

No Restrictions

2475/3785

MONASH UNIVERSITY
THESIS ACCEPTED IN SATISFACTION OF THE
REQUIREMENTS FOR THE DEGREE OF
DOCTOR OF PHILOSOPHY

ON..... 30 November 2004.....

Sec. Research Graduate School Committee

Under the Copyright Act 1968, this thesis must be used only under the normal conditions of scholarly fair dealing for the purposes of research, criticism or review. In particular no results or conclusions should be extracted from it, nor should it be copied or closely paraphrased in whole or in part without the written consent of the author. Proper written acknowledgement should be made for any assistance obtained from this thesis.

BOREHOLE ELECTROMAGNETIC PROSPECTING FOR WEAK CONDUCTORS

Candidate: John Apostolis Theodoridis B.Sc.(Hons)

Institution: School of Geosciences;
Faculty of Science;
Monash University.

Date of Submission: *23 November 2004.*

TABLE OF CONTENTS

ABSTRACT.

1. INTRODUCTION.

1.1. Project Introduction.....	1-1
1.2. Phenomena of Current Channelling.....	1-8
1.2.1. The mechanism of galvanic excitation.....	1-8
1.2.2. Galvanic saturation.....	1-10
1.2.3. Saturation estimates and the current channelling number.....	1-11
1.3. Review of Downhole TEM Case Histories.....	1-14
1.3.1. Review of the Que River deposit.....	1-15
1.3.2. Review of the Thalanga deposit.....	1-17
1.3.3. Drive Delay and Resulting Effects.....	1-20
1.3.4. Review of the Hellyer Ore Deposit.....	1-23
1.3.4.1. Introduction.....	1-23
1.3.4.2. DHTeM with drill-hole HL3.....	1-24
1.3.4.3. Decay analysis.....	1-25
1.3.4.4. Surface UTEM on Line 10400N.....	1-26
1.3.4.5. Surface UTEM on Line 10700N.....	1-27
1.3.4.6. IP effects and the UTEM data.....	1-28
1.3.4.7. Comments and conclusions.....	1-29
1.3.5. Review of the Que-Hellyer Volcanics Experience.....	1-31
1.3.5.1. DHTeM surveys at Que River.....	1-31
1.3.6. Review of the Aguas Tenidas East Deposit.....	1-34
1.3.6.1. Introduction.....	1-34
1.3.6.2. EM-37 survey overview.....	1-35
1.3.6.3. Numerical modelling.....	1-37
1.3.6.4. Summary.....	1-39
1.4. Project Aims and Objectives.....	1-40
1.4.1. Cadjebut mineralisation.....	1-40
1.4.2. Flying Doctor Deposit.....	1-41

TABLE OF CONTENTS.

2. CLASSICAL ELECTROMAGNETIC THEORY.

2.1. Introduction.....2-1

2.2. Maxwell's Equations2-3

 2.2.1. The auxiliary equations2-5

 2.2.2. Current density2-7

 2.2.3. Boundary conditions.....2-8

 2.2.4. Relaxation time2-9

2.3. The Electromagnetic Wave Equations2-11

2.4. The Quasi-Static Approximation.....2-14

2.5. 1-D Solutions to the Wave Equations.....2-17

2.6. Transient Response of a Vertical Magnetic Dipole2-19

2.7. Transient Response of a Circular Loop.....2-23

2.8. The "smoke ring" Approximation.....2-26

3. NUMERICAL PACKAGES.

3.1. Modelling Classes and Attributes3-1

 3.1.1. Model dimensionality3-2

 3.1.2. Numerical Methods3-3

 3.1.3. Source representation3-4

 3.1.4. Host and target representation.....3-5

3.2. LEROI3-6

 3.2.1. Program description and philosophy.....3-6

 3.2.2. Discretization3-6

 3.2.3. Program history3-8

 3.2.4. Origins of LEROI thin sheet theory3-8

 3.2.5. Developments and modifications3-9

3.3. MARCO3-10

 3.3.1. Program description and philosophy.....3-10

 3.3.2. Discretization3-11

 3.3.3. Group theory and increased computational efficiency.....3-11

3.4. Technical Aspects and Functionality Common to LEROI and MARCO3-13

 3.4.1. File conventions and program execution.....3-13

 3.4.2. Computations.....3-13

 3.4.3. Late-time source switching3-14

 3.4.4. Reusing previous computations.....3-15

 3.4.5. Time domain system conventions.....3-16

TABLE OF CONTENTS.

3.4.6. Arbitrary waveform options3-17

3.5. Implementation of LEROI and MARCO.....3-18

4. INDUCTIVE AND GALVANIC DECAY ANALYSIS.

4.1. Introduction.....4-1

4.2. Inductive Decay Analysis.....4-2

4.3. Galvanic Decay Analysis.....4-6

 4.3.1. Introduction.....4-6

 4.3.2. Galvanic excitation of a near surface target4-6

 4.3.3. Inference of the late-time power law for galvanic decay4-11

 4.3.3.1. Summary4-13

 4.3.4. Galvanic excitation of a target at depth4-13

5. CADJEBUT LEAD-ZINC ORE BODY.

5.1. Introduction.....5-1

 5.1.1. Discovery of Cadjebut5-1

 5.1.2. Mineralisation.....5-1

 5.1.3. Trial surveys5-3

5.2. Methods5-3

 5.2.1. Technical matters5-3

 5.2.2. Early Interpretations of Data.....5-6

 5.2.3. Background level in Line E.....5-6

 5.2.4. Absence of a definitive anomaly.....5-7

 5.2.5. The ineffectiveness of TEM methods over Cadjebut5-7

5.3. Modelling of the Field Data5-8

 5.3.1. Development of a five layered earth model.....5-8

 5.3.2. Construction of the coincident-loop and downhole TEM models.....5-10

 5.3.3. Inference of target resistivities5-13

 5.3.4. Target discretization.....5-13

5.4. Results5-14

 5.4.1. The coincident-loop MARCO model5-14

 5.4.2. The downhole TEM MARCO model.....5-17

 5.4.3. Verification of the Galvanic Response5-19

5.5. Discussions and Interpretations5-22

 5.5.1. Proposed mechanism for the coincident-loop M-shaped anomaly5-22

TABLE OF CONTENTS.

5.5.2. Proposed mechanism for the DHTEM intersection anomaly	5-22
5.6. Conclusions.....	5-24
5.7. Guidelines for modelling galvanic effects.....	5-25
6. FLYING DOCTOR DEPOSIT: UPPER LENS.	
6.1. Introduction.....	6-1
6.2. Overview of Model Development.....	6-2
6.3. STAGE 1: Description and Analysis of the Field Data.....	6-6
6.3.1. Classification of the field TEM response.....	6-6
6.3.2. Borehole ID3039 with Loop 1.....	6-8
6.3.2.1. Middle times: windows 5 (0.345 ms) to 10 (0.995 ms)	6-9
6.3.2.2. Intermediate times: windows 10 (0.995 ms) to 15 (2.495 ms).....	6-11
6.3.2.3. Late times: windows 15 (2.495 ms) to 20 (5.895 ms).....	6-11
6.3.3. Borehole ID3039 with Loop 3.....	6-12
6.3.4. Borehole ID3071.....	6-13
6.3.5. Conclusions	6-15
6.4. STAGE 2: Model Development.....	6-16
6.4.1. Development of Plate 1.....	6-18
6.4.1.1. Borehole ID3039 with Loop 1	6-18
6.4.1.2. Borehole ID3039 with Loop 3	6-23
6.4.1.3. Borehole ID3071 with Loop 1	6-24
6.4.1.4. Borehole ID3071 with Loop 3	6-28
6.4.2. Development of Plate 2.....	6-31
6.4.2.1. Borehole ID3039 with Loop 1	6-31
6.4.2.2. Borehole ID3039 with Loop 3	6-38
6.5. STAGE 3: Linear Superposition of the Plate 1 and 2 Model Data	6-40
6.5.1. Introduction.....	6-40
6.5.2. Simultaneous modelling of inductive and galvanic effects.....	6-40
6.5.3. Linear superposition of Plates 1 and 2	6-41
6.5.4. Conclusions	6-43
6.6. Power-Law Decay Analysis and Program LEROI: A Final Remark.....	6-44
6.6.1. Introduction.....	6-44
6.6.2. Decay analysis of Plate 2	6-44
6.6.3. Decay analysis of Plate 1	6-46
6.6.4. Power law decay indices and plate-receiver separation.....	6-48

TABLE OF CONTENTS.

6.6.5. Dependence of the decay index upon cell discretization.....	6-50
6.6.6. Conclusions.....	6-51
7. LIMITATIONS OF LEROI.	
7.1. Introduction.....	7-1
7.2. Inductive Decay Rates of LEROI.....	7-1
7.3. Chaotic Behaviour of Multiple Plate Models	7-2
7.3.1. Sign reversals of inductive responses	7-2
7.3.2. Non-linear responses with unrealistic amplitudes	7-10
7.4. Instabilities Associated with Discretization.....	7-13
7.5. Conclusions	7-16
8. FLYING DOCTOR DEPOSIT: LOWER LENS.	
8.1. Introduction.....	8-1
8.2. Geology of the Mineralisation	8-2
8.3. Single Plate Model.....	8-2
8.3.1. Active time windows.....	8-5
8.3.2. Active stations	8-6
8.3.3. Artificial extension of boreholes	8-7
8.3.4. Presentation of data	8-7
8.4. Limitations of the Single Plate Model.....	8-8
8.4.1. End-of-hole anomaly within the ID3418 - Loop 1 field response	8-8
8.4.2. End-of-hole anomaly within the ID3419 - Loop 1 field response	8-10
8.4.3. Amplitude matching and inference of the target conductance.....	8-11
8.5. Galvanic Component of the LEROI Response	8-19
8.6. Galvanic Stripping.....	8-21
8.6.1. Galvanic stripping of the ID3418 model data	8-22
8.6.2. Galvanic stripping of the ID3419 model data	8-26
8.7. Discussions of the Loop 3 Field Data.....	8-33
8.7.1. ID3418 field data	8-33
8.7.2. ID3419 field data	8-36
8.8. Conclusions	8-36
9. CONCLUSIONS.	
9.1. The Cadjebut Case Study	9-1

TABLE OF CONTENTS.

9.2. The Flying Doctor Case Study 9-5
 9.2.1. The Flying Doctor deposit: upper lens 9-5
 9.2.2. The Flying Doctor deposit: lower lens 9-8
 9.3. Industry Software Tests 9-10
 9.4. Concluding Remarks 9-12

APPENDICES.

Appendix A.

Appendix A.1: Symbol listing A.1

Appendix B.

Appendix B.1: LEROI - Program version B-1

Appendix B.2: MARCO - Program version B-2

Appendix C.

Appendix C.1: Discretization of MARCO model C-1

Appendix C.2: MARCO execution times C-2

Appendix C.3: Theodoridis and Asteri (2001) C-3

Appendix D.

Appendix D.1: Downhole TEM Field Data D-1

Appendix D.2: Downhole TEM Model Data - Plate 1 D-5

Appendix D.3: Downhole TEM Model Data - Plate 2 D-9

Appendix E.

Appendix E.1: Downhole TEM Field Data E-1

Appendix E.2: Downhole TEM Model Data E-5

Appendix E.3: Borehole Station Coordinates E-9

Appendix E.4: SIROTEM Composite Times E-12

FOLD-OUT MAPS (REAR SLEEVE):

PLATE I: Plan view of Cadjebut mineralisation.

PLATE II: Borehole section of Cadjebut mineralisation.

PLATE III: Geologic section of Flying Doctor deposit.

ABSTRACT.

Traditionally, the TEM method has been regarded amongst interpreters as a purely inductive technique, to be used primarily in the exploration of massive sulphides and other good conductors. The downhole TEM prospecting technique has been demonstrated to be effective in the exploration of other economic, but weakly conducting targets, where detection is achieved by means of TEM induced galvanic excitation, an effect that can be enhanced by use of long-offset loops.

The following industry standard modelling software were tested and implemented within this project: program MARCO, which permits full 3D modelling of tabular-prisms within a layered host; and program LEROI, which can model multiple thin-sheets in a layered earth. These programs were chosen on the basis that they could simultaneously model inductive and galvanic excitation within a TEM survey. Limitations were identified for program LEROI, with numerical instabilities documented for multiple plate systems, and single plate systems where over discretization had occurred.

Two case studies are presented, in which numerical models and interpretations were carried out for the following: surface EM and downhole TEM data acquired from the Cadjebut MVT (Mississippi Valley Type) sphalerite (ZnS) galena (PbS) mineralisation; and downhole MMR and TEM data from surveys at the Flying Doctor lead-zinc deposit situated North of Broken Hill, New South Wales.

The downhole TEM survey conducted at the Cadjebut mineralisation utilised a single intersecting borehole and two transmitter loops. Modelling with program MARCO reproduced the key features of the field profiles, namely: a null response for the inductively well-coupled transmitter loop overlying the target; and a prominent negative intersection anomaly within the early-time response, for the adjacent loop that lay offset to the mineralisation. Decay analysis confirmed galvanic excitation as the mechanism responsible for the offset loop response within both the field and model data. Numerical modelling confirmed that the Cadjebut mineralisation is too weakly conducting for detection by a moving loop survey. This case study demonstrated the

ability of an offset loop to excite galvanically a weakly conducting target, which would otherwise be invisible to traditional inductive based exploration methods.

The upper and lower massive sphalerite galena lenses of the Flying Doctor deposit, were each surveyed with a pair of boreholes, utilizing an inductively well-coupled near-loop and a weakly-coupled long-offset loop. Inductive effects were prominent within the near-loop data of both lenses, but diminished with use of the long-offset loop, permitting galvanic effects to dominate. Interpretations of the inductive and galvanic profiles of the upper lens response yielded conflicting estimates for the target conductivity and depth extent. Consequently, two independent single plate models were developed to represent the target; a high conductivity plate, and a low conductivity plate of greater depth-extent, which were inferred from the inductive and galvanic components respectively. Attempts to combine both plates in a multiple plate system failed, due to inherent numerical instabilities within program LEROI. Based on the assumption that the two plates shall exhibit a weak inductive interaction, a satisfactory composite model response was synthesised for the near-loop by the linear superposition of the host and scattered response of each plate.

A galvanic stripping process was developed to investigate the effects of a long-offset loop on the relative contributions made by the inductive and galvanic components comprising the scattered model response. Determining the lowest conductance for a given model for which galvanic saturation occurred yields an estimate for galvanic component, and subtraction of this subsequent response from the original total model response yields an estimate for the inductive component. It is envisaged that this new technique be employed to aid future designs of offset loop configurations, for the exploration of weakly conducting targets.

Declaration:

This thesis contains no material that has been accepted for the award of any other degree or diploma in any university or other institution. Nor to the best of my knowledge, does this thesis contain material previously published or written by another person, except where due reference is made in the text of the thesis.

Signature of Candidate:



23 November 2004.

Acknowledgments:

This project was supported by a Strategic Partnership with Industry - Research and Training (SPIRT) grant through the collaboration between Monash University Department of Earth Sciences, and the participating industry partners: BHP Minerals International, Mt Isa Mines (MIM) Exploration Ltd, North Ltd and Pasminco Exploration Ltd. Personal financial benefits were received through an Australian Post-Graduate Award – Industry (APA - I). I wish to express my gratitude to the aforementioned industry sponsors for accepting my candidature and for providing ongoing support and encouragement. The assistance of Neil Hughes, Robin Scott, Art Raiche and Andrew Duncan is acknowledged. Many personal thanks are due to my supervisor Michael Asten for his support and infinite patience over the years and for our many stimulating discussions within which he imparted to me but a fraction of his extensive knowledge of TEM theory. Thanks are due also to my co-supervisor - Jim Cull, for providing assistance on all matters academic and bureaucratic and helping me over the final hurdle to thesis submission. Farewell to my friends within the department and in particular to Duncan Massie who helped ease my transition from astrophysics to geophysics - from stars to mud!

I wish also to express my deepest gratitude to selected family members and closest friends, which of whom offered me emotional support. I dedicate this thesis to my parents - Ruth & Peter, my cousin - Ilias and my fiancée - Angela.

CHAPTER ONE

INTRODUCTION.

1.1. PROJECT INTRODUCTION.

Time domain electromagnetic methods (TEM), also known as transient EM techniques (Nabighian and Macnae, 1991), have been used extensively in prospecting for massive sulphide ore deposits residing both near surface and at great depth (Nabighian and Macnae, 1991; Palacky, 1988).

Massive sulphides are traditional EM targets, since they are often highly conductive and exhibit strong conductivity contrasts with their host rocks (Swift, 1988). In most cases, the resistivities of massive sulphide deposits lie within the range of 0.01 to 1.0 ohm.m (Palacky, 1988); however, some poorly conductive and even entirely non-conductive sulphides, which yield no geophysical signature at all, have been documented within the literature (Palacky, 1988).

The TEM Method

In a TEM survey, an ungrounded current carrying transmitter loop is laid upon the surface of the earth, as shown in Figure 1.1. Inductive excitation of a nearby conducting body will occur when the current flowing in the transmitting loop is abruptly terminated and, by Faraday's law of induction, the collapsing primary magnetic field induces a system of closed vortex currents within the body. A remote receiver, which may be located above or below ground, then measures the secondary magnetic fields associated with the induced currents as a transient voltage response in the absence of the source primary field (Nabighian and Macnae, 1991). Downhole TEM data discussed within this thesis was normalised by the transmitter (Tx) loop current, thereby incurring the units of microvolts per ampere [$\mu\text{V}\cdot\text{A}^{-1}$]. In a highly resistive earth, or near free-space environment, the inductive excitation of a body is impulsive, whereas a

conductive host will delay, distort and attenuate the induced host currents supporting the collapsing primary field (McNeill *et al.*, 1984).

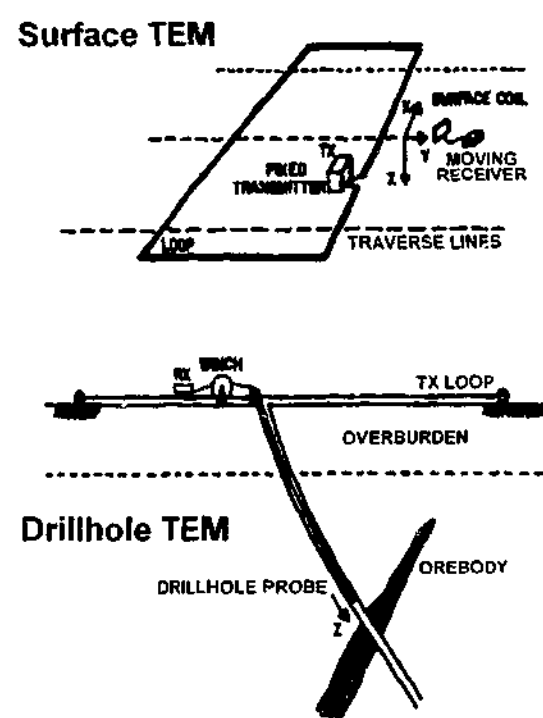


Figure 1.1: Schematic representations of a surface and downhole TEM survey. This particular surface configuration is referred to as a fixed-loop survey, as opposed to a coincident loop survey, in which both the transmitter and receiver move together coinciding with each other. Only downhole TEM surveys are considered within this thesis. (After Nabighian and Macnae, 1991).

Inductive Geophysical Interpretations

The secondary fields associated with vortex currents are dipolar in form; as such, the inductive response of a target will be greatly dependent upon its orientation and physical attributes (McNeill *et al.*, 1984). In particular, profile analysis of an inductive response may yield valuable information, such as strike-length, depth-extent and dip. In addition to this, the electrical properties of a target, namely its conductivity-thickness product or conductance, may also be inferred. At early times, an inductive response consists of a multitude of exponential components decaying at different rates (McNeill *et al.*, 1984; see also Section 4.2). Eventually, at late time, only the component with the largest time-constant will remain. This fundamental time-constant, which can be obtained by means of decay curve analysis, is characteristic of both target conductance and geometry (Nabighian and Macnae, 1991; McNeill *et al.*, 1984). Thus, the

target conductance is not directly observable, and its determination requires an interrelated quantitative procedure, which requires knowledge of both the fundamental time constant and the physical dimensions of the target (see Section 4.2 for further discussion on inductive decay).

Variability of Target Conductance

Although massive sulphides are intrinsically highly conductive, their in-situ electrical properties, such as the bulk resistivity may be quite large (Palacky, 1988), thereby rendering them undetectable to inductive based EM exploration methods. Table 1.1 lists some common sulphides and their intrinsic resistivities. By order of magnitude, these resistivities lie within the range of 10^{-6} to 10^4 ohm.m, this in stark contrast to the typical range of resistivities found for massive sulphide ores, *i.e.*, 10^{-2} to 10^0 ohm.m (Palacky, 1988).

The bulk resistivity of a massive sulphide deposit is dependent upon composition, texture and mineral habit (Keller, 1988; Palacky, 1988), and cannot be inferred from the quantity and percentage content of the constituent sulphides, nor from a simple combination of the resistivities of the native elements alone.

The presence of a highly conducting mineral in an ore body will have minimal effect on the bulk resistivity if it takes the form of small isolated inclusions (Palacky, 1988). Indeed, even at high concentrations, isolated conductive grains will not greatly influence the bulk resistivity (Palacky, 1988). For example, pyrite often forms non-interconnecting blobs, as such a deposit rich in this sulphide will tend to have a low to moderate conductivity (Palacky, 1988).

If, however, the conducting mineral is in the form of connected veins, the bulk resistivity will be substantially lowered, since the veins will constitute multiple conduction paths (Palacky, 1988). Pyrrhotite-rich deposits are typically highly conductive for this reason (Palacky, 1988). In addition to this, minerals such as graphite that form thin continuous films along grain boundaries can significantly reduce the bulk resistivity of an ore, even if they are present at very low concentrations (Keller, 1988).

Table 1.1: Resistivities of some common sulphides (After Keller, 1988).

NATIVE SULPHIDES	RESISTIVITY (ohm.m)
Galena, PbS	6.8×10^{-6} to 9.0×10^{-2}
Sphalerite, ZnS	2.7×10^{-3} to 1.2×10^4
Chalcopyrite, $\text{Fe}_2\text{S}_3 \cdot \text{Cu}_2\text{S}$	1.5×10^2 to 9.0×10^{-3}
Pyrite, FeS_2	1.2×10^0 to 6.0×10^{-1}

TEM Induced Galvanic Excitation

In the event that a massive sulphide deposit is weakly conducting, inductive based TEM methods will be largely ineffectual. In such instances, the exploration methods resorted to are those for which the mode of excitation is galvanic rather than inductive, e.g., the magnetometric resistivity (MMR) method.

Galvanic excitation occurs during a TEM survey when the diffusing host currents, induced by the collapsing primary field, are concentrated within a locally more conductive target. The overall effect of the current concentration is as if an additional anomalous poloidal current has arisen within the conductor. This galvanic current flow is responsible for the characteristic unipolar secondary magnetic fields associated with current gathering.

Since, however, galvanic excitation is dependent upon the relative conductivity between target and host, i.e., the conductivity contrast, and not the absolute conductance (conductivity-thickness product) as with inductive excitation, current gathering effects associated with TEM methods can be exploited for the exploration of weakly conducting targets.

The presence of a galvanic component within TEM data is often perceived as a nuisance amongst EM interpreters, since it can severely hinder an otherwise routine inductive modelling procedure. The unipolar nature of the secondary fields associated with galvanic excitation has negative implications for conventional geophysical interpretations. Information acquired from galvanic anomalies within TEM data are less diagnostic than that derived from inductive excitation. For example, although target location and

depth can still be determined, attributes such as distance, target dimensionality and orientation will be poorly constrained (Asten, 1991b; McNeill *et al.*, 1984). One advantageous aspect of the unipolar field, however, is the absence of the directional ambiguity associated with induction related dipolar fields (Asten, 1991a), this attribute is invaluable when determining the direction to a target located off-hole within a downhole TEM survey.

In regards to the electrical properties of a target, only minimal information can be derived from a galvanic anomaly, since the temporal behaviour of a galvanic response is determined by the half-space current flow, and not the target conductance as with inductive excitation (see Chapter Four for relevant theory). Moreover, when a conductor is in a state of galvanic saturation, good conductors are difficult to distinguish from poor ones, since both will yield an essentially equivalent galvanic response (McNeill *et al.*, 1984).

TEM Overview

An informal overview of the TEM response types that can be expected for a range of host environments and target conductivity is presented within Figure 1.2. This schematic overview is arranged with the earth resistivity varying in the horizontal - decreasing from left to right, and with target conductivity varying in the vertical - decreasing from the top downward. In this scheme, target conductivity is categorised into three basic groups, namely: highly conductive, moderately or partially conductive, and weakly conducting. Here the term partially conductive, pertains to a body with an inhomogeneous conductivity distribution, such as one comprised of a highly conductive core encompassed by a less conductive halo or expanse. The points noted within the numbered cells of Figure 1.2 are discussed below:

1. In a highly resistive earth, the host response will be negligible, resulting in a target response that is entirely due to induced vortex currents. The combination of a good conductor embedded within a resistive earth is idyllic for inductive based TEM interpretations, allowing for the reliable use of "free-space" approximations that neglect host-target interactions. In such situations, a great deal of diagnostic information will be available about the

target, although accessibility of this information will diminish as host conductivity increases.

2. Inductive methods are only effective in delineating moderately to highly conductive zones of mineralisation, thus a partially conductive body will appear smaller than its respective geologic interpretation. Moreover, weakly conducting bodies may be devoid of any detectable inductive signature, this is especially true in more conductive environments.
3. As the half-space conductivity increases, the host response will become significant, requiring removal before traditional "free-space" inductive interpretations can commence. In addition to this, increased geologic noise will tend to degrade any diagnostic information (McNeill *et al.*, 1984).
4. At low earth resistivities, current gathering effects will tend to dominate a response, obscuring the inductive component, and thereby resulting in a loss of valuable diagnostic information (McNeill *et al.*, 1984). A typical response may be observed to evolve from one mode of excitation to another (see Chapter Six for an example); at early times galvanic excitation will dominate, but as inductive effects become more prevalent, an intermediate stage will arise in which the response will be an indiscernible mixture of galvanic and inductive components. Finally, at late times, the galvanic component will have decayed sufficiently to allow induction to be the dominant mode of excitation. Moreover, depending on the inductive time constant, galvanic effects may become apparent again at very late times (McNeill *et al.*, 1984).
5. Galvanic excitation is advantageous for the delineation of both partially and entirely weakly conducting mineralisations. In particular, partially conducting targets will appear larger when galvanically excited, allowing a greater appreciation of a deposit's true geological extent; whereas weakly conducting targets, which may have eluded inductive based methods, may yield a detectable response when galvanically excited.

Research conducted within this thesis has contributed to the understanding of TEM induced galvanic excitation from the viewpoint of borehole electromagnetic prospecting. In respect to Figure 1.2, the area of research

covered by this thesis relates to cells 4 and 5. In particular, archival downhole TEM data acquired from the Cadjebut Pb-Zn mineralisation was used to demonstrate the ability of galvanic excitation to detect a weak conductor that, in a previous field report, was concluded to be impervious to inductive based methods (see Chapter Five). Moreover, specially acquired downhole TEM data, from the Flying Doctor Pb-Zn deposit, illustrated the ability of galvanic excitation to reveal the true geologic extent of a partially conducting target (See Chapter Six). Thus it has been demonstrated, that galvanic target anomalies within TEM data can be isolated, modelled and interpreted, permitting both the detection and acquisition of valuable diagnostic information about a partially or weakly conducting target.

EARTH RESISTIVITY.				
HIGH.	MEDIUM.	LOW.		
1. • Little or no host response. Ideal conditions for inductive based TEM methods, permitting rapid "free-space" inductive interpretations.	3. • Prevalent host response requiring removal so as to isolate target anomaly. • Degradation of the target response may occur due to geologic noise, and the possible shielding by overburden effects.	4. • TEM induced current gathering effects become prominent, and may frustrate conventional inductive type interpretations.	HIGHLY CONDUCTIVE.	TARGET CONDUCTIVITY.
2. • Inductive based TEM methods ineffectual in the complete delineation of partially conductive targets. • Weakly conducting targets are unlikely to be detected.		5. • Galvanic excitation permits the delineation of partially conductive deposits, and is advantageous over inductive methods for the detection of weak conductors.	MODERATELY & PARTIALLY CONDUCTIVE.	
		WEAKLY CONDUCTING.		

Figure 1.2: Schematic overview of the anticipated TEM response types associated for a range of earth resistivities and target conductivities (refer to text for further explanation).

1.2. PHENOMENA OF CURRENT CHANNELLING.

1.2.1. THE MECHANISM OF GALVANIC EXCITATION.

Consider a finite conductor embedded within a conductive half-space excited by a step-function (turn-off) current source. At the time of current termination, a current image will be induced within the earth so as to oppose the collapsing primary field, this system of host currents will propagate outward and downwards attenuating and diffusing with time, and in a manner analogous to a smoke ring in air (Nabighian, 1979). As the diffusing *smoke ring* propagates past the target, the host current electric field will instantaneously induce a distribution of electric charge at the conductor boundaries (Nabighian and Macnae, 1991). The electric field due to these displaced charges will oppose

and tend to cancel the smoke ring electric field within the target (Nabighian and Macnae, 1991). Despite the effect of the displaced charges to reduce the primary electric field inside the target, the actual internal current density will be greater than that of the surrounding earth if the conductivity of the target is larger than that of the host medium (Newman *et al.*, 1989). The accumulation of these charges is dependent upon the magnitude of the discontinuity of the normal component of the electric field at the conductivity boundaries (Nabighian and Macnae, 1991). Moreover, the induced electric polarisation of a conductor is sufficiently rapid that it may be described in terms of direct current (DC) flow in a conducting medium (Nabighian and Macnae, 1991). Assuming DC current flow in a source free heterogenous conducting medium, electric charges will accumulate whenever there exists a non-vanishing gradient of conductivity and the electric field has a component parallel to it (Nabighian and Macnae, 1991). In the simple case of an abrupt conductivity change at the boundary between two homogenous media, surface electric charges will appear at that boundary whenever there is a conductivity contrast and the electric field has a component perpendicular to the boundary (Nabighian and Macnae, 1991). Thus, the galvanic current flow within a target originates from the secondary electric field due to displaced charges residing at the conductivity boundaries. Specifically galvanic current flow is poloidal current flow due to the induced polarisation of a conductor by the primary *smoke ring* electric field (Nabighian and Macnae, 1991).

Alternately, one may interpret the above description of the mechanism of galvanic excitation in the following manner. Consider the uniform electric field in the interior region between two large electrified (electrostatic) plates. If a conductive body is placed within this region free charges, according to sign, will tend to migrate to the edges of the body where the normal component of the primary field in respect to the boundary is greatest. Although the net charge of the body remains zero, it is said to be polarised due to the partial separation of charges. The degree of polarisation will be dependent upon the strength of the applied field, since increasing its strength will offset the mutual attraction (repulsion) of the displaced charges. Conceptually, one may replace

the induced polarised conductor with an equivalent static electric dipole. In this respect one may envisage the interaction of the conductor with the primary field to be sum of this field with that of the equivalent electric dipole. If the surrounding medium is conductive, then polarisation of the body will still occur but to a lesser degree, as one may envisage charge "leakage" from the body into the medium. Again as within free-space, the total electric field can be represented as the summation of the primary and induced secondary dipolar fields. The secondary field will oppose and tend to cancel the primary electric field within both the body and its immediate surrounding regions. Again, by Ohm's law, the current density will be larger within the body despite the reduced internal electric field. The overall effect of this process is the concentration of the host current stream into the body, whilst leaving a zone of partial depletion around the conductor. The gathering of all available current by the body from its immediate surroundings is referred to as *current saturation* (Walker and West, 1992).

1.2.2. GALVANIC SATURATION.

The capacity of a conductivity inhomogeneity to gather host currents is dependent upon both geometry of the body and its conductivity contrast with its host medium (Nabighian *et al.*, 1984). Initially, current channelling effects will increase linearly within increasing conductivity contrast. Eventually, however, current saturation will occur (Nabighian *et al.*, 1984). Two extreme states of current saturation are recognised:

i. **UNDER-SATURATED:** A conductor is regarded to be galvanically under-saturated when the strength of the secondary depolarising electric field, arising from the induced surface charges on the conductor, is small relative to the primary field from the source. Thus due to the insignificance of the scattered field, the total electric field may be approximated by the primary field to yield the under-saturated estimate of galvanic excitation, *i.e.*, currents within the body may be estimated by assuming the internal electric field to be equal to that of the source in the vicinity of the body (Walker and West, 1992).

ii. **SATURATED:** Galvanic saturation of a conductor occurs when the depolarising electric field arising from the surface charges completely cancels the internal primary field. In this situation, the maximum available current is being gathered from the surrounding host medium and driven through the conductor (Walker and West, 1992). Furthermore, the saturated galvanic current density may be estimated by equating the total current available for gathering within the host medium to the total current flowing through the conductor (Walker and West, 1992).

1.2.3. SATURATION ESTIMATES AND THE CURRENT CHANNELLING NUMBER.

The present understanding of galvanic effects within TEM data lends itself heavily to MMR theory; in both instances a galvanic anomaly will arise from the perturbation of host currents into a locally more conductive target, which will in effect, result in an anomalous poloidal current flow.

Consider the galvanic response of a body within a conductive half-space. The amplitude of this anomaly will be found to be proportional to the product $F(\alpha) \cdot A_p$; where $F(\alpha)$ is some function of the dimensionless *current channelling number* α , and A_p is the amplitude of the galvanically saturated anomaly profile when the conductivity of the body is much greater than that of the surrounding host medium (Edwards and Nabighian, 1981). Otherwise stated, the amplitude of an MMR anomaly is directly proportional to, and limited by, the amplitude of the galvanically saturated response. Moreover, the associated term of proportionality will be dependent upon the current channelling number for a given system. Edwards and Nabighian (1981), defined the current channelling number as the "ratio of conductance per unit length to the effective conductance of the host medium per unit length". Or rather, the channelling number is the ratio of current channelled into a body to the total available current flowing in the vicinity of the body (Nabighian *et al.*, 1984).

One application of the current channelling number is in the estimation of the state of saturation of the galvanic mode of excitation (Nabighian *et al.*, 1984; Walker and West, 1992). In one example, Walker and West (1992) used parametric analysis to predict whether the dominant mode of excitation was

inductive or galvanic. The authors estimated the current channelling number for a thin plate by considering it to be composed of numerous infinitesimal dipoles. These dipoles lay adjacent to each other within the plane of the plate, oriented in the direction of the ambient current flow in the surrounding host medium. The total ambient current collected by each dipole is approximately equal to that of the original host current contained within a cylinder of dipole length and whose axis is coincident with the dipole.

Taking the product of the plate conductance and source primary electric field yields the estimate for the under-saturated current density. By this approach, Walker and West (1992) obtained an estimate for the current channelling number α of a thin plate of side length L :

$$\alpha \approx \tau \cdot (\sigma L)^{-1}; \quad (1.1)$$

where τ is the conductance (conductivity-thickness product) of the plate, σ is the conductivity of the half-space. That is, the current channelling number for a thin plate is proportional to the ratio of target to host conductivity per unit length. Furthermore, Nabighian *et al.* (1984) quotes independently that the currently channelling number of a square plate of side length L , and conductance S , in a host medium of resistivity ρ , can be also be expressed as

$$\alpha = \rho \cdot S \cdot L^{-1}. \quad (1.2)$$

Moreover, the galvanic response of such a plate will be found to increase with increasing current channelling number α as

$$f = \alpha \cdot (1 + \alpha)^{-1}; \quad (1.3)$$

where f is the dimensionless *current channelling response parameter* which indicates the degree of current saturation within a body and has the following range: $f = 0$ no current channelling and $f = 1$ galvanic saturation (Asten, 1991b; McNeill *et al.*, 1984). When the current channelling number α is less than one, the target will be galvanically under-saturated, and the galvanic response will increase linearly with respect to α , whereas for values of α much greater than one, current saturation will occur limiting the amplitude of the response to that of its galvanically saturated state (Walker and West, 1992).

It is noted, that during the development of Plate 2, a low conductance thin-sheet model within Chapter Six, the model response was observed to

converge to galvanic saturation in a manner described by Equation 1.3, as its conductance was increased in small increments.

Asten (1991b) noted that for a typical host resistivity (100 to 1000 ohm.m), target conductance (10 S to 100 S) and size (100 m), the *current channelling number* α will be large, and the *current channelling response parameter* f will be close to unity. As such, galvanic saturation is likely to be observed for many geophysical targets in the field (Asten, 1991b). It was further noted by Asten (1991b), that under these conditions the galvanic response will, to a first order approximation, be a function of the ambient host currents. This result can be readily obtained as follows: by Ohm's law (see Equation 2.14 of Section 2.2.2) and Equation 1.2, the ambient host current density can be shown to be inversely proportional to both the host resistivity and the *current channelling number*. By rearranging Equation 1.3 to make α^{-1} the dependent variable, and taking the binomial expansion, which is permissible under the aforementioned field conditions, one will yield an expression in which the parameter f is to a first order approximation a function of α^{-1} , and in turn the ambient host current density.

In summary, the magnitude (strength) of an inductive TEM anomaly will be found to be dependent upon a target's absolute conductance (conductivity thickness product) and characteristic dimensions; whereas the magnitude of a galvanic anomaly (induced by either TEM or MMR methods), will depend upon the relative host-target conductivity contrast and target geometry. Thus, unlike induction, a galvanic response is dependent upon host resistivity (Asten, 1991b).

1.3. REVIEW OF DOWNHOLE TEM CASE HISTORIES.

The following exploration case histories highlight some of the important aspects that need to be considered when including current channelling within both surface and downhole TEM interpretations. The lessons learnt from these case histories were of twofold value to the project: firstly, these lessons helped establish theoretical guidelines and a practical framework necessary for the study of TEM induced galvanic excitation. Secondly, they helped to maintain the relevance of the work undertaken, with that of the broader research into current gathering effects associated with TEM exploration methods as a whole.

These case histories illustrate how previous interpreters have perceived current channelling within TEM data as a problem or undesirable effect, given that its presence could not be confirmed or modelled. As such, interpreters have often invoked current gathering without justification, to explain discrepancies that have occurred between field data and free-space inductive models. Unfortunately, early TEM interpretations were restricted to computing the inductive response of a thin plate in free-space (infinite resistivity), mimicking a highly conductive target embedded within a host of large resistivity. Although the effects of a conductive overburden were understood, the complex interactions that occur between a conductor and its conductive host could not be modelled. Indeed, recent developments in numerical modelling, and in particular, by those algorithms that allow for the full interactions of a conductor embedded within a conductive half-space, has spurred greater interest in TEM induced galvanic effects observed in the field. In this respect, the work presented within this thesis can be viewed as part of the ongoing research into techniques for the identification, verification, and modelling of TEM induced galvanic effects. Research was conducted within this project under the pretext of, development and application of, techniques for the detection and delineation of weakly conducting ore-bodies. Moreover, contribution to this area of research was made possible by the availability of the following industry standard software:

1. Program MARCO, which is capable of modelling the EM response of 3D rectangular prisms in a multi-layered half-space (see Section 3.3 for additional information).
2. Program LEROI, which can model one or more interacting thin sheets in a uniform half-space, or the basement of a two layer half-space (Raiche *et al.*, 1998b; see also Section 3.2 for additional information).

1.3.1. REVIEW OF THE QUE RIVER DEPOSIT.

The Que River Cu-Pb-Zn-Ag-Au base-metal deposit is located 75 km south of Burnie, within the Tasmanian Cambrian Mt Read Volcanics (Staltari, 1986). The two main zones of mineralisation that constitute the deposit are the S and the P lens (see Figure 1.3). The main constituents of the S lens are the sulphides: Pyrite (FeS_2), Chalcopyrite ($\text{Fe}_2\text{S}_3 \cdot \text{Cu}_2\text{S}$), and Galena (PbS) in most parts; whereas the P lens is mostly comprised of the sulphides: sphalerite (ZnS) and galena (PbS), with only minor Pyrite (FeS_2) and Chalcopyrite ($\text{Fe}_2\text{S}_3 \cdot \text{Cu}_2\text{S}$) (Staltari, 1986).

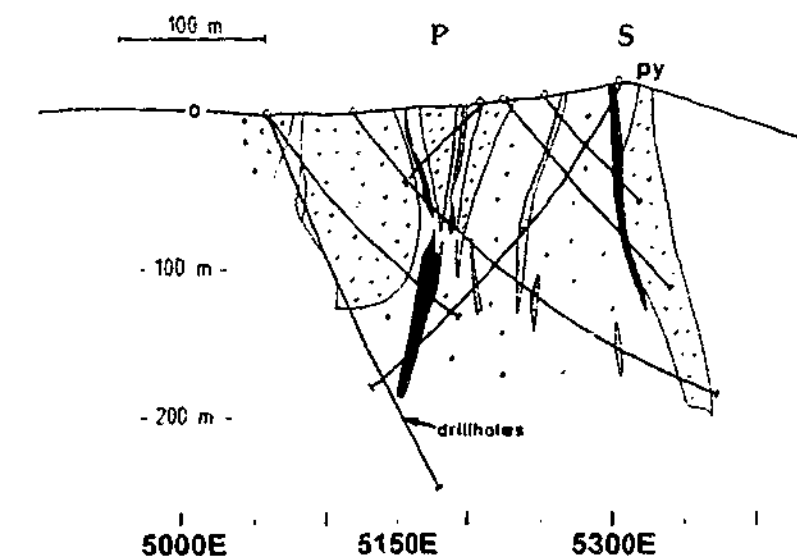
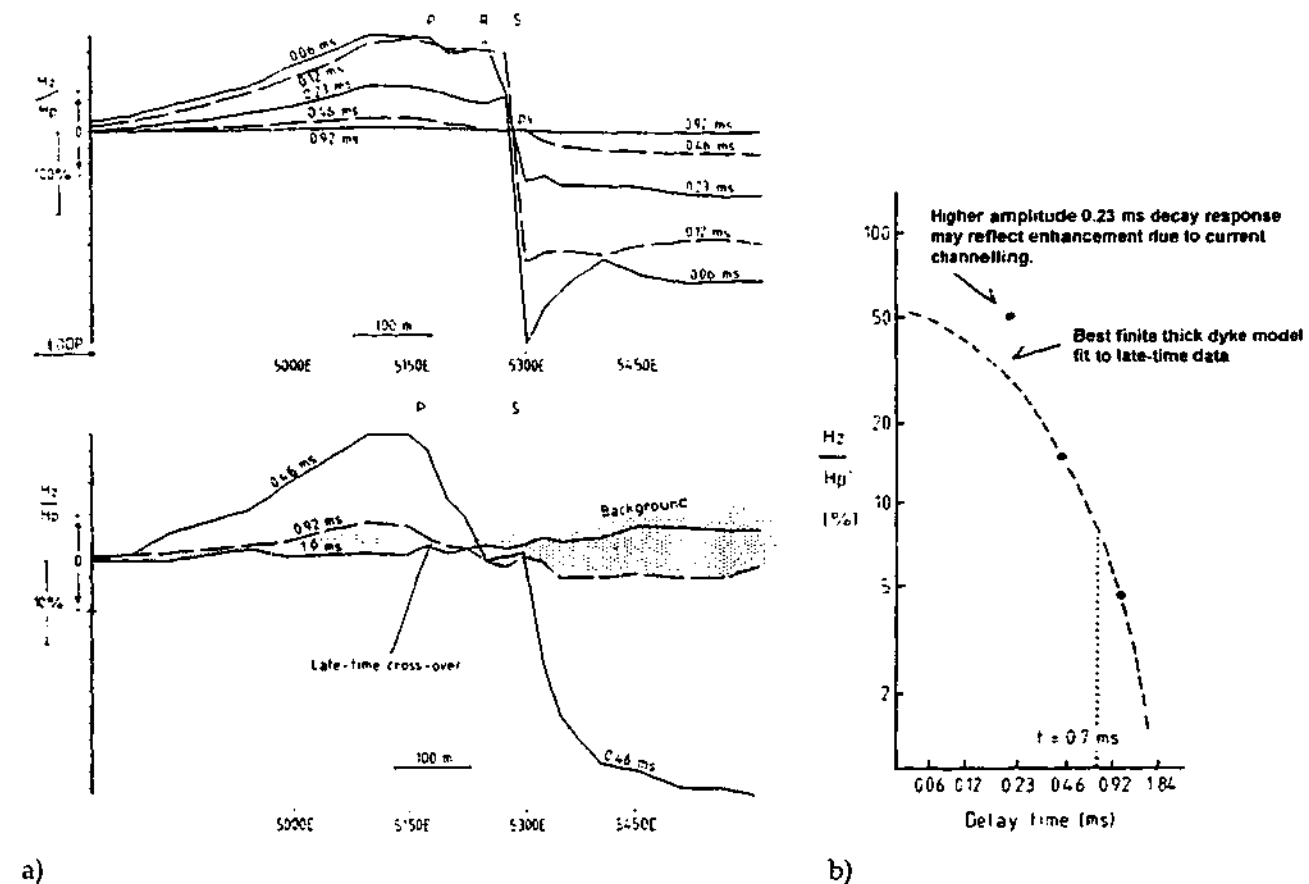


Figure 1.3: Geologic cross-section across the Que River ore body along the UTEM fixed-loop survey line, Line 7400N (After Staltari, 1986).

The following account is taken from a semi-quantitative analysis by Staltari (1986) of the experimental UTEM surveys that were performed over the deposit in order to determine the system's effectiveness in the search of similar type mineralisations. The UTEM survey consisted of a fixed-loop transmitter, 800 m x 600 m, placed to the west of both the P and S lenses, with readings

taken every 25 m with a roving receiver for 850 m, along line 7400N from 4780E to 5600E (Staltari, 1986). The results of the UTEM survey are shown within Figure 1.4a. Staltari (1986) identified the S lens anomaly as the asymmetric crossover about Station 5300E, with its sharpness being a manifestation of the shallow depth of the lens; whereas, the anomaly attributed to the P lens, was the late-time (0.46 ms and 0.92 ms) broad crossover anomaly, which is superimposed upon a regional, and located about Station 5150E.

Refer to Figure 1.4b for the peak-to-trough (P-T) anomaly decay curve, prepared by Staltari (1986), for the late-time crossover anomaly at Station 5150E. In brief, Staltari (1986) states that the 0.23 ms decay response can be ignored since its anomalous amplitude could not be accounted for by the best finite dyke model, which was fitted to late-time data. This exclusion was justified by Staltari (1986) as it permitted a conductance estimate of 15 Siemens and depth estimate of 70 m to the main portion of the conductor, the later being consistent with the results of Silic *et al.* (1985). Unfortunately, the discrepancy was large enough to be of concern, but the only explanation offered by Staltari (1986) was that the higher amplitude data point might reflect enhancement due to current channelling. It appears that the author has assumed that if reasonable attributes can be computed by ignoring the data point, then the discrepancy if not due to error, must be attributable to another mechanism whose effects are indifferent to the computation of those attributes, namely galvanic excitation. This case study illustrates an example in which current gathering effects were invoked to explain deficiencies in an inductive interpretation of TEM data, and without further justification or verification.



a) Figure 1.4: a) Fixed-loop UTEM vertical component profile for Line 7400N, scale is continuously normalised. Note that the late-time crossover corresponds with the P lens position. b) Peak-to-trough anomaly decay curve at 5150E (After Staltari, 1986).

1.3.2. REVIEW OF THE THALANGA DEPOSIT.

In this section, a paper by Irvine (1987) is reviewed. The borehole under consideration within this paper is DDH 135, and as shown within the geologic cross-section Figure 1.5, DDH 135 is noted to pass closely beneath a zone of mineralisation. Downhole TEM surveys were conducted using this hole for the southern (1984/5) and northern (1984/6) transmitter loops. This survey configuration was implemented so that the primary field of each loop would complement the other in coupling with the target. The associated DHEM profiles for DDH 135 with transmitter loops 1984/5 and 1984/6 are displayed Figure 1.6.

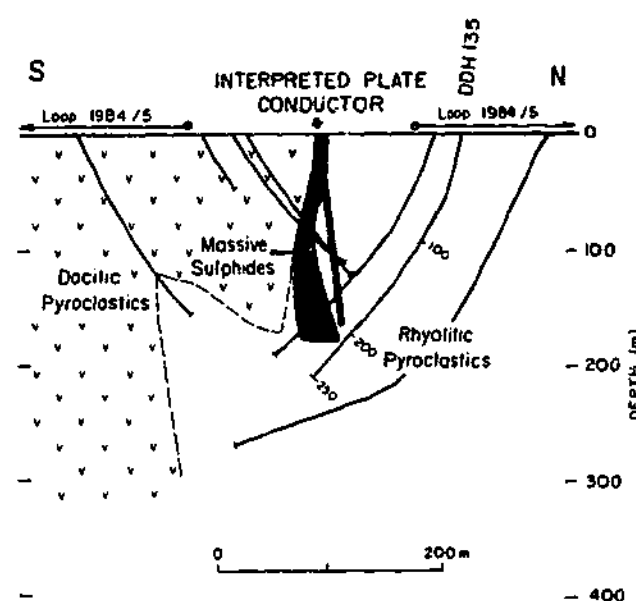
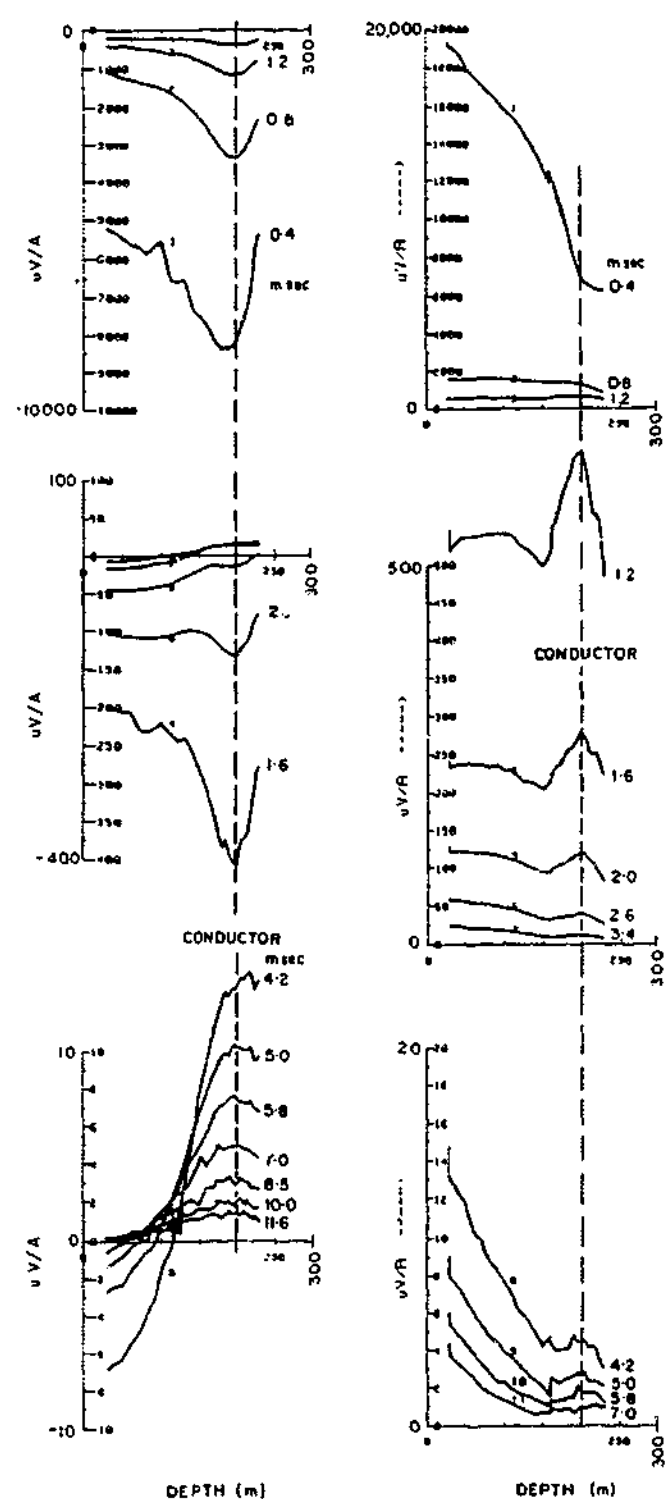


Figure 1.5: Geologic cross-section of DDH 135 showing the locations of both the northern (1984/6) and southern (1984/5) transmitter loops. Borehole DDH 135 is shown and is noted to pass but a few metres below the known massive sulphides. The associated DHTeM profiles for these loops are shown within Figure 6. (After Irvine, 1987).

Irvine (1987) noted that the response due to the southern loop, in contrast to the northern loop, is essentially without a host response. A negative-to-positive crossover occurs for the southern loop, whereas the opposite occurs for its northern counterpart. Of particular importance, is the behaviour of the anomalies due to both loops located 200 m down-hole. Specifically, these anomalies undergo a sign change from early to late times Irvine (1987). These sign reversals were interpreted by Irvine (1987) to be due to the predominance of current channelling effects at early times, yielding to inductive effects at later times. The schematic diagram of Figure 1.7 illustrates a mechanism for Loop 1984/5, for which inductive and galvanic excitation of a vertical target can account for anomalies of opposite sign. The plan view within Figure 1.7 crudely shows how a current image induced by the transmitter loop within the earth at the time of current termination, will proceed to expand outward and propagate downwards as a diffusing toroid of current, much like a smoke ring in air (Nabighian, 1979). See also Section 2.8 for further discussion of the smoke ring concept. As the smoke ring passes the mineralisation, regions of greater conductivity relative to the host gather up the ambient host currents. It is this condensed current stream that produces the typical unipolar magnetic fields

that are associated with galvanic excitation (see Figure 1.7). The secondary magnetic fields due to induction are dipolar in nature, producing field lines that circulate in an anticlockwise sense at the top edge of the plate, reinforcing the fields due to current channelling at the surface. Whilst at the base of the plate, the secondary inductive field lines circulate in a clockwise sense (directed down hole), resulting in a positive response for the southern loop. The magnetic field lines, however, due to current channelling at the base of the conductor are directed up hole, and subsequently form a negative anomaly. Thus, if galvanic effects dominate at early times and inductive effects at later times, the anomaly would be expected to pass from negative to positive from early to late times. In regards to the northern transmitter loop, Loop 1984/6, the resulting secondary fields of both the inductive and galvanic excitations of the target were reversed. See Figure 1.6b for response profiles of Loop 1984/6. The effects of the reverse coupling are evident where the anomalies are of similar shape but of opposite sign to that of those due to the southern loop. This case study is an excellent example in which galvanic excitation was proposed to explain a sign reversal which could not be accounted for by induction alone. Most importantly, however, the author was able to justify this explanation by means of profile analysis and provide a description of the proposed excitation mechanism.



a) b)
Figure 1.6: DHTEM profiles of DDH135 with a) Loop 1984/5, and b) Loop 1984/6. Sign reversals were noted within the profiles of both surveys, and were attributed by Irvine (1987) to the dominance current channelling at early times and induction at late times. (After Irvine, 1987).

1.3.3. DRIVE DELAY AND RESULTING EFFECTS.

The effect termed *drive delay* by McNeill *et al.* (1984) was proposed as an alternative to current channelling as the mechanism behind the sign reversals noted within DDH135 (Irvine, 1987). A brief discussion on this effect is provided in the following, however, this effect shall not be considered further within the thesis.

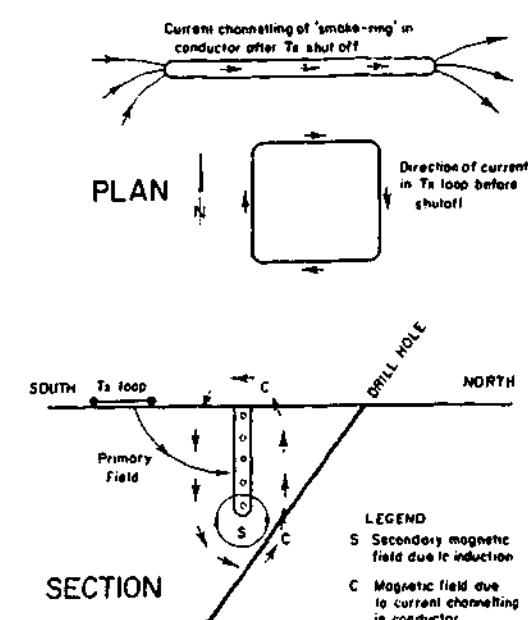


Figure 1.7: Schematic diagram illustrating the contributions made by both induction and current channelling for a vertical finite plate conductor. The dipolar field associated with induction, and the unipolar fields associated with galvanic excitation will be opposed to each other at the lower edge of the plate, whilst at the top edge of the plate they will be reinforced. (After Irvine, 1987).

Drive delay is the term used to describe the time delay of the driving magnetic field impulse between transmitter turn-off and the time at which secondary field decay commences in a deep conductor (Asten *et al.*, 1987). Immediately after transmitter turn-off a current image forms at the surface of the earth so as to support the collapsing primary field (McNeill *et al.*, 1984). Conceptually, the delay arises from the finite time required for the transmitter current image or smoke ring (Nabighian, 1979) to propagate down and outwards through a conductive host towards the target conductor (Asten *et al.*, 1987). McNeill *et al.* (1984) used the term *drive* to describe the behaviour of the primary-field field impulse dB/dt after transmitter turn-off. An ideal instantaneous transmitter turn-off within free-space would result in an impulse *drive* that would propagate outward from the source at the speed of light (Ward and Hohmann, 1988). Increasing the conductivity of the halfspace, however, will both delay and broaden the infinitely narrow free-space impulse drive. Moreover, for a given time the delay and broadening of the *drive* impulse will increase with depth and radial distance from the transmitter (McNeill *et al.*, 1984). The process of drive delay is illustrated within calculations performed by McNeill *et al.* (1984) for a 500 m transmitter loop on a conductive halfspace, the results of which were reproduced in Asten *et al.* (1987) and are presented here in Figure 1.8(a & b). The drive of the primary field for a receiver at a depth of 300 m was noted by Asten *et al.*, 1987) to undergo an initial increase after transmitter turn-off then decreasing after reaching a maximum and changing sign when $\rho t \approx 0.06$ ohm.m.s; where ρ is the halfspace resistivity and t is time in seconds (Asten *et al.*, 1987). The cause of the sign change in the drive and hence the target response is best understood in terms of the behaviour of the primary-field (see Figure 1.8b) which is obtained simply by integrating the drive impulse dB_z/dt (see Figure 1.8a) (Asten *et al.*, 1987). The initial increase in the vertical magnetic field component B_z below the halfspace surface after turn-off can be attributed to the approach of the smoke ring (Nabighian, 1979); it is at these times that the geometric coupling between the transmitter and receiver increases faster than the rate of decay of the source magnetic moment (Asten *et al.*, 1987).

Thus in summary, if the magnitude of the inductive coupling between source and target first increases then decreases as result of drive delay then a sign change within the induced target response will be found. Furthermore, Asten *et al.* (1987) noted that sign changes of this type would not occur with an instrument that transmits a step-response drive dB/dt such as the UTEM system. Indeed Irvine (1987) suggested that the UTEM system, which uses a triangular-wave, should be capable of resolving this ambiguity, since a sign reversal will still occur for current channelling but not for the temporary increase in magnetic field arising from drive delay.

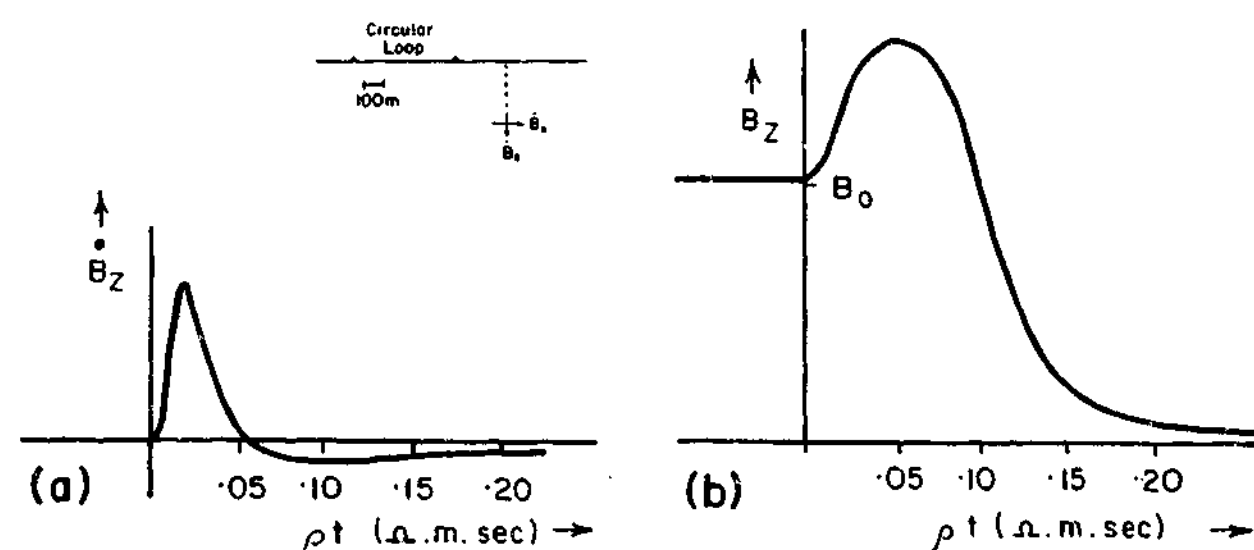


Figure 1.8: a) Behaviour of the primary field drive dB_z/dt at a depth of 300 m in a conductive homogenous halfspace. The effect of the conductive medium is to both broaden and delay the drive impulse. A change of sign is noted for $\rho t \approx 0.06$ ohm.m.s; where ρ [ohm.m] is the halfspace resistivity. And, b) the resulting primary field can be obtained by integrating the drive impulse a), and is noted to increase after turn-off as the smoke ring emitted from the transmitter loop approaches. (Profiles are reproduced from Asten *et al.* (1987), and the schematic insert from McNeill *et al.* (1984))

In general, drive delay and broadening will result in an inductive response which is both delayed and attenuated by an amount proportional to the time constant (τ) of the target (McNeill *et al.*, 1984). McNeill *et al.* (1984) illustrated this by computing the drive impulse within a conductive half-space for a point located 500 m from the centre of a circular loop transmitter and at a depth of 300 m. Simulated inductive responses of a single wire loop were computed by McNeill *et al.* (1984) by convolving the drive with simple exponentials of the form $e^{-t/\tau}$ for various time constants (τ). McNeill *et al.* (1984) showed by that for an extended drive pulse at early times the loop current follows the drive for all time constants (τ). At later times for values of τ large in comparison with the

drive duration the characteristic exponential decay is eventually seen, whereas for small values of τ the current continues to follow the drive for all time (McNeill *et al.*, 1984). Furthermore, for time constants which are large compared with the drive duration, the peak amplitude response will remain approximately equal to that resulting from an impulse which is of finite speed, whereas the peak amplitude for smaller time constants will be attenuated with decreasing τ (McNeill *et al.*, 1984). Restated, for a plate embedded in a conductive halfspace, only the eigencurrents with time constants greater than the drive duration will have amplitudes approximately equal to their equivalent free-space value, whereas eigencurrents with shorter time constants will experience reduced amplitudes (McNeill *et al.*, 1984).

1.3.4. REVIEW OF THE HELLYER ORE DEPOSIT.

1.3.4.1. INTRODUCTION.

The Hellyer ore deposit is located in North Western Tasmania and resides within the Cambrian Mt Read Volcanics 3 km north of the Que River mine (Eadie, 1987). This deposit is a massive sulphide mineralisation with base metal constituents (Zn/Pb, Ag and Au). In particular, 24 m of massive sulphides averaging 17% Zn/Pb, 160 g/t Ag and 2 g/t Au were intersected at a depth of 198 m down the discovery hole HL3 (Eadie, 1987). Following its discovery, performance based trial surface and DHTeM surveys were performed over the Hellyer deposit with the purpose of comparing and testing the effectiveness of several EM systems within this environment (Eadie, 1987). The principal holes and loops used within the surveys were HL3 with Loop 1 at the southern end spur and HL19 with Loops 2 and 1 at the central or main portion to the north, whereas the NEWMONT system was assigned its own loop (Eadie, 1987).

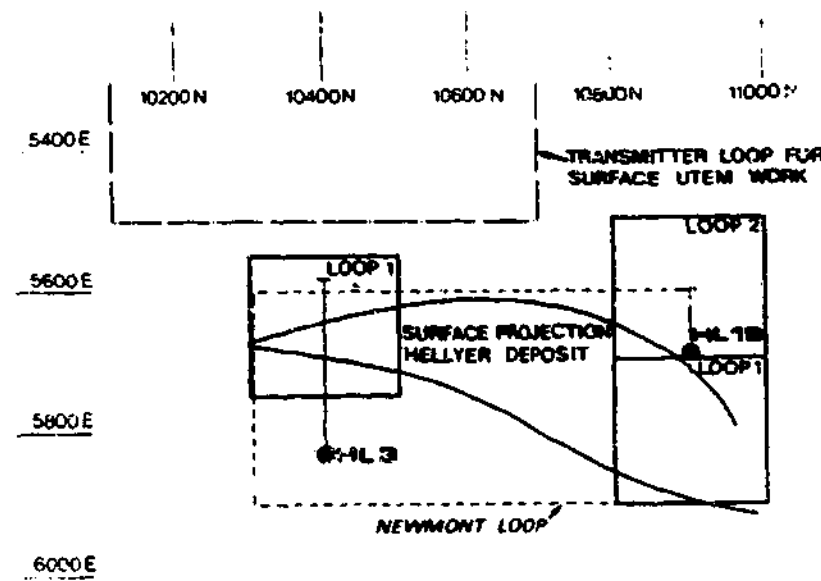


Figure 1.9: Plan showing the positions of the transmitter loops used within the surface UTEM and downhole Newmont EMP surveys, whilst the 200 m by 200 m loops, Loops 1 and 2, were used for the Sirotec, EM37 and Crone PEM surveys. (After Eadie, 1987).

1.3.4.2. DHTEM WITH DRILL-HOLE HL3.

A DHTEM survey was conducted with drillhole HL3 at the southern end spur with Loop 1 (see Figure 1.9). The following instrumentations were used: the SIROTEM system with standard times, the EM-37 system with 25Hz wave form, the CRONE PEM and NEWMONT EMP systems (Eadie, 1987). The generic characteristics of the response profiles for all systems at early, moderate and late-times were summarised by Eadie (1987):

- **EARLY TIMES (LESS THAN 1.5 ms):** The down-hole response begins with a positive sign at shallow depths, which decreases rapidly forming a large negative spike type response 20 m above the conductor. On intersection with the body, the anomaly ends abruptly resuming a positive response that peaks in amplitude before decreasing monotonically with depth. This early time response can be explained in terms of the horizontal current flow induced by the decay of the vertically coupled primary field (Eadie, 1987).
- **MODERATE TIMES (BETWEEN 1.5 ms AND 2.0 ms):** At moderate times, the current plane within the conductor will undergo a clockwise rotation, thereby permitting the current distributions to occupy the maximum dimension of the body. As such, the resulting current plane will be orientated nearly perpendicular to the borehole, resulting in a positive response at all depths (Eadie, 1987).

- **LATE TIMES (GREATER THAN 2.0 ms):** At late times a broad negative response begins to form below the body near the base of the borehole. This is due to the migration of the current distribution, which results in it flowing along the strike length of the north plunging ore body (Eadie, 1987).

1.3.4.3. DECAY ANALYSIS.

Refer to Figure 1.10 for a compilation of decay curves, prepared by Eadie (1987), for the response profiles of the four EM systems. It is apparent, that the decay curve of each system appears to exhibit a two-tier decay mode. The first mode is defined within the interval of moderate times (2 to 6 ms), with each system response noted to decay exponentially with a time constant ranging from 0.75 ms to 1.1 ms. The second mode of decay lies within the late time interval (7 ms onwards), and is typified by the exponential decay with a time constant of 3 ms. Eadie (1987) reasoned that the late time decay mode originates from current distributions within the main part of the conductor north of HL3.

Eadie (1987) proposed two mechanisms to explain the origin of the 1 ms decay mode, and thus reconcile the two different time constants exhibited within the SIROTEM and NEWMONT decay curves:

- i. Either a small-localised current system has been established within the southern spur of the body, and decays with a characteristic time constant of 1 ms. This is implied by the near perfect exponential decay at moderate times. Or;
- ii. the smaller time constant noted at moderate times may in part arise from effects due to current channelling (Eadie, 1987).

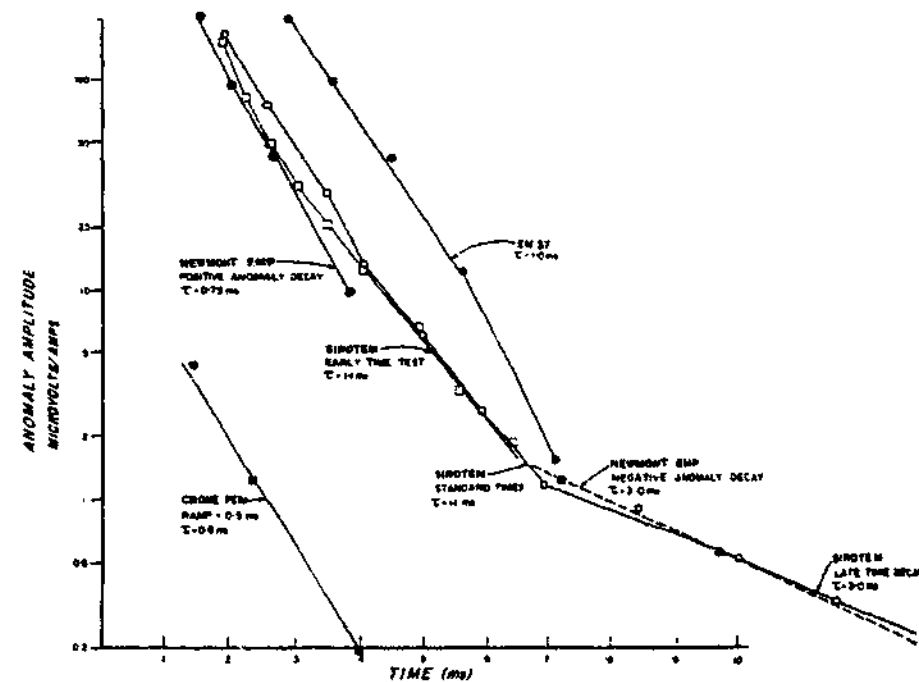


Figure 1.10: Multiple decay curves obtained at an axial depth of 200 m down drillhole HL3, for the CRONE PEM, EM 37, NEWMONT EM and SIROTEM systems. Note all systems suggested to Eadie (1987) an exponential decay with time constant of about 1 ms at moderate times, whilst the SIROTEM and NEWMONT systems indicate a two tier decay mode with an additional slower decaying current system with a time constant of 3 ms at later times. (After Eadie, 1987).

1.3.4.4. SURFACE UTEM ON LINE 10400N.

A surface survey was performed by use of the UTEM system along Line 10400N from 5500E to 5900E, with a fixed transmitter loop located west of the target (see Figure 1.9). Inductive free-space modelling was applied to two time windows, 0.9 ms and 1.9 ms, of the UTEM field response with background removed (Eadie, 1987). A vertical thin plate model, with a conductance of 125 S, was used by Eadie (1987) to represent the induced vertical current plane within the body. The stripped field data and associated model response are reproduced within Figure 1.11. It was noted, by Eadie (1987), that although the model provided a poor fit to the field data at 0.9 ms, it was in very good agreement at 1.9 ms. The failure of the model at 0.9 ms suggested to Eadie (1987) that galvanic currents dominated the response at early times and vortex currents dominated at moderate times. However, the author was cautious in making this conclusion as the interpretations included only two time windows.

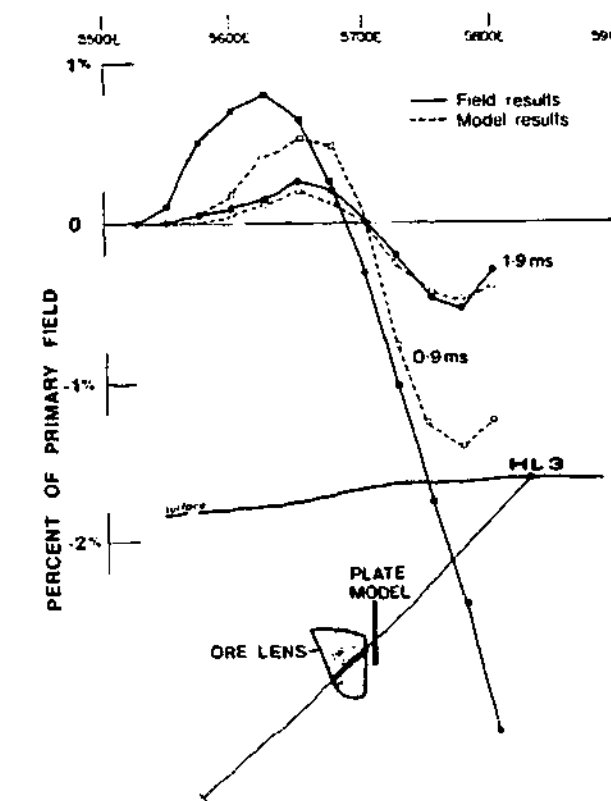


Figure 1.11: Profiles at 0.9 ms and 1.9 ms of the UTEM field data on line 10400N with the background response removed, compared with a 125 siemens plate model with a strike length of 500 m. The poor fit to the inductive model at window 5 (0.9 ms) suggested to Eadie (1987) galvanic current flow dominates the response at early times, whilst inductive effects dominate at later times. (After Eadie, 1987).

1.3.4.5. SURFACE UTEM ON LINE 10700N.

A surface survey was also performed along Line 10700N from station 5550E to 5950E across the thick central portion of the ore body (Eadie, 1987). The anomaly featured within the response profiles of Figure 1.12, extends to later times than on 10400N, and is thus indicative of a deeper body of greater conductance (Eadie, 1987). A peak to trough decay curve is for the UTEM data is shown within Figure 1.13. Current channelling effects were assumed by Eadie (1987) to dominate from early to moderate times, whilst at later times the response exhibits an inductive decay with a time constant of 3.8 ms, a result which is consistent with the DHTM data (Eadie, 1987). The vertical thin-plate model yielded a peak-to-trough decay curve that is in reasonable agreement with the field data. Note the model could only match the inductive decay mode, due to its incapacity to replicate the effects associated with galvanic current flow (Eadie, 1987).

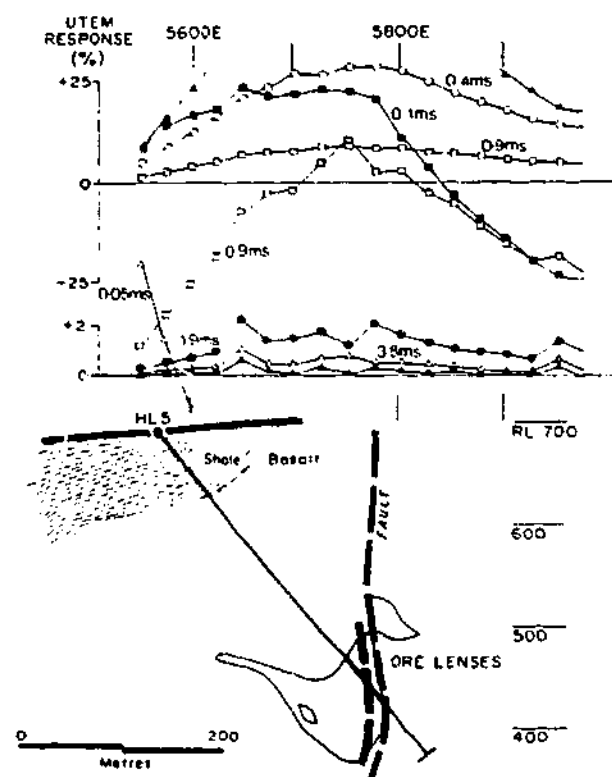


Figure 1.12: Profiles of the UTEM field data on line 10700N, the position of the transmitter loop is shown in Figure 2. (After Eadie, 1987).

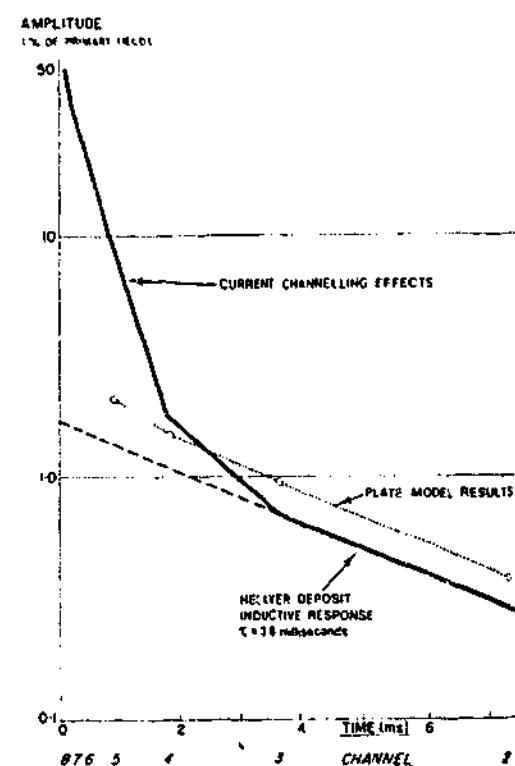


Figure 1.13: Peak to trough decay curve for the field UTEM data on line 10700N, compared to that of a 200 siemens vertical plate model with a strike length of 500 m, a depth extent of 100 m, and depth to top of 225 m. Current channelling effects are apparent at early times with inductive effects dominating after 3 ms. (After Eadie, 1987).

1.3.4.6. IP EFFECTS AND THE UTEM DATA.

Flis (1987) explored the proposition that induced polarisation (IP) effects may be responsible for negative responses within coincident-loop TEM data, which may otherwise be attributed to factors including instrumental error, conductor geometry and current channelling. IP effects are characterised by early time enhancement of inductive anomalies, followed by a period of rapid decay at middle time and a sign reversal at late time (Flis, 1987). In particular Flis (1987) refers to surface UTEM data within Eadie *et al.* (1985) collected over line 10300N of the Hellyer ore deposit (see Figure 1.14) and notes that the normal crossover anomaly at 5675E at early times undergoes a sign reversal by 3.7 ms, a feature pointed out by Flis (1987) to be typical of IP effects in fixed-loop data. Rather than disregarding this subtle late time feature as noise, Flis (1987) sought justification for the IP interpretation by noting that a similar late time sign reversal is present within the adjacent line, line 10400N. Recall Section 1.3.4.4,

within which a review is given of the UTEM profile along line 10400N together with the tentative conclusion, drawn by Eadie (1987), that the poor match between the free-space inductive model and field data for a single time window (0.9 ms) suggests the dominance of galvanic current flow at early time. Although current channelling is an early time effect, the work of Eadie (1987) and Flis (1987) exemplifies the need for caution when seeking an explanation for the divergence of a field response from free-space inductive interpretations.

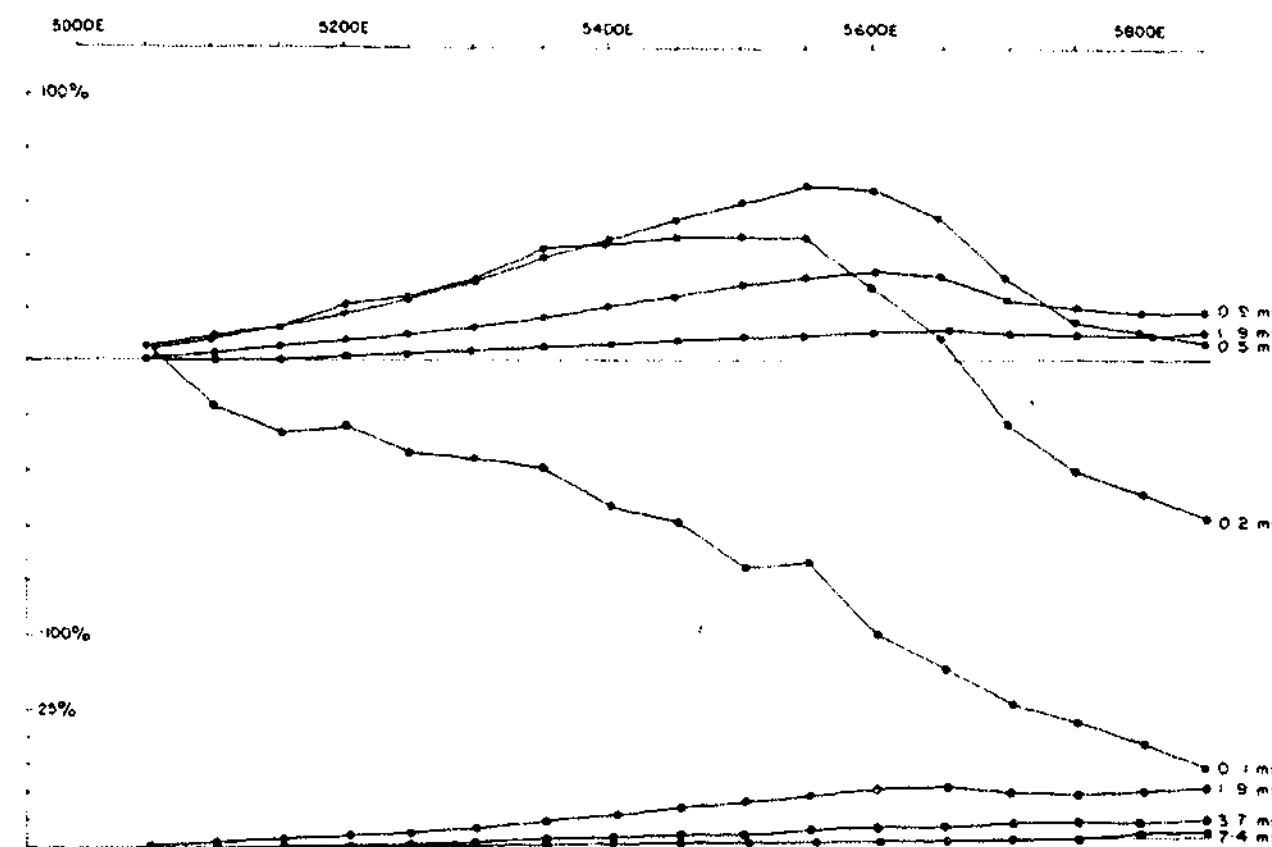


Figure 1.14: Profiles of the vertical component UTEM field data from line 10300N. Note, the sign reversal by 3.7 ms of the normal early time crossover was attributed by Flis (1987) to IP effects. (After Flis, 1987).

1.3.4.7. COMMENTS AND CONCLUSIONS.

Eadie (1987) expresses the possibility of current channelling within both the DHTM and UTEM surveys, but is purely speculative in his suggestions. Unfortunately, the suspected galvanic components within the field data were not confirmed by numerical modelling, due to the unavailability of such algorithms at the time. The inference of current channelling within the field data was made from decay curves for both the DHTM surveys and the surface UTEM survey on line 10700N. Specifically, Eadie (1987) interpreted the rapid decay at early times within the peak-to-trough decay curve of the UTEM data and the 1 ms decay mode in the DHTM data to be a manifestation of current

channelling effects at early to moderate times. In regards to the UTEM survey on line 10400N, Eadie (1987) attributed the poor amplitude matching between the thin plate inductive free-space model response and the stripped field response to the dominance of a galvanic component at early times.

Eadie (1987) noted that the galvanic and inductive effects dominated the field response for the following times:

- UTEM ON LINE 10400N:
Current channelling effects dominate the target response until at least .09 ms, whilst inductive effects appear to dominate after 1.90 ms.
- UTEM ON LINE 10700N:
Current channelling occurs at early to moderate times, whilst the inductive response dominated at late-times (3 ms and onwards) and decayed exponentially with a time-constant of 3.8 ms.
- DHTEM WITH HOLE HL3:
All systems exhibited an exponential decay mode with a time-constant of approximately 1 ms at moderate times (1 to 5 ms) and was attributed in part to current channelling. In regards to the SIROTEM and NEWMONT systems, inductive effects were assumed to dominate at late-times (7 ms and onwards), and decayed with a time-constant of 3 ms."
- INDUCED POLARISATION EFFECTS:
Furthermore, the UTEM data for lines 10300N and 10400N were interpreted by Flis (1987) to exhibit IP effects at late time (by 3 ms), and were manifest as sign reversals in the 5675E crossover anomaly. Although galvanic effects are not expected to occur at late-times, the observation by Flis (1987) represents another situation where the field response will diverge from free-space inductive interpretations.

1.3.5. REVIEW OF THE QUE-HELLYER VOLCANICS EXPERIENCE.

The Cambrian Mt Read Volcanics sequence hosting both the Que River and Hellyer ore deposits, known as the Que-Hellyer volcanics, is a relatively resistive volcanic sequence exhibiting an average resistivity of 500 ohm.m, and features a conductive overburden in the form of overlying black shales with resistivities as low as 100 ohm.m (Silic and Eadie, 1989). Historically, the Que River and Hellyer mined-deposits have been the only strong conductors detected, demonstrating that the intermediate volcanic sequence is an ideal environment for EM exploration techniques (Silic and Eadie, 1989).

The detection of the more conductive and deeper P lens at Que river by the fixed loop UTEM surveys, prompted further UTEM surveys to be conducted in the areas surrounding Que River; these follow up surveys led to the discovery of the Hellyer ore deposit (Staltari, 1986).

Silic and Eadie (1989) examined the experience and techniques of the DHTEM method in the Que-Hellyer volcanics, observing that although the region is favourable to EM methods, there remain factors that will complicate DHTEM interpretations. These factors include:

- i. Effects arising from the overlying moderately conducting black shales.
- ii. Instrumentation responses from the SIROTEM unit, *e.g.*, probe self response.
- iii. Cultural noise associated with existing deposits.
- iv. Responses from nearby conductors whose presence is either known or unknown (Silic and Eadie, 1989).

Although all factors were discussed by Silic and Eadie (1989) only one example is considered relevant here and deals with the Que River mine.

1.3.5.1. DHTEM SURVEYS AT QUE RIVER.

The exploration program at Que River included the drilling of two deep holes, Boreholes QR1001 and QR1060A, beneath the mine at a spacing of 400 m from one another. Subsequent TEM surveys of both these holes employed the SIROTEM system in conjunction with transmitter loop 2 (See Figure 1.15 for survey configuration). The TEM response acquired from Borehole QR1060A featured a broad late time negative trough (See Figure 1.15). This trough is

centred about an axial depth of 975 m and is at least 700 m wide at 4.8 ms, whilst its *half-width* (the anomaly at half the peak amplitude) is greater than 500 m. Two questions arose from these findings, firstly:

- i. is the response due only to the Que River massive sulphides of the culture associated with the mine 500 m above the hole? The answer to this question was concluded to be no, since no late anomaly is observed in QR1001 which is located the same distance from the deposit. And secondly;
- ii. what is the origin of the anomalous sign change around 2 ms?

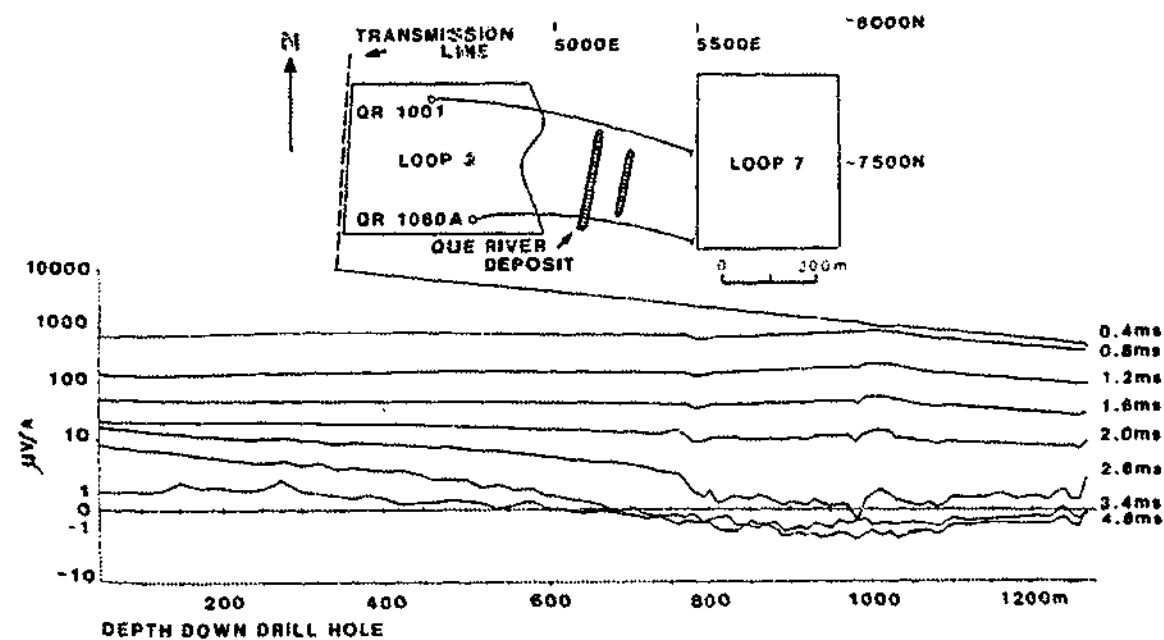


Figure 1.15: Composite figure showing the downhole TEM SIROTEM response profiles for Borehole QR1001 with Loop 2, and a schematic insert showing the locations of Boreholes QR1001 and QR1060A together with Loops 2 and 7. Note the broad anomaly centred about 975 m is found to change from positive to negative with increasing delay time. (After Silic and Eadie, 1989).

Both holes were resurveyed with the EM-37 system using two additional loops, loops 2 and 7. See Figure 1.16 for selected windows from the response of Borehole QR10610A. A strong broad cultural response, which decreases slowly with depth, is present within the Loop 2 data at early times. This cultural effect is responsible for artificially inducing the large *half-width* noted in both the EM-37 and SIROTEM Loop 2 data. Given that, the Loop 7 response possesses no such cultural contamination it was deemed suitable for interpretation (Silic and Eadie, 1989).

The Loop 7 data (see Figure 1.16) exhibits a broad negative anomaly centred about an axial depth of 975 m that undergoes an anomalous sign change at late time. Silic and Eadie (1989) proposed two possible mechanisms for the sign reversal:

- i. The first explanation was in reference to Asten *et al.* (1987) who in turn noted a similar effect and attributed it to *drive delay*, but was later dismissed as the effect could be calculated to die out by 0.1 ms.
- ii. The second explanation suggested that current channelling effects dominated over inductive effects at early time producing a broad negative anomaly, which in turn, yielded to an inductive dominated response at late-times (Silic and Eadie, 1989).

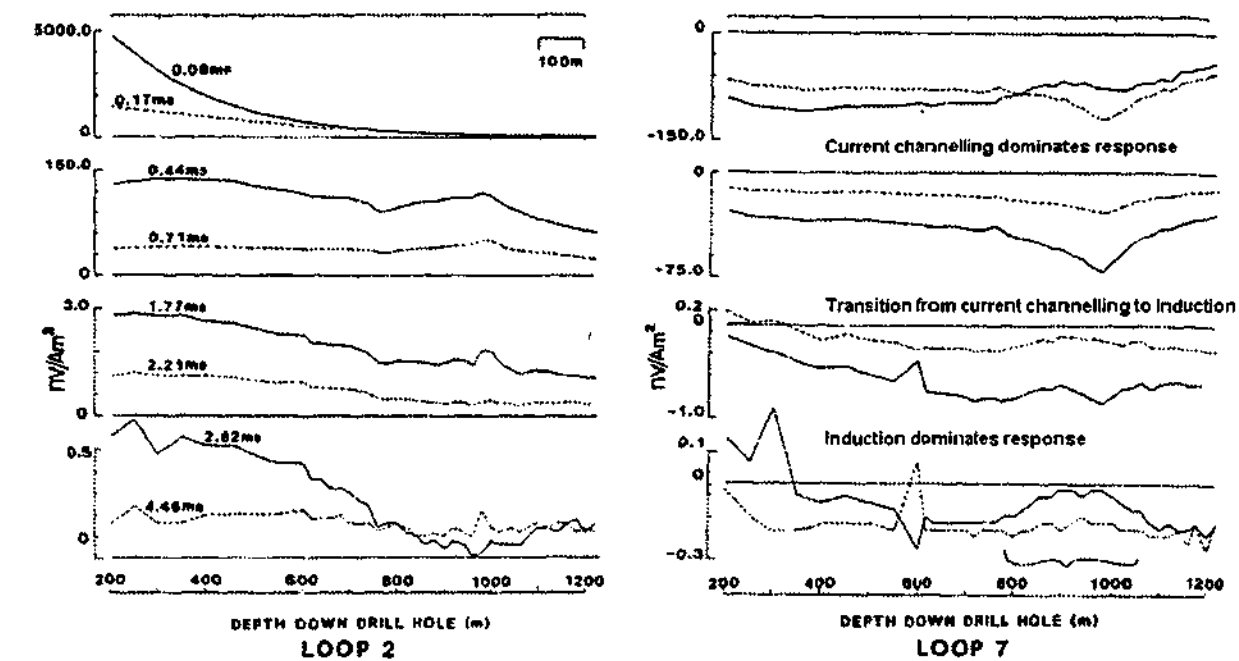


Figure 1.16: Profiles of the downhole EM-37 response for QR1060A with transmitter loops, loops 2 and 7. (After Silic and Eadie, 1989).

Silic and Eadie (1989) also provided justification that current channelling is the underlying mechanism behind the anomalous sign changes. Firstly, it explains the data well. Secondly, within these types of volcanics strong current channelling effects are found from experience to have a lifetime of up to 2 ms. Thirdly, the sign inversion between 1.77 ms and 2.21 ms possesses the characteristic of both galvanic and vortex flow rather than traversing a zero amplitude state (Silic and Eadie, 1989). Furthermore, the authors used current channelling to their advantage by applying the additional information to

resolve the directional ambiguity of the conductor relative to the borehole. That is the opposite polarity of the galvanic and inductive response permitted them to interpret the target to lie above the borehole as shown in Figure 1.17. Unfortunately, it was not possible for the authors to ascertain whether current channelling was occurring by means of numerical modelling, due to the unavailability at the time of computer algorithms which could simultaneously model both galvanic and inductive current flow.

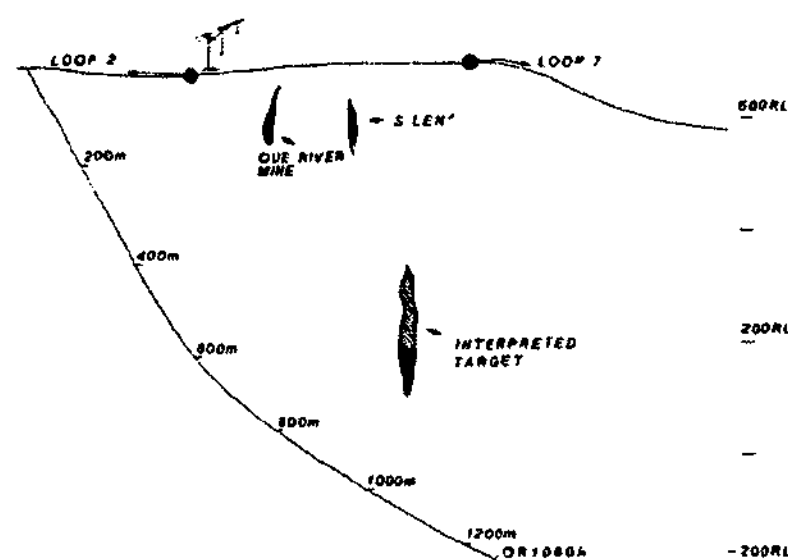


Figure 1.17: Cross section showing the location of borehole QR1060 with transmitter loops and the interpreted conductor. (After Silic and Eadie, 1989).

1.3.6. REVIEW OF THE AGUAS TENIDAS EAST DEPOSIT.

1.3.6.1. INTRODUCTION.

The Aguas Tenidas East (ATE) volcanogenic deposit was discovered in 1985 and is located in SW Spain. Its composition consists predominantly of massive pyrite with a few percent sphalerite ZnS , chalcopyrite $CuFeS_2$ and galena PbS (Hopgood and Hungerford, 1994). Numerous TEM surveys using the EM-37 system were performed over the ATE deposit in 1985 and 1986 following its discovery so as to better define the position and attitude of the mineralisation (Hopgood and Hungerford, 1994). The following account of the initial pre-discovery TEM survey conducted in 1984 is taken from Hopgood and Hungerford (1994), it is considered in detail here as it illustrates an excellent example in which current channelling was both inferred and verified through numerical modelling.

1.3.6.2. EM-37 SURVEY OVERVIEW.

The pre-discovery 1984 surface EM-37 survey was performed over the ATE deposit, utilising a fixed 600 x 300 m transmitter loop with a frequency of 25Hz. Measurements were taken along north-south survey lines spaced at 100 m or 200 m with stations located at 50 m intervals. The results of the survey revealed an EM anomaly located at the eastern end of the horizon and signalled the presence of the mineralisation.

The initial, and incorrect, interpretation was that of a steeply dipping source located at a depth of about 100 m, inferred by extrapolating the sub-vertically dipping surface geology on the southern flank of the San Telmo anticline. As a consequence of this the conductor was incorrectly modelled as a vertical plate (see Figure 1.18) and led to the drilling of borehole AE-1 to a depth of 294 m falling short of the true mineralisation. Although no mineralisation was intersected a borehole EM37 survey indicated a substantial off-hole and deeper conductor. Although the region identified to contain mineralisation was not considered very prospective given that the rock-type identified at base of borehole AE-1 was of the same type as that found 300 m to the south at the footwall of the minor outcropping mineralisation. A second borehole AE-2 was drilled 200 m along strike west of AE-1 to depth of 297 m, but failed also to intersect any mineralisation. The discovery hole AE-3 was drilled 70 m to the east of AE-1 after improved delineation of the conductor was made through further surface EM-37 surveys (Hopgood and Hungerford, 1994).

Results from the 1984 EM-37 survey featuring the z-component profiles on a log-linear plot are shown within Figure 1.19. Decay analysis on the surface EM-37 data yielded time constant estimates of 2.2 ms for the x-component and 3.0 ms for the z-component (Hopgood and Hungerford, 1994).

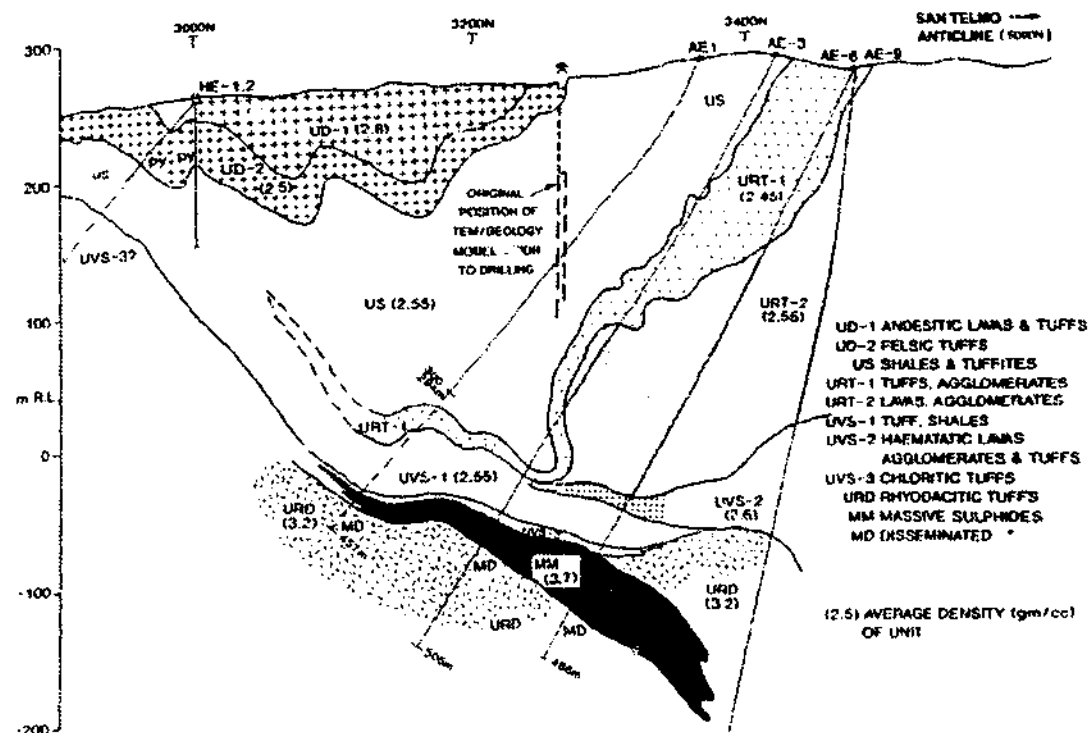


Figure 1.18: Geological cross-section of the ATE deposit along line 90900E. Featured also is the original free-space inductive interpretation of the TEM anomaly which was constrained by the extrapolation of surface geology. The failure to include current channelling within the interpretation incorrectly placed the mineralisation at a shallow depth, and resulted in drillhole AE-1 falling short of the true mineralisation. (After Hopgood and Hungerford, 1994).

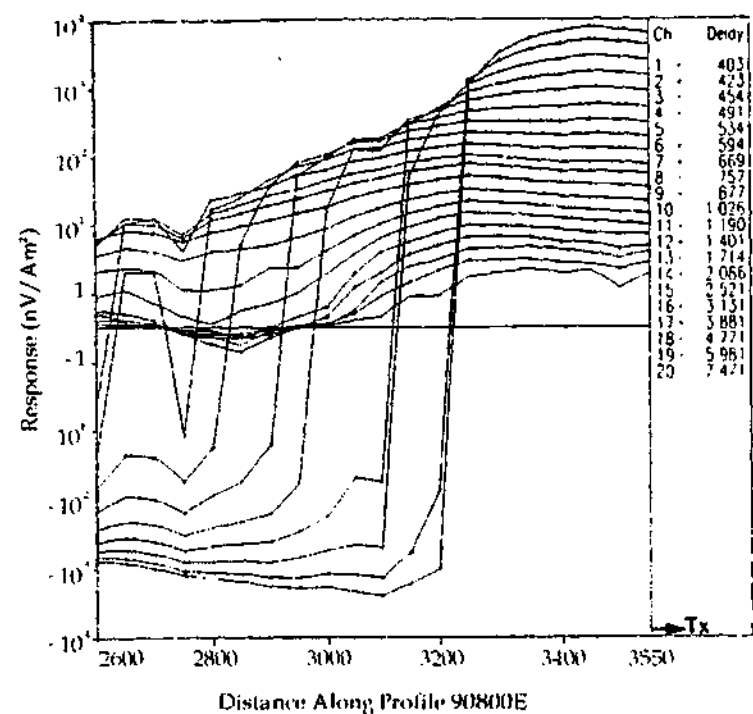


Figure 1.19: TEM response profile, z-component (log-linear), of surface EM-37 field data from Line 90800E: Roving surface Rx with fixed loop Tx. (After Hopgood and Hungerford, 1994).

1.3.6.3. NUMERICAL MODELLING.

Thin-Plate Inductive Free-Space Model

The z-component data of the Line 90800 EM-37 response was initially modelled with the SIROEX program OZPLTE. Figure 1.20 shows the comparison between the model and field profile. Both the model and field profiles display similar asymmetries suggesting the attitude of the body is correct. The amplitude of the field response, however, greatly exceeds that of the free-space model, with a field to model amplitude ratio of about 1000:1. This large difference forced the authors to consider one of two possible explanations: firstly, the plate model is inappropriate; secondly, current gathering effects dominate the field response. The authors considered the second option.

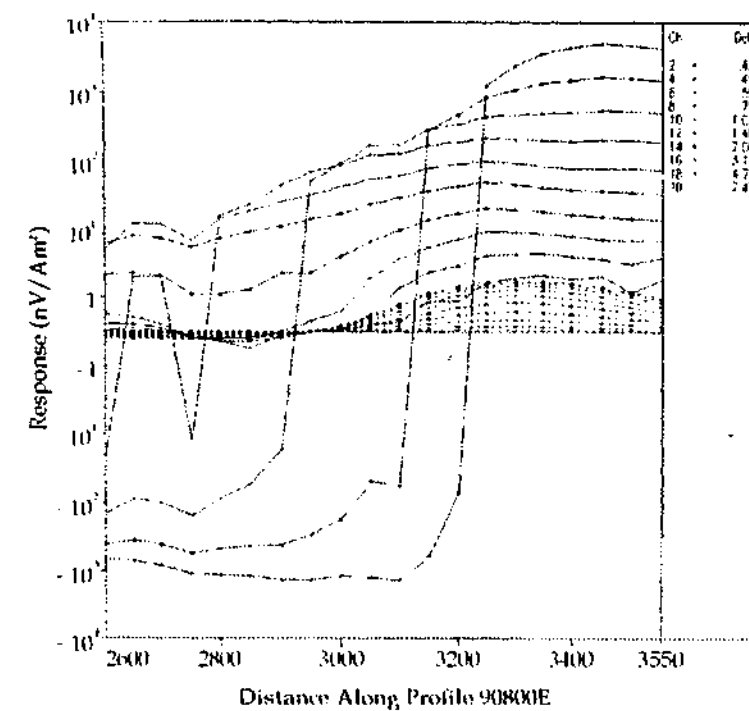


Figure 1.20: z-component surface EM-37 field response (solid line) along line 90800E with the associated model data (dashed line). The inductive free-space model response is that due to a thin plate computed with the algorithm OZPLTE. Inadequate amplitude matching was attributed to the absence of the galvanic effects within the model. (After Hopgood and Hungerford, 1994).

2.5D Galvanic and Inductive Model

In order to model the effects of both vortex currents and current channelling Hopgood and Hungerford (1994) implemented a 2.5D finite element algorithm developed by the CSIRO. In this case the thin plate was replaced with a conductor of infinite strike length embedded within a conductive 300 ohm.m half space. See Figure 1.21 for the z-component profile of the 2.5D model and field data. Although the field response is greater for all time windows, especially at early times, its amplitude is of the similar order of magnitude as the model response. In summary, a large component of the ATE TEM response can be attributed to current channelling effects.

The authors Hopgood and Hungerford (1994), however, were concerned by the results of the modelling performed by San Filippo *et al.* (1985). These models suggested that for a moderate host resistivity of 300 ohm.m, contributions due to current channelling should be negligible after 1 ms, whereas the ATE field data suggests that current channelling effects may persist till later times (Hopgood and Hungerford, 1994).

It was remarked by Hopgood and Hungerford (1994) that given the 300 ohm.m host resistivity of the ATE region is by no means unique, the occurrence of anomalously large field TEM data relative to pure induction may indeed be common. The Thalanga base metal deposit in Queensland which resides in a similarly resistive environment was quoted as an example. See Section (1.3.2) for an account of suspected galvanic effects at Thalanga.

Finally, Hopgood and Hungerford (1994) ascribed the predominance of the galvanic component over inductive effects to possible galvanic bias due to the orientation of the conductor; in this instance a horizontal prism, in contrast to vertical prism, is more favourable to galvanic excitation, and less favourable to inductive excitation due to poorer coupling.

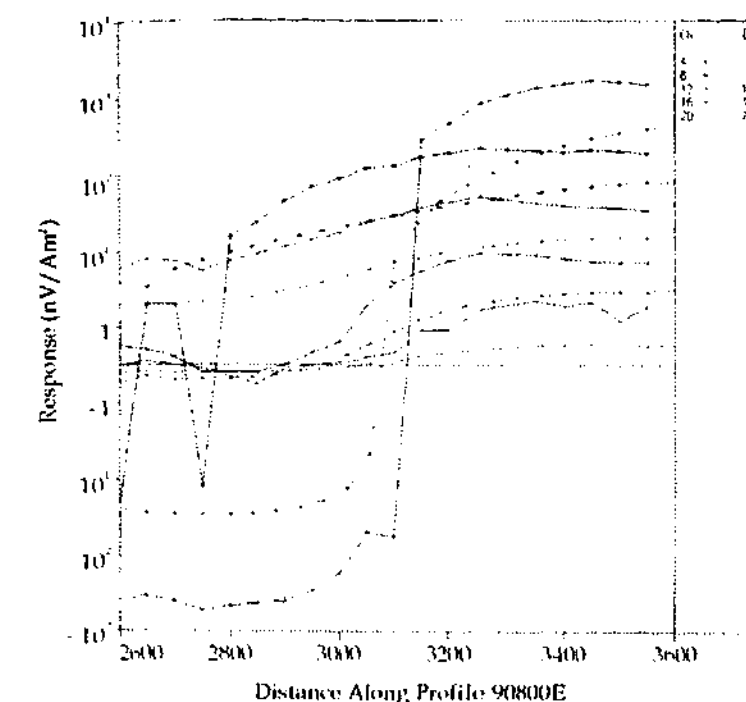


Figure 1.21: z-component surface EM-37 field response (solid line) along line 90800E with the associated model data (dashed line). The 2.5D model response is due to a conductor of infinite strike length in a 300 ohm.m host. The inclusion of galvanic effects has enhanced the model response and thus improved amplitude matching. (After Hopgood and Hungerford, 1994).

1.3.6.4. SUMMARY.

In summary, this account of TEM exploration at ATE from Hopgood and Hungerford (1994), is an example in which current channelling was inferred by numerical modelling, in as much as it was invoked to reconcile the differences between field and inductive thin plate interpretations. In particular, current channelling was proposed to explain the 1000:1 field to model amplitude ratio noted from the EM-37 surface surveys. Moreover, the inferred presence of a galvanic component within the field response was later verified by a 2.5D finite element algorithm, which calculated the combined galvanic and inductive response due to a target of infinite strike and excited by a 3D transmitter source. Although no additional information was attained from the presence of current channelling, the inclusion of a galvanic component within the model response improved the amplitude matching between the model and field data. If, however, galvanic effects were included within the initial interpretation, the ATE deposit may have been discovered earlier, since the original interpretation was based upon the free-space inductive response of thin plate conductor and

placed the deposit at an erroneously shallow depth. The essential aspects of this case study can be summarised as follows:

- i. Galvanic effects were both inferred and verified by numerical modelling.
- ii. Failure to include galvanic effects within the initial interpretation resulted in drilling error.
- iii. The discovery of the ATE deposit is testament to the benefits of the DHTEM method: the early extrapolation of the surface geology misled the initial interpretations, whereas DHTEM correctly identified a deeper off-hole conductor.

1.4. PROJECT AIMS AND OBJECTIVES.

Investigations into TEM induced galvanic effects were carried out within two case-studies featuring the Cadjebut Pb-Zn deposit, and the Flying Doctor Pb-Zn-Ag deposit respectively. The principal project tasks and aims which were specific to each case-study are provided below.

1.4.1. CADJEBUT MINERALISATION.

The Cadjebut lead-zinc ore body is located in north Western Australia on the Leonard Shelf, and is an example of a Mississippi Valley-type (MVT) mineralisation (Scott *et al.*, 1994). Given the difficult nature of MVT mineralisations as geophysical targets, their characteristics were studied within surveys performed by BHP Minerals in 1987 at Cadjebut (Lebel, 1987). Of the tests performed, only the results of the surface and downhole transient EM (DHTEM) surveys were considered within the thesis project.

PROJECTS AIMS: Investigation into the underlying mechanisms behind the production of both the M-anomaly and prominent galvanic intersection anomaly found within the moving-loop and downhole TEM surveys respectively. The following objectives were pursued by means of forward numerical modelling with industry standard software:

- a) To determine if the M-anomaly noted with the response of the moving loop survey can be attributed solely to the Cadjebut mineralisation.

- b) To confirm whether or not the prominent intersection anomaly in the DHTEM data was due to galvanic excitation of the target from use of an offset loop.

It is noted, that the downhole TEM surveys were regarded to be good candidates for current channelling, since the weakly-coupled offset loop yielded a prominent target signature, whereas the inductively well-coupled loop was devoid of any such response.

1.4.2. FLYING DOCTOR DEPOSIT.

Located near Broken Hill, NSW, the Flying Doctor Deposit (FDD) has been used extensively as a test site for many geophysical systems and surveying techniques (Macnae *et al.*, 1991). It is estimated that the deposit consists of 200 000 metric tons of 6 percent lead, 3 percent zinc, and 2 percent pyrrhotite (Fe_7S_8) (Macnae *et al.*, 1991). Furthermore, the Broken Hill galena (PbS) and sphalerite (ZnS) type mineralisation is invariably conductive enough to yield good EM responses (Bishop *et al.*, 1997). Downhole transient electromagnetic (DHTEM) and magnetometric resistivity (DHMMR) surveys were conducted at the Flying Doctor site in June 1998, as part of the SPIRT project under Monash University and the collaborating industry partners. The aim of the field trip was not only to collect data specifically for the thesis project but also provided the opportunity for the trial of new geophysical equipment.

- a) Testing of the experimental VECTEM probe developed by Monash University. The trials, if successful would have yielded valuable 3-component TEM data that would have permitted the construction of inductive models by inversion. Unfortunately, the probe suffered a misfortune on the first day of testing when it began leaking water at the shallow depth of 20 m. Although regrettable, this trial highlights the stresses and high water pressures many probes encounter, and the design considerations that need to be made in order to address it. Because of this, both the DHTEM and DHMMR surveys were conducted with a single axis probe. The disadvantage with using single component data is that inversion methods are unable to produce unique models due to the lack of *information*.

Consequently, all interpretations were made by the time consuming process of forward modelling, in which model development proceeded in a heuristic manner through successive alterations of model parameters.

- b) The receiver used was an early prototype of the SMARTem system, which at the time was still at the pre-commercial stage. The system featured a 486 processor which enabled the user to remove cultural noise and perform signal analysis. Improved data visualisation is also noted. For an in-depth technical description of the SMARTem and its capabilities, the reader is referred to Duncan *et al.* (1998). The system designer, Andrew Duncan, was actively present during the surveys demonstrating the receiver's capabilities.

The two geophysical survey techniques employed, together with their respective aims were:

- a) the Downhole Transient Electromagnetic (DHTEM) method, which utilised both an inductively well coupled and offset transmitter loop, and;
 c) the Downhole Magnetometric Resistivity (DHMMR) method, with grounded dipoles placed along strike of the mineralisation.

Note, the purpose of the DHTEM survey was to investigate further the ability of an offset loop to galvanically excite a target, in conjunction with the traditional inductive excitation with a near loop. In both cases four boreholes were surveyed; surveys conducted with boreholes ID3071 and ID3039 (Chapter Six) were used to study the shallow lode, whilst the boreholes ID3418 and ID3419 (Chapter Eight) were used for the deep lode.

CHAPTER TWO

CLASSICAL ELECTROMAGNETIC THEORY.

2.1. INTRODUCTION.

The origins of both inductive and current channelling phenomena, within downhole TEM surveys for impulse systems, can be traced from the expanding host current systems established by a rectilinear transmitter loop in which the current has been terminated abruptly. Current channelling effects arise within downhole TEM surveys from the concentration of the host currents into local conductivity inhomogeneities or targets; inductive effects will arise from closed current vortices induced, within such targets, by the collapsing primary magnetic field of the diffusing host current system (McNeill *et al.*, 1984). A review of classical electromagnetic theory is provided within this chapter, in addition to an introductory discussion on the mathematical theory of propagating electromagnetic disturbances within conductive media. Unnecessary derivations and rigorous proofs have been avoided to maintain clarity and coherency.

Topics discussed within this chapter include:

- Revision of the fundamentals of electromagnetic theory, namely Maxwell's equations.
- The derivation of the vector Helmholtz equations in terms of the electric **E** and magnetic **H** field intensities, and discussion of the diffusive nature of EM wave propagation in conductive media.
- The quasi-static approximation.
- Solutions to the 1D Helmholtz equations are presented for the following:
 - i. A plane wave with a sinusoidal time dependence (which are used to illustrate the concept of skin depth).

- ii. Impulsive electric and magnetic field sources within a homogeneous whole-space (which are used to illustrate delay, broadening, attenuation and propagation of a source impulse in conductive media).
- The respective theories of propagation of an induced current image, and transient response of a circular loop (finite source) and vertical magnetic dipole VMD (point source) are discussed.

The review of electromagnetic theory is completed with a discussion on the concept of the "smoke ring" approximation, proposed by Nabighian (1979), which is often used to explain diffusing electromagnetic fields established in a conductive homogeneous half-space by a VMD.

2.2. MAXWELL'S EQUATIONS.

Maxwell's equations are four uncoupled partial differential equations that form the basis of classical electromagnetic theory. They describe the interactions between electric and magnetic fields, and their sources such as charge and current density. Encompassed within these equations are the empirical laws of Gauss, Faraday and Ampère (Hecht, 1987). In the presence of charge and current sources, Maxwell's equations will assume an inhomogeneous form (Strauss, 1992).

- MAXWELL'S EQUATIONS IN DIFFERENTIAL OR POINT FORM¹:

$$\nabla \cdot \mathbf{D} = \rho_T \quad (\text{Gauss's law for electricity}), \quad (2.1a)$$

$$\nabla \cdot \mathbf{B} = 0 \quad (\text{Gauss's law for magnetism}), \quad (2.1b)$$

$$\nabla \times \mathbf{E} + \partial_t \mathbf{B} = 0 \quad (\text{Faraday's law}), \quad (2.1c)$$

$$\nabla \times \mathbf{H} - \partial_t \mathbf{D} = \mathbf{J}_T \quad (\text{Ampère-Maxwell law}). \quad (2.1d)$$

(After Halliday and Resnick, 1988; Lorrain and Corson, 1990).

The operator ∂_t denotes the partial derivative with respect to time. Application of the Divergence Theorem and Stokes' Theorem to Equations (2.1) yields the integral form of Maxwell's equations:

- DIVERGENCE THEOREM:

$$\int_{\partial D} \mathbf{A} \cdot d\mathbf{x}^2 = \int_D (\nabla \cdot \mathbf{A}) dx^3, \quad (2.2a)$$

- STOKES' THEOREM:

$$\oint_{\partial S} \mathbf{A} \cdot d\mathbf{x} = \int_S (\nabla \times \mathbf{A}) \cdot d\mathbf{x}^2, \quad (2.2b)$$

where D is a closed region bounded by the surface ∂D .
(After Kreyszig, 1988).

where S is closed surface bounded by the curve ∂S .

- MAXWELL'S EQUATIONS IN INTEGRAL FORM (After Lorrain and Corson, 1990):

$$\epsilon_0 \int_{\sigma} \mathbf{E} \cdot d\mathbf{x}^2 = Q_T, \quad (2.3a) \quad \oint_{\lambda} \mathbf{E} \cdot d\mathbf{x} = -\partial_t \int_{\sigma} \mathbf{B} \cdot d\mathbf{x}^2 = -\Phi_T, \quad (2.3c)$$

$$\int_{\sigma} \mathbf{B} \cdot d\mathbf{x}^2 = 0, \quad (2.3b) \quad \oint_{\lambda} \mathbf{B} \cdot d\mathbf{x} = \mu_0 \int_{\sigma} (\mathbf{J}_M + \epsilon_0 \partial_t \mathbf{E}) \cdot d\mathbf{x}^2 = \mu_0 I_T, \quad (2.3d)$$

where σ is a closed surface.

Where λ is the closed curve or boundary of the surface σ .

¹ See Table 2A.1 of Appendix 2A for a list of the symbols used within this chapter.

In respect to the integral form of Maxwell's Equations, Equation (2.3a) merely states that the total electric flux ($\epsilon_0 \mathbf{E}$) through a closed surface σ will be proportional to the total quantity of free charge Q_T enclosed within that surface. Whilst Equation (2.3d) states that the circulation of the magnetic field intensity about the closed curve λ , is directly proportional to component of the current normal to the surface enclosed by that path \mathbf{J}_M , in addition to the time rate of change of the electric displacement ($\epsilon_0 \partial_t \mathbf{E}$).

Maxwell's Equations in differential form can be summarised as follows:

- Gauss's law for electricity, Equation (2.1a), states that the divergence of the total electric flux \mathbf{D} from a region of space will be equal to the total charge density ρ_T contained within that region. For example, the electric field associated with a point negative, or positive, charge in free space will be found to be directed radially inwards, or outwards, respectively from each charge. Gauss's law equates to the conservation of charge, and by application of Ohm's law, see Section 2.2.2, it can be re-expressed as the equation of continuity: $\nabla \cdot \mathbf{J} + \partial_t \rho = 0$.
- Gauss's law for magnetism, Equation (2.1b), states that the divergence of all magnetic fields \mathbf{B} are identically zero, that is *magnetic monopoles*, or *magnetic charges*, do not exist or at least they have not been observed.
- Faraday's law, Equation (2.1c), states that a divergence free circulating electric field \mathbf{E} , may be established by a time varying magnetic field \mathbf{B} . For example a current may be induced within a closed loop of wire if a bar magnet is permitted to pass through it.
- The Ampère-Maxwell law, Equation (2.1d), states that a divergence free circulating magnetic field \mathbf{H} may be established about a current density \mathbf{J} , such as a current carrying wire, or from a time varying electric flux density \mathbf{D} , such as the collapsing electric field between two electrified plates².

² The term $\partial_t \mathbf{D}$, or $\epsilon_0 \partial_t \mathbf{E}$, within the Ampère-Maxwell law of Maxwell's equations is referred to as the *displacement current*, and has units of amperes as does the more familiar *conduction current* (Lorrain and Corson, 1990).

2.2.1. THE AUXILIARY EQUATIONS.

Typically, Maxwell's equations are coupled by use of the associated linear free-space (vacuum) *constitutive* or *auxiliary* equations (Hayt, 1981; Ward and Hohmann, 1988; Weeks, 1964), which relate the *magnetic induction* \mathbf{B} to the *magnetic field intensity* \mathbf{H} :

$$\mathbf{B} = \mu_0 \mathbf{H}, \quad (2.4)$$

and the *electric displacement* \mathbf{D} to the *electric field intensity* \mathbf{E} :

$$\mathbf{D} = \epsilon_0 \mathbf{E}. \quad (2.5)$$

In the presence, however, of an electrically polarizable material, or *dielectric*, of *polarization*³ \mathbf{P} , the expression for the *electric displacement* \mathbf{D} will become

$$\mathbf{D} = \epsilon_0 \mathbf{E} + \mathbf{P}. \quad (2.6)$$

The class of materials referred to as dielectrics, or insulators, differ from conductors in that their conductivity is presumed to be zero (Weeks, 1964; Lorrain and Corson, 1990). Charges within dielectrics are bounded, so that on application of an electric field, for example, there will be no transportation or migration of charge within the material. Although conduction currents cannot be initiated within dielectrics, charges can be displaced by an applied electromotive force (Weeks 1964; Lorrain and Corson, 1990). It is by this mechanism in which dielectrics interact with an electric field. In particular, polarisation of a dielectric can occur in the following ways:

1. Dipole moments can be induced within molecules by means of charge displacement (Weeks, 1964; Lorrain and Corson, 1990).
2. Some dielectrics possess permanent microscopic electric dipoles that, in their natural state, are randomly orientated resulting in a zero net field. Alignment of these dipoles, however, may occur either singly or within groups called domains, by application of an external electric field (Weeks, 1964; Lorrain and Corson, 1990).

³ The *polarization* \mathbf{P} of a *dielectric*, pertains to the macroscopic properties of a collection of electric dipoles within a material, and can be defined as the electric-dipole moment \mathbf{p} of the material per unit volume. The concept of the dipole moment \mathbf{p} , arises from the observation that an electric dipole, will in general, experience a torque that is proportional to the strength of the applied electric field, and to the magnitude of the charges that comprise the dipole, and to their separation (Weeks, 1964).

In the presence of magnetically polarizable materials, of *magnetic polarization*⁴ \mathbf{M} , the *auxiliary* equation relating the *magnetic induction* \mathbf{B} to the *magnetic field intensity* \mathbf{H} will become

$$\mathbf{B} = \mu_0(\mathbf{H} + \mathbf{M}). \quad (2.7)$$

The magnetisation of a substance can be considered to be the cumulative effect of the alignment of *microscopic magnetic dipoles* (Weeks, 1964). These dipoles occur as closed current loops, or *Amperian currents* (Hayt, 1981), whose dimensions are comparable to that of atoms and molecules. In most materials, these microscopic dipoles are of random orientation and so exhibit a zero net field (Weeks, 1964). On application of an external field, however, these dipoles will experience a torque and will tend to align themselves with the applied field (Weeks, 1964). Consequently, the field contributions made by the aligned dipoles will reinforce one another resulting in a non-zero net field (Weeks, 1964). It is by this mechanism that a *magnetised* substance can interact with an external magnetic field (Weeks, 1964).

Unfortunately, the *auxiliary* equations relating \mathbf{D} , \mathbf{E} and \mathbf{P} , Equation (2.6), and \mathbf{B} , \mathbf{H} and \mathbf{M} , Equation (2.7), are somewhat impractical due to the complicated dependence of the *polarization* \mathbf{P} , and the *magnetization* \mathbf{M} , upon the electric and magnetic field intensities, \mathbf{E} and \mathbf{H} (Weeks, 1964). The relationships, however, between \mathbf{D} and \mathbf{E} , and, \mathbf{B} and \mathbf{H} , are essentially linear for many materials with fields of moderate strengths (Weeks, 1964). That is, one may write:

$$\mathbf{B} = \mu \mathbf{H}, \quad (2.8)$$

and

$$\mathbf{D} = \epsilon \mathbf{E}. \quad (2.9)$$

Thus for linear, homogeneous, isotropic materials, it is often possible to characterise both the electric and magnetic properties of a material in terms of its *relative permittivity* ϵ_R (Lorrain and Corson 1990; Weeks, 1964), defined as:

$$\epsilon = \epsilon_0 \epsilon_R, \quad (2.10)$$

⁴ In a manner analogous to *dielectrics*, the *magnetic polarization* or *magnetization* \mathbf{M} of a magnetic material, pertains to the macroscopic properties of a collection of microscopic magnetic dipoles within a material, and can be defined as the magnetic-dipole moment \mathbf{m} of the material per unit volume (Weeks, 1964).

and its *relative permeability* μ_R , defined as:

$$\mu = \mu_0 \mu_R. \quad (2.11)$$

In the event of an encounter with an *anisotropic* material, the *permittivity* ϵ and/or the *permeability* μ will necessarily assume the form of a *tensor*, as opposed to that of a *scalar* (Weeks, 1964). It is to be noted that for this situation the expressions (2.8) and (2.9) will remain true, except \mathbf{B} , \mathbf{H} and \mathbf{M} , and, \mathbf{D} , \mathbf{E} and \mathbf{P} , will in general be no longer parallel (Weeks, 1964).

2.2.2. CURRENT DENSITY.

In general, the total current density \mathbf{J}_T depicted in Maxwell's Equations can be expressed as the sum of current density of free charges, the polarization current density and the equivalent current density within magnetised matter:

$$\mathbf{J}_T = \mathbf{J}_f + \partial_t \mathbf{P} + \nabla \times \mathbf{M}, \quad (2.12)$$

(Lorrain and Corson, 1990). The portion of current density arising from free charges \mathbf{J}_f can in turn be decomposed into three components⁵, namely *conduction*, *convection* and *source* currents (Lorrain and Corson, 1990; Weeks, 1964):

$$\mathbf{J}_f = \mathbf{J}_{\text{conduction}} + \mathbf{J}_{\text{convection}} + \mathbf{J}_{\text{source}}. \quad (2.13)$$

The first term of Equation (2.13), represents *conduction currents*, those currents which will arise within a *conductor* upon application of an electromotive force. Indeed, for many ordinary conducting linear, homogeneous, isotropic materials, the current density will be directly proportional to the applied electric field intensity:

$$\mathbf{J}_{\text{conduction}} = \sigma \mathbf{E} \quad (\text{Ohm's law}), \quad (2.14)$$

where σ is the *conductivity* of the conductive medium and has the SI unit of Siemens (Lorrain and Corson, 1990). Materials that obey Ohm's Law are termed *Ohmic*. In the event that a conductor is anisotropic, the scalar conductivity term in Equation (2.14), will necessarily assume a tensor or matrix form (Weeks, 1964).

⁵ Note: Contributions to total current flow depend upon the electrodynamic system under consideration. In particular, one may need to include an electrostatic current term to account for the migration of ions within a solution (Lorrain and Corson, 1990). However, for geophysical applications and modelling dealt within this project, it sufficed to consider only the conduction and source current terms.

The second term of Equation (2.13) is the *convection current*, and represents the component of the current that moves within free-space according to the laws of mechanics and the Lorentz force equation:

$$\mathbf{F} = q \mathbf{E} + q(\mathbf{v} \times \mathbf{B}), \quad (2.15)$$

where \mathbf{F} is the force exerted upon a charge q moving with velocity \mathbf{v} , within a electric \mathbf{E} and magnetic \mathbf{B} field (Hayt, 1981; Weeks, 1964).

The last term of Equation (2.13) is the *source current density*, and represents a current that is injected into a region and is able to be maintained independently of any external influences, *i.e.*, by either \mathbf{E} or \mathbf{H} (Weeks, 1964). Note that in free-space the current components $\mathbf{J}_{\text{convection}}$ and $\mathbf{J}_{\text{source}}$ may exist but $\mathbf{J}_{\text{conduction}}$ cannot, whilst within an insulator only the source current may remain non-zero (Weeks, 1964). Furthermore, it should be noted that both permittivity and permeability might also be dependent on position regardless if their form is scalar or tensor (Weeks, 1964).

Once the form of the generalised constitutive relations have been established for the problem at hand, both the electric displacement and magnetic induction can be eliminated from Maxwell's equations (Weeks, 1964). Assuming the current density is known either explicitly or implicitly as a function of either \mathbf{E} or \mathbf{H} , or both, there will remain two equations for the two unknowns \mathbf{E} and \mathbf{H} (Weeks, 1964). Hence in brief, the electromagnetic effects within material bodies can be described by the electrical parameters ϵ , μ and σ (Lorrain and Corson, 1990; Weeks, 1964).

2.2.3. BOUNDARY CONDITIONS.

Materials with inhomogeneous electrical properties can be simplified by subdivision into smaller homogenous portions, Ward and Hohmann (1988); such that, within each portion the permittivity, permeability and conductivity are presumed to be constant. The electric and magnetic field quantities, on opposing sides of an interface between two adjoining regions, relate to one another by a set of *boundary conditions* prescribed for that interface. These relations are also known as the *continuity conditions* (Lorrain and Corson, 1990). The boundary conditions which relate the normal and tangential components of

the vector quantities \mathbf{B} and \mathbf{H} , and, \mathbf{D} and \mathbf{E} , may assume a variety of forms, including the following (Stratton, 1941; Seely and Poularikas, 1979):

- TANGENTIAL COMPONENT OF \mathbf{E} IS CONTINUOUS:

$$\hat{\mathbf{n}}_1 \times [\mathbf{E}_2(\mathbf{r}) - \mathbf{E}_1(\mathbf{r})] = 0. \quad (2.16)$$

- NORMAL COMPONENT OF \mathbf{D} IS DISCONTINUOUS:

$$\hat{\mathbf{n}}_1 \cdot [\mathbf{D}_2(\mathbf{r}) - \mathbf{D}_1(\mathbf{r})] = \rho_s(\mathbf{r}). \quad (2.17)$$

- TANGENTIAL COMPONENT OF \mathbf{H} IS DISCONTINUOUS:

$$\hat{\mathbf{n}}_1 \times [\mathbf{H}_2(\mathbf{r}) - \mathbf{H}_1(\mathbf{r})] = \mathbf{J}_s(\mathbf{r}). \quad (2.18)$$

- NORMAL COMPONENT OF \mathbf{B} IS CONTINUOUS:

$$\hat{\mathbf{n}}_1 \cdot [\mathbf{B}_2(\mathbf{r}) - \mathbf{B}_1(\mathbf{r})] = 0. \quad (2.19)$$

Subscripts 1 and 2 refer to the two adjacent regions to which the conditions are to be applied; $\hat{\mathbf{n}}_1$ denotes the outward unit normal of region 1, and points into region 2. The vector \mathbf{r} denotes the position vector.

It is noted, that the discontinuity in the normal component of the electric displacement \mathbf{D} , is proportional to the accumulated surface charge density $\rho_s(\mathbf{r})$; the discontinuity in the tangential component of the magnetic field intensity \mathbf{H} , is proportional to the presence of surface currents $\mathbf{J}_s(\mathbf{r})$.

2.2.4. RELAXATION TIME.

Any net charge on a finite conductor must reside on its surface (Lorrain and Corson, 1990). As stated by Stratton (1941): "Within a region of non-vanishing conductivity there can be no permanent distribution of free charge". This theorem was demonstrated by Stratton (1941), for an infinite, electrically homogeneous, ohmic material. By application of both Ohm's and Gauss's laws, and the Equation of Continuity, an initial charge distribution throughout a conductor was shown to decay exponentially with time, at every point, and in a manner wholly independent of the applied field. The actual time required for a charge distribution at a point to decay to e^{-1} of its initial value, within a particular material, is referred to as the *relaxation time*. In all but the weakest conductors, such as quartz, the relaxation time is exceedingly small, *e.g.*, the relaxation time of sea water is in the order of 100 picoseconds, as opposed to microseconds for distilled water (Stratton, 1941). Given that the relaxation time

for many conductors is of this order of magnitude, the diffusion of free charges within a conductor can be considered instantaneous (Stratton, 1941). Thus for most applications (at least for those considered here), Gauss's law can be equated to zero within a homogenous conductive region (Stratton, 1941):

$$\nabla \cdot \mathbf{D} = 0 \quad (\text{No free charges}). \quad (2.20)$$

Free charges, however, do not vanish entirely, so that for finite regions these charges will accumulate at the boundary interface (Stratton, 1941), and will become important when formulating the boundary conditions for that system, see Equation (2.17).

2.3. THE ELECTROMAGNETIC WAVE EQUATIONS.

The interpretation of electrical prospecting methods requires an understanding of electromagnetic theory, subsequent modelling often involves the formulation and solution of a boundary value problem (BVP) for a given system (Ward and Hohmann, 1988). Simplification of the associated mathematics can be achieved by making assumptions about the electrical properties of the given media; these may include the following as discussed within Ward and Hohmann (1988):

1. All media are considered to be homogenous, linear and isotropic in respect to the conductivity σ , permittivity ϵ , and magnetic permeability μ .
2. Inhomogeneous media are represented as the composition of numerous homogeneous regions.
3. Both the electric permittivity ϵ , and magnetic permeability μ , are assumed to be non-dispersive, *i.e.*, independent of time.

Many of the BVP's encountered can be solved in terms of the vector electric \mathbf{E} , and magnetic field \mathbf{H} , intensity functions (Ward and Hohmann, 1988). The computations for these vector field quantities arise from solving the respective wave equation for each homogeneous, isotropic and linear region. The wave equation for a given region, will assume an inhomogeneous form if sources are present, and a homogeneous form if the region is source-less (Ward and Hohmann, 1988). Solutions of the wave equations for adjacent regions are then connected by application of the prescribed boundary conditions (Ward and Hohmann, 1988). Although each wave equation is formulated specifically for each region of a given system, a generic form of these equations is presented here for the sake of discussion.

Following the procedures of Strauss (1992) and Hecht (1987), one may easily derive the electromagnetic vector wave equations for the electric \mathbf{E} and magnetic \mathbf{H} field intensities. Commencing with Maxwell's equations, see Section 2.2:

$$\nabla \times \mathbf{E} + \partial_t \mathbf{B} = 0 \quad (\text{Faraday's law}), \quad (2.21a)$$

$$\nabla \times \mathbf{H} - \partial_t \mathbf{D} = \mathbf{J} \quad (\text{Ampère-Maxwell law}). \quad (2.21b)$$

By the aforementioned assumptions, one may use the auxiliary equations, Section 2.2.1, and Ohm's Law, Section 2.2.2, to rewrite these expressions solely in terms of \mathbf{E} and \mathbf{H} :

$$\nabla \times \mathbf{E} + \mu \partial_t \mathbf{H} = 0, \quad (2.22a)$$

$$\nabla \times \mathbf{H} - \varepsilon \partial_t \mathbf{E} - \sigma \mathbf{E} = 0. \quad (2.22b)$$

Taking the curl of both expressions:

$$\nabla \times \nabla \times \mathbf{E} + \mu \partial_t \nabla \times \mathbf{H} = 0, \quad (2.23a)$$

$$\nabla \times \nabla \times \mathbf{H} - \varepsilon \partial_t \nabla \times \mathbf{E} - \sigma \nabla \times \mathbf{E} = 0, \quad (2.23b)$$

and resubstituting Equations (2.22), will yield

$$\nabla \times \nabla \times \mathbf{E} - \varepsilon \mu \partial_{tt} \mathbf{E} - \sigma \mu \partial_t \mathbf{E} = 0, \text{ and} \quad (2.24a)$$

$$\nabla \times \nabla \times \mathbf{H} - \varepsilon \mu \partial_{tt} \mathbf{H} - \sigma \mu \partial_t \mathbf{H} = 0. \quad (2.24b)$$

By application of the following vector identity⁶:

$$\nabla \times \nabla \times \mathbf{A} = \nabla(\nabla \cdot \mathbf{A}) - \Delta \mathbf{A} \quad (2.25)$$

and recalling Gauss's laws for electric and magnetic fields, see Section 2.2, one will acquire:

• THE ELECTROMAGNETIC WAVE EQUATIONS (See also Hecht, 1987):

$$\Delta \mathbf{E} - \varepsilon \mu \partial_{tt} \mathbf{E} - \sigma \mu \partial_t \mathbf{E} = \nabla(\rho/\varepsilon), \quad (2.26a)$$

$$\Delta \mathbf{H} - \varepsilon \mu \partial_{tt} \mathbf{H} - \sigma \mu \partial_t \mathbf{H} = 0. \quad (2.26b)$$

These are the electromagnetic wave equations, or alternately, the vector Helmholtz equations for a conductive homogeneous, linear, isotropic medium.

These equations can be rewritten in a compact form:

$$(\Delta + k^2) \mathbf{H} = 0, \quad (2.27a)$$

$$(\Delta + k^2) \mathbf{E} = 0, \quad (2.27b)$$

where the operator k is defined as

$$k^2 = -(\varepsilon \mu \partial_{tt} + \sigma \mu \partial_t). \quad (2.28)$$

The vector Helmholtz equations form the essence of interpreting inductive and TEM induced galvanic effects. Although programs⁷ MARCO and LEROI implement wave equations such as these without the attention of the user,

⁶The Laplacian operator Δ , when applied to a vector quantity in Cartesian coordinates is treated as such: $\Delta \mathbf{A} = \Delta A_1 \mathbf{i} + \Delta A_2 \mathbf{j} + \Delta A_3 \mathbf{k}$ (Kreyszig, 1988).

⁷Descriptions of the numerical packages MARCO and LEROI are provided within Chapter Three. These programs were chosen for use within this project to forward model the data sets of the Cadjebut mineralisation - Chapter Five, and the Flying Doctor Deposit - Chapters Six and Eight.

understanding the generic form the electromagnetic wave equation will equip one with insight into the physics of the problem. At this stage, I shall take the opportunity to attach some physical meaning to the generic Helmholtz equations, Equations (2.26). Firstly, if one were to evaluate these equations for a non-conducting and source-less medium, namely the vacuum of free space, one would obtain

$$\Delta \mathbf{E} - \varepsilon_0 \mu_0 \partial_{tt} \mathbf{E} = 0, \quad (2.29a)$$

$$\Delta \mathbf{H} - \varepsilon_0 \mu_0 \partial_{tt} \mathbf{H} = 0. \quad (2.29b)$$

Now comparing Equations (2.29) with that of the prototype scalar wave equation:

$$\Delta \Psi(\mathbf{x}, t) - \frac{1}{v^2} \partial_{tt} \Psi(\mathbf{x}, t) = 0, \quad (2.21)$$

(After Strauss, 1992)

which describes the propagation of a disturbance Ψ travelling at speed v , one may immediately infer that the solution to the Helmholtz equation in free space, would describe the propagation of an electromagnetic wave, with speed c given by

$$\mu_0 \varepsilon_0 \cdot c^2 = 1. \quad (2.22)$$

What physical meaning may one infer from the terms with a 1st order time derivative within Equations (2.26)? Consider the prototype diffusion equation, which describes phenomena such as conduction:

$$\Delta \Psi(\mathbf{x}, t) - k \cdot \partial_t \Psi(\mathbf{x}, t) = 0, \quad (2.23)$$

(After Strauss, 1992)

where k is a constant of proportionality. By comparing the form of the diffusion equation with that of the electromagnetic wave equations, Equations (2.26), one may infer that for a host medium of non-zero conductance, diffusion of the electric \mathbf{E} , and magnetic \mathbf{B} , field intensities will occur. Thus in conjunction with the Laplacian operator, one may intuitively attribute the terms within Equations (2.26) with a 1st and 2nd order time derivative to diffusion and wave phenomena respectively.

2.4. THE QUASI-STATIC APPROXIMATION.

Consider now, as in Ward and Hohmann (1988), a harmonic or sinusoidal time dependence for the electric and magnetic fields:

$$\mathbf{E}(\mathbf{x}, t) = \mathbf{E}_0(\mathbf{x}, t) e^{i\omega t}, \quad (2.33a)$$

$$\mathbf{H}(\mathbf{x}, t) = \mathbf{H}_0(\mathbf{x}, t) e^{i\omega t}, \quad (2.33b)$$

where,

$$\omega = 2\pi\nu \quad (\text{Angular Frequency}). \quad (2.34)$$

By use of the effective operator exchange

$$\partial_t \leftrightarrow i\omega \quad \text{and} \quad \partial_{tt} \leftrightarrow -\omega^2,$$

the wave number defined in Equation (2.28), can be rewritten for the frequency domain:

$$k^2 = \omega^2 \mu \epsilon - i\omega \mu \sigma. \quad (2.35)$$

The parameter k , is referred to as either the propagation constant, as within Telford *et al.* (1990), or the wave number, as within Keller (1988) and Ward and Hohmann (1988). In reference to the electromagnetic wave equations, Equations (2.27), the first term of Equation (2.35) pertains to displacement currents and the second term to conduction currents. In non-conducting media of zero conductivity ($\sigma_n = 0$), Equation (2.35) reduces to

$$k^2 = \omega^2 \mu \epsilon, \quad (2.36)$$

so that one deals exclusively with wave phenomena. Moreover, the wave formula

$$\lambda = c\tau = c/\nu, \quad (2.37)$$

describing a wave of wavelength λ , period τ and frequency ν combined with Equations (2.31) and (2.34), permits the wave number k in free-space, Equation (2.36), to be expressed in a more familiar form as in Hecht (1987):

$$k = 2\pi/\lambda. \quad (2.38)$$

Unlike free-space, an EM wave attenuates as it travels through a conducting medium (Telford *et al.*, 1990). A basic measure of attenuation is the concept of *skin depth*, a measure that is inversely proportional to the product of the harmonic (plane wave) field frequency and host medium conductivity (see Section 2.5). To minimise attenuation in the earth, geophysical EM prospecting

methods typically employ low frequencies, within the frequency domain, or late times, within the time domain (Ward and Hohmann, 1988). At very low frequencies, less than 10^5 Hz for earth materials, the inequality $\omega^2 \mu \epsilon \ll \omega \mu \sigma$ is observed and displacement currents can be considered to be significantly less than conduction currents (Ward and Hohmann, 1988). Under these conditions the wave equations, Equations (2.27), reduce to diffusion equations as the wave number k , Equation (2.35), simplifies to

$$k^2 \approx i\omega \mu \sigma. \quad (2.39)$$

It is this dependence upon diffusion effects, which accounts for the attendant lack of resolution of conductivity anomalies within EM surveys (Ward and Hohmann, 1988). If in the instance that displacement currents are negligible within non-conducting media, the wave number can be approximated to zero, permitting the reduction of the homogeneous wave equations, Equations (2.27), to Laplace's equation; whereas the inhomogeneous form of the wave equations will reduce to Poisson's equation. Note Laplace's equation describes both diffusion and wave processes that are time independent (Strauss, 1992). Electric and magnetic field intensities are said to be quasi-stationary or quasi-static, if they are sufficiently slow varying that displacement currents ($\partial_t \mathbf{D}$) and in turn wave propagation effects can be neglected (Ward and Hohmann, 1988; West and Macnae, 1991; Zaky, 1974). The spatial dimensions of EM surveys are usually much less than the corresponding free space wavelength of the harmonic field frequencies employed in EM methods, resulting in negligible phase variation due to propagation; as such the quasi-static approximation is applicable in most cases of geophysical interest (Telford *et al.*, 1990; Ward and Hohmann, 1988). Alternatively, delays times and transmitter-receiver separation distances, typically employed within TEM surveys, are well within the quasi-static limit such that time delays arising from the finite speed of light can be regarded as insignificant (Nabighian and Macnae, 1991).

The quasi-static approximation is a useful tool that can drastically simplify a given problem. Ward and Hohmann (1988) provides general expressions, within the frequency domain, for the EM field components of a step source vertical magnetic dipole (VMD) on or above the surface of a layered

earth, but the complexity of the integrands within these solutions means evaluation must proceed by numerical integration. Quasi-static analytical solutions for the time domain step and impulse response were obtained, however, for the specific case of both source and receiver residing upon the surface of a homogeneous half-space. Under the quasi-static approximation Ward and Hohmann (1988) neglected displacement currents, thereby reducing the wave number in the air layer to zero and the wave number of the conductive homogeneous earth to a simplified form as in Equation (2.39). The analytical solutions by Ward and Hohmann (1988) for a VMD source and small circular loop are discussed within Sections 2.6 and 2.7 respectively.

2.5. 1-D SOLUTIONS TO THE WAVE EQUATIONS.

Current gathering phenomena occurring in downhole TEM surveys result from the perturbation of host currents by a conductivity anomaly (McNeill *et al.*, 1984; Newman *et al.*, 1989). To begin the discussion of the behaviour of induced host currents within a homogeneous half space, consider first the solution of the wave equations, Equations (2.26), given by Ward and Hohmann (1988), for an impulsive electric and magnetic field source at $z = 0$ in a homogeneous whole-space under the quasi-static approximation:

$$\begin{bmatrix} \mathbf{E} \\ \mathbf{H} \end{bmatrix} = \begin{bmatrix} \mathbf{E}_0^+ \\ \mathbf{H}_0^+ \end{bmatrix} \frac{(\mu\sigma)^{1/2} z}{2\pi^{1/2} t^{3/2}} e^{-\mu\sigma z^2 (4t)^{-1}}. \quad (2.40)$$

The behaviour of both fields with time, and distance z , is illustrated within Figure 2.1. In the case of the free space solution, namely $\sigma = 0$, one would find the fields to be an impulse response at time (z/c) , where c is the speed of light in a vacuum. For a conductive medium, however, this impulse will be delayed, broadened and attenuated (Ward and Hohmann, 1988). By taking the derivative of Equation (2.40), it is possible to compute both the temporal and spatial loci of the maximum of the propagating impulse. Thus for a given position along the z -axis, the time of arrival of the impulse maxima t_{max} , will be

$$t_{max} = \frac{\mu\sigma z^2}{6}, \quad (2.41)$$

and the position of the field maximum z_{max} , or *penetration depth*, at time t will be

$$z_{max} = \left(\frac{2t}{\mu\sigma} \right)^{1/2}. \quad (2.42)$$

Finally, by taking the derivative of Equation (2.42), one will obtain the speed of propagation of the field maximum:

$$V = \frac{dz_{max}}{dt} = \frac{1}{(2\mu\sigma t)^{1/2}}. \quad (2.43)$$

(After Ward and Hohmann, 1988: Eq. 1.64).

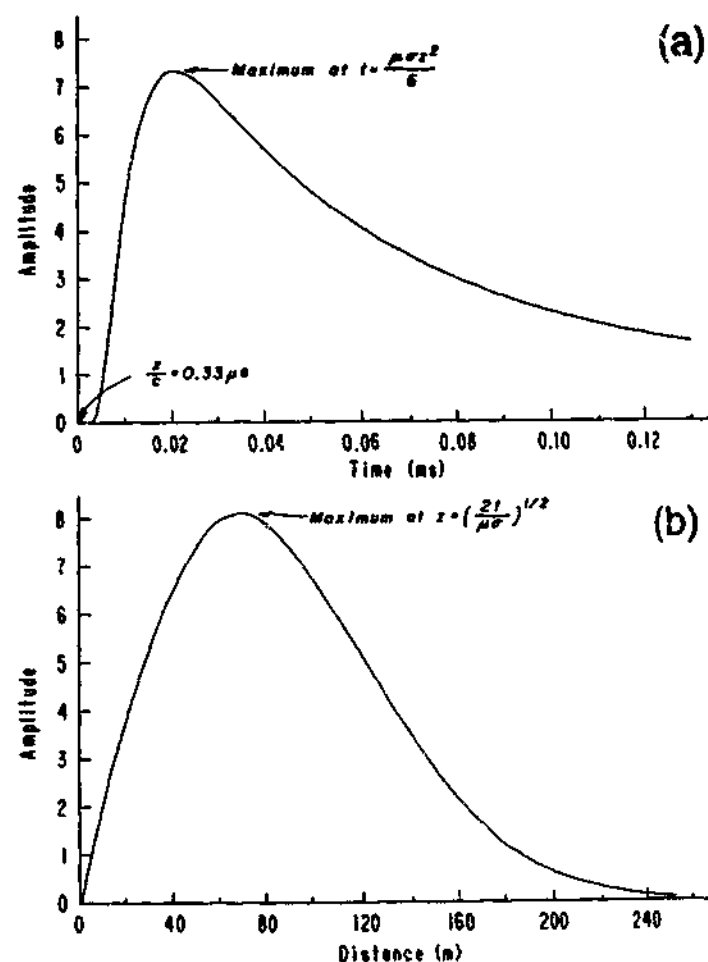


Figure 2.1: The electric and magnetic fields as a function of a) time, and b) distance, for a 1D impulse source in a 0.01 Sm^{-1} whole space at 0.03 ms . Note that in free space the fields would remain an impulse with the propagation speed equal to the speed of light in a vacuum. (After Ward and Hohmann, 1988: Fig. 1.2).

An interesting comparison was made by Ward and Hohmann (1988): there is a conceptual similarity between the *penetration depth* of an impulsive source, and the *skin depth*⁸ δ of a 1D sinusoidal time-dependent plane wave undergoing attenuation as it propagates along the z -axis, notably

$$\delta = \left(\frac{2}{\omega \mu \sigma} \right)^{1/2}. \quad (2.44)$$

Comparing Equations (2.44) and (2.42), it is noted that the skin depth is proportional to $\omega^{-1/2}$, whereas the penetration depth is proportional to $t^{1/2}$, as suggested by Ward and Hohmann (1988).

⁸ In the current context, the skin depth refers to the distance to be traversed by a plane wave for its amplitude to be attenuated by a factor of $1/e$.

2.6. TRANSIENT RESPONSE OF A VERTICAL MAGNETIC DIPOLE.

Presented within this section are the analytic expressions for the transient response of a vertical magnetic dipole whose moment has been terminated abruptly. It is emphasised that these expressions were derived under the quasi-static approximation for the special case in which both the transmitter and receiver reside upon the surface of a homogenous earth (Ward and Hohmann, 1988). The original derivations of these analytic solutions by Ward and Hohmann (1988) include the general expressions for the horizontal, or azimuthal, electric field, and both the horizontal and vertical components of the magnetic field intensity on or above the surface of a layered earth. Unfortunately, these expressions are cumbersome and can only be evaluated by numerical means. The derivations by Ward and Hohmann (1988), for the expressions describing the EM fields of a VMD on a homogenous earth which has been terminated abruptly, are quite involved and shall not be reproduced here, hence the expressions for the azimuthal electric field, and the radial and vertical components of the magnetic field intensity, shall be stated here without proof. All expressions are stated in cylindrical coordinates, namely (r, ϕ, z) : r is the radial distance measured from the z -axis (in this case the centre of the VMD since the receiver resides at the surface), ϕ is the azimuthal or angular position defined to be positive if its circulation (in terms of the curl operator) is in the positive z -direction, and z has its usual meaning, but is defined as positive pointing down. The radial position r is defined in terms of the Cartesian coordinates (x, y) as

$$r^2 = x^2 + y^2. \quad (2.45)$$

The azimuthal component of the TD electric field measured at the surface of a homogeneous earth and a radial distance r from a VMD is given by

• STEP RESPONSE (After Ward and Hohmann, 1988: Eq. 4.64):

$$E_\phi(r, t) = -\frac{m}{2\pi\sigma r^2} \left[3\text{erf}(\theta r) - 2\pi^{-1/2}\theta r(3 + 2\theta^2 r^2)e^{-\theta^2 r^2} \right], \quad (2.46)$$

where the parameter θ , with units of metres^{-1} , is defined by

$$\theta^2 = \left(\frac{\mu_0 \sigma}{4t} \right). \quad (2.47)$$

The step response for the vertical component of the magnetic field intensity is

- STEP RESPONSE (After Ward and Hohmann, 1988: Eq. 4.69a):

$$H_z(r,t) = \frac{m}{4\pi r^3} \left[\operatorname{erf}(\theta r) \left(\frac{9}{2\theta^2 r^2} - 1 \right) - \pi^{-1/2} \left(\frac{9}{\theta r} + 4\theta r \right) e^{-\theta^2 r^2} \right]. \quad (2.48)$$

Furthermore, the magnetic field impulse response can be obtained by taking the time derivative of the step response, Equation (2.48):

- IMPULSE RESPONSE (After Ward and Hohmann, 1988: Eq. 4.70):

$$\partial_t H_z(r,t) = -\frac{m}{2\pi\mu_0\sigma r^5} \left[9\operatorname{erf}(\theta r) - 2\theta r \pi^{-1/2} (9 + 6\theta^2 r^2 + 4\theta^4 r^4) e^{-\theta^2 r^2} \right]. \quad (2.49)$$

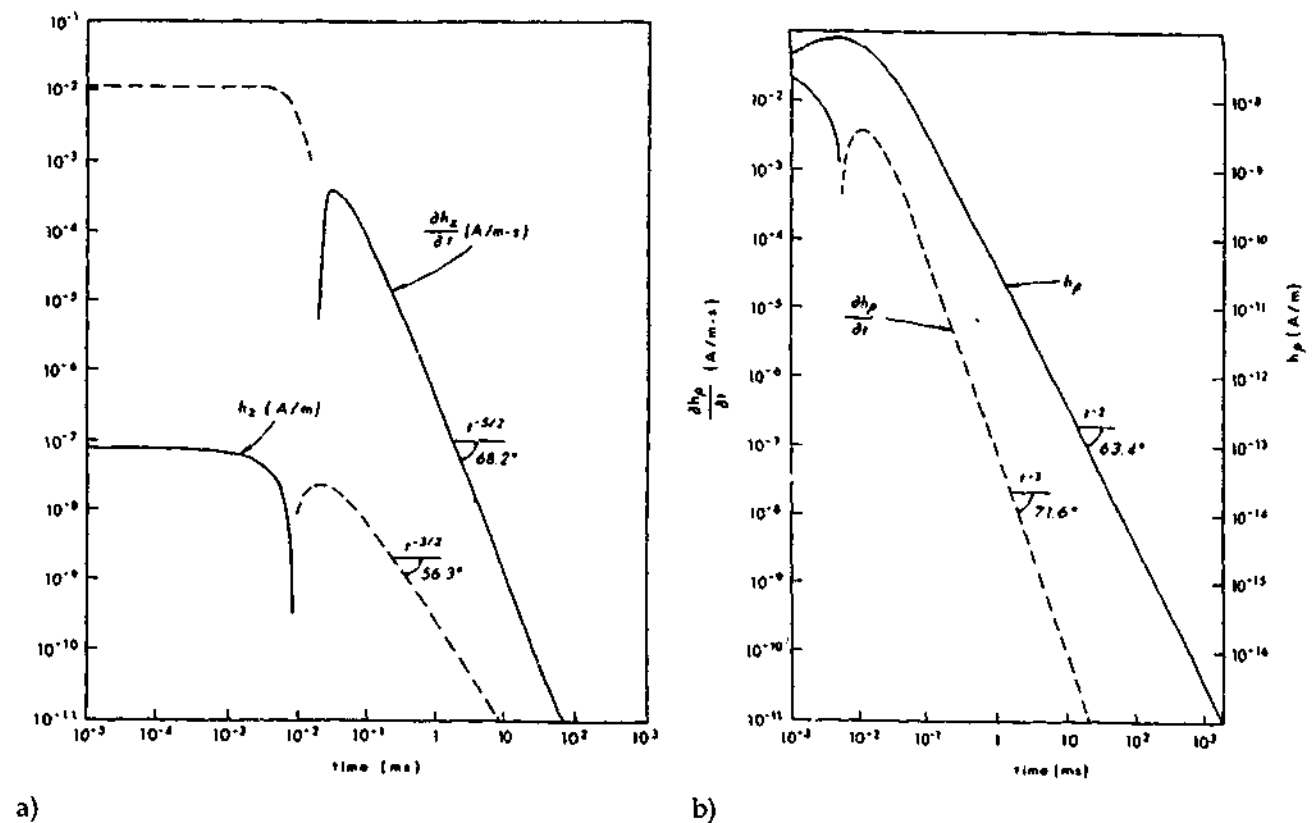
The behaviour of the vertical components of the magnetic field intensity and its time derivative, as governed by Equations (2.48) and (2.49), are illustrated within an example reproduced from Ward and Hohmann (1988), and shown within Figure 2.2a. In this example, the receiver was located at a radial distance of 100 m from a unit vertical magnetic dipole, both of which resided upon the surface of a homogeneous 100 ohm.m half-space.

At the time of termination of the dipole moment a current image will be established at the surface of the earth, these induced surface currents will be distributed in such a manner so as to oppose the collapse of the primary field. This current system will in turn propagate outward and downwards into the earth whilst diffusing with time, and shall be responsible for the decaying magnetic field as described by Equation (2.48) at subsequent times, Ward and Hohmann (1988) (See also discussions by Nabighian and Macnae, 1991, and McNeill *et al.*, 1984).

The effects of the expanding host current system are clearly shown within Figure 2.2. Although the dipole is directed upward, the z-component of the fields at the receiver is considered positive if directed downward. In particular, the vertical component of the magnetic field is seen to undergo a positive to negative sign change, near the time the current maximum passes beneath the receiver. Likewise, the time derivative of the magnetic field also changes in sign from negative to positive, but at a short time later. This can be understood in terms of the "smoke ring" concept as proposed by Nabighian (1979), who demonstrated that the magnetic field intensity at the surface of a

homogeneous earth due to currents induced by a VMD can be approximated by an equivalent single circular filament of current, or "smoke ring".

Thus for a "smoke ring" whose current circulation (in terms of the curl operator) is directed upwards, the vertical component of the associated magnetic field intensity at the surface directly above the loop interior will be negative in sign, whilst for regions above the loop exterior the vertical component will be positive. Thus, as the current maximum within the "smoke ring" expands past the region of earth beneath the receiver, the magnetic field will be expected to pass from being a positive to a negative decaying field, in turn its derivative will pass from being negative to positive in sign accordingly.



a)

b)

Figure 2.2: The a) vertical, and b) horizontal, magnetic field and its time derivative at a distance of 100 m from a vertical magnetic dipole which has been terminated abruptly. Both the source and receiver reside upon the surface of a 100 ohm.m homogeneous half-space. Dashed lines indicate a negative response. (After Ward and Hohmann, 1988: Figs. 4.4 and 4.5).

The late-time asymptotic forms for the *step* and *impulse* responses, Equations (2.48) and (2.49), are given by the following expressions, Equations (2.50) and (2.51) respectively.

- ASYMPTOTIC STEP RESPONSE (After Ward and Hohmann, 1988: Eq. 4.70a):

$$H_z(t) = \frac{m}{30} \left(\frac{\sigma\mu_0}{\pi} \right)^{3/2} t^{-3/2}, \quad (2.50)$$

- ASYMPTOTIC IMPULSE RESPONSE (After Ward and Hohmann, 1988: Eq. 4.70b):

$$\partial_t H_z(t) = -\frac{m}{20} \left(\frac{\sigma \mu_0}{\pi} \right)^{3/2} t^{-5/2}. \quad (2.51)$$

Finally, the associated equations for the horizontal component of the magnetic field intensity and its time derivative are given by the following:

- STEP RESPONSE (After Ward and Hohmann, 1988: Eq. 4.72):

$$H_\rho(r,t) = -\frac{m\theta^2}{2\pi r} e^{-\frac{1}{2}\theta^2 r^2} \left[I_1 \left(\frac{\theta^2 r^2}{2} \right) - I_2 \left(\frac{\theta^2 r^2}{2} \right) \right], \quad (2.52)$$

- IMPULSE RESPONSE (After Ward and Hohmann, 1988: Eq. 4.74):

$$\partial_t H_\rho(r,t) = \frac{m\theta^2}{2\pi r t} e^{-\frac{1}{2}\theta^2 r^2} \left[(1 + \theta^2 \rho^2) I_0 \left(\frac{\theta^2 r^2}{2} \right) - \left(2 + \theta^2 \rho^2 + \frac{4}{\theta^2 \rho^2} \right) I_1 \left(\frac{\theta^2 r^2}{2} \right) \right]. \quad (2.53)$$

The associated late-time asymptotic expressions for Equations (2.52) and (2.53), are

- ASYMPTOTIC STEP RESPONSE (After Ward and Hohmann, 1988: Eq. 4.73):

$$H_\rho(r,t) \approx -\frac{mr\mu_0^2\sigma^2}{128\pi} t^{-2}, \quad (2.54)$$

- ASYMPTOTIC IMPULSE RESPONSE (After Ward and Hohmann, 1988: Eq. 4.75):

$$\partial_t H_\rho(r,t) \approx \frac{mr\mu_0^2\sigma^2}{64\pi} t^{-3}. \quad (2.55)$$

Plots of Equations (2.52) and (2.53) representing the horizontal component for the magnetic step and impulse responses respectively, are shown within Figure 2.2b and are reproduced from Ward and Hohmann (1988). As before, the receiver is located at a radial distance of 100 m from a unit dipole, whilst the resistivity of the homogeneous earth assumed a value of 100 ohm.m. Both the source and receiver are located at the surface. As this figure shows, the horizontal component of the magnetic field intensity will remain positive for all time. Although initially positive, the time derivative of this field becomes negative as the current maximum passes beneath the receiver. This event also coincides with maxima of the magnetic step impulse.

2.7. TRANSIENT RESPONSE OF A CIRCULAR LOOP.

In practise, a vertical magnetic dipole is approximated by a flat-lying horizontal loop of finite-size. The most widely used source within EM surveys is a large rectangular loop. Unfortunately, no analytical solutions exist for the general case of a rectangular loop on either a layered or homogeneous earth (Ward and Hohmann, 1988). Analytical solutions do exist, however, for particular source-receiver configurations that utilise a circular transmitter loop. One is justified in using these solutions, given that a circular loop will provide a reasonable approximation to a square loop of equal area, in configurations where the receiver is located either at the centre of the loop, or at a considerable distance from it (Ward and Hohmann, 1988). The analytic solutions reproduced here from Ward and Hohmann (1988), are for the transient response of a *central-loop* configuration on the surface of a homogenous half-space.

The vertical component of the magnetic field after current shut-off, or step response, is given by Equation (2.56).

- STEP RESPONSE (After Ward and Hohmann, 1988: Eq. 4.98):

$$H_z(t) = \frac{I}{2a} \left[\frac{3}{\pi^{1/2} \theta a} e^{-\theta^2 a^2} + \left(1 - \frac{3}{2\theta^2 a^2} \right) \text{erf}(\theta a) \right]. \quad (2.56)$$

Note, that the coefficient $I/2a$ is the magnetic field intensity due to a circular loop in free space with a steady current I . The adjacent term enclosed by square brackets, results from currents flowing within the conductive earth. These currents are responsible for the decaying magnetic field after current shut-off (Ward and Hohmann, 1988). By taking the time derivative of the negative step response, Equation (2.56), one will obtain an expression for the impulse response:

- IMPULSE RESPONSE (After Ward and Hohmann, 1988: Eq. 4.97):

$$\partial_t H_z(t) = \frac{-I}{\mu_0 \sigma a^3} \left[3 \text{erf}(\theta a) - \frac{2}{\pi^{1/2}} \theta a (3 + 2\theta^2 a^2) e^{-\theta^2 a^2} \right]. \quad (2.57)$$

The late-time asymptotic relations ($\theta \ll 1$) for the step and impulse responses, Equations (2.56) and (2.57), are given by the following expressions, Equations (2.58) and (2.59) respectively.

- ASYMPTOTIC STEP RESPONSE (After Ward and Hohmann, 1988: Eq. 4.98a):

$$H_z(t) \approx \frac{I\sigma^{3/2}\mu_0^{3/2}a^2}{30\pi^{1/2}} t^{-3/2}, \quad (2.58)$$

- ASYMPTOTIC IMPULSE RESPONSE (After Ward and Hohmann, 1988: Eq. 4.98b):

$$\partial_t H_z(t) \approx \frac{-I\sigma^{3/2}\mu_0^{3/2}a^2}{20\pi^{1/2}} t^{-5/2}. \quad (2.59)$$

Thus, the vertical component of the magnetic field intensity, and its time derivative, will at the centre of a circular loop exhibit $t^{-3/2}$ and $t^{-5/2}$ power law decays respectively.

The behaviour of the magnetic field and its time derivative, as governed by Equations (2.56) and (2.57), are illustrated with Figure 2.3. It is to be noted that both the step and impulse response remain positive in sign at the centre of the loop (Ward and Hohmann, 1988). As in the case of a vertical magnetic dipole, the transient magnetic field intensity after current shut-off, is due to a system of circular currents within the earth, which circulate in the same direction as the loop current (Nabighian, 1979). These current distributions, originating as the current image of the transmitter loop, will propagate outward and downward whilst diffusing with time. It was further showed by Nabighian (1979), that these diffuse current distributions can be approximated by a circular current filament, or "smoke ring".

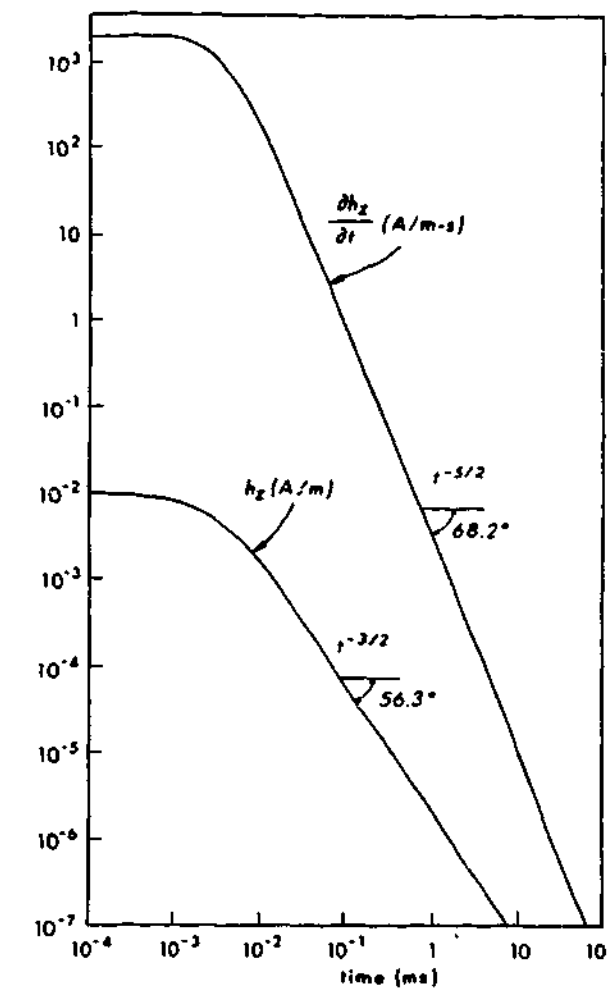


Figure 2.3: The vertical magnetic field and its time derivative computed at the centre of a circular loop of radius 50 m residing on the surface of a 100 ohm.m homogeneous half-space. (After Ward and Hohmann, 1988: Fig. 4.8).

2.8. THE "SMOKE RING" APPROXIMATION.

Nabighian (1979) demonstrated that the magnetic Hertz potential describing the transient response due to an aperiodic vertical magnetic dipole (VMD) residing upon a homogeneous half-space, possesses a first order term, which is precisely the magnetic Hertz potential of circular current filament which migrates outward and downward with decreasing speed and diminishing amplitude. These current filaments, which approximate the true induced diffuse toroidal current systems, were noted by Nabighian (1979) to resemble a system of "smoke rings" blown from the VMD or equivalent transmitter loop, see graphical representation in Figure 2.4.

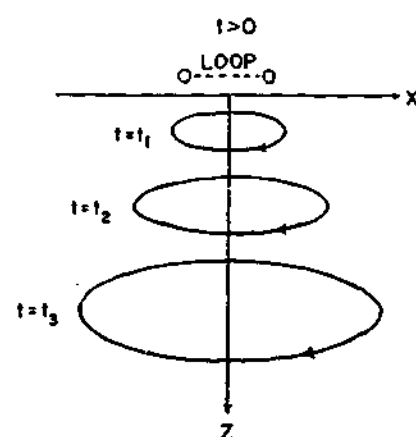


Figure 2.4: An equivalent current filament, or "smoke ring", sketched at different times as it propagates downward and outward from a circular transmitter loop. (After Nabighian, 1979).

The motion of an equivalent current filament, for an aperiodic VMD residing upon the surface of a homogeneous half-space of conductivity σ_H , can be described by the equations of kinematics given by Nabighian (1979) which yield the radius, depth and downward vertical speed of the induced "smoke ring".

- THE EQUATIONS OF KINEMATICS OF A "SMOKE RING" (After Nabighian, 1979):

$$r(t) = \sqrt{\frac{(64/\pi - 16)t}{\sigma_H \mu_0}} \quad (\text{Radius of current filament}), \quad (2.60a)$$

$$z(t) = \sqrt{\frac{16t}{\pi \sigma_H \mu_0}} \quad (\text{Depth}), \quad (2.60b)$$

$$\partial_t z(t) = \frac{2}{\sqrt{\pi \sigma_H \mu_0 t}} \quad (\text{Downward vertical speed}), \quad (2.60c)$$

$$I(t) = \frac{\sigma_H \mu_0}{(16 - 8\pi)t} \quad (\text{Current intensity}). \quad (2.60d)$$

In summary, the transient EM response observed on or above a conducting half-space, or layered earth, can be approximated by a current filament of the same shape as the transmitting loop, e.g., a circular current filament in the case of a VMD or circular loop (Nabighian, 1979). In the case of a VMD, the equivalent "smoke ring" will propagate outward, with a radius given by Equation (2.60a), and downward with depth and decreasing vertical speed given by Equations (2.60b) and (2.60c) respectively, whilst the current intensity given by Equation (2.60d) will diminish in time as t^{-1} . By equations (2.60a) and (2.60b), the angle of descent of the current filament into a homogeneous earth will be found to be approximately 47 degrees, steeper than the 30 degrees for the true current system (Nabighian, 1979). Although the actual induced current systems will propagate downwards with time, all currents for a homogeneous or layered earth will be restricted to horizontal flow, that is, no downward component of the current density is required in order to accomplish the observed downward diffusion (Nabighian and Macnae, 1991).

Nabighian (1979) noted that the generalisation of the "smoke ring" approximation to a layered earth is possible but algebraically cumbersome. A smoke ring would be expected to propagate in a similar fashion within a layered conductive medium as in a half space, with the exception that it possesses different velocities and rates of attenuation within each homogeneous layer (Nabighian, 1979). Indeed, for a layered earth the diffusing current system will remain longer in higher conductivity beds (Telford *et al.*, 1990).

Although the equivalent current filament approximation may facilitate a basic understanding of current diffusion within a conductive half-space, such a concept may prove deceiving. Reid and Macnae (1998) identified a common misconception amongst many geophysicists, namely Ampère's Law supposedly implies that the time-domain magnetic fields arising from currents distributed within a homogeneous half-space will circulate about the electric field, and

thus, the current density maximum. Whilst such an intuitive understanding of Ampère's Law may hold true for current flow restricted to a filament residing in free-space, the relationship between magnetic fields and current densities, as described by Ampère's Law, becomes considerably more complicated when the currents are dispersed throughout a conductive medium (Reid and Macnae, 1998). Consider the current density induced within a homogeneous half-space by a VMD source (see Figure 2.5). The time-domain magnetic field vectors will circulate at approximately twice the radius of and about the same depth as the electric field and current density maxima, whereas the time derivative of the magnetic field will circulate at approximately one and a half times the radius of and about the same depth as the electric field maximum. So although for a half-space the maximum curl of the magnetic field coincides with the electric field and current density maximum, the magnetic field does not circulate about the its maximum curl (Reid and Macnae, 1998).

Thus, one needs to exercise caution when performing a single current filament inversion on TEM data with the intent of deducing the conductivity structures within the earth, since the inverted filament will not coincide with the true current density maximum.

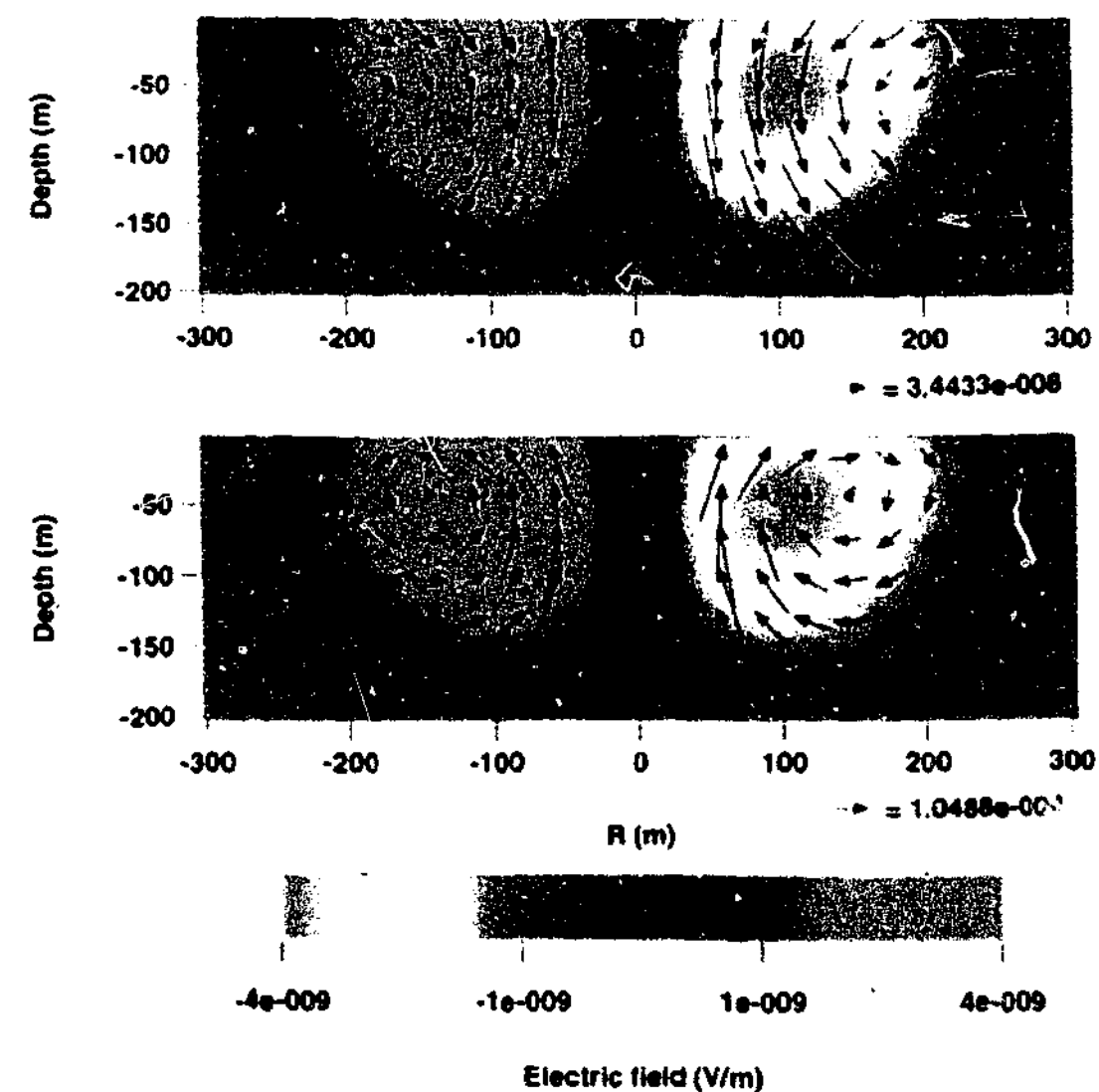


Figure 2.5: The vector components of both the magnetic field (top image) and its time derivative (bottom image) superimposed upon the colour images of the electric field intensity for a 0.1 S m^{-1} homogeneous half-space at time 0.5 ms . A vertical magnetic dipole source was used and is located at the origin. (After Reid and Macnae, 1998).

CHAPTER THREE

NUMERICAL PACKAGES.

3.1. MODELLING CLASSES AND ATTRIBUTES.

The TEM response of a target residing in a resistive host can be sufficiently interpreted using numerical models which assume the target to be suspended in free-space. By applying the free-space approximation to TEM data, one assumes a priori that induction is the dominant mode of excitation. In situations, however, where the host medium can no longer be regarded as resistive, one must take into account any host-target EM interactions which may occur; namely current channelling. Thus, it is this more generalised approach which must be taken when interpreting a TEM response which features both an inductive and galvanic component. Unfortunately, no universal program exists which is capable of computing the TEM response, and all associated EM interactions, of any generalised system of arbitrary complexity. As such, modelling software developed within the industry are based upon, and classed in respect to, some sort of simplification or approximation.

TEM numerical models are often classed in terms of their representation of the source, host and targets, and by their dimensionality and mathematical approach. Familiarity of these modelling classes to an interpreter is essential. To emphasise this importance, one must realise that due to the limiting physics applied within the industry software, the results of a particular TEM model will be dependent upon the class of the modelling software employed. For example, not all model classes will take into account the inductive interaction between two adjacent bodies.

Summarised in the following subsections, are some of the main distinguishing features, and basic constituents, of the TEM modelling software available within the industry.

3.1.1. MODEL DIMENSIONALITY.

TEM numerical models incorporating conductive hosts can usually be classed in terms of their degrees of freedom in respect to conductivity distribution. There are three classes of model dimensionality; these are 1-D, 2-D, 2.5-D and 3-D models, each of which can be defined as follows:

1. **1-D MODELS:** 1-D models are typified by layered earth models, for which conductivity varies only as depth. Due to the simplified physics, analytical solutions commonly exist for 1-D models permitting both fast and reliable computations to be made. An example of this is the use of layered earth models to partially test the computed response of a 2-D or 3-D program (Raiche *et al.*, 1998b). Here, large finite tabular bodies within the higher dimensional models are used to simulate the response of a layer of infinite extent within the 1-D model. Such trials, however, are valid only at early and middle delay times. At some point in time the induced "smoke ring" (Nabighian, 1979) will expand beyond the boundaries of the finite target, resulting in a departure in response from the 1-D approximation (Raiche *et al.*, 1998b). It is at these times the differences between a tabular body of finite (2-D and 3-D models) and infinite (1-D models) extent become apparent. Moreover, the times at which the divergence occurs will be delayed with increasing target size (Raiche *et al.*, 1998b).
2. **2-D MODELS:** 2-D models are comprised of 1-D host and 2-D conductivity structures of infinite strike length excited by a 2-D source. The source of practical interest is the line source of time-varying current at the surface of the earth approximating a long grounded wire or one side of a large loop (Hohmann, 1988). Namely an infinite line of current parallel to a 2-D conductive geometry (Nabighian and Macnae, 1991). Two-dimensional modelling is sometimes used to simulate the response of an elongated conductor buried in a conductive host and energised by a large-loop source (San Filippo *et al.*, 1985). For example Oristaglio (1982) used two parallel line sources to simulate the effects of a rectangular loop on a homogenous halfspace. Furthermore, Oristaglio and Hohmann (1984) used an explicit finite-difference technique to simulate the response of a tabular body with

infinite strike length embedded in a conductive homogenous medium with a conductive overburden layer.

3. **2.5-D MODELS:** 2.5-D models are characterised by 2-D conductivity structures residing in a 1-D host excited by a source of 3-D geometry (Nabighian and Macnae, 1991). In this case like the 2-D models conductivity does not vary in the strike direction, but the source is finite in size as is a circular loop replacing infinite line currents sources. This problem is of practical importance as discretization is necessary only over a cross-section, and not throughout a volume (Hohmann, 1988).
4. **3-D MODELS:** 3-D models are characterised by 3-D conductivity structures residing in a 1-D host and excited by a source of 3-D geometry. Examples include the forward modelling numerical packages used within this project: program LEROI, see Section 3.2, and program MARCO (Xiong, 1992; Xiong and Tripp, 1995), see Section 3.3.

3.1.2. NUMERICAL METHODS.

The two most commonly implemented numerical schemes, for the solution of a prescribed set of equations governing a given system, include the integral equation and differential equation methods:

1. **DIFFERENTIAL EQUATIONS (DE):** This class of numerical schemes includes the finite-difference (FDM) and finite-element (FEM) methods, both of which are derived from the differential forms of the governing (physical) equations (Xu, 2001). The FDM and FEM are classified as regional methods, *i.e.*, the entire geologic domain must be incorporated within the model and discretized (Xu, 2001). These techniques are effective for solving boundary value problems (BVP) where regions of complex geology are to be simulated (Hohmann, 1988; Xu, 2001).
2. **INTEGRAL EQUATIONS (IE):** Despite the increased difficulty in the mathematics, IE methods are regarded to be advantageous over DE methods in situations where the response due to small, finite targets, such as an isolated ore-body, are to be computed. The efficiency of the IE method

stems from the requirement that only anomalous conductivity inhomogeneities need be discretized (Hohmann, 1988; Xu, 2001).

In addition to these numerical schemes in the boundary element method (BEM), its classification seats it somewhere in between the DE and IE methods. The BEM can be considered as a FEM used for the solution of boundary integral equation problems (Xu, 2001). The predecessor of the BEM is the boundary integral equation method, in which a given BVP, expressed as a partial DE, is transformed into an IE over the boundary of a region by Green's formula (Xu, 2001). A large amount of integration is involved within the BEM: conductivity boundaries are divided into multiple elements, and over each element an integration is performed (Xu, 2001). The BEM is regarded as efficient due to the requirement that only the boundary separating regions of contrasting physical properties need to be discretized. This feature can prove advantageous in some instances over the regional type DE methods, and the IE method that requires gridding over an entire 2-D surface, or 3-D target volume.

3.1.3. SOURCE REPRESENTATION.

Rectangular transmitter loops used within TEM surveys are usually represented by either rectangular or circular loops of equal area, a time-varying vertical magnetic dipole (VMD) or parallel line sources. Magnetic dipoles are often used as either an approximation to a circular or rectangular loop when a transmitter size is small relative to the dimensions of a model (Raiche *et al.*, 1998b), or in theoretical applications when analytical solutions are sought. For example, analytical expressions for both the vertical magnetic field step and impulse (time derivative of step response) responses are available for the limited case of receiver and VMD source residing upon the surface of a homogeneous earth; however, analytic expressions for a circular loop exist only for the central-loop configuration (Ward and Hohmann, 1988).

3.1.4. HOST AND TARGET REPRESENTATION.

Real earth structures are typically complicated in form consisting of conductivity inhomogeneities other than the designated target. Layering may also occur but not necessarily as horizontal strata. In the case of a highly conductive target embedded in a resistive medium, good inductive interpretations can be made by modelling a finite conductive body (traditionally a thin sheet) suspended in free-space. When current gathering and attenuation effects are to be accounted for, representations such as a homogenous conductive halfspace and a horizontally layered earth are commonly used. In the latter case, layered earth models are often employed to simulate the effects of a conductive overburden on a target response.

Common geometrical representations used for targets include rectangular sheets and tabular bodies of finite thickness. Algorithms implementing IE methods, however, are advantageous in that they permit more general conductivity structures to be constructed from rectilinear blocks or prisms, as with program MARCO, see Section 3.3.

3.2. LEROI.

Refer to Appendix B.1 for the version of LEROI adopted for use within this thesis.

3.2.1. PROGRAM DESCRIPTION AND PHILOSOPHY.

Program LEROI computes the forward time domain (TD) response of single or multiple thin sheets within a conductive earth for a loop source (Raiche *et al.*, 1997). The earth itself may either be a homogeneous half-space or composed of two homogeneous layers (Raiche *et al.*, 1997). In the latter case, the thin sheets are restricted to lie within the bottom layer, or basement, without electrical contact with the top layer or overburden (EM Vision, 1996). Complex or Cole-Cole resistivities may also be specified for both the thin sheet targets and the conductive earth layers (Raiche *et al.*, 1997). The assignment of the receiver locations is completely general, as LEROI allows receivers to be placed within the air, and on and below the surface for borehole applications (Raiche *et al.*, 1997). In particular, LEROI was designed specifically to operate with a variety of field and survey configurations, with either single or multiple TEM readings (Raiche *et al.*, 1997).

3.2.2. DISCRETIZATION.

When choosing an appropriate discretization for a particular plate model the user is forced to take a heuristic approach to the problem as there are no set recommendations. In general, but not always, the accuracy of a model response will increase with cell size reduction. Unfortunately, execution times can increase, sometimes quite dramatically, as the discretization becomes finer (Raiche *et al.*, 1998b). Thus, LEROI can be computationally intensive with run times ranging from minutes to hours, the user needs to weigh up carefully the benefits and disadvantages associated with fine cell discretizations. In general, the choice on appropriate discretization depends upon a number factors which include frequency, time-range, relative conductivities, plate geometry and the relative positions between the source and receivers (Raiche *et al.*, 1998b). In addition to this, both the method of model computation and the representation of scattering currents need also to be considered (Raiche *et al.*, 1998b). It should be noted, that previous guidelines based upon skin depth arguments are now

considered to be over simplistic (Raiche *et al.*, 1998b). Thus technically, model computations should use different discretizations for each frequency, but this is deliberately avoided as dynamic cell sizes can cause problems during the conversion of the frequency model response into the time domain (Raiche *et al.*, 1998b).

Some simple rules for choosing appropriate discretization have been established by the program developers. These rules are based upon the time domain results obtained from the execution of a limited number of models. It is recommended that for flat-lying targets, or sheets, a cell size of about 40 m is acceptable for most applications, but for more accurate work a reduction to 20 m is advised. Whilst for general work with vertical targets 20 m cells are to be used. Again, if greater accuracy is required then the cells should be reduced to around 10 m in size if the total number of cells is less than 800 (Raiche *et al.*, 1998b). Given that the choice of discretization is at ones own discretion, it is advisable to commence all modelling with a reasonably large cell size of say 50 m and progressively decrease it from 20 m to 10 m to 5 m, so as to gauge the dependency of the response with respect to cell size. One should never accept a model without conducting such a trial. Finally it is noted that for all LEROI models presented within this thesis, only models with 10 m and 20 m cells were constructed.

Moreover as a practical guideline, reduced cells sizes are recommended when vortex current dominate over galvanic currents, or when strong inductive interactions occur between multiple sheets (Raiche *et al.*, 1998b). Increased plate conductance, decreased host conductivity and in some situations orientating the target vertically as opposed to horizontally will serve to increase the inductive component (Raiche *et al.*, 1998b).

Finally, numerical instabilities associated with too fine a discretization and inductive interactions between multiple sheets, have been noted for models constructed within the project. For a comprehensive discussion on these problems encountered with discretization within LEROI the reader is referred to Chapter Five: Limitations of LEROI.

3.2.3. PROGRAM HISTORY.

The initial coding of the LEROI algorithm began around the late 1980's and early 1990's; further development of the program commenced under the sponsorship of the Australian Mineral's Industry Research Association (AMIRA) until its final release to sponsors in March of 1990 (EM Vision, 1996). The origins of LEROI reside within program SCHEIBE¹ developed by Peter Weidelt of the Technical University of Braunschweig in Germany (EM Vision, 1996). The original program SCHEIBE, computed the frequency domain response of a thin sheet residing in the basement of a two-layered earth for vertical magnetic dipole source (EM Vision, 1996). Although theoretically based upon SCHEIBE, LEROI was essentially rewritten allowing for improvements in both accuracy and use within applications. Modifications to the original program were made so as to accommodate for a rectangular loop source in replacement of the vertical magnetic dipole (EM Vision, 1996). In addition to this, algorithms for the conversion of the response from the frequency to the time domain were implemented enabling broader application and use within EM Vision (EM Vision, 1996).

3.2.4. ORIGINS OF LEROI THIN SHEET THEORY.

Peter Wiedelt developed the thin-sheet theory implemented by program LEROI that occurred originally within program SCHIEBE. This theory involves the solution of integral equations within the frequency domain (FD): these integral equations arise from Green's functions that Wiedelt had separated into divergence-free (vortex) and curl-free (current gathering) modes (Raiche *et al.*, 1997). By performing this decomposition, both the vortex and galvanic currents could be determined by taking the curl and gradient of the normal vector potentials respectively. Moreover, Weidelt proved that such a formulation would eliminate the inverse conductance term that was present in previous calculations, thus preventing the program from failing at high conductivity contrasts that occur for very resistive hosts (Raiche *et al.*, 1997).

¹ The word Scheibe comes from the German for sheet; pronounced 'shyber'.

3.2.5. DEVELOPMENTS AND MODIFICATIONS.

Despite inheriting the aforementioned thin sheet theory from SCHEIBE, program LEROI does not implement any of the computational algorithms contained within the original SCHEIBE code. Instead, the CSIRO Mathematical Geophysics Group completely redesigned all of the algorithms for LEROI, which included those for computing the electric and magnetic Green's functions, primary fields, frequency stepping, frequency to time domain transforms and matrix algorithms, resulting in improved stability, accuracy and speed (Raiche *et al.*, 1997).

3.3. MARCO.

Refer to Appendix B.2 for the version of MARCO adopted for use within this thesis.

3.3.1. PROGRAM DESCRIPTION AND PHILOSOPHY.

The algorithm MARCO, which is based upon the volume 3-D integral equation method, was designed to model the EM response of arbitrary structures which can be represented by multiple 3-D rectilinear prisms residing in a multi-layered earth (Raiche *et al.*, 1998b). Although each prism can be assigned an arbitrary but uniform conductivity, its orientation is restricted to be parallel to the three component axes, and thus cannot be assigned neither dip or plunge specifications. Moreover, the simulation of strike can only be achieved through the orientation of the survey lines (Raiche *et al.*, 1998b). Despite these restrictions, MARCO is capable of modelling relatively complicated structures such as stepped and variable overburdens, and multiple target structures which may traverse host layer boundaries.

MARCO will initially compute the frequency domain response for a given model, and by user option the associated time domain response (Raiche *et al.*, 1998b). Cole-Cole resistivities may also be specified for both the targets and host layers, whilst receivers can be located in the air, down hole, or on the surface of the earth (Raiche *et al.*, 1998b). Furthermore, MARCO is able to compute high frequency radio imaging responses for grounded sources and downhole magnetic dipole sources (Raiche *et al.*, 1998b). In this project, however, only surface and downhole time domain models were computed, where real resistivities were used for both target and host (see Chapter Six: Cadjebut Lead-Zinc Body).

Unfortunately, unlike the thin sheet formulation within LEROI the inverse conductivity term in the Green's function could not be eliminated within MARCO (Raiche *et al.*, 1998b). As a consequence of this MARCO is restricted to models with conductivity contrasts of up to about a 1000 to 1 between the 3-D targets and the immediate host surroundings (Raiche *et al.*, 1998b). In situations such as tabular models residing within resistive hosts with no conductive overburden, the conductivity contrast is not recommended to exceed the 300 to 1 limit (Raiche *et al.*, 1998b).

3.3.2. DISCRETIZATION.

The rectilinear blocks or prisms within a MARCO model constitute the survey targets, which in turn are discretized into a number of 3-D cells of specified size. By application of the 3-D integral method, both the magnitude and direction of the induced current within each cell are treated as constant. Hence discretization must be sufficiently fine in order for the discrete cells to adequately resolve the induced current system (Raiche *et al.*, 1998b). As stipulated within Section 3.2.2 ascertaining whether the targets are sufficiently discretized is of the users discretion, since time constraints must also be considered. As for LEROI the authors of MARCO made some basic recommendations in regards to cells size, namely 40 m to 20 m cells were noted to be effective for vertical targets, whilst 10 m cells are preferable for thin horizontal targets (Raiche *et al.*, 1998b). Again, finer discretization is recommended when induction predominates over current channelling (Raiche *et al.*, 1998b), this can be attributed in part to the increased complexities in geometry of the divergence free vortex current systems. The authors of MARCO advise that such recommendations require testing within one's own models before acceptance. It is noted, however, that these recommendations held true for models constructed within this project. Namely, both LEROI and MARCO models required much finer discretization when inductive effects predominated, and in particular when the receivers were in close proximity to a target. This situation was most greatly appreciated when modelling the surface and downhole data from Cadjebut (see Chapter Six), notably the surface survey models were found to be more tolerant of larger cells than those of downhole surveys. Moreover, in the modelling conducted coarse discretizations were found to be sufficient when current gathering dominated, and often only minor enhancements were noted in the target response when the cell size was reduced.

3.3.3. GROUP THEORY AND INCREASED COMPUTATIONAL EFFICIENCY.

MARCO boasts the use of group theory to greatly enhance the computational efficiency of particular models which exhibit appropriate symmetries without

sacrificing accuracy, a feature which is unique amongst EM modelling programs (Raiche *et al.*, 1998b).

The two types of symmetries recognised are translational cell symmetry, and block symmetry (Raiche *et al.*, 1998b). For translational cell symmetry to be active, all target prisms are to be discretized into cells of equal size, and spaced such that the distances between them are of integer multiples of the universal cell dimensions. That is, the target prisms can be considered to be composed of cells which form a uniformly distributed super-mesh containing the model entire (Raiche *et al.*, 1998b). Whereas block symmetry is activated when the model displays two-fold symmetry in respect to both the North-South and East-West axes, thus permitting group symmetric reductions to reduce the computations to just one quadrant of the model. Furthermore, symmetry is only necessary in respect to the model targets, and not the transmitter or receiver positions (Raiche *et al.*, 1998b).

3.4. TECHNICAL ASPECTS AND FUNCTIONALITY COMMON TO LEROI AND MARCO.

3.4.1. FILE CONVENTIONS AND PROGRAM EXECUTION.

For the most part, both MARCO and LEROI obey similar conventions for the construction of a model control file and its subsequent execution. All models begin with the creation of a control file which is labelled as "input.dat". Survey details of a given model are provided by the user via the control file. Some model specifications include the stipulation of delay times, the choice of time domain system, transmitter and receiver configurations, layered earth parameters, and waveform description. A number of user options are also available, giving the user greater modelling flexibility and control. Detailed instructions for the creation of a control file and listing of the various user options available for both LEROI and MARCO can be found within the documentation attached to the respective FORTRAN code.

On running the MARCO or LEROI executable files "MARCO.exe" and "LEROI.exe", data is imported from the model control file "input.dat" and execution begins (Raiche *et al.*, 1997 & 1998a). Once completed, the file "output.out" is created, in which the total time domain response is printed, in addition to the percent-scattered field response or percentage target effect, *i.e.*, (vortex + galvanic component)/total field response. An option is available to print the un-normalized scattered field response, *i.e.*, the vortex + galvanic component, if so desired (Raiche *et al.*, 1997 & 1998a). Furthermore, the scattered frequency domain data are stored within the file "output.frq"; its use within subsequent calculations is optional (see also Section 3.4.4). Finally, the AMIRA formatted output file "AMIRA.fmt", allowed one to import the TD impulse data or voltage response into EM Vision for display and interpretation (Raiche *et al.*, 1997 & 1998a).

3.4.2. COMPUTATIONS.

The scattered field response defined as total field less the regional response, is initially computed within the frequency domain (FD) before transformation into the time domain (TD) (Raiche *et al.*, 1997 & 1998a). Computation of the frequency domain response is made within the frequency range of 1 Hz to 100 kHz in intervals of six points per decade. In the event the time domain

measurements are made for very early channels, including those within the signal on-time, or very resistive host mediums, ie resistivities around 100,000 ohm.m and over, then the frequency domain computations are extended from 46 kHz to 1 Mhz with an increased spectral density of 12 points per decade (Raiche *et al.*, 1997 & 1998a). Once computed, the frequency domain response is extrapolated back to zero frequency or DC response (Raiche *et al.*, 1997 & 1998a). Finally, the frequency domain response, of the imaginary component of the magnetic field for the entire frequency spectrum, is obtained by means of a cubic spline interpolation (Raiche *et al.*, 1997 & 1998a).

The computation of the time domain magnetic fields use digital filter coefficients derived from the fast Hankel transform program of Johansen and Sorensen (1979) (Raiche *et al.*, 1997 & 1998a). Once computed, a cubic spline interpolation is fitted to the time domain magnetic fields, the coefficients of which permit the computation of the time derivatives of these fields (dB/dt). Finally, this scattered voltage response is convolved within the source function, thus yielding the observed field voltages with units of area by time derivative (area x dB/dt) (Raiche *et al.*, 1997 & 1998a).

3.4.3. LATE-TIME SOURCE SWITCHING.

At early times the normal fields computed within LEROI and MARCO are due to a transmitter loop represented by a line integration of horizontal electric dipoles (Raiche *et al.*, 1997 & 1998a). Thus the fields due to the dipoles on opposite sides of the loop are of opposite sign. Unfortunately at late times, these fields tend to be of the same order of magnitude resulting in numerical chaos if their summation is attempted (Raiche *et al.*, 1997 & 1998a). For times after the "smoke ring" has passed the transmitter boundary the transmitter loop may be regarded as a single vertical magnetic dipole (VMD). Thus before numerical instabilities occur, LEROI and MARCO will test for the suitability of the VMD approximation and will switch to this representation accordingly (Raiche *et al.*, 1997 & 1998a). The benefit to be gained from late time source switching is that such an approximation does not suffer from numerical

instabilities at late time. Note that the horizontal fields will be affected more than the vertical with this approximation (Raiche *et al.*, 1997 & 1998a).

The late time switching begins with the simulation of the finite loop with a line integration of horizontal electric dipoles (HED) (Raiche *et al.*, 1997 & 1998a). Once computed, the validity of the VMD approximation is checked. Note that the circular loop approximation (CLA) is also verified and if it is found to fail then the VMD approximation is also assumed to fail (Raiche *et al.*, 1997 & 1998a). When the difference between the VMD approximation and line integral methods converges to within a given tolerance, source switching is validated but not made. Once this tolerance is met, and the difference begins to increase, then the switch to the VMD approximation is made (Raiche *et al.*, 1997 & 1998a). If the original tolerance is not met, and the difference is found to increase with time, then the conversion to a VMD is made anyway (Raiche *et al.*, 1997 & 1998a).

3.4.4. REUSING PREVIOUS COMPUTATIONS.

At completion of the frequency domain computations, the imaginary components of the 'raw' frequency-domain scattered magnetic field responses are written to the file "output.frq" (Raiche *et al.*, 1997 & 1998a). The reason for this is that these frequency domain computations are responsible for around 95% to 99% of the LEROI run time (Raiche *et al.*, 1998b). Thus if the model, ie the plate and layered earth attributes, together with the transmitter and receiver locations remain unchanged from a previous execution, then it is possible to reuse the old frequency responses stored within the file "output.frq" (Raiche *et al.*, 1998b). The main purpose of this option was to enable the user to experiment with different time domain system options. Specifically trials utilising different waveforms, pulse lengths and receiver windows can be performed (Raiche *et al.*, 1998b). Note this facility of recycling the frequency domain response, together with the alternate options of creating an entirely new 3-D model or computing a layered earth response with no target, is activated by the appropriate parameter within the control file "input.dat", see (Raiche *et al.*, 1998b) for more information. In addition to this, various data

output modes can also be accessed. For example, if the original data output was in profile mode then the frequency domain computations can be reused to generate an output in the decay curve mode. Alternatively, if the initial response was chosen to be displayed in terms of voltages, then the response for subsequent executions may then be displayed in terms of the magnetic fields (Raiche *et al.*, 1993b).

3.4.5. TIME DOMAIN SYSTEM CONVENTIONS.

The transmitter waveform and properties are dependent upon the instrument selected or may be defined by the user. When the SIROTEM or EM37 instrument option is selected within the control file "input.dat", the program assumes a bipolar waveform with an exponential rise-time and a ramp turn-off time. The off-time and on-time are defined to be of equal duration and are user defined. Note the on-time, the length of time for which the current is defined to be on in a square wave signal, is defined to start at the beginning of the exponential rise of the waveform (Raiche *et al.*, 1998b). Furthermore, the zero time-reference for the SIROTEM option, from which delay times are measured, occurs at the start of the ramp turn-off. Alternatively, for both the EM37 instrument and the user delay time options, the delay times are actually referenced from the base or end of the ramp turn-off not its start (Raiche *et al.*, 1998b).

For user supplied delay times, the employed waveform is a pulsed bipolar boxcar waveform with linear ramps consisting of four specified non-overlapping parts (Raiche *et al.*, 1997; Raiche *et al.*, 1998a; Raiche *et al.*, 1997b):

1. A linear ramp turn-on (not exponential).
2. An on time of constant current (1 amperes).
3. A linear ramp turn-off.
4. An off-time of zero current.

3.4.6. ARBITRARY WAVEFORM OPTIONS.

In addition to the user specifying the delay times and widths, an arbitrary waveform option is also available. A general waveform can be specified which may be either mono-polar or bi-polar in form (Raiche *et al.*, 1997 & 1998a). Furthermore, the user may also specify whether the arbitrary waveform will be composed of linear segments with corners, or be a smooth function. Specifically, the arbitrary waveform may either be composed of multiple linear segments or consist of a single smooth curve connecting specified points (Raiche *et al.*, 1997 & 1998a). Again, either of these type waveforms can be repeated as bi-polar pulses, or as a series of positive sign mono-polar pulses (Raiche *et al.*, 1997 & 1998a).

Regardless of whether the waveform used is standard or user defined, measurements made are restricted to lie within the off-time. The UTEM standard option, however, permits measurements during the on-time as this system has no off-time (Raiche *et al.*, 1997 & 1998a).

3.5. IMPLEMENTATION OF LEROI AND MARCO.

The criteria for the selection of modelling software for use within this project were largely based upon survey requirements, the geology of a mineralisation and the half-space complexity. Outlined below are the requirements which were considered when programs LEROI and MARCO were chosen for their designated application within the Cadjebut and Flying Doctor case studies. An essential feature common to both programs is the ability to account for the full interaction between half-space and target; both LEROI and MARCO compute the galvanic and inductive components of a TEM response.

Case Study of Cadjebut Pb-Zn Deposit

Program MARCO was selected to model archival surface EM and downhole TEM data acquired from the Cadjebut Pb-Zn mineralisation (see Chapter Five for entire case study, and see Section 5.1.2. for the geological attributes of the deposit).

MARCO's ability to model the response of multiple rectilinear prisms in a multi-layer half-space, meant that it was well suited to representing the slab like nature of the Cadjebut ore-body, with its relatively large thickness, and in particular the complicated host environment in which it resides (refer to Section 5.3.2 for model attributes).

Unfortunately, targets within MARCO cannot be assigned a non-zero dip. This restriction, however, did not pose problems during modelling, for the Cadjebut mineralisation possesses only a slight dip which, in regard to the scale of the EM surveys, can be treated as insignificant. A further restriction imposed on model construction within MARCO, is the limitation on the target-to-host resistivity contrast. In general, it is recommended that this ratio does not exceed the value of 1 : 1000, and for situations in which the target resides within a resistive host with no overburden, this ratio is reduced to 1 : 300 (Raiche *et al.*, 1998b). It is noted that the target-to-host resistivity contrast adopted within the Cadjebut model, namely 1 : 229, did not violate the aforementioned conditions.

The Flying Doctor Case Study

Program LEROI was chosen to model downhole TEM data acquired from the Flying Doctor Pb-Zn deposit (See Chapters Six and Eight). The suitability of the Flying Doctor deposit to thin-sheet representation, lends itself to the planar type form of the upper and lower ore lenses constituting the mineralisation. Unlike MARCO, targets within LEROI can be an assigned arbitrary dip, an essential attribute for this case study. One major limitation of LEROI is its inability to deal with a multi-layered earth; the interpreter is limited, at most, to a two layer host with the target confined to the basement layer. This limitation, however, did not pose any problems for this particular case study, as a simple half-space sufficed.

Preliminary interpretations, of the inductive and galvanic components, of the upper lens TEM response yielded conflicting estimates for the target conductivity and depth-extent. Since LEROI is restricted to modelling sheets with a homogeneous conductivity distribution, modelling proceeded in a novel manner by first computing the independent response of a high conductivity sheet, and a low conductivity sheet of greater depth-extent, and then synthesizing a complete model response by taking the linear combination of the host and scattered response of each plate. This approach was necessary, for during the course of modelling LEROI was found to be unstable for closely spaced multiple plate systems, and in instances where over discretization had occurred (see Chapter Seven for more information).

CHAPTER FOUR

INDUCTIVE AND GALVANIC DECAY ANALYSIS.

4.1. INTRODUCTION.

A procedure was devised to facilitate the interpretation of the downhole TEM data considered within this thesis, and to streamline model construction. This interpretational procedure is outlined within Section 6.2 of Chapter Six. The first stage of this method entails the identification of the excitation mechanisms responsible for the target anomalies present within the downhole TEM field profiles. In regards to the downhole TEM data considered within this thesis, a typical field response was found to consist of essentially two basic components: a background or host response and a target anomaly, where the latter of which can be either inductive or galvanic in origin, or a mixture of both.

As emphasised within Chapters Six and Eight, it is in general difficult to completely distinguish between the inductive and galvanic components of a downhole TEM response. Preliminary interpretations utilised profile analysis: the comparison of the field response with an inferred target response, which is estimated by assuming either a unipolar or bipolar secondary field, depending on whether the dominant excitation mechanism is deemed to be galvanic or inductive. Once an anomaly within the field data has been deduced by means of profile analysis to be unambiguously either inductive or galvanic in origin, the suspected dominating excitation mechanism is then verified by decay-curve analysis. The theory of inductive and galvanic decay-curve analysis is the subject of this chapter.

4.2. INDUCTIVE DECAY ANALYSIS.

Inductive downhole TEM interpretations and modelling were carried out for the thin tabular conductive ore bodies which constituted the Flying Doctor Deposit, see Chapters Six and Eight. These targets were modelled as thin finite rectangular conductive sheets, buried within a conductive homogenous earth. The thin sheet models constructed to replicate the field response required the assignment of physical dimensions and electrical conductance. In most instances the depth-extent of each body could be derived from a geological cross-section of the deposit, whereas the strike-length remained more or less unknown. Deducing the conductance of the target, however, required determining the exponential inductive time constant from the target anomaly. By use of the fundamental inductive time constant and the characteristic length, namely the depth-extent, the conductance for an isolated tabular conductor can be estimated.

A revision of eigencurrent theory is included here, as it provides a practical understanding of the behaviour of induced currents within a conductor and their evolution with time. Almost all induced vortex currents, or eddy currents, which are spatially finite, can be decomposed into a set of predetermined current patterns of fixed geometry; these current patterns are referred to as a basis (West and Macnae, 1991). Such systems can be analysed as if the elements of the basis are a set of simple closed current loops, for which of each the resistance, mutual inductance and self inductance have been taken into consideration (West and Macnae, 1991). In general, it will be possible to find n sets of n basis current loops such that each set is completely independent of one another. These sets are referred to as eigencurrents (West and Macnae, 1991). The most important property of an eigencurrent, or a set of basis currents, is that it behaves collectively and independently as if it were a unified flow of current within a single isolated circuit. Consequently, each eigencurrent will have an associated self inductance and a unique time constant (West and Macnae, 1991).

The total current distribution $\mathbf{J}(\mathbf{x}, t)$ for a given finite induced current system can be determined by taking the infinite sum of these non-interacting

eigencurrent sets (Nabighian and Macnae, 1991). In practice, however, only a small number of eigencurrents will be known. This summation can be written generically as

$$\mathbf{J}(\mathbf{x}, t) = \sum_{n=1}^{\infty} \mathbf{J}_n(\mathbf{x}) a_n e^{-t/\tau_n}, \quad (4.1)$$

where \mathbf{x} is a position vector, $\mathbf{J}_n(\mathbf{x})$ describes the fixed geometry of the n^{th} eigencurrent and a_n are the amplitude coefficients which account for the effects of the source field. The only time dependent term is the exponential which decays inversely with τ_n , the time constant of the n^{th} eigencurrent, where $\{\tau_1 : \tau_2 < \tau_3 \dots\}$ (Nabighian and Macnae, 1991).

This expression illustrates clearly how an induced current distribution can be decomposed into a set of eigencurrents, and that system can then be evolved with time by simply re-scaling each eigencurrent term with e^{-t/τ_n} (West and Macnae, 1991). The patterns exhibited by the higher-order eigencurrents are more complex than those of lower-order eigencurrents, and will also decay faster due to their smaller time constants (Barnett, 1984). Hence at early times the response from such a system will be non-exponential, since it will be composed of a mixture of high and low order eigencurrents (Nabighian and Macnae, 1991). Eventually, however, the response will become purely exponential (Nabighian and Macnae, 1991) as the induced vortex currents assume the form of the eigencurrent with the largest time constant (West and Macnae, 1991). The high-order eigencurrents contribute significantly to the secondary fields at early times, whilst the contribution made by the low-order eigencurrents will dominate at late times (Barnett, 1984). The largest time constant τ_1 is commonly referred to as the fundamental time constant, and is characteristic of the target geometry and conductance (McNeill *et al.*, 1984). Fundamental time constants have been determined for a small number of bodies of simple geometry, *e.g.*, a sphere, cylinder and prism (Nabighian and Macnae, 1991). This project employed the empirical formula of Lamontagne (1975) for determining the inductive time constant of a thin prism:

$$\tau = \frac{\mu(\sigma l)L}{10}, \quad (4.2)$$

where μ is taken to be equal to μ_0 the permeability of free-space, L is the intermediate or characteristic length of the prism, and $(\sigma \cdot t)$ is the conductivity-thickness product (for other occurrences of this and similar thin slab formulae see Dyck and West, 1984; Gallagher *et al.*, 1985; Nabighian and Macnae, 1991; Newman *et al.*, 1989; Newman and Hohmann, 1988; San Filippo *et al.*, 1985). Gallagher *et al.* (1985) reports that the decay rate of the response of a thin plate is very weakly dependent upon strike-length but strongly dependent upon depth-extent, and will increase in direct proportion to a reduction in either dimension; Gallagher *et al.* (1985) thereby concluded that the depth-extent is the principal dimension that controls the time constant of a plate. This result is in agreement with Dyck and West (1984), which of whom found the time constant of a thin finite plate to be dependent upon the product of the strike-length and the intrinsic eigenvalue of the fundamental eigencurrent, where the latter term is a function of the depth-extent to strike-length ratio. In this thesis, the fundamental inductive time constant of a thin tabular body (or prism), with dimensions of strike-length by depth-extent by thickness, is determined by equating the characteristic length invoked by Equation (4.2) to the shortest dimension of the prism, namely its depth-extent, and taking the conductivity-thickness product to be the target's conductance S . Hence, the adopted form of Equation (4.2) is

$$\tau_{thin\ sheet} = \frac{\mu S (depth\ extent)}{10}. \quad (4.3)$$

The theory of eigencurrents was applied by Annan (1974) to the problem of determining the inductive response of an isolated thin rectangular plate; a problem for which no simple analytical solutions are available (Nabighian and Macnae, 1991). In the numerical treatment by Annan (1974), the individual eigencurrents, see Figure 4.1, were initially determined and depended only upon the plate geometry, then the mutual inductances between each of the eigencurrents, source and receiver, were computed and combined to obtain the inductive response of the plate (West and Macnae, 1991).

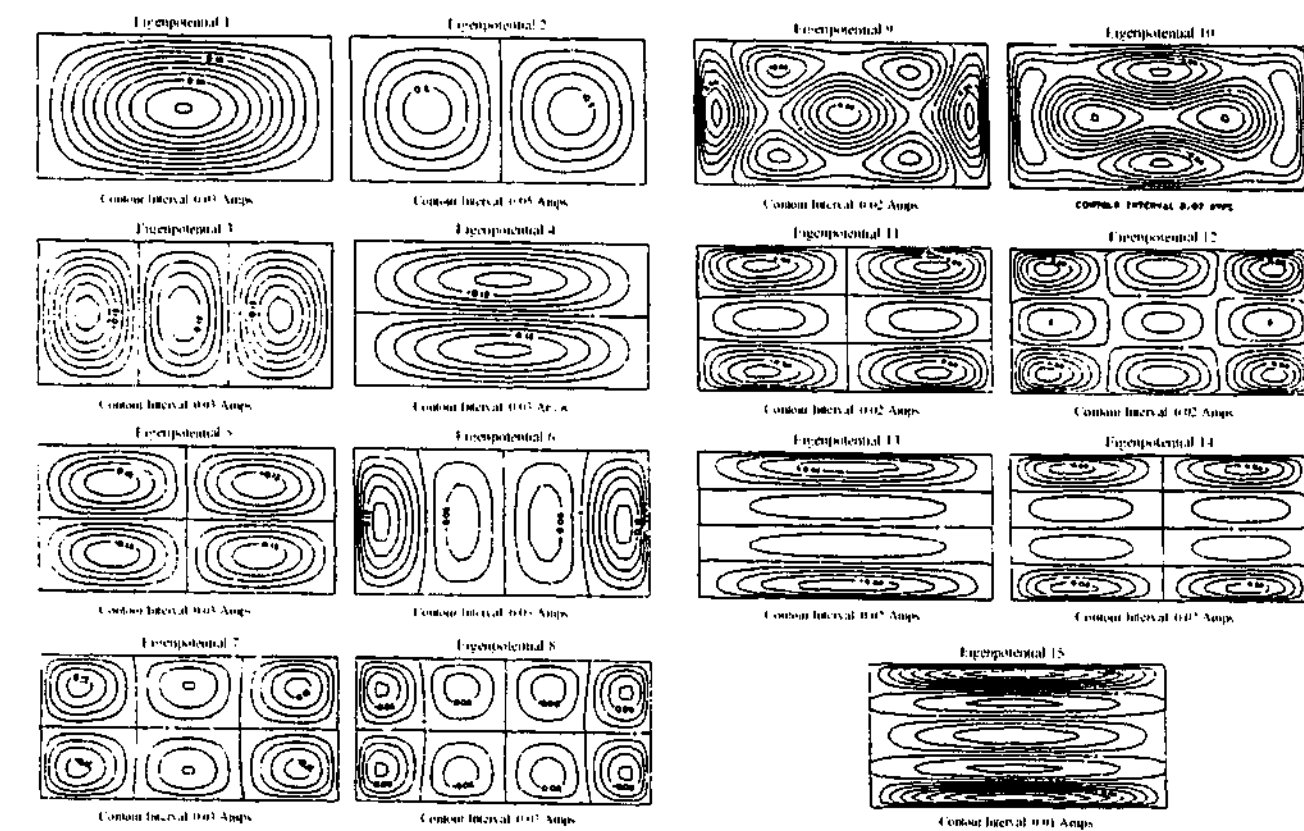


Figure 4.1: Eigenpotential streamlines of the 15 principal eigencurrents computed by Annan (1974) for an isolated 2-by-1 thin plate. (After Dyck and West, 1984).

In theory, an infinite set of eigencurrents is required to completely represent the induced vortex currents in a continuous conductor (West and Macnae, 1991). In practice, however, as in the case of Annan (1974) only a finite number of eigencurrents can be determined. Because of this limitation, it is not possible in practice to represent accurately an induced current system that is highly localised within a portion of the plate (West and Macnae, 1991). Such is the case where the transmitter and receiver are in close proximity to the plate in relation to the dimensions of that plate (West and Macnae, 1991), or if the plate is significantly larger than the transmitter loop (Nabighian and Macnae, 1991).

An induced current system within a thin isolated conductor can be approximated by a single equivalent current filament at any instant in time (Barnett, 1984). Single current loops provide reasonable matches at late-time, but will underestimate the response at early-time (McNeill *et al.*, 1984). It is interesting to note that the equivalent current filament will only match the first order eigencurrent expansion term at late-time (Barnett, 1984); this is intuitive when considering the single loop geometry of the first order eigencurrent computed by Annan (1974), see Figure 4.1.

4.3. GALVANIC DECAY ANALYSIS.

4.3.1. INTRODUCTION.

In this section, the theoretical investigations into the late-time behaviour of a galvanic TEM response due to a small finite target embedded within a homogenous half-space are investigated. Two cases are considered: the first deals with the restricted case of near-surface targets and the second, with the generalised case of a target at depth.

A galvanic TEM dB/dt impulse response, induced by an abruptly terminated (aperiodic) vertical magnetic dipole (VMD), will exhibit a $t^{-7/2}$ power-law decay at late-times (McNeill *et al.*, 1984; Silic, 1989; Asten, 1991a); this behaviour is demonstrated here to be strictly limited to near-surface targets, and very late times for targets at depth.

Silic (1989) observed that an anomalous galvanic current density has essentially the same time dependence as the local primary electric field. The author further noted that the late-time asymptotic power-law decay of the primary electric field possesses an exponent of $-5/2$ for impulse response systems, *e.g.*, SIROTEM, and an exponent of $-7/2$ for step response systems, *e.g.*, UTEM (see West *et al.*, 1984); hence, unlike inductive time constants, the exponents of galvanic power-law decays are excitation dependent.

An informal mathematical derivation of the $t^{-7/2}$ power law is presented within Sections 4.3.2 and 4.3.3. This work is has been extended to include targets at depth, see Section 4.3.4.

4.3.2. GALVANIC EXCITATION OF A NEAR SUFRACE TARGET.

An analytical solution for the electric field induced by an aperiodic VMD exists only for the special case where both source and receiver (test point) reside upon the surface of a homogenous earth (Ward and Hohmann, 1988). Before stating the actual analytical solution for the induced electric field at the surface $\mathbf{E}_{\text{surface}}$, consider its generic form in (ρ, ϕ, z) cylindrical-polar coordinates with the VMD placed at the origin, see Figure 4.2:

$$\mathbf{E}_{\text{surface}} = E_{\rho}(\rho, \phi) \hat{e}_{\rho} + E_{\phi}(\rho, \phi) \hat{e}_{\phi} + E_z(\rho, \phi) \hat{e}_z, \quad (4.4)$$

where the radial \hat{e}_{ρ} , azimuthal \hat{e}_{ϕ} and vertical \hat{e}_z unit basis vectors are defined in terms of the (x, y, z) Cartesian coordinate \mathbf{i}, \mathbf{j} and \mathbf{k} system:

$$\hat{e}_{\phi} = -\sin \phi \mathbf{i} + \cos \phi \mathbf{j}, \quad (4.5a)$$

$$\hat{e}_{\rho} = \cos \phi \mathbf{i} + \sin \phi \mathbf{j}, \quad (4.5b)$$

$$\hat{e}_z = \mathbf{k}. \quad (4.5c)$$

The transformation from (x, y, z) Cartesian to (ρ, ϕ, z) cylindrical-polar coordinates is defined as:

$$\rho^2 = x^2 + y^2, \quad (4.6a)$$

$$x = \rho \cos \phi, \quad (4.6b)$$

$$y = \rho \sin \phi. \quad (4.6c)$$

Whereas the transformation of the individual electric field components can be achieved using

$$E_{\phi} = (-y E_x + x E_y) \rho^{-1}, \quad (4.7a)$$

$$E_{\rho} = (x E_x + y E_y) \rho^{-1}, \quad (4.7b)$$

$$E_z = E_z. \quad (4.7c)$$

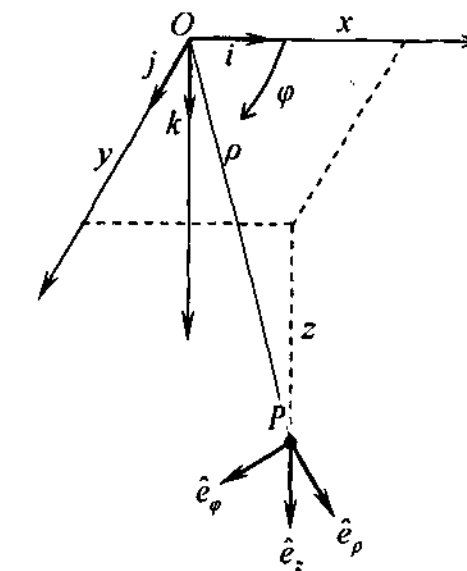


Figure 4.2: A schematic diagram illustrating how a point P can be defined within 3-space relative to an origin O, by means of the (x, y, z) rectangular Cartesian coordinate system, and the (ρ, ϕ, z) curvilinear cylindrical polar coordinate system. In cylindrical coordinates the position of the point P is specified by the radial distance ρ , the angle ϕ and the depth z . It is noted that the base vectors which define the Cartesian coordinate system \mathbf{i}, \mathbf{j} and \mathbf{k} are position invariant, whereas the base vectors of the cylindrical coordinate system $\hat{e}_{\rho}, \hat{e}_{\phi}$ and \hat{e}_z are position dependent. The equations of transformation for the coordinates of these two systems are given by Equations (4.6), whilst those for the base vectors are given by Equations (4.5).

Due to the axial symmetry of the system, there will be no radial or vertical component within the induced electric field, and so only the azimuthal field component will be non-zero (Ward and Hohmann, 1988). That is to say, the induced host currents will be restricted to circulate about the VMD axis in a horizontal flow. Recalling Equations (2.48) and (2.49), the analytical solution due to Ward and Hohmann (1988) for the azimuthal component of the time domain electric field step response, measured at the surface of a homogenous earth of conductivity σ_H and radial distance ρ from a step source (aperiodic) VMD, is given by

$$|\mathbf{E}_{\text{surface}}| = E_{\phi}(\rho, \varphi) = \frac{m}{2\pi\sigma_H\rho^4} \left(3 \operatorname{erf}(\theta\rho) - 2\pi^{-1/2} (3\theta\rho + 2\theta^3\rho^3) e^{-\theta^2\rho^2} \right), \quad (4.8)$$

where m is the magnetic dipole moment, and the parameter θ [m^{-1}] is defined as

$$\theta = \left(\frac{\mu_0 \sigma_H}{4t} \right)^{1/2}. \quad (4.9)$$

A late-time expression for the azimuthal component of the electric field E_{ϕ} can be obtained by expanding Equation (4.8) in a power series in terms of the dimensionless parameter ξ , defined by the product

$$\xi = (\theta\rho). \quad (4.10)$$

Consider first, the series expansion of each significant term of Equation (4.8) separately. Given the Maclaurin power series expansion of the exponential function e^{ξ} , see Kreyszig (1988):

$$e^{\xi} = \sum_{n=0}^{\infty} \frac{\xi^n}{n!} = 1 + \xi + \frac{\xi^2}{2!} + \frac{\xi^3}{3!} + \dots, \quad (4.11)$$

it is possible to determine the series expansion for the term $e^{-\xi^2}$:

$$e^{-\xi^2} = \sum_{n=0}^{\infty} \frac{(-1)^n \xi^{2n}}{n!} = 1 - \xi^2 + \frac{\xi^4}{2!} - \frac{\xi^6}{3!} + \dots \quad (4.12)$$

Moreover, the error-function (see Kreyszig, 1988) which is defined as

$$\operatorname{erf}(\xi) = \frac{2}{\pi^{1/2}} \int_0^{\xi} e^{-u^2} du, \quad (4.13)$$

has the Maclaurin power series

$$\operatorname{erf}(\xi) = \frac{2}{\pi^{1/2}} \sum_{n=0}^{\infty} \frac{(-1)^n \xi^{2n+1}}{n!(2n+1)} = \frac{2}{\pi^{1/2}} \left[\xi - \frac{\xi^3}{1!3} + \frac{\xi^5}{2!5} - \dots \right]. \quad (4.14)$$

Applying Equations (4.10), (4.12) and (4.14) to Equation (4.8) yields

$$\begin{aligned} E_{\phi} &= \frac{m}{\pi^{3/2} \sigma_H \rho^4} \sum_{n=0}^{\infty} \left[3 \frac{(-1)^n}{n!(2n+1)} \xi^{2n+1} - 3 \frac{(-1)^n}{n!} \xi^{2n+1} - 2 \frac{(-1)^n}{n!} \xi^{2n+3} \right] \\ &= \frac{m}{\pi^{3/2} \sigma_H \rho^4} \sum_{n=0}^{\infty} \left[\frac{-6n(-1)^n}{n!(2n+1)} \xi^{2n+1} - 2 \frac{(-1)^n}{n!} \xi^{2n+3} \right] \\ &= \frac{m}{\pi^{3/2} \sigma_H \rho^4} \sum_{n=1}^{\infty} \left[\left(\frac{-6n(-1)^n}{n!(2n+1)} + \frac{2(-1)^n}{(n-1)!} \right) \xi^{2n+1} \right] \\ &= \frac{m}{\pi^{3/2} \sigma_H \rho^4} \left(\frac{4}{5} \xi^5 - \frac{4}{7} \xi^7 + \frac{2}{9} \xi^9 - \dots \right). \end{aligned} \quad (4.15)$$

The first term within the series of Equation (4.15) will dominate when

$$\xi = \theta\rho = \rho \left(\frac{\mu_0 \sigma_H}{4t} \right)^{1/2} \ll 1.0 \quad (\text{late-time condition, } z = 0). \quad (4.16)$$

Silic (1989) also arrived at this criterion, and suggested that it served as a practical definition of what is meant by "late-time". By truncating the series of Equation (4.15) and applying Equations (4.9) and (4.10), a late-time expression for the azimuthal component of the electric field E_{ϕ} measured at the surface of a homogenous earth can be determined, and is found to be

$$E_{\phi} \approx \frac{m \mu_0^{5/2} \sigma_H^{3/2} \rho}{40 \pi^{3/2}} t^{-5/2} + O(t^{-7/2}) \quad (\text{late-time approximation, } z = 0). \quad (4.17)$$

In addition to this, the late-time approximation for the magnetic field intensity \mathbf{H} can be determined by applying Faraday's law of Maxwell's equations (see Equation 2.1c) to Equation (4.17):

$$\nabla \times \mathbf{E}_{\text{surface}} + \partial_t \mathbf{B} = 0, \quad (4.18)$$

where the magnetic induction \mathbf{B} is related to the magnetic field intensity \mathbf{H} by the auxiliary equation

$$\mathbf{B} = \mu_0 \mathbf{H}. \quad (4.19)$$

Recalling the definition of the curl of a vector in cylindrical-polar coordinates, Equation (4.18) becomes

$$\frac{1}{\rho} \begin{vmatrix} \hat{\mathbf{e}}_{\rho} & \rho \hat{\mathbf{e}}_{\phi} & \hat{\mathbf{e}}_z \\ \partial_{\rho} & \partial_{\phi} & \partial_z \\ E_{\rho} & \rho E_{\phi} & E_z \end{vmatrix} + \mu_0 \partial_t \mathbf{H} = 0. \quad (4.20)$$

Since $E_{\rho} = 0$ and $E_z = 0$, Equation (4.20) will simplify to

$$\frac{1}{\rho} \partial_{\rho} (\rho E_{\phi}) \hat{e}_z + \mu_0 \partial_t \mathbf{H} = 0. \quad (4.21)$$

Substituting Equation (4.17) into Equation (4.21), and rearranging terms yields

$$\partial_t \mathbf{H}(t) = -\frac{m}{20} \left(\frac{\mu_0 \sigma_H}{\pi} \right)^{3/2} t^{-5/2} \hat{e}_z \quad (\text{late-time approximation, } z = 0); \quad (4.22)$$

an expression which is in agreement with Ward and Hohmann (1988). Finally, by associating Equation (4.17) with Equation (4.22), a late-time relationship between the surface azimuthal electric field E_{ϕ} and the vertical component of the magnetic field impulse response $\partial_t H_z(t)$ can be obtained:

$$E_{\phi} \approx -\frac{\mu_0 \rho}{2} \frac{\partial}{\partial t} H_z(t). \quad (4.23)$$

In summary, the localised late-time behaviour of the surface azimuthal electric field is found to vary in direct proportion to the vertical magnetic field impulse response, and increase linearly with distance from the VMD source. Equations (4.17) and (4.23) are key results that are used within the next section to infer the late-time $t^{-7/2}$ power law of a decaying galvanic anomaly.

Some caution must be exercised when interpreting Equation (4.23), for at first glance, this expression seems to suggest that the electric field will actually increase without bound, with increasing radial distance from the source. To overcome such an unreasonable conclusion, one must enforce the late-time condition upon which the expression was derived. In reference to the late-time criteria of Equation (4.16), one may state that the late-time approximation for a set half-space conductivity will be valid for a sufficiently large time, at a particular radial distance from the VMD source. This criteria stems from the finite amount of time it takes for the induced system of diffusing host currents or "smoke ring" to expand beyond the location of the receiver, at which instant late-time is achieved. Increasing the host conductivity will slow the expansion of the diffusing current system; this in turn will delay the onset of "late-time". Those times at which the "smoke ring" approaches and is in close proximity to the receiver can be loosely defined as early to middle times.

It is apparent from Equation (4.16) that as the radial distance ρ of the receiver from the VMD is increased, the temporal range of validity of a late-time asymptotic expression will be pushed back to later times. Alternatively,

the times at which a late-time expression holds for a particular value of ρ will in general not hold for another. Hence, for any given time the radial distance ρ cannot be increased indefinitely without breaching the late-time condition. Moreover, if the late-time condition is indeed satisfied for a given time and position, then Equation (4.23) dictates the azimuthal electric field will be found to have only a localised linear dependence upon the radial distance of the test point from the source.

4.3.3. INFERENCE OF THE LATE-TIME POWER LAW FOR GALVANIC DECAY.

An informal derivation is presented within this section of the $t^{-7/2}$ power law, proposed by Asten (1991a), which describes the late-time decay of a TEM galvanic response. The following derivations are based upon a series of lecture notes prepared by Asten (1998).

Consider a finite inhomogeneity, or target, residing within an otherwise homogeneous earth, and let this system be excited by an aperiodic VMD situated at the surface. Galvanic currents will arise within the target as the circulating host currents, induced within the earth by the VMD, are perturbed into the locally more conductive region (see Section 1.2 for a full description of the mechanism of current gathering). It is possible by means of Ohm's law (see Equation 2.14) to compute the current density \mathbf{J} at each point in the earth, once the conductivity distribution σ_T and the electric field function \mathbf{E}_T is known:

$$\mathbf{J} = \sigma_T \mathbf{E}_T. \quad (4.24)$$

This problem can be simplified by introducing the concept of anomalous target conductivity σ_A , which is defined as the difference between the absolute target conductivity σ_{target} and the conductivity of the surrounding host σ_H :

$$\sigma_A = (\sigma_{\text{target}} - \sigma_H). \quad (4.25)$$

Implementing this concept, Equation (4.24) can be expanded by representing the conductivity distribution within the earth σ_T , as the sum of the host conductivity σ_H and the anomalous target conductivity σ_A :

$$\begin{aligned} \mathbf{J} &= \sigma_T \mathbf{E}_T \\ &= (\sigma_H + \sigma_A) \mathbf{E}_T \\ &= \sigma_H \mathbf{E}_T + \sigma_A \mathbf{E}_T. \end{aligned} \quad (4.26)$$

Applying Ohm's law to each term of Equation (4.26) yields, in order

$$\mathbf{J} = \mathbf{J}_{\text{host}} + \mathbf{J}_{\text{galvanic}}; \quad (4.27)$$

thus it is recognised that the total earth current density \mathbf{J} , can be separated into its host \mathbf{J}_{host} and galvanic $\mathbf{J}_{\text{galvanic}}$ components. In this treatment, the galvanic currents have been equated to the anomalous current flow, and not the total current flow, within the target. In order to compute the galvanic current density $\mathbf{J}_{\text{galvanic}}$, the electric field \mathbf{E}_T in the vicinity of the target is required. Unfortunately, an analytical solution for \mathbf{E}_T is in general unavailable. If, however, the conductivity inhomogeneity is regarded to be relatively insignificant in respect to the computation of \mathbf{E}_T , it can be assumed that \mathbf{E}_T can be replaced with an expression determined for a simple half-space. Hence, for the special case of a near surface target, and by Equation (4.23), a suitable approximation for the galvanic current density at late-time can be obtained:

$$\begin{aligned} \mathbf{J}_{\text{galvanic}} &= \sigma_A \mathbf{E}_T \\ &\approx \sigma_A \mathbf{E}_{\phi(\text{half-space})} \\ &\approx \frac{-\mu_0 \sigma_A \rho}{2} \frac{\partial}{\partial t} H_z(t). \end{aligned} \quad (4.28)$$

The Ampere-Maxwell law for time-dependent fields relates the curl of the magnetic field intensity \mathbf{H} to both the conduction \mathbf{J} and displacement \mathbf{D} currents (see Equation 2.1d):

$$\nabla \times \mathbf{H} - \partial_t \mathbf{D} = \mathbf{J}. \quad (4.29)$$

Neglecting displacement currents and applying Equation (4.28), the secondary magnetic fields associated with the anomalous galvanic currents can be approximated:

$$\begin{aligned} \nabla \times \mathbf{H}_{\text{galvanic}} &\approx \mathbf{J}_{\text{galvanic}} \\ &\approx -\frac{1}{2} \mu_0 \sigma_A \rho (\partial_t H_z) \hat{e}_{\phi} \\ &\propto t^{-5/2}. \end{aligned} \quad (4.30)$$

Since time-domain systems, employed within geophysical surveys, measure the voltage induced by the decaying secondary fields within the receiver sensor, the recorded galvanic response will be expected to behave as the temporal derivative of Equation (4.30):

$$\begin{aligned} \nabla \times \partial_t \mathbf{H}_{\text{galvanic}} &\approx \partial_t \mathbf{J}_{\text{galvanic}} \\ &\propto t^{-7/2}. \end{aligned} \quad (4.31)$$

Hence it is inferred, that the galvanic impulse response $\partial_t (\mathbf{H}_{\text{galvanic}})$ of a near surface target will, at late-time, exhibit a $t^{-7/2}$ power law decay.

4.3.3.1. SUMMARY.

In the case of a conductive half-space, analytic expressions for a vertical magnetic dipole VMD which has been terminated abruptly only exist for the situation in which both the dipole and receiver reside upon the boundary surface (Ward and Hohmann, 1988). Using a power series expansion, a late-time approximation can be derived from these expressions for the local surface azimuthal electric field. In turn, the conduction currents arising from the anomalous conductivities within the host, and driven by this late-time electric field, will result in a decaying unipolar magnetic field. Given that only measurements of the voltages induced within the receiving coils are made, the temporal derivative of the decaying magnetic field is required and was shown to decay at late-times by a power law with a decay index of $-7/2$, as was inferred by Asten (1991a).

4.3.4. GALVANIC EXCITATION OF A TARGET AT DEPTH.

The validity of the late-time behaviour of the galvanic magnetic field impulse response, established within the previous section after the work of Asten (1991a) and Asten (1998), is restricted to the special case of near surface targets. This limitation stems from the late-time expression, Equation (4.23), employed to approximate the primary electric field, an expression which is valid only at the surface of a homogeneous earth. As noted earlier, in Section 4.3.2, no analytical solutions are available, for computing at any given depth or time, the primary electric field induced within a half-space by a VMD source. In such a generalised situation, one must resort to numerical methods to compute the primary electric field. Fortunately, however, a late-time analytical asymptotic solution is obtainable for the determination of the primary electric field at any depth. A half-space solution from Silic (1989), which describes the late-time behaviour of the primary electric field E'_{ϕ} normalised to the transmitter-loop

current, will be used within this section to infer the time dependence of the anomalous galvanic current flow within a target at an arbitrary depth z :

$$E'_\phi \approx \frac{a^2 \mu_0^{5/2} \sigma_H^{3/2} \rho}{40 \pi^{1/2}} t^{-5/2} + \frac{5\Gamma(5/2)}{96} \cdot \frac{a^2 \mu_0^3 \sigma_H^2 \rho}{\pi^{1/2}} z t^{-3} \quad (\text{late-time approximation}), \quad (4.32)$$

where a is the radius of the aperiodic current-loop source, which is located at the origin of the system described by (ρ, ϕ, z) cylindrical-polar coordinates, z is the depth and ρ is the radial distance from the source axis. The gamma function of x , denoted by $\Gamma(x)$, appearing within the second term of Equation (4.32) is defined as

$$\Gamma(x) = \int_0^\infty e^{-u} u^{x-1} du, \quad (4.33)$$

so that, $\Gamma(5/2) \approx 1.32934$, see Kreyszig (1988). Moreover, the late-time condition imposed by Silic (1989) on Equation (4.32), is given by

$$(a^2 + z^2 + \rho^2) \left(\frac{\mu_0 \sigma_H}{4t} \right) \ll 1.0 \quad (\text{late-time condition}). \quad (4.34)$$

Recall, that for an infinitesimal loop of radius a carrying a current I , the magnetic dipole moment m is given by

$$m = I \pi a^2. \quad (4.35)$$

By application of Equation (4.35) to Equation (4.32), the late-time expression for the primary electric field can be rewritten in terms of m :

$$E'_\phi \approx \frac{m \mu_0^{5/2} \sigma_H^{3/2} \rho}{40 \pi^{3/2}} t^{-5/2} + \frac{5\Gamma(5/2)}{96} \cdot \frac{m \mu_0^3 \sigma_H^2 \rho z}{\pi^{3/2}} t^{-3} \quad (\text{late-time approximation}); \quad (4.36)$$

a form which is equivalent to Equation (4.17). By following the procedure within Section 4.3.3, and substituting the new depth dependent expression for the primary electric field, Equation (4.32), for the previously determined expression restricted to surface solutions, Equation (4.17), one can immediately infer the late-time behaviour of the galvanic TEM voltage response associated with a small finite target residing at a depth z :

$$\begin{aligned} \nabla \times \partial_t \mathbf{H}_{\text{galvanic}} &\approx \partial_t \mathbf{J}_{\text{galvanic}} \\ &\approx \partial_t (\sigma_A E_\phi) \\ &\approx -\frac{\sigma_A m \mu_0^{5/2} \sigma_H^{3/2} \rho}{16 \pi^{3/2}} t^{-7/2} - \frac{5\Gamma(5/2)}{32} \cdot \frac{\sigma_A m \mu_0^3 \sigma_H^2 \rho}{\pi^{3/2}} z t^{-4}. \end{aligned} \quad (4.37)$$

Hence, unlike near surface targets, the galvanic TEM response due to a target residing at an arbitrary depth z , will not strictly exhibit a $t^{-7/2}$ power law decay at late-time. Indeed, if a single power law were fitted to a late-time galvanic response, decaying as Equation (4.37), the resulting decay index will be expected to lie within the indicial range of -3.5 to -4.0. It is noted, however, that for the special case of $z = 0$, the second term of Equation (4.37) will vanish resulting in an expression which is identical to Equation (4.31). The extent to which the depth of the target will affect the decay index can be inferred from the ratio (V_1 / V_2) , where V_1 and V_2 are the first and second terms of Equation (4.37) respectively:

$$\frac{V_1}{V_2} = \frac{2}{5\Gamma(5/2)} \cdot \frac{1}{z} \sqrt{\frac{t}{\mu_0 \sigma_H}}. \quad (4.38)$$

This section shall now be concluded with a final analysis of the late-time behaviour of Equation (4.37). The decaying magnetic field associated with the diffusing host current system induced by a VMD within a simple half-space, was demonstrated by Nabighian (1979) to be representable by an expanding and attenuating current-loop or "smoke ring", see Section 2.8 for further discussion. A set of equations describing the evolution and kinematics of a "smoke ring" were provided by Nabighian (1979), amongst this set is an expression for the determination of the "smoke ring" depth:

$$z(t) = \sqrt{\frac{16t}{\pi \sigma_H \mu_0}}. \quad (4.39)$$

Recall the earlier definition of "late-time" put forward in Section 4.3.2: late-time can be regarded as those times after which the electric field maxima of the diffusing host current system has passed beyond the region of concern. By this definition, a critical value for the ratio (V_1 / V_2) can be obtained by equating the target depth z_{target} to the depth of the "smoke ring" $z_{S,R}$, thus substitution of Equation (4.39) into Equation (4.38) yields

$$\begin{aligned} z_{target} &= z_{S-R} \\ \left(\frac{V_1}{V_2}\right)_{critical}^{-1} \cdot \frac{2}{5\Gamma(5/2)} \cdot \sqrt{\frac{t}{\mu_o \sigma_H}} &= \frac{4}{\pi^{1/2}} \sqrt{\frac{t}{\mu_o \sigma_H}} \\ \left(\frac{V_1}{V_2}\right)_{critical}^{-1} &= 10\Gamma(5/2)\pi^{-1/2} \end{aligned} \quad (4.40)$$

Thus, for Equation (4.38) to be valid the following condition must be imposed:

$$\left(\frac{V_1}{V_2}\right) > \left(\frac{V_1}{V_2}\right)_{critical} \quad (4.41)$$

Moreover, by re-substitution of Equation (4.40) and Equation (4.38), this criterion can be rewritten as

$$z_{target}^2 \frac{\mu_o \sigma_H}{(16\pi^{-1})t} < 1.0; \quad (4.42)$$

which is precisely the late-time condition, Equation (4.34), originally imposed by Silic (1989) on the asymptotic expression for the primary electric field, Equation (4.32). Recapitulating the key results of this section: it is inferred that the late-time decay of a galvanic TEM response will not strictly obey a $t^{-7/2}$ power law for a target at depth. The requirement, however, for the depth independent term of Equation (4.37) to dominate, is none other than the late-time condition itself. Thus at late-time, not only will Equation (4.37) be valid, but it will essentially decay by a $t^{-7/2}$ power law. It is emphasised, that the late-time condition for a target at depth, given by Equation (4.34), is a much stricter criterion than that for near surface targets, given by Equation (4.16). Thus, by Equation (4.42), it is inferred that for the range of host conductivities, target depths and times at which decay analysis is likely to be applied in the field, only a slight increase, if any, within the galvanic decay index is likely to be observed. Moreover, the errors incurred within galvanic decay analysis from the preparation of field data, are more than likely to mask the subtle relationship between the observed decay index of a target and its depth. The follow caveat concludes this section: before performing decay analysis on a suspected galvanic TEM anomaly, it is imperative that the target under consideration (located at a depth z and radial distance ρ from the VMD source) satisfies the generalised galvanic late-time condition given by Equation (4.34).

CHAPTER FIVE

CADJEBUT LEAD-ZINC ORE BODY.

Material from this chapter has been published within a peer-reviewed paper (see Appendix C.3):
Theodoridis, J.A., and Asten, M.W., 2001. Galvanic excitation of the Cadjebut Pb-Zn ore body: Extended Abstracts of the ASEG 15th Geophysical Conference and Exhibition, 5-8 Aug. 2001, Exploration Geophysics, v. 32, p. 176-180.

5.1. INTRODUCTION.

5.1.1. DISCOVERY OF CADJEBUT.

In 1976, exploration of the Leonard shelf in North Western Australia commenced under a joint Venture between BHP and Billiton (Scott *et al.*, 1994). A combination of geology, geochemistry and geophysics defined areas of interest to focus exploration efforts. Following the experiences with the North American Mississippi Valley-Type (MVT) deposits, statistical and systematic grid-drilling programmes were undertaken within the areas of noted importance (Scott *et al.*, 1994). This rigorous exploration programme resulted in the discovery of a number of significant MVT occurrences, which included the Cadjebut, Blendevale and Twelve Mile Bore deposits (Scott *et al.*, 1994).

5.1.2. MINERALISATION.

Discovered in 1984, the Cadjebut lead-zinc deposit is situated on the Leonard Shelf at the southern end of the Emanuel Range in North Western Australia. Exhibiting typical MVT characteristics, the Cadjebut ore body is hosted by silty, shallow shelf-facies dolomite (lower dolomite) situated at the base of the Devonian Pillara Limestone unit (Scott *et al.*, 1994). The mineralisation is epigenetic and essentially strata bound, featuring coarse-grained galena, sphalerite, marcasite and sparry calcite. These constituents are found to be either infilling open spaces or replacing the original host rock (Scott *et al.*, 1994). A geologic plan and cross-section of the Cadjebut mineralisation are shown within Figure 5.1a and Figure 5.1b respectively. The deposit is comprised of

two high-grade lenses running parallel to each other dipping gently in the east-south-east direction. The strike length of the deposit is approximately 3 km, with its width ranging from 50 m to 150 m and its thickness from 2 m to 8 m (Scott *et al.*, 1994).

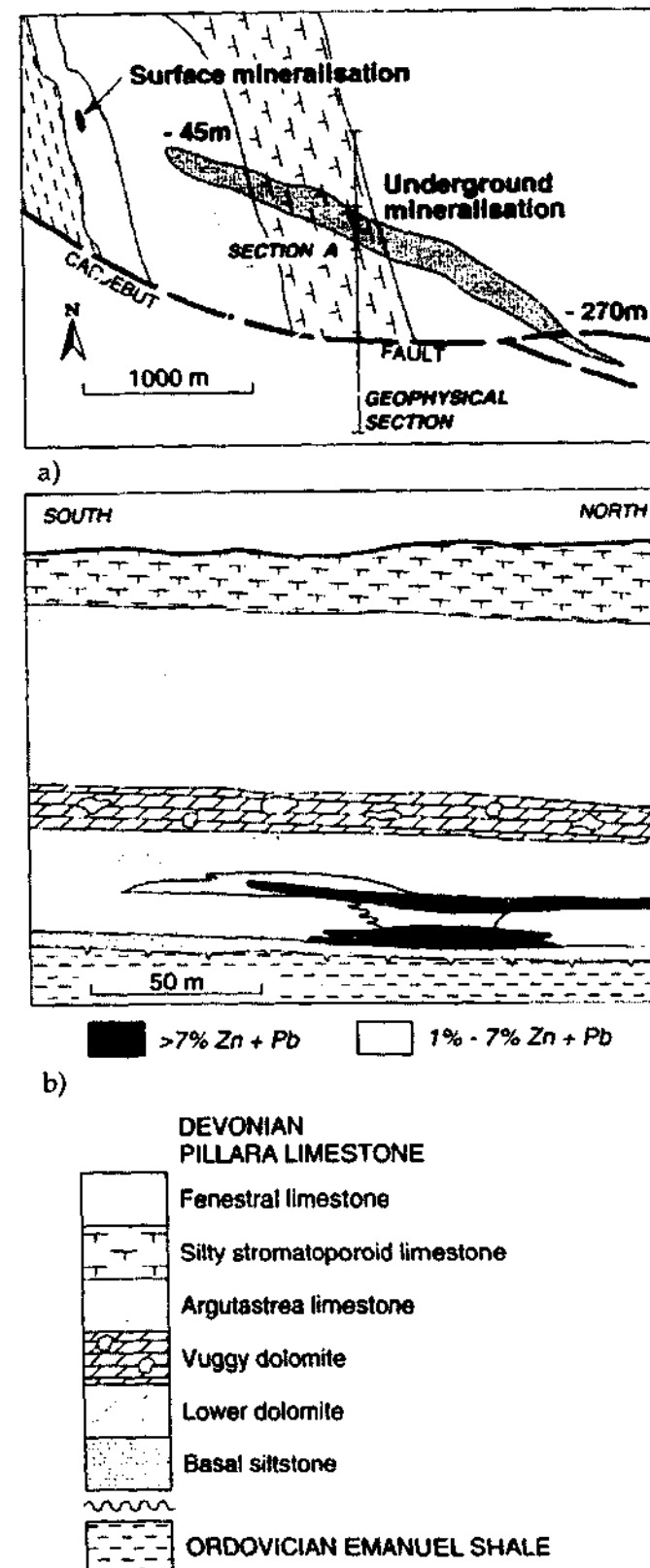


Figure 5.1: Geologic plan a), and cross-section b), of the Cadjebut mineralisation, which is, comprised of two high-grade Pb-Zn ore lenses running parallel to each other. Note the gentle dip of the deposit, which varies in depth from 45 m in the northwest to 270 m in the southeast. (Scott *et al.*, 1994).

5.1.3. TRIAL SURVEYS.

Mississippi Valley-type lead-zinc deposits are difficult geophysical targets, requiring extensive exploration programmes at high cost. Studies of the geophysical characteristics of MVT's on the Leonard Shelf provided a practical guide for more cost efficient exploration methods on both the Leonard Shelf and elsewhere (Scott *et al.*, 1994).

Lebel (1987) documented geophysical test surveys performed over BHP/Shell's Cadjebut Pb-Zn ore body in August and September of 1987; these tests included surface and downhole transient electromagnetic (DHTEM) surveys and induced polarisation (IP) methods. The purpose of these tests was to determine the effectiveness of the aforementioned survey techniques on the Cadjebut mineralisation, and to exploit findings that correlated with the known properties of the deposit to improve the efficiency of exploration at adjacent sites (Lebel, 1987).

5.2. METHODS.

5.2.1. TECHNICAL MATTERS.

This case study revisited archival data sourced from Lebel (1987) for re-interpretation, namely: two downhole TEM surveys and a 100 m coincident-loop survey. See the foldout survey map (Plate I) located in the rear sleeve for the configuration of the coincident-loop and downhole TEM surveys. Marked upon Plate I are the locations of the collar of Borehole ID159 and the associated transmitter loops - Loop Tx1 (inductively well-coupled near loop) and Loop Tx2 (weakly-coupled offset loop), and Line E of the coincident-loop survey. See also Plate II located in the rear sleeve for the cross-sectional view of the mineralisation with Borehole ID159.

The coincident-loop survey utilised a 100 m square loop with station spacings of 50 m, in conjunction with a SIROTEM MK II receiver operating at early-delay times and an RVR unit; readings at each station were recorded up to window 26 (8.404 ms). See Figure 5.2 for the vertical component of the coincident-loop TEM field response.

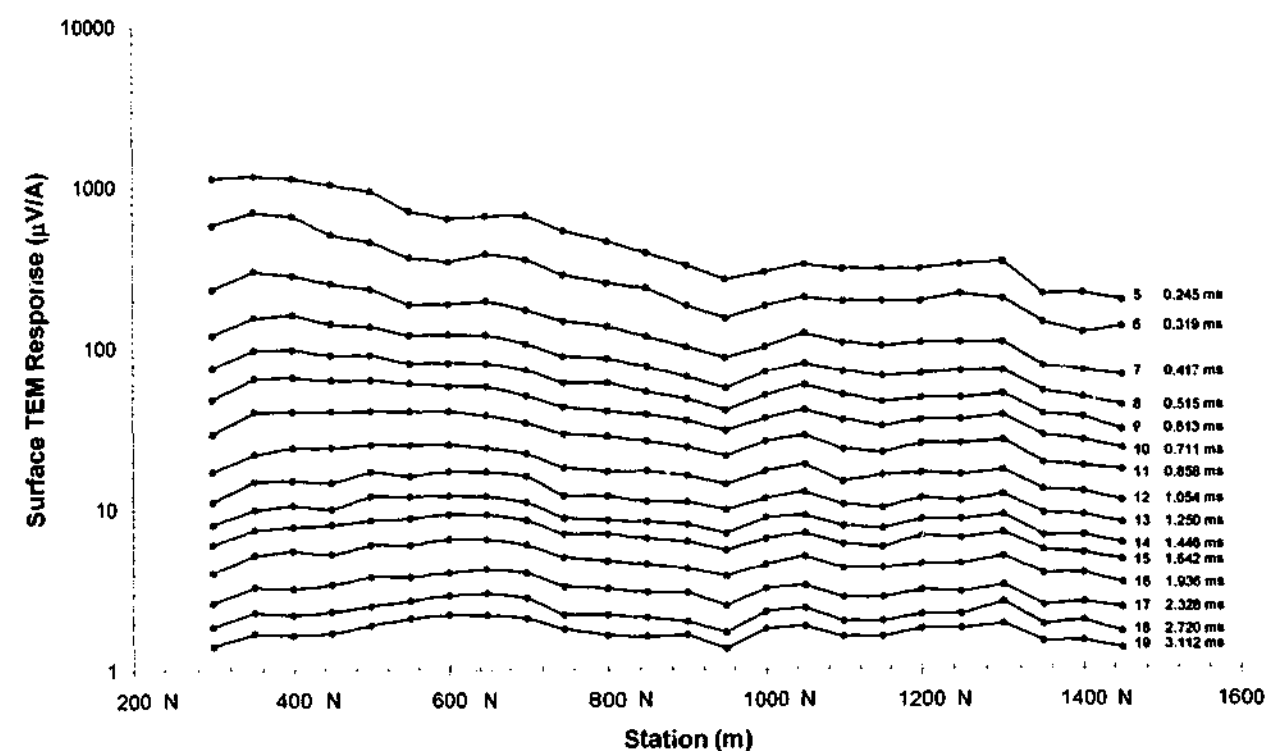


Figure 5.2: Logarithmic profiles of the Line E vertical-component Field TEM response. The 100 m coincident-loop survey, was conducted with 50 m spacings and a SIROTEM MKII instrument operating at early-delay times.

Consider the downhole TEM survey line, Line H, which crosses the Pb-Zn mineralisation (see Plate I, foldout survey map). Upon this line resides the collar of Borehole ID159; the borehole itself dips at an angle of 29 degrees taken from the vertical into northerly direction (see Plate II, foldout cross-section of mineralisation). Readings were taken with a single axis component probe at borehole axial depths of 20 m to 125 m in intervals of 10 m, and then in intervals of 5 m to a final depth of 155 m. The probes at these positions measured the component of the secondary magnetic field parallel to the axis of the borehole, where the primary field is generated by the surface 150 m x 150 m square loops labelled Tx1 and Tx2. The instrument used was a SIROTEM MK II receiver, which recorded standard-delay times up to window 20 (20.110 ms).

Logarithmic profiles of the Tx1 and Tx2 field data are shown in Figure 5.3 and Figure 5.4 respectively. The induced voltage response of the decaying secondary fields was measured and normalised against the current within the associated transmitter loop, thereby acquiring the units of microvolts per ampere. Unfortunately, the archival field data had to be manually digitised for it was only available within hardcopy graphical form (the original data tapes

are thought to be lost). Moreover, this procedure was susceptible to error since the plots were of logarithmic scale.

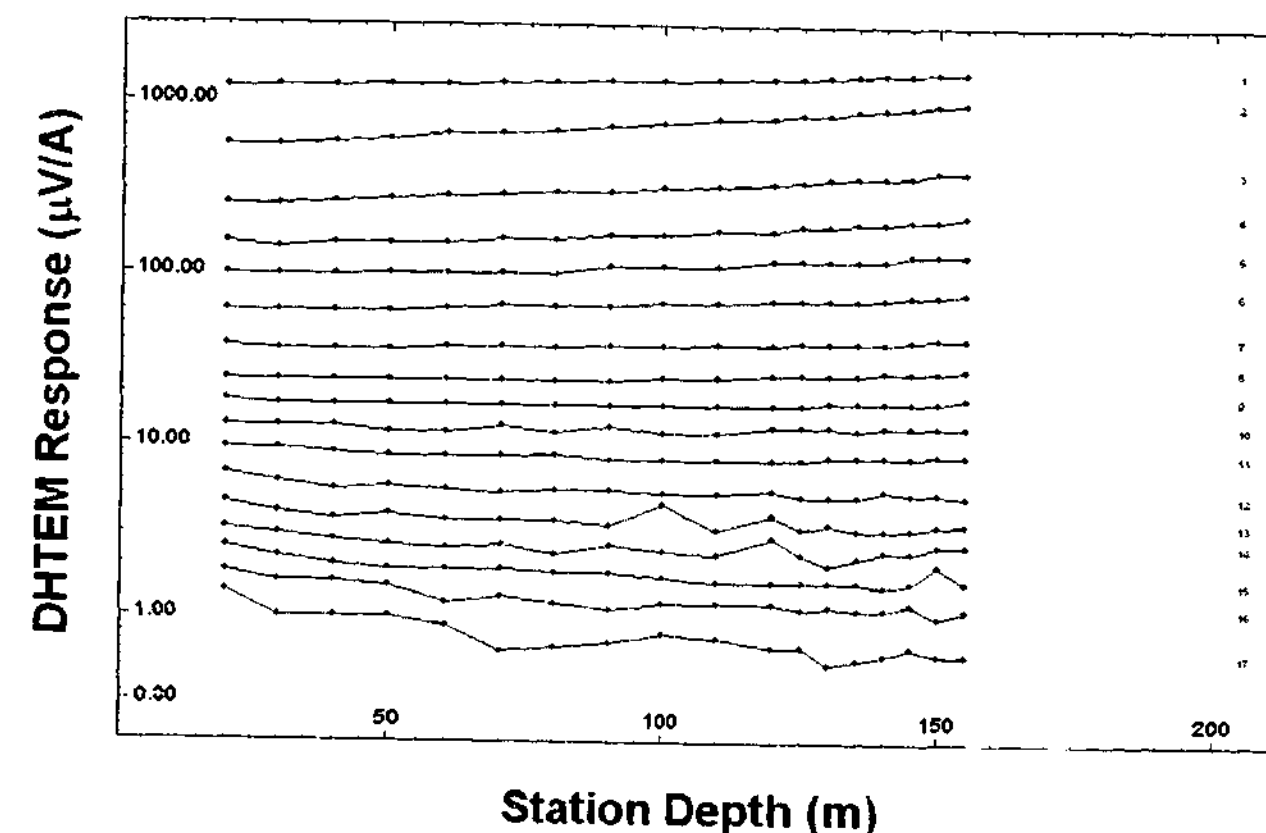


Figure 5.3: Logarithmic profile of the axial-component field response of Borehole ID159 due to Tx1. The first four time windows are window 1 (0.474 ms), window 2 (0.866 ms), window 3 (1.258 ms) and window 4 (1.650 ms).

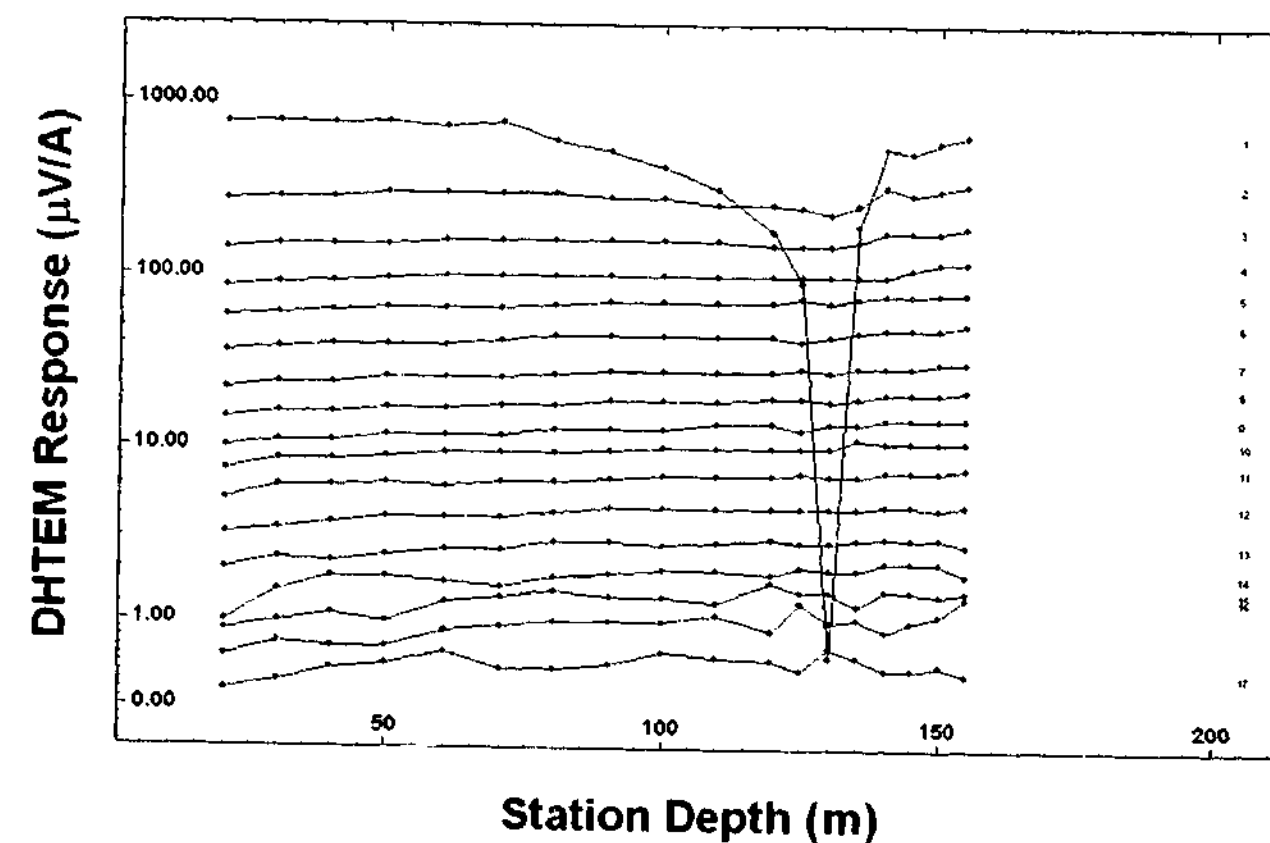


Figure 5.4: Logarithmic profile of the axial-component field response of Borehole ID159 due to Tx2. The first four time windows are the same as those in Figure 5.3.

5.2.2. EARLY INTERPRETATIONS OF DATA.

Two aspects of the field data warranted further investigation: the M-shaped anomaly within the Line E moving loop data, and the prominent signature within the Tx2 downhole TEM data. As shown within Figure 5.2, the M-shaped anomaly consists of two peaks centred about Stations 1000N and 1250N. The anomaly is first recorded at window 5 (0.245 ms) and persists to window 18 (2.720 ms) without any significant attenuation. Interpretations of the moving loop data within this thesis began with the premise that the M-shaped anomaly was a signature of the Cadjebut mineralisation; subsequent modelling has indicated this to be unlikely (see Section 5.4).

Secondly, in regards to the downhole TEM surveys, a surprising result was obtained. The response due to the transmitter loop Tx1, which lies directly over the deposit and is thus inductively well-coupled with it, is devoid of any target signature (see Figure 5.3), whereas transmitter loop Tx2, which lies offset to the mineralisation and is weakly-coupled with the deposit, features a prominent intersection anomaly at Station 130 (see Figure 5.4).

No previous comprehensive modelling of the Line E or Line H data sets has been undertaken. Lebel (1987), however, made some preliminary interpretations, and to a greater degree, so did Scott *et al.* (1994). Their work provided a foundation for the modelling undertaken within this thesis.

5.2.3. BACKGROUND LEVEL IN LINE E.

Another prominent feature of the moving loop data is the gradual decrease in the background signal strength when traversing the survey line from south to north. This trend within signal strength correlates well with the apparent resistivities obtained from the surface induced polarisation survey performed along Line E. Specifically, the IP survey yielded apparent resistivities ranging from 30 ohm.m at Station 400N up to values of 500 ohm.m near Station 1600N (Lebel, 1987). In addition to this, Scott *et al.* (1994) attributed the decrease in signal strength to a tapering in thickness of the black soil and shale overburden south of the limestone outcrop (see also Figure 5.1b).

5.2.4. ABSENCE OF A DEFINITIVE ANOMALY.

Apart from the strong overburden effects, previous authors have noted the absence of any definitive inductive signature of the Cadjebut mineralisation. Scott *et al.* (1994) noted a very weak anomalous response centred about Station 1050N apparent at late-times out to window 26 (8.404 ms), but concluded the amplitude of the response is too weak to be definitive. Lebel (1987) noted that although there are no anomalies in the chargeability associated with the ore body, there is however, a resistivity high (500 to 600 ohm.m) between stations 1000N and 1200N. Unfortunately, the resistivity high found within the IP data has no such equivalent within the TEM data. As such, Lebel (1987) concluded that neither the fault nor the ore body are sufficiently conductive to cause any prominent, visual anomalies.

5.2.5. THE INEFFECTIVENESS OF TEM METHODS OVER CADJEBUT.

Despite the abundance of the conductive sulphides galena, marcasite and pyrite within the Cadjebut mineralisation, the deposit itself is only weakly conducting (Scott *et al.*, 1994). The poor conductivity of the deposit can be attributed to the constituent sulphides, which are in general disseminated and perhaps massive in form, being electrically unconnected due to interlayering with the predominant colloform sphalerite, calcite and limestone (Scott *et al.*, 1994). Factors that influence the variability of target conductance were discussed within Section 1.1. Thus, due to its low conductivity, Cadjebut is essentially impervious to EM methods that utilize induction as the primary mechanism in detection. Furthermore, in areas of conductive cover, similar type weak conductors will yield an EM response that would be highly attenuated by the overburden response (Scott *et al.*, 1994).

To summarise Scott *et al.* (1994) and Lebel (1987), the Cadjebut mineralisation is neither sufficiently conductive nor chargeable, or shallow enough, to permit detection by either IP, surface or downhole TEM methods. In conclusion, TEM methods are not an effective exploration technique for Cadjebut style mineralisations under conductive cover.

5.3. MODELLING THE FIELD DATA.

The coincident-loop and downhole TEM data sets yielded geologic information about the host and electrical properties of the ore body: inversions on the coincident-loop data yielded layer resistivities and thickness for a five-layer host model, whilst the downhole TEM data permitted indirect conductivity estimates of the Cadjebut mineralisation itself.

5.3.1. DEVELOPMENT OF A FIVE LAYERED EARTH MODEL.

Preliminary models of the downhole TEM data employed only simple conductive half-spaces to represent the earth; however, these models inadequately matched the regional component of the field response. Attempts to acquire a suitable host conductivity structure by trial and error proved impractical. The geologic cross-section of the Cadjebut mineralisation prepared by Scott *et al.* (1994) (see Figure 5.1b) provided the basis for the inference of a layered earth structure. Although the cross-section contained information about layer thickness and composition, it did not provide information about the electrical properties of those layers. Instead, a series of inversions of the coincident-loop data with program GRENDL permitted the determination of the layer resistivities. A five-layered model derived from the six layered earth section of Scott *et al.* (1994), by the combination of layers four and five, served as an initial model for the GRENDL inversions (see Table 5.1 for model attributes). The field data inversions performed with neither the layer resistivities nor thickness fixed yielded a unique layered earth structure for each station with an average standard error of 3.9% (see Figure 5.5). Subsequent averaging of the different layer resistivities and thickness yielded the final single five-layered earth model (see Table 5.1 for model attributes).

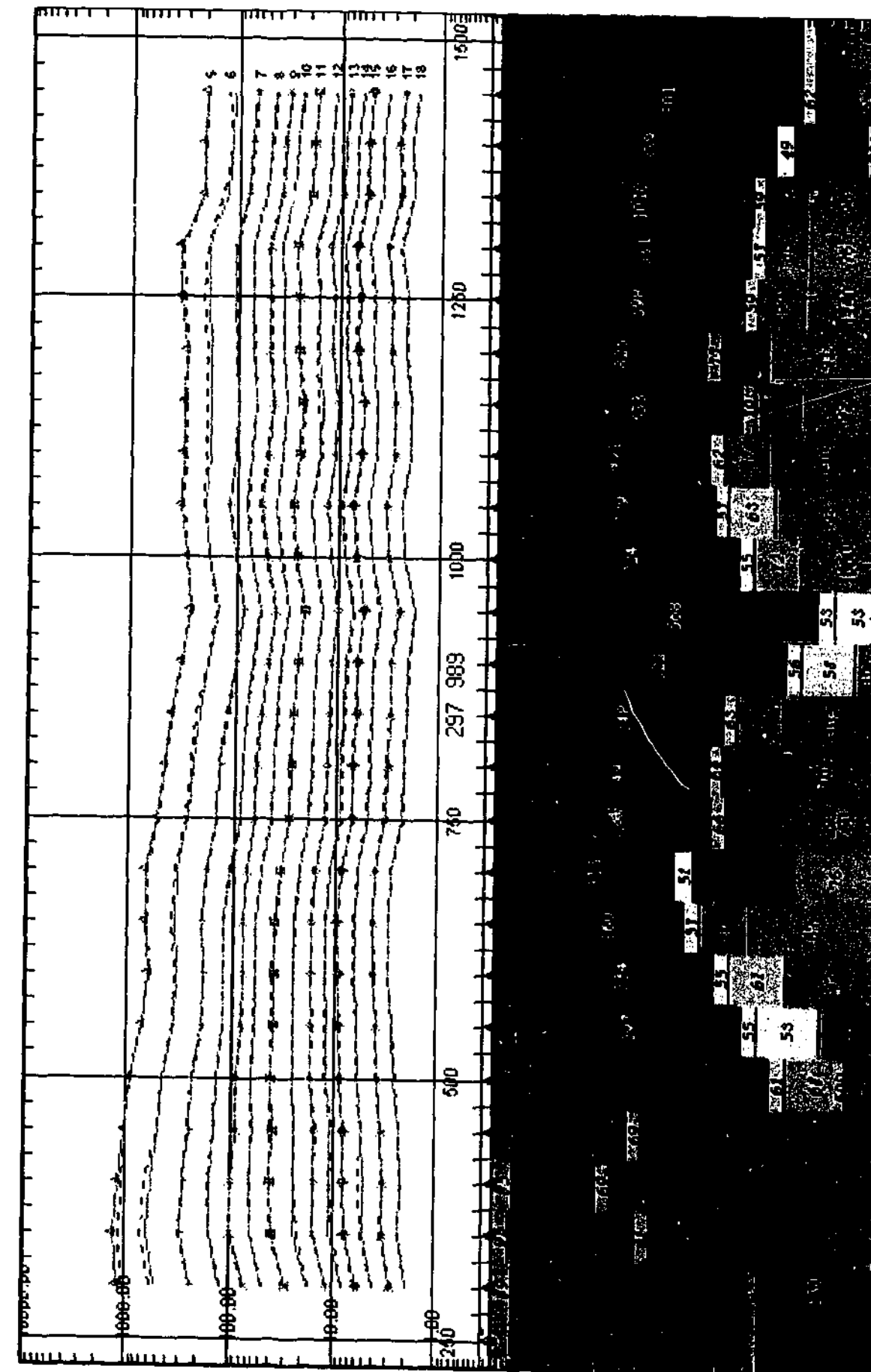


Figure 5.5: Layered earth structure acquired with program GRENDL by inversion of the Line E coincident-loop field data (host resistivities shown in ohm.m). The associated inverted model response is shown in solid lines, whilst the field data is shown in dashed lines. Each station was inverted in isolation of each other, so that the resulting earth structure is simply the independent layered earth models for each station placed side-by-side one another.

Table 5.1: Initial model used for GRENDL inversion and resulting GRENDL layered earth model. Note the increased thickness of the second layer after inversion. The thicknesses of each layer within the initial model are based upon the geologic section of Scott *et al.* (1994).

Layer	INITIAL MODEL.		GRENDL MODEL.	
	Thickness (m)	Resistivity (ohm.m)	Thickness (m)	
1	20	210	25	
2	55	538	175	
3	13	61	14	
4	38	135	54	
5	Basement	104	Basement	

Curiously, the model inverted to is remarkably different from the initial obtained from the geological cross-section acquired from Scott *et al.* (1994). Moreover, Scott *et al.* (1994) shows the ore body to lie at a depth of about 100 m along the survey line E, Figure 5.1b, this is in disagreement with the survey map of the region provided by Lebel (1987), which suggests a depth of about 80 m, Figure 5.1b.

Nevertheless, the five layered model proposed within Scott *et al.* (1994) seems credible, as it possesses important features such as the conductive overburden of silty limestone and a conductive basement of emanuel shale. Hence, the layered structure inverted to was deemed suitable as a host in which the ore body may reside.

5.3.2. CONSTRUCTION OF THE COINCIDENT-LOOP AND DOWNHOLE TEM MODELS.

Three models were construction within Program MARCO: one for the coincident-loop survey along Line E, and two for the downhole TEM surveys which featured Borehole ID159 in conjunction with transmitter loops Tx1 (overlying loop) and Tx2 (offset loop). Each of the models utilised an identical host-target representation. Physical attributes for the dual-slab model, representing both the upper and lower constituents of the ore body, were derived directly from both Plate I (survey map) and Plate II (cross-section of mineralisation and borehole), acquired from the original test survey report prepared by Lebel (1987). See Figure 5.6 for a cross-sectional view of the down

TEM survey model and Figure 5.7 for the associated plan-view. See also Figure 5.8 for a plan-view of the coincident-loop model. Figure 5.6 is also relevant to the coincident-loop model, as it shows the specifications of the host-target representation that were common to all three models, *e.g.*, layer thicknesses and resistivities; target size and depth.

Two conductive horizontal slabs represented the mineralisation; both slabs were of equal thickness (4 m) and strike-length (400 m). The upper-slab was of width 165 m and was located at a depth of 115 m; whereas the width of the lower-slab was 100 m, and resided 7 m below the upper-slab at a depth of 126 m (slab depth is in reference to its top surface). Although the strike-length of the Cadjebut mineralisation extends to around 3km (see Figure 5.1a), a model strike-length of 400 m is sufficient for the scale of the surveys: the coincident-loop survey used 100 m loops, and the downhole TEM surveys used 150 m loops. Modelling trials, which tested the effects of variation of strike-length, revealed that strike-lengths greater than 400 m produced no significant change in the amplitude of the downhole TEM galvanic anomalies, and only caused a slight increase in the persistence of the coincident-loop M-anomaly to later times.

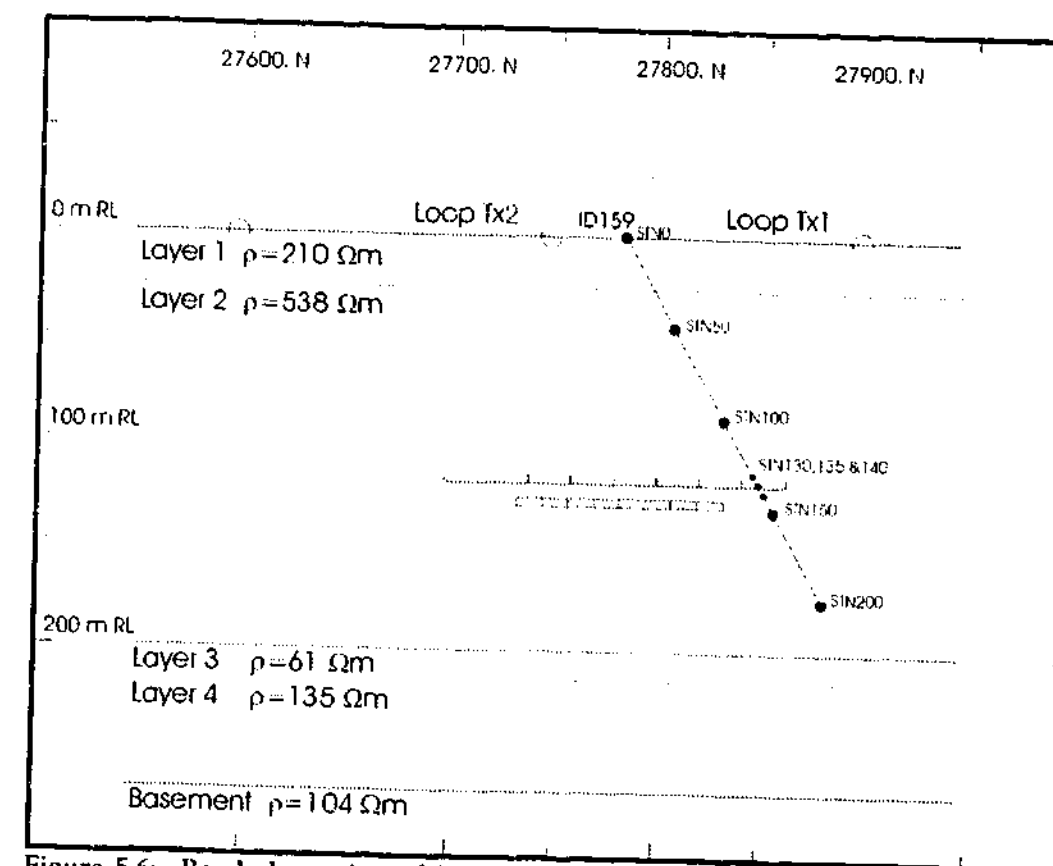


Figure 5.6: Borehole section of ID159 with both loops Tx1 and Tx2, showing the MARCO model which was comprised of a dual-slab target embedded within a five layer host. Both slabs were assigned a resistivity of 2.35 ohm.m. (See Figure 5.7 for the associated plan view of the downhole TEM MARCO model).

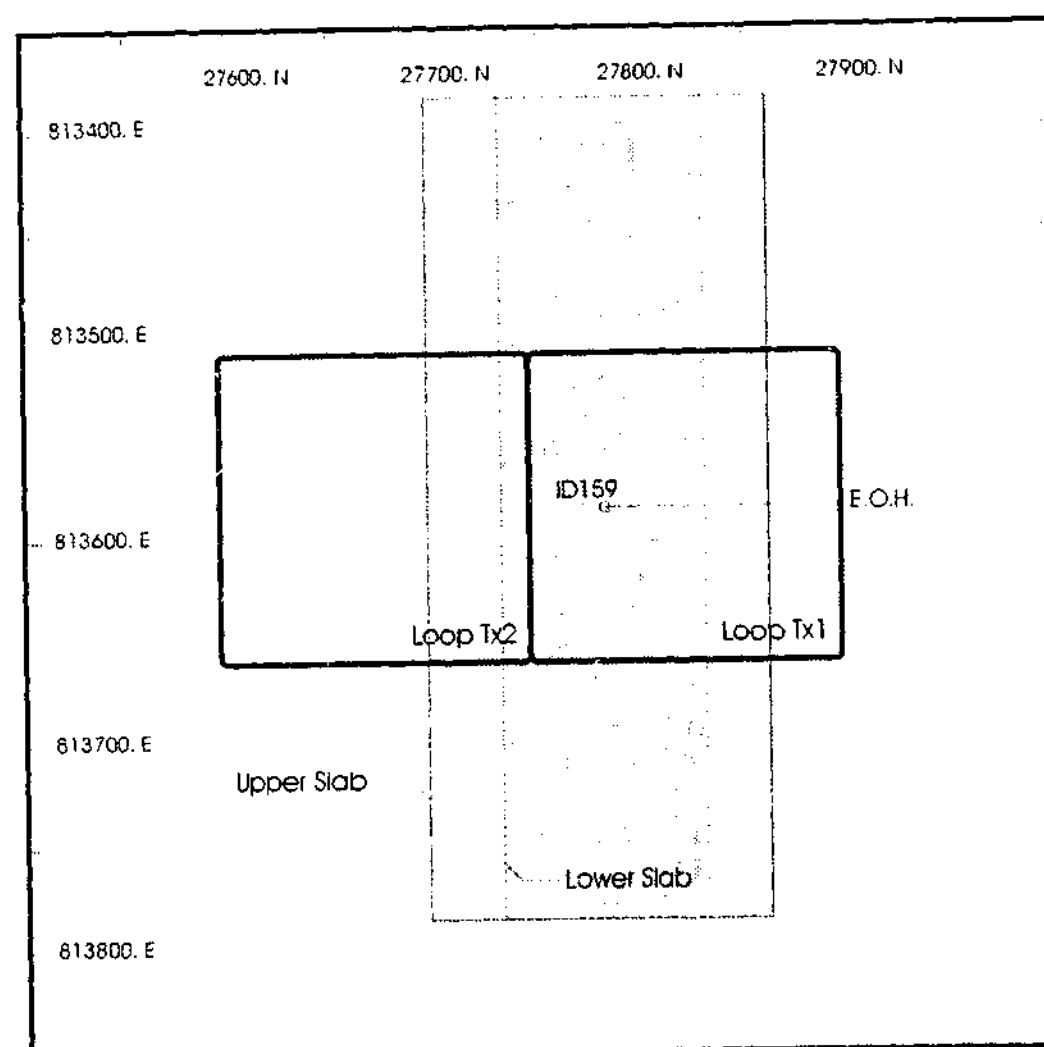


Figure 5.7: Plan view of the downhole TEM MARCO model showing the position of transmitter loops Tx1 and Tx2 with Borehole ID159. The boundary of the lower slab is delineated by the dashed lines. (Note, the surface EM survey was performed 396 m to the west of Borehole ID159, and ran north-south over the Cadjebut mineralisation).

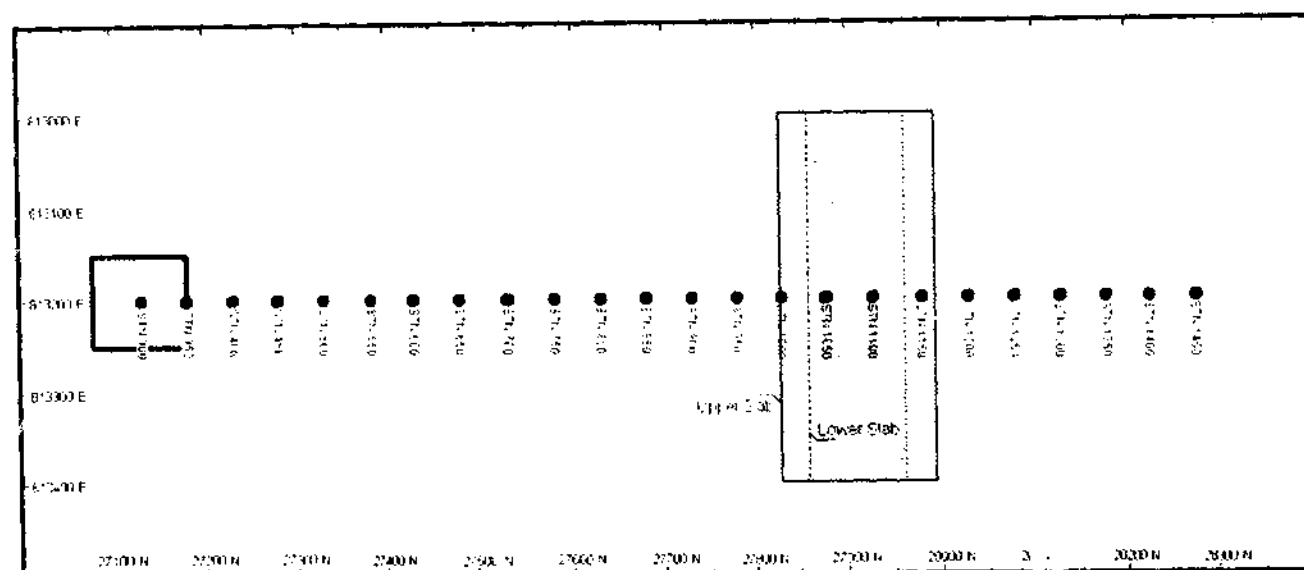


Figure 5.8: Plan view of the MARCO model of the 100 m coincident-loop survey along Line E. The survey line consisted of 24 stations; STN300 to STN1450, at 50 m spacings. The dual-slab target is shown, and was assigned a resistivity of 2.5 ohm.m (refer to Figure 5.6 for specifications of host-target representation).

5.3.3. INFERENCE OF TARGET RESISTIVITIES.

Explicit resistivity estimates of the Cadjebut mineralisation were not possible in the absence of an inductive component within the target response. Instead, resistivity estimates for mineralisation were sought indirectly by seeking a range of target model resistivities that were low enough to inhibit inductive excitation, but high enough to maintain a suitable host-target resistivity contrast to permit galvanic saturation. Subsequent refinement of the target resistivity involved matching the Tx2 intersection anomalies of the model and field downhole TEM data. Early downhole TEM modelling yielded a robust target resistivity of 2.5 ohm.m, this value was adopted for the coincident-loop model, whereas the Tx1 and Tx2 downhole TEM models employed a more refined target resistivity of 2.35 ohm.m. Note, that the highly refined value of 2.35 ohm.m represents the sensitivity of the Tx2 intersection anomaly to slight changes in model parameters within program MARCO, rather than dramatic changes in the galvanic saturation. In all three models, however, the upper and lower slabs of the dual-slab target were of equal resistivity. Regardless of the slightly different resistivities employed within the downhole TEM and coincident-loop models, the order-of-magnitude of the target conductance remains the same, *i.e.*, the conductance of the Cadjebut mineralisation is estimated to be in the order of 1 to 2 S.

5.3.4. TARGET DISCRETIZATION.

Program MARCO requires the user to stipulate the number of cells in which to discretize a target. There are no strict guidelines on discretization, other than the requirement that the cells are sufficiently small to resolve the toroidal inductive currents and poloidal galvanic currents. Recalling the eigencurrent theory of thin-sheets, as discussed within Section 4.2, it is apparent that a target undergoing inductive excitation will require a finer discretization in order to resolve sufficiently the complex geometry of the induced vortex current system. This is particularly true for high-order current systems established at early times. In addition to this, the user is to be mindful of excessive computation times arising from over-discretization. Determination of an appropriate target

discretization proceeded here in a heuristic manner. The requirement for sufficient eddy current resolution has strong implications for the associated secondary fields and the subsequent target response, and in particular, for situations when the receiver is located in close proximity to the target. This became apparent during preliminary work, which revealed the downhole TEM model to be more susceptible to an increase in target discretization than the coincident-loop model.

The upper and lower slabs constituting the target of the coincident-loop model were discretized into 8 by 4 by 2 parts in the strike-length, depth-extent and thickness dimensions respectively, thereby dividing the upper-slab into 50 m x 41.25 m x 2 m cells, and the lower-slab into 50 m x 25 m x 2 m cells. The downhole TEM models required, and employed, a more finely discretized target, which was discretized into 16 by 8 by 2 parts, thereby dividing the upper and lower slabs into 25 m x 20.625 m x 2 m cells and 25 m x 12.5 m x 2 m cells respectively. Unlike the finely discretized model, the coarsely discretized model did not produce a well-defined negative-to-positive intersection anomaly centred about Station 134 (refer to Section 5.4.2 for a detailed discussion of the Tx2 model response), but instead produced a response that oscillated chaotically between Stations 128 and 142 (see Figure C.1.1 of Appendix C.1 for comparison profiles). This result provided the basis for the selection of the finely discretized model for use within the downhole TEM models. Execution times for the MARCO models are given within Table C.2.1 of Appendix C.2.

5.4. RESULTS.

5.4.1. THE COINCIDENT-LOOP MARCO MODEL.

The vertical-component TEM response profiles generated with the coincident-loop MARCO model (see Figure 5.9) are similar to those of the field data (see Figure 5.2). At early times, the target anomaly within the model data appears as a single positive anomaly centred about Stations 1050N and 1100N, evolving with time, this anomaly splits into an M-shaped anomaly at window 7 (0.417 ms) with peaks centred about Stations 950N and 1200N, until finally rapidly diminishing and persisting for another six windows or so.

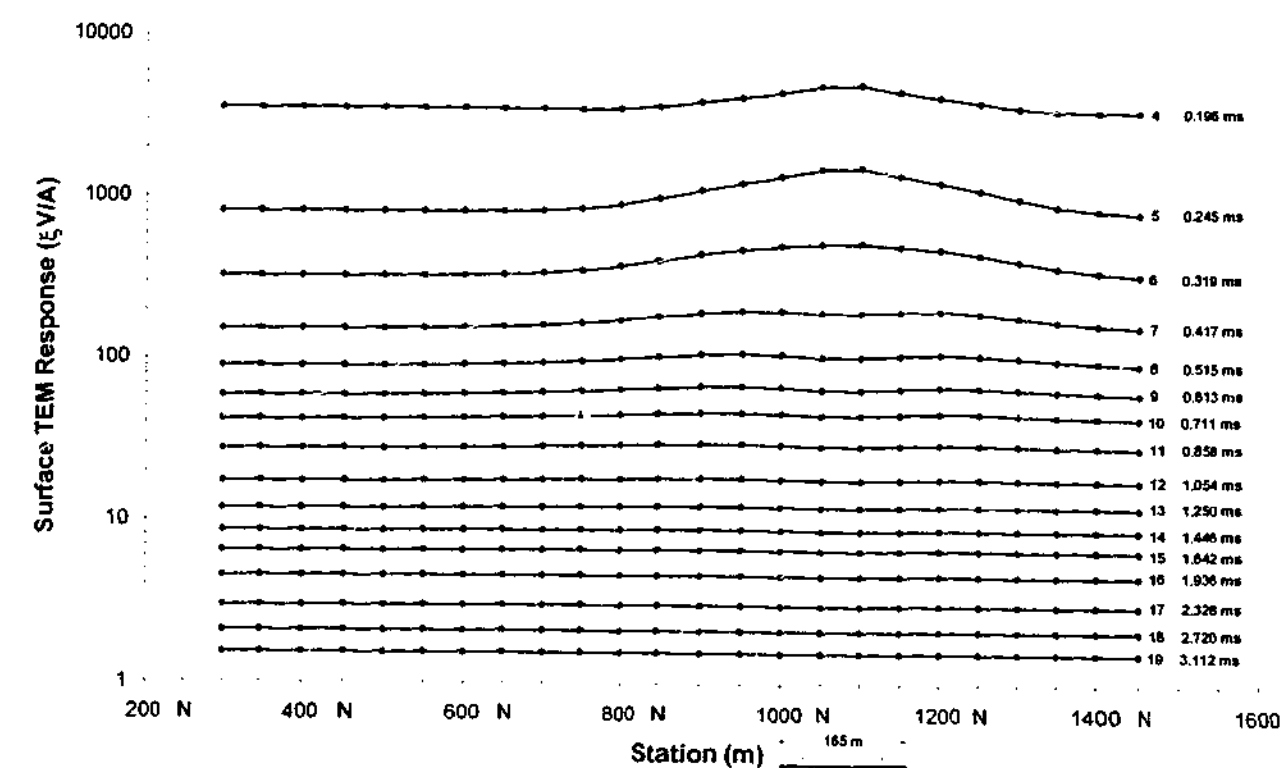


Figure 5.9: Vertical-component TEM response of the 100 m coincident-loop MARCO model. Note the evolution of the response with time, from a single positive anomaly to an M-shaped anomaly with peaks centred about stations 950N and 1200N. The schematic insert indicates both the horizontal position and depth-extent (165 m) of the dual-slab target.

Unfortunately, the MARCO model could not replicate the persistence of the M-shaped anomaly to late-times, as did the anomaly within the field data. Subsequent attempts to sustain the anomaly to later times proved unsuccessful. The original coincident-loop MARCO model served as a control model for investigations involving four additional models. In each variation of the control model, however, the M-shaped anomaly diminished by window 12 (1.054 ms), as opposed to the field data in which the anomaly remained essentially unchanged until window 17 (2.328 ms). The following is a summary of results of the four attempts designed to sustain the M-shaped anomaly to later times:

1. REDUCTION OF TARGET RESISTIVITY:

Modelling trials, which tested target resistivities of 1.5 ohm.m, 2.5 ohm.m and 3.6 ohm.m, revealed that a reduction in target resistivity resulted in a slight increase in the anomaly amplitude, but not its longevity.

2. REDUCTION OF TARGET DEPTH:

Reducing the depth of the target by 65 m, namely the upper-slab depth from 115 m to 50 m and the lower-slab depth from 126 m to 61 m, resulted in a dramatic increase in the amplitude of the anomaly at early times but had

little effect on its longevity. Due to the gentle dip of the mineralisation in the southeast direction, a reduction in depth would have been justifiable. In particular, Figure 5.1a shows the body depth to vary from 45 m in the west to 240 m for the eastern portion. Interpolation of these end depths imply the body to be at a depth of around 60 m near the coincident-loop survey. The trial depth of 50 m tested the extremes of depth variation on the model.

3. INCLUSION OF A CONDUCTIVE BODY BENEATH TARGET:

The key idea here is that the longevity of the field M-shaped anomaly is due to the persistence of induced current distributions at great depth. In an attempt to mimic such an effect, a large conductive body was placed directly beneath and in electrical contact with the lower-slab. The width and strike-length of the additional body were equal to that of the upper-slab, namely 165 m and 400 m respectively, whereas its depth extent was 100 m and its resistivity 60 ohm.m. Despite an increase in the amplitude of the anomaly at early times, its longevity remained essentially unchanged.

4. ALTERATION OF LAYER 1 AND 2 RESISTIVITIES:

Altering the resistivities of both Layer 1 and Layer 2 to values above and below those of the control model, namely 210 ohm.m to 150 ohm and 300 ohm.m for Layer 1 and 538 ohm.m to 450 ohm.m and 600 ohm.m for Layer 2, excluded the possibility of a poor choice in host layer resistivity. For each layer considered, however, an increased conductivity resulted in only a slight attenuation of the amplitude of the M-shaped anomaly.

Two aspects of the field data need addressing: firstly, no explanation is available for the persistent M-shaped anomaly within the field data. Secondly, although the coincident-loop MARCO model featuring a dual-slab target produced an M-shaped anomaly, this result is not a reproduction of aforementioned anomaly within the field data. Indeed, the MARCO model has shown that if the signature of the Cadjebut ore body is comparable to that of its associated dual-slab model, its TEM response is unlikely to be detectable in the context of the current field environment. Hence, modelling has verified the conclusions of Lebel (1987) and Scott *et al.* (1994), that the Cadjebut ore body is too weakly conducting to be detectable by surface TEM methods.

5.4.2. THE DOWNHOLE TEM MARCO MODEL.

The two downhole TEM Marco models successfully reproduced the anomalous features of the field data: namely a null response for the inductively well-coupled loop, Loop Tx1, and a prominent negative anomaly for the weakly coupled offset loop, Loop Tx2. Refer to Figure 5.10 and Figure 5.11 for the logarithmic profiles of the downhole TEM model response for Borehole ID159 due the transmitter loops Tx1 and Tx2, respectively. See also Figure 5.3 and Figure 5.4 for the associated logarithmic profiles of the downhole TEM field data. It is apparent, that the amplitude of the regional response of the field data is greater by a factor of three than that generated by the MARCO model. Despite this, the decay rates of the regional response within both the model and field data are essentially the same, with the model response decaying only slightly faster. Window 1 (0.474 ms) of the Tx2 model response features a prominent negative galvanic anomaly centred about Station 140. Linear profiles of the first three time windows reveal the fine structure within both the model (Figure 5.12a) and field (Figure 5.12b) anomalies. Decay curve analysis performed at the minima of the model anomaly at Station 140, verified the primary excitation mechanism to be galvanic in origin (see Section 5.4.3). Superimposed upon the model galvanic anomaly, is a well-defined intersection anomaly centred about Station 134, which passes from negative (Station 133) to positive (Station 135) in sign. Similarly, the galvanic anomaly within the field data also possesses an intersection anomaly with extrema at Stations 130, 140 and 145 (see Figure 5.12b). Station spacings of 1 m, between Stations 128 and 142, were required to resolve the intersection anomaly within the model data. Unfortunately, the field data employed only 5 m spacings, thereby rendering it to be of inferior resolution. Although the Loop Tx1 model response also features a similar type composite galvanic anomaly as that due to Loop Tx2, it is of significantly lower amplitude.

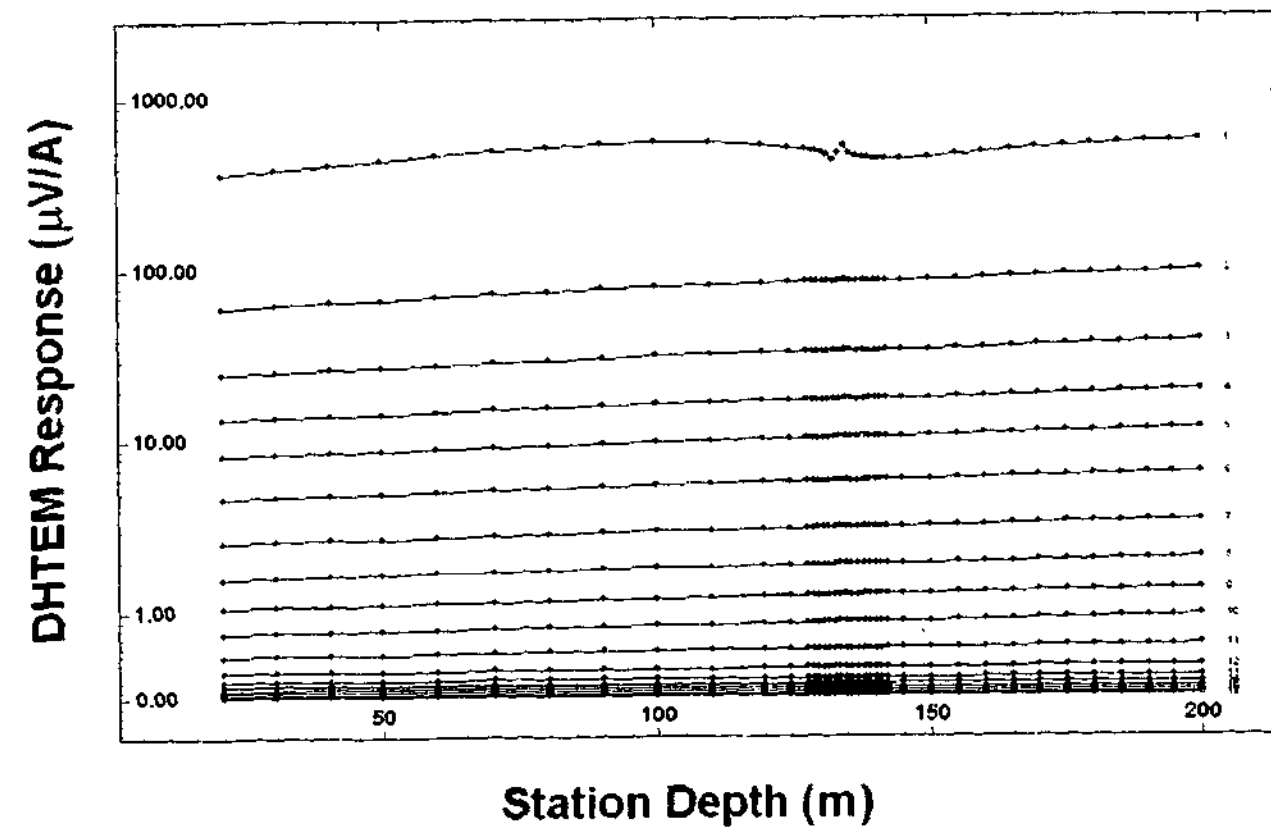


Figure 5.10: Logarithmic profile of axial component of model response of Borehole ID159 due to Loop Tx1. The first four time windows are window 1 (0.474 ms), window 2 (0.866 ms), window 3 (1.258 ms) and window 4 (1.650 ms).

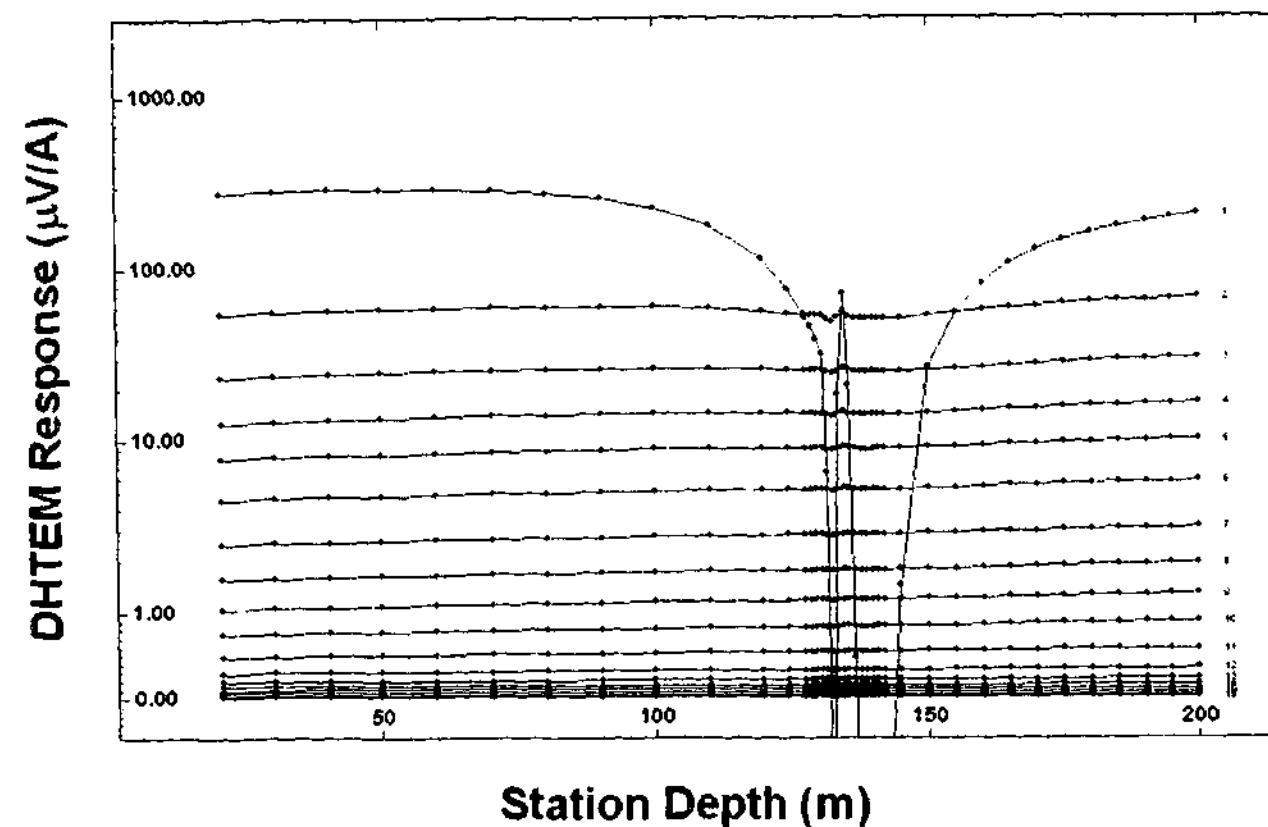
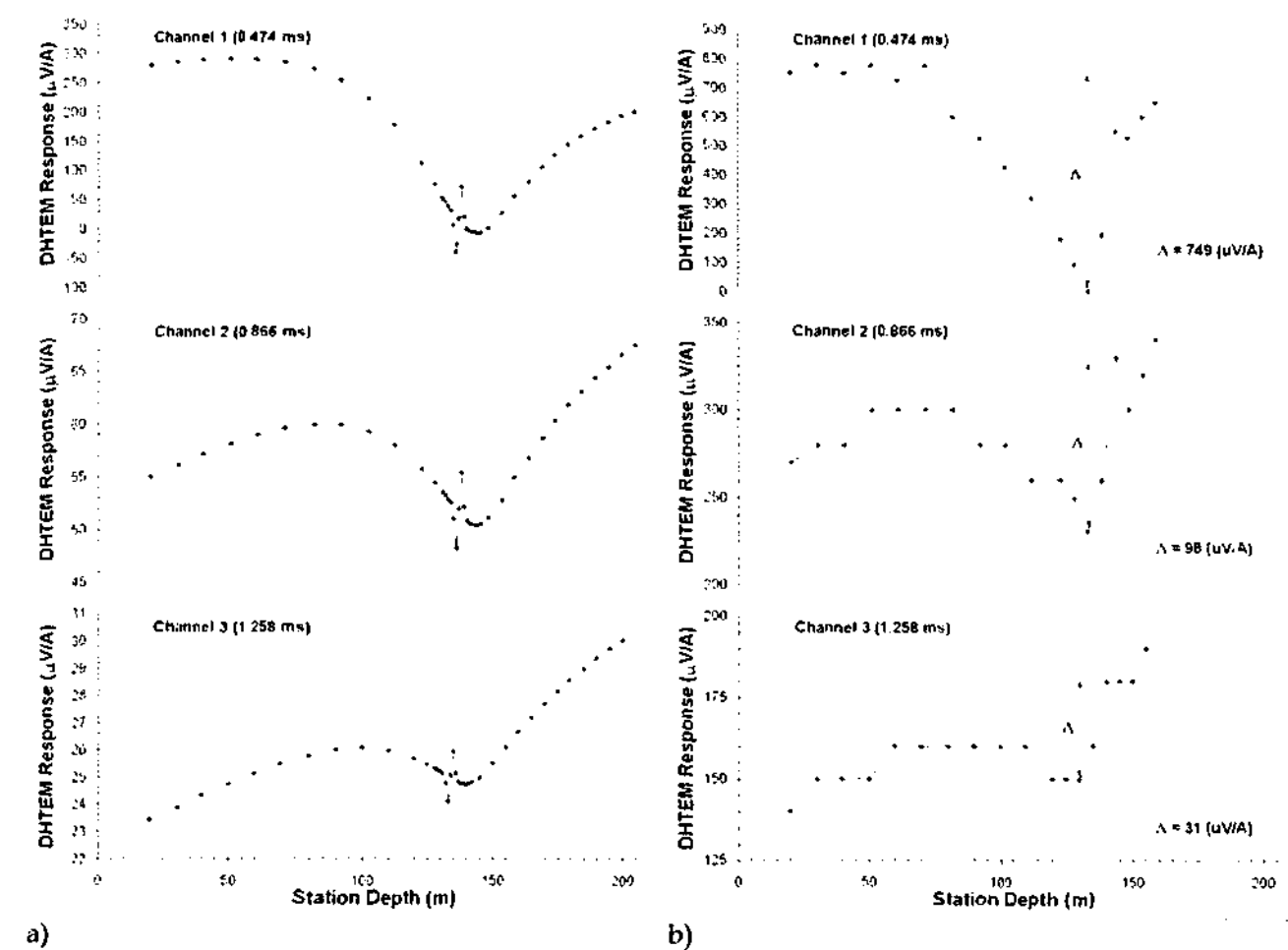


Figure 5.11: Logarithmic profile of axial component of model response of Borehole ID159 due to Loop Tx2. See Figure 5.12a for linear profiles of the first three time windows.



a) b)
Figure 5.12: Linear profiles of the axial component of the model (a), and field (b) response due to Loop Tx2, for time windows 1 (0.474 ms), 2 (0.866 ms) and 3 (1.258 ms). (a) A negative to positive intersection anomaly centred about Station 134 m can be clearly seen, which in turn is superimposed upon a broad negative galvanic anomaly with a minimum at Station 140. (b) Again, superimposed upon a broad negative galvanic anomaly, is an apparent negative to positive intersection anomaly at Stations 130, 135 and 140. Unfortunately, due to station intervals of 5 m the structure of the anomaly is poorly resolved. Shown also are the estimated regional profiles (dashed lines), which were used in stripping the field data so as to obtain the scattered anomaly response at Station 130. The scattered anomaly amplitudes (Δ) are noted for each time window.

5.4.3. VERIFICATION OF THE GALVANIC RESPONSE.

Decay-curve analysis identified the intersection anomalies within the model and field Tx2 data as galvanic in origin. This process entailed determining if the scattered Tx2 anomalies decayed by a $-7/2$ power law, a successful fit implied galvanic excitation (Asten, 1991a). See also Section 4.3 for additional theory on galvanic decay-curve analysis. The evaluation of a scattered anomaly or scattered galvanic anomalous response requires the identification and removal of the regional response; a process commonly referred to as *stripping*. It is here that the difficulty arises, as identifying a regional response is often non-trivial. Stripping of the model data, however, employed a simple but reliable technique: subtracting the layered earth model response (target absent) from the complete model response (target present) will immediately yield the scattered anomalous galvanic model response. Applied to Station 140 and time

windows 3 (1.258 ms) to 15 (13.214 ms) of the model data, this technique yielded a decay index of -3.47, a value compatible with current channelling (see Figure 5.13).

In respect to the field data, stripping proceeded manually by sketching an estimated regional upon a hard copy of the field linear profiles. See Figure 5.12b for linear profiles of the field data for the time windows 1 (0.474 ms), 2 (0.866 ms) and 3 (1.258 ms). Subtraction of the estimated regional response from the total field response yielded the scattered anomalous galvanic field response. Unfortunately, the quality of the data restricted the analysis to the first three time windows. Decay-curve analysis, utilizing only three data points at Station 130, yielded a decay index of -3.27 (see Figure 5.14).

Some justification is needed for performing decay analysis on the model data with windows 3 (1.258 ms) and onwards, whilst only using the time windows 1 (0.474 ms) to 3 (1.258 ms) for the field data. The decay of the scattered model response at Station 140 is not asymptotically stable at early times (see Figure 5.13). Indeed, a power law fit to time windows 1 (0.474) to 3 (1.258) of the model data yields a decay index of -4.5. In the absence of late time analysis, the question of whether the decay of the anomalous scattered field response has approached its asymptotic decay remains unanswered. Moreover, the decay index computed for the field data is subject to error, due to both the poor quality of the data, and the difficulty in estimating the regional response. Nevertheless, the decay analysis performed on both the field and model data, have yielded decay indices which are consistent with that of galvanic excitation.

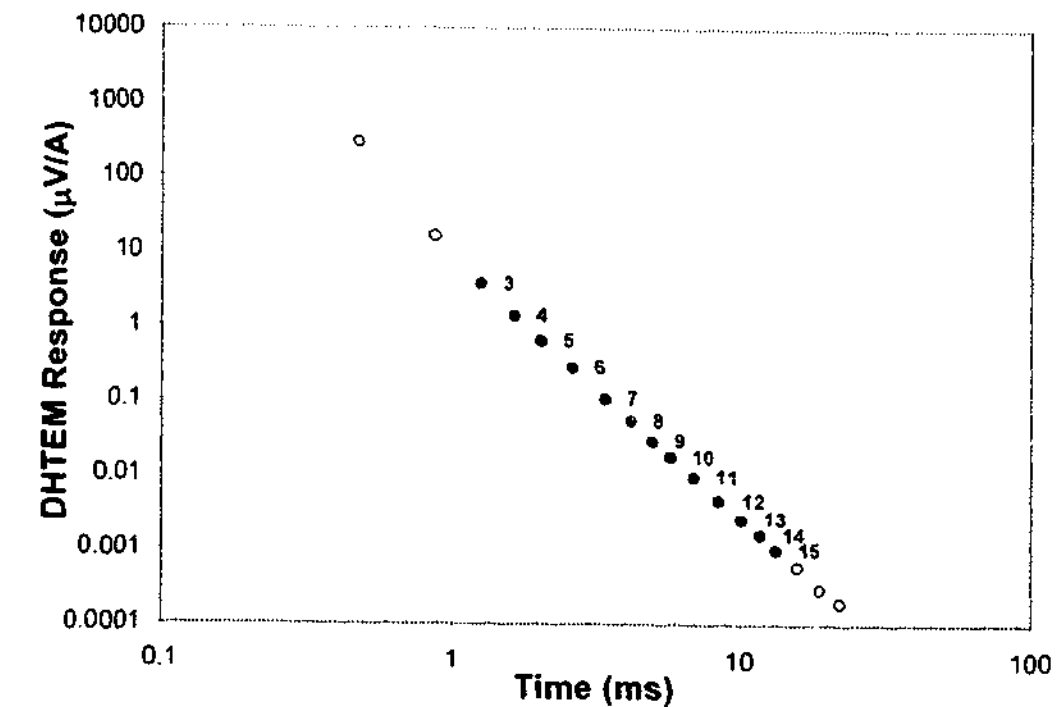


Figure 5.13: Log - Log decay plot for the MARCO model data at Station 140 with the regional response removed. A power law (solid line) was fitted to time windows 3 (1.258 ms) to 15 (13.214 ms) and yielded a decay index of -3.47 (Note: fitted windows are indicated by filled circles).

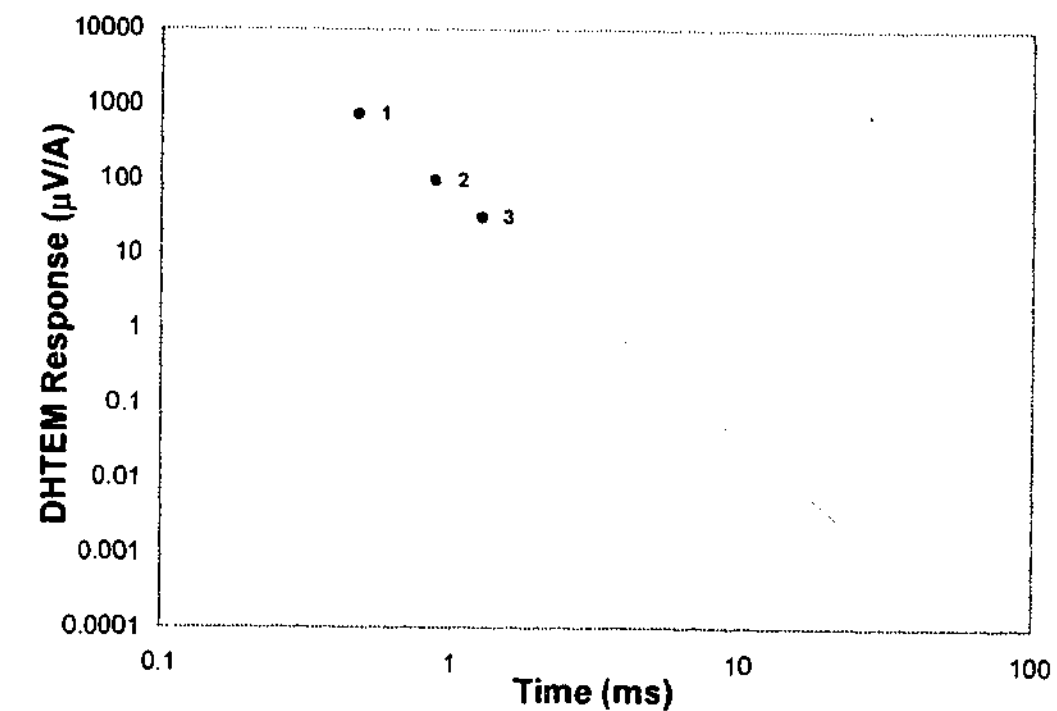


Figure 5.14: Log - Log decay plot for the field data at Station 130 with the regional response removed. A power law (solid line) was fitted to time windows 1 (0.474 ms) to 3 (1.258 ms) and yielded a decay index of -3.27 (Note: fitted windows are indicated by filled circles).

5.5. DISCUSSIONS AND INTERPRETATIONS.

5.5.1. PROPOSED MECHANISM FOR THE COINCIDENT-LOOP M-SHAPED ANOMALY.

The M-shaped anomaly within the 100 m coincident-loop model response (Figure 5.9) is a result of differing degrees of galvanic excitation of the dual-slab target with each loop position. Galvanic excitation¹ will occur when the diffusing host currents, or smoke rings, emanating from the transmitter loop are 'gathered' into the locally more conductive target. As the loop approaches the dual-slab target along Line E, the target will undergo a steady increase in galvanic excitation as it is increasingly exposed to the host current electric fields associated with the encroaching smoke rings. Eventually galvanic excitation will peak as the loop passes through the optimal configuration for the inducement of current gathering. In this case, the optimal configuration for galvanic excitation occurred for loop positions Stations 950N and 1200N. As the loop moves over the centre of the target, the smoke rings tend to propagate past the target unperturbed, thereby reducing current gathering effects. In summary, the characteristic M-shaped anomaly noted within Figure 5.9, originates from the steady increase, peaking, and then slight reduction in galvanic excitation, and then slight reduction in galvanic excitation, followed by the same processes in reverse order, as the coincident-loop approached and passed over the target.

5.5.2. PROPOSED MECHANISM FOR THE DHEM INTERSECTION ANOMALY.

A mechanism for the production of the galvanic anomaly is proposed within the expanded view of the model cross-section (Figure 5.15). At the time of transmitter shut-off, a current image arises within the conductive earth directly beneath Loop Tx2. Through interactions with its own fields, and in manner analogous to a smoke ring in air, the induced currents will propagate outward and downwards, attenuating in amplitude and diffusing with time (Nabighian, 1979). As the smoke ring expands past the mineralisation, the host currents are gathered into the locally more conductive zones, producing in effect, an anomalous current stream that flows along strike within the body. This

¹ Refer to Section 4.3 for a comprehensive explanation of the mechanism of galvanic excitation.

anomalous current stream can be understood in terms of a ribbon of current, lying in the plane of the body and directed along strike, or in reference to Figure 5.15 into the page. Furthermore, the secondary B-fields established by these gathered currents will be unipolar in form, which when viewed from the east as in Figure 5.15, will circulate in a clockwise fashion around the body.

In the case of the dual-slab model, the anomaly due to Loop Tx2 can be viewed as a superposition of the individual galvanic responses of both the upper and lower slabs. Specifically when modelled in isolation, the top slab produced a sharp intersection anomaly superimposed upon a broad negative anomaly, whilst the lower-slab produced only a broad negative single signed anomaly centred about Station 135.

In reference to Figure 5.15, and in regards to the production of the lower-slab anomaly, it is immediately apparent that the axial component of the secondary galvanic fields will remain negative for all borehole stations. Furthermore, the magnitude of the field strength will increase with reduced receiver-target distance. Thus, one would expect the anomaly to peak for the receivers nearest the body, namely Station 135. The breadth of the anomaly, however, is attributable to the distance at which the borehole passes the body. That is, the anomaly will become narrower with reduced borehole-target distance.

An understanding, however, of the mechanism for the production of the intersection anomaly due to the upper-slab, requires knowledge of the behavior of the surface galvanic secondary B-fields on the opposing surfaces of the slab. See Figure 5.15 for a representation of the poloidal anomalous galvanic currents flowing within the upper-slab, and the associated surface secondary B-fields. The depicted anomalous galvanic currents flow along strike, from east to west (into page). Observe also, that for regions on or near the upper-slab, the secondary fields established by the galvanic currents will be essentially tangential to the slab surface. Thus, for receiver stations in close proximity to the surfaces of the upper-slab, the tangential surface fields will yield an axial component directed down-hole just above the slab, and up-hole just below the slab respectively, *i.e.*, the resulting borehole response will undergo a rapid

negative-to-positive change in sign. Although the borehole intersects the top and bottom surfaces of the upper-slab at borehole depths of 131.5 m and 136.1 m respectively, the actual negative and positive peaks occur at Stations 133 and 135, within the body itself. Thus, the negative-to-positive intersection anomaly, centred at a depth of 134 m down-hole, has a width comparable to the thickness of the slab.

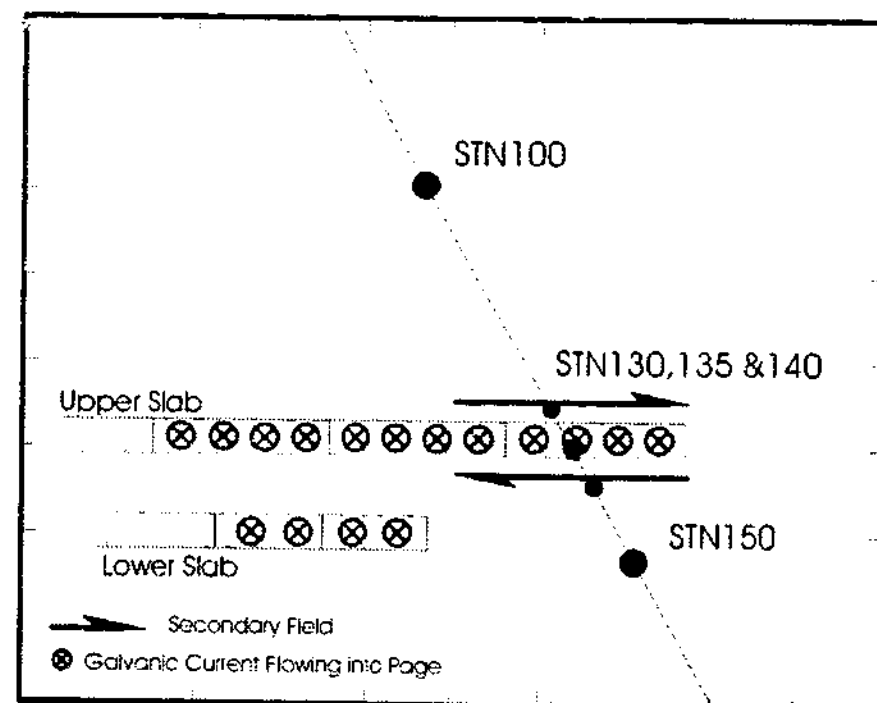


Figure 5.15: Schematic diagram illustrating the secondary galvanic fields in the vicinity of the upper-slab. The galvanic currents can be approximated as current ribbons flowing into the page. By noting the sign of the field response at the surface of the upper-slab, the Tx2 data computed from the MARCO model, can be reasoned to have a negative-to-positive intersection anomaly centred about Station STN135. (Note: A positive up-hole sign convention is adopted here)

5.6. CONCLUSIONS.

The purpose of modelling the coincident-loop field data was to attempt to explain the M-shaped anomaly found within the field data, and to verify whether it originated from the Cadjebut mineralisation. It has been demonstrated, that by representation of the Cadjebut mineralisation as a dual-slab body embedded within a five-layer host, an M-shaped anomaly similar to that found within the field data is produced. Unfortunately, the coincident-loop MARCO model failed to duplicate the decay-rate, position and width of the M-shaped anomaly observed within the field data. It was found, that the anomaly within the field data persisted to window 18 (2.720 ms) without significant attenuation, whilst the associated model yielded a much larger

decay rate, with the anomaly all but gone by window 10 (0.711 ms). The peaks of the M-shaped anomaly in the field response, see Figure 5.2, are centred about stations 1050N and 1250N, whilst the peaks in the model response, see Figure 5.9, are centred about stations 950N and 1200N. Thus, the width of the M-shaped anomaly in the field data is 200 m, less than that of the model anomaly, namely 250 m. In addition to this, the M-shaped anomaly within the field data is displaced approximately 50 m to 100 m northward in respect to the model anomaly, and so is not centred over the Cadjebut mineralisation.

Recapitulating the findings of Section 5.4.1, no explanation is available for the persistent M-shaped anomaly within the field data. Moreover, although the coincident-loop MARCO model featuring a dual-slab target produced an M-shaped anomaly, this result is not a reproduction of the aforementioned anomaly within the field data. Despite these shortcomings, the MARCO model has demonstrated that if the signature of the Cadjebut ore body is comparable to that of its associated dual-slab model, then its detection is unlikely in its current geologic environment. Hence, the MARCO models successfully verified the conclusions of Lebel (1987) and Scott *et al.* (1994): that the Cadjebut ore body is too weakly conducting to be detectable by surface TEM methods.

The downhole TEM MARCO models successfully reproduced the characteristic features of the field data of Borehole ID159 with both Loops Tx1 and Tx2. In summary, the intersection anomaly featured in window 1 (0.474 ms) of the offset loop Tx2 data set, and the null response within the inductively well coupled loop Tx1 data set, can be fully explained in terms of current gathering without recourse to inductive effects. The modelling performed on the downhole field data has confirmed the ability of an offset loop to induce galvanic excitation of a weakly conducting target that would otherwise be unresponsive to inductive based TEM methods.

5.7. GUIDELINES FOR MODELLING GALVANIC EFFECTS.

Some important diagnostic features of current channelling became apparent during the course of modelling with MARCO. Unlike inductive methods, which permit explicit conductivity estimates, *i.e.*, by the use of time constants,

galvanic methods can provide subtle but useful information regarding the electrical properties of a target and its host. The absence of an inductive response within the field data, prevented explicit conductivity estimates of the Cadjebut mineralisation. By determining the range of conductivities for the dual-slab target within the MARCO model that yielded an insignificant inductive response, it was possible to obtain an estimate for an upper bound of the target conductance. Once this was achieved, the final slab conductivity for use within the model was chosen so that the amplitude of the resulting galvanic anomaly would match that found within the field data. Thus, in brief, the conductance of the Cadjebut mineralisation was estimated by minimising the model inductive response by lowering the slab conductivity, whilst trying to maximise the galvanic response by means of galvanic saturation.

Due to its unipolar field, current channelling can provide unambiguous information about target position relative to a borehole. Furthermore, information about the location and possible even depth extent of a target can be gained from offset and null response loops. The distance at which a borehole passes a body can be inferred from the breadth of a galvanic anomaly. That is the width of an anomaly is expected to decrease as the distance is reduced, thus tending to a sharp anomaly on intersection with the body.

Hence, in cases where traditional inductive methods have failed, optimisation of surveys to enhance downhole TEM induced current channelling may prove useful in supplementing valuable information regarding the location and electrical properties of weakly conducting ore bodies.

CHAPTER SIX

FLYING DOCTOR DEPOSIT: UPPER LENS.

6.1. INTRODUCTION.

In June 1998, down hole TEM test surveys were conducted over the Flying Doctor lead-zinc deposit situated North of Broken Hill, New South Wales. These surveys were carried out specifically for this project, to test the effectiveness of long-offset loops in detecting weakly conducting mineralisations.

The upper and lower massive sphalerite galena lenses of the deposit were targeted, where each lens was surveyed with a pair of boreholes: ID3071 and ID3039 for the upper lens, and ID3418 and ID3419 for the lower lens, utilising the same transmitter loops, namely an inductively well coupled near loop, Loop 1, and a weakly coupled long-offset loop, Loop 3. In total, four TEM data sets were acquired for each lens. Downhole MMR surveys were also conducted, but were only of secondary importance to the project; the purpose of these surveys in the current context was to facilitate the identification of the galvanic components within the TEM data.

The Flying Doctor case study is presented in two parts; the upper lens of the deposit is discussed within this chapter, Chapter Six, and the lower lens in Chapter Eight.

6.2. OVERVIEW OF MODEL DEVELOPMENT.

Thin-sheet models were constructed within program LEROI for interpreting the ID3039 and ID3071 DHTEM field data sets. A three-stage process was implemented to aid model construction, the details of which are summarised below:

STAGE 1: DESCRIPTION AND ANALYSIS OF THE FIELD DATA.

[Refer to Section 6.3]

The first stage entailed analysis of the field data, with the primary objective of identifying the excitation mechanisms responsible for each of the anomalies present within the field profiles. Unfortunately, distinguishing between the galvanic and inductive effects within the DHTEM data was not straight forward. Nevertheless, it was necessary to do so in order to construct the appropriate thin-sheet LEROI models to independently represent these two excitation mechanisms, and thus enable the construction of a composite model to describe the response as a whole.

Three surveys were conducted for boreholes ID3039 and ID3071, a DHMMR survey, and two DHTEM surveys that utilised a near-loop, Loop 1, and a far-loop, Loop 3, respectively. The procedure adopted to identify, and differentiate, inductive and galvanic anomalies within the profiles of the field data, involved the cross correlation of the three data sets acquired for each borehole. In brief, inductive excitation was much reduced with the far-loop, allowing the effects of galvanic excitation to dominate the response. Consequently, the far-loop data aided the identification of galvanic, and indirectly inductive, anomalies within the inductively well-coupled near-loop response. Comparisons with the DHMMR profiles further aided the identification of suspected galvanic anomalies, due to this data being devoid of any inductive effects. Verification of each excitation mechanism was performed by means of both profile matching, and decay analysis comparisons with the associated LEROI thin-sheet models (see Section 6.4). In some situations, inference of an excitation mechanism responsible for a particular anomaly could be made by estimating a response profile, *i.e.*, anomaly sign and the location of

any cross-overs, peaks or troughs, for a target with an assumed bi-polar or uni-polar field.

STAGE 2: MODEL DEVELOPMENT.

[Refer to Section 6.4]

Once the excitation mechanism for each anomaly was identified and its associated profile was isolated, it was then possible to develop independent plate models to describe each response type separately. In summary two plate models were constructed, namely a high conductivity body Plate 1, and a low conductivity body Plate 2, which were designed specifically to match the inductive and galvanic response of the mineralisation respectively.

STAGE 3: LINEAR SUPERPOSITION OF THE PLATES 1 AND 2 MODEL DATA.

[Refer to Section 6.5]

It was anticipated that it would be possible to take the two independent thin-sheet models, Plates 1 and 2, and use them simultaneously in a single multiple plate model. Unfortunately, any attempt to do so proved unsuccessful (see Section 6.4). Instead, a composite thin-sheet model was procured from the linear-superposition of the scattered field response of the Plate 1 and Plate 2 models. This approach was justified by assuming that minimal inductive coupling would occur between the two plates. It is noted, that this composite model was only constructed to represent the field response of Borehole ID3039 with Loop 1.

The successful synthesis of a composite model response by the linear superposition of a host response and the scattered responses of Plates 1 and 2 assumed that the two plates, of high and low conductance, would exhibit a weak inductive and galvanic interaction. Various host-target interactions do occur for a 3-D target residing within a conductive host. In the current context the terms scattered and secondary responses are synonymous with one another and refer the resultant response obtained by the subtraction of the host from the target response.

Despite the occurrence of complex interactions between a target and its host medium, interpreters, have for the most part, been successful in procuring

the scattered target response for the purpose of free-space interpretations (McNeill *et al.*, 1984). In this approach, the total field response is treated as the superposition of the host and inductive response of the target; so that by equating the secondary response to a free-space model response information regarding the location, dimensions and conductivity of the target can be obtained (San Filippo *et al.*, 1985). This technique is well suited to responses characterised by inductive effects, but will fail when a suitable host estimate cannot be obtained or when superposition is no longer valid (San Filippo *et al.*, 1985). In instances where effects arising from charge accumulation on the target are no longer negligible, an example of host-target interaction, interpretations must account for galvanic excitation (San Filippo *et al.*, 1985).

McNeill *et al.* (1984) extended the practice of superposition by first treating the total response as the sum of the target and host responses, and then treating the target response as the sum of independent inductive and galvanic components. The authors demonstrated this technique with the synthesis of the transient EM response of a plate within a conductive earth, representing the inductive and galvanic components with a simple current loop and a distribution of current dipoles respectively. These superpositions will be valid for particular target geometries over certain time ranges; moreover, some of the coupling terms describing interactions between inductive and galvanic currents within a thin plate have been demonstrated by Lajoie and West (1976) to be negligible (McNeill *et al.*, 1984). Inductive and galvanic currents do engage in complex interactions; however, these interactions are in general weak, so that at predictable times, in general intermediate times, superposition of these two effects is practical (McNeill *et al.*, 1984; Nabighian and Macnae, 1991; San Filippo *et al.*, 1985).

The inducement of inductive currents occurs by the decay of the primary (host) magnetic field, and the decay of the magnetic fields associated with galvanic currents, *i.e.*, self-induction (San Filippo *et al.*, 1985). In free-space, the primary field due to a step-off VMD will vanish abruptly resulting in an impulsive dB/dt inductive excitation of a target, whereas within a conductive medium inductive excitation arises from the decay of the relatively slowly

varying magnetic fields of the expanding and diffuse host currents (McNeill *et al.*, 1984). Thus, the resulting effect of a conductive medium is to alter the impulsive nature of excitation and to delay, distort and attenuate the inductive component in comparison to the free-space response (McNeill *et al.*, 1984).

The treatment of inductive and galvanic effects as non-interacting components presupposes Green's functions that are free-space and static half-space functions respectively (McNeill *et al.*, 1984). A generalised form of the Green's functions is more complicated, as these functions must account for the direct interactions between the anomalous target currents and those within the host medium, and the internal interactions between the inductive and galvanic currents (West and Edwards, 1985).

6.3. STAGE 1: DESCRIPTION AND ANALYSIS OF THE FIELD DATA.

6.3.1. CLASSIFICATION OF THE FIELD TEM RESPONSE.

The field data was categorised into four window ranges or sets, in recognition of the various stages of evolution of the TEM response profiles with time (see Table 6.1). In brief, the near-loop field profiles were found to evolve from a predominately galvanic response at early times, to a predominately inductive response at late times; Hanneson (1992) reported similar observations whilst investigating the TEM step response of a dipping plate within conductive half-space. Hanneson (1992), reported that the late time currents within sufficiently conductive plates were toroidal (inductive in origin) and were similar to those induced within in plate situated in a free-space environment, whereas at earlier times, or at all times for poorly conducting plates, the currents are poloidal (galvanic in origin). The transition to toroidal currents, if they occur, was found to be gradual. An intermediate stage was also noted for the Flying Doctor field data, during which time the response was found to evolve from one excitation mechanism to another. It was also noted by Hanneson (1992), that since the toroidal currents decay exponentially, whereas the poloidal currents decay more slowly with the host currents, the poloidal currents will ultimately come to dominate the response. This effect, Hanneson (1992) cautions, is rarely observed in the field. Indeed, this very late time effect was not observed within the Flying Doctor field, or model, TEM data.

The excitation mechanisms responsible for the anomalies characteristic of each time window set, were identified by means of both profile and decay analysis. In doing so, the inductive and galvanic anomalies present within the field data profiles were effectively isolated. This facilitated the development of the thin-sheet models, Plate 1 and Plate 2, which were designed specifically to independently represent the inductive and galvanic components of the field data. Although this classification scheme was originally developed for the ID3039 - Loop 1 data set, it nevertheless proved useful in the interpretations of the ID3039 - Loop 3 and the ID3071 field data sets.

Bimodal algorithms account for the full interactions between inductive and galvanic modes of excitation, whereas unimodal algorithms only account

for one mode of excitation, Hanneson (1992). Although program LEROI can be classed as bimodal, it was implemented in a pseudo unimodal fashion, *i.e.*, the conductance of Plate 2 was reduced to a degree which inhibited inductive current flow, but was retained high enough so as to ensure galvanic saturation.

It was recognised during model development and by Hanneson (1992), that although a composite field response can be interpreted by applying unimodal algorithms to the isolated galvanic and inductive components, one must recognise when each mechanism dominates in order to address the appropriate part of the decay. This procedure is in general difficult, but the classification scheme devised within Table 1 served to address this problem in a methodical manner. The work of Walker and West (1992) on *parametric analysis* is also of interest, in which the following was demonstrated: current excitation ratios, which are computed by dividing the galvanic current estimators; or channelling number, by the inductive estimators; or induction number, can be used to ascertain whether either induction or current channelling will dominate the current excitation of a given conductive body. By this approach, the inductive and galvanic modes of excitation within the Flying Doctor field data are to be regarded as either saturated or under-saturated, with a transition zone separating the two limiting states. In this respect, the purpose of the classification scheme shown in Table 6.1 was to facilitate the determination at which times each mode of excitation is saturated and dominant.

Table 6.1: Classification of window times for the field response.

SET 1:	WINDOWS: 1 (0.120 ms) TO 5 (0.345 ms) VERY EARLY TIMES. (Note: Dominated by near surface effects)
SET 2:	WINDOWS 5 (0.345 ms) TO 10 (0.995 ms) EARLY TIMES. (Note: Predominantly galvanic)
SET 3:	WINDOWS: 10 (0.995 ms) TO 15 (2.495 ms) INTERMEDIATE STAGE. (Note: neither galvanic nor inductive effects predominate at these times)
SET 4:	WINDOWS: 15 (2.495 ms) TO 20 (5.895 ms) LATE TIMES (Note: Predominantly inductive)

6.3.2. BOREHOLE ID3039 WITH LOOP 1.

The axial component field DHTeM data, for Borehole ID3039 with Loop 1, are shown within Figure D.1.1 of Appendix D.1. The field response can be divided into four window sets, or time series, so that each set features a response due to a particular excitation mechanism (see Table 6.1). The field response at very early times, windows 1 (0.120 ms) to 5 (0.345 ms), can be attributed to near surface or overburden effects (see Figure 6.1). As such, these window times were not addressed within the interpretations and numerical models.

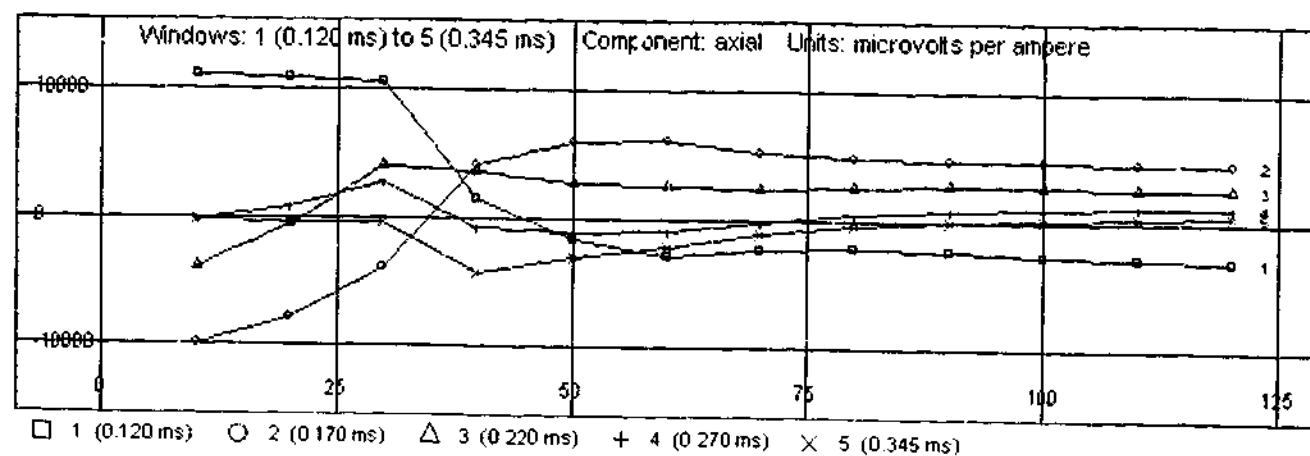


Figure 6.1: Field DHTeM response for Borehole ID3039 with Loop 1 (windows 1 to 5).

6.3.2.1. MIDDLE TIMES: WINDOWS 5 (0.345 ms) TO 10 (0.995 ms).

The field response at middle times, Figure 6.2, consists of a narrow, negative, single signed anomaly centred about Receiver Station 40. The anomaly is also noted to possess a slight asymmetry, with the deeper wing extending down-hole being of slightly greater amplitude than that of the shallow wing extending up-hole. This response can be attributed to uni-polar secondary fields established by anomalous currents flowing within the mineralisation in a south-to-north direction; a mechanism consistent with current gathering. Thus if one were to consider the region of the body below Borehole ID3039 (refer to the fold-out geological section - Plate III, located within rear sleeve), it can be seen that the axial components of these fields will be directed down hole for all stations, resulting in a negative single-signed anomaly as expected. Furthermore, the asymmetry biased toward the wing of the anomaly is attributable to the angle at which the mineralisation is inclined in respect to the borehole. Since the breadth of a galvanic anomaly due to a planar type body will be directly proportional to its distance from a borehole, it may then be concluded that the mineralisation has either glanced or actually intersected the borehole. Finally, a negative-to-positive cross-over is noted between Stations 100 and 110.

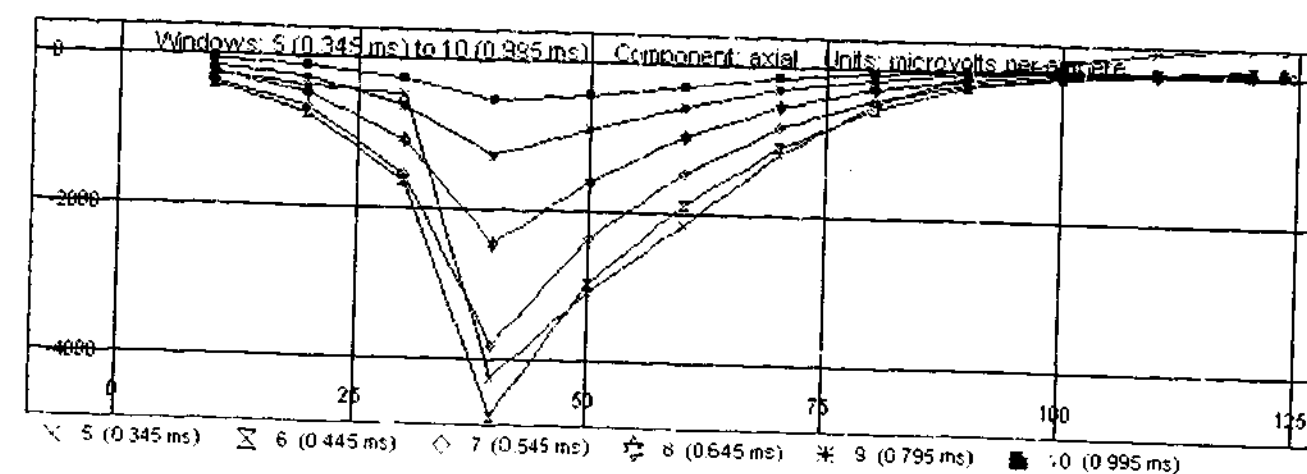


Figure 6.2: Field DHTeM response for Borehole ID3039 with Loop 1 (windows 5 to 10).

Verification of the galvanic origin of the anomaly within the field data was performed by means of both profile matching and decay analysis comparisons with the low conductivity model, Plate 2 (see Section 6.4.2). The most striking evidence, however, for the galvanic origin of the negative

anomaly at Station 40 for both loops Loop 1, Figure 6.2, and Loop 3, Figure 6.3, can be found within the DHMMR data for borehole ID3039, Figure 6.4.

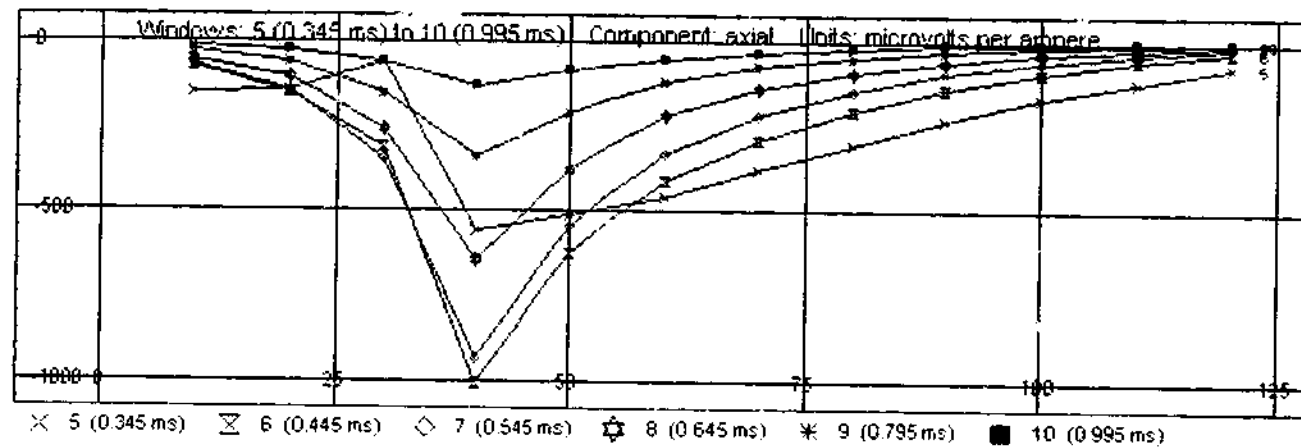


Figure 6.3: Field DHTEM response for Borehole ID3039 with Loop 3 (windows 5-10).

Although some subtle differences in respect to symmetry are noticeable, the anomalies noted within the DHTEM and DHMMR profiles are almost identical. This similarity can be attributed to the equivalence of the eastern portion of the diffusing azimuthal electric field, *i.e.*, *smoke ring*, established by each of the transmitter loops in the vicinity of the mineralisation, with the north-south aligned electric fields established within the DHMMR survey, Figure 6.11.

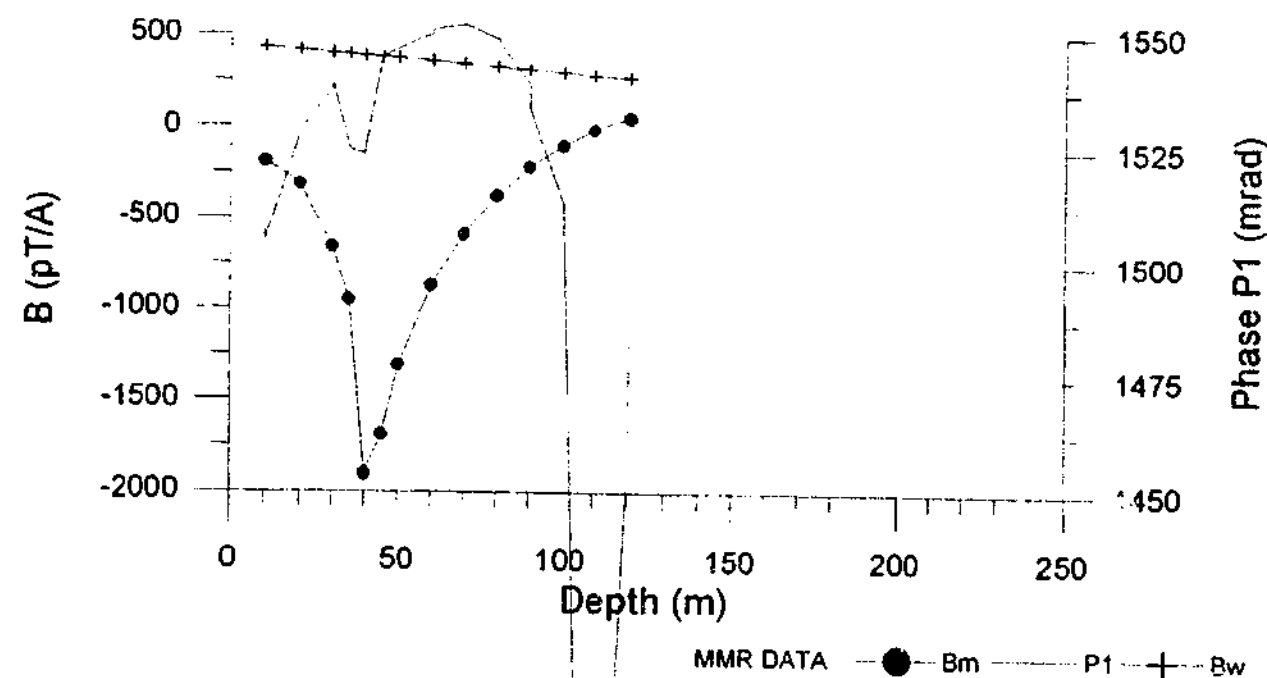


Figure 6.4: DHMMR response for Borehole ID3039, (collected June 1998; See Figure 8.1 of Chapter Eight for survey configuration). Measurements were made with a DHTEM probe, of both the phase ($P1$) and magnitude, of the transient magnetic field at each station. The magnetic B field data (B_m), was then obtained after the effects of the wire field (B_w), were removed from the converted (dB/dt) response. See also Asten (2001), for a comprehensive review of the Monash University - SPIRT research project, to which this thesis belongs: a project that is aimed at developing processing and interpretation techniques for borehole EM and MMR methods for the exploration of weakly conducting targets. The Flying Doctor MMR data was also used by Elders and Asten (2000, 2001) for research into noise reduction of the phase responses of MMR data.

6.3.2.2. INTERMEDIATE TIMES: WINDOWS 10 (0.995 ms) TO 15 (2.495 ms).

The time windows 10 (0.995 ms) to 15 (2.495 ms), Figure 6.5, represent an intermediate or transitional stage of the field response, where the primary excitation mechanism passes from being galvanic to inductive in nature. Here the remnants of the galvanic anomaly can be seen at window 10 (0.995 ms), but with increasing time the sharp negative anomaly centred about Station 40 is found to evolve into a broad anomaly now centred about Station 50, whilst the cross-over is noted to migrate up-hole.

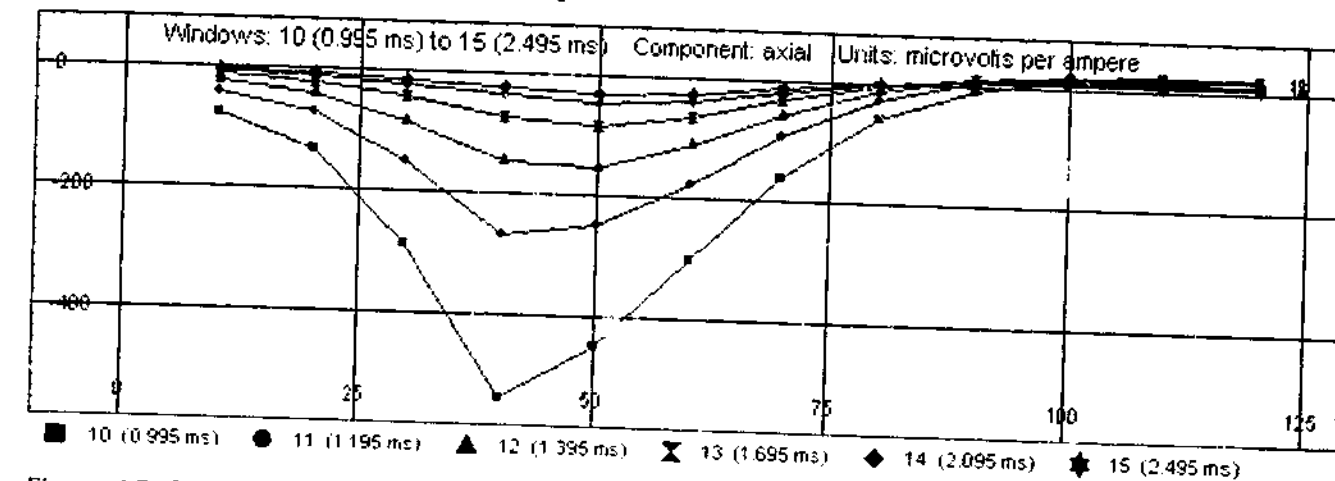


Figure 6.5: Field DHTEM response for Borehole ID3039 with Loop 1 (windows 10 to 15).

6.3.2.3. LATE TIMES: WINDOWS 15 (2.495 ms) TO 20 (5.895 ms).

A negative single signed anomaly is no longer present within with field profile at time windows 15 (2.495 ms) to 20 (5.895 ms) (see Figure 6.6). Instead, the field profile possesses the following features: a broad negative anomaly centred about Station 50, a crossover at Station 80, and a broad positive anomaly centred about Station 100. It should be noted that the negative portion of the response possesses a slight asymmetry. Specifically, the amplitude of the downhole wing is slightly greater than that of the up-hole wing of the anomaly. Again this can be attributed to the inclination of the mineralisation with respect to the borehole (ID3039), see fold-out geologic section Plate III (located in sleeve of back cover). The formation of this response can be understood in terms of induction, by considering only the portion of the mineralisation beneath Borehole ID3039, and assuming it to be essentially planar in nature. The normal component of the primary field due to Loop 1 at the surface of the body is thus directed upward pointing into a westerly direction. The dipolar fields associated with the induced vortex currents, can be reasoned to have a negative

axial component for stations within close proximity to the top edge of the body, whereas the axial component, however, would be expected to become positive further down the borehole namely about Station 100. Thus the cross-over located at Station 80 seems reasonable. Again, verification of induction as the primary excitation mechanism is provided within Section 6.4.1, by performing both profile matching and decay analysis comparisons with the high conductivity model, Plate 1.

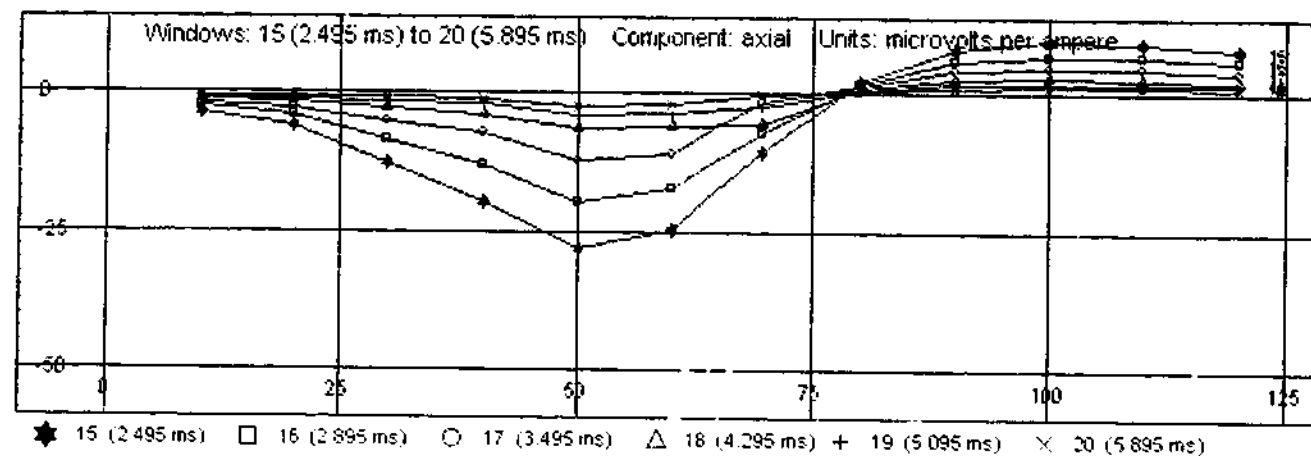


Figure 6.6: Field DHTEM response for Borehole ID3039 with Loop 1 (windows 15 to 20).

6.3.3. BOREHOLE ID3039 WITH LOOP 3.

The most noticeable feature of the ID3039 - Loop 3 field TEM profiles, in comparison to the Loop 1 data, is the complete absence of any inductive response. At time windows 15 (2.495 ms) to 20 (5.895 ms) no apparent target anomaly is present within the Loop 3 profiles, Figure 6.7b, whereas at these times the Loop 1 profiles feature a prominent inductive anomaly, Figure 6.6. Consequently, the intermediate stage noted within the Loop 1 data, Figure 6.5, is no longer present for Loop 3, Figure 6.7a, allowing the galvanic response to dominate from window 5 (0.345 ms) through to window 15 (2.495 ms). One of the most striking features of the Loop 3 galvanic response is that even though its amplitude is approximately one quarter that of the Loop 1 response, these galvanic anomalies are essentially of the same shape and form, position and symmetry. The only noticeable difference between the two profiles is the migration of the cross-over down hole to a depth greater than Station 125. This migration can be attributed to a change in half-space response resulting from moving the transmitter loop westward back 200 m from the target.

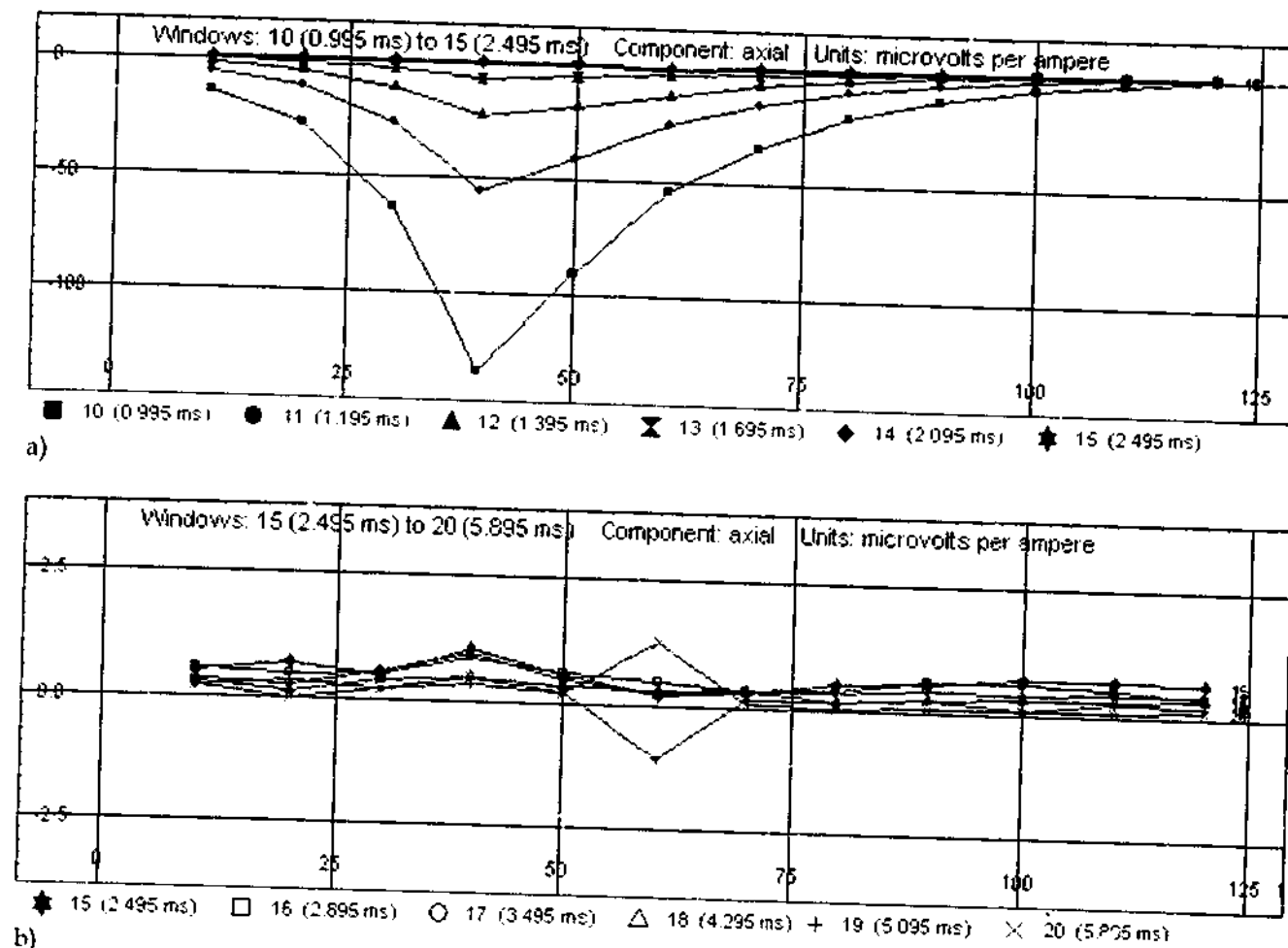


Figure 6.7: Field DHTEM response for Borehole ID3039 with Loop 3: a) intermediate times (windows 10 to 15) and b) late times (windows 15 to 20).

6.3.4. BOREHOLE ID3071.

Distinguishing between galvanic and inductive anomalies in the Borehole ID3071 data set, was a little more difficult than it was for Borehole ID3039. In particular for Borehole ID3071 the M-shaped galvanic anomaly centred about Station 110 within the DHMMR data set, Figure 6.8, although clearly visible within the DHTEM Loop 3 data set, Figure 6.9, is almost unrecognisable within the Loop 1 data, Figure 6.10. Despite this difficulty, the Loop 1 data for Borehole ID3071 can still be crudely divided into four window sets in which each of the differing excitation mechanisms dominate. As before, windows 1 (0.120 ms) to 5 (0.345 ms) were not be considered. In regards to windows 6 (0.445 ms) to 10 (0.995 ms), Figure 6.10a, current gathering effects do appear to dominate, although inductive effects are apparently more significant than they were for the same time series within the Borehole ID3039 data set with Loop 1, Figure 6.2. The main attributes here are the two positive anomalies peaking at Stations 90 and 150, the second being of lesser amplitude. Residing within the valley between these two peaks is a small but sharp positive anomaly centred

upon Station 120. The field response at time windows 10 (0.995 ms) to 15 (2.495 ms), Figure 6.10b, appears to be an intermediate stage showing a transition from galvanic to inductive effects. It is noted, that with the passage of time, the peaks at Stations 90, 150 and 120 will diffuse away.

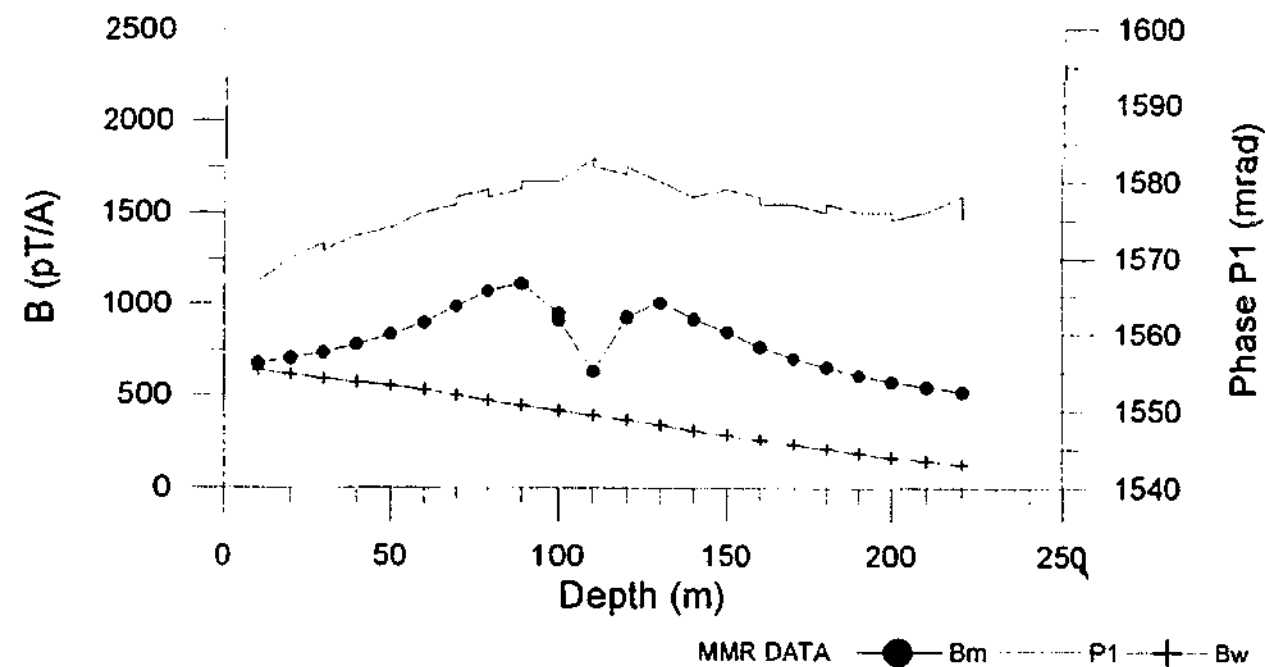


Figure 6.8: DHMMR response for Borehole ID3071 (see also Figure 6.4 for addition information).

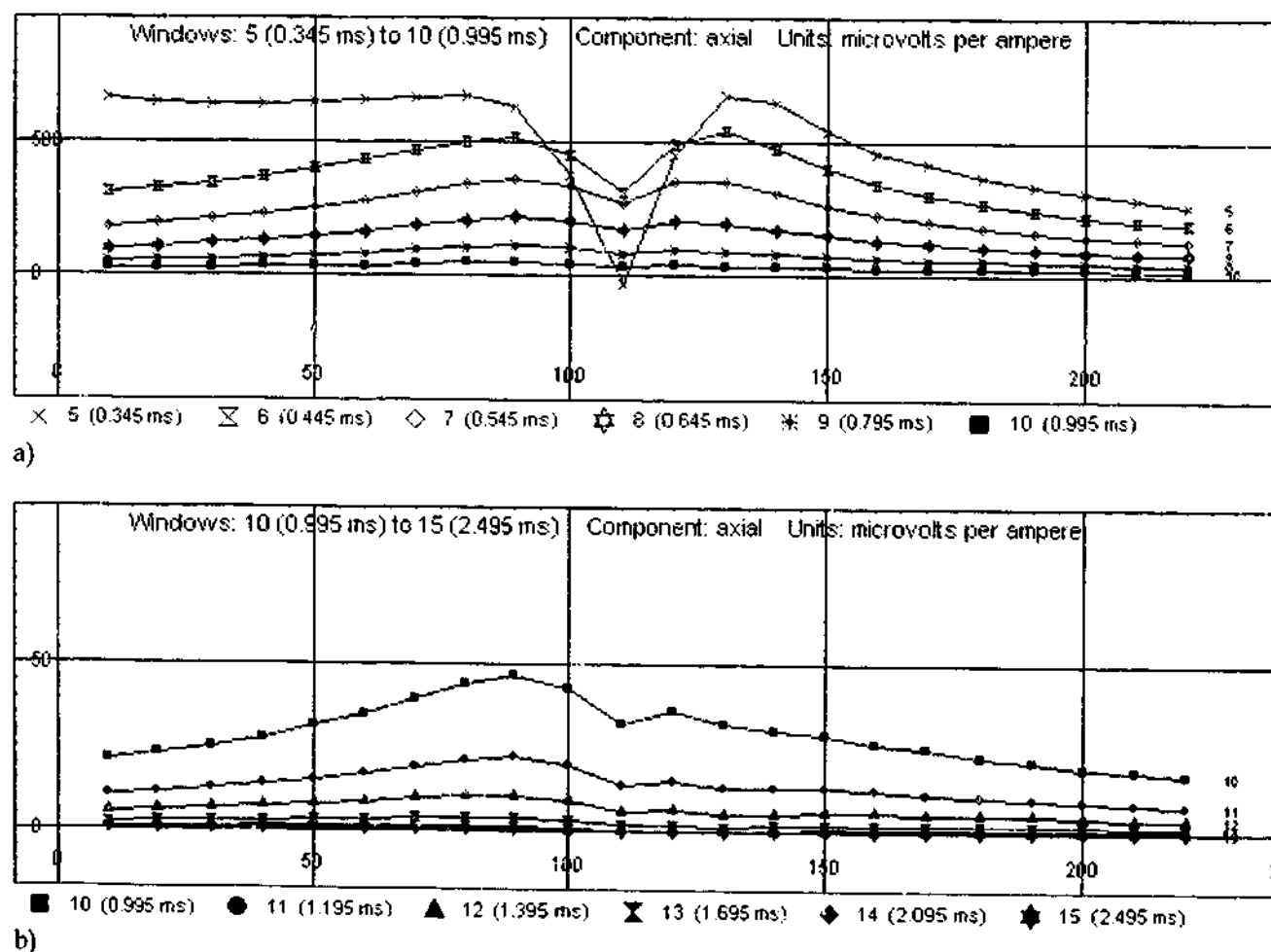


Figure 6.9: Field DHTEM response for Borehole ID3071 with Loop 3: a) middle times (windows 5 to 10) and b) intermediate times (windows 10 to 15).

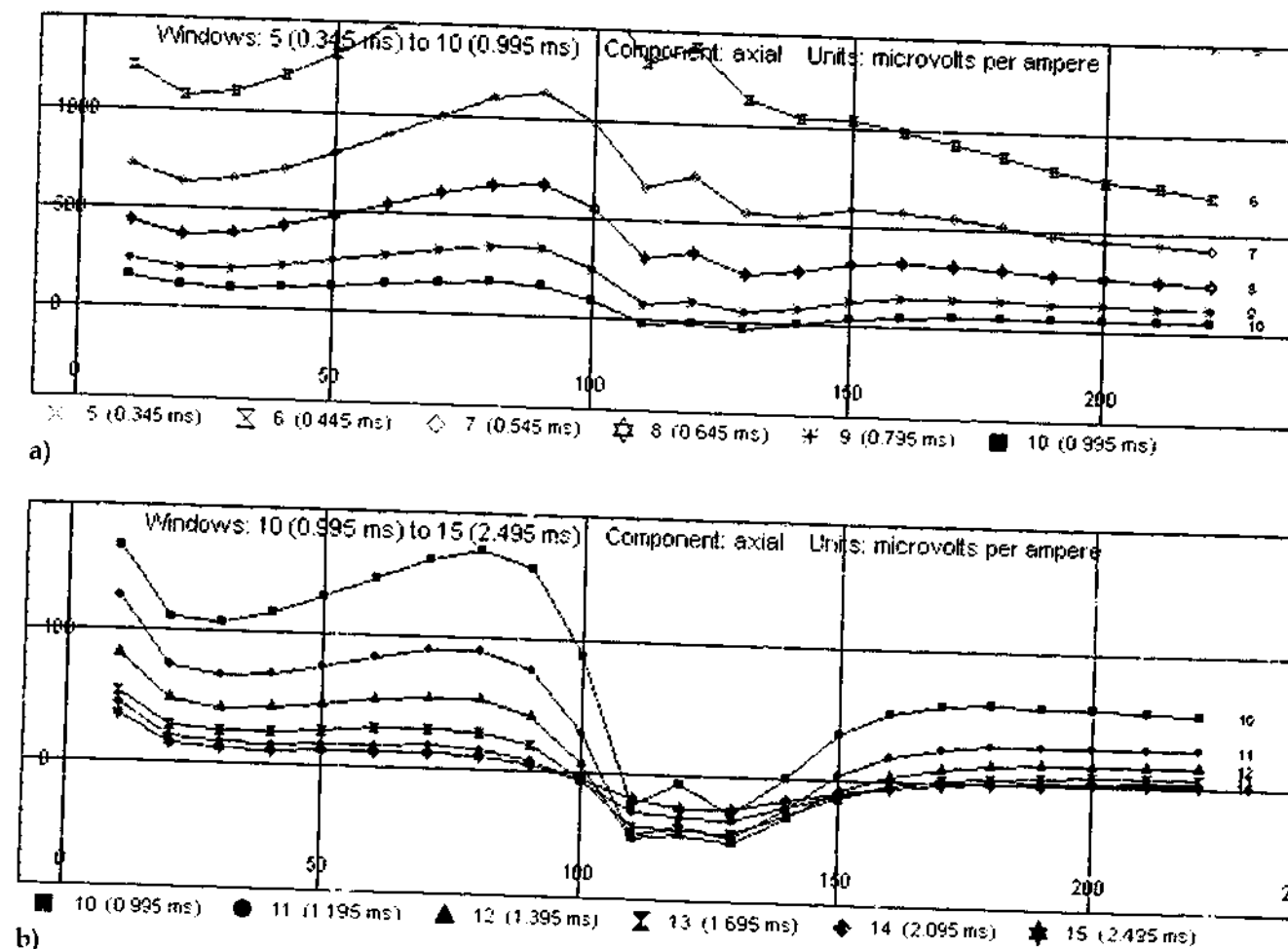


Figure 6.10: Field DHTEM response for Borehole ID3071 with Loop 1 at a) middle times (windows 5 to 10) and b) intermediate times (windows 10 to 15).

6.3.5. CONCLUSIONS.

In regards to Borehole ID3039, the DHMMR profile was found to be equivalent to the galvanic anomaly noted within the DHTEM survey. In addition to this, the benefit in using near and far loops to excite a body inductively and, or solely galvanically, have been clearly illustrated for both Boreholes ID3039 and ID3071. Furthermore, by discriminating between the two different modes of excitation it is possible to construct a classification scheme that essentially recognised three states; that is, the field response was seen to be either dominantly galvanic or inductive in nature, or within a state of transition between these two saturation modes. In general for both holes, the Loop 1 data consisted of a transition zone within windows 10 (0.995 ms) to 15 (2.495 ms) and an inductive response within windows 15 (2.495 ms) to 20 (5.895 ms), whilst for the Loop 3 data current gathering was able to dominate the response in the absence of significant inductive effects.

6.4. STAGE 2: MODEL DEVELOPMENT.

The initial model that was constructed for the upper lens of the Flying Doctor deposit was comprised of only a single plate, the attributes of which were determined by the late-time inductive field response. It was soon realised, however, that a single plate model was incapable of simultaneously replicating both the galvanic and inductive effects noted within the field data. As a consequence of this, two separate plate models were developed independently of each other so as to deal with each of these two principal excitation mechanisms isolated with the field data. The final model can be regarded as a dual plate composite model, which consists of the two plates, Plates 1 and 2. Specifically, Plate 1 a high conductance plate, and Plate 2 a low conductance plate, were developed specifically to match the inductive and galvanic responses respectively of the near surface mineralisation for boreholes ID3039 and ID3071. Specifications for the dual plate model are listed within Table 6.2, and the model and field survey configuration is shown within Figure 6.11.

Complete TEM profiles for both the field data and LEROI models are provided within Appendices D.1, D.2 (Plate 1) and D.3 (Plate 2) respectively. Note also SIROTEM composite times were used and are listed within Appendix E.4.

Table 6.2: Specifications of the dual-plate model.

	PLATE 1. (INDUCTIVE MODEL)	PLATE 2. (GALVANIC MODEL)
HOST RESISTIVITY (ohm.m):	500	500
LOCATION†:		
EASTING (m):	4780	4778
NORTHING (m):	20400	20400
DEPTH (m):	-87.4	-85.4
DIP (degrees):	-70	-70
STRIKE-LENGTH (m):	400	400
DEPTH-EXTENT (m):	40	60
PLATE CONDUCTANCE (siemens):	190	23

† In reference to the midpoint of the top edge of the plate.

FLYING DOCTOR SURVEY CONFIGURATION.

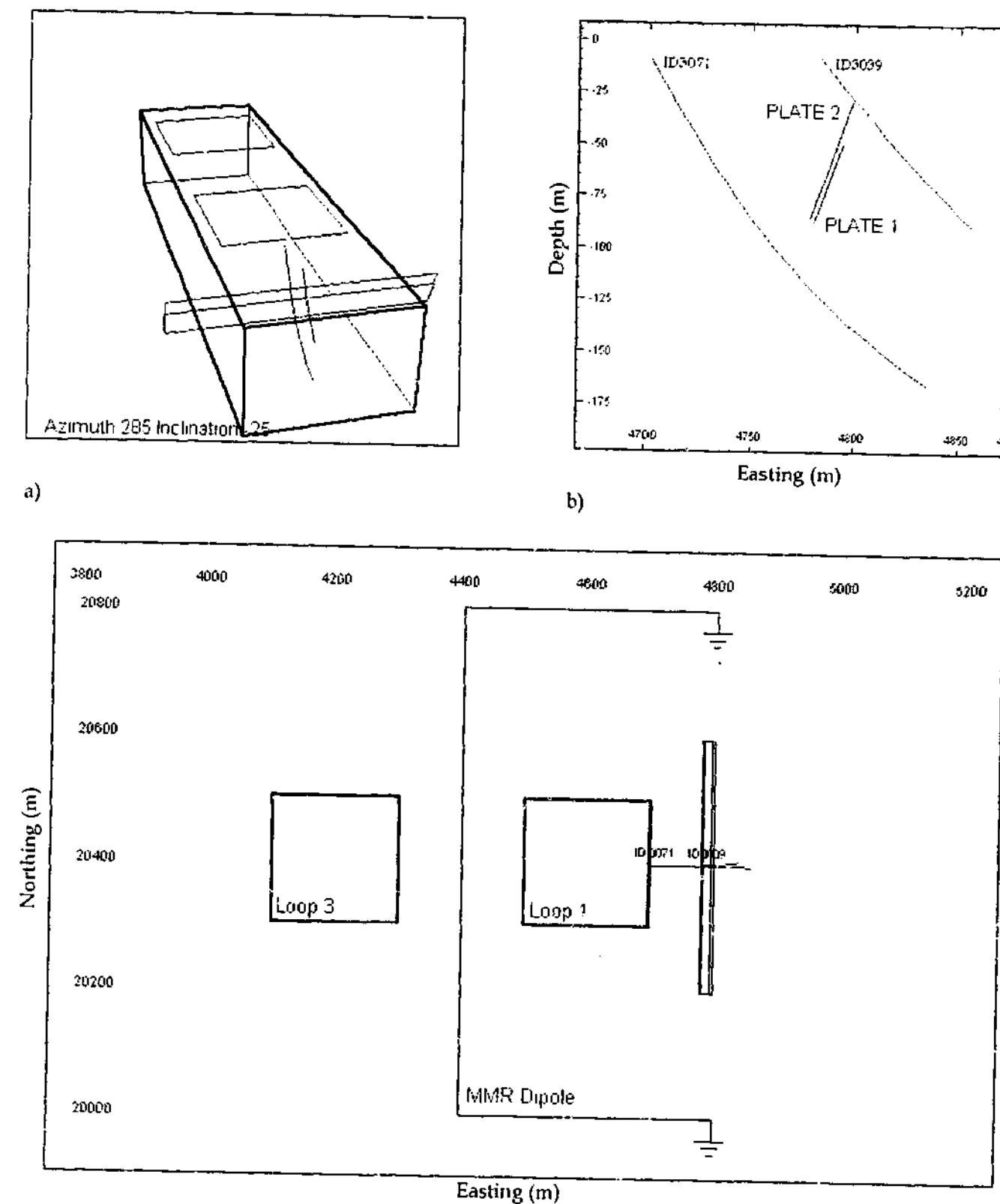


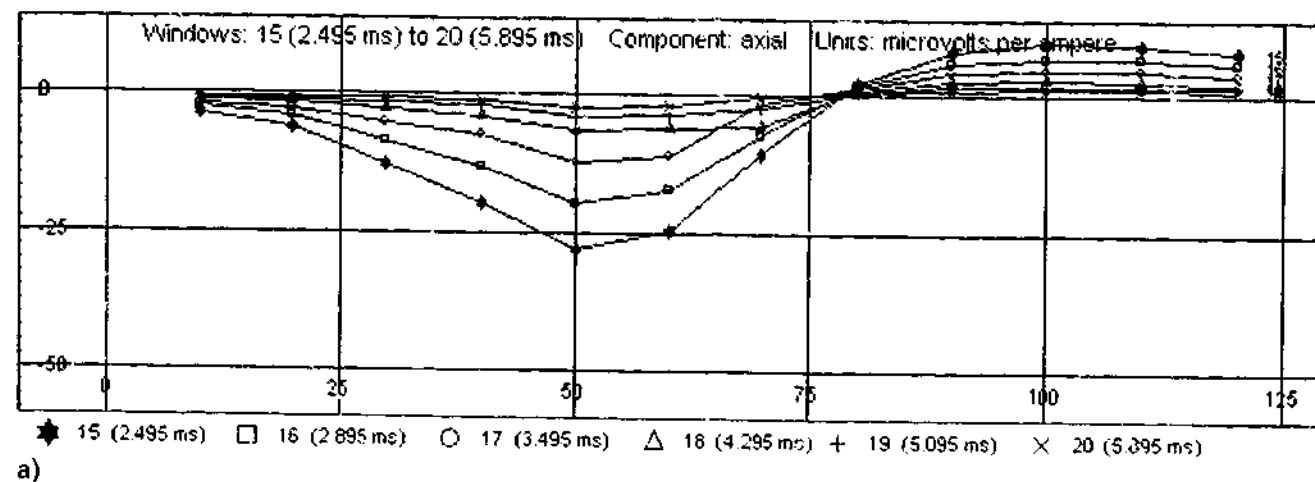
Figure 6.11: Survey configuration featuring Loops 1 and 3 with Boreholes ID3039 and ID3071, together with the DHMMR dipole: a) borehole perspective, b) borehole section and c) survey map.

6.4.1. DEVELOPMENT OF PLATE 1.

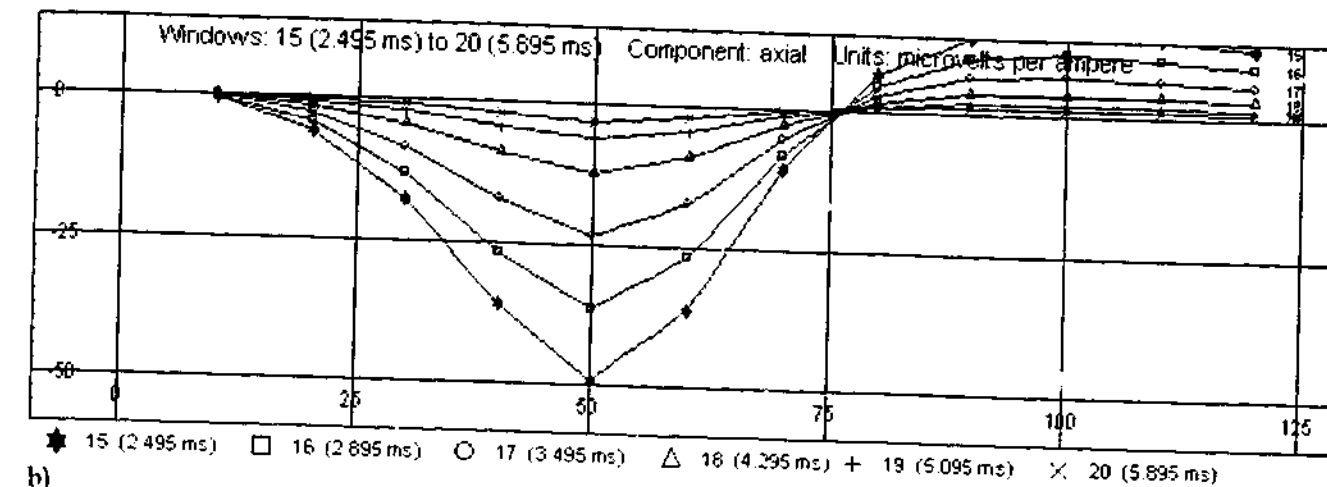
A high conductivity thin-sheet model, Plate 1, was developed within program LEROI. The purpose of this model was to aid the interpretation of the inductive components within both the ID3039 and ID3071 field DHTeM data. Specifications for Plate 1 are given within Table 6.2; whereas details of the model survey configuration can be found within Figure 6.11, which features a survey map, borehole perspective and borehole section respectively. The main constituents of the survey include the Plate 1 model; boreholes ID3039 and ID3071; and the near, Loop 1, and long-offset, Loop 3, transmitter loops.

6.4.1.1. BOREHOLE ID3039 WITH LOOP 1.

The Plate 1 model response computed with program LEROI, for Borehole ID3039 with Transmitter Loop 1, is shown within Figure D.2.1 of Appendix D.2. This model response is to be compared with the field DHTeM data presented within Figure D.1.1 of Appendix D.1. It is noted that although Plate 1 was unable to duplicate the field data at early to middle times, windows 1 (0.120 ms) to 15 (2.495 ms), it was capable of reproducing the inductive response seen within the field data at late-times, windows 15 (2.495 ms) to 20 (5.895 ms). Note for these late times both the field, Figure 6.12a, and model, Figure 6.12b, data possess a negative minimum at Station 50 passing through a negative-to-positive crossover at station 75 down to a positive maximum at Station 100. Although the amplitude of the model minimum is nearly twice as great as that of the field response, the two data sets are observed to decay at similar rates.



a)



b)

Figure 6.12: a) Field DHTeM response for Borehole ID3039 with Loop 1 (windows 15 to 20) and b) the associated thin-sheet LEROI model response of Plate 1 (windows 15 to 20).

The inductive nature of the late-time response was confirmed by decay analysis, in which log-linear decay plots were prepared for both the field and Plate 1 model data, see Figure 6.13a and Figure 6.14a respectively. Idealistically, decay analysis is to be performed on the scattered field response of an anomaly. In this instance, this was achieved for the model data by simple subtraction of the computed host response. Decay analysis, however, is still permissible in instances where an irreducible but insignificant regional is present; this was the case for the field data. Exponential curves were fitted to six late-time windows of Station 50, windows 15 (2.495 ms) to 20 (5.895 ms), yielding inductive time constants of 1.38 ms for the field data, and 1.25 ms for the model data. Although the anomaly within the field data decays slightly faster than that within the Plate 1 model data, the two time constants are considered to be reasonably well matched.

Additional inductive time constants were obtained for Plate 1 using program OZPLTE: 0.97 ms (determined with windows 15 to 20 at Station 50), and the modified formula of Lamontagne (1975) for a thin prism, see Equation 4.3 of Section 4.2: 0.96 ms.

The apparent linear fit to both the field and model data on the log-linear plots, suggests they are exponential in form and thus inductive in origin. To test this result, additional decay plots were prepared but with log-log axes (see Figure 6.13b and Figure 6.14b respectively). On the log-log plot, a poor apparent linear fit is observed for the Plate 1 data, thus providing verification

that model response within this time range is indeed dominated by an exponentially decaying inductive component. This finding is quantified by the lower RMS fit of 98% for the log-log plot compared to nearly 100% for the log-linear plot. Although a similar observation is made for the field data, its apparent linear fit on the log-log plot, suggesting a power law decay, is slightly better than that found for model data. Since a host response will decay by a power law, the improved fit could be attributable to the presence of a regional component within the field response.

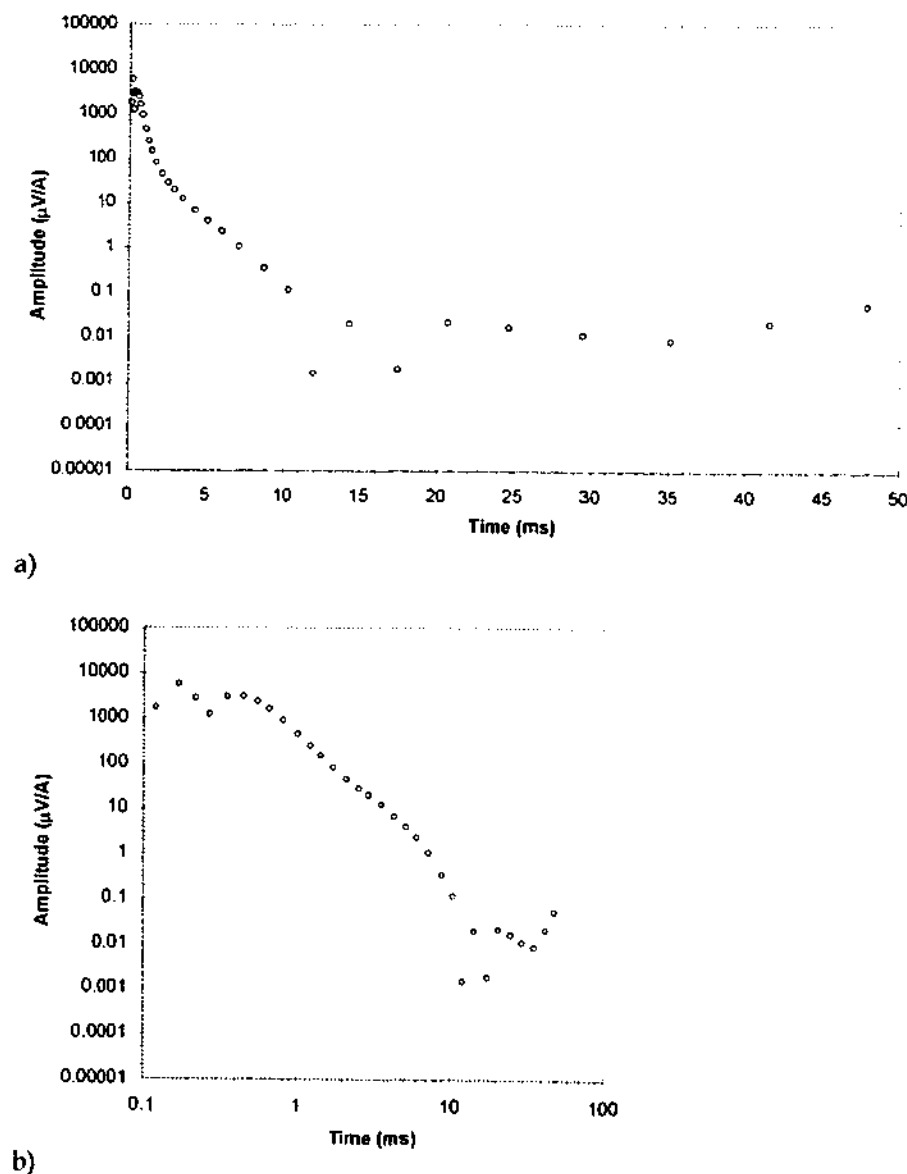


Figure 6.13: Decay analysis of field data at Station 50, for Borehole ID3039 with Loop 1: a) log-linear decay and b) log-log decay.

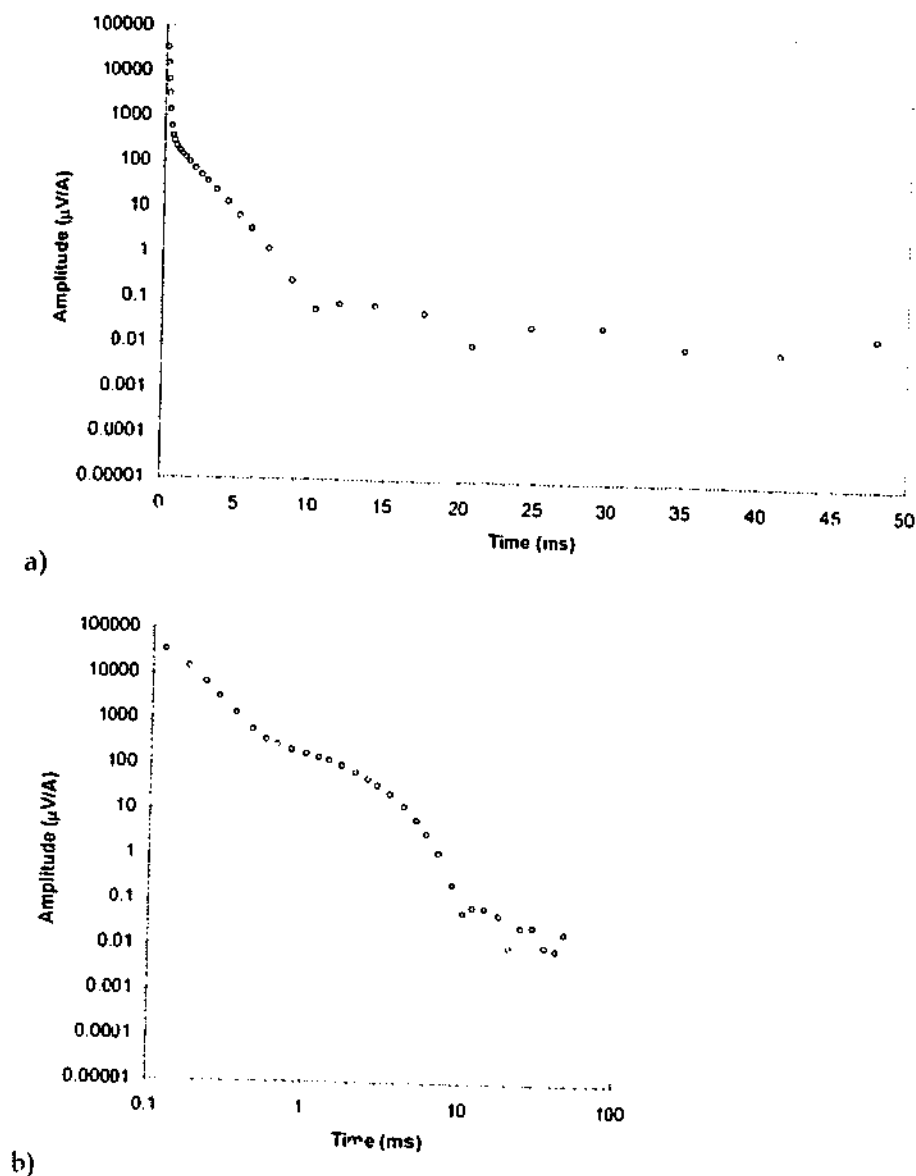
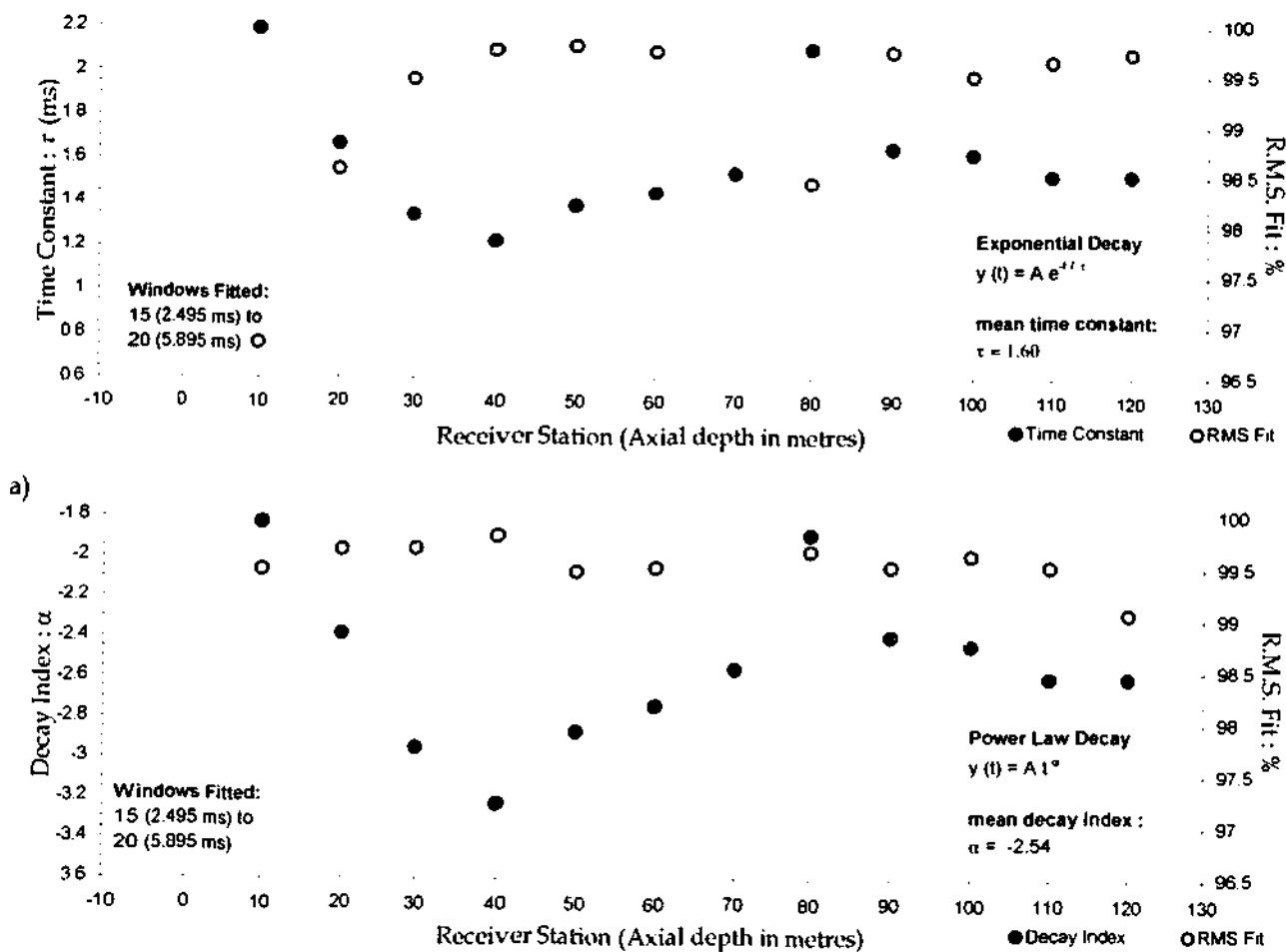
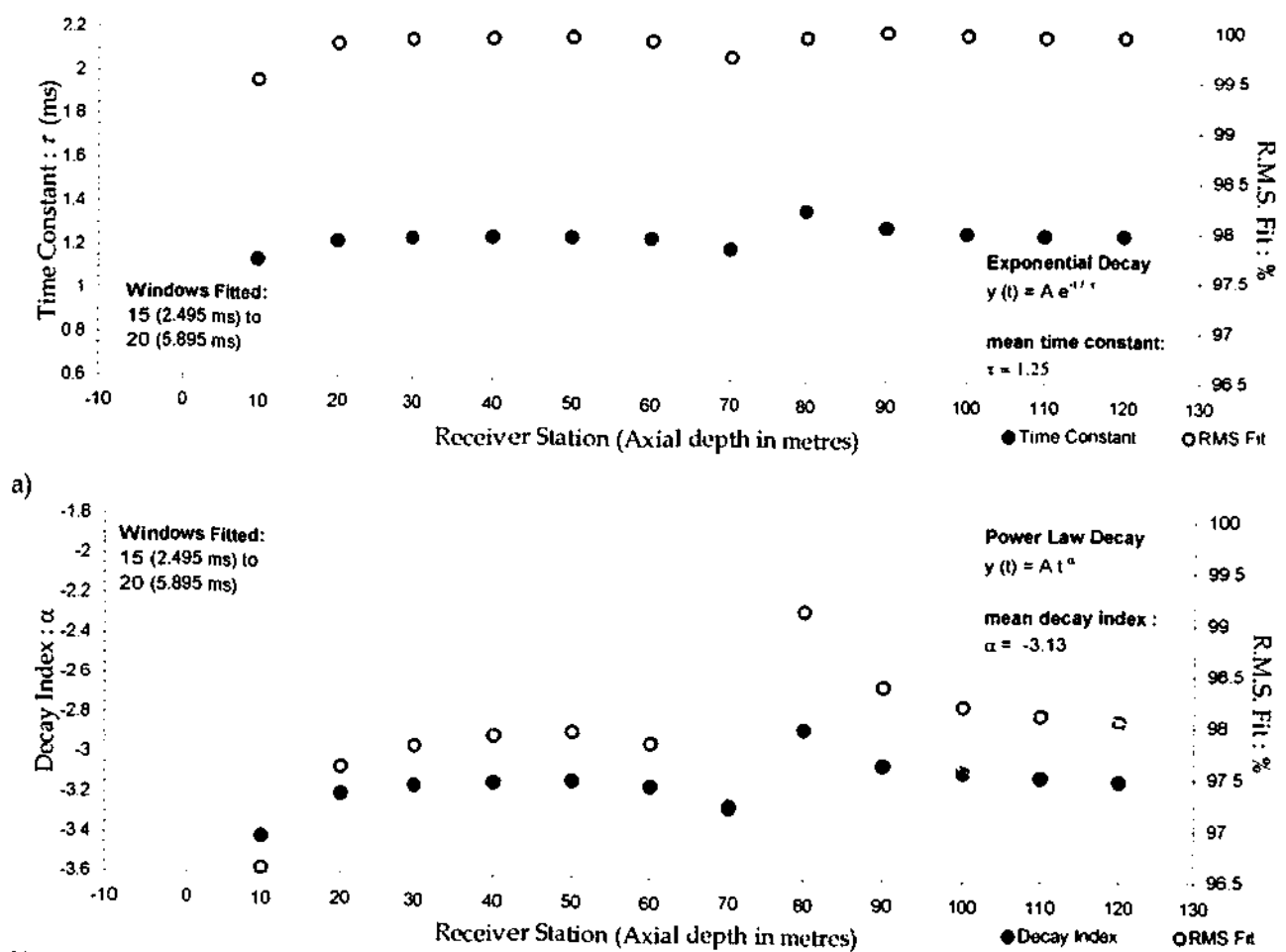


Figure 6.14: Decay analysis of the Plate 1 LEROI model data at Station 50, for Borehole ID3039 with Loop 1 (regional removed): a) log-linear decay and b) log-log decay.

Decay analysis was also performed at multiple stations; where both time constant and decay index profiles were prepared for the field data, Figure 6.15, and Plate 1 model data, Figure 6.16. A predominantly exponential decay is observed within the Plate 1 model decay profiles, notably the RMS fit values within the decay index profile, Figure 6.16b, are of consistently lower value than those within the time constant decay profile, Figure 6.16a. Curiously, the intersection anomaly at Station 80 within the DHTEM field and Plate 1 TEM profiles is manifested within the decay profiles as a discontinuity.



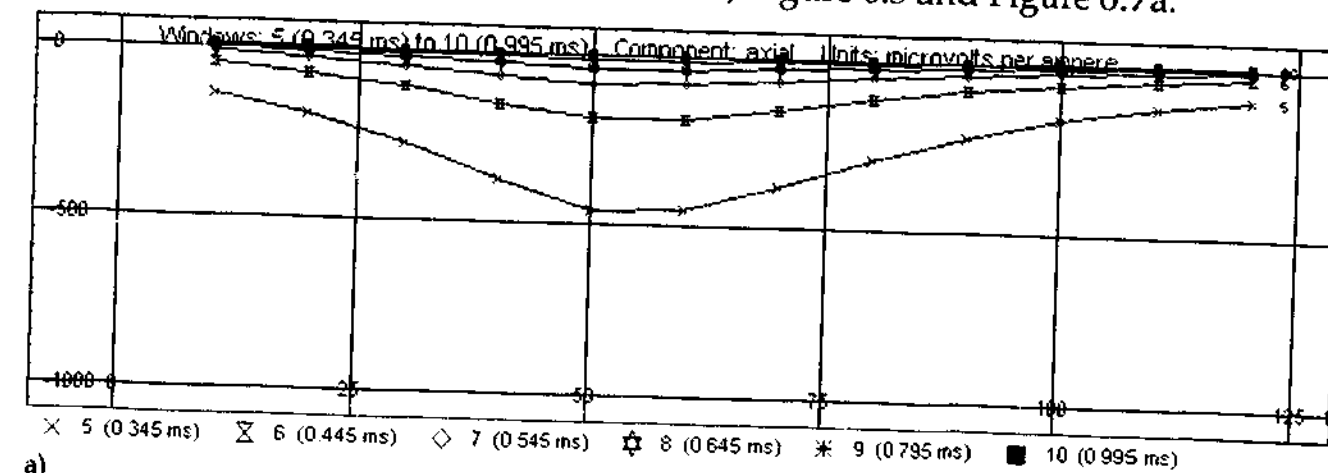
b) Figure 6.15: Decay analysis of the ID3039 - Loop 1 field data (regional retained): a) time-constant profile and b) decay-index profile.



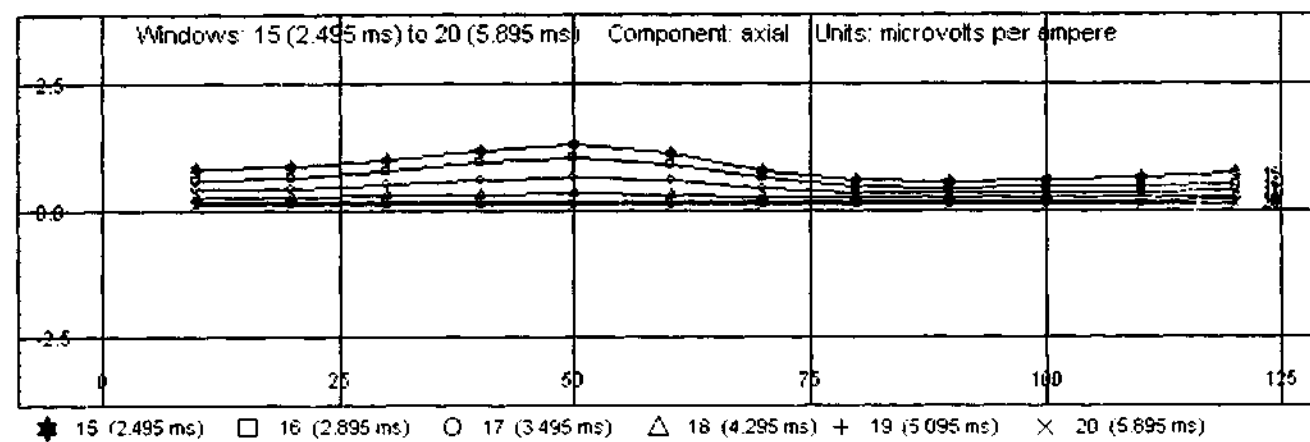
b) Figure 6.16: Decay analysis of the ID3039 - Loop 1 Plate 1 LEROI model data (regional removed): a) time-constant profile and b) decay-index profile.

6.4.1.2. BOREHOLE ID3039 WITH LOOP 3.

The axial component of the LEROI model response of Plate 1 for Borehole ID3039 with Loop 3 is shown within Figure D.2.2 of Appendix D.2. This model response is to be compared with the field axial component DHTEM data within Figure D.1.2 of Appendix D.1. The Plate 1 model response is noted to feature a broad negative anomaly centred about stations 50 and 60 for windows 2 (0.17 ms) through to 10 (0.995 ms), Figure 6.17a. This feature is consistent with current gathering, and can be inferred by consideration of the unipolar secondary fields associated with an anomalous galvanic current, flowing northward, within the plane of the plate. If Plate 1 is extended, thereby reducing the distance from the edge of the plate to the borehole, the galvanic anomaly will sharpen and migrate up hole, approaching the station depth at which the plate intersects the borehole. Unfortunately, attempting to match the field data by this procedure is not permitted, as the depth extent of Plate 1 is constrained by the inductive field response of Loop 1. It was this observation that led to the development of an additional extended, but weakly conducting plate, Plate 2. A negligible inductive response is also noted within windows 15 (2.495 ms) through to 20 (5.895 ms), Figure 6.17b. When compared to the response due to Loop 1, this inductive response has been noted to have undergone a sign reversal due to the change in coupling with the receded loop, Loop 3. Note, that if an inductive response was present within the field data, it would remain undetected due the high level of noise within this window range, Figure 6.7b. Even though the response of Plate 1 is reminiscent of that of the field data, a second plate, Plate 2, was introduced to explain the strong sharp galvanic response centred about Station 40, Figure 6.3 and Figure 6.7a.



a)



b) Figure 6.17: DHTEM LEROI model response of Plate 1 for Borehole ID3039 with Loop 3: a) middle times (windows 5 to 10) and b) late times (windows 15 to 20).

6.4.1.3. BOREHOLE ID3071 WITH LOOP 1.

The axial component of the Plate 1 LEROI model data and its associated field DHTEM response for Borehole ID3071 with Loop 1 are displayed within Figures D.2.3 and D.1.3 respectively. The inductive response present within windows 15 (2.495 ms) to 20 (5.895 ms), Figure 6.16a, of the field data has been reproduced adequately by the Plate 1 model, Figure 6.18. Specifically, at a depth of 70 m the Plate 1 response passes through a positive maximum while the field profile does so at 60 m. Then for both the model and field profiles a positive to negative crossover is reached at the depth of 95 m, while a negative minimum is attained for both the model and field profiles at depths of 120 and 125 m respectively. Finally, a negative to positive crossover is reached at a depth of 160 m in the Plate 1 profile and 180 m in the field profile.

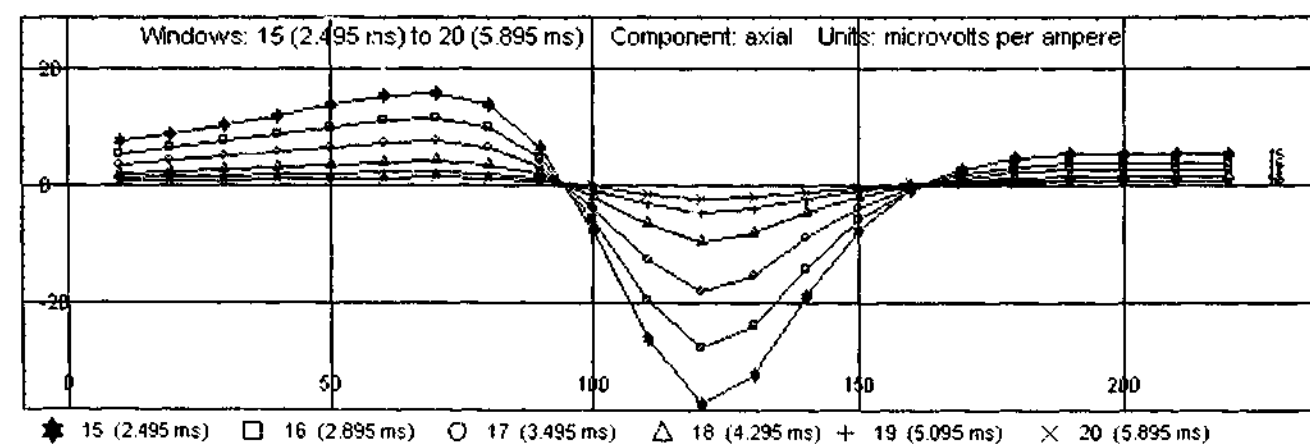
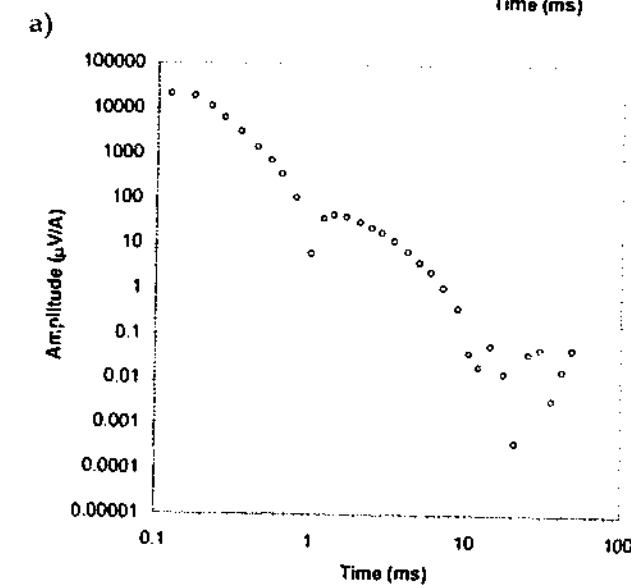
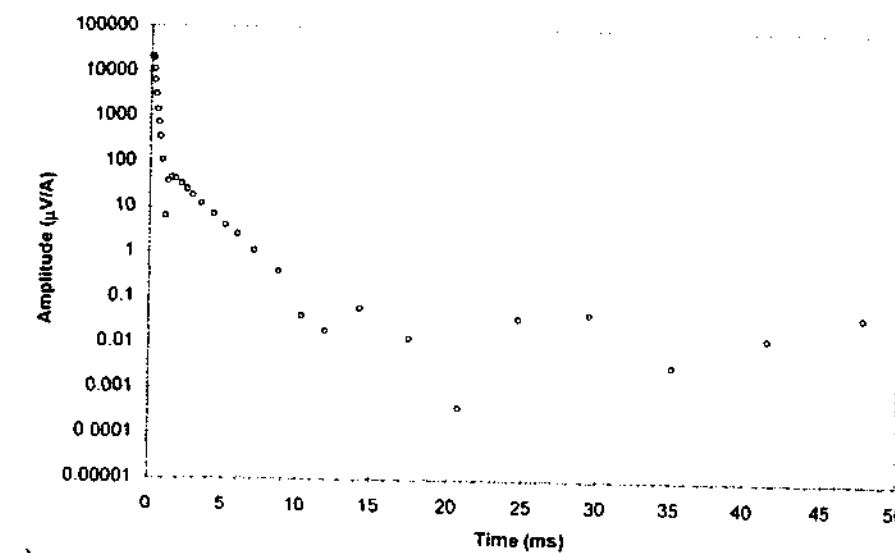


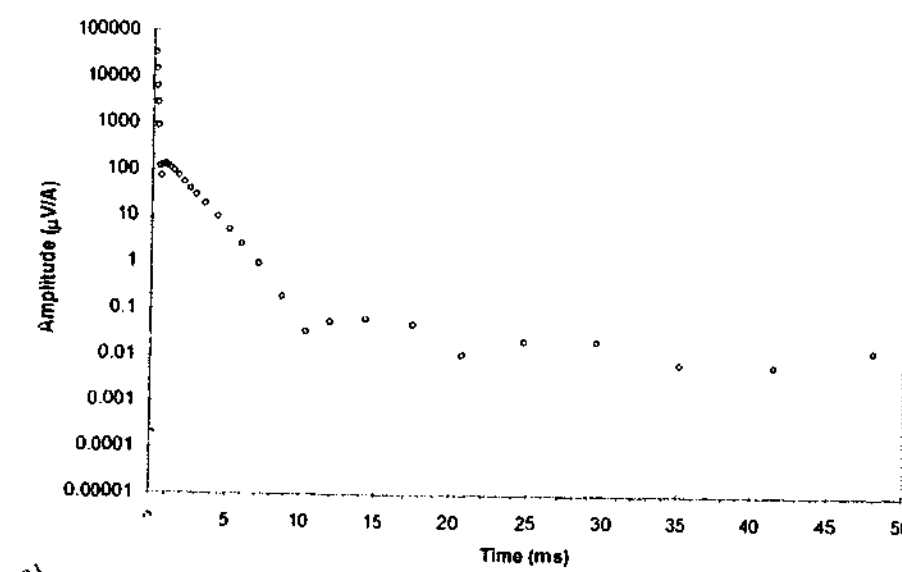
Figure 6.18: DHTEM LEROI model response of Plate 1 for Borehole ID3071 with Loop 1 (windows 15 to 20).

Decay analysis was performed at Station 50 with windows 15 (2.495ms) to 20 (5.895ms), on both the field and Plate 1 model data, yielding inductive time

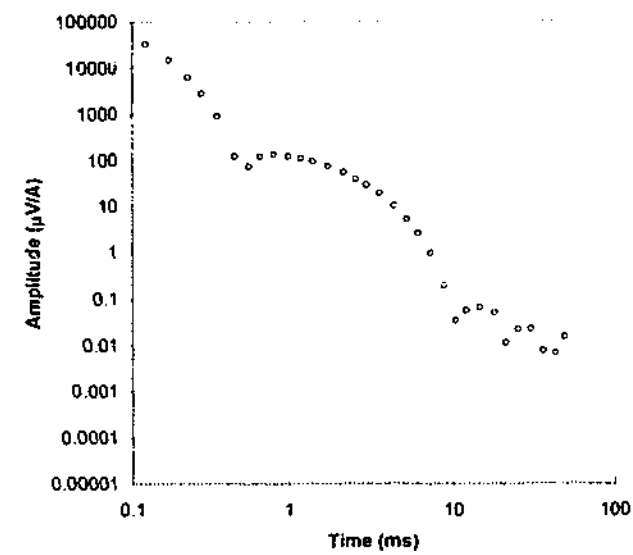
constants of 1.49 ms and 1.25 ms respectively. In addition to this, comparative log-linear and log-log plots were prepared for the field, Figure 6.19, and Plate 1 model, Figure 6.20, data. A late-time exponential decay is evident in both instances.



b) Figure 6.19: Decay analysis of field data at Station 120, for Borehole ID3071 with Loop 1: a) log-linear decay and b) log-log decay.



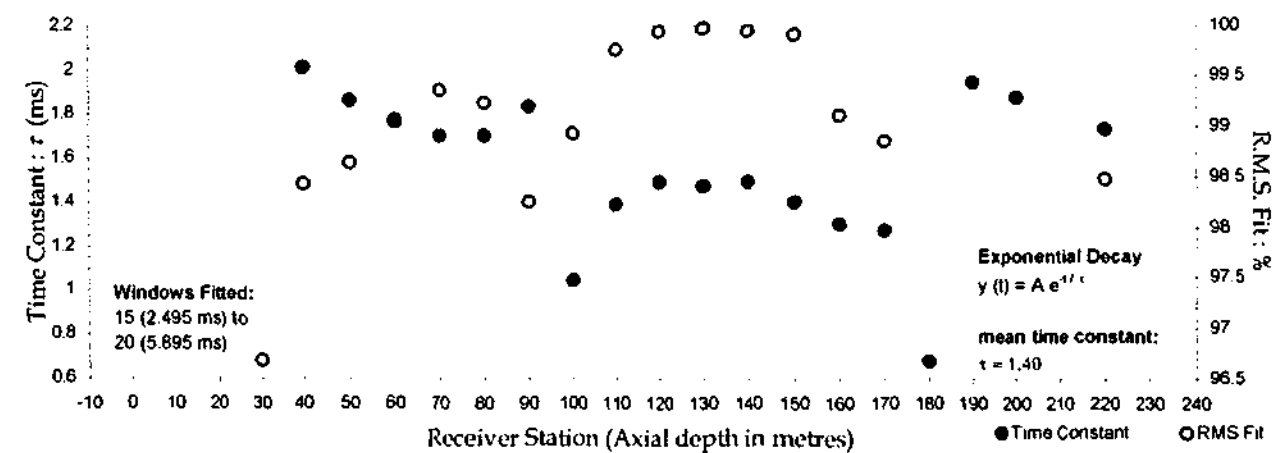
a)



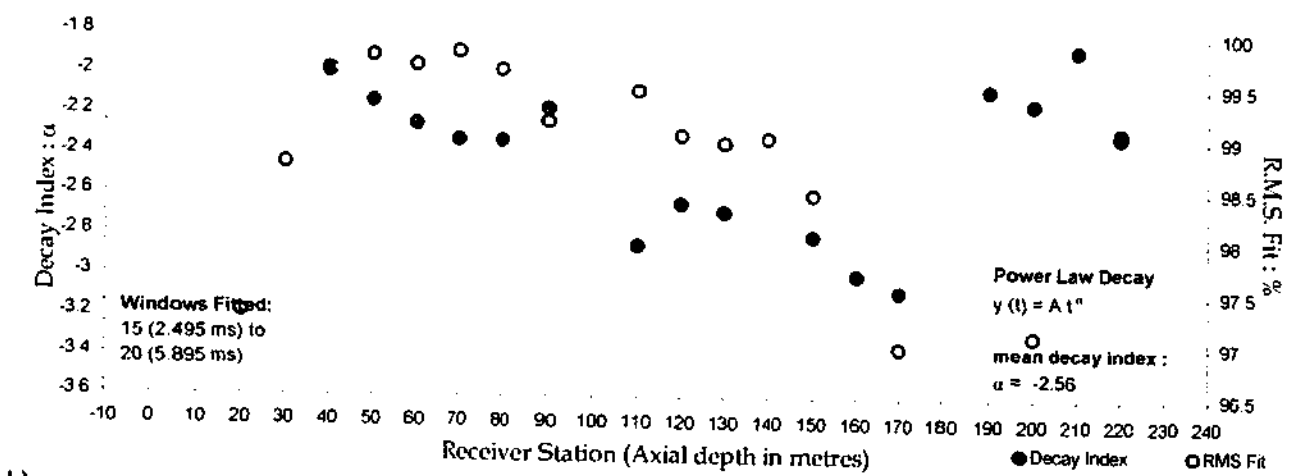
b) Figure 6.20: Decay analysis of the Plate 1 LEROI model data at Station 120, for Borehole ID3071 with Loop 1: a) log-linear decay and b) log-log decay.

Decay profiles were also prepared, for the inductive time constants and power-law decay indices derived from the field, Figure 6.21, and model, Figure 6.22, data. As before, a dominant inductive component is confirmed for both data sets by the large RMS fit values obtained for the time constant decay profile. The zero-amplitude crossovers within the field and model data were manifested in the decay profiles as discontinuities.

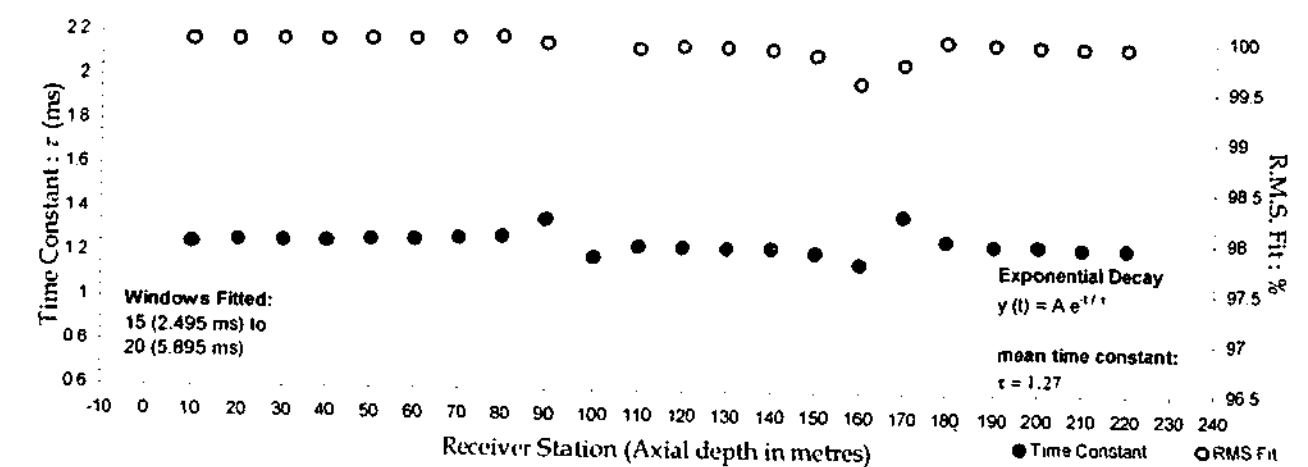
An additional time constant decay profile was prepared for the Plate 1 model using program OZPLTE, Figure 6.22c. An average time constant of 0.97 ms was obtained; a result that is in excellent agreement with that derived from the modified formula of Lamontagne (1975) for a thin prism: 0.96 ms, see Equation 4.3 of Section 4.2.



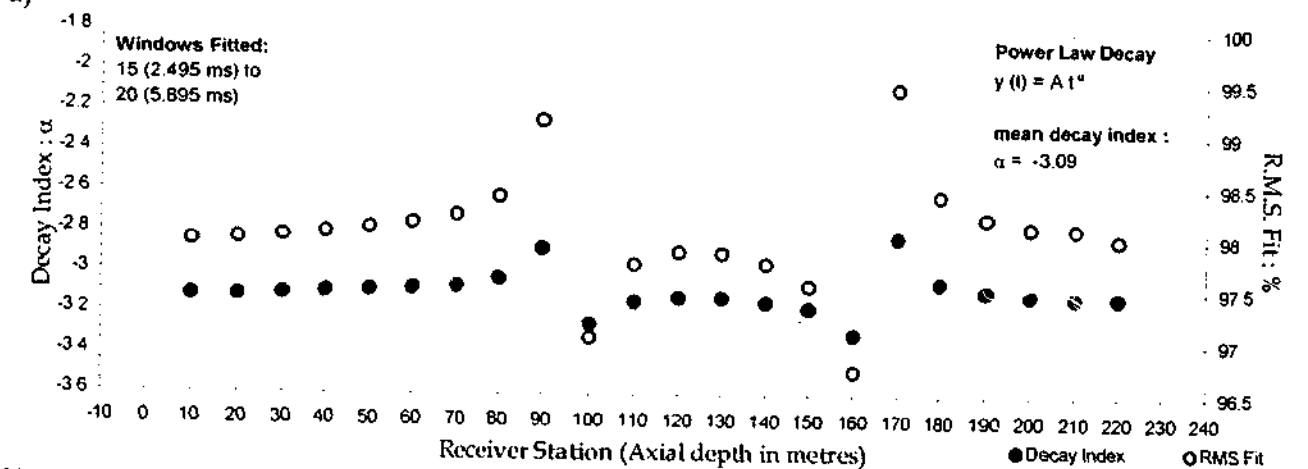
a)



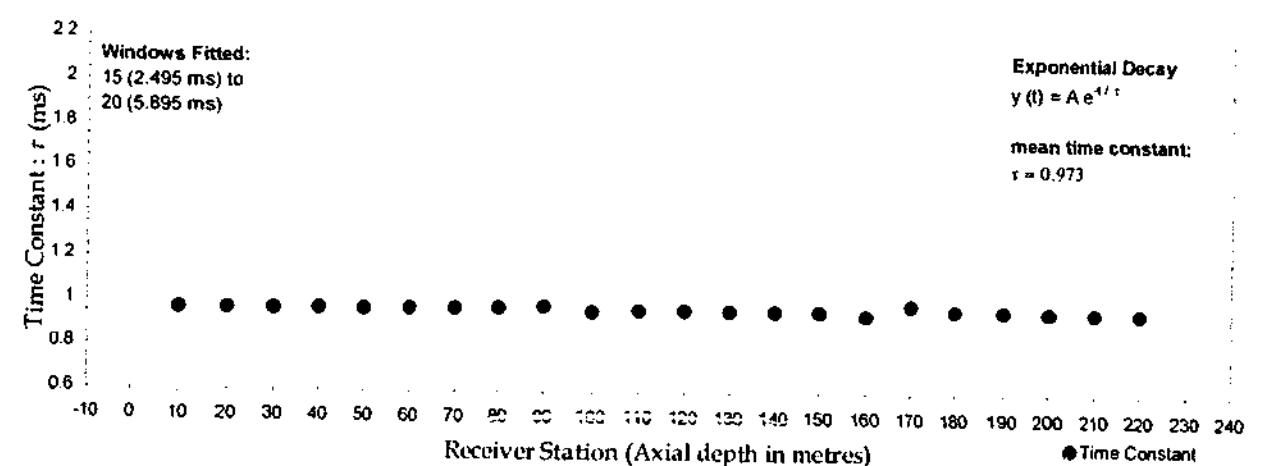
b) Figure 6.21: Decay analysis of field DHTM data for Borehole ID3071 with Loop 1: a) time-constant profile and b) power law decay index profile.



a)



b)



c) Figure 6.22: Decay analysis of the Plate 1 DHTM LEROI model data, for Borehole ID3071 with Loop 1: a) time-constant profile, b) decay-index profile and c) time-constant profile of the equivalent OZPLTE model.

Featured within windows 5 (0.345 ms) to 10 (0.995 ms) of the model data, is a broad positive anomaly centred about Station 110, Figure 6.23. The origin of this anomaly can be traced to current gathering effects within the plate. In reference to the model section, Figure 6.11b, the mechanism for the production of this anomaly can be understood in terms of the unipolar secondary fields associated with a galvanic anomalous current stream, or ribbon of current, flowing northward within the plate (into page). The secondary fields will be found to circulate around the plate, with the curl of their circulation aligned with the direction of the galvanic current flow (clockwise within the figure). Thus, the axial component of these fields will be directed up-hole for all receiver stations in Borehole ID3071, thereby resulting in a single signed positive anomaly peaking at the station most closest to the lower edge of the plate, namely Stations 110 and 120.

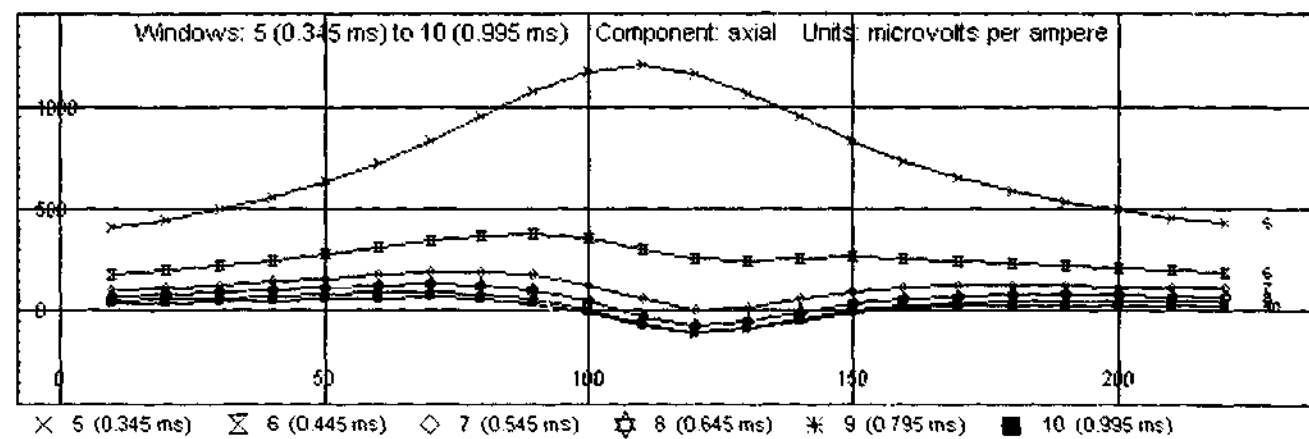
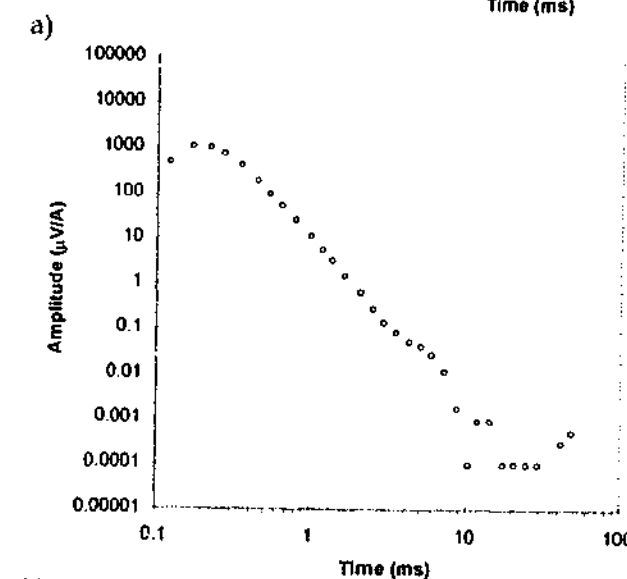
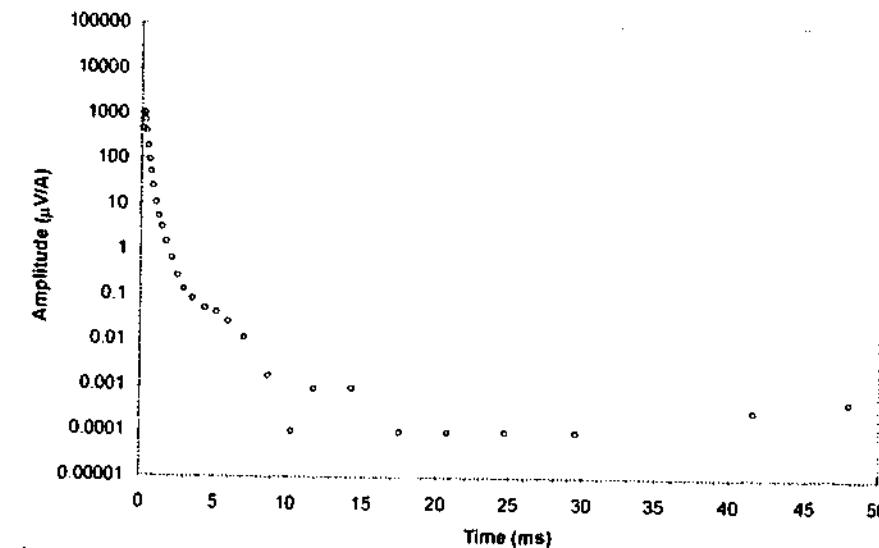


Figure 6.23: Downhole TEM model response of Plate 1 using program LEROI, for Borehole ID3071 with Loop 1 (windows 5 to 10).

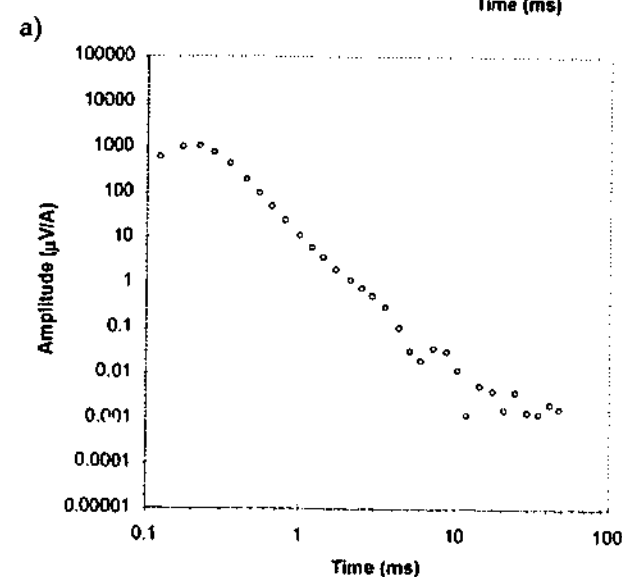
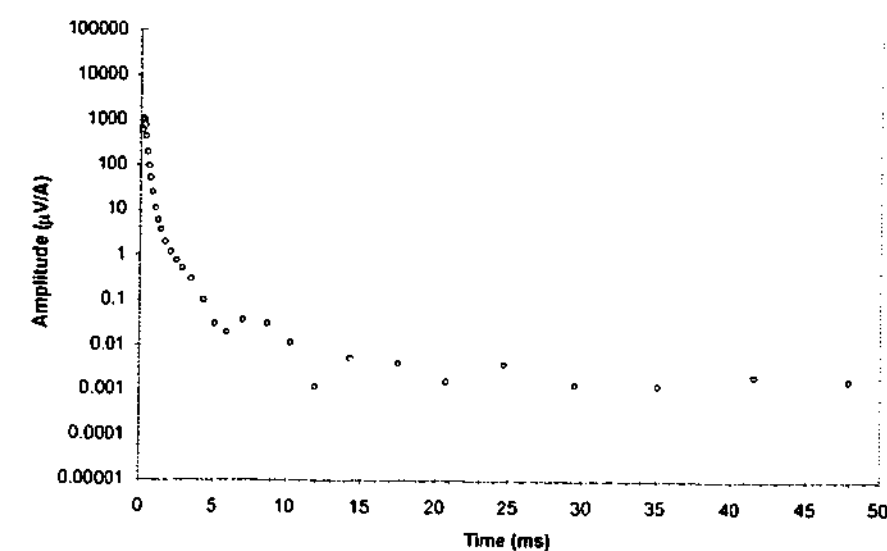
6.4.1.4. BOREHOLE ID3071 WITH LOOP 3.

The axial component of the LEROI model response of Plate 1 for Borehole ID3071 with Transmitter Loop 3 is shown within Figure D.2.3. This model response is almost identical to that due to Plate 2, Figure D.2.4. Specifically, the profiles of both Plates 1 and 2 feature a broad positive anomaly centred about Station 120. A reasonable match has been attained with the field data, which also possesses a broad positive anomaly that is centred about Station 110 for windows 5 (0.345 ms) through to 15 (2.495), Figure D.1.4. Unfortunately, the presence of a negative intersection anomaly at this depth prevented any meaningful decay analysis on the main positive anomaly.

Decay analysis was performed on both the Plate 1 and 2 model anomalies at Station 110 using windows 6 (0.445 ms) through to 12 (1.395 ms). In both cases each model anomaly was found to decay by a power-law. The decay indices obtained were -3.5 for Plate 1, Figure 6.25b, and -3.58 for Plate 2, Figure 6.24b, these values are in excellent agreement with the theoretical value of $-7/2$ for current channelling (Asten 1991a; see also Section 4.3). It should be noted that these decay indices were obtained from the model data that had been stripped of its host response; specifically a simple subtraction between the total (LEROI) and regional response was performed. Finally, log - linear plots for both the Plate 1, Figure 6.25a, and Plate 2, Figure 6.24a, model data were prepared, noting that the slight positive curvature of the data for windows 6 to 10 verifies the power-law relationships.



b) Figure 6.24: Decay analysis of the Plate 2 LEROI model data at Station 110, for Borehole ID3071 with Loop 3: a) log-linear decay and b) log-log decay.



b)
Figure 6.25: Decay analysis of the Plate 1 LEROI model data at Station 110, for Borehole ID3071 with Loop 3: a) log-linear decay and b) log-log decay.

The Plate 1 anomaly remains prominent within windows 15 (2.495 ms) to 20 (5.895 ms), whereas the Plate 2 anomaly does not. This is attributable to the enforcement of the galvanic response with inductive effects, since an inductive component is apparent at these times. In particular, the stripped LEROI response (see Figure 6.26) reveals an anomaly that possesses a minimum and maximum at Stations 60 and 120 respectively, together with a negative-to-positive crossover centred about Station 80. In comparison, Figure D.2.3 shows an inductive anomaly for Loop 1; this anomaly features a maximum and minimum at Stations 70 and 120, and a positive-to negative crossover between Stations 90 and 100. The reverse coupling of Loop 1 with respect to Loop 3 has resulted in an inductive anomaly of opposite sign. Despite the occurrence of the Loop 1 and Loop 3 minima at different depths, a positive galvanic anomaly would explain the up-hole migration of the Loop 3 minimum and crossover.

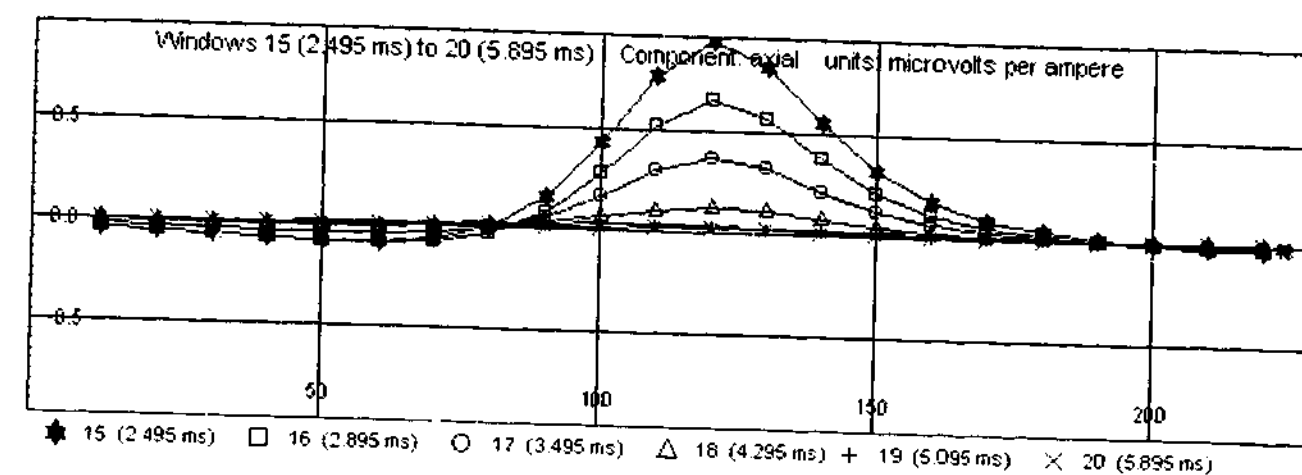


Figure 6.26: Stripped LEROI model response of Plate 1 for Borehole ID3071 with Loop 3 (windows 15 to 20).

6.4.2. DEVELOPMENT OF PLATE 2.

The thin-sheet model, Plate 2, is a low conductivity body that was developed with program LEROI, for the benefit of the galvanic response within the ID3039 and ID3071 field data. Specifications for Plate 2 are given within Table 6.2; whereas details of the model survey configuration can be found within Figure 6.11, which features a survey map, borehole perspective and borehole section respectively. The main constituents of the survey include the Plate 2 model; boreholes ID3039 and ID3071; and the near, Loop 1, and long-offset, Loop 3, transmitter loops.

6.4.2.1. BOREHOLE ID3039 WITH LOOP 1.

Complete axial-component TEM profiles, for Borehole ID3039 with Loop 1, for both the LEROI model response of Plates 2 and its associated field data, are shown within Figures D.3.1 and D.1.1 respectively.

The field response at early times features a prominent negative galvanic anomaly centered about Station 40. This anomaly first appears at window 5 (0.345 ms); peaks at window 6 (0.445); and persists until around window 10, Figure 6.27a. At middle-times, windows 10 (0.995 ms) to 15 (2.495 ms), an intermediate stage is observed, during which the target undergoes a change in its primary mode of excitation, and the field response becomes a indiscernible mixture of galvanic and inductive effects. Eventually, however, the galvanic component diminishes entirely, permitting inductive effects to dominate the response at late-time, namely windows 15 (2.495 ms) to 20 (5.895 ms).

It is recalled, that although Plate 1 successfully reproduced the late-time inductive field response, it failed to replicate the early-time galvanic component, yielding only a broad, low amplitude, galvanic anomaly which was centred about Stations 50 to 60. Since the inductive response within the field data constrained the depth extent of the model, Plate 1 could not be extended so as to match the sharp galvanic anomaly noted within the field data, Section 6.4.1.2. This prompted the development of a second plate, Plate 2, whose conductance was chosen to be of a sufficiently low value, namely 23 S as opposed to 190 S, so as to eliminate its inductive response and the associated constraints on depth extent.

The Plate 2 LEROI model using a depth extent of 60 m achieved an excellent match with the early-time galvanic field response, see Figure 6.27, comparative TEM profiles of the model and field data for windows 5 (0.345 ms) to 10 (0.995 ms); this an important result, since the depth extent inferred from the inductive component was only 40 m. These apparently conflicting estimates for the depth extent of the target have revealed that the upper lens of the deposit is comprised of a highly conductive core and weakly conducting extension.

In detail, the Plate 2 model response with LEROI, is noted to be devoid of an inductive component, but features a sharp negative galvanic anomaly of large amplitude, centred about Station 40, which diminishes rapidly after window 10 (0.995 ms) (see Figure 6.C.1). Unlike the field response, however, a galvanic anomaly is present at very early-times, windows 1 (0.120 ms) to 5 (0.345 ms), within the Plate 2 model response, compare Figures 6.A.1 and 6.C.1. This may be attributed to the masking of the galvanic component within the field data by near surface EM effects. In addition to this, the galvanic anomaly within the field data exhibits a stronger asymmetry than that due to Plate 2, Figure 6.27. Consequently, the negative-to-positive crossover within the field profiles is located at a greater borehole axial depth, namely 100 m, than the crossover within the Plate 2 profiles, namely 65 m.

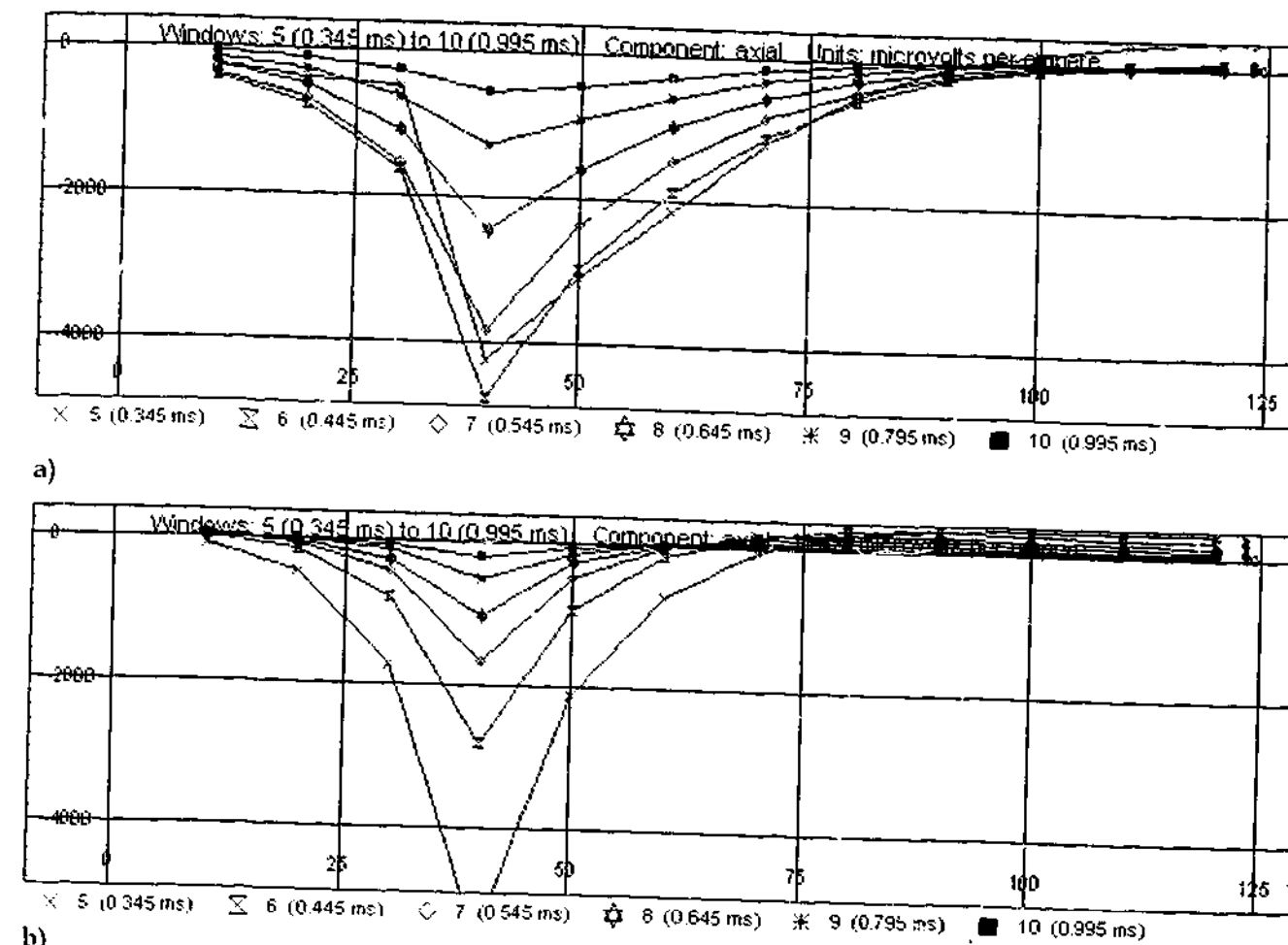


Figure 6.27: a) Field DHTM response for Borehole ID3039 with Loop 1 (windows 5 to 10) and b) the associated LEROI model response of Plate 2 (windows 5 to 10).

Verification of the galvanic origin of the early-time anomalies, noted within both the Plate 2 and field data sets, was achieved by means of decay analysis in which a power-law decay was sought. Comparative log-log and log-linear decay plots were also prepared for the field, Figure 6.28, and Plate 2, Figure 6.29, data.

A power-law decay fitted to the field data, using windows 7 (0.545 ms) to 10 (0.995 ms) at Station 40, yielded a decay index of -3.27 , whereas for the Plate 2 model data, a decay index of -3.05 was obtained using windows 7 (0.545 ms) to 9 (0.795 ms) at Station 40. These results are consistent with current gathering (see Section 4.3). For the same respective window ranges, however, a near linear relation is also noted on the log-linear plots prepared for both the Plate 2 model, Figure 6.29a, and field data, Figure 6.28a, implying an exponential decay. The poor RMS¹ fit within the decay index profile, Figure 6.30b, in

¹ The Root-Mean-Square error employed here is defined as: $R.M.S. \text{ error} = \sqrt{N^{-1} \sum_{i=1}^N \delta_i^2}$, where N is the sample number, and the δ_i are the differences between each data point and the fitted curve; this result is expressed as a percentage: 0 % worst fit, 100% best fit (EM Vision, 1996).

respect to the RMS fit within the time constant profile, Figure 6.30a, generated from the field data again seems to imply an inductive decay. In the case of the Plate 2 data, however, the RMS fit values about Station 40 for both the time constant and decay index profiles, Figure 6.31a and Figure 6.31b, are essentially equivalent. This coupled with the mean time constant, namely 0.7 ms, of the Plate 2 time constant profile generated from OZPLTE, Figure 6.31c, appears to indicate that although the profile is predominantly galvanic in nature a residual inductive component may also be present.

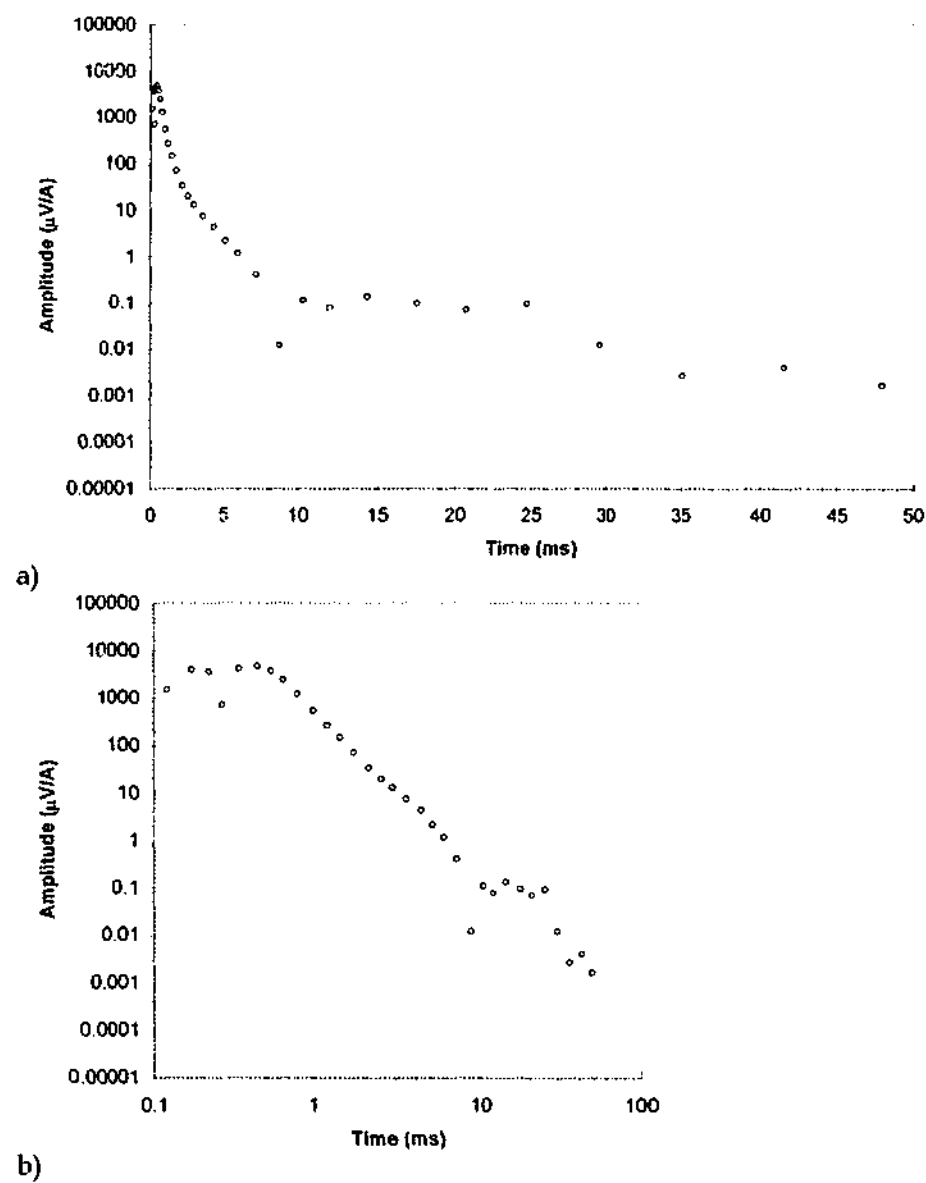


Figure 6.28: Decay analysis of the field data at Station 40, for Borehole ID3039 with Loop 1: a) log-linear decay and b) log-log decay.

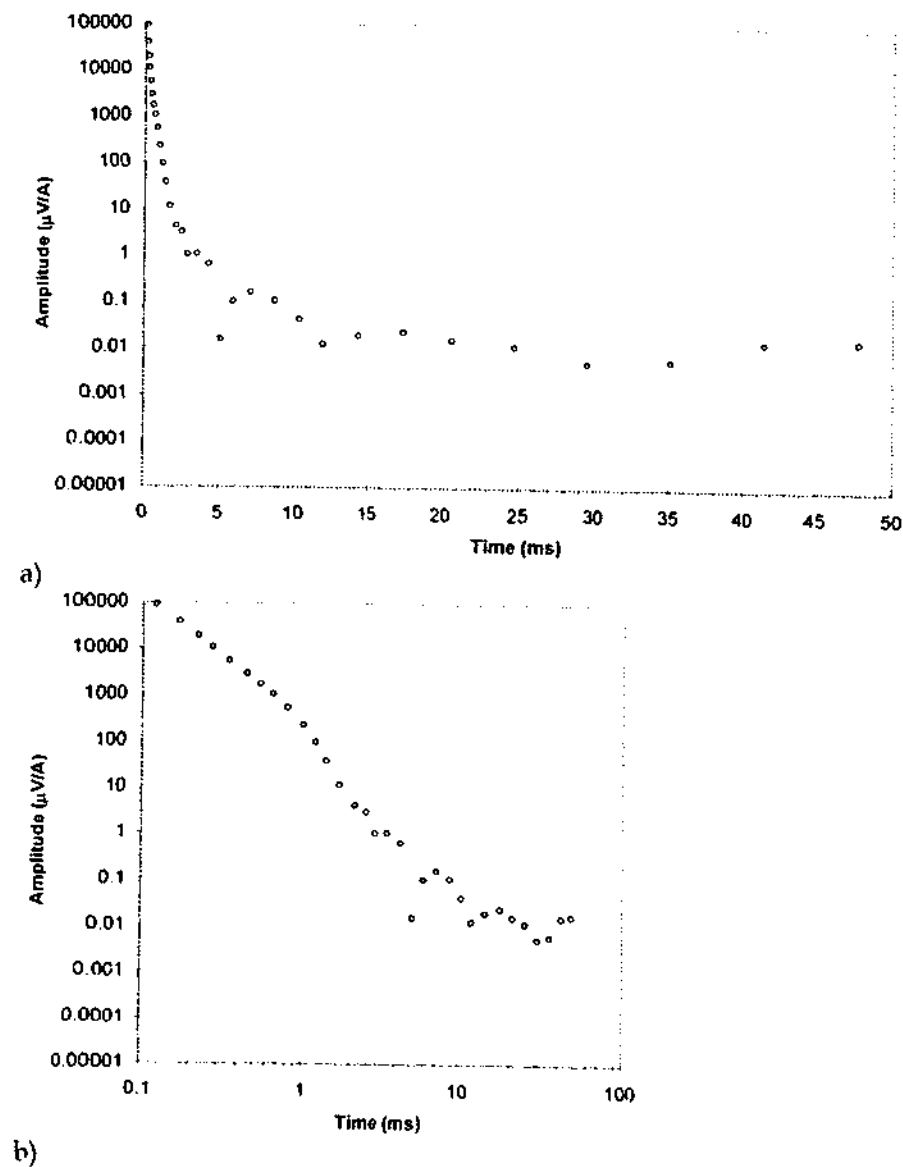


Figure 6.29: Decay analysis of the Plate 2 LEROI model data at Station 40, for Borehole ID3039 with Loop 1: a) log-linear decay and b) log-log decay.

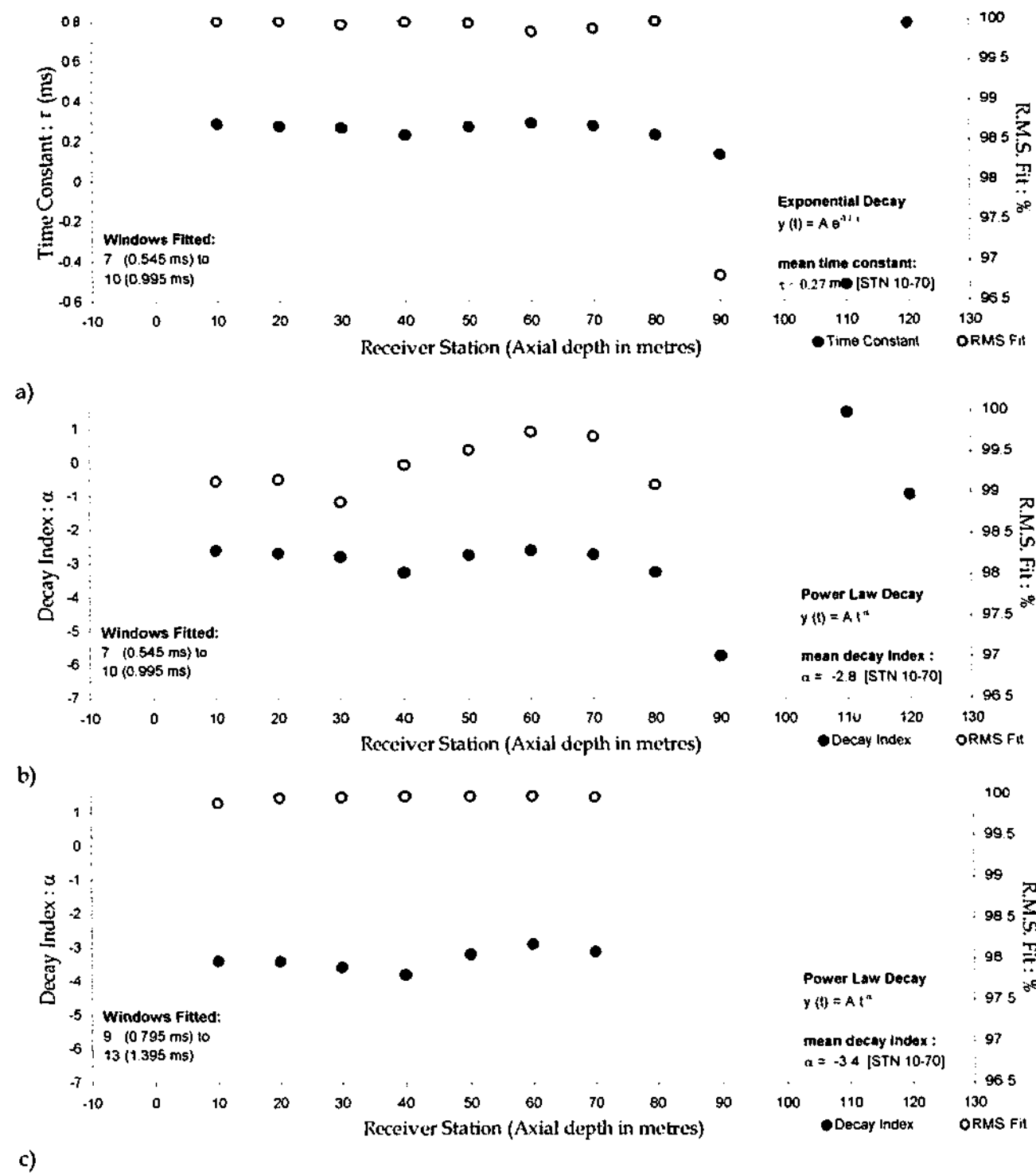


Figure 6.30: Decay analysis of the field response, see Figure 6.27a), for Borehole ID3039 with Loop 1, with regional retained. Profiles for the time-constants a), and decay-indices b) and c) were prepared for the analysis.

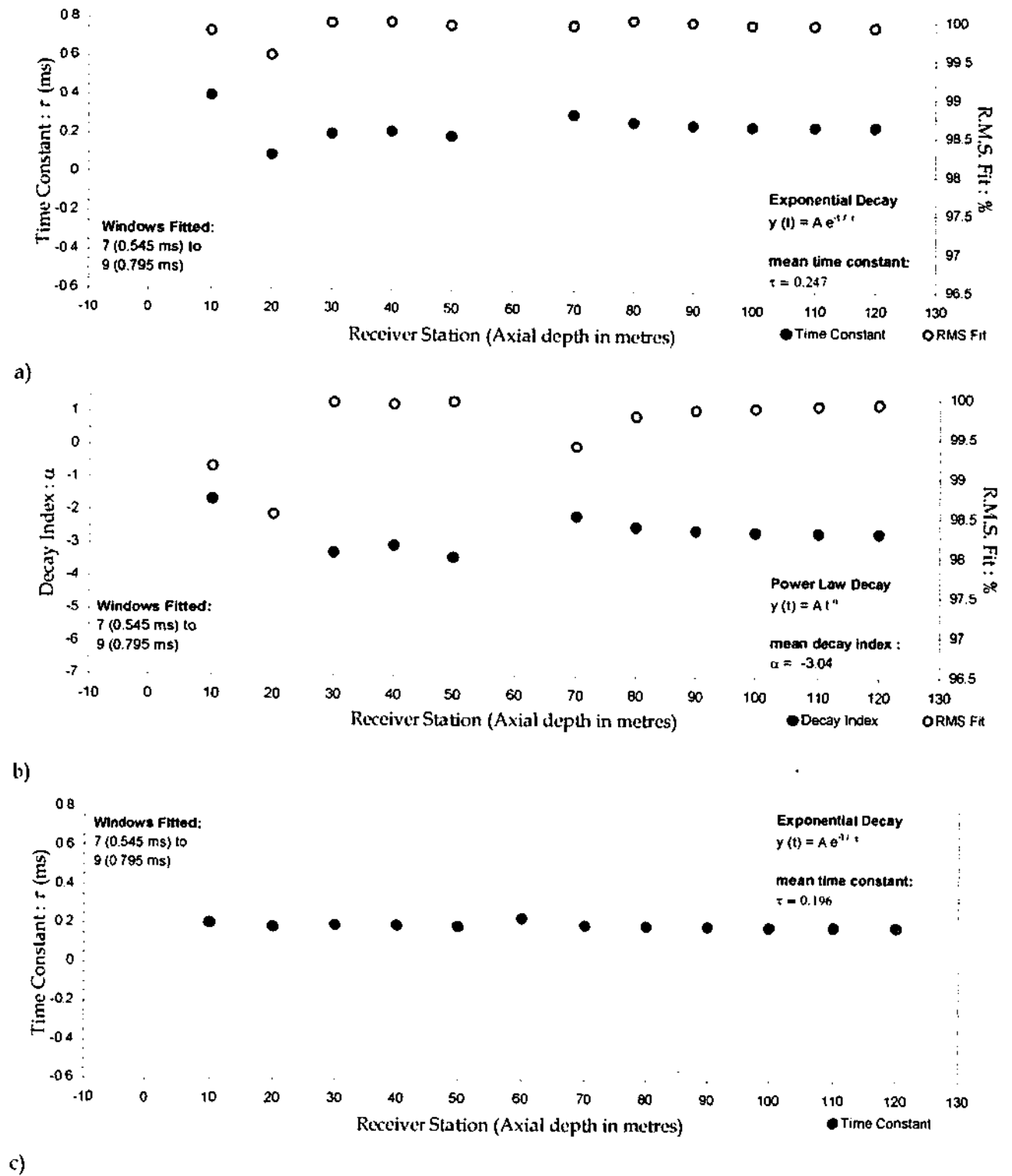


Figure 6.31: Decay analysis of the LEROI model response of Plate 2 for Borehole ID3039 with Loop 1 (see Figure 6.27b) with the regional removed. Profiles for the time-constants a), and decay-indices b), were prepared for the analysis. c) Time-constant profile of the equivalent free-space OZPLTE model.

6.4.2.2. BOREHOLE ID3039 WITH LOOP 3.

The axial component of the Plate 2 LEROI model and field DHTeM data for Borehole ID3039 with Transmitter Loop 3, are shown within Figures D.3.2 and D.1.2 respectively. Reduced inductive coupling between the target and transmitter loop, with the use of Loop 3, has resulted in the absence of an inductive response. Indeed the time windows for which the inductive profiles were noted to be prominent within the Loop 1 data, windows 15 to 25, were found to be devoid of any target EM signature with Loop 3. Consequently, the intermediate stage noted in the Loop 1 data set is no longer present, so that the anomaly at these times appears to be entirely galvanic, with its profile unperturbed by inductive effects. It is interesting to note, however, that at the time in which the intermediate stage occurred, the galvanic anomaly is found to decay to background levels, and does not persist beyond window 15 (2.495 ms). Finally, a sharp negative single signed galvanic anomaly of the type noted within windows 5 (0.345 ms) to 10 (0.995 ms) of the Loop 1 data Figure 6.2a, is present within the Loop 3 data Figure 6.32a. Unfortunately, with its depth extent constrained, Plate 1 was unable to replicate this response, and produced only a broad single signed galvanic anomaly, Figure D.2.2. The response of the Plate 2 model data at middle times, Figure 6.32b, features a negative anomaly with a profile that has the same shape and location as the anomaly described within the field data. It is noted, however, that unlike the field anomaly, the Plate 2 anomaly does not persist to window 13 (1.695 ms) (see Figure C.2b).

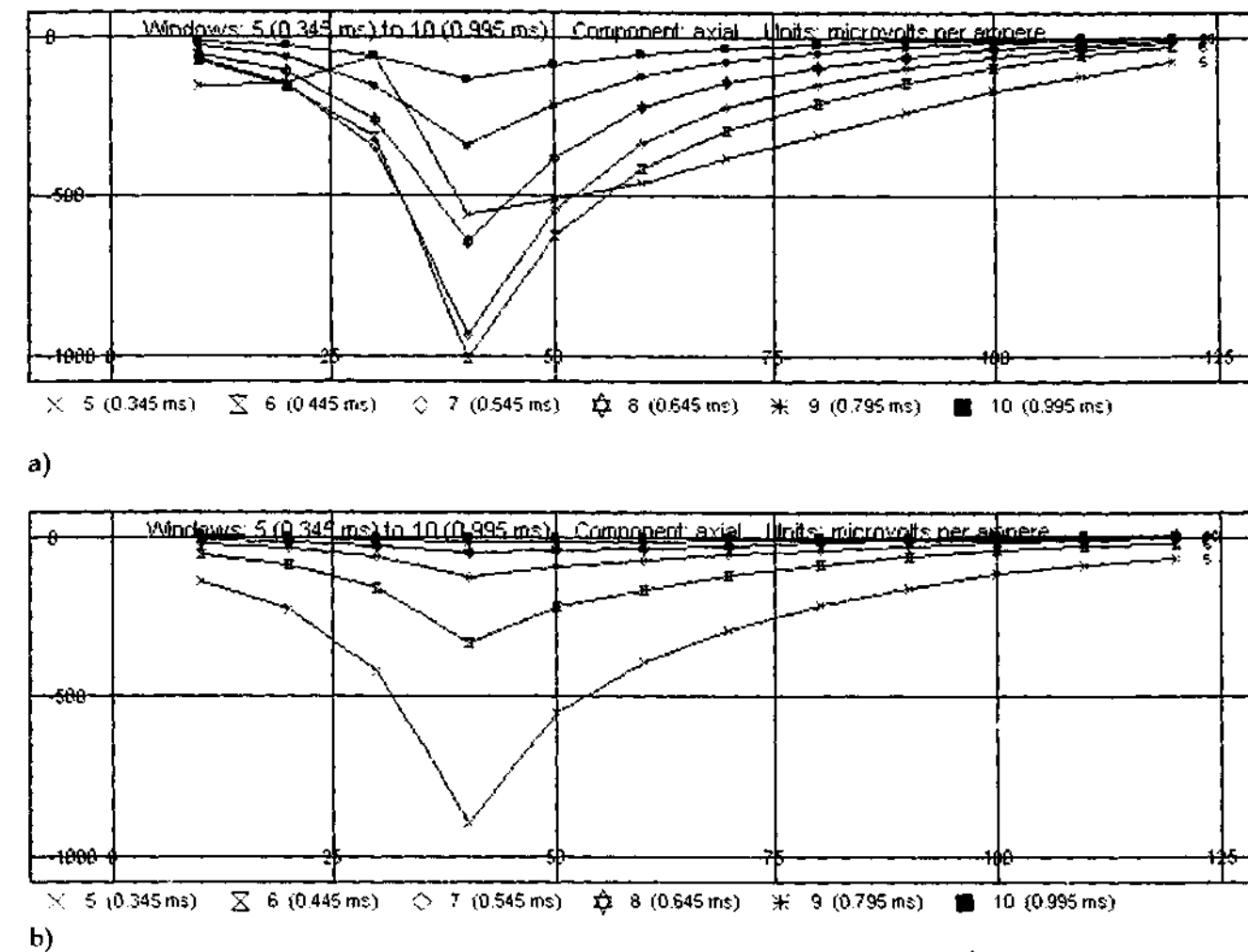


Figure 6.32: a) Field DHTeM response for Borehole ID3039 with Loop 3 (windows 5 to 10) and b) the associated LEROI model response of Plate 2 (windows 5 to 10).

6.5. STAGE 3: LINEAR SUPERPOSITION OF THE PLATE 1 AND 2 MODEL DATA.

6.5.1. INTRODUCTION.

The construction of the composite LEROI model for the ID3039 and ID3071 field data sets followed a three stage process, the methodology of which is outlined within Section 6.1. The first stage of this process entailed analysis of the field data, in which investigations of the Loop 1 and Loop 3 field data sets, in conjunction with the associated downhole MMR data, resulted in the identification of the inductive and galvanic components of the field TEM response. Subsequent verification of the excitation mechanisms responsible for each response component was achieved by decay curve analysis. In the second stage, two independent thin sheet models Plates 1 and 2 were developed specifically to represent the inductive and galvanic components of the field data.

6.5.2. SIMULTANEOUS MODELLING OF INDUCTIVE AND GALVANIC EFFECTS.

As noted within Section 6.4.2.1, the requirement for two independent models to represent the field data, stems from the fact that the upper lens of the deposit is comprised of a conductive core and weakly conducting extension. The traditional approach to modelling field data with a composite response type such as this commonly involved the construction of a hybrid model: the inductive component is represented either as a simple current loop or a free-space thin-sheet model, and the galvanic component is represented by approximating the anomalous galvanic current stream within the target, with either a bundle of current filaments, or a ribbon of current. The difficulty with this unimodal approach is that one is left with two independent models, or rather interpretations, of the mineralisation.

Program LEROI, however, allows for the full interaction between a target and its surrounding host medium; its computations account for the effects arising from the confined eddy currents established by induction, and current gathering effects arising from the host-target conductivity contrast. In addition to this, LEROI also computes the inductive coupling between targets within a multiple plate system.

In this respect, application of LEROI and other such bimodal algorithms is superior to the traditional method, as it permits an integrated approach to modelling a composite field response. In this particular case study, however, different interpretations of the inductive and galvanic components of the field data were attributed to the intrinsic differences of each mode of excitation, *e.g.*, the different depth extents of Plates 1 and 2 were understood to indicate a possible conductivity gradient within the mineralisation. The traditional method, as opposed to this, would have required two physically different unimodal models, thereby introducing computational artefacts into the interpretations.

6.5.3. LINEAR SUPERPOSITION OF PLATES 1 AND 2.

In the third and final stage of model development, attempts were made to combine Plates 1 and 2 within a single multiple plate system. Unfortunately, each of these attempts proved unsuccessful, resulting in unrealistically large response amplitudes that were greater than the sum of the individual contributions made by each plate. This unforeseen complication prompted rigorous tests to be conducted on program LEROI, for both single and multiple plate systems, see Chapter Seven for results and further discussions. In summary, LEROI was demonstrated to be unstable for models with too fine a discretization, and multiple plate systems in which the plate-to-plate and plate-to-borehole receiver separation is of the order of, or less than, the cell discretization. These tests, despite being a digression from the original aims of the project, were a valuable exercise, the findings of which were relayed back to the principal developer of program LEROI - Dr Art Raiche.

Despite these problems, some interaction between the two plates was anticipated, but not to this degree. Specifically, given the low conductance of Plate 2, only a minimal inductive interaction between it and Plate 1 was expected. It was possible to circumvent these difficulties, however, by assuming a weak inductive interaction, and synthesising a composite model response for the ID3039-Loop 1 field data, by computing the linear superposition of the host and scattered field response of Plates 1 and 2.

The synthesised model response is shown within Figure 6.33, and is to be compared with the respective field data, Figure D.1.1 of Appendix D.1. The composite model successfully replicated the three essential features of the field data: the dominant early-time galvanic response, windows 5 (0.345 ms) to 10 (0.995 ms); the dominant late-time inductive response, windows 15 (2.495 ms) to 20 (5.895 ms); and the intermediate stage, windows 10 (0.995 ms) to 15 (2.495 ms). It is noted, that the asymmetry of the early-time galvanic anomaly within the composite model response, Figure 6.33, is slightly greater than that due to Plate 2 alone (see Section 6.4.2.1). As such, the negative-to-positive crossover within the galvanic anomaly occurs at a slightly greater depth of 75 m.

The success of this linear model in describing the field data is understood to imply that the initial assumption of weak interaction between high and low conductance sheets is correct. Although it may also be noted, that the ability to distinguish between the galvanic and inductive response within the field data, and to model them independently, assumes linear superposition as a priori.

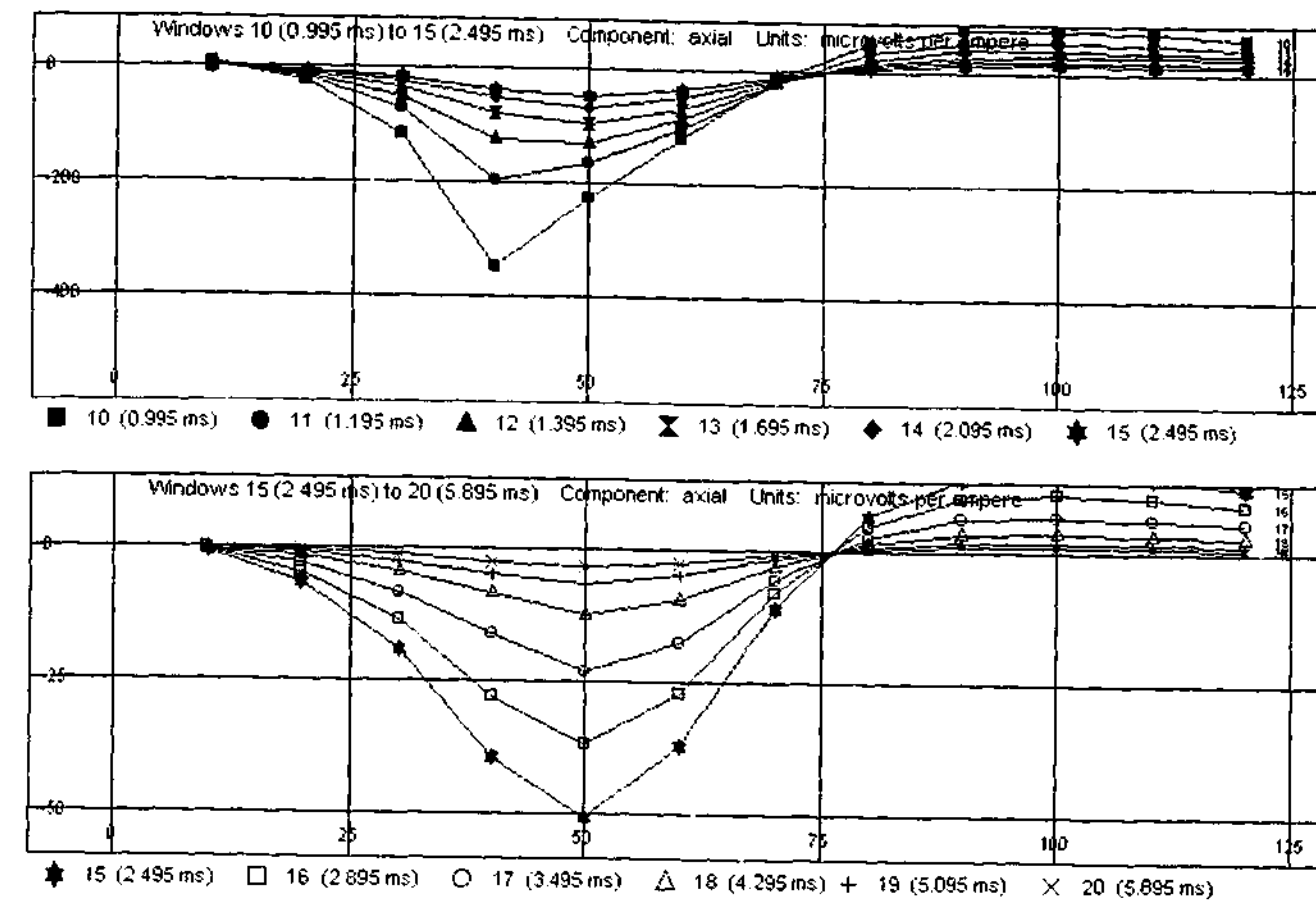
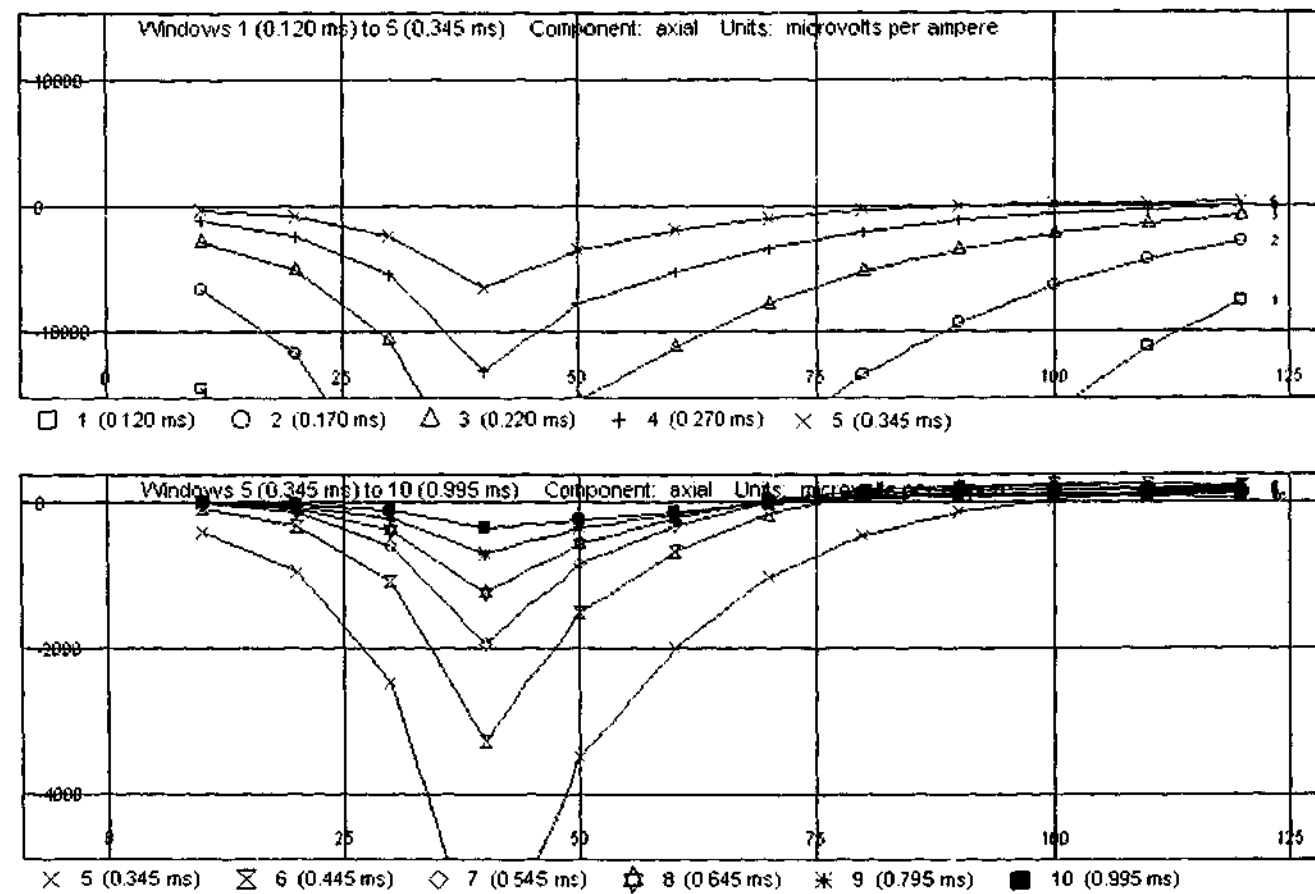


Figure 6.33: The composite model response for Borehole ID3039 with Loop 1, which was derived from the linear superposition of the scattered response of Plate's 1 and 2 (windows 1 to 20).

6.5.4. CONCLUSIONS.

It has been demonstrated that by the use of two plates, both the inductive and galvanic response of the Flying Doctor field data can be modelled. Namely, the inductive response present within both the ID3039 and ID3071 Loop1 data sets, can be attributed to a highly conductive plate, Plate 1, while the early time galvanic response most noticeable within the ID3039 data set, can be attributed to a larger but less conductive plate, Plate 2. In addition to this, modelling the two excitation modes with conductive plates proved advantageous, as a direct inference of the conductivity distribution within the mineralisation could be made by noting the depth extent of each plate model. Finally in situations such as this, it appears linear superposition is a suitable approximation for generating the combined response of a dual plate system comprised of both a high and low conductance plate.

6.6. POWER-LAW DECAY ANALYSIS AND PROGRAM LEROI: A FINAL REMARK.

6.6.1. INTRODUCTION.

Decay analysis performed on the galvanic component of the stripped LEROI model response of Plate 2, for Borehole ID3039 with Loop 3, yielded unexpected results which warranted further investigation. The details of this analysis are given within Section 6.6.2, in which the following questions were raised: why is the form of the negative galvanic anomaly, present within the model DHTEM profiles, Figure 6.34, reflected within the associated decay index profile, Figure 6.35? Does this result suggest that the power law decay indices are dependent upon the amplitudes of the DHTEM response? But most importantly, why did the Plate 2 model data yield power law decay indices of unusually large magnitude?

In an attempt to answer these questions, three possible explanations were proposed: a residual inductive component may have prevented meaningful decay indices to be determined, as addressed within Section 6.6.2; the decay indices may be dependent upon the plate-receiver (p-r) distance (see Section 6.6.4); and finally the degree of discretization of Plate 2 may effect how LEROI computes galvanic currents, see Section 6.6.5.

6.6.2. DECAY ANALYSIS OF PLATE 2.

Consider the DHTEM model response of Plate 2 within the window range of 5 (0.345 ms) to 10 (0.995 ms), for Borehole ID3039 with Loop 3, see Figure 6.32b. A negative intersection anomaly is present within this time window set, and was inferred to be galvanic in origin (see Section 6.4.2.2). To substantiate this inference, a decay index profile was prepared from the stripped Plate 2 data (see Figure 6.34) within the time window range of 6 (0.445 ms) to 10 (0.995 ms), and is presented within Figure 6.35.

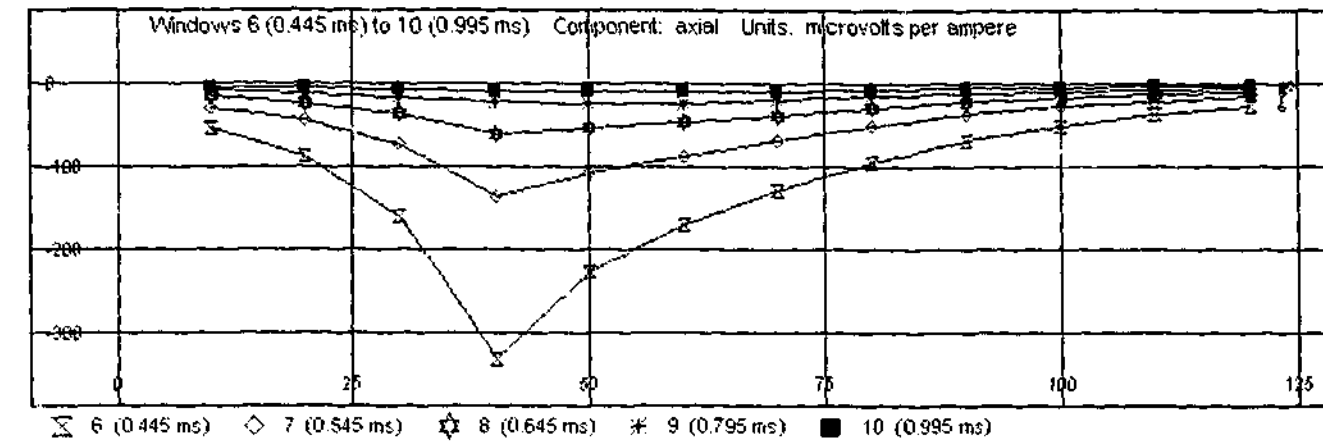


Figure 6.34: The DHTEM LEROI response of Plate 2 with the regional removed for Borehole ID3039 with Loop 3 (windows 6 to 10). The original unstripped model data is shown within Figure 6.32b.

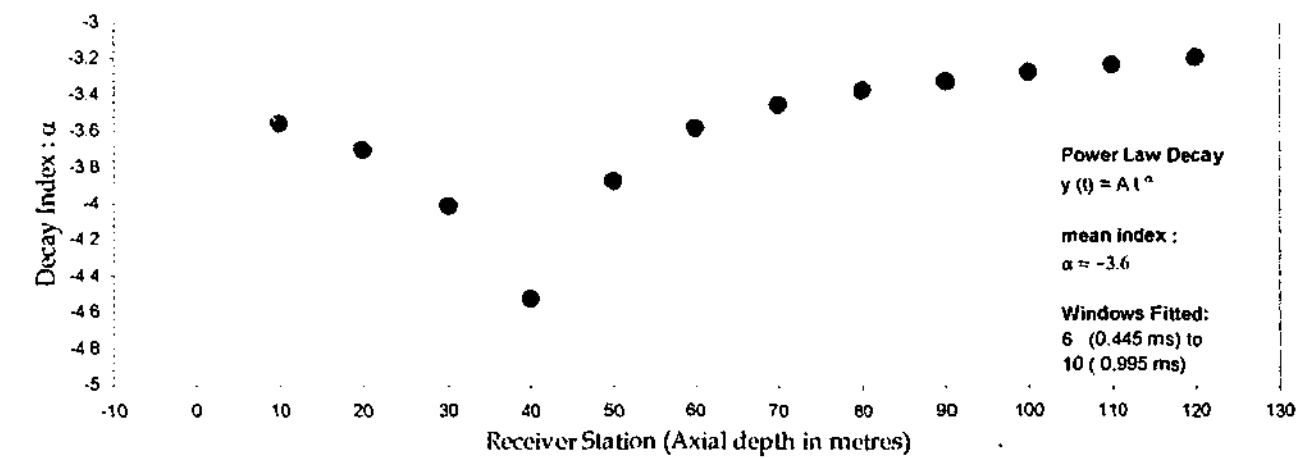


Figure 6.35: Decay index profile prepared from the stripped LEROI response of Plate 2, see Figure 6.34, for Borehole ID3039 with Loop 3.

The magnitude of the power law decay index obtained at the anomaly peak, Station 40, was found to be unusually large, namely $\alpha = -4.52$ (Station 40, windows 6 to 10). It is recalled that a galvanic anomaly will be expected to decay by a power law with a decay index of $\alpha = -3.5$, Asten (1991a); see also Section 4.3. In respect to the un-stripped field data (see Figure 6.32a) a power law decay index of $\alpha = -3.62$ (Station 40, windows 8-10) was obtained. Although the regional component of the field data was but a small fraction of the total response, its presence unnoticed within the DHTEM profiles was, however, manifested within the decay profiles preventing a linear fit for the entire window range 6 (0.445 ms) through to 10 (0.995 ms). The question now arises as to why the stripped model data did not yield a result as good as the un-stripped field data, especially when the opposite outcome would have been expected? It is also noted, that the shape and form of the galvanic anomaly within the Plate 2 DHTEM profiles, Figure 6.34, is also reflected within the

associated decay index profile, Figure 6.35? A comprehensive discussion on these issues is deferred until Sections 6.6.4 and 6.6.5.

Although the magnitude of the decay index of the model response computed at Station 40 for windows 6 (0.445 ms) to 10 (0.995 ms) was found to be unreasonably large, the average decay index computed from all stations is more acceptable, namely $\alpha = -3.6$, Figure 6.35. The inductive response of Plate 2 computed using OZPLTE and was found to be less than 10% of the total LEROI response for windows 6 (0.445 ms) to 10 (0.995 ms), Figure 6.36. Furthermore, the decay index profile obtained from the LEROI response stripped of both the regional and inductive (OZPLTE) response, not shown, was found to be essentially the same as that derived from the LEROI response stripped of the regional alone Figure 6.34. Thus, it seems that the inductive component can be neglected, and that its presence is unlikely to be responsible for the anomalous decay index profile. Although an inductive component of less than 10% of the total model response has been shown to be insignificant when determining the decay index, the question of what the *inductive tolerance* is for this system remains unanswered.

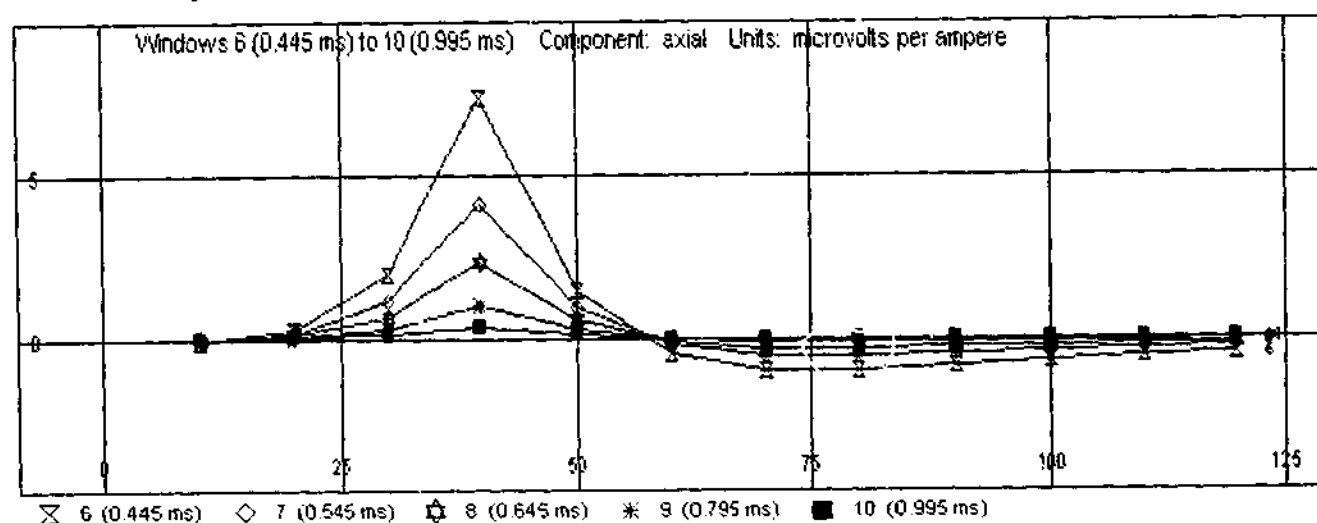


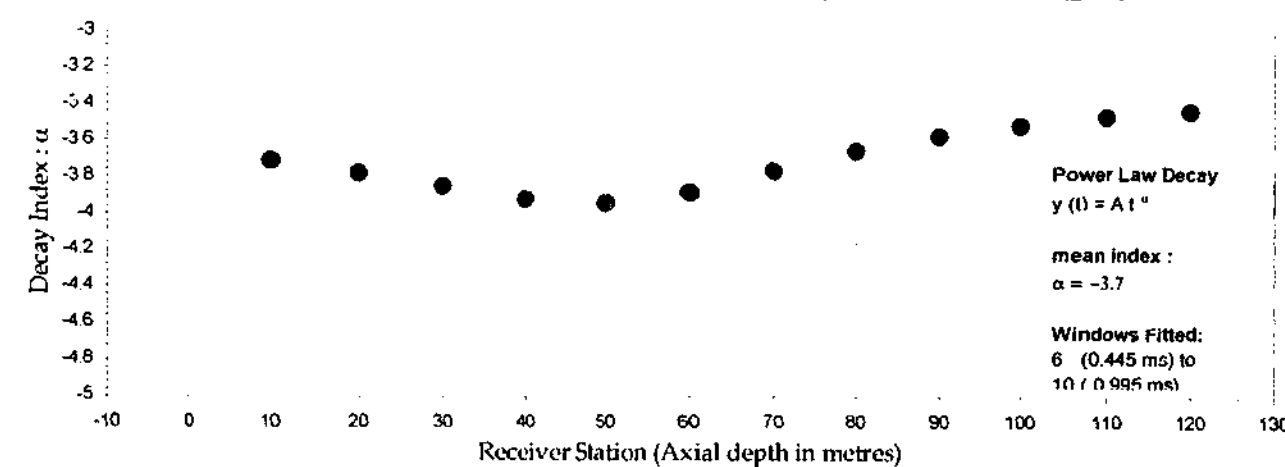
Figure 6.36: The free-space OZPLTE model response of Plate 2 (windows 6 to 10), to be compared with the associated stripped LEROI response, for Borehole ID3039 with Loop 3.

6.6.3. DECAY ANALYSIS OF PLATE 1.

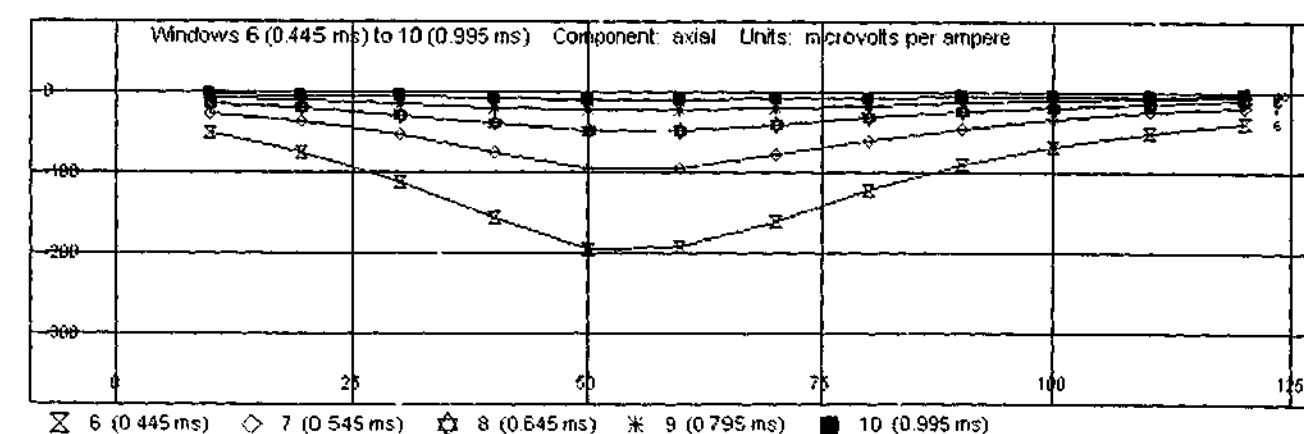
Plate 1 is a high conductivity galvanically saturated plate capable of sustaining significant eddy current distributions. Set 20 m further back from the borehole than Plate 2, Plate 1 was found to produce an improved decay index profile, Figure 6.37a, with a reduced anomalous amplitude. In light of this, the question

now arises: is the improvement of the decay index profile due to the reduced component of the inductive response, less than half a percent for windows 6 (0.445 ms) through to 10 (0.995 ms), Figure 6.37c, or rather to the reduced anomaly amplitude in the DHTEM response, Figure 6.37b? In answer to the first part of this question, it is unlikely that the reduced inductive component is responsible for the improvement. For if it were, it would contradict the previous findings of Section 6.6.2 which suggested that a inductive component of less than 10% can be regarded as insignificant.

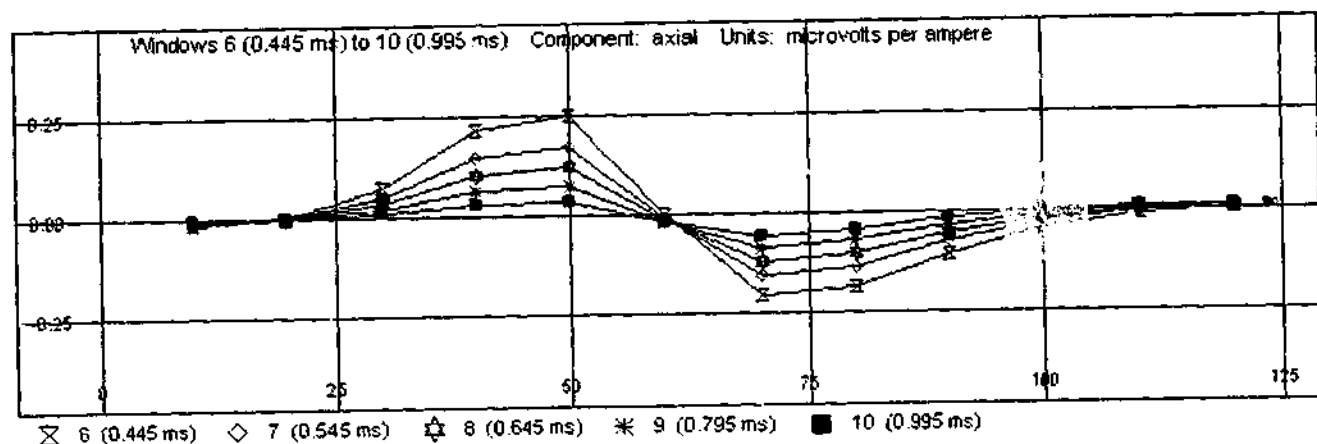
It is proposed that a final confirmation of this would be to take the Plate 1 model and to increase the plate conductivity so as to acquire a significant inductive component. If the computed decay index profile undergoes little change than insignificance of the inductive component is confirmed, but if this is not the case then more work is required. One must also be conscious of the inductive tolerance, and thus it would be advisable not to allow the inductive component to be greater than that of Plate 2. The improvement of the decay index profile for Plate 1 may in fact be due to the reduced amplitude of the DHTEM galvanic anomaly or rather the increased plate-receiver (p-r) distance.



a)



b)



c) Figure 6.37: a) Decay index profile of the stripped LEROI response; b) DHTEM LEROI model response (regional removed; windows 6 to 10); c) Equivalent free-space OZPLTE model response for Borehole ID3039 with Loop 3 (windows 6 to 10).

6.6.4. POWER LAW DECAY INDICES AND PLATE-RECEIVER SEPARATION.

A possible dependency of the power law decay indices upon the plate-receiver separation distance within the Plate 2 LEROI model was investigated. It was anticipated, that as the plate-receiver distance is increased, the associated decay index profile of each model would converge to its mean decay index. This test, was motivated in part to the previously noted limitations of program LEROI, see Chapter Seven, and in particular, to the proposed recommendation advising that the plate-receiver distance be kept greater than the dimensions of the cells of discretization.

Four additional models were constructed within LEROI, in which the plate-receiver distance, of the original Plate 2 model, was increased in 10 m increments by sliding Plate 2, within its own plane, in the down-dip direction. Model specifications are provided within Table 6.3. These models were implemented within LEROI using 20 m cells, and the resulting response of each was stripped of its regional by simple subtraction of the host response. Decay index profiles were prepared from the stripped model data by fitting power laws to windows 6 (0.445 ms) through to 10 (0.995 ms), the results of which are shown within Figure 6.38.

Table 6.3: Model specifications for the increasing down-dip displacement of Plate 2. The coordinates given, define the plate reference point, which is located at the midpoint of the bottom edge of the plate.

DISPLACEMENT. (m)	EASTING. † (m)	NORTHING. (m)	DEPTH. ‡ (m)
0	4777.6	20400	-85.4
10	4774.2	...	-94.8
20	4770.8	...	-104.2
30	4767.3	...	-113.6
40	4763.9	...	-123.0

Note, the entries for zero displacement are the original Plate 2 coordinates.
 † Easting (new) = 4777.6 - Displacement x cos (Dip)
 ‡ Depth (new) = -85.4 - Displacement x sin (Dip); Dip = 70 degrees.

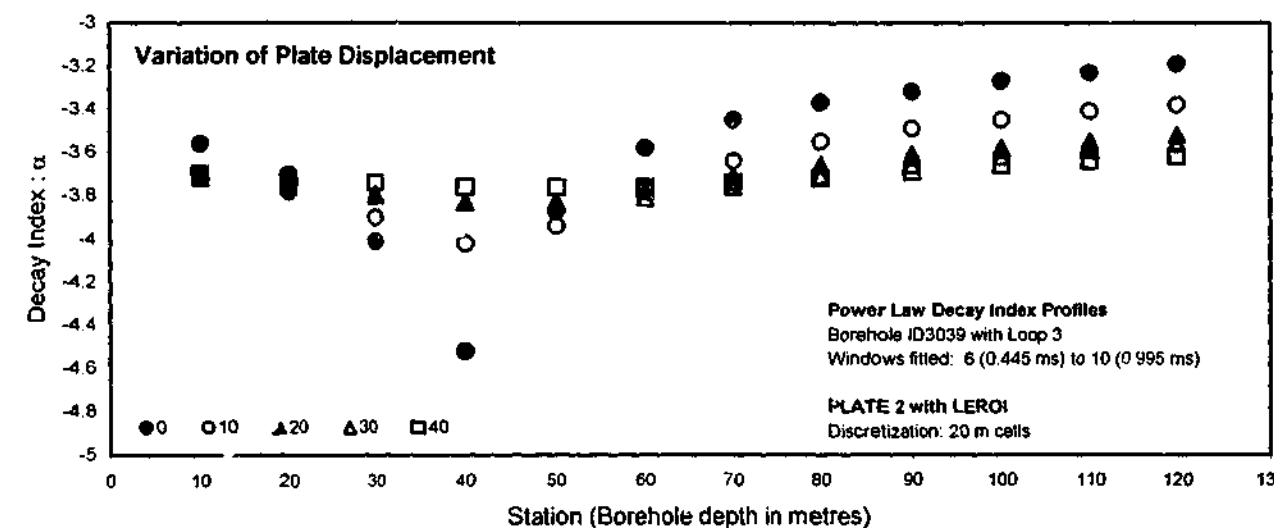


Figure 6.38: Power law decay-index profiles for various plate positions (see Table 9.3).

It is apparent, that with increased plate displacement, the variation of the decay indices from one station to another is significantly reduced. In particular, the original Plate 2 data (zero plate displacement) yielded a decay index at Station 40 with an anomalously large magnitude, namely -4.52. This result, however, was revised down considerably to a more acceptable value of -3.76, by increasing the plate displacement to 40 m. To illustrate further the convergence of the decay index profiles, the decay indices for each station were plotted against plate displacement (Figure 6.39).

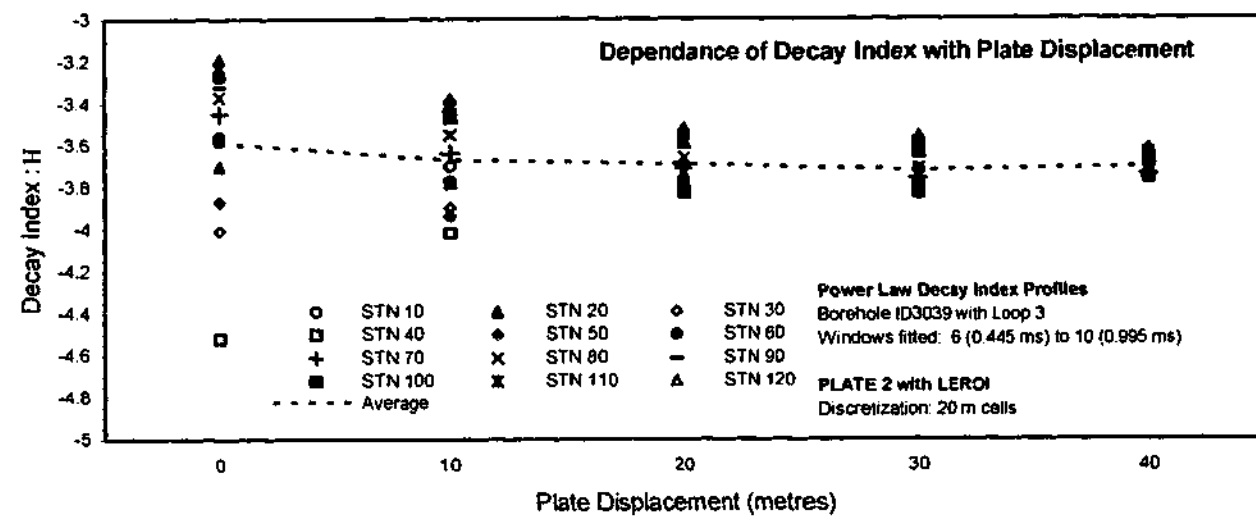


Figure 6.39: Behaviour of decay indices computed at each station for increasing plate displacement.

It is clearly evident, that for all receiver stations the associated decay indices do indeed converge to a more acceptable value with increasing plate displacement, namely $\alpha = -3.7$. Note for a plate displacement of 0 m the decay indices were found to lie within the range $\alpha = -3.6 \pm 0.9$, i.e., 50% of the indicial average, whilst for a plate displacement of 40 m this range was constrained to $\alpha = -3.7 \pm 0.1$, i.e., 5% of the indicial average. Furthermore, the indicial average for each plate displacement, indicated by the dashed line in Figure 6.39, was found to fluctuate in magnitude by as little as 3% of its total value.

6.6.5. DEPENDENCE OF THE DECAY INDEX UPON CELL DISCRETIZATION.

Although the above modelling scheme demonstrated the decay indices are dependent upon the plate-receiver (p-r) distance, one cannot conclude that there exists a dependency on the ratio of (p-r) distance to cell size. Specifically, if the decay indices were indeed dependent upon this ratio, one would expect that a reduction in cell size would be equivalent to increasing the (p-r) distance. Thus as a final test for this dependency, the previous LEROI models which featured a 0 m and 10 m plate displacement were repeated with a reduced cell size of 10 m. The associated decay index profiles for these models are shown within Figure 6.40 together with those profiles derived from the original 20 m cell models. Surprisingly, no significant improvement was made in reducing the cell discretization. In particular, the decay indices for the station which features the galvanic minimum, Station 40, were actually found to be lower for the model utilising 10 m cells. Given that the decay indices were found to be

only weakly dependent upon cell size reduction, it is concluded that the anomalous behaviour noted within the decay index profiles is independent of plate discretization. Thus the recommendation made for LEROI within Chapter Seven enforcing that the (p-r) distance be kept greater than the plate cell size to ensure stability of response, cannot be enforced in regards to the computation of decay indices of the galvanic response of a plate.

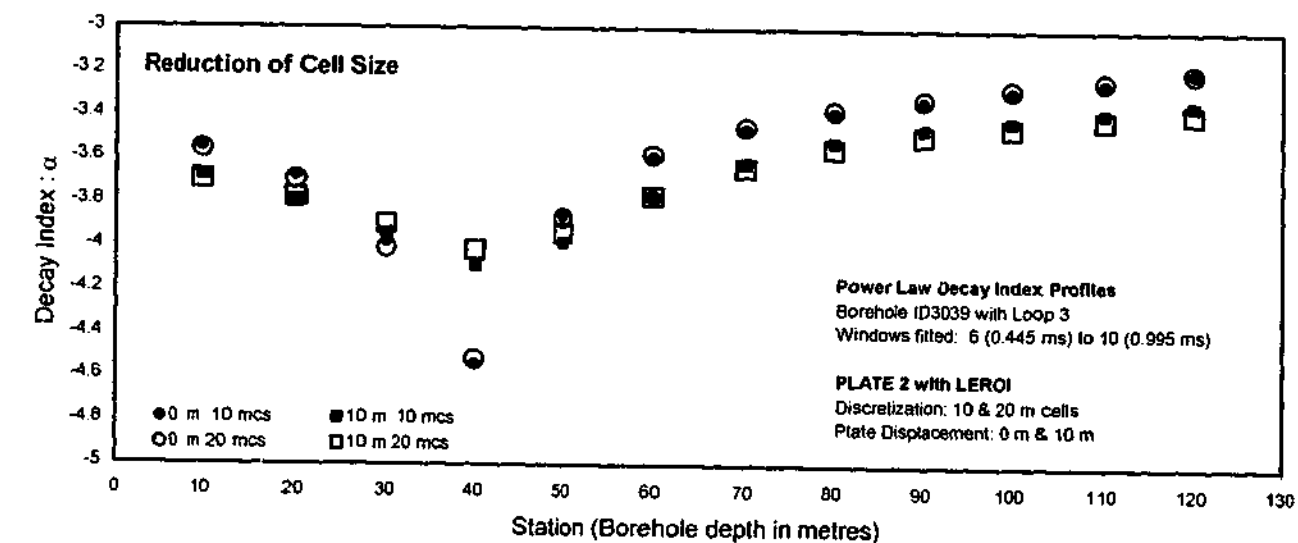


Figure 6.40: Comparison of decay-index profiles for two plate positions with reduced cell size.

6.6.6. CONCLUSIONS.

Power-law decay indices derived from the galvanic component of the LEROI model response of Plate 2 were found to be strongly dependent upon the distance between the plate and the borehole receivers. Subsequently, the decay indices were found to increase in magnitude in direct proportion to the amplitude of the resulting galvanic anomaly. No significant dependence of the decay indices on plate discretization was found.

CHAPTER SEVEN

LIMITATIONS OF LEROI.

7.1. INTRODUCTION.

Numerous difficulties were encountered with the numerical package LEROI during the course of downhole TEM modelling within the Flying Doctor case study. These problems only became known when constructing downhole TEM models, and in particular, when more than one plate was used. The purpose of this chapter is to provide the reader with a listing and brief description of the problems encountered to date. Although the limitations of LEROI were noted and discussed with the principal program developer Dr Art Raiche, no satisfactory resolutions to these problems have been neither proposed nor made. Unfortunately because of this, it was not possible to conduct downhole TEM modelling of closely spaced multiple plates with LEROI within this project.

7.2. INDUCTIVE DECAY RATES OF LEROI.

A comparative model study was performed with a 200 m square plate, with equivalent conductance, using both MARCO (Version 2.6, see Section 3.3) and LEROI (Version 5.0, see Section 3.2). The purpose of this study was to compare the inductive decay rates of LEROI with MARCO. A full report was prepared for the industry sponsors but no details will be given here. In summary, it was found that inductive currents appear to persist for greater times when modelled using LEROI compared to MARCO. The cause of this discrepancy, as proposed by Dr Art Raiche, may arise from the delta function secondary source implemented within MARCO. Models, however, constructed using the free-space algorithm OZPLTE produced time constants that were in reasonable agreement with MARCO.

In the case of a free-space host, it is expected that LEROI will approach the behaviour of OZPLTE. Nevertheless, LEROI produced larger decay rates than OZPLTE; OZPLTE in turn produced decays which were in good agreement with the theoretical inductive time-constants computed using the formula of Lamontagne (1975), see Equation 4.2 of Chapter Four. It has been found from my experience that for most models run to date, LEROI has yielded decay rates that are approximately 1.2 times greater than those derived from OZPLTE.

7.3. CHAOTIC BEHAVIOUR OF MULTIPLE PLATE SYSTEMS.

7.3.1. SIGN REVERSALS OF INDUCTIVE RESPONSES.

One of the more severe errors noted within LEROI, is the occurrence of sign reversals within a multiple plate response. In general, these sign reversals have only been found to apply to the inductive component, and of all the modelling conducted to date, such sign changes were confined to multiple plate systems. It has been suggested by Dr Art Raiche, that such sign reversals are believed to occur as a result of the host electric field rising and falling above and below the scattered field, *i.e.*, such sign changes are a relative effect based upon the difference between the host and scattered fields. These sign changes first became apparent when the total response due to two parallel plates was compared to that of each individual plate. It was soon realised that these sign inversions were dependent upon cell size, indeed their existence has now been attributed to poor discretization.

An example in which the inductive component within a LEROI response undergoes a sign reversal is illustrated by use of a downhole TEM multiple thin-plate model. This model consisted of two parallel sheets, which shall be referred to as Plates 1 and 2, embedded within a 500 ohm.m half-space, see Figure 7.1 for model configuration. Although both plates were of equal dimensions, namely 400 m x 40 m, Plate 1 was assigned a conductance of 90 S, whilst Plate 2 was assigned a much lower conductance of 7 S. The independent response profiles of Plates 1 and 2 are shown with Figure 7.2 and Figure 7.3 respectively. In brief, the response profiles of Plate 1 feature a broad negative

single signed galvanic anomaly centred about Station 60 at early times, evolving into a negative-to-positive inductive anomaly at later times. In respect to Plate 2, the response profiles feature a sharp, galvanic anomaly centred about Station 40. It should be noted, that conductance of Plate 2 is much too low to sustain inductive excitation, thus allowing the galvanic anomaly to predominate.

The response of the multiple plate system comprised of Plates 1 and 2, was synthesised by computing the linear superposition of the host and scattered¹ field response of each plate (see Figure 7.4). In this case, a weak inductive interaction between the plates was assumed, an assumption that is justified by the low conductance of Plate 2. When, however, the complete multiple plate response was computed with LEROI, thereby allowing for the inductive interactions between the two plates, a reversal in sign of the inductive component of the model response was observed (see Figure 7.5). These sign reversals have been attributed to erroneous plate-to-plate interactions within LEROI.

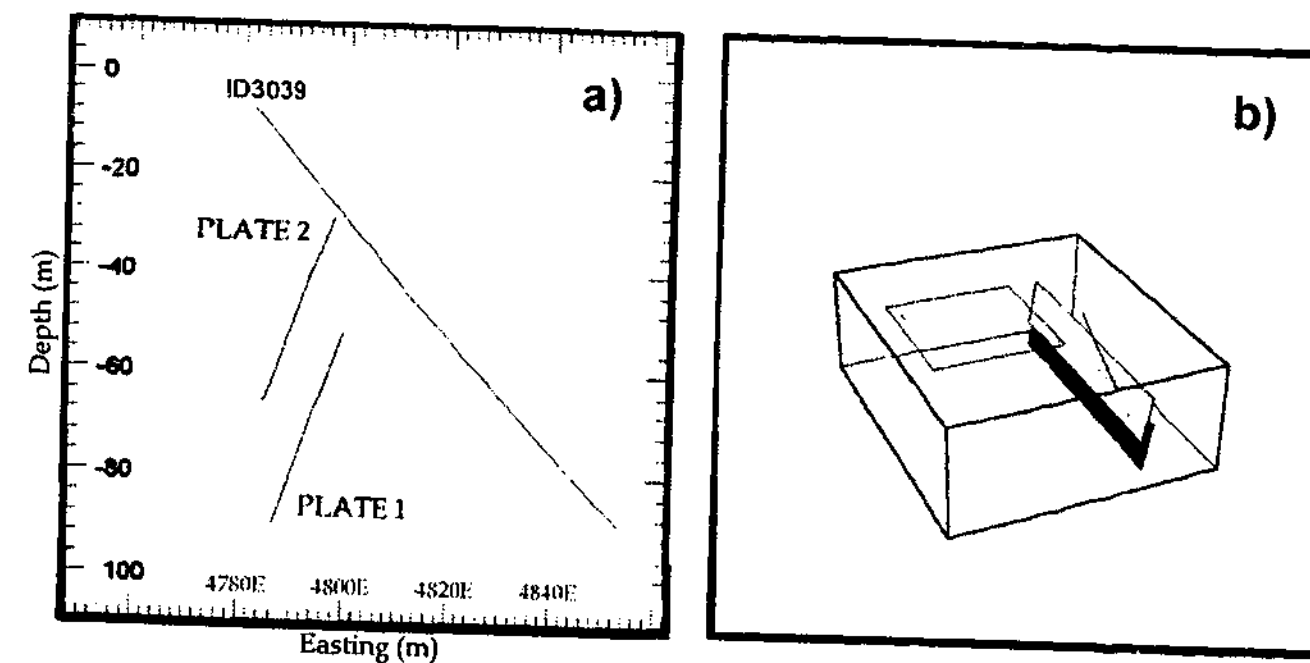


Figure 7.1: The model configuration of the multiple plate system featuring the parallel plates, Plates 1 and 2, showing a) the cross-section and, b) the perspective views respectively. In this example, the spacing between the plates was set to 10 m.

¹ Note: the scattered field response of each plate was obtained by subtracting the host response, computed without the plate, from the total field response, computed with the plate.

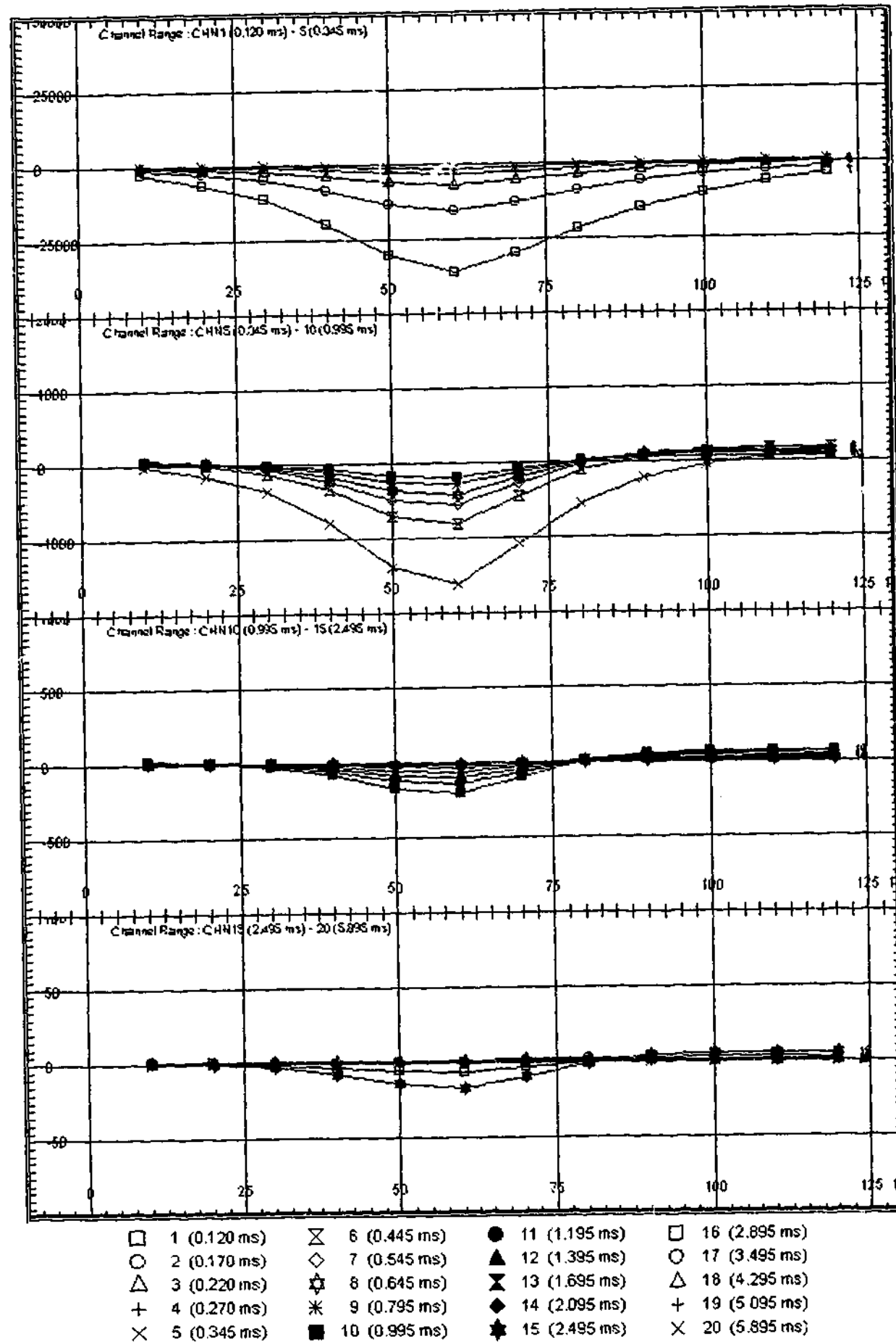


Figure 7.2: Linear profiles of the axial component of the downhole TEM response computed using LEROI of Plate 1 with Borehole ID3039 and Loop 1.

MODEL SPECIFICATIONS FOR PLATE 1.

Plate Dimensions: 400 m x 40 m
 Discretization Cell Size: 10 m x 10 m
 Conductance: 90 S
 Host Resistivity: 500 ohm.m

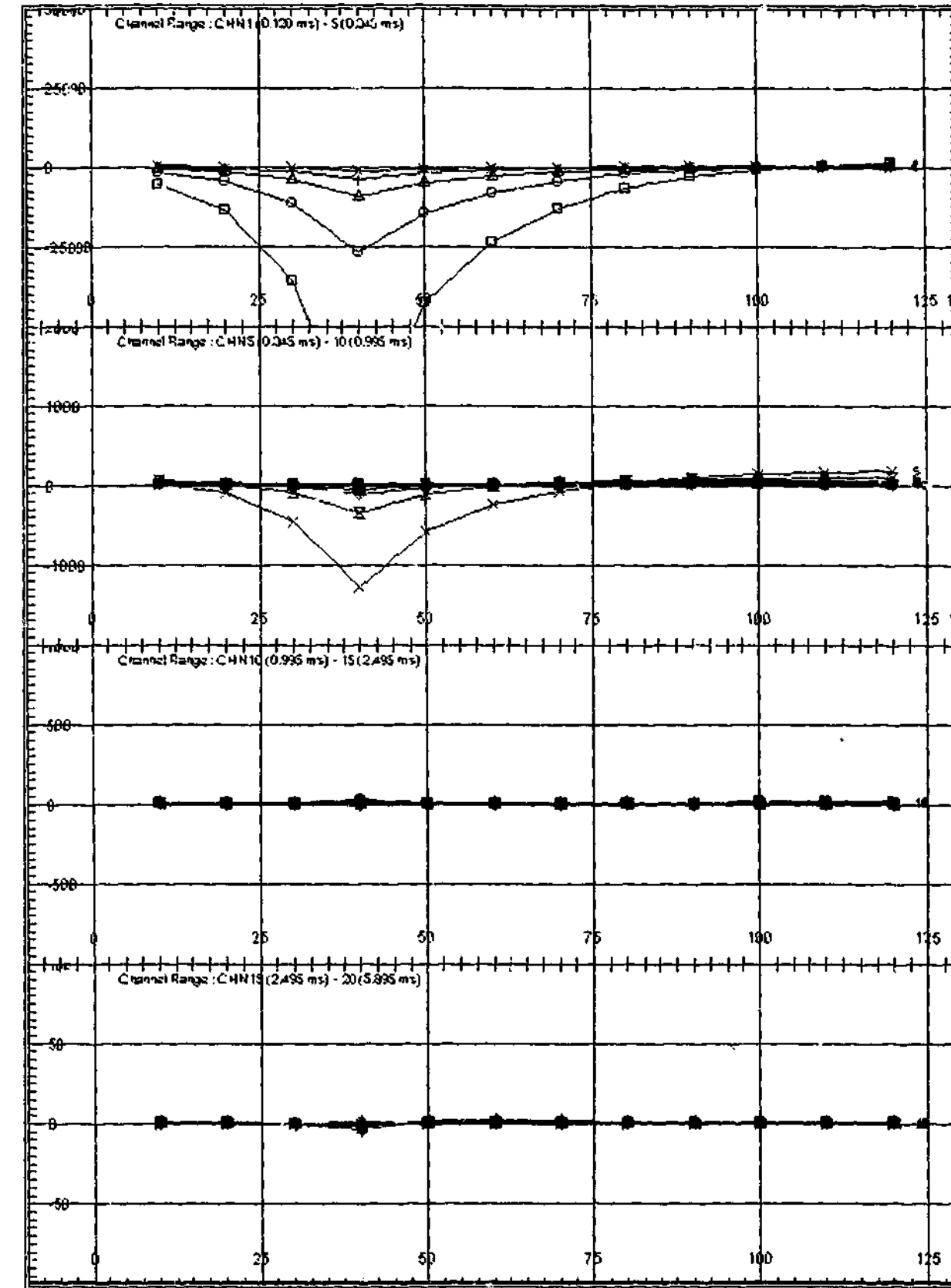


Figure 7.3: Linear profiles of the axial component of the downhole TEM response computed using LEROI of Plate 2 with Borehole ID3039 and Loop 1.

MODEL SPECIFICATIONS FOR PLATE 2.

Plate Dimensions: 400 m x 40 m
 Discretization Cell Size: 10 m x 10 m
 Conductance: 7 S
 Host Resistivity: 500 ohm.m

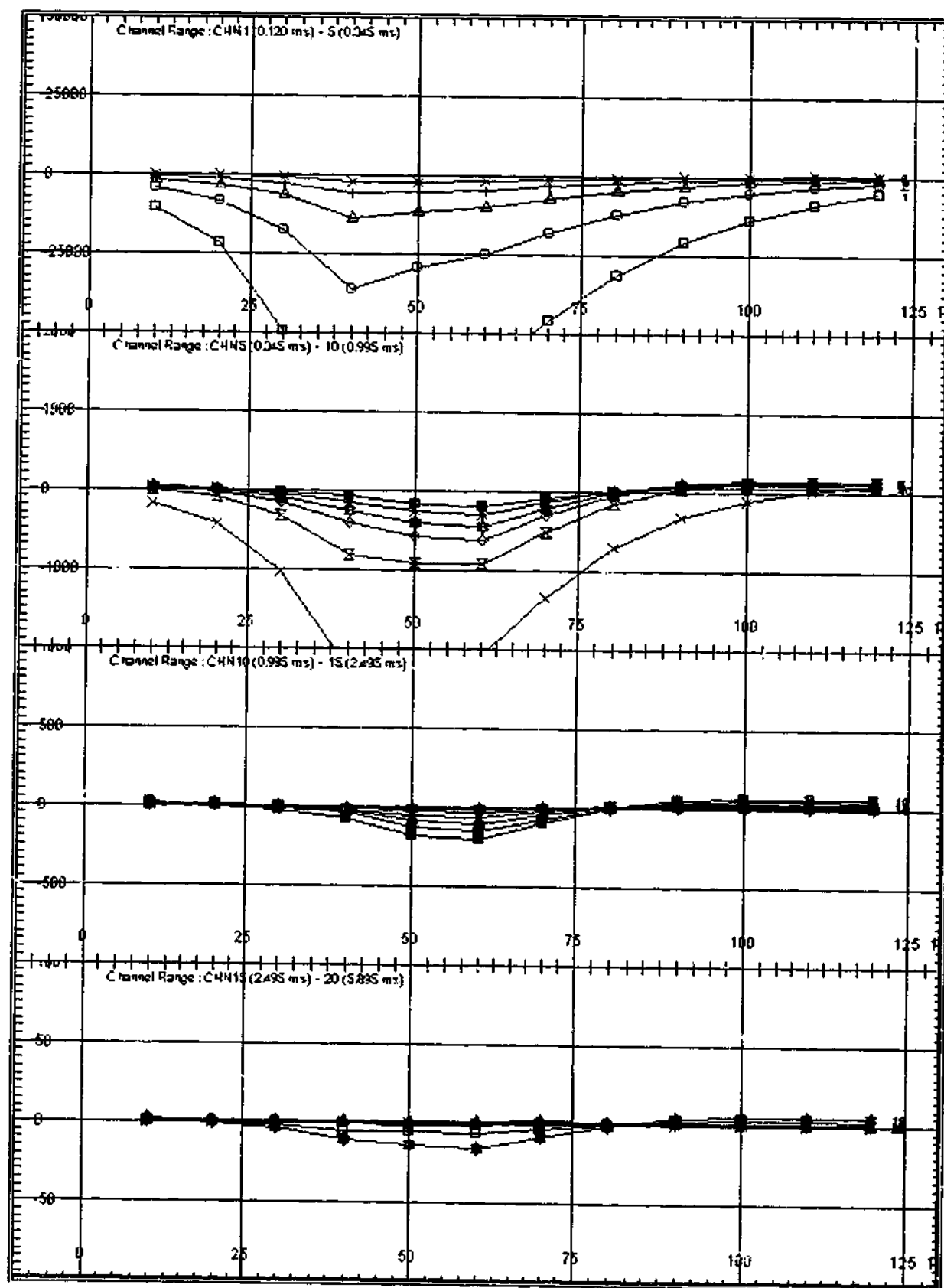


Figure 7.4: Linear profiles of a downhole TEM multiple plate model, constructed by the linear superposition of the axial components of the host response, and the individual scattered field responses of Plates 1 and 2. Note each scattered field response was obtained by subtracting the host response, computed without the plates, from the total field response.

MODEL SPECIFICATIONS.

Dimensions of Plates 1 and 2: 400 m x 40 m
 Discretization Cell Size of Plates 1 and 2: 10 m x 10 m
 Plate Separation: 10 m
 Conductance of Plate 1: 90 S
 Conductance of Plate 2: 7 S
 Host Resistivity: 500 ohm.m

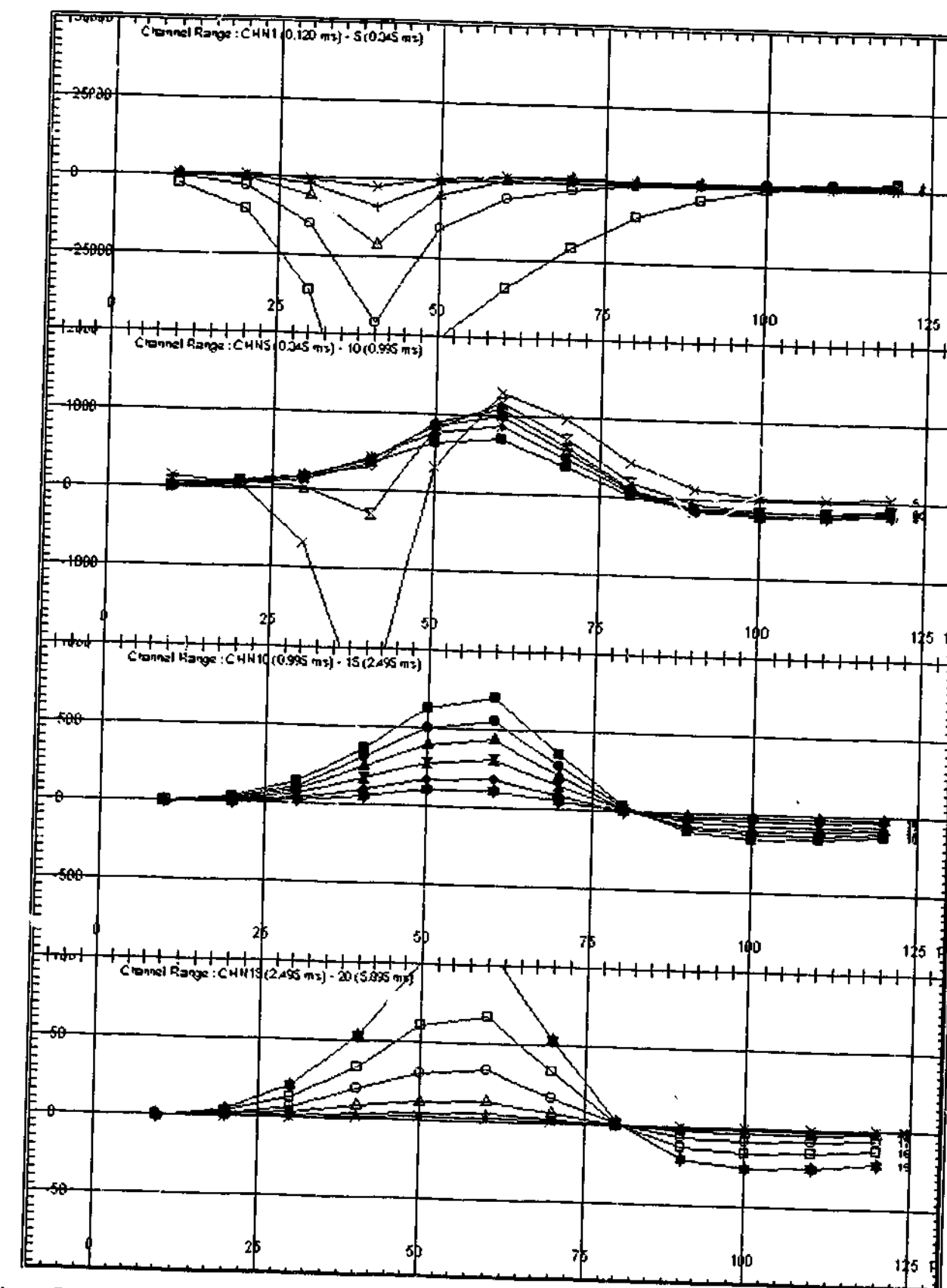


Figure 7.5: Linear profiles of the axial component of a downhole TEM multiple plate model comprising of Plates 1 and 2, with Borehole ID3039 and Loop 1. The model response was computed using LEROI and thus allowed for inductive interactions between the two plates. Sign reversals within the inductive component of this model become apparent when comparing it to that of the linear superposition model (see Figure 7.4). These sign reversal occur as a result of erroneous plate-to-plate interactions within LEROI.

MODEL SPECIFICATIONS.

Dimensions of Plates 1 and 2: 400 m x 40 m
 Discretization Cell Size of Plates 1 and 2: 10 m x 10 m
 Plate Separation: 10 m
 Conductance of Plate 1: 90 S
 Conductance of Plate 2: 7 S

Host Resistivity: 500 ohm.m

It is emphasised, that the instabilities illustrated so far have only been demonstrated for plates with a relatively large strike-length to depth-extent ratio, namely 400 m x 40 m. To test the possibility that such a large plate dimensional ratio could be the source of these errors, the multiple plate model featuring the parallel plates, Plates 1 and 2, was altered so that the strike length of each plate was reduced by half to 200 m. The results for this altered model are shown within Figure 7.6.

Instabilities are noted to occur at very early times, namely windows 2 (0.170 ms) and onwards. In particular, the galvanic component has been so severely affected it is no longer recognisable within windows 2 (0.170 ms) to 5 (0.345 ms), as it was within the original (see Figure 7.5) and linear superposition (see Figure 7.4) models. In addition to this, the inductive component of the model response is noted to have undergone a sign reversal, an instability that also occurred with the 400 m x 40 m model. The response amplitudes of the altered model at early to middle times was also found to be proportionately larger than the response of the original 400 m x 40 m model (see Figure 7.5). Specially, the amplitude of the inductive component within the window range 5 (0.345 ms) to 10 (0.995 ms), was found to be approximately four times greater than that within the 400 m x 40 m linear superposition model, Figure 7.4, and as such was deemed unrealistically large.

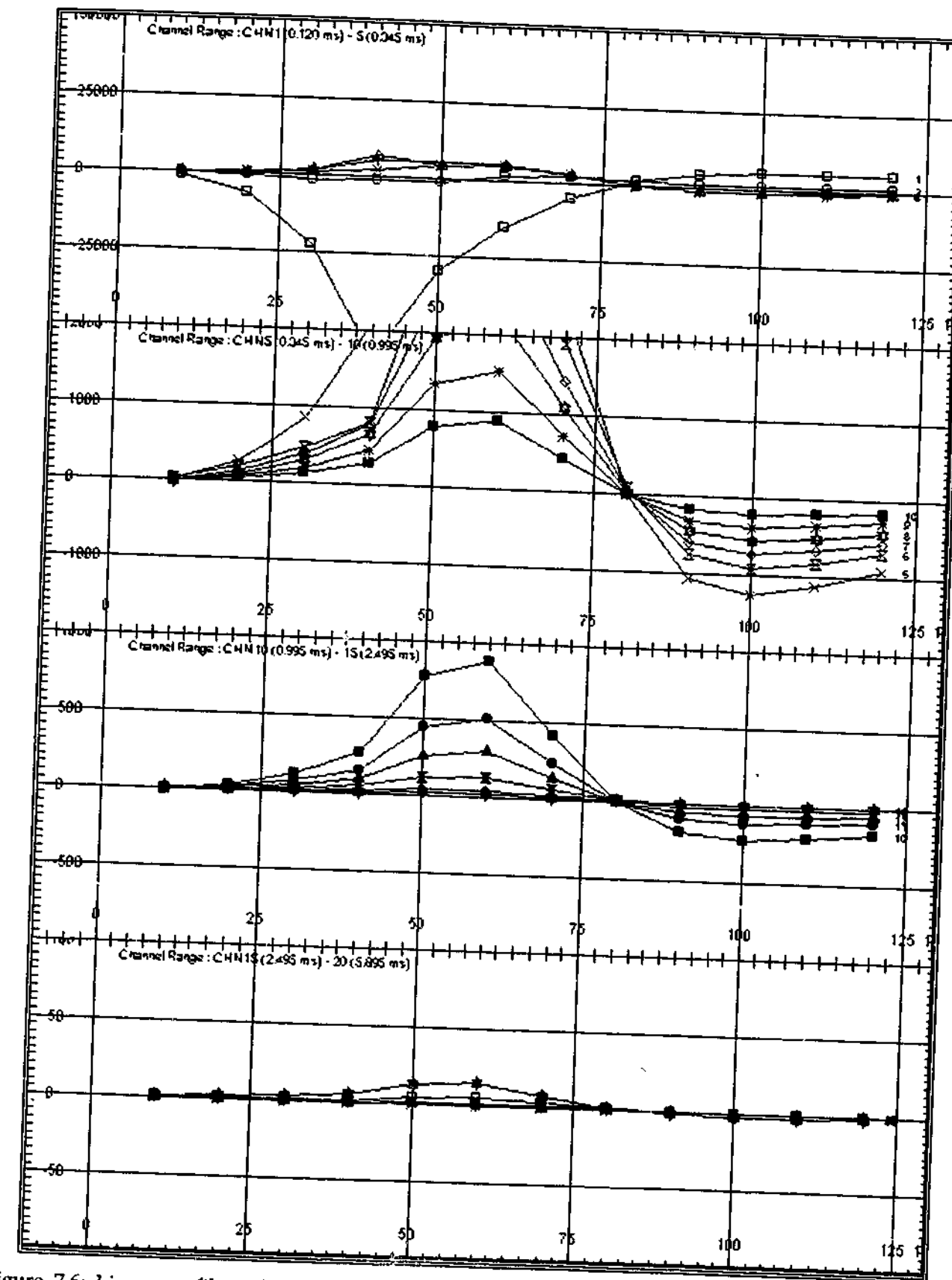


Figure 7.6: Linear profiles of the axial component the downhole TEM altered multiple plate model comprising of Plates 1 and 2, with a reduced strike length of 200 m. Again, the model response was computed using LEROI with Borehole ID:3039 and Loop 1, and thus allowed for inductive interactions between the two plates. The main features to be noted here are; a) the early times in which instabilities set in and thus disrupting the galvanic component, namely windows 2 (0.170 ms) and onwards; b) the unrealistically large model response within windows 5 (0.345 ms) to 10 (0.995 ms), and; c) the sign reversal of the inductive component, which is apparent within windows 5 (0.345 ms) to 20 (5.895 ms).

MODEL SPECIFICATIONS.

Dimensions of Plates 1 and 2: 200 m x 40 m
 Discretization Cell Size of Plates 1 and 2: 10 m x 10 m
 Plate Separation: 10 m
 Conductance of Plate 1: 90 S
 Conductance of Plate 2: 7 S

Host Resistivity: 500 ohm.m

7.3.2. NON-LINEAR RESPONSES WITH UNREALISTIC AMPLITUDES.

One of the benefits of LEROI is its ability to compute the full inductive and galvanic interaction between multiple plates and a conductive half-space. However, of the downhole TEM modelling performed to date, it appears that the highly non-linear interactions exhibited within multiple plate systems are not physically correct. It has been noted, that parallel plates with a separation distance of 4 m can produce a response that is in the order of 5 times greater than an equivalent linear combination. Indeed, an extreme case was found where two dipping but abutting plates produced a response that was around 100 times greater than their linear sum. Even though the effects of coupling can be reduced by increasing plate separation, there are still many problems concerning response stability of multiple plate systems.

A multiple plate system comprising of Plates 1 and 2, was used to demonstrate a situation where adjacent plates can be considered to close in respect to their discretization. In this example, the plate spacing was set to 5 m and each plate was discretized into 10 m x 10 m cells (see Figure 7.7). The response profiles for this model are shown within Figure 7.8. This reduction in plate spacing from 10 m (see Figure 7.5) to just 5 m (see Figure 7.8) resulted in unrealistically large response amplitudes. Moreover, on comparison with the linear superposition model (see Figure 7.4) an erroneous sign reversal in the inductive component can be observed.

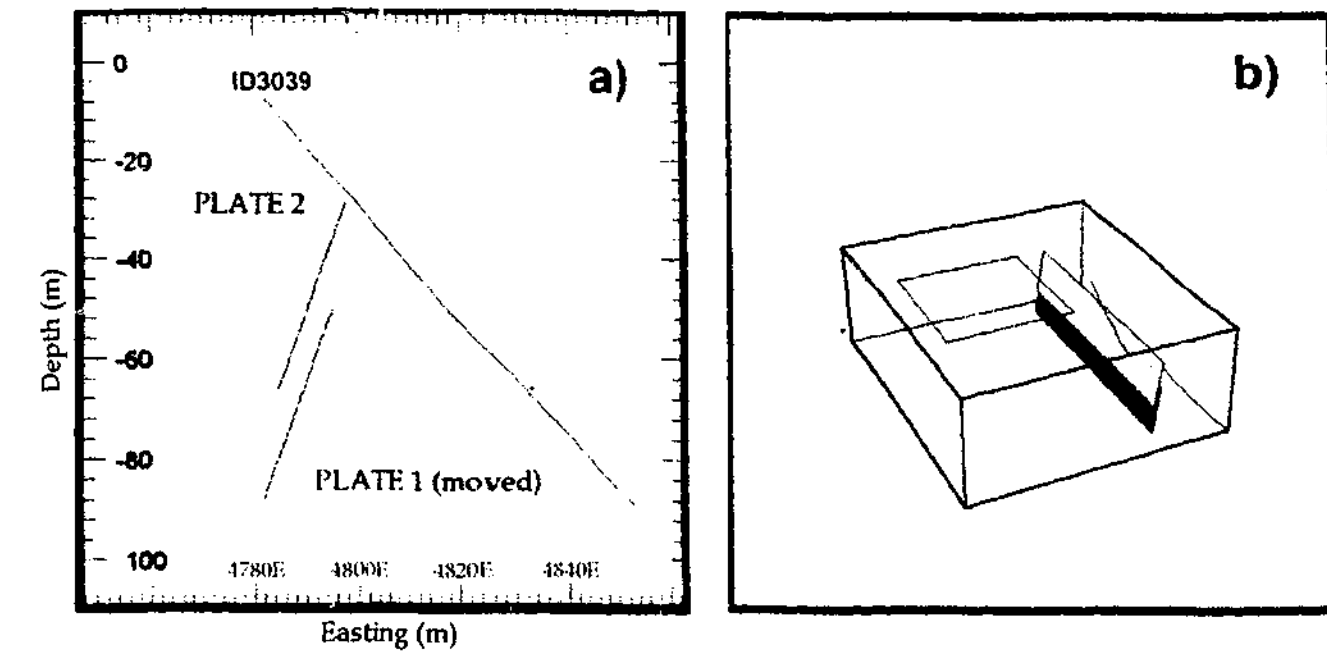


Figure 7.7: The model configuration of the multiple plate system featuring the parallel plates, Plates 1 and 2, showing a) the cross-section view which illustrates the plate spacing and the respective distances between the borehole and the upper edge of each plate, and b) the perspective view of the system which illustrates the relative positions of each plate in respect to the transmitter loop and borehole. (Note: This multiple plate model is identical to that presented within Section 7.3.1., with the exception that Plate 1 has been moved so as to reduce the plate spacing from 10 m to just 5 m)

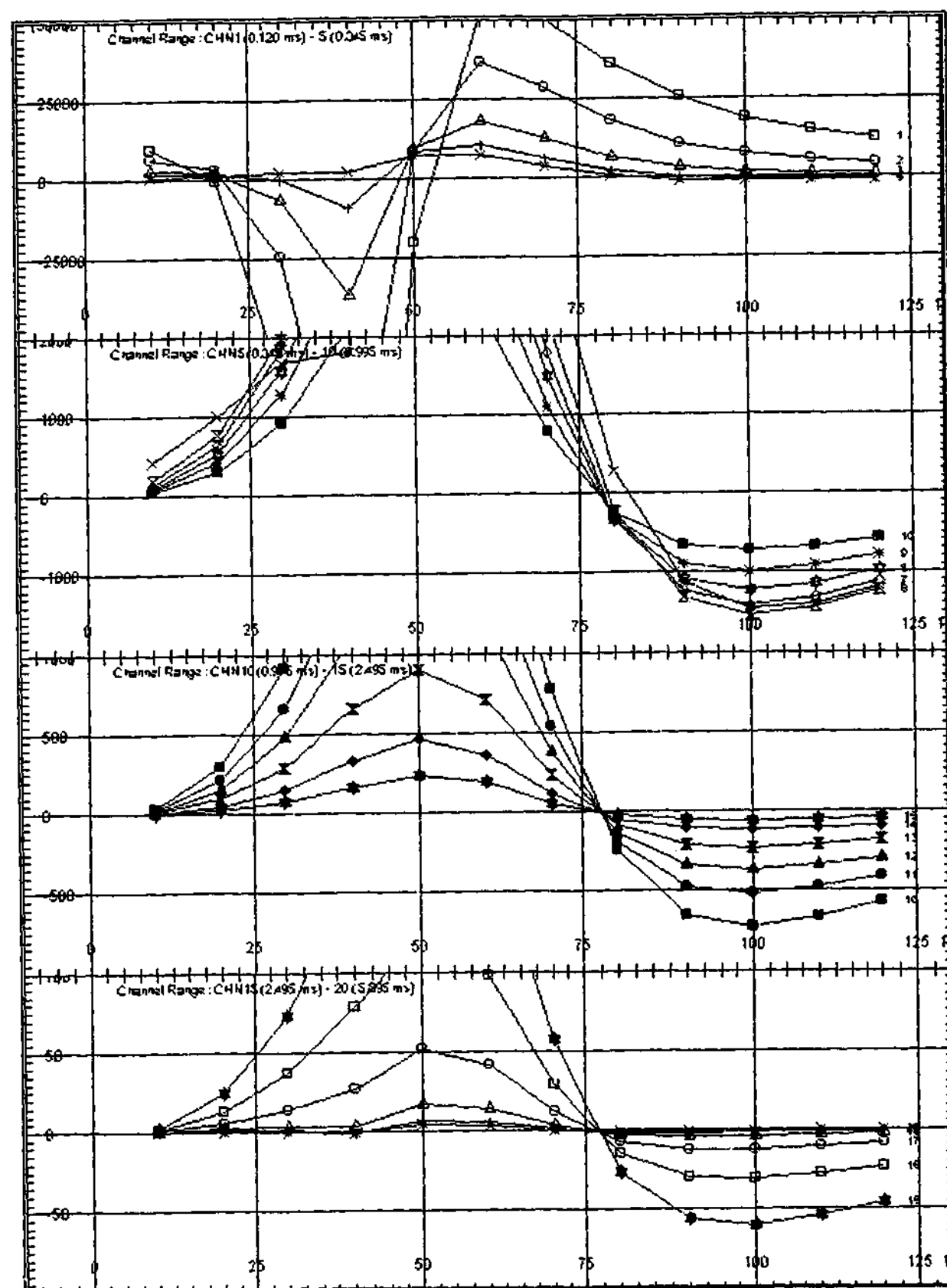


Figure 7.8: Linear profiles of the axial component of a downhole TEM multiple plate model comprising of Plates 1 and 2, with Borehole ID3039 and Loop 1, computed using LEROI. By reducing the plate separation from 10 m (see Figure 7.5) to just 5 m, an unrealistically large increase in the amplitude of the inductive response is noted. Again, on comparison with the linear superposition model (see Figure 7.4) an erroneous sign reversal in the inductive component can be observed.

MODEL SPECIFICATIONS.

Dimensions of Plates 1 and 2: 400 m x 40 m
 Discretization Cell Size of Plates 1 and 2: 10 m x 10 m
 Plate Separation: 5 m
 Conductance of Plate 1: 90 S
 Conductance of Plate 2: 7 S
 Host Resistivity: 500 ohm.m

7.4. INSTABILITIES ASSOCIATED WITH DISCRETIZATION.

Program LEROI failed to converge to well-behaved solutions as sheets within a particular model were progressively discretized into cells of ever decreasing size. Two models, featuring Plates 1 and 2, are presented within this section, to illustrate examples where instabilities have occurred within single plate systems due to over discretization. Both models are identical to those presented within Figures 7.2 and 7.3, with the exception that the discretization has been increased by using 5 m x 5 m cells instead of 10 m x 10 m cells. In the first example, a comparison is made between the 5 m cell, Figure 7.9, and 10 m cell, Figure 7.2, single plate models featuring the high conductance plate, Plate 1. Attributes common to the response profiles of both the 5 m and 10 m models include the following: a broad negative single signed galvanic anomaly at early times; an intermediate stage within windows 5 (0.345 ms) to 10 (0.995 ms), in which neither galvanic nor inductive excitation predominates; and a predominant negative-to-positive inductive anomaly at middle to late times, windows 10 (0.995 ms) and onwards. At late times, however, instabilities are noted to occur within the response profiles of the 5 m cell model (see Figure 7.9). In particular, the inductive response within windows 18 (4.295 ms), 19 (5.095 ms) and 20 (5.895 ms), can be seen to undergo a complete reversal in sign.

In the second example, two comparative single plate models were run featuring the low conductance plate - Plate 2, employing discretizations of 5 m x 5 m cells, Figure 7.3, and 10 m x 10 m cells, Figure 7.10, respectively. Again, instabilities arose within the 5 m cell model, but unlike the high conductance plate, they occurred at much earlier times, namely windows 5 (0.345 ms) and onwards. Moreover, the amplitudes of these instabilities were so great, that the predominating galvanic anomaly was distorted beyond recognition. This increase in the erratic behaviour of the response profiles is attributable to the reduced spacing between the borehole receivers and the lower edge of the plate.

Dr Art Raiche suggested that instabilities associated with over discretization might originate from the amplification of small errors within the frequency domain, during the transformation of the response into the time domain; indeed, reduction of cell size will exacerbate this effect.

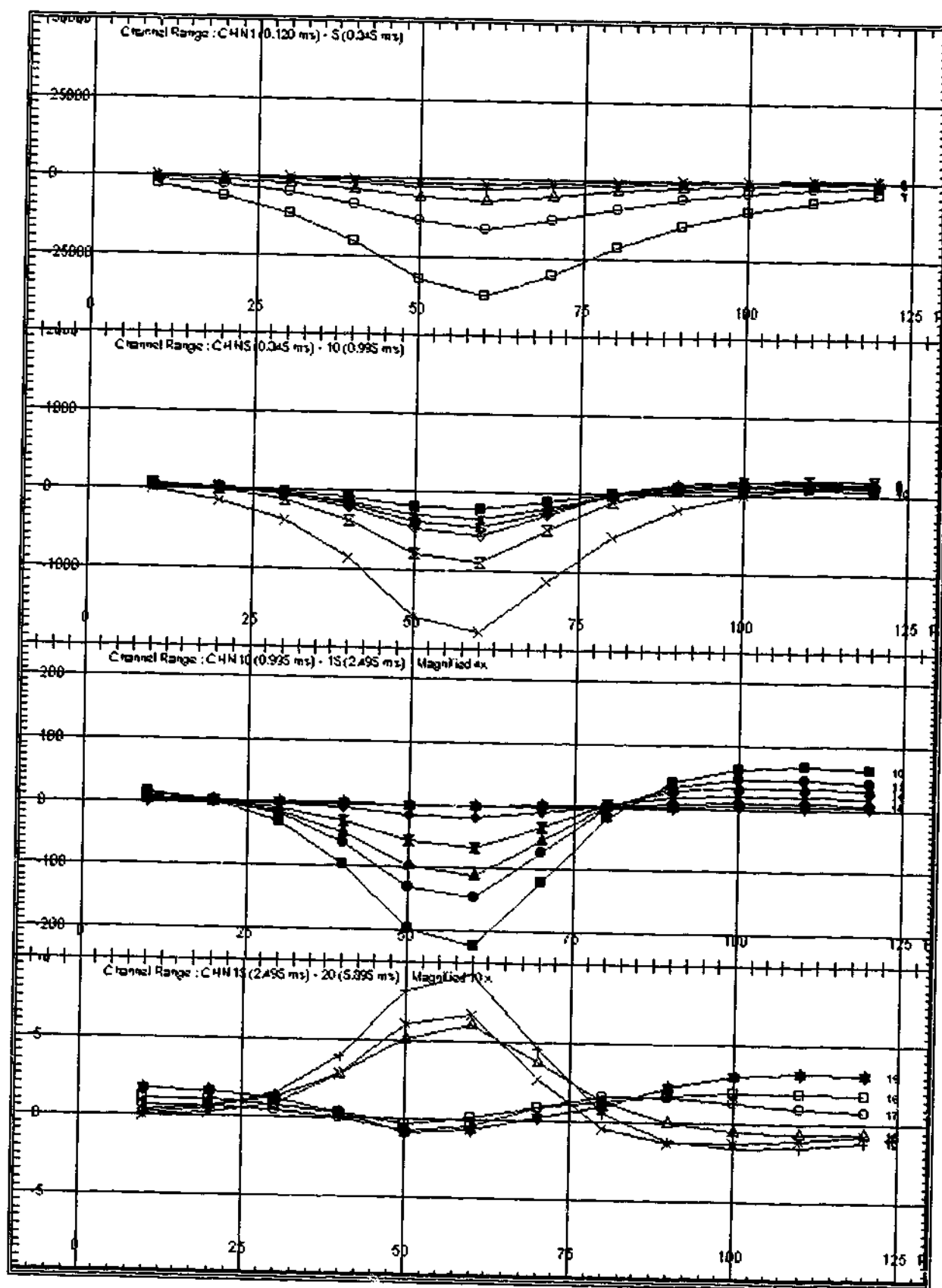


Figure 7.9: Linear profiles of the axial component of the downhole TEM response computed using LEROI of Plate 1 with Borehole ID3039 and Loop 1. By reducing the discretization of Plate 1 from 10 m (see Figure 7.2) to 5 m cells, instabilities were found to occur within the inductive response at late times. Note also the apparent sign reversal within the late-time inductive component.

MODEL SPECIFICATIONS FOR PLATE 1.

Plate Dimensions: 400 m x 40 m
 Discretization Cell Size: 5 m x 5 m
 Conductance: 90 S
 Host Resistivity: 500 ohm.m

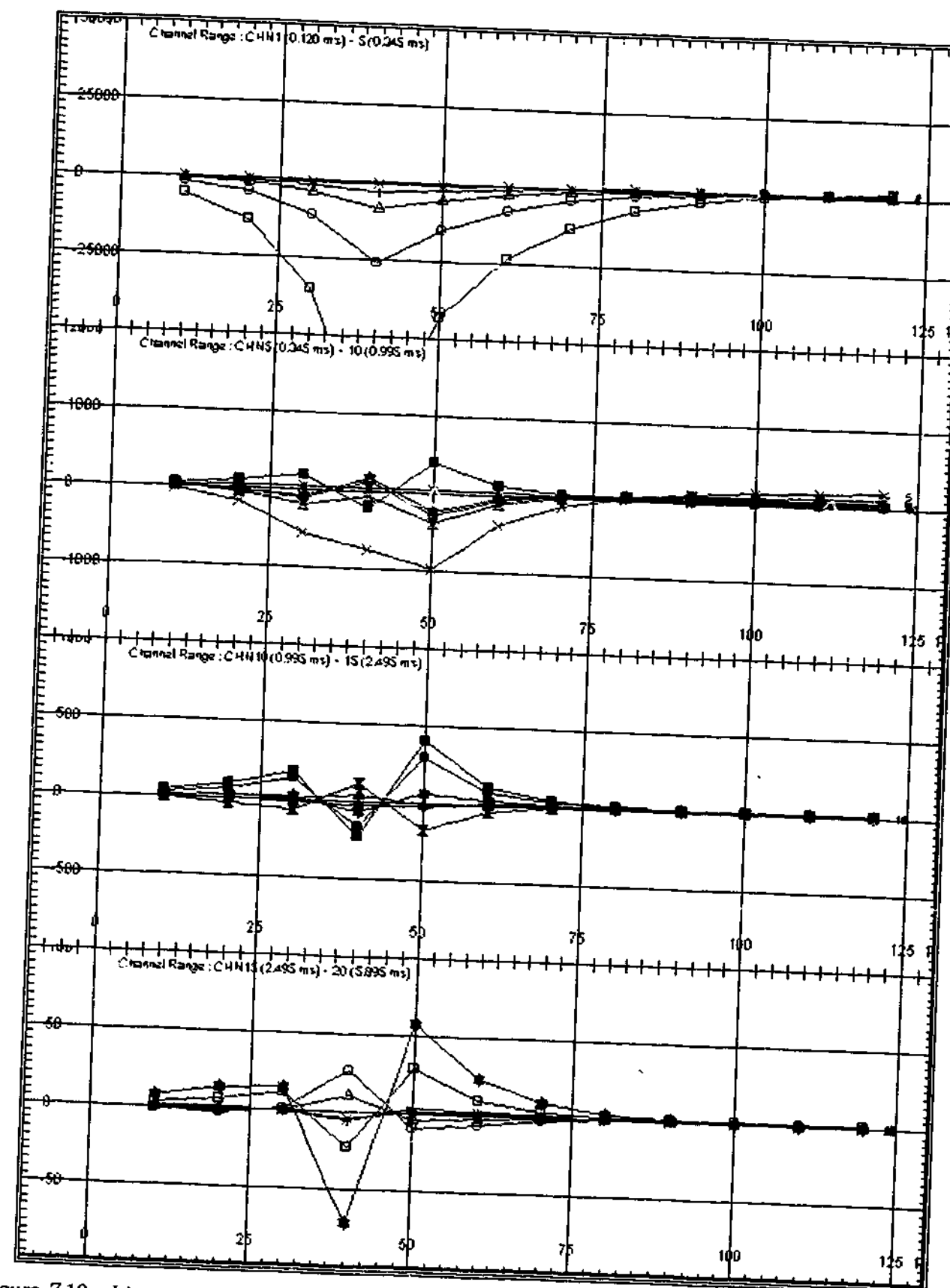


Figure 7.10: Linear profiles of the axial component of the downhole TEM response computed using LEROI of Plate 2 with Borehole ID3039 and Loop 1. As with Plate 1, by reducing the discretization of Plate 2 from 10 m (see Figure 7.3) to 5 m cells, instabilities were found to occur within the galvanic response. In this case however, the instabilities set in at much earlier times, namely window 5 (0.345 ms) and onwards. The severity of these instabilities, in respect to the scenario with Plate 1, was attributed to the relatively small spacing between the lower edge of Plate 2 and Borehole ID3039.

MODEL SPECIFICATIONS FOR PLATE 2.

Plate Dimensions: 400 m x 40 m
 Discretization Cell Size: 5 m x 5 m
 Conductance: 7 S
 Host Resistivity: 500 ohm.m

7.5. CONCLUSIONS.

Even if the coupling computations between multiple plates are correct, there lies one fundamental problem with the implementation of LEROI. To begin with, it is advisable that the user keep the ratio of cell size to separation distance as small as possible. It is noted, that this separation distance relates to the spacing between two adjacent plates (p-p), or a plate and borehole receiver (p-r). Any attempt, however, to minimise this ratio by indefinite reduction of cell size will incur instabilities, thus a lower limit is imposed on both the p-p and p-r distances. Recommendations regarding plate-to-plate and plate-to-receiver separation distances for a given discretization have yet to be formulated, so at present the user must ascertain appropriate parameters by trial and error. Unfortunately, such restrictions will prevent a large class of models to be constructed within LEROI.

In summary, LEROI has been demonstrated to be relatively well behaved for single plate models, save for errors due to over discretization, but highly unstable for multiple plate systems.

CHAPTER EIGHT

FLYING DOCTOR DEPOSIT: LOWER LENS.

8.1. INTRODUCTION.

A single plate thin-sheet LEROI model is presented within this chapter, for downhole TEM data acquired from surveys of the lower massive sphalerite galena lens at the Flying Doctor deposit, situated north of Broken Hill, New South Wales. These surveys incorporated Boreholes ID3418 and ID3419 with Loop 1 (near loop) and Loop 3 (long offset loop). The main contributions of this case study include:

- i. Development of a single plate thin-sheet model to represent the lower lens of the mineralisation.
- ii. Development of the technique of galvanic stripping, which enabled the decomposition of total LEROI response into its constituent inductive and galvanic components.
- iii. Quantitative study of the effect of time and loop position on the relative contributions of the inductive and galvanic components within the total model response.
- iv. Brief observation on the equivalence of the ID3418 DHMMR response and its associated galvanic DHTeM Loop 3 field response.

8.2. GEOLOGY OF THE MINERALISATION.

The lower portion of mineralisation at the flying doctor deposit is located some 300 m below the near surface mineralisation discussed in Chapter Six. As illustrated within the geologic cross-section (see Plate III; fold-out geologic cross-section, located within the sleeve of the back cover), the lower mineralisation is located at a depth of around 380 m and at an easting of 4715 m. Known attributes of the body include the 100 m depth-extent, and westerly down dip of 63 degrees. Unfortunately, no information is available for either the strike bearing nor strike-length of the target.

As seen within the geologic section, the mineralisation possesses a central bulge that tapers off toward the edges. In particular, Borehole ID3415 passes through the central region of the body and intersects only 24.2 m of the mineralisation. Whereas Boreholes ID3418 and ID3419, both of which pass through opposite edges of the body, intersect only 13.1 m and 8.7 m of the mineralisation respectively. The actual midpoints of the intersection of the boreholes with the mineralisation are located at axial depths of 376 m for Borehole ID3418, and 415 m for Borehole ID3419. Thus, a response from a DHEM or DHMMR survey carried out with Borehole ID3418 is anticipated to have an anomaly around Stations 370 and 380. Regrettably, a blockage within Borehole ID3419 just before Station 400 prevented the complete passage of the downhole probe through the mineralisation.

8.3. SINGLE PLATE MODEL.

The Flying Doctor case study of the upper lens of the mineralisation (see Chapter Six) demonstrated the ability of a long offset loop to galvanically excite a strong and weakly conducting target. The identification and isolation of the galvanic and inductive components within the field response permitted the construction of a composite dual-sheet model within LEROI; this model reflected the inhomogeneous conductivity of the mineralisation. Application of this modelling technique to the downhole TEM response of the lower lens met with only limited success, due to the inability to unambiguously identify or completely isolate either the inductive or the galvanic components of the field

response. Instead, a model comprising of a single thin sheet residing within a homogenous half-space was developed with program LEROI to match the field response of Boreholes ID3418 and ID3419 due to loops 1 and 3. See Figure 8.1 for the survey configuration and Table 8.1 for the model specifications. Initial estimates for the dip and strike of the plate were obtained from the geologic section provided (see Plate III; located in back sleeve), but were later altered as the model was refined to suit the field response. Specifically, the negative anomaly within the field data for Borehole ID3418 (see Figures E.1.1 and E.1.2 within Appendix E.1) enabled the location of the upper edge of the plate to be determined with reasonable accuracy. Unfortunately, the mineralisation extended below Borehole ID3419, making the positioning of the lower edge of the plate more difficult. As such, the depth extent and to a lesser degree the dip of the plate could not be well constrained, and may require some revision as additional information becomes available with an extension of Borehole ID3419. Determination of strike length is typically difficult; anomaly width and to some extent anomaly amplitude implied 200 m to be an appropriate value. Decay-curve analysis on the field data yielded unreliable inductive time constants; as such, target conductance estimations relied upon profile analysis with amplitude matching.

Table 8.1: Specifications of the single plate model.

	SINGLE PLATE MODEL
HOST RESISTIVITY (ohm.m):	500
LOCATION†:	
EASTING (m):	4718.9
NORTHING (m):	20398.2
DEPTH (m):	-358.0
DIP (degrees):	120
STRIKE-LENGTH (m):	200
DEPTH-EXTENT (m):	48
PLATE CONDUCTANCE (m):	30

† In reference to the midpoint of the top edge of the plate.

FLYING DOCTOR SURVEY CONFIGURATION.

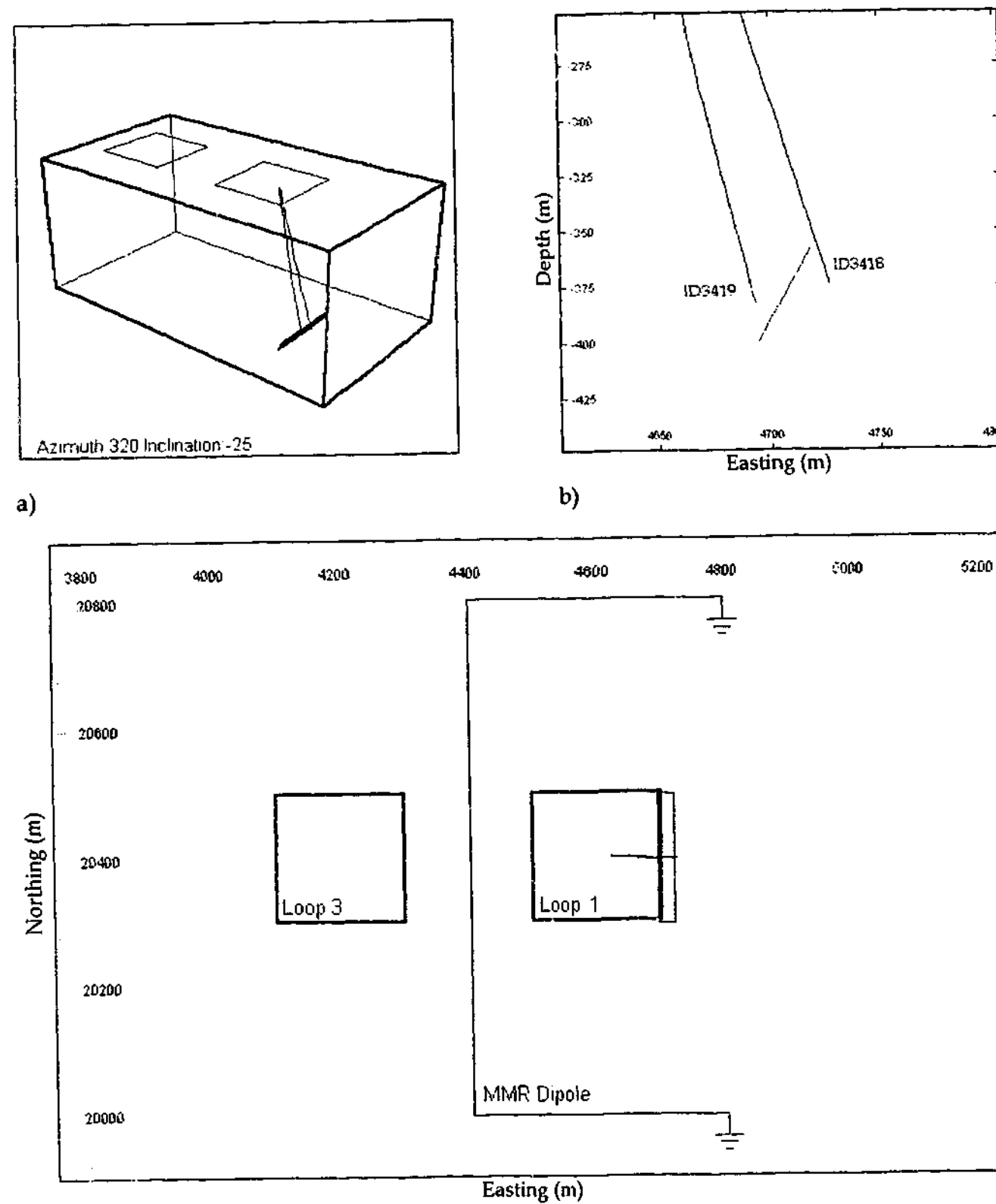


Figure 8.1: Survey configuration: a) Borehole perspective, b) borehole section and c) survey map of Loops 1 and 3 with Boreholes ID3418 and ID3419 together with the DHMMR dipole.

8.3.1. ACTIVE TIME WINDOWS.

Only two sets of time windows were considered suitable for interpretation: windows 6 (0.445 ms) to 10 (0.995 ms), and windows 10 (0.995 ms) to 15 (2.495 ms). The response profiles for windows 15 (2.495 ms) and onwards were regarded to be of little value and so were ignored entirely (see Appendix E.1). As within Chapter Six, the first five windows, windows 1 (0.120 ms) to 5 (0.345 ms), were ignored. Apart from being common practice when interpreting downhole EM, these early times were excluded due to possible contamination of the field response with spurious effects such as probe self response, incomplete transmitter loop turn-off and the likelihood of the early time response lying within the ramp turn-off time. Evidence for these effects and thus justification for the exclusion of the first five windows, was found within the ID3418 data set, and include:

- the evolution of the positive anomaly within windows 1 (0.120 ms) to 5 (0.345 ms) of the Loop 1 data set at Station 380, into a negative anomaly centred about Stations 370 to 380 within windows 6 (0.445 ms) and onwards (see Figure 8.2). Note, the negative sign of the response of window 1 (0.120 ms) is also indicative of early time system effects.

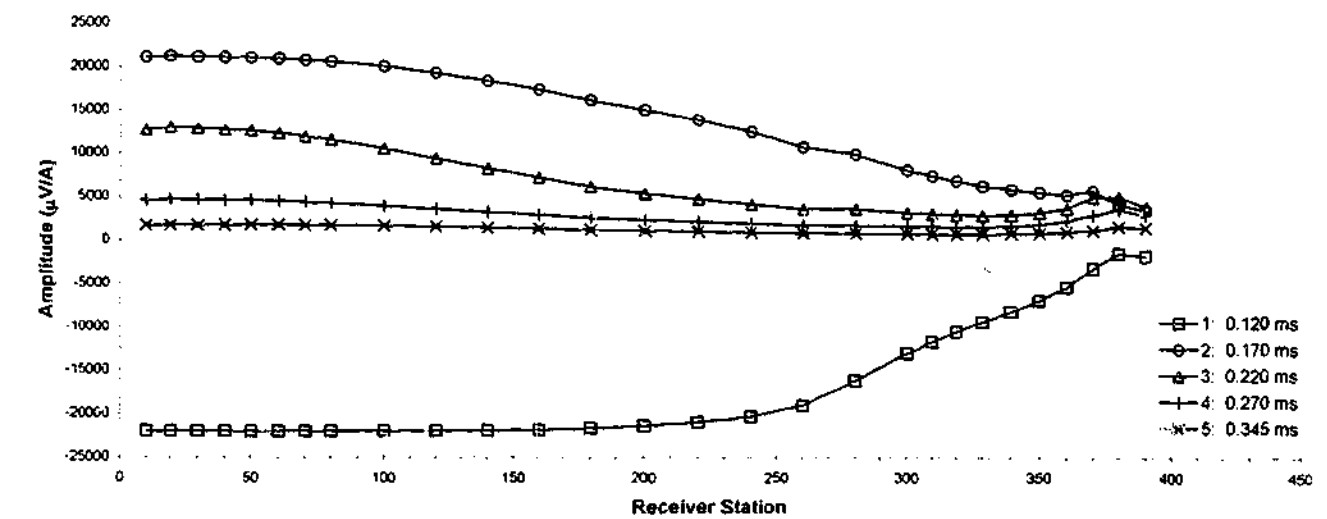


Figure 8.2: DHTM field response of Borehole ID3418 due to Loop 1.

- b) Further evidence is available from the Loop 3 data set, in which the anomaly at Station 380 begins as negative for window 1 (0.120 ms), flips to positive for window 2 (0.170 ms), then back to negative for windows 3 (0.220 ms) and onwards, see Figure 8.3. Such a sign change at these early times implies windows 1, 2 and possibly even 3 are still within the ramp turn-off time.

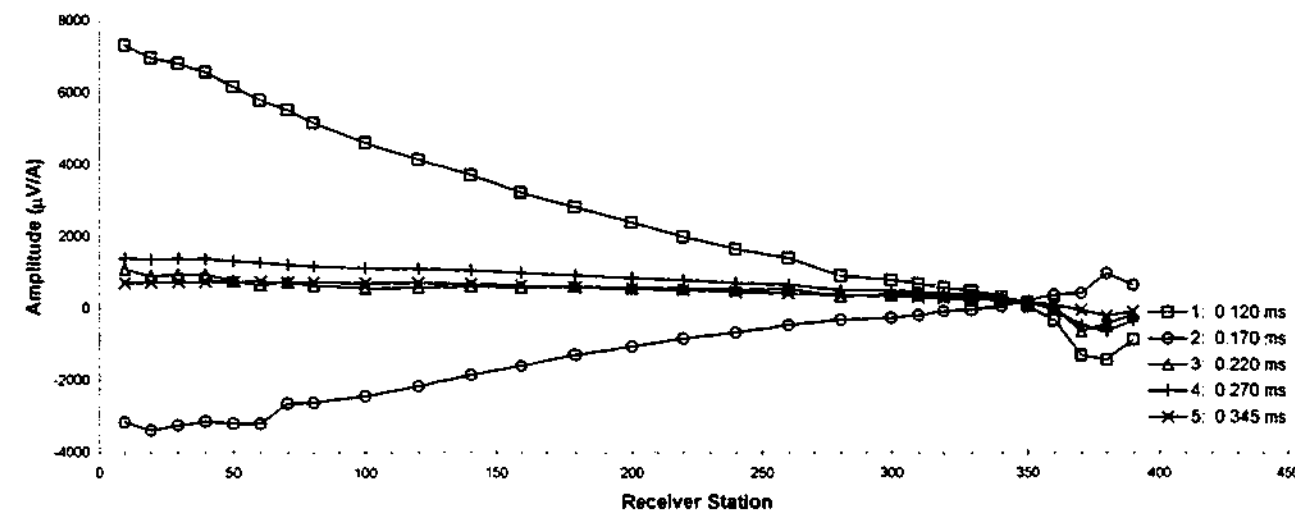


Figure 8.3: DHTM field response of Borehole ID3418 due to Loop 3.

8.3.2. ACTIVE STATIONS.

In general, the field data collected for both boreholes can be broken down into two main parts, namely a shallow and deep-hole response. The shallow-hole response, Stations 10 to 200, is most likely due to a culmination of surface effects, near surface mineralisation and unknown host structure or layering; the single plate model did not address any of these response components. Rather, the purpose of the modelling was to facilitate the interpretation of the deep-hole response, Stations 300 to 390, of the mineralisation; thereby confining the interpretations of the lower mineralisation and LEROI model to these greater depths. Hence, despite the availability of field data for Stations 10 to 390 only Stations 300 to 390 contributed to model development.

8.3.3. ARTIFICIAL EXTENSION OF BOREHOLES.

Boreholes ID3418 and ID3419 terminated near the mineralisation preventing the capture of entire response profiles. The incomplete anomalies, especially those at the base of the boreholes (see sections 8.4.1 and 8.4.2 for further discussion) severely hindered model development. Artificial extension of the boreholes, however, enabled the capture of the entire thin-sheet model response. This additional information aided in the profile analysis of the field data, and in turn, facilitated the identification of the predominating excitation mechanisms. The artificial extension of Boreholes ID3418 and ID3419, involved the linear extrapolation of the holes, using Stations 380 and 390, to a new axial depth of 450 m in spacings of 5 m (See Figure 8.4 for model section view; refer also Tables E.3.3 (ID3418) and E.3.4 (ID3419) of Appendix E.3 for the Cartesian coordinates of the borehole receiver stations and their extensions).

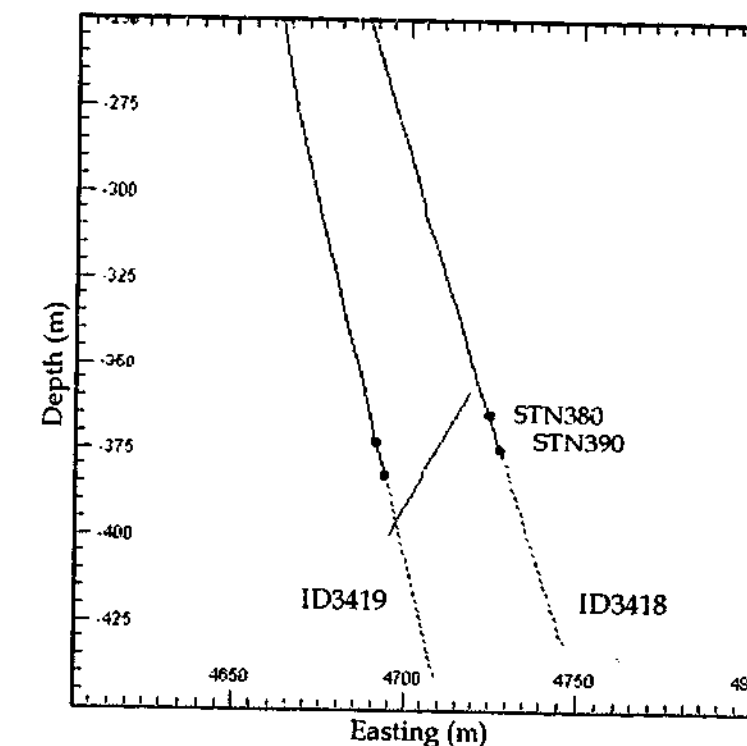


Figure 8.4: Borehole section illustrating both Borehole ID3418 and ID3419 (solid lines), and their artificial extensions (dotted lines). The single plate model specified within Table 8.1 is also shown.

8.3.4. PRESENTATION OF DATA.

To improve clarity, only data specific to a particular discussion are included within the text. Refer to Appendices for E.1 and E.2 for complete response profiles of the DHTM field data and LEROI model data respectively, refer also to Table E.4.1 of Appendix E.4 for the associated composite delay times.

8.4. LIMITATIONS OF THE SINGLE PLATE MODEL.

The single plate model implemented with program LEROI inadequately matched the field profiles for all stations within the active time range of windows 6 (0.445 ms) to 15 (2.495 ms); the model failed to replicate the following features of the field response:

- The positive end-of-hole anomaly present within the early-time Loop 1 field profiles at the base of Borehole ID3418.
- The negative end-of-hole anomaly present within the early-time Loop 1 field profiles at the base of Borehole ID3419.
- The amplitudes of the target anomalies within both boreholes (modelling trials that tested variants of the accepted model specifications were to no avail).
- The near surface field response (this feature, however, was not considered during model development).

The following sections deal with these issues in more detail. Note, that the time windows 6 (0.445 ms) to 10 (0.995 ms) shall be referred to as early times.

8.4.1. END-OF-HOLE ANOMALY WITHIN THE ID3418-LOOP 1 FIELD RESPONSE.

The regional response of the field data for Borehole ID3418 with Loop 1 at early times increases from the collar down, peaking at Station 80 (see Figure 8.5). After which, the regional steadily decreases until about Station 330 before rising once again. The initial rise in the regional is attributable in part to the galvanic response of the near surface mineralisation. The mechanism, however, behind the increase in regional at the base of the borehole eluded identification. Note, in the current context, the term regional is synonymous with the term background response.

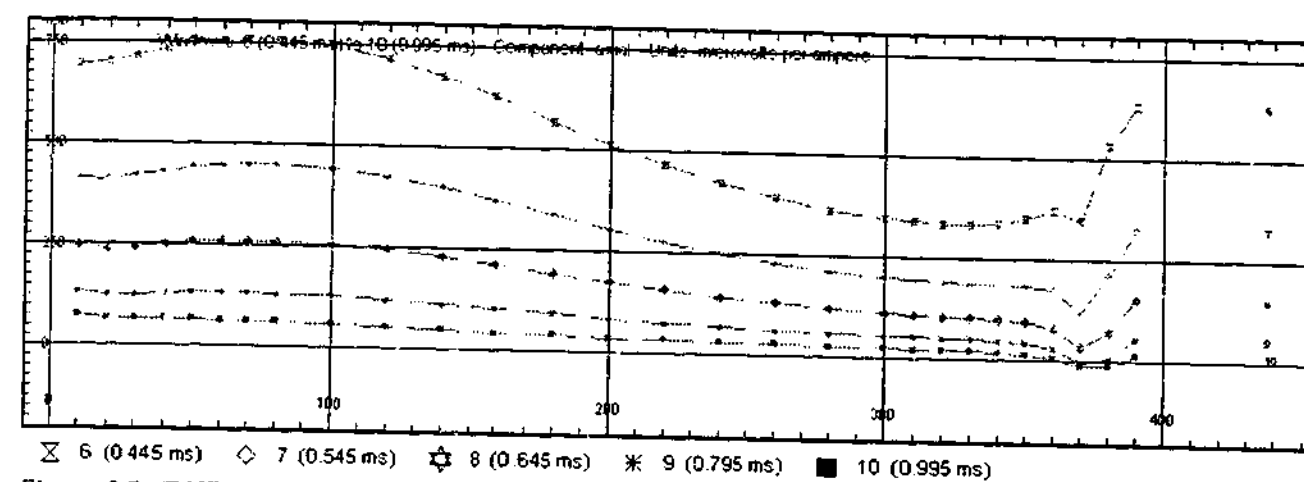


Figure 8.5: DHTM field response profiles of Borehole ID3418 due to Loop 1.

The question as to whether the increase in amplitude of the field response at the base of Borehole ID3418 is associated with the host or target remains unanswered. Indeed, if it is a target response then it appears to be only the up-hole portion of a more significant end-of-hole anomaly. Given that the anomaly exists only at early times up to window 8 (0.645 ms), implied a galvanic origin. The absence, however, of the anomaly within the Loop 3 data (Figure 8.6) suggests this to be unlikely. Unfortunately, the termination of the borehole at Station 390 prevented the capture of the complete anomaly. Knowledge of the entire anomaly profile may provide some indication as to its origin, namely as galvanic or inductive. Moreover, difficulties in estimating a true regional at these depths prevented identification by decay-curve analysis. Thus, the mechanism responsible for the production of the positive end-of-hole anomaly within Borehole ID3418 could not be determined due to insufficient information.

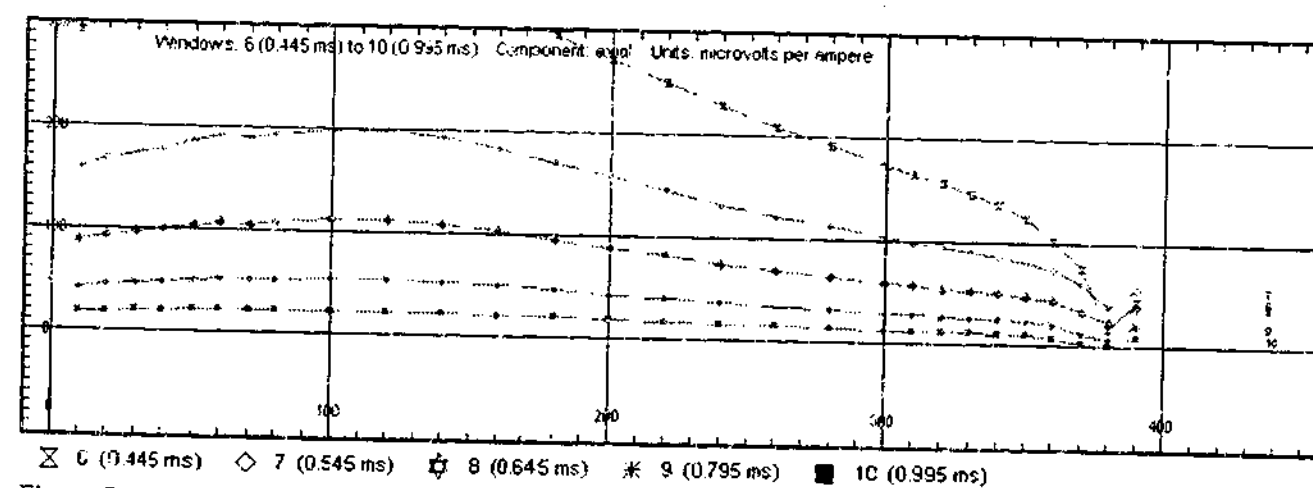
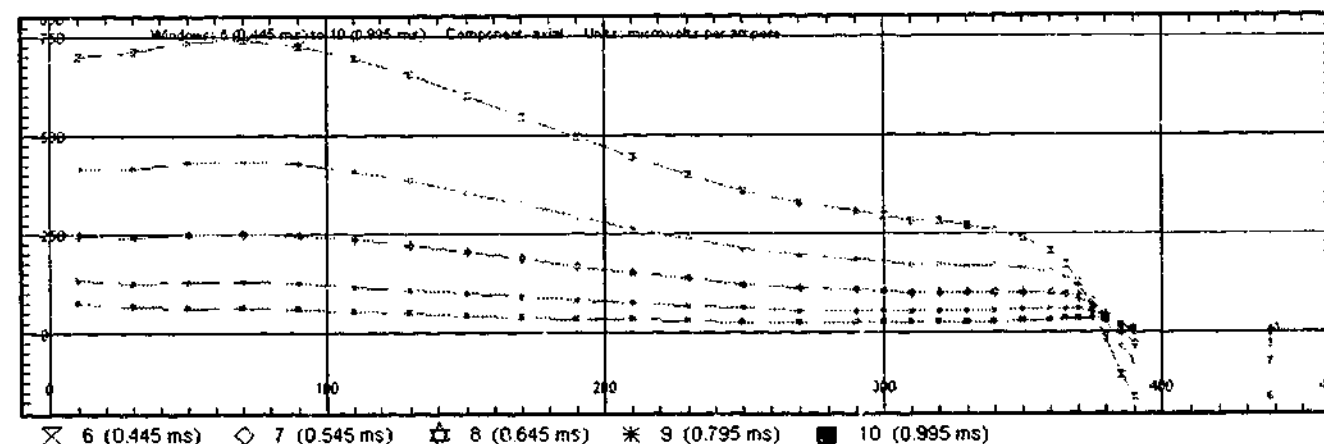


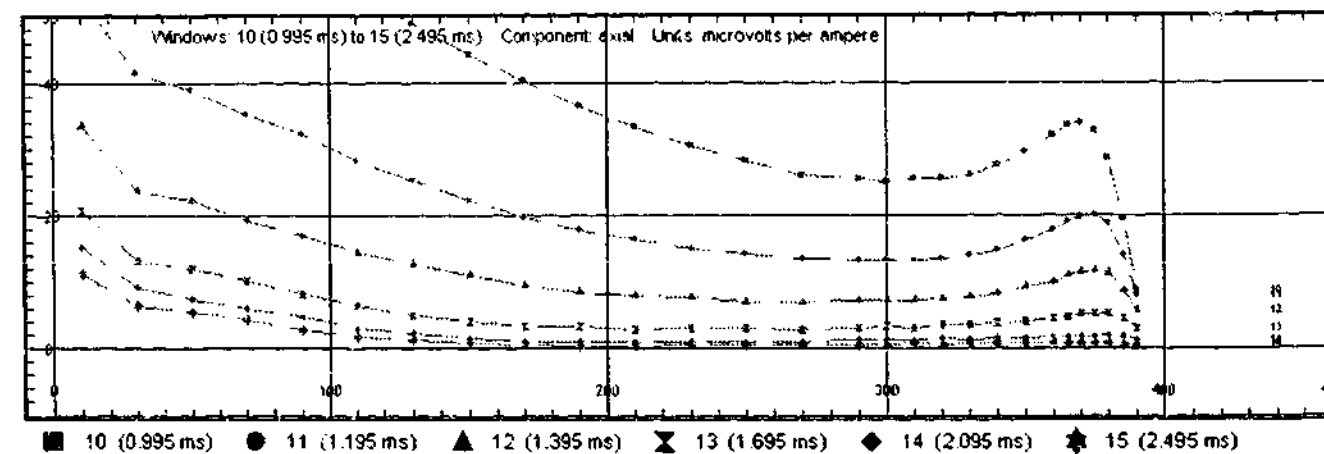
Figure 8.6: DHTM field response profiles of Borehole ID3418 due to Loop 3.

8.4.2. END-OF-HOLE ANOMALY WITHIN THE ID3419-LOOP 1 FIELD RESPONSE.

There appears to be a negative single-signed anomaly centred about Station 400 within the ID3419 Loop 1 field response at early times (see windows 6 (0.445 ms) to 10 (0.995 ms) of Figure 8.7a); this anomaly decays without any noticeable change in profile until about window 8 (0.645 ms). For windows 9 (0.795 ms) and onwards, however, the profile is noted to develop a positive anomaly centred about Station 375 (see Figure 8.7b). The positive end-of-hole anomaly within the ID3418 Loop 1 data and the negative end-of-hole anomaly within the ID3419 Loop 1 data share the following attributes: both anomalies occur only within their respective Loop 1 data sets at early times (compare Figures 8.5 and 8.7a); both anomalies are located in the vicinity of the known mineralisation (apparent from stations 340 onwards). The mechanisms responsible for the production of the ID3418 and ID3419 end-of-hole anomalies have eluded identification, and the known geology does not appear to account for the presence of these anomalies; however, it is suspected, although not demonstrated, that the ID3418 and ID3419 anomalies do have a common origin.



a)



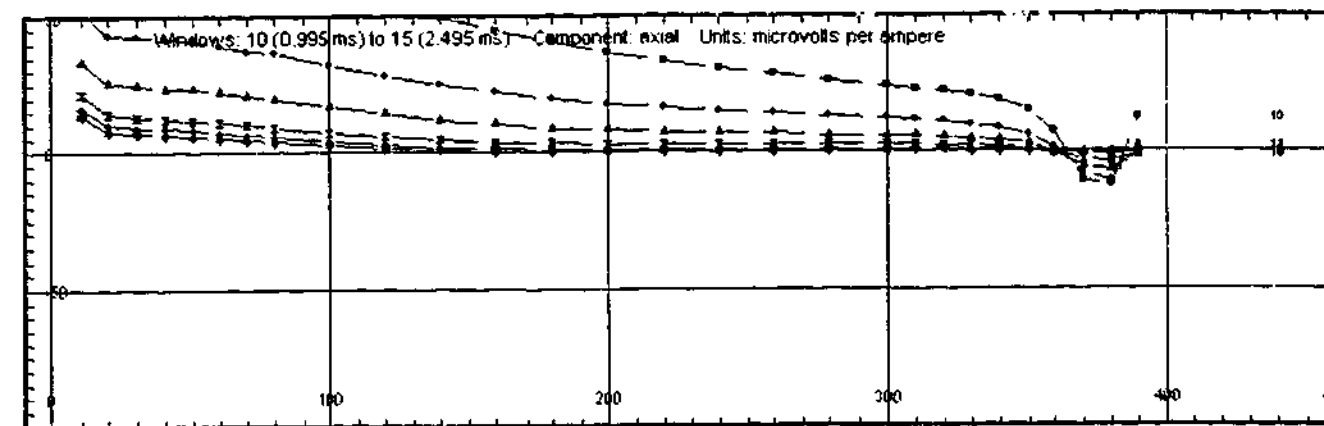
b)

Figure 8.7: DHTM field response profiles of Borehole ID3419 due to Loop 1.

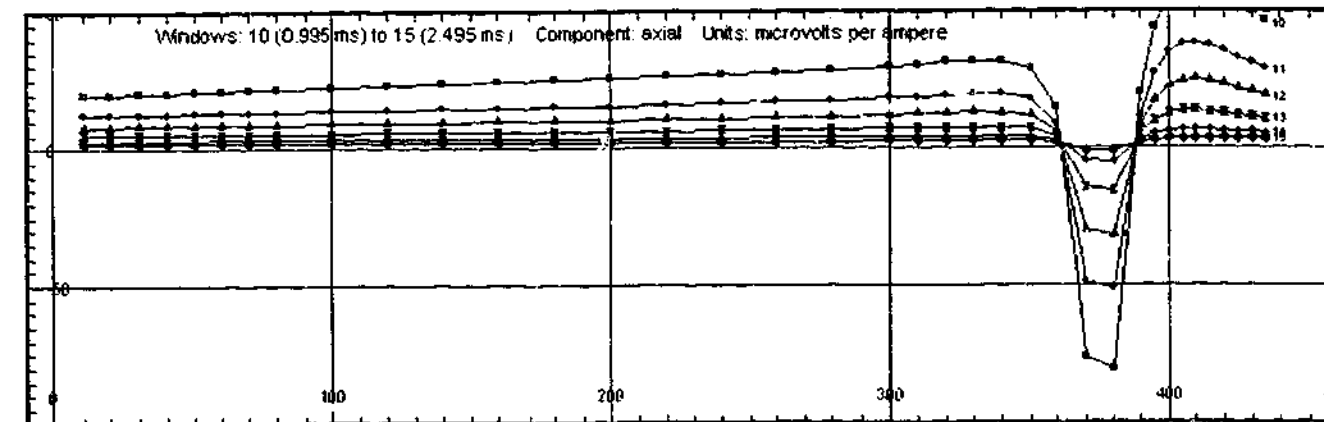
The downhole migration of the negative-to-positive crossover is attributable to the formation of the positive anomaly centred about Station 370 (see Figure 8.7b). This anomaly decays steadily from windows 10 (0.995 ms) and onwards, and is still visible up until window 15 (2.495 ms), after which the field response deteriorates rapidly with increasing noise. Only a portion of the anomaly could be captured due to the termination of Borehole ID3419 at Station 390; thereby hindering interpretation. Moreover, difficulties encountered in estimating a regional that would be suitable for the determination of a scattered field response prevented any meaningful decay-curve analysis on the positive anomaly at Station 370. Thus, in the absence of profile and decay-curve analysis, a mechanism for the production of the STN370-anomaly could not be determined.

8.4.3. AMPLITUDE MATCHING AND INFERENCE OF THE TARGET CONDUCTANCE.

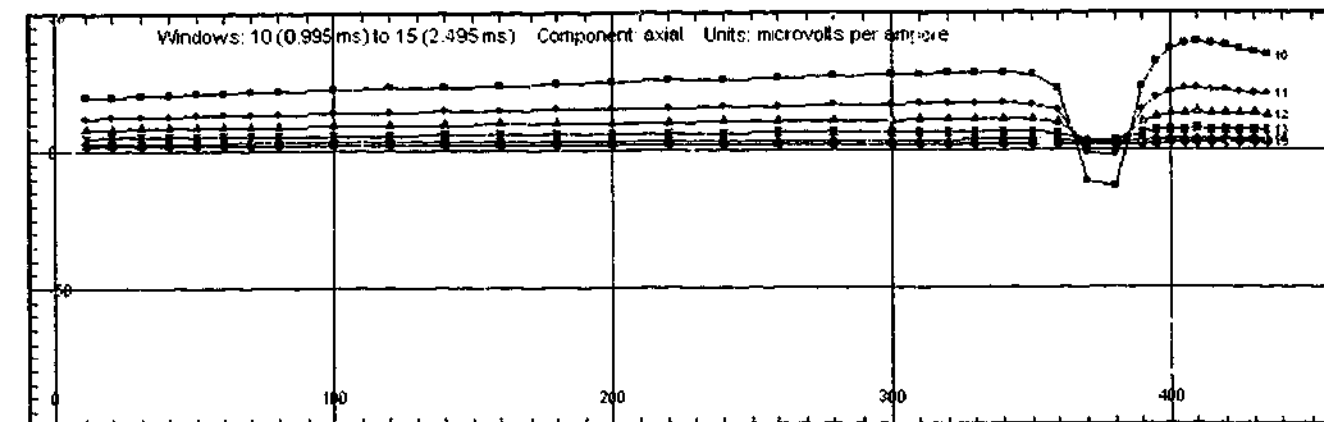
Consider the negative anomaly centred about Station 370 within the Borehole ID3418 data due to Loop 1 (see Figure 8.8). The amplitude of the negative anomaly for time windows 10 (0.995 ms) to 15 (2.495 ms) is on average 3.5 times greater within the original 55 S LEROI model than within the field data. This deficiency initiated trials that investigated the effects of conductance and strike-length on the magnitude of the Station 370 anomaly. Initial interpretations suggested that a poor choice in target conductance caused the excessive amplitude of the anomaly within the LEROI data, this initiated a modelling series that tested the single plate model with the following conductances: 45 S, 40 S, 35 S, 30 S and 25 S. The independent results of each of these trials will not be discussed, although profile analysis on each data set suggested that a sheet conductance of approximately 30 S is more appropriate than the original estimate of 55 S. Specifically for Loop 1, the amplitude of the negative anomaly for the 30 S model (Figure 8.8c) was about 1.5 times greater than that within the field data (Figure 8.8a), less than the factor of 3.5 obtained for the 55 S model (Figure 8.8b).



a)



b)

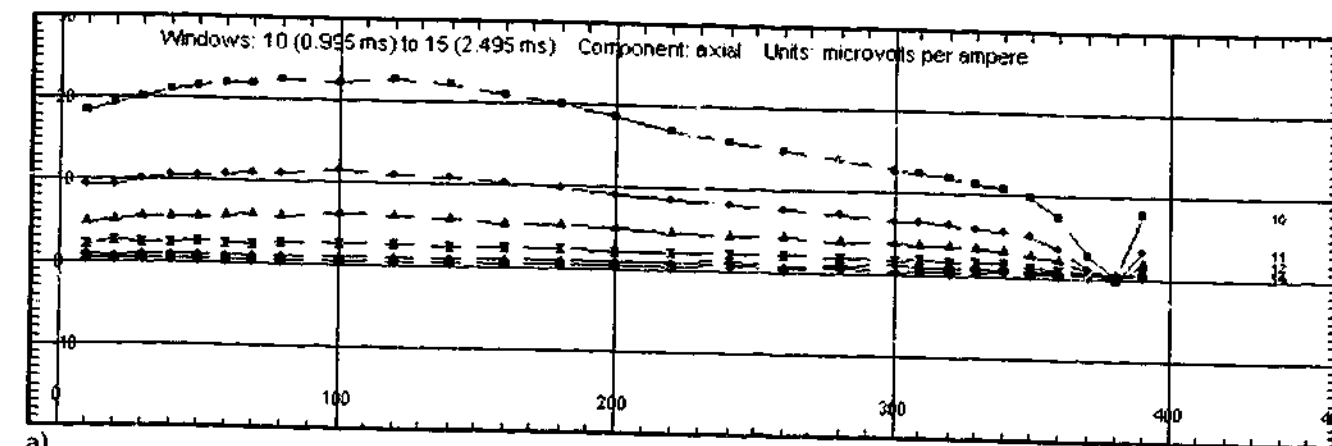


c)

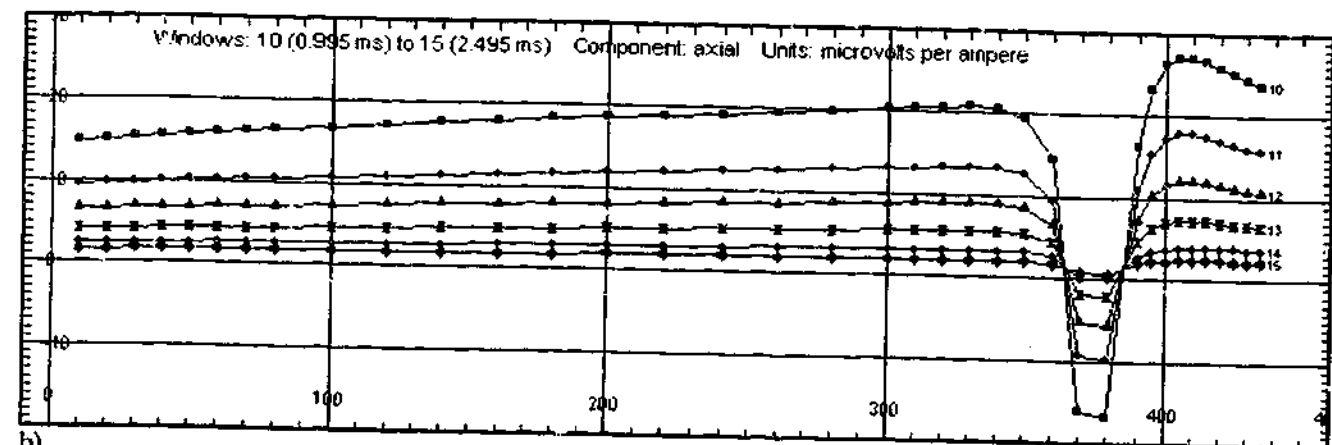
■ 10 (0.995 ms) ● 11 (1.195 ms) ▲ 12 (1.395 ms) ✕ 13 (1.695 ms) ◆ 14 (2.095 ms) ★ 15 (2.495 ms)

Figure 8.8: DHTM response profiles of Borehole ID3418 due to Loop 1: a) field data, b) LEROI model with a plate conductance of 55 S and c) LEROI model with a plate conductance of 30 S.

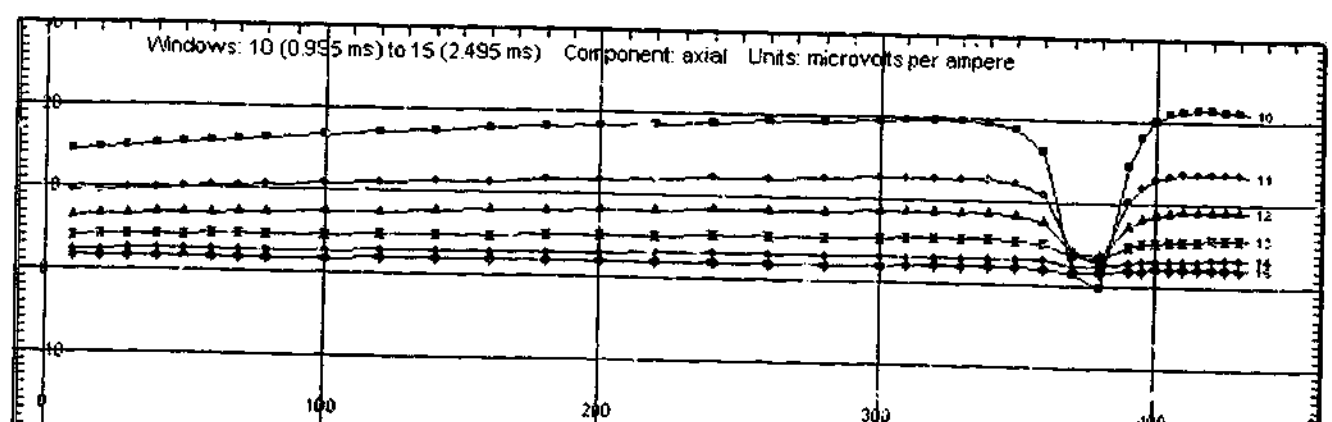
The improved model-field amplitude match is more noticeable within the Loop 3 data than the Loop 1 data. In particular, the 30 S model (Figure 8.9c) yields an anomaly amplitude greater by about a factor of 3 in respect to that found within the field data (Figure 8.9a), compared to the 50 S model (Figure 8.9b) which is greater by about a factor of 5.5. Note, however, the 55 S model (Figure 8.8b) appears to replicate the decay rate of the field anomaly (Figure 8.8a) better than the 30 S model (Figure 8.8c).



a)



b)

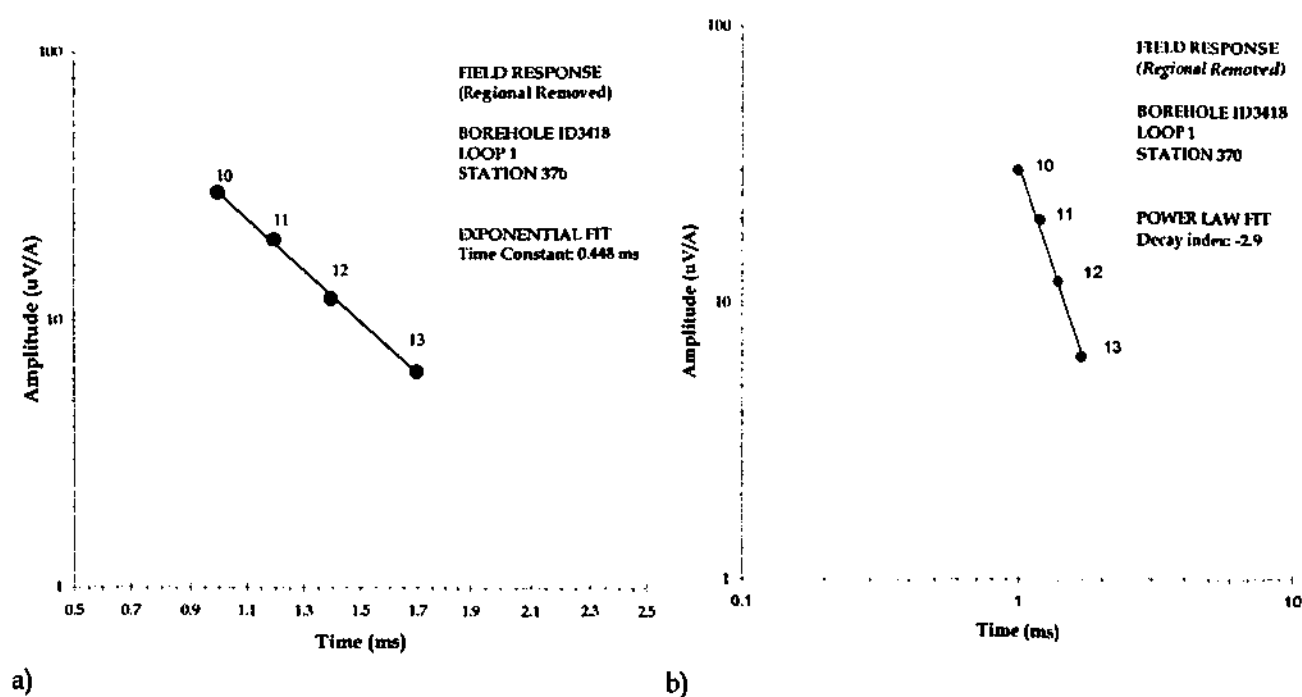


c)

■ 10 (0.995 ms) ● 11 (1.195 ms) ▲ 12 (1.395 ms) ✕ 13 (1.695 ms) ◆ 14 (2.095 ms) ★ 15 (2.495 ms)

Figure 8.9: DHTM response profiles of Borehole ID3418 due to Loop 3: a) field data, b) LEROI model with a plate conductance of 55 S and c) LEROI model with a plate conductance of 30 S.

Justification for reducing the plate conductance to 30 S was sought by means of decay analysis. Unfortunately, the field response for both the ID3418 and ID3419 data sets proved to be notoriously resistant to any unambiguous and thus meaningful decay analysis. As previously mentioned, the reason for this lies in the inability to identify and then isolate the host, inductive and galvanic components of the field response. Regardless of this, a decay plot was prepared for the scattered response of the field data for the time windows 10 (0.995 ms), 11 (1.195 ms), 12 (1.395 ms) and 13 (1.695 ms) about the anomaly minimum, Station 370 (see Figure 8.8a). The scattered response was acquired in the same manner employed within Chapter Five, namely by computing the difference between the total field response and an estimated regional sketched over a hardcopy form of the field data. In summary, an exponential function provided a reasonable fit to the data, thereby implying the anomaly to be inductive with a time constant of 0.448 ms (see Figure 8.10a). The same data, however, also seems to imply that the anomaly is due in part to current channelling, as a reasonable fit can be achieved from a power law with a decay index of -2.9 (see Figure 8.10b). These findings are in conclusion ambiguous; as such, additional information is required to identify the galvanic and inductive components of the field response.

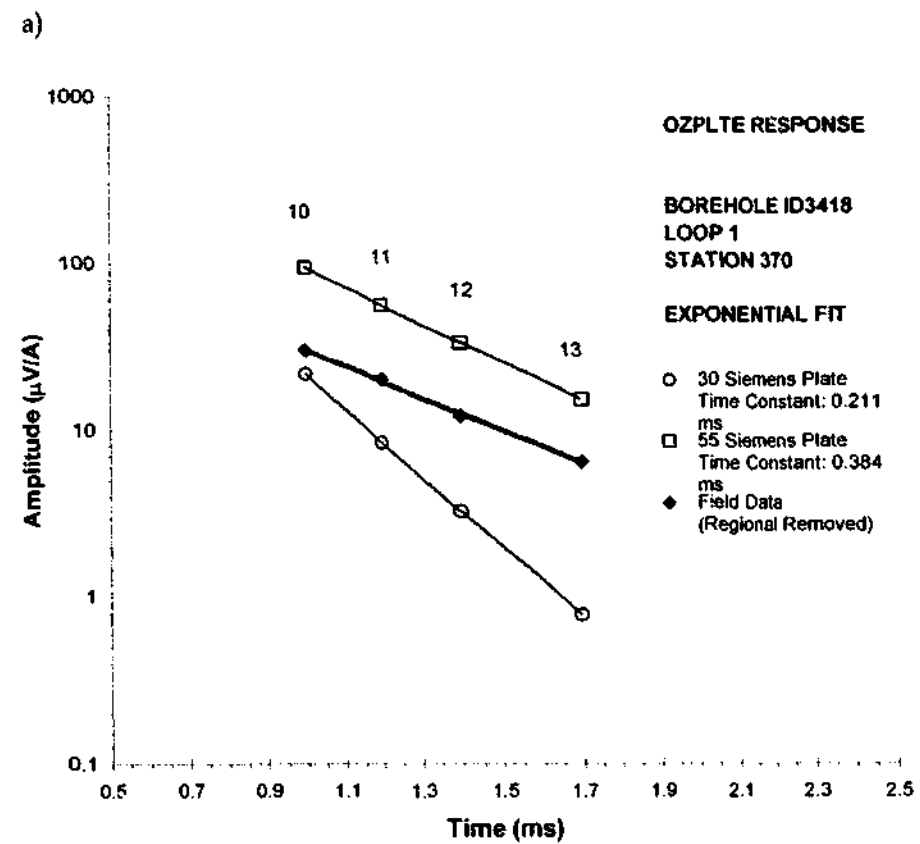
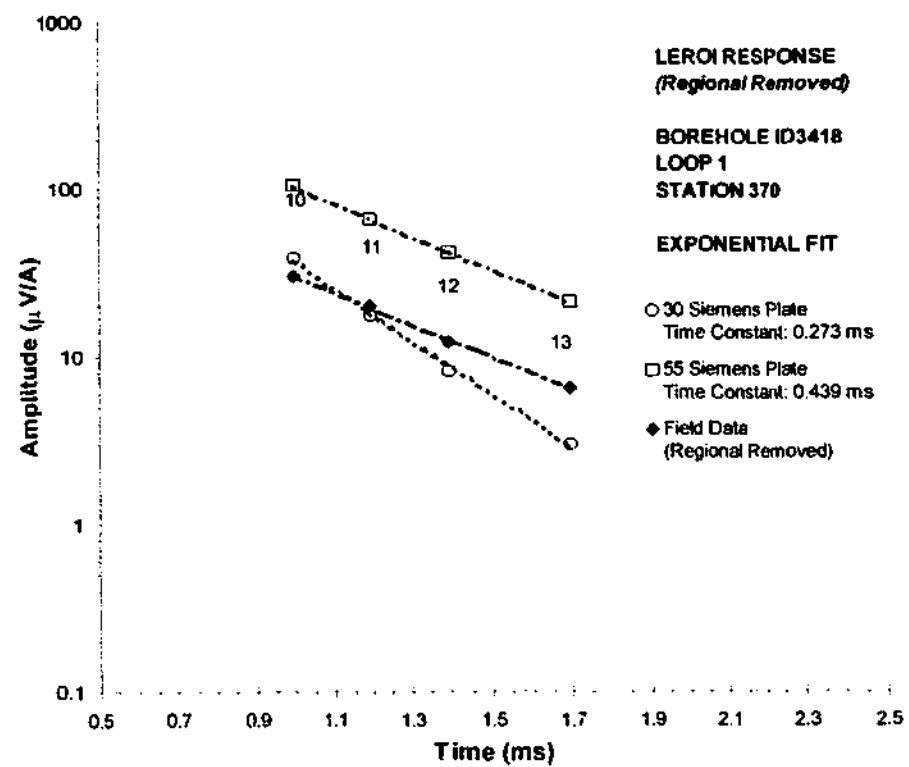


a) Figure 8.10: Decay analysis of the scattered field response estimated for Station 370 of Borehole ID3418 with Loop 1.

Decay-curve analysis performed on the scattered LEROI response of both the 30 S and 55 S plate models, yielded the following exponential time constants, fitted to windows 10 (0.995 ms) to 13 (1.695 ms), for Stations 360, 370 and 380 respectively: 0.438 ms, 0.439 ms and 0.441 ms (55 S model), and 0.280 ms, 0.273 ms and 0.274 ms (30 S model). See Figure 8.11a for the decay plot prepared for Station 370. Recall also, that the scattered or stripped LEROI response is the difference between the total LEROI response and its associated host response.

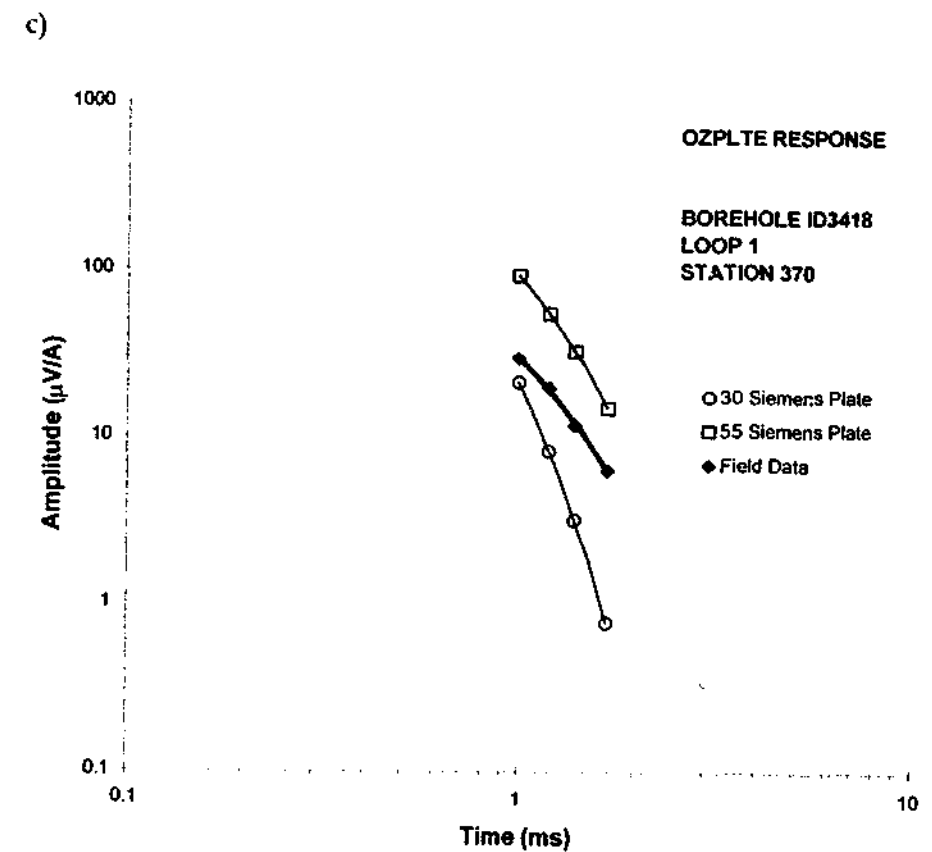
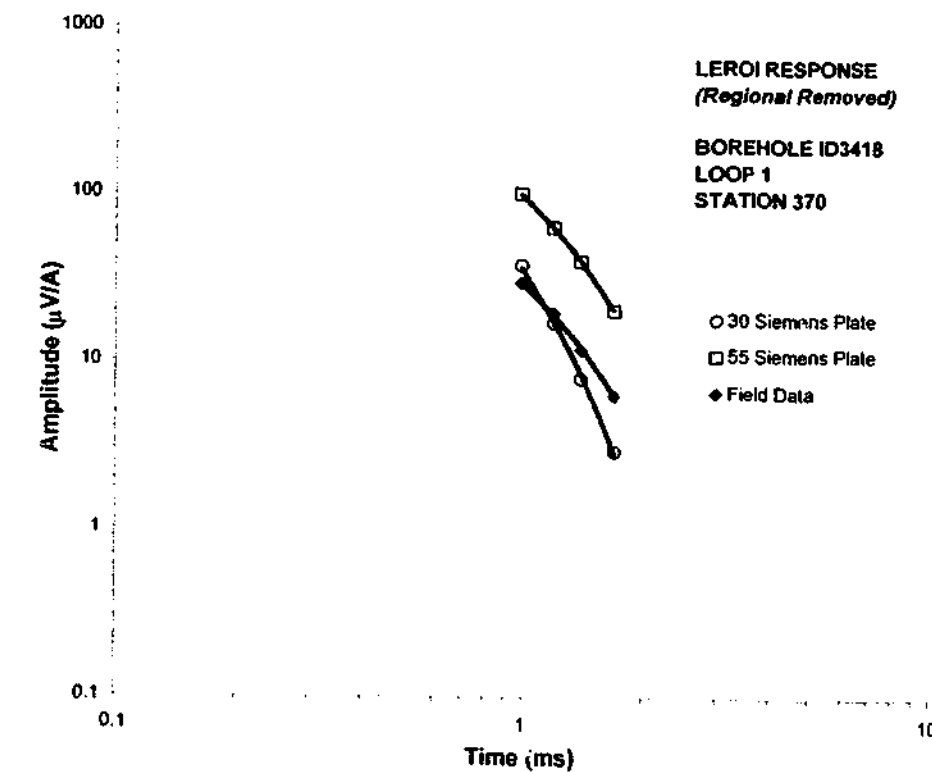
Decay analysis performed on the purely inductive OZPLTE response (Figure 8.11b) at Station 370 for the same time windows yielded a time constant of just 0.384 ms for the 55 S model, and 0.211 ms for the 30 S model. The theoretical time constants for a thin prism obtained from the formula of Lamontagne (1975), see Equation 4.2 of Chapter Four, were slightly lower yet again, specifically 0.336 ms (55 S model) and 0.183 ms (30 S model). Since OZPLTE and the formula of Lamontagne (1975) yielded equivalent time constants for both models, and are both significantly smaller than the time constants acquired from LEROI, it is concluded that the negative anomalies within the LEROI models are not entirely inductive. The beneficial aspects of the competing models are succinctly illustrated within Figure 8.11a: a plate conductance of 55 S is required for decay rate of the model and field anomalies to be matched, whereas a reduced conductance of 30 S is required to match the amplitudes.

Note also, the curved lines of best fit within the complementary log-log decay plots prepared for both the LEROI and OZPLTE models confirm the exponential decay of the LEROI anomaly (see Figure 8.11 c and d).



a)

b)



c)

d)

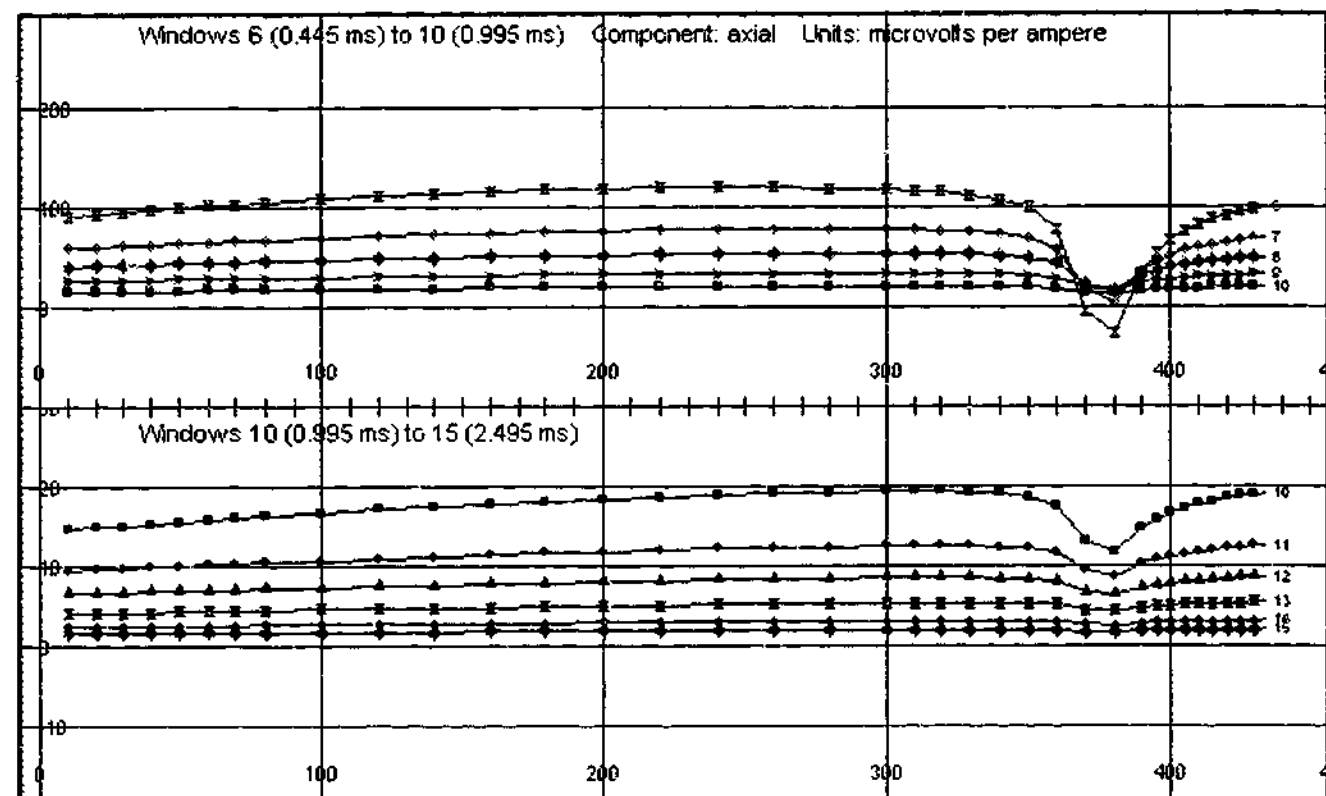
Figure 8.11: Decay plots for both the 30 S and 55 S plate models implemented with a) LEROI and b) OZPLTE. Included for reference are the scattered field data previously shown within Figure 8.10 a). The curved lines of best fit in the log-log plots c) and d), confirm the exponential relations found within both the LEROI and OZPLTE model data.

In summary, conductance estimates for the single plate LEROI model began with matching the decay rates of the negative anomalies centred about Station 370 of the Loop 1 - ID3418 model and field data sets. Exponential time constant matching, namely 0.448 ms (scattered field response) and 0.439 ms (scattered model response), implied a target conductance of 55 S. Decay-curve analysis, however, on the field data yielded ambiguous results implying that the field anomaly is not entirely inductive, thereby nullifying its inferred time constant and the original conductance estimate. Subsequent profile analysis with amplitude matching yielded an estimate of 30 S for the target conductance.

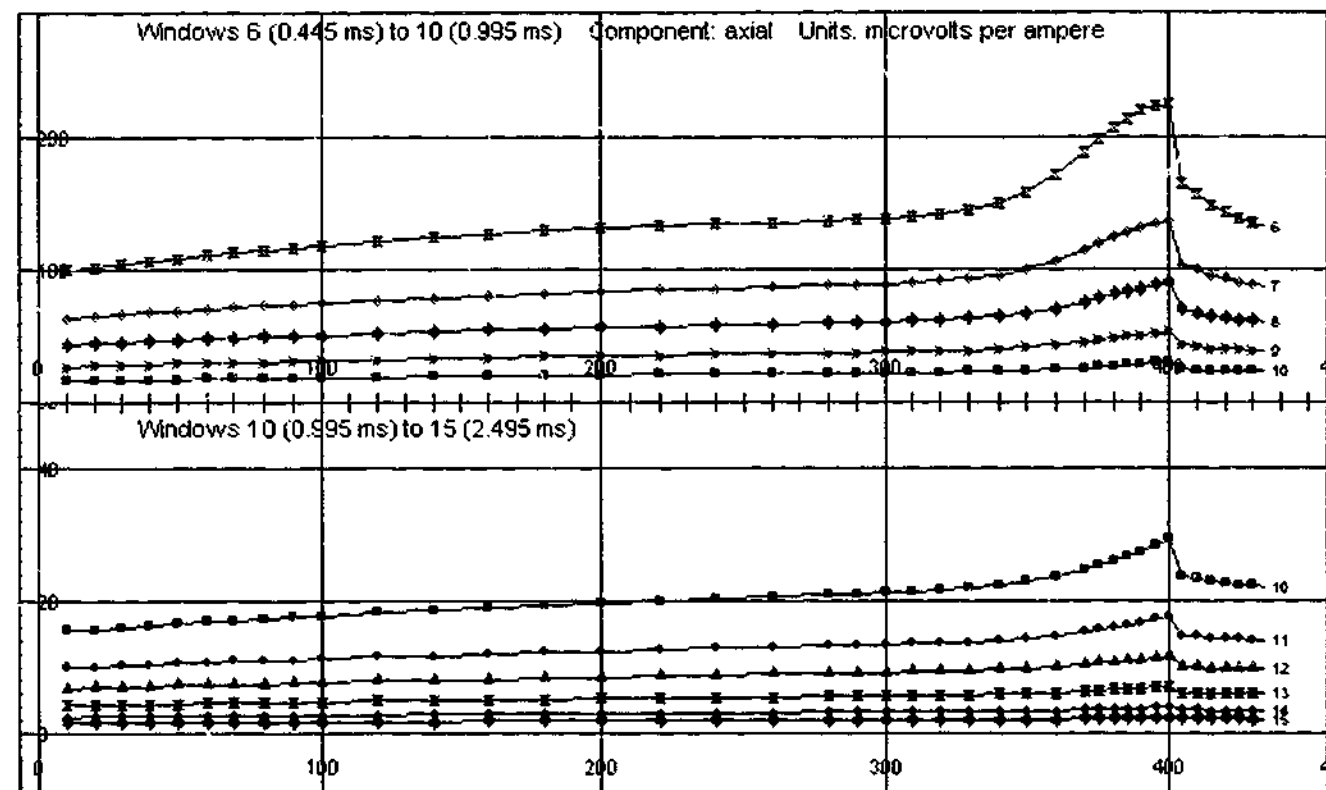
Furthermore, it is unreasonable to expect the single plate LEROI model to provide an adequate match to the amplitudes of the field response for Stations 300 to 390, given that there is significant deviation of the LEROI response from the field data between Stations 10 and 300. In particular, the LEROI model employed only a simple conductive half-space, since the structure of the true host could not be determined. Moreover, program LEROI restricts host representations to just two layers, with all targets confined to the basement layer. Thus, in the event of a multi-layered host regional matching would prove impossible.

8.5. GALVANIC COMPONENT OF THE LEROI RESPONSE.

The inability to determine the conductance of the lower lens by means of decay analysis alone is attributable to the presence of a galvanic component within the field data. Decay analysis performed on the field data yielded ambiguous results, thus preventing the identification of the predominating excitation mechanism (see Section 8.4.3). In addition to this, the scattered LEROI response yielded time constants larger than the associated free-space OZPLTE response, which again, confirmed a galvanic component within the LEROI model data. The inference of a galvanic component within the LEROI response was later illustrated in a more eloquent manner. Reducing the plate conductance to just 10 S, significantly reduced the inductive component within the Loop 3 LEROI response of both boreholes (see Figure 8.12). In particular, the positive-to-negative anomalies noted within the 30 S and 55 S models were no longer present within the 10 S model. Instead, a positive singled signed anomaly centred about Stations 390 and 400 occurred for Borehole ID3419 (Figure 8.12b), and a negative singled signed anomaly centred about Station 380 occurred for Borehole ID3418 (Figure 8.12a). The ID3418 and ID3419 anomalies are not symmetrical, and exhibit prominent down-hole and up-hole wings respectively. Decay-curve analysis verified the dominant excitation mechanism of the scattered LEROI response to be galvanic in origin. Power laws fitted to time windows 6 (0.445 ms) to 15 (2.495 ms) at Stations 360, 370 and 380 yielded decay indices of -3.51, -3.57 and -3.56 respectively for Borehole ID3418, and decay indices of -3.64, -3.6, and -3.56 for Borehole ID3419. See Figure 8.13 for the decay curves prepared for Boreholes ID3418 and ID3419 at Station 370. These findings indicate that the galvanic component within window 10 (0.995 ms) of the Loop 3 LEROI response for both boreholes is of the order of 45% of the scattered total LEROI response for Stations 370 and 380.



a)



b)

- ⊗ 6 (0.445 ms) ◇ 7 (0.545 ms) ☆ 8 (0.645 ms) * 9 (0.795 ms) ■ 10 (0.995 ms)
- 11 (1.195 ms) ▲ 12 (1.395 ms) ✕ 13 (1.695 ms) ◆ 14 (2.095 ms) ★ 15 (2.495 ms)

Figure 8.12: DHTM response profiles of the LEROI model with a plate conductance of 10 S: a) Borehole ID3418 with Loop 3 and b) Borehole ID3419 with Loop 3.

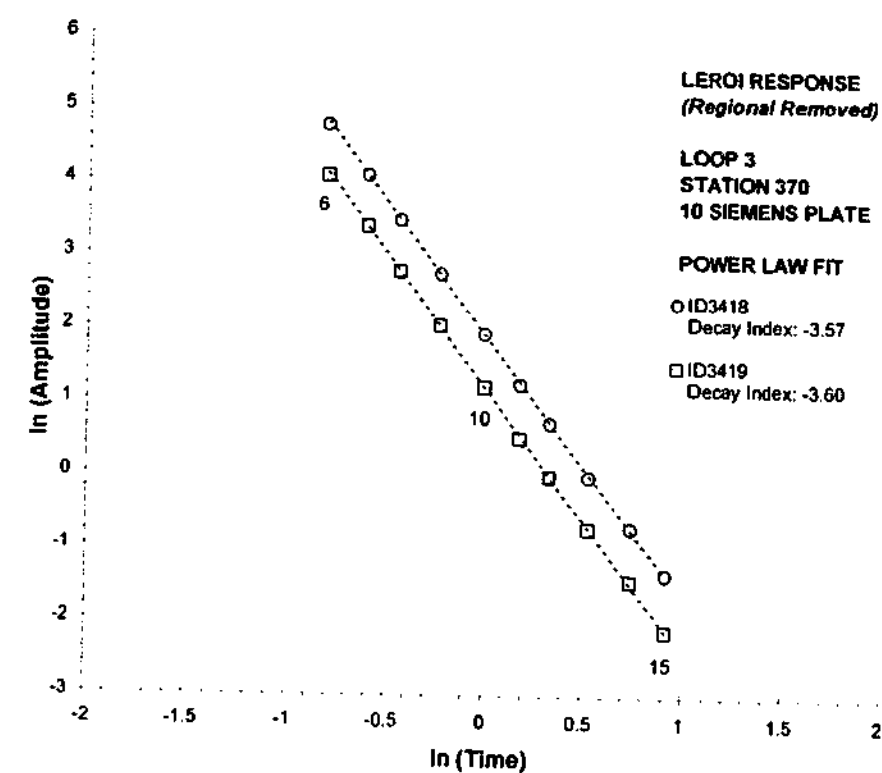


Figure 8.13: Decay curves of the 10 S scattered LEROI response for Borehole ID3418 and ID3419 at Station 370. The slightly higher amplitude of the ID3418 data is due to the plate being in close proximity to the borehole.

8.6. GALVANIC STRIPPING.

The ability to confirm and isolate the galvanic components of the LEROI response has proven to be advantageous in understanding the evolution of the model response with time and loop position. Moreover, the ability to isolate the galvanic component led to the development of the technique of *galvanic stripping*. It is possible to isolate the galvanic component of the LEROI response by reducing the plate conductance to inhibit inductive excitation. In this process, the interpreter successively reduces the sheet conductance until a transition stage is reached, thereby identifying a range of conductances for which the response is predominantly galvanic. As the target conductance increases from zero, a state of saturation eventually occurs, after which any increase in conductance will result in only a minimal rise in current channelling. Inductive effects, however, may become significant before galvanic saturation, thus hindering the ability to isolate the components of each excitation mechanism. Subsequent subtraction of the galvanic response from the original LEROI response yields the isolated inductive component. Presented within the following sections are examples for which *galvanic*

stripping has been implemented as an interpretational aid, facilitating the understanding of the mechanisms responsible for the formation of composite anomalies. Note, from here on, the original LEROI response before galvanic stripping shall be referred as the *total* LEROI response.

8.6.1. GALVANIC STRIPPING OF THE ID3418 MODEL DATA.

A prominent negative single signed anomaly is centred about Stations 370 and 380, within windows 6 (0.445 ms) to 10 (0.995 ms) of the 30 S LEROI model data for Borehole ID3418 with Loop 3 (see Figure 8.14.a). By windows 10 (0.995 ms) to 15 (2.495 ms), however, this anomaly has decreased in amplitude, whilst at Station 410, a weak-positive anomaly begins to developed (see Figure 8.14a). This evolution of response is attributable to the predominance of the galvanic component at early times: a negative galvanic anomaly centred about Stations 370 and 380, inferred from the 10 S model, enforces the minimum of the inductive anomaly whilst offsetting its low-amplitude down-hole wing maximum. See Figure 8.14a for the response profiles of both the 30 S and 10 S LEROI models. The response of the 10 S model approximates the galvanic component of the 30 S model (see Section 8.5). Note for late times, the amplitude of the *isolated galvanic component* relative to the *total* LEROI response has decreased. The *isolated inductive component*, obtained by subtraction of the 10 S response from the 30 S response, is compared with the pure inductive OZPLTE response within Figure 8.14b. The excellent match between the two profiles indicates that the galvanic stripping was successful. In particular, note the recovered crossovers located at Stations 350 and 390 that were not visible within the original 30 S data.

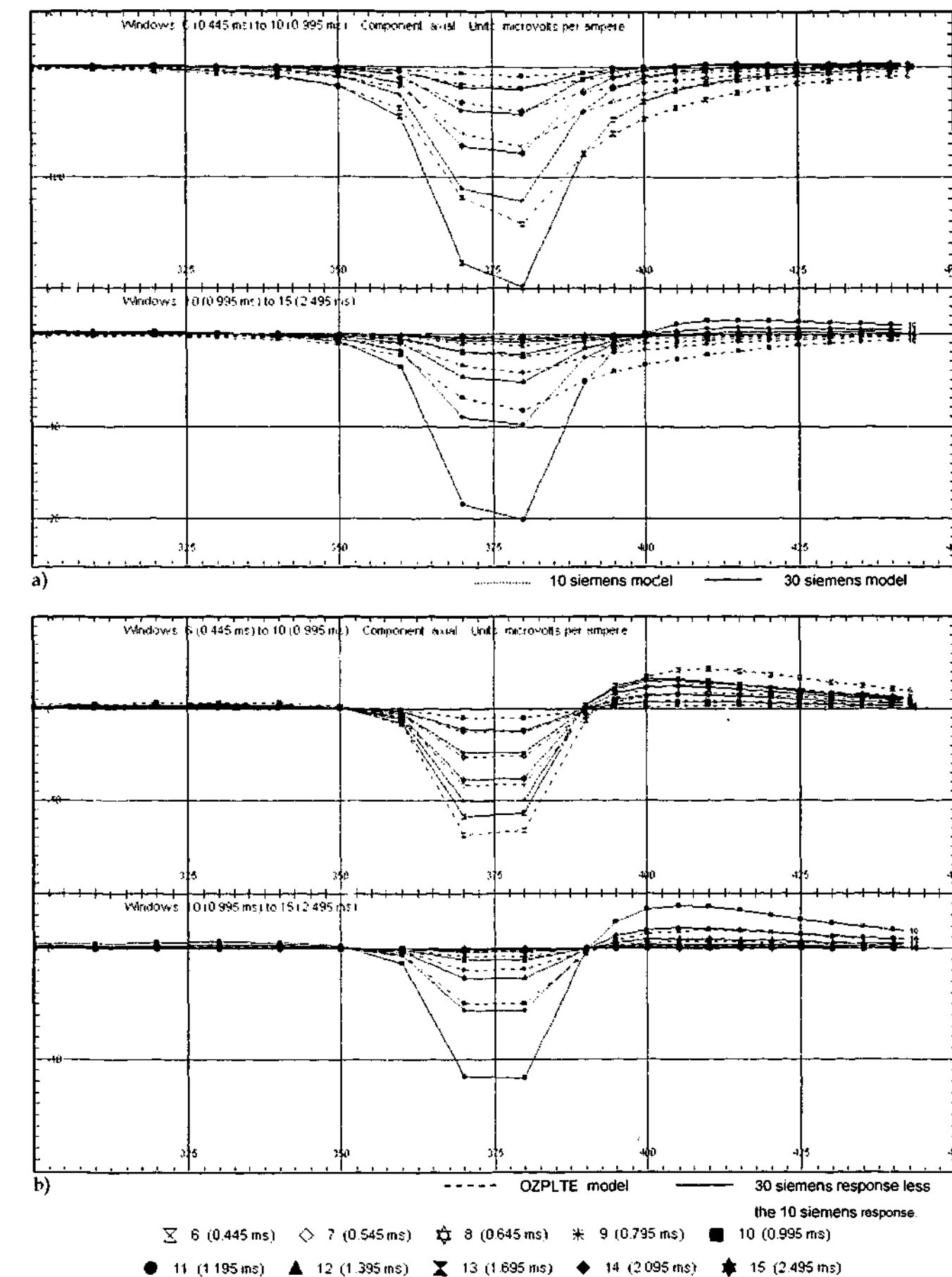


Figure 8.14: An example of galvanic stripping: a) Scattered LEROI response profiles of the ID3418 Loop 3 models with conductances of 30 S and 10 S. The response due to the 10 S model was found to be predominantly galvanic, whilst an increased conductance resulted in a composite inductive and galvanic response for the 30 S model. A positive-to-negative inductive profile is revealed b) after removal of the galvanic component, namely the 10 S response, from the 30 S response. Both profile and amplitude matching with the respective 30 S OZPLTE model, confirms the inductive nature of the stripped LEROI response.

Response profiles of the 30 S LEROI model for Borehole ID3419 with Loop 1, before and after galvanic stripping are shown within Figure 8.15a and Figure 8.15b respectively. The isolated galvanic component of the 30 S model, approximated by the response of the 10 S model, see Figure 8.15a, is negative in sign and weak in amplitude. The galvanic response features a minimum about Station 375, and predominates at early times; windows 6 (0.445 ms) to 10 (0.995 ms), representing less than half of the total scattered 30 S model response. Subtraction of the isolated galvanic component from the 30 S model, reduced the minimum of the inductive anomaly at Stations 370 and 380, and slightly increased its maximum at Station 410. The resulting isolated inductive component after stripping, was found to be well matched with the response profiles of the associated 30 S OZPLTE model (see Figure 8.15b). Note, that the Loop 1 data, in contrast to Loop 3, is predominantly inductive due to improved coupling between the plate and transmitter loop.

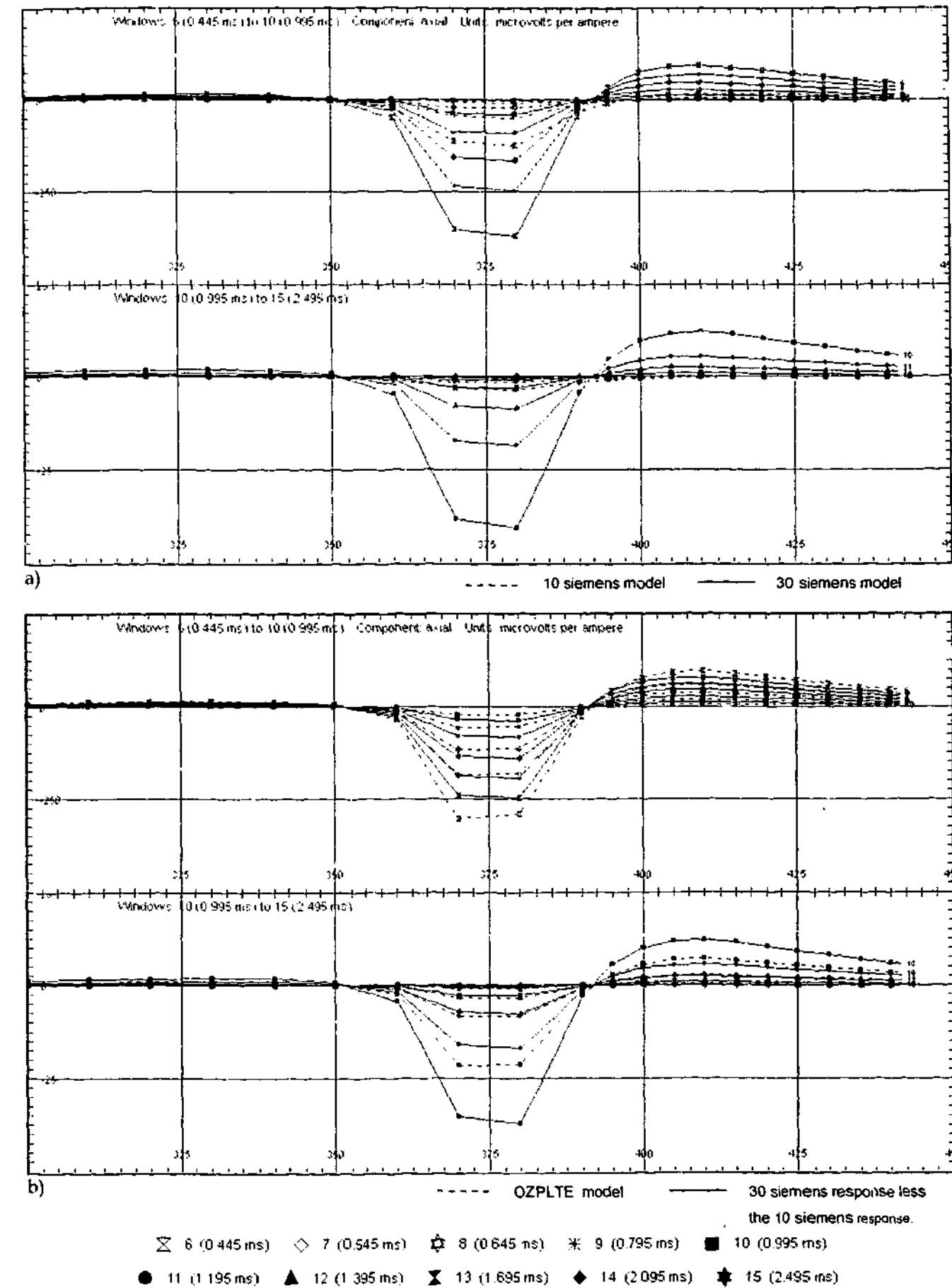


Figure 8.15: Galvanic stripping of the ID3418-Loop 1 model data set: a) Scattered total LEROI response of models with plate conductances of 30 S and 10 S. b) Comparison of the 30 S OZPLTE response with the isolated inductive response.

8.6.2. GALVANIC STRIPPING OF THE ID3419 MODEL DATA.

For the following discussion, refer to Figure 8.16 for profiles of the scattered LEROI response, before and after stripping, for Borehole ID3419 with Loop 3. At early times windows 6 (0.445 ms) to 10 (0.995 ms), the total scattered LEROI response features a broad positive anomaly centred about Station 375, in addition to an intersection anomaly centred about Station 400 (see Figure 8.16a). At later times (windows 10 to 15) a positive-to-negative anomaly is noted to form within the total 30 S LEROI response (see Figure 8.16a), with the negative intersection anomaly, initially positive in window 6 (0.445 ms), increasing in amplitude. A reduced plate conductance of 10 S reveals a significant galvanic component with a broad positive single signed asymmetric profile (see Figure 8.16a). Indeed, its presence is apparent within the total LEROI response as a small positive peak at Station 400. Removal of this galvanic component (see Figure 8.16b) recovered a positive-to-negative inductive profile, which in turn, closely matches the pure inductive response obtained from the associated OZPLTE model. In summary, galvanic stripping successfully isolated a predominating early time positive galvanic anomaly. This anomaly reinforced and reduced the positive and negative portions of the inductive component respectively.

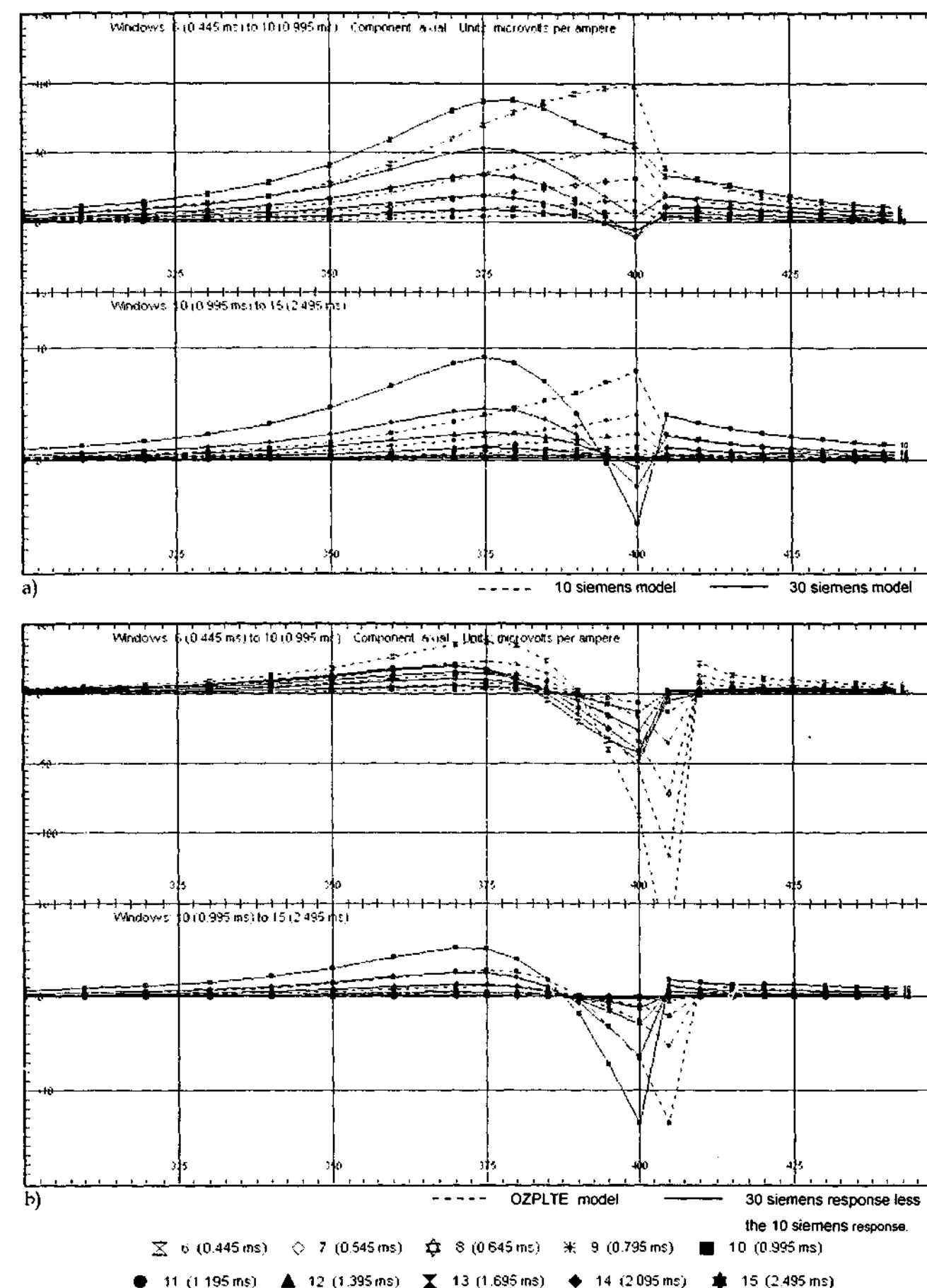


Figure 8.16: Galvanic stripping of the ID3419-Loop 3 model data set: a) Scattered total LEROI response of models with plate conductances of 30 S and 10 S. b) Comparison of the OZPLTE response with the difference between the scattered 30 S and 10 S model response.

Refer to Figure 8.17 for profiles of the scattered 30 S model response, before and after galvanic stripping, for Borehole ID3419 with Loop 1. At early times windows 6 (0.445 ms) to 10 (0.995 ms), a weak isolated positive galvanic component is noted, inferred from the 10 S LEROI model, but diminishes at later times. Removal of the galvanic component reduced slightly the positive anomaly centred about Station 375. The resulting isolated inductive component after stripping (see Figure 8.17b) matched well with the response profiles of the associated 30 S OZPLTE model. The Loop 1 data, in contrast with Loop 3, is predominantly inductive due to improved target-loop coupling.

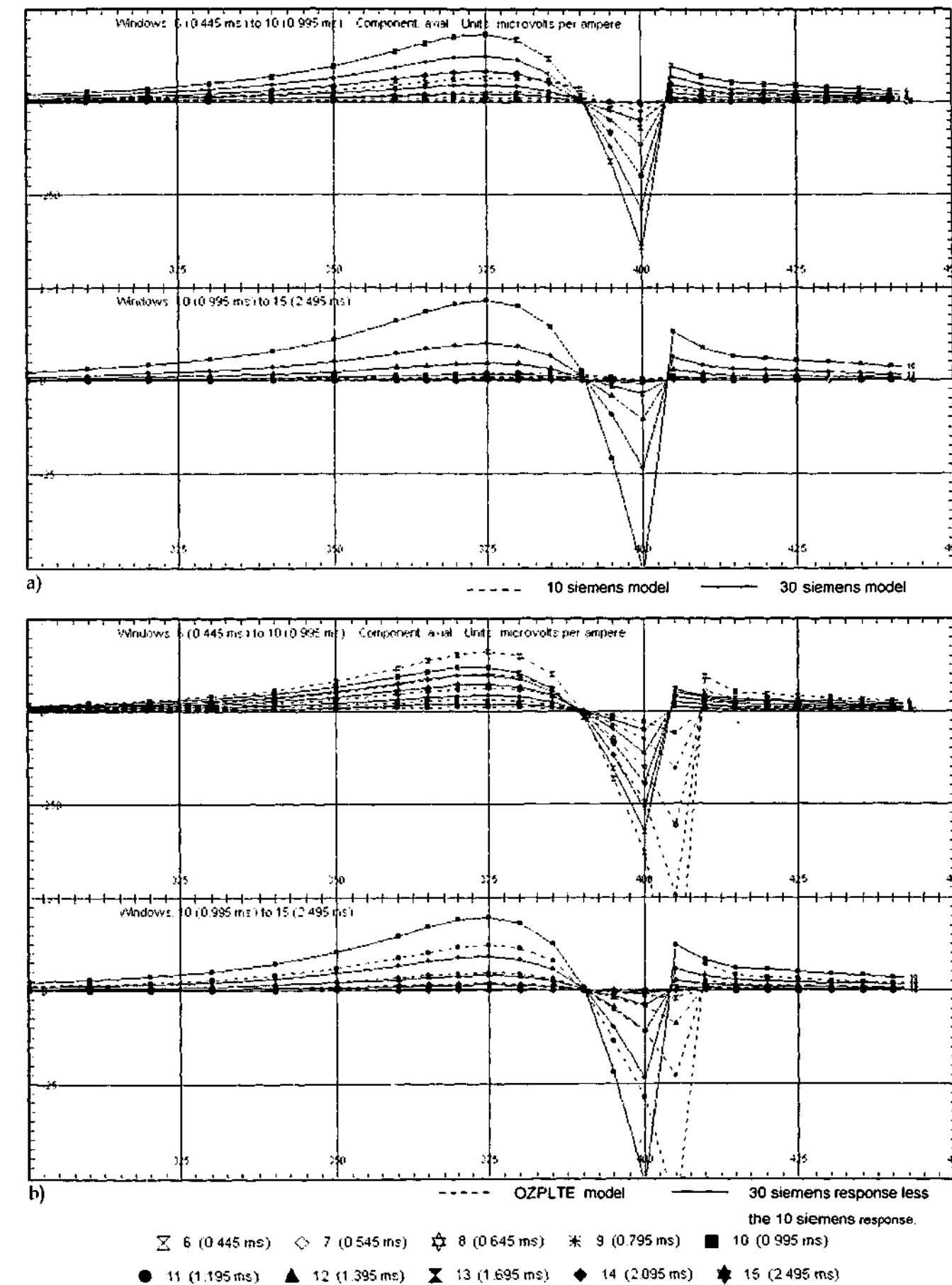


Figure 8.17: Galvanic stripping of the ID3419-Loop 1 model data set. a) Scattered *total* LEROI response of models with plate conductances of 30 S and 10 S. b) Comparison of the 30 S OZPLTE response with the isolated inductive response.

Profile amplitude analysis, performed at Station 375, quantified the late time predominance of current channelling within the 30 S LEROI model data for Borehole ID3419 with Loop 3. See Table 8.2, for the results of this analysis. Station 375 was selected for analysis since a positive anomaly occurs at this depth in both the field and the 30 S LEROI model. See Table 8.2a for the amplitudes of the scattered total LEROI, isolated galvanic and inductive response profiles for windows 6 (0.445 ms) and 10 (0.995 ms) and Loops 1 and 3. The ratio of the response amplitudes of Loop 3 with Loop 1, reflect the change in behaviour of each response type with a change in loop position.

The Loop 3 to Loop 1 response amplitude ratio of the scattered *total* LEROI data is 47% for window 6 (0.445 ms) and 43% for window 10 (0.995 ms).

The amplitudes, however, of the scattered isolated galvanic response are found to increase with Loop 3 by a factor of 6% for window 6 (0.445 ms) and 122% for window 10 (0.995 ms). This result is in agreement with the findings of the Cadjebut (see Chapter Five) and Flying Doctor Deposit: Shallow Lens (see Chapter Six) case studies that showed offset loops will increase galvanic excitation of a target. Finally, the response amplitudes of the scattered isolated inductive LEROI data and the associated OZPLTE model data both decreased with Loop 3 by about a factor of four.

The actual contributions made by the inductive and galvanic components to the total LEROI response can be seen within Table 8.2b, in which both the scattered isolated galvanic and inductive components are expressed in terms of percentages of the total LEROI response. The behaviour of the isolated inductive and galvanic components can be summarised as follows:

- i. For both Loops 1 and 3, the inductive and galvanic components increase and decrease respectively with time.
- ii. For both windows 6 (0.445 ms) and 10 (0.995 ms), the inductive and galvanic components are found to decrease and increase respectively with Loop 3.

Note that, the inductive component dominated the Loop 1 data, accounting for 64.2% and 91.4% of the total LEROI response in windows 6 (0.445 ms) and 10 (0.995 ms) respectively. In respect to Loop 3, however, a significant galvanic

component is noted in window 6 (0.445 ms) accounting for 80% of the total LEROI response, whilst for window 10 (0.995 ms) neither the inductive nor the galvanic components can be said to predominate with respective contributions of 55.8% and 44.2%.

In summary, the galvanic component of the LEROI model response is greater than the inductive component for Loop 3 at early times up to window 10 (0.995 ms). The galvanic component has greater influence on the evolution of the LEROI response within the Loop 3 data, than the Loop 1 data. This result is attributable to the stronger inductive component within the near loop or Loop 1 response. In particular, the OZPLTE response is greater within the Loop 1 data by about a factor of four.

Table 8.2: Results of the amplitude analysis on the 30 S LEROI and OZPLTE models for Borehole ID3419.

RESPONSE TYPE.	RESPONSE AMPLITUDE AT STATION 375. (microvolts per ampere)		AMPLITUDE RATIO: LOOP 3/LOOP 1.
	LOOP 1	LOOP 3	
<i>WINDOW 6 (0.445 ms)</i>			
Scattered Total LEROI	184.5	87.6	0.47
Isolated Galvanic†	66.1	70.0	1.06
Isolated Inductive†	118.4	17.6	0.15
OZPLTE	160.2	37.4	0.23
<i>WINDOW 10 (0.995 ms)</i>			
Scattered Total LEROI	21.5	9.2	0.43
Isolated Galvanic†	1.8	4.0	2.22
Isolated Inductive†	19.7	5.1	0.26
OZPLTE	12.2	2.8	0.23

a) † Inferred from galvanic stripping of the total LEROI response.

RESPONSE TYPE.	RELATIVE COMPONENT OF THE TOTAL LEROI RESPONSE.	
	LOOP 1	LOOP 3
<i>WINDOW 6 (0.445 ms)</i>		
Isolated Galvanic†	35.8%	80.0%
Isolated Inductive†	64.2%	20.0%
<i>WINDOW 10 (0.995 ms)</i>		
Isolated Galvanic†	8.6%	44.2%
Isolated Inductive†	91.4%	55.8%

b) † Inferred from galvanic stripping of the total LEROI response.

8.7. DISCUSSIONS OF THE LOOP 3 FIELD DATA.

Unlike the Loop 1 field data set in which the regional exhibits an anomalous behaviour, there are no significant changes in the field response profiles for Loop 3 within the window range 6 (0.445 ms) to 15 (2.495 ms) for either Borehole ID3418 nor ID3419. The following subsections contain discussions on the profile analysis performed on the ID3418 and ID3419 field data sets, together with proposed mechanisms for the production of the respective profiles noted in the field response.

8.7.1. ID3418 FIELD DATA.

It is noted that there is a slight broadening of the negative anomaly within Borehole ID3418 at Station 380 for windows 9 (0.795 ms) and onwards for both loops, Loop 1 (see Figure E.1.1b) and Loop 3 (see Figure E.1.2b). Given the poor resolution of the profile, it is difficult to ascertain whether this change is real. Furthermore, the relative amplitude of the Station 380 anomaly in respect to the regional response, decreases by about a factor of three for window 10 (0.995 m) with Loop 3.

Inferences made from the LEROI modelling within Section 8.6.1, suggest that the Station 380 anomaly in the field data is the resultant of the superposition of a single signed negative galvanic anomaly with the up-hole portion of a negative-to-positive inductive anomaly.

The galvanic component within the LEROI data decreased by at least 50% between windows 6 (0.445 ms) and 10 (0.995 ms) for both Loops 1 and 3. Thus, the apparent broadening of the Station 380 anomaly noted within the field data may well be a similar type transition from a predominantly galvanic to inductive response. Indeed, if the edge of the mineralisation near Borehole ID3418 is more tenuous, and so of lower conductance, than the central region of the body, it would be expected that an anomaly due to current channelling would be 'sharper' than an anomaly arising from induction alone.

The downhole magnetometric resistivity (DHMMR) response of the lower mineralisation (see Figure 8.18) may provide some indication of what the galvanic component of the DHTM response may look like. A sharp negative

anomaly is noted at an axial depth of around 380 m, which implies that the galvanically excited a portion of the mineralisation that is in close proximity to the borehole. It is also noted that the profile of window 6 (0.445 ms) from the Loop 3 DHTEM data set (see

Figure 8.19) is quite similar to the profile of the DHMMR response. This observation may lend itself to the results from the LEROI modelling (see Table 8.2) which show that the galvanic component is most prominent within the Loop 3 data at early times. Note also, that the similarity between the shapes of the positive anomalies centred about Station 100 within both data sets strengthens the argument that the origin of the anomaly within the DHTEM response is primarily galvanic, and possibly due to current channelling within the surface mineralisation.

Finally, the decrease in the relative amplitude of the Station 380 anomaly with Loop 3 is attributable to the decrease in the inductive component. Note also, that the associated OZPLTE response diminishes by a factor of four with Loop 3 (see Table 8.2).

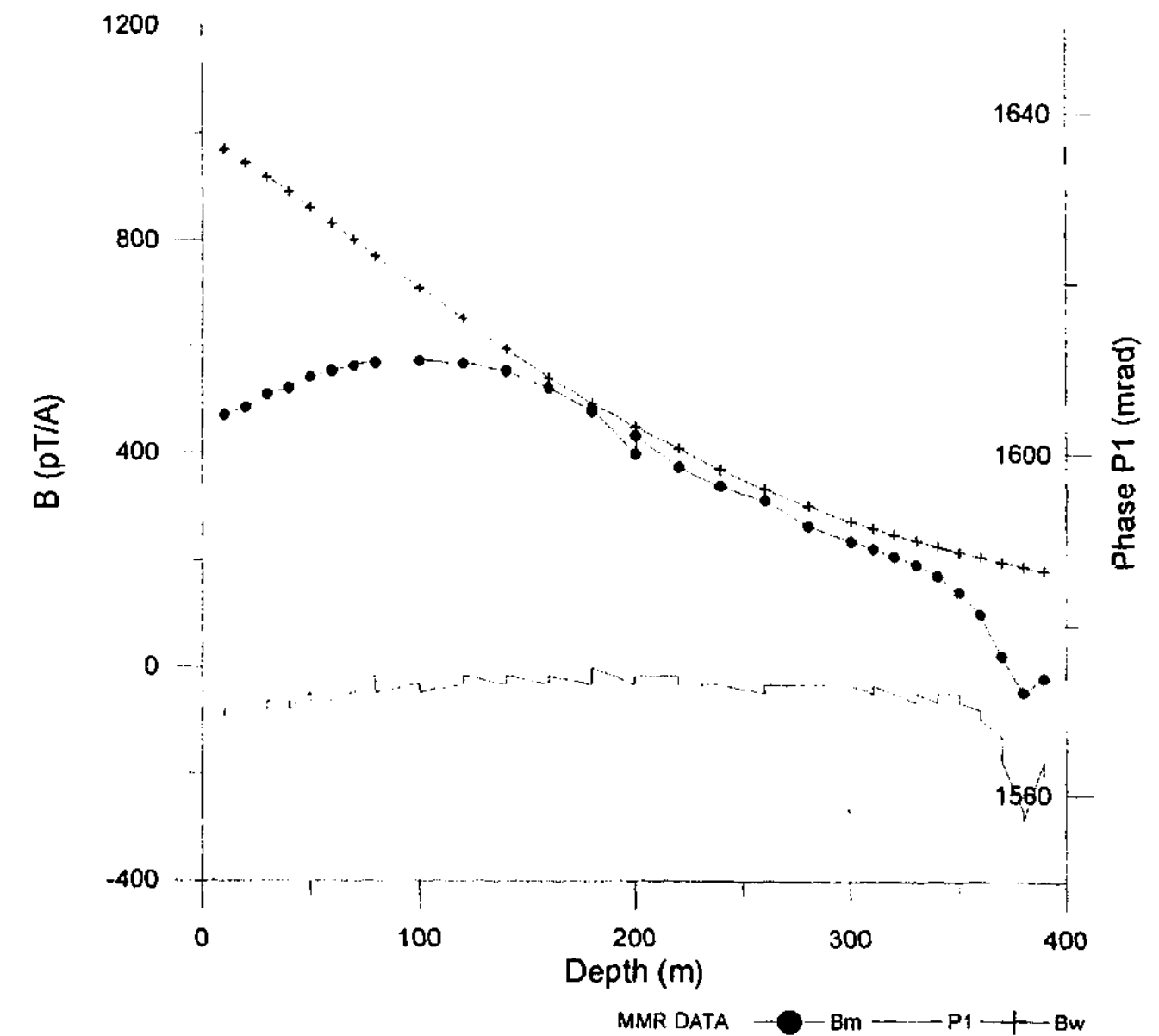


Figure 8.18: DHMMR field response of Borehole ID3418 (See Figure 8.1 for the dipole configuration used within the survey). Measurements were made with a DHTEM probe, and of both the phase (P1) and magnitude, of the transient magnetic field at each station. The magnetic B field data (Bm), was then obtained after the effects of the wire field (Bw), were removed from the converted (dB/dt) response. Refer to Figure 6.4 of Chapter Six for additional information on this related DHMMR surveys.

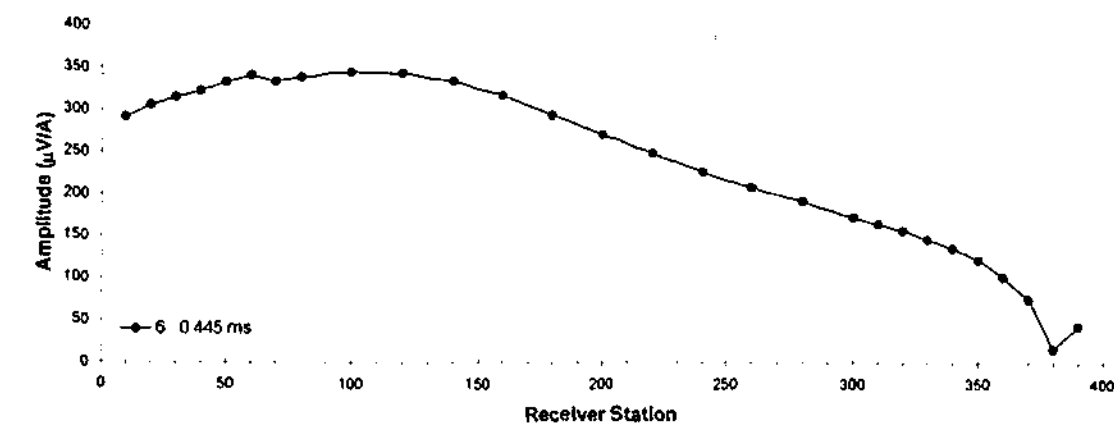


Figure 8.19: Window 6 (0.445 ms) of the DHTEM field response of Borehole ID3418 with Loop 3. Note, the remarkable similarity with the DHMMR profile in Figure 8.18, implying the DHTEM response arose primarily from current channelling effects.

8.7.2. ID3419 FIELD DATA.

The response profiles of the ID3419-Loop 1 data set for the late time windows 10 (0.995 ms) to 15 (2.495 ms) were noted to have a positive peak centred about Station 370, and an assumed positive-to-negative intersection anomaly near Station 400 (See Figure E.1.3b). Profiles of a similar nature were also noted within the Loop 3 response at both early, windows 6 (0.445 ms) to 10 (0.995 ms), and late times, windows 10 (0.995 ms) to 15 (2.495 ms), Figure E.1.4b. In respect to the Loop 1 response, there appears to be a slight broadening of the peak at Station 370 and a downhole migration of the positive-to-negative crossover.

An understanding of the evolution of the field response with a change of loop only became known after the mechanisms within the LEROI models were revealed by means of galvanic stripping. Indeed, the LEROI models (see Section 8.6.2) suggest that the positive peak at Station 370 noted within both the Loop 1 and 3 data sets is the resultant of the superposition of the up-hole portion of a positive-to-negative anomaly, and a positive single signed galvanic anomaly. So that with Loop 3, a predominating galvanic component would both broaden the Station 370 anomaly and force the crossover downhole.

8.8. CONCLUSIONS.

A thin-sheet single plate model was developed with program LEROI for the benefit of the field response of Boreholes ID3418 and ID3419 due to the near and far loops, Loops 1 and 3. Although field data was available for time windows 1 (0.120 ms) to 32 (47.895 ms) and Stations 10 to 400 for both boreholes and loops, the amount of data beneficial for interpretation was restricted to just 10 windows: windows 6 (0.445 ms) to 15 (2.495 ms), and 10 stations: Stations 300 to 390. The single plate model successfully replicated the main features of the field data, namely the composite inductive and galvanic anomalies centred about Stations 370 and 380 within both boreholes. The single plate model, however, did not reproduce the end-of-hole anomalies within the early time - Loop 1 data sets. Unfortunately, decay-curve analysis yielded ambiguous results, thereby hampering estimates on the conductance of the mineralisation. Decay rate matching of the negative anomaly within the late time ID3418 -

Loop 1 data yielded an initial conductance of 55 S. Subsequent profile analysis by amplitude matching, revised the conductance estimated down to 30 S.

A new technique, referred to as galvanic stripping, aided the identification of the excitation mechanisms within the LEROI models. In this method, suppression of the induction currents enabled the inference of the galvanic component of the *Total LEROI* response, or that of the 30 S model. This process entailed lowering the plate conductance to 10 S, yielding the *isolated inductive* component. The *isolated inductive* component could then be immediately determined by subtracting the *isolated inductive* component from the *Total LEROI* response. Comparisons with the associated free-space OZPLTE model response, helped ascertain the degree of success of galvanic stripping. The inability to obtain any unambiguous or consistent results from the decay analysis performed on both the field ID3418 and ID3419 anomalies implied that neither inductive nor galvanic effects predominated; galvanic stripping confirmed that this was at least the case for the model data. This case study has also highlighted the need to consider the response amplitudes in addition to decay analysis in determining the electrical properties of a conductor. The use of anomaly amplitudes as a diagnostic tool arose from the inability to isolate the host, inductive, and galvanic components of the field response.

CHAPTER NINE

CONCLUSIONS.

9.1. THE CADJEBUT CASE STUDY.

The following archival TEM data sets, acquired from the Cadjebut Pb-Zn ore body in 1987, were the subject of interpretation and numerical modelling:

- i. a surface coincident-loop survey conducted along Line E; and
- ii. a downhole TEM survey conducted using Borehole ID159 with an inductively well-coupled near loop (Loop Tx1) and a weakly-coupled offset loop (Loop Tx2).

Both TEM data sets were sourced from the original field report prepared by Lebel (1987). There were two primary objectives for the Cadjebut case study: identification of the underlying mechanisms for both the M-shaped anomaly within the coincident-loop profiles, and the intersection anomaly within the offset loop downhole TEM profile.

Interpretations were carried out by forward modelling with the industry standard software program MARCO (see Section 3.3 for a detailed program description), which is based upon a 3D integral equation method, and was designed to model the EM response of 3D rectilinear prisms in a multi-layered half-space (Raiche *et al.*, 1998b). The choice of the algorithm was based upon its ability to model both inductive and galvanic excitation, and deal with multiple tabular bodies of finite thickness. Three models were constructed: one to represent the surface survey and two to represent the down-hole TEM surveys that utilised Loops Tx1 and Tx2 respectively. All three models employed the same five-layer host and dual-slab target of zero dip and equal resistivities; however, the surface model implemented a target discretization of $8 \times 4 \times 2$ parts and a resistivity of 2.5 ohm.m, whereas the down-hole TEM models implemented a target discretization of $16 \times 8 \times 2$ parts and a more refined

resistivity of 2.45 ohm.m (discretizations refer to the dimensions *strike-length* x *depth-extent* x *thickness*). Specifications for the three models drew upon information acquire from both the surface and down-hole TEM field data sets: inversions of the coincident-loop data, with program GRENDL, yielded layer thicknesses and resistivities for a multi-layered host; whereas profile matching between model and field yielded an estimate for conductivity of the mineralisation. The physical aspects of this dual-slab model, such as thickness and depth extent, were obtained from a previously prepared geologic cross-section within Lebel (1987).

Although the MARCO model produced an M-shaped anomaly, it is not a reproduction of the aforementioned anomaly within the field data; namely, the model failed to duplicate the following attributes:

- i. Decay-rate: the field anomaly persists to much later times.
- ii. Position: the field anomaly sits offset from the mineralisation 50 m to 100 m north of the model anomaly.
- iii. Width: the field and model anomalies have widths of 200 m and 250 m respectively.

Three variations of the original model were trialled in an attempt to match the decay-rates of the field and model anomalies, namely: a decrease in target depth, inclusion of a large conductive body beneath the target, and alteration of the host layer resistivities; each attempt failed. No explanation is currently available for the persistence of the M-shaped anomaly within the field data. Despite these shortcomings, numerical modelling confirmed the findings of Lebel (1987) and Scott *et al.* (1994): that the Cadjebut mineralisation is too weakly conducting for a coincident-loop survey to provide a detectable inductive response.

The Cadjebut Pb-Zn ore deposit is classified as a Mississippi Valley-type (MVT) mineralisation (Scott *et al.*, 1994). The attributes of MVT deposits make them difficult geophysical targets requiring extensive exploration programmes at high cost (Scott *et al.*, 1994). Thus in this context, the benefits gained from implementing survey practices exploiting TEM induced galvanic excitation, by

means of offset loops, are immediately recognised (Theodoridis and Asten, 2001).

Although the origin of the M-shaped anomaly within the field data remains unknown, some understanding of a possible mechanism for its production was inferred from the MARCO model, in which its resulting M-shaped anomaly could be described in terms of the "smoke ring" concept. It appears that as currents are induced within the model target, they will diffuse and expand without restriction until a conductivity boundary is encountered. Thus, the coincident loop response will be greater at the edges of the slab than over its interior, thereby accounting for the M-shaped anomaly (see Section 5.5.1).

The 3D dual-slab MARCO model successfully reproduced the essential features of the downhole TEM field data: the inductively well-coupled loop (Loop Tx1) overlying the target yielded a null response, and the adjacent loop (Loop Tx2) that lay offset to the target yielded a strong intersection anomaly (see Section 5.4.2).

Decay-curve analysis confirmed galvanic excitation as the mechanism responsible for the offset loop response within both the field and model Tx2 data. Specifically, the *scattered galvanic anomalies* within both data sets decayed by a power law, with decay indices -3.27 (field) and -3.47 (model) (see Section 5.4.3). These values are in excellent agreement with the theoretical decay index of -3.5 as shown by Asten (1991a) for current gathering phenomena (see also Section 4.3 for an elaboration of the theory of galvanic decay-curve analysis).

The term *scattered galvanic anomaly* in the current context refers to the *estimated galvanic response* computed by subtracting the *background response* from the *total response*. Although effects due to induction will contaminate the scattered galvanic response if present, no evidence of inductive excitation within the model or field data was found. In respect to the model data, the background or layered earth response was computed directly by running the model in absence of the dual slab target. In respect to the field data, however, the regional response within the vicinity of the deep galvanic anomaly was

estimated by extrapolation of the assumed regional response that occurred at a shallow borehole depth.

The TEM induced galvanic response within the model Tx2 data features a composite negative-to-positive anomaly superimposed upon a broad negative single signed anomaly. Although this feature is also present within the near loop Tx1 model profiles, it is greatly enhanced within the offset loop Tx2 data.

Modelling each slab in isolation revealed that the upper slab of the target produced a negative-to-positive intersection anomaly, the peaks of which were dependent upon the thickness of the slab. Whereas, the lower slab produced a prominent broad negative single signed anomaly, whose width was directly proportional to the distance from the edge of the slab to the borehole (see Section 5.4.5).

Representing the galvanic currents as anomalous poloidal current streams within each slab, and studying the axial component of the associated secondary fields at each receiver station, permitted an understanding of the effects of current gathering within the dual-slab target. Refer to Section 5.4.5 for further discussion on the mechanisms responsible for the formation of each of the model anomalies.

9.2. THE FLYING DOCTOR CASE STUDY.

Downhole TEM surveys were performed at the Flying Doctor lead-zinc deposit, situated North of Broken Hill, New South Wales. The upper and lower massive sphalerite galena lenses of the deposit, were each surveyed with a pair of boreholes: ID3071 and ID3039 for the upper lens, and ID3418 and ID3419 for the lower lens, utilising the same inductively well-coupled and long-offset transmitter loops, Loops 1 and 3 respectively. Thus, four independent data sets were acquired for each lens. Although downhole MMR surveys were also conducted, they were regarded to be of only secondary importance to the project. The Flying Doctor case study is divided into two parts: the upper lens of the deposit is discussed within Chapter Six, and the lower lens in Chapter Eight.

Interpretations carried out for the downhole TEM field data involved forward numerical modelling using the industry standard thin-sheet modelling software, program LEROI. These models were, in respect to both the upper and lower lenses, in agreement with the known geology. Inversion of field data is not possible with program LEROI. A summary of the key results and modelling techniques developed within the case study are provided below. The fundamental finding of the Flying Doctor case study, however, shall be stated from the outset: induction was the prominent mode of excitation within the near-loop data of both lenses, but its relative contribution to the field response was diminished with use of the far-loop, permitting galvanic effects to dominate.

9.2.1. THE FLYING DOCTOR DEPOSIT: UPPER LENS.

A composite thin-sheet model was assembled within program LEROI for the upper lens of the Flying Doctor deposit. Conflicting estimates obtained for the conductivity and depth extent of the upper lens, and the subsequent inference that the upper lens was comprised of a highly conductive core and a weakly conducting expanse or halo, motivated the development of the composite modelling technique.

Traditionally, the solution to a problem such as this involved the construction of a hybrid model: a free-space model represents the inductive response component, and current filaments or ribbons approximate the galvanic response. In contrast to the traditional approach, the composite modelling technique possesses an important quality: any discrepancies that may arise between inductive and galvanic interpretations will be intrinsic to each particular excitation mechanism, rather than computational artefacts arising from the differing procedures adopted to interpret each response component.

The composite modelling technique was applied to the upper lens in a three-stage process, an overview is provided below.

Stage One: Analysis of the field data

Profile analysis of the field data began with identifying the excitation mechanisms responsible for each anomaly (see Section 6.2). Response attributes consistent with a dipolar or unipolar secondary field source indicated inductive or galvanic excitation respectively. Cross correlation of the field data with the model data verified the results of the initial profile analysis; decay-curve analysis confirmed the underlying excitation mechanisms within the models (see Section 6.3).

The following interpretational techniques facilitated the identification and isolation of the inductive and galvanic components of the upper lens TEM response:

- i. A classification scheme was devised for the field data (see Section 6.3.1), in which the response profiles were categorised into four time window sets (see Table 6.1) in recognition of the evolution of the field response from one dominant mode of excitation to another. In brief, galvanic effects were found to dominate a response at early to middle times, whereas inductive effects dominated at late times.
- ii. Shape correlation between anomalies within the TEM and associated MMR response profiles aided the identification of the galvanic components within the field data (see Section 6.3.2.1 and Section 6.3.4). This technique

exploits the spatial similarity between the electric field distributions, established by an aperiodic VMD and a MMR dipole, in the vicinity of a localised conductivity inhomogeneity or target, and the subsequent galvanic anomalies, which are comparable in form, that arise from the gathering of the respective induced host currents by that target.

Stage Two: Model Construction

Representation of the upper lens TEM response required the development of two independent single plate models: a high conductivity plate (Plate 1) and a low conductivity plate (Plate 2) of greater depth-extent; these models matched the inductive and galvanic components respectively of the near loop field response for Boreholes ID3039 and ID3071. Refer to Section 6.3.1 for a full account of the development of Plate 1, and Section 6.3.2 for Plate 2.

Stage Three: Synthesis of a composite response

A composite model response was synthesised by the linear superposition of the host and scattered response of each plate (see Section 6.5.3). The completed model response adequately matched the field data; it featured the evolution of the target response from being predominantly galvanic to predominantly inductive, and an intermediate stage in which neither mode of excitation dominated, exhibiting the transition of the response from one state to another. Attempts to combine both plates in a single multiple plate system within program LEROI yielded erroneous results (see Section 9.3 for further discussion).

Theoretical justification of linear superposition in TEM

Despite the occurrence of complex interactions between a target and its host medium, interpreters, have for the most part, been successful in the practice of removing the regional component, by simple subtraction, from a combined host-target TEM response (McNeill *et al.*, 1984). This concept of linear superposition was employed within the composite modelling technique, and extended to the representation of a target response as the summation of two

independent and distinct components; namely inductive and galvanic. McNeill *et al.* (1984) took a similar approach and successfully synthesised the TEM response of a plate within a conductive earth by summing the host and target response; the latter of which was obtained by superposing the inductive and galvanic components approximated by a simple current loop and a distribution of current dipoles respectively. This application of linear superposition, to estimate the scattered response of a target, was noted by McNeill *et al.* (1984) to be valid for particular target geometries and over certain time ranges. However, development of the composite modelling technique depended upon the assumption that two plates, of high and low conductance, shall only exhibit a weak inductive interaction. Moreover, Nabighian and Macnae (1991) noted that although the interactions that occur between vortex and galvanic currents are in general of a complex nature, they are nonetheless weak.

Ramifications for future interpretations

Based upon the experience of the upper lens of the Flying Doctor deposit, it would be prudent for interpreters to recognise and state as to whether the depth extent of a mineralisation, derived from a downhole TEM survey, is inferred from either the inductive or the galvanic component of the response.

Inductive excitation tends to illuminate only the highly conductive portions of a mineralisation, whereas methods utilising current gathering will tend to detect any additional expanse of weakly conducting material, and so will in general appear larger. It should also be stressed, that inductively or galvanically inferred depth extents are electrical interpretations of a mineralisation, these and additional physical properties derived from which may in turn differ from the known geology.

9.2.2. THE FLYING DOCTOR DEPOSIT: LOWER LENS.

A robust thin-sheet single plate model, utilizing a homogeneous half-space, was constructed within program LEROI for the benefit of the field response of Boreholes ID3418 and ID3419 due to Loop 1 (near loop) and Loop 3 (long offset loop), for selected time windows and stations. Despite the availability of field

data for time windows 1 (0.120 ms) to 32 (47.895 ms) and Stations 10 to 400 for both boreholes and loops, interpretations were restricted to windows 6 (0.445 ms) to 15 (2.495 ms), so as to exclude early time effects and late time noise (see Section 8.3.1), and Stations 300 to 390, so as to isolate the deep-hole response of the lower lens (see Section 8.3.2). A single plate model sufficed, for unlike the upper lens, the lower lens possessed a homogenous conductivity distribution. Refer to Section 8.3 for model specifications and Section 8.4 for discussion of results.

The termination of Boreholes ID3418 and ID3419 at the lower lens prevented the capture of its entire response profiles (see Section 8.3.3). Incomplete target anomalies inhibited identification and isolation of the inductive and galvanic components, thereby hindering model development: notably the plate conductance, depth extent and dip were poorly constrained.

Additional complications arose in respect to conductance estimates for the lower lens. The field data proved notoriously resistant to any unambiguous and thus meaningful decay-curve analysis, without which the fundamental time constant of the inductive decay could not be determined. Decay-curve analysis yielded a significantly larger conductance of 55 siemens compared with the 30 siemens deduced from profile amplitude matching alone (see section 8.4.3). Decay-curve analysis proved unsuccessful in this situation due to the contamination of the downhole TEM field response with a residual galvanic response and, to a lesser degree, host response. It was not possible to remove either the host or galvanic response components.

Idealistically, one performs decay-curve analysis on the scattered field response of a target anomaly that is either solely inductive or galvanic in origin. In general, however, decay-curve analysis is still practicable for situations where a regional or host response is present, but insignificant relative to the component of the predominating excitation mechanism. In situations where a TEM response consists of a significant regional, inductive and galvanic component, it is necessary but difficult to isolate the governing relations of each excitation mechanism within the decay curve of the total response. Consequently, the associated diagnostic parameters of each excitation

mechanism within a composite response will often remain undetermined; such was the case for the ID3418 and ID3419 downhole TEM data sets.

Galvanic Stripping of model data

Whilst conducting interpretations of the downhole TEM field data of both the upper and lower lens, a reliable means of gauging the relative contributions of the galvanic and inductive components within the near-loop and offset-loop field data sets was sought.

Preliminary interpretations of field data began with identifying any fundamental changes within the response profiles, for each borehole, with a change of loop. Differences within profile structure often reflected a change in excitation mechanism, or an alteration in the inductive coupling between the target and transmitter. Studies of models that replicated the field data provided insight into the processes involved in the formation of the field response.

A novel technique referred to as galvanic stripping, developed with program LEROI, aided the identification and isolation of both the inductive and TEM induced galvanic components within a model response (see Section 8.6). This technique proved valuable in studying the evolution of the isolated galvanic and inductive components in respect to time, and the dependence of these components with loop position. Determining the relative inductive and galvanic components in terms of percentages of the total model response, permitted a quantitative validation that galvanic effects predominate at early times, and that long-offset loops will enhance TEM induced current gathering (see Table 8.2 of Section 8.6.2).

9.3. INDUSTRY SOFTWARE TESTS.

Limitations were identified for the industry software LEROI, with numerical instabilities documented for the following cases: multiple plate systems in which the plates are in close proximity to one another; and, single plate systems where the dimensions of the cells of discretization were less than 10 m (see Chapter Seven). The chaotic behaviour of program LEROI documented for multiple plate systems, include:

- i. Sign reversals of the inductive components; and
- ii. highly non-linear interactions between closely spaced plates (in respect to discretization), resulting in unrealistically large inductive response amplitudes.

Instabilities associated with discretization disrupted both the galvanic and inductive components of the model response; reduction of the plate-to-borehole distance aggravated these problems.

Recommendations

Whilst modelling multiple plates within LEROI it is advisable that the user keeps the ratio of cell size to separation distance between adjacent plates, and that between the plates and the borehole receiver, as small as possible. Any attempt to minimise this ratio by indefinite reduction of cell size will incur instabilities, thereby imposing a lower limit upon the plate-to-plate and plate-receiver distances.

9.4. CONCLUDING REMARKS.

The Cadjebut and Flying Doctor case studies confirmed the effectiveness of downhole TEM surveys in the exploration of weakly conducting mineralisations, whilst also providing further validation that long-offset loops can enhance TEM induced current gathering within a target. Two important capabilities of the downhole TEM method were demonstrated; namely the ability to:

- i. detect a weakly conducting target which is otherwise non-responsive to traditional inductive based methods; and
- ii. delineate the true geologic extent of a partially conducting target which is comprised of a conductive core and weakly conducting extension.

In addition to this, the following interpretational aids were developed:

- i. the composite modelling technique, which permitted the representation of a partially conductive target by superposing the scattered response of two thin-sheets of high and low conductance; and
- ii. the method of galvanic stripping, which enabled the percentage contribution of the inductive and galvanic components within a target model response to be determined.

Moreover, the case studies illustrated how a galvanic component within a target TEM anomaly can be isolated, modelled and interpreted, permitting the acquisition of valuable diagnostic information.

In summary, one may recognize three types of conductors: highly conducting; partially conducting, *i.e.*, highly conductive core with a poorly conducting halo or expanse; and entirely weakly conducting. The first type of target is ideal for inductive TEM techniques (see Section 1.1); however, the Flying Doctor deposit case study of the upper lens demonstrated, by means of a dual-plate model, the ability of the downhole TEM method to delineate a partially conducting target. The Cadjebut case study demonstrated, by the mechanism of TEM induced galvanic excitation, the ability of the downhole TEM method to detect an entirely weakly conducting mineralisation that is non-responsive to inductive excitation.

APPENDIX A

APPENDIX A.1: SYMBOL LISTING.

Table A.1: Some common symbols used within electromagnetic theory and their SI units. (Sourced from Hayt, 1981; Lorrain and Corson, 1990).

PHYSICAL QUANTITY.	SYMBOL.	DIMENSIONS.	PHYSICAL QUANTITY.	SYMBOL.	DIMENSIONS.
Electric field intensity:	E	[V.m ⁻¹]	Electric (Displacement/Flux Density):	D	[C.m ⁻²]
Magnetic field intensity:	H	[A.m ⁻¹]	Magnetic (Induction /Flux Density):	B	[T]
Magnetisation:	M	[A.m ⁻¹]	Electric Polarisation:	P	[C.m ⁻²]
Total volume charge density:	ρ_T	[C.m ⁻³]	Total current density:	J_T	[A.m ⁻²]
Permittivity:	ϵ	[F.m ⁻¹]	Permeability	μ	[H.m ⁻¹]
Relative permittivity:	ϵ_R	-	Relative permeability:	μ_R	-
Permittivity of vacuum:	ϵ_0	[F.m ⁻¹]	Permeability of vacuum:	μ_0	[H.m ⁻¹]

APPENDIX B

APPENDIX B.1: LEROI - PROGRAM VERSION.

- IMPLEMENTED WITHIN PROJECT:

Version 5.0 June 1997

- PREVIOUS RELEASES:

Version 4.0 1996

- RELEASED BY:

*Cooperative Research Centre for
Australian Mineral Technologies; CRC AMET.
Mathematical Geophysics Group.
Macquarie University, NSW 2109, Australia.*

PROGRAM MANAGER:

Dr Art Raiche

RESEARCH STAFF:

Dr Fred Sugeng

Dr Zonghou Xiong

LEROI was released for the use of sponsors of AMIRA project P223C.

APPENDIX B.2: MARCO - PROGRAM VERSION.

- IMPLEMENTED WITHIN PROJECT:

Version 2.6 June, 1998

Version 2.3p January, 1998

- PREVIOUS RELEASES:

Version 2.2 October, 1997

Version 2.1 May, 1997

Version 2.0 October, 1996

Version 1.2 February, 1996

Version 1.1 September, 1995

- RELEASED BY:

Cooperative Research Centre for

Australian Mineral Technologies; CRC AMET.

Mathematical Geophysics Group.

Macquarie University, NSW 2109, Australia.

PROGRAM MANAGER:

Dr Art Raiche

RESEARCH STAFF:

Dr Fred Sugeng

Dr Zonghou Xiong (Primary author of MARCO)

MARCO was released for the use of sponsors of AMIRA project P223D.

APPENDIX C

APPENDIX C.1: DISCRETIZATION OF THE MARCO MODEL.

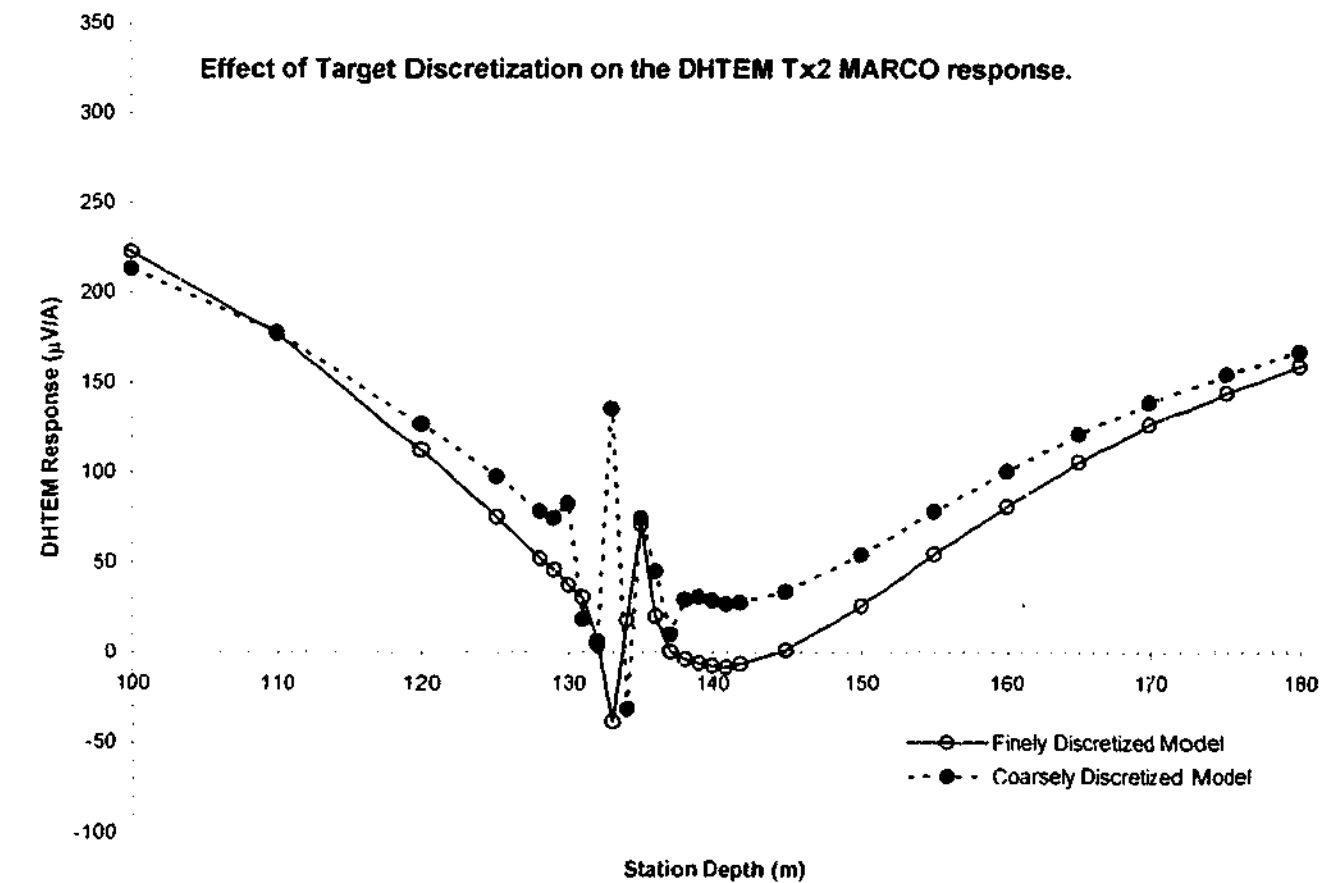


Figure C.1.1: Comparison profiles illustrating the effect of insufficient discretization of the target adopted for the downhole TEM MARCO model representing the Cadjebut mineralisation. The response of the coarsely discretized target exhibits chaotic oscillations between Stations 128 and 142, whereas the response of the finely discretized target features a well-defined negative-to-positive intersection anomaly centred about Station 134, superimposed upon a prominent, and slightly more enhanced, negative galvanic anomaly centred about Station 140. These comparison profiles were prepared for window 1 (0.474 ms). (Refer to Section 5.3.4 for relevant discussion).

COARSELY DISCRETIZED MODEL.

No. of Cells: 8 x 4 x 2.

Upper Slab Cell Size: 50 m x 41.25m x 2 m.

Lower Slab Cell Size: 50 m x 25 m x 2 m.

FINELY DISCRETIZED MODEL.

No. of Cells: 16 x 8 x 2.

Upper Slab Cell Size: 25 m x 20.625 m x 2m.

Lower Slab Cell Size: 25 m x 12.5 m x 2 m.

(Dimensions stated as *strike-length x depth-extent x thickness*)

APPENDIX C.2: MARCO EXECUTION TIMES.

Table C.2.1: Execution times for the downhole and coincident-loop MARCO models discussed within Chapter Five; a reduction in execution time by a factor of six is observed for the Pentium 4 processor. Note that two downhole TEM models were computed for each loop: models Tx1-a and Tx2-a implemented the same station spacings as the field data, whereas models Tx1-b and Tx2-b implemented spacings of 1 m from Stations 128 to 142 so as to fully resolve the galvanic anomaly (see Figures 5.10 and 5.11 for the responses of models Tx1 and Tx2 respectively; see Figure 5.9 for the responses of model Line E).

MARCO MODELS.	COMPUTER PROCESSOR AND PLATFORM.	
	PENTIUM II - 233 MHZ. WINDOWS 95.	PENTIUM 4 - 2.8 GHZ. WINDOWS XP.
<i>DOWNHOLE TEM MODELS.</i>		
Tx1-a	3h24m	34m
Tx1-b	-	30m
Tx2-a	3h22m	33m
Tx2-b	-	30m
<i>COINCIDENT-LOOP MODEL.</i>		
Line E	-	5m

APPENDIX C.3: THEODORIDIS AND ASTEN (2001).

Published peer-reviewed paper:

Theodoridis, J.A., and Asten, M.W., 2001. Galvanic excitation of the Cadjebut Pb-Zn ore body: Extended Abstracts of the ASEG 15th Geophysical Conference and Exhibition, 5-8 Aug. 2001, Exploration Geophysics, v. 32, p. 176-180.

Galvanic excitation of the Cadjebut Pb-Zn ore body

John A. Theodoridis* Michael W. Asten*

Key words: downhole transient electromagnetic (DHTEM), borehole, current channelling, galvanic

ABSTRACT

Numerical modelling was used to investigate the results from a downhole transient electromagnetic (DHTEM) test survey, which was performed over the Cadjebut lead-zinc ore body in 1987. Unexpectedly, the response due to the inductively well-coupled near-loop contained no signature of the known ore-body, whilst the response due to the offset loop contained a prominent negative intersection anomaly.

A dual-slab block model representing the known mineralisation was constructed using a 3D integral equation program MARCO. This algorithm was used because it permitted modelling of both inductive and galvanic effects. The response generated from this model for both the near and far loops contained a weak and strong single-signed galvanic anomaly, respectively. Current channelling was recognised as the primary excitation mechanism after consideration of the anomaly sign and verification with decay analysis. Specifically, decay analysis of the anomaly within the offset loop data yielded decay indices $\alpha = -3.27$ and $\alpha = -3.47$ for the field and model data, respectively. These results are in agreement with the decay index identifiable with current channelling, namely $\alpha = -3.5$.

The modelling has demonstrated the importance of offset loops in the production of detectable current channelling effects, which in turn enables the detection of weakly conducting targets which may otherwise be invisible to traditional inductive exploration methods.

INTRODUCTION

Located on the Leonard shelf in north western Australia, the Cadjebut lead-zinc ore body was discovered in 1984 as a direct result of an extensive drilling programme, the high cost of which motivated the testing of several geophysical techniques over the deposit (Lebel, 1987). The three survey types tested were surface EM, downhole transient EM and induced polarisation methods. A preliminary interpretation on the surface EM survey is available within Scott et al. (1994). It is the downhole EM survey for Borehole ID159 with loops Tx1 and Tx2 that is considered here.

In response to these geophysical surveys, research was undertaken to investigate the origins of the underlying mechanisms behind the production of the intersection anomaly found within the offset loop (Tx2) DHTEM survey. The original findings in the report prepared by Lebel (1987) concluded that no anomalies were found within the borehole surveys, and thus the mineralisation was not sufficiently conductive to be detectable by downhole TEM.

Department of Earth Sciences
P.O. Box 28E
Monash University, Victoria 3500

*Masten@math.cmu.edu

Presented here are the results for the numerical modelling of the DHTEM survey conducted for Borehole ID159 with both the near and far loops Tx1 and Tx2.

METHOD AND RESULTS

Time-domain downhole EM

The DHTEM test survey was carried out for Borehole ID159 with two surface (150 m x 150 m) transmitter loops Tx1 and Tx2, see Figures 1 and 2. Measurements were made with an axial-component probe in conjunction with a SIRDTEM MKII receiver. Standard delay times were used and recorded out to window 20 (20,110 ms). The field response was normalised against the transmitter loop current and thus its amplitude is given in units of microvolts per ampere. Finally, logarithmic profiles of the field response due to both Loops Tx1 and Tx2 are shown within Figures 3 and 4, respectively.

Modelling Software

The numerical package used for modelling the DHTEM data was MARCO version 2.6, and was released in 1998 strictly for the use of sponsors of AMIRA project D223D and their authorized agents. The choice in use of this program was made upon its ability to model both galvanic and inductive effects. MARCO is based upon a 3D integral equation method, and is designed to model the EM response of 3D rectangular prisms in a multi-layered half-space (Ranche et al., 1998).

MARCO Model

Physical attributes for the dual slab model representing the ore body were derived directly from both a survey map and drill hole

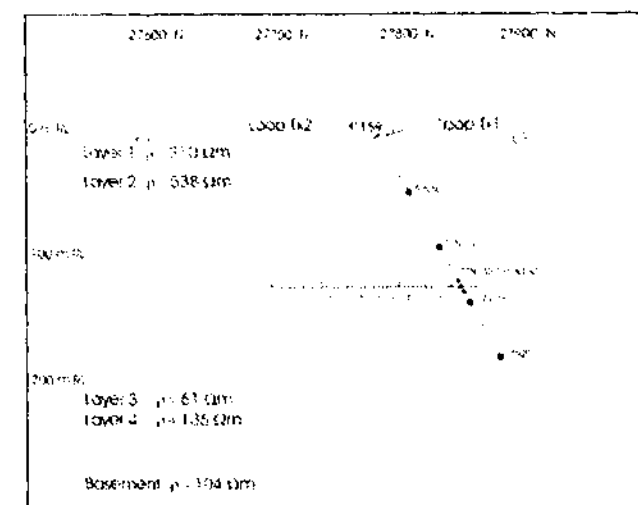


Fig. 1. Borehole section of ID159 with both loops Tx1 and Tx2, showing the MARCO dual-slab model within a five layer earth. Both the upper and lower slabs were 4 m thick and were assigned a resistivity of 2.35 Ohm.

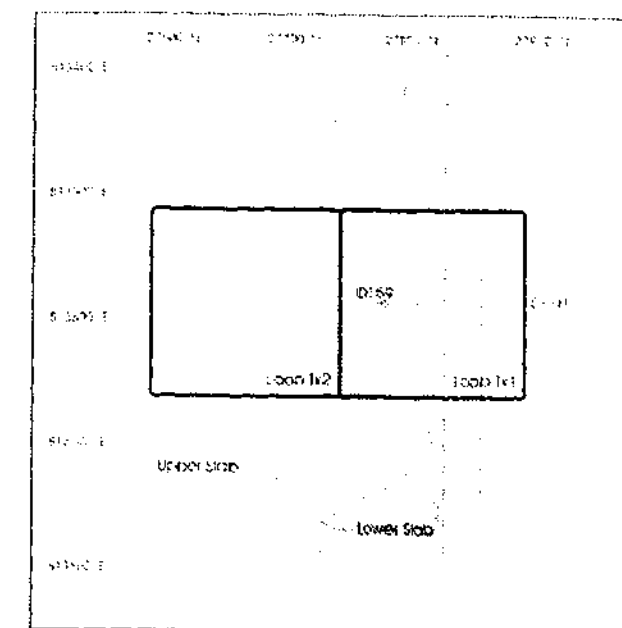


Fig. 2. Survey map showing the position of Transmitter Loops Tx1 and Tx2 and Borehole ID159. The boundary of the lower slab is delineated by the dashed lines. Note, the surface EM survey was performed 396 m to the west of Borehole ID159, and ran North-South over the Cadjebut mineralisation.

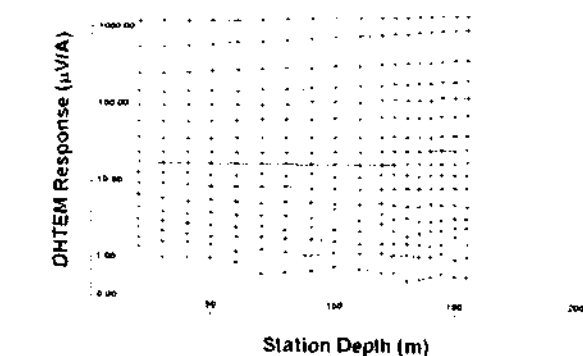


Fig. 3. Logarithmic profile of axial component of field response of Borehole ID159 due to Loop Tx1. The first four time windows are window 1 (0.474 ms), window 2 (0.866 ms), window 3 (1.258 ms) and window 4 (1.650 ms).

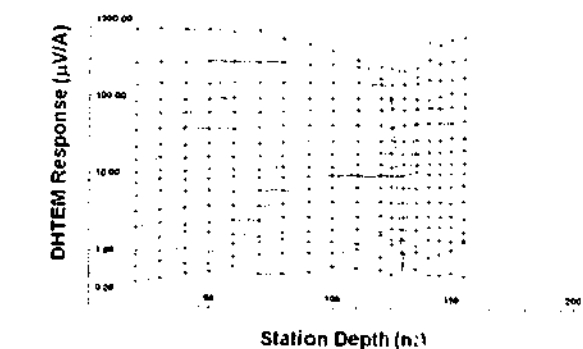


Fig. 4. Logarithmic profile of axial component of field response of Borehole ID159 due to Loop Tx2. See also the associated linear profiles in Fig. 7b.

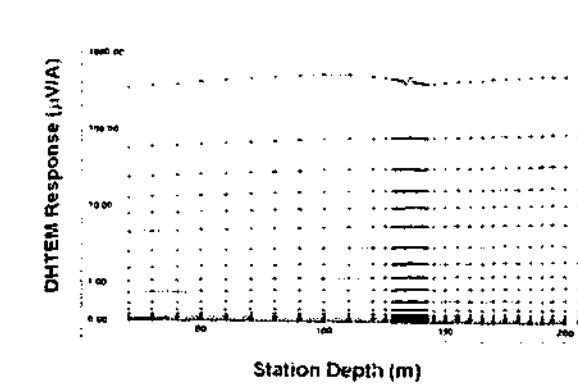


Fig. 5. Logarithmic profile of axial component of the model response for Borehole ID159 due to Loop Tx1.

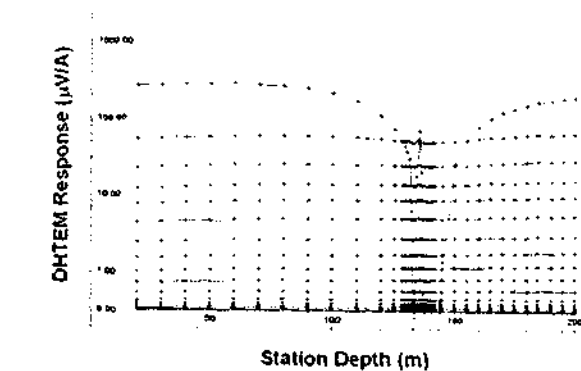


Fig. 6. Logarithmic profile of axial component of the model response for Borehole ID159 due to Loop Tx2. See also the associated linear profiles in Fig. 7a.

cross-section provided within the original test survey report prepared by Lebel (1987). In addition to this information regarding the geology of the Cadjebut mineralisation and the host in which it resides was acquired from a paper by Scott et al. (1994). The resistivities for the layered host were determined by inversion of the surface EM data. Specifications for the model are shown in Figures 1 and 2. It should be noted that although the field DHTEM data was collected down to a borehole depth of just 155 m, Borehole ID159 was artificially extended within the model by 40 m, to a new borehole depth of 200 m, so as to view the entire model anomaly.

Comparison of Model and Field Response

Shown within Figures 5 and 6 are the logarithmic profiles of the downhole TEM model response for Borehole ID159 due to the transmitter loops Tx1 and Tx2, respectively. Comparing these figures with associated logarithmic profiles of the field data (Figures 3 and 4), it is noted that the amplitude of the regional response of the field data is greater by a factor of three than that generated by the numerical model. Despite this, the decay rates of the regional response due to both the model and field data are essentially the same, with the model response decaying only slightly faster. However, the broad features of the field data have been reproduced by the model, namely a null response for the inductively well-coupled loop, Loop Tx1, and a negative anomaly within the response due to Loop Tx2. Specifically, window 1 (0.474 ms) of the model response due to Loop Tx2 features a broad, negative galvanic anomaly centred about Station 140. The fine structure of this anomaly is clearly visible in Figure 7a, in which linear profiles of the first three time windows are shown. Note, that verification of current channelling as the primary

Theodoridis & Asten

Galvanic excitation of the Cadjebut Pb-Zn ore body

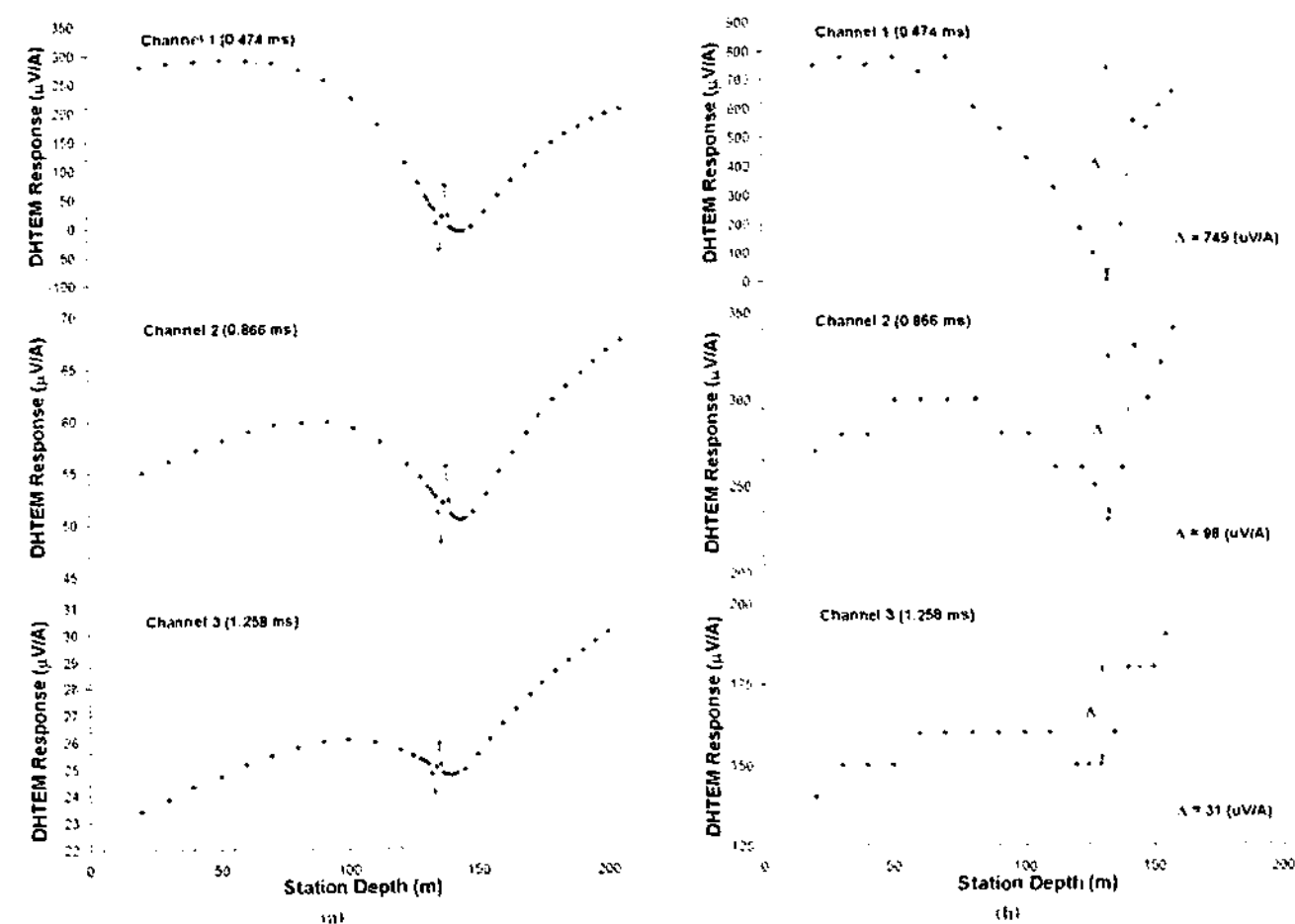


Fig. 7. Linear profiles of the axial component of the model (a), and field (b) response due to Loop Tx2, for time windows 1 (0.474 ms), 2 (0.866 ms) and 3 (1.258 ms). (a) A negative to positive intersection anomaly centred about Station 134 m can be clearly seen, which in turn is superimposed upon a broad negative galvanic anomaly with a minima at Station 140. (b) Again, superimposed upon a broad negative galvanic anomaly, is an apparent negative to positive intersection anomaly at Stations 130, 135 and 140. Unfortunately, due to station intervals of 5 m the structure of the anomaly is poorly resolved. Shown also are the estimated regional profiles (dashed lines), which were used in stripping the field data so as to obtain the scattered anomaly response at Station 130. The scattered anomaly amplitudes have been noted for each time window, and are plotted in Fig. 9.

excitation mechanism was performed by decay analysis, at the minima of the broad anomaly at Station 140, and is discussed later. Superimposed upon this galvanic anomaly, is a well defined intersection anomaly centred about Station 134, and is noted to pass from negative (Station 133) to positive (Station 135). This is to be compared with the galvanic anomaly within the field data, which also appears to possess an intersection anomaly at Stations 130, 140 and 145, see Figure 7b. Unfortunately, the field data was collected with station spacings of 5 m in the vicinity of the anomaly, and so lacks the resolution of the model data which was computed with spacings of 1 m between Stations 128 and 142. Finally, the model response due to transmitter loop Tx1 is also noted to feature a similar composite anomaly as Loop Tx2 but of significantly lower amplitude. This should be compared with the field data for Loop Tx1, where the galvanic anomaly is barely visible. In general, the DHEM field data has been matched adequately, and is believed to be a good example of current channelling.

Verification of Galvanic Response

Assuming the anomaly due to Loop Tx2 is a galvanic response, it would be expected to decay as such. Specifically, the anomaly should be governed by a power law and decay with index $\alpha = -1.5$ (Asten 1991). Unfortunately, the procedure for determining the decay index of the anomaly is not straightforward. The decay

curve generated for the anomaly is not that of its absolute magnitude, but rather the difference between the amplitude of the anomaly and the regional response, i.e. the scattered galvanic response. It is here that the difficulty arises, as identifying a regional response is non-trivial. However, when considering the model data a simple but reliable technique may be employed. Namely the regional response for the model was removed by subtraction of the response of the model without the slabs from the model with the slabs. Thus the scattered galvanic response at Station 140 can be computed immediately. This procedure was applied to the time windows 3 (1.258 ms) to 15 (13.214 ms) and yielded the decay index $\alpha = -3.47$, a value compatible with current channelling, see Figure 8.

The removal of the background response from the field data was performed by graphical means. Shown within Figure 7b are linear profiles of the field data for the time windows 1 (0.474 ms), 2 (0.866 ms) and 3 (1.258 ms), upon which the estimated regional response is sketched (dashed lines). The scattered response of the galvanic anomaly at Station 140, was computed by subtracting the estimated regional from the total field response. Unfortunately, due to the quality of the data the analysis was restricted to these three time windows. A decay curve composed of three data points was obtained, from which the decay index was computed and found to be $\alpha = -3.27$, see Figure 9.

Theodoridis & Asten

Galvanic excitation of the Cadjebut Pb-Zn ore body

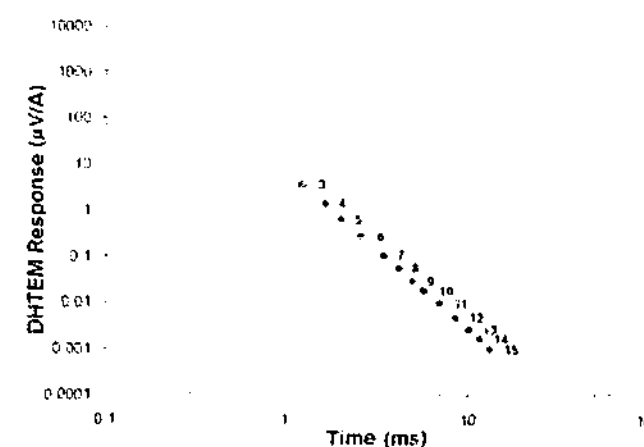


Fig. 8. Log - Log decay plot for stripped MARCO model data at Station 140. A power law (dashed line) with decay index $\alpha = -3.47$ was fitted to time windows 3 (1.258 ms) to 15 (13.214 ms).

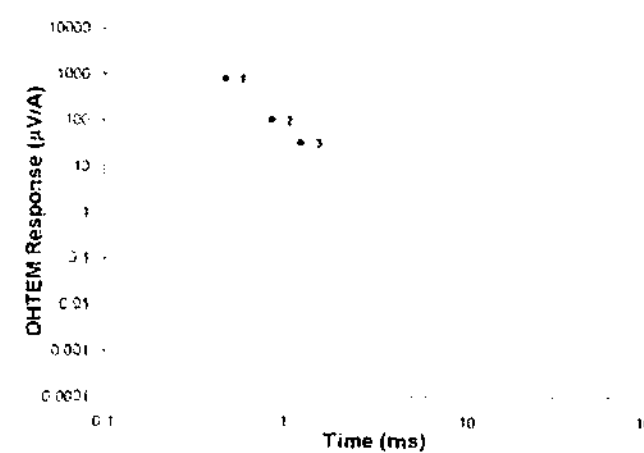


Fig. 9. Log - Log decay plot for stripped field data at Station 130. A power law (dashed line) with decay index $\alpha = -3.27$ was fitted to time windows 1 (0.474 ms) to 3 (1.258 ms).

Some justification is needed for performing decay analysis on the model data with windows 3 and onwards, whilst only using the time windows 1 to 3 for the field data. As can be seen within Figure 8, the decay of the scattered model response at Station 140, is not asymptotically stable at early times. Indeed, if a power law were to be fitted to the time windows 1 to 3, a decay index α of -1.5 would be obtained. Whether the decay of the scattered response of the field data, has approached its asymptotic decay remains uncertain, as analysis at late times was not possible. Moreover, the decay index computed for the field data is subject to error, due to both the poor quality of the data, and the difficulty in estimating the regional response. Nevertheless, the decay analysis performed on both the field and model data, have yielded decay indices which are consistent with that of galvanic excitation.

Proposed Mechanism for the Galvanic Intersection Anomaly due to Loop Tx2

A mechanism for the production of the galvanic anomaly is proposed within the expanded view of the model cross-section, Figure 10. At the time of transmitter shut-off, a current image arises within the conductive earth directly beneath Loop Tx2. Though interactions with its own fields, and in a manner analogous to a 'smoke ring' in air, the current ring will propagate outward and downwards, attenuating in amplitude and diffusing with time

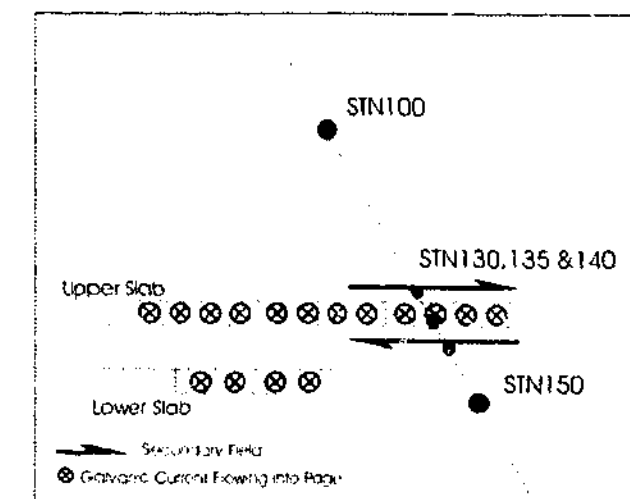


Fig. 10. Schematic diagram illustrating the secondary galvanic fields in the vicinity of the upper slab. The galvanic currents can be approximated as current ribbons flowing into the page. By noting the sign of the field response at the surface of the upper slab, the Loop Tx2 data computed from the MARCO model, can be reasoned to have a negative to positive intersection anomaly centred about Station 135. (Note: A positive up-hole sign convention is adopted here)

Naghian (1979). As the smoke ring expands past the mineralisation, the host currents are gathered into the locally more conductive zones, producing in effect, an anomalous current stream that flows along strike within the body. This anomalous current stream can be understood in terms of a ribbon of current, lying in the plane of the body and directed along strike, or in reference to Figure 10 into the page. Furthermore, the secondary B-fields established by these gathered currents will be unipolar in form, which when viewed from the east as in Figure 10, will circulate in a clockwise fashion around the body.

In the case of the dual-slab model, the anomaly due to Loop Tx2 can be approximated as the superposition of the individual galvanic responses of both the upper and lower slabs. Specifically when modelled in isolation, the top slab was found to produce a sharp intersection anomaly superimposed upon a broad negative anomaly, whilst the lower slab produced only a broad negative single signed anomaly centred about Station 135.

With regard to the production of the lower slab anomaly and in reference to Figure 10, it is immediately apparent that for all stations down the borehole, the axial component of the secondary galvanic field remains negative. Furthermore, the magnitude of the field strength will increase with reduced distance to the body. Thus one would expect the anomaly to peak for the receivers nearest the body, namely Station 135. Finally, the broadness of the anomaly can be attributed to the distance at which the borehole passes the body. That is, the width of the anomaly is expected to decrease as the distance is reduced.

The mechanism, however, for the production of the intersection anomaly due to the upper slab, is best understood by considering what happens immediately before and after the intersection of the borehole with the body. The schematic diagram within Figure 10 shows a representation of the anomalous currents within the upper slab and the secondary B-fields near its surface. Here the anomalous currents are approximated by ribbons of uniform current directed along strike flowing from east to west (into page). For regions on or near the upper slab, the secondary galvanic fields set up by the ribbon of current can be considered to be tangential to the slab surface. In particular, for stations which are in close

Theodoridis & Asten

Galvanic excitation of the Cadjebut Pb-Zn ore body

proximity to the upper slab, the axial components of the tangential fields are reasoned to be directed down-hole above the slab and up-hole below the slab, respectively i.e. to be negative and positive in sign. Thus as the receiver moves down the borehole through the slab, the secondary field response will rapidly change from being negative to positive in sign. Although the borehole intersects the top and bottom surfaces of the upper slab at borehole depths of 131.5 m and 136.1 m respectively, the actual negative and positive peaks occur at stations 133 and 135, within the body itself. Thus the negative to positive intersection anomaly is centred at a depth of 134 metres down the borehole, and has a width comparable to the thickness of the slab.

CONCLUSIONS

We have demonstrated by means of numerical modelling, that although the Cadjebut mineralisation is not sufficiently conductive to be detectable by traditional inductive based DHTM methods, its detection is still possible by means of TEM induced galvanic excitation. Whilst a null response is noted for the inductively well coupled loop, Loop Tx1, a strong negative galvanic anomaly is present within the response due to Loop Tx2 within the field data. This result was attributed to the enhancement of current channelling within the mineralisation due to the offset configuration of Loop Tx2.

During the course of modelling, some important diagnostic features of current channelling have been noted. Unlike inductive methods which allow explicit conductivity estimates to be made i.e. by the use of time constants, galvanic methods can provide subtle but useful information regarding the electrical properties of a target and its host. Due to the absence of an inductive response within the field data, explicit conductivity estimates of the Cadjebut mineralisation could not be made. However, by determining the range of conductivities for the slabs within the MARCO model which yielded an insignificant inductive response, it was possible to obtain an estimate for an upper bound of the target conductance. Once this was achieved, the final slab conductivity for use within the model was chosen so that the amplitude of the resulting galvanic anomaly would match that found within the field data. Thus in brief, the conductance of the Cadjebut mineralisation was estimated by minimising the model inductive response by lowering

the slab conductivity, whilst trying to maximise the galvanic response by means of galvanic saturation.

Due to its unipolar field, current channelling can provide unambiguous information about the target position relative to a borehole. Furthermore, information about the location and possibly even the depth extent of the target could be gained from offset and null response loops. The distance at which a borehole passes the body could be inferred from the broadness of the galvanic anomaly. That is, the width of the anomaly is expected to decrease as the distance is reduced, thus tending to a sharp anomaly on intersection with the body.

Hence, it is concluded, that in cases where traditional inductive methods have failed, optimisation of surveys to enhance DHTM induced current channelling may prove useful in supplementing valuable information regarding the location and electrical properties of weakly conducting ore bodies.

ACKNOWLEDGEMENTS

This research was undertaken as part of the SPIRE project 'Borehole EM for weak conductors' and is supported by the Australian Research Council, BHP Minerals Exploration, North Limited, Pasminco Exploration and MIM Exploration.

REFERENCES

Allen, M.W., 1991. A study of galvanic response to the TEM response of conductive ore bodies. Abstracts of the Australian Soc. of Expl. Geophys. 8th Conference, Sydney, p124.

Label, A., 1987. Geophysical tests at Cadjebut 1987. Surface and downhole MR011 M and IP. BHP Minerals International Exploration Dept.

Nabighian, M.N., 1979. Quasi-static transient response in a conducting half space. An approximate representation. *Geophysics* 44: 1700-1705.

Raiche, A., J. Sogren, and Z. Xiong, 1998. P223 software manual. Description and Use of P223 Software with P223D Updates, prepared for AMIRA project P223-3D.

Scott, R.J., Whiting, T.H. and Turner, R., 1991. *Reflected Geophysics: an exploration for MVT lead-zinc deposits on the Eastern Shelf, Western Australia.* In: Dennis, M.C., Frankowski, K.T., Ho, S.L., Sheppard, E.M., Gimes, P.L.A., Jenck, A., (eds). *Geophysical signatures of Western Australian Minerals Deposits: Geology and Geophysics Department (Key Centre), UWA, Fremantle, The University of Western Australia, Publication 26, and Australian Society of Exploration Geophysicists, Special Publication 7, 32.*

APPENDIX D

[DATA FOR FLYING DOCTOR DEPOSIT - UPPER LENS.]

APPENDIX D.1: DOWNHOLE TEM FIELD DATA.

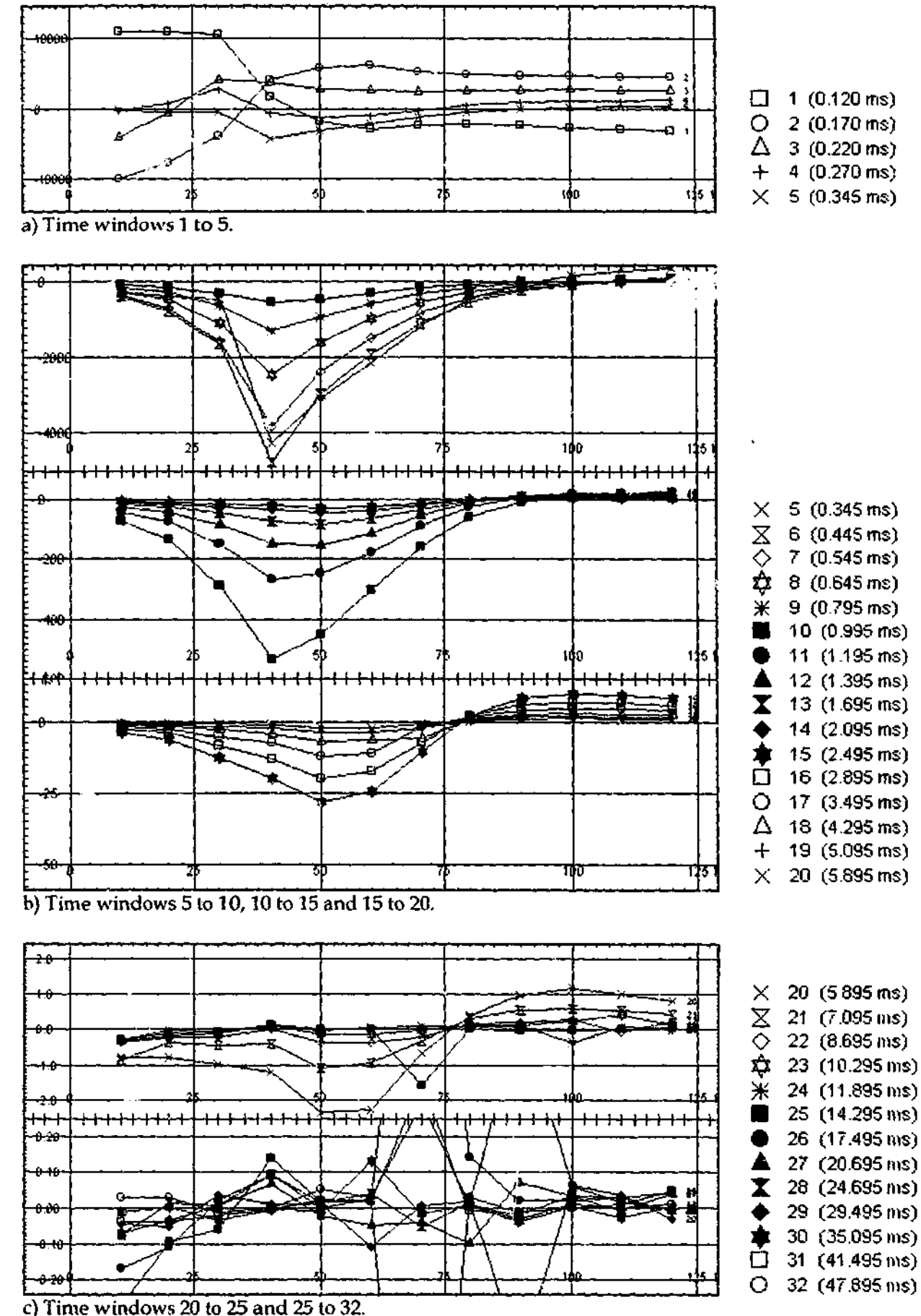
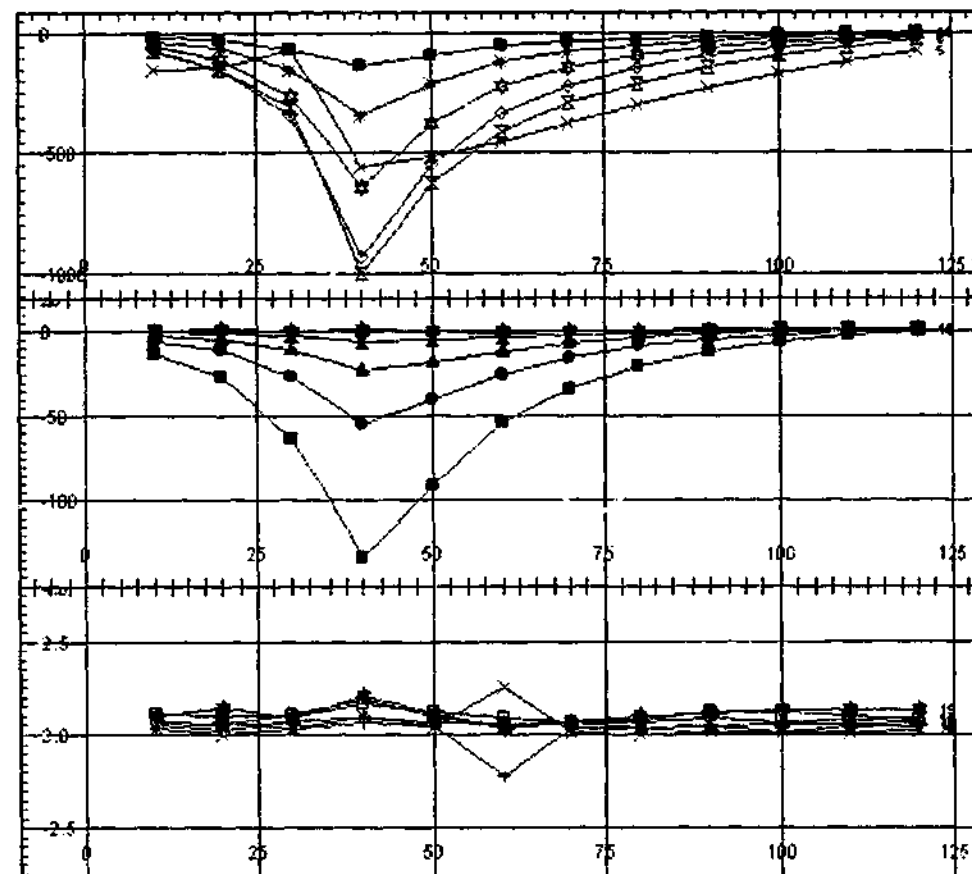


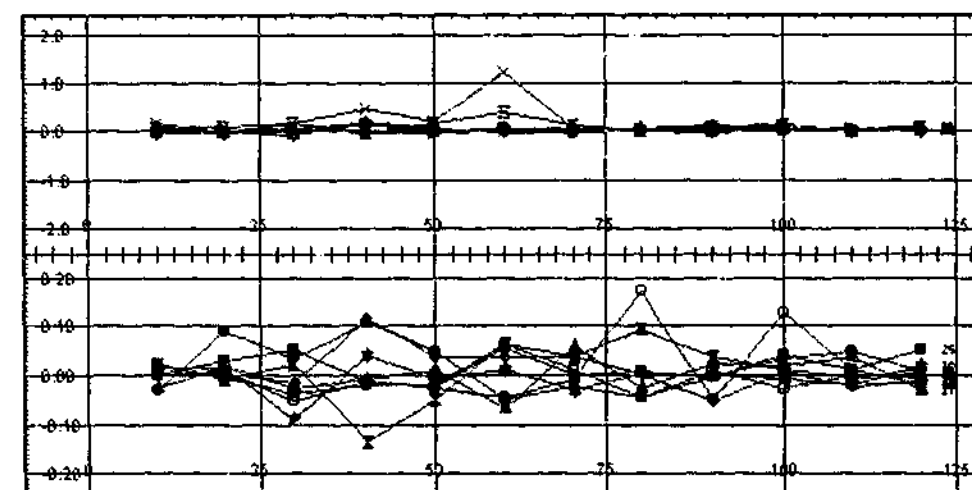
Figure D.1.1: Linear profiles of the axial component DHTM field data for Borehole 1D3039 with Loop 1.



a) Time windows 1 to 5.

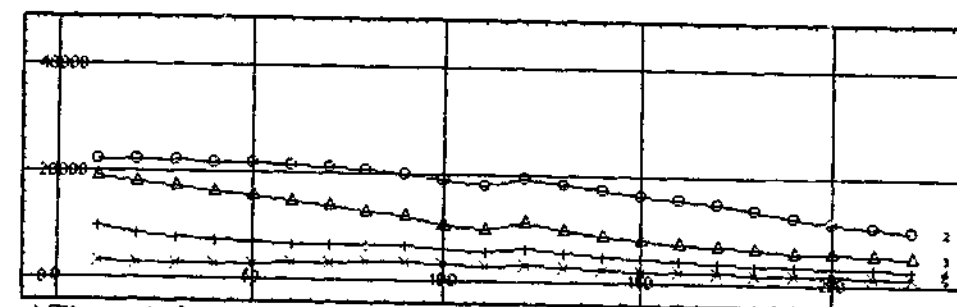


b) Time windows 5 to 10, 10 to 15 and 15 to 20.

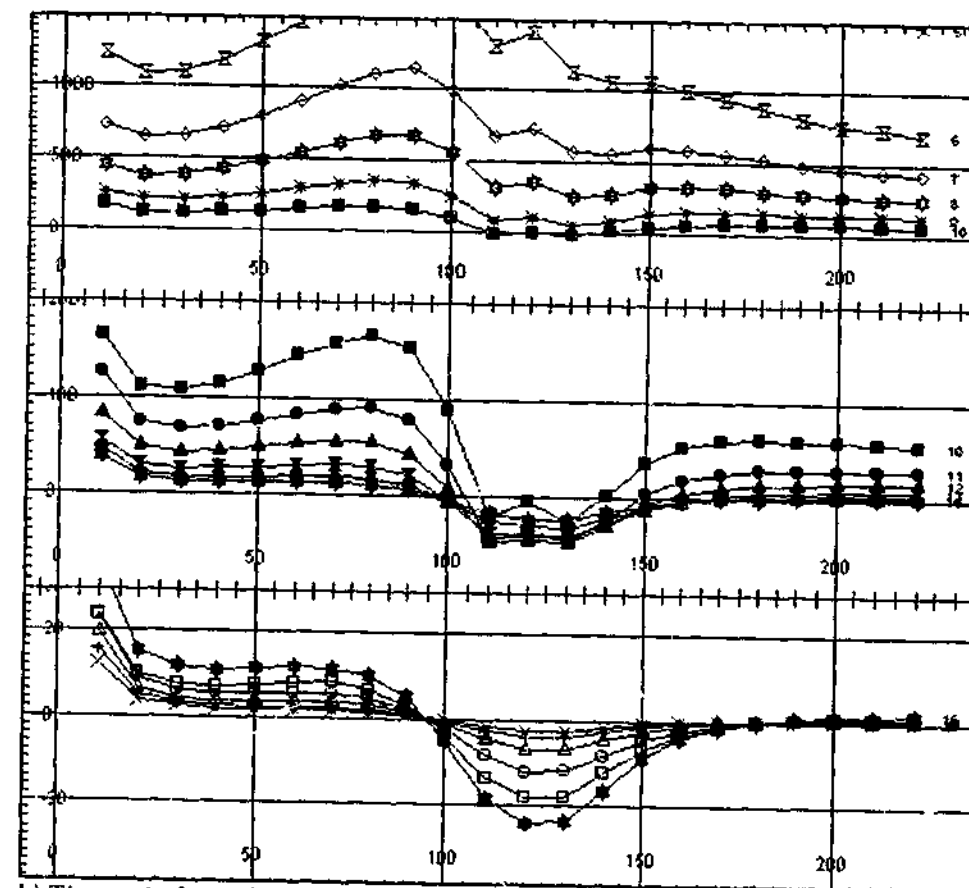


c) Time windows 20 to 25 and 25 to 32.

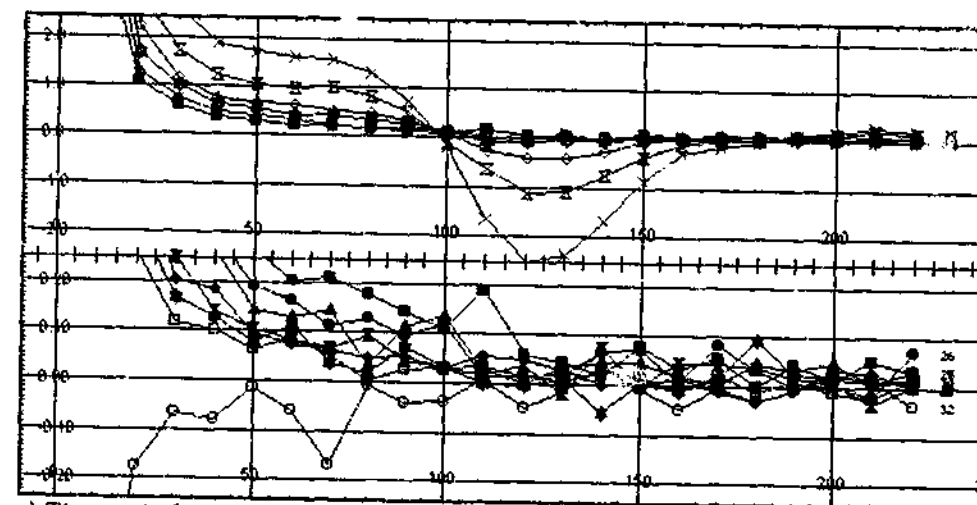
Figure D.1.2: Linear profiles of the axial component DHTEM field data for Borehole ID3039 with Loop 3.



a) Time windows 1 to 5.

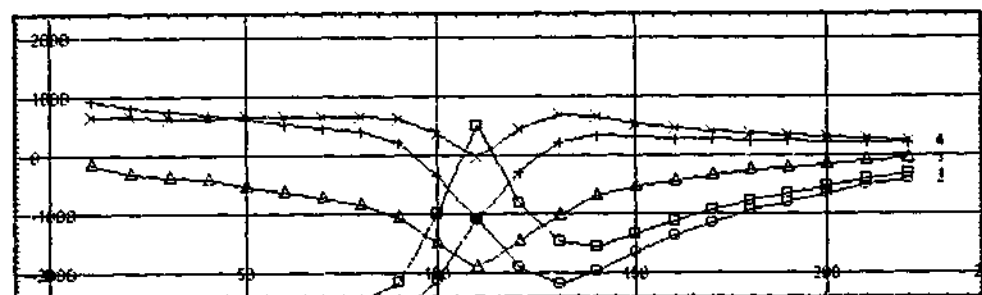


b) Time windows 5 to 10, 10 to 15 and 15 to 20.

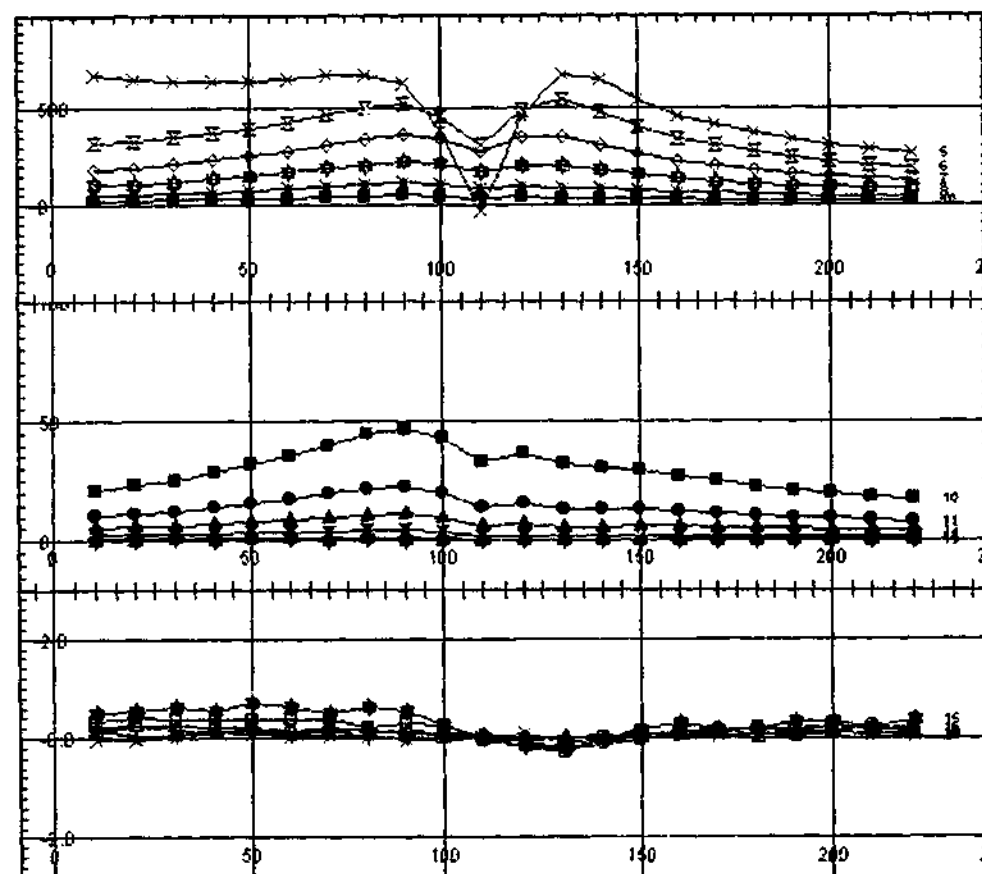


c) Time windows 20 to 25 and 25 to 32.

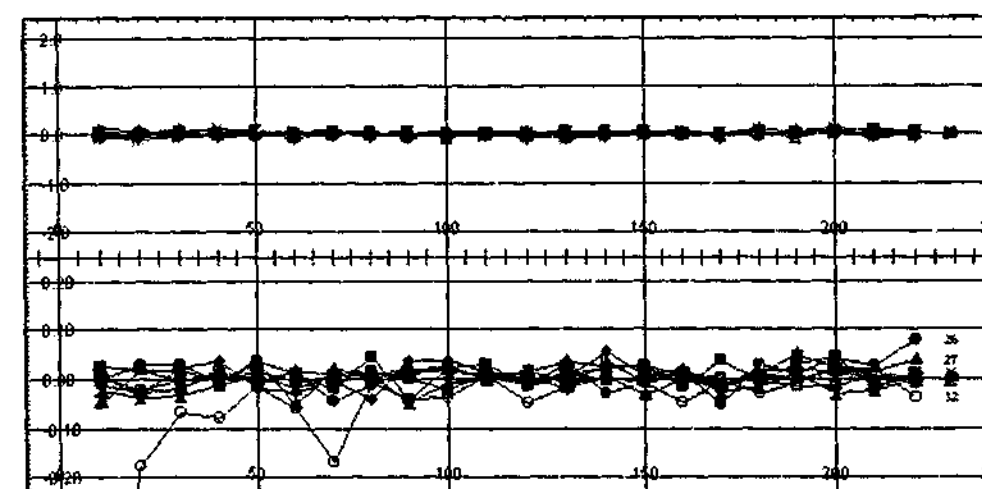
Figure D.1.3: Linear profiles of the axial component DHTEM field data for Borehole ID3071 with Loop 1.



a) Time windows 1 to 5.



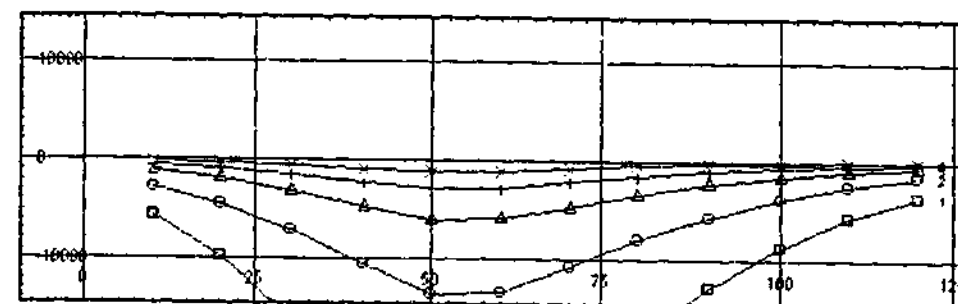
b) Time windows 5 to 10, 10 to 15 and 15 to 20.



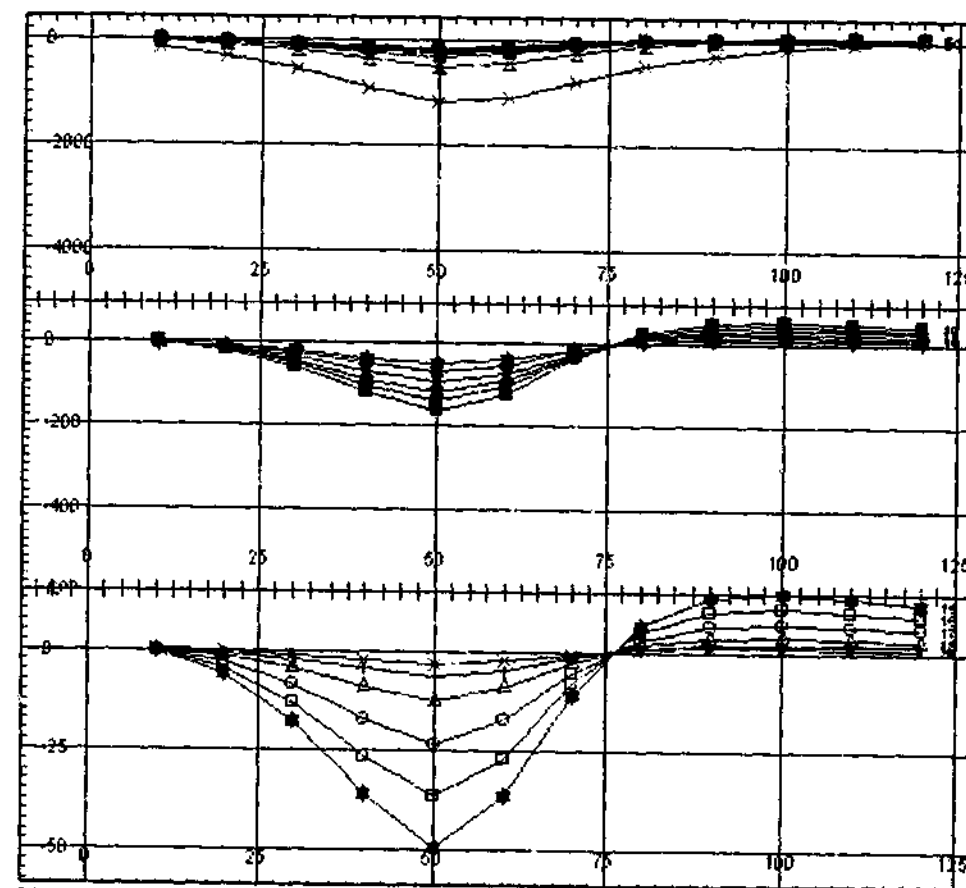
c) Time windows 20 to 25 and 25 to 32.

Figure D.1.4: Linear profiles of the axial component DHTEM field data for Borehole ID3071 with Loop 3.

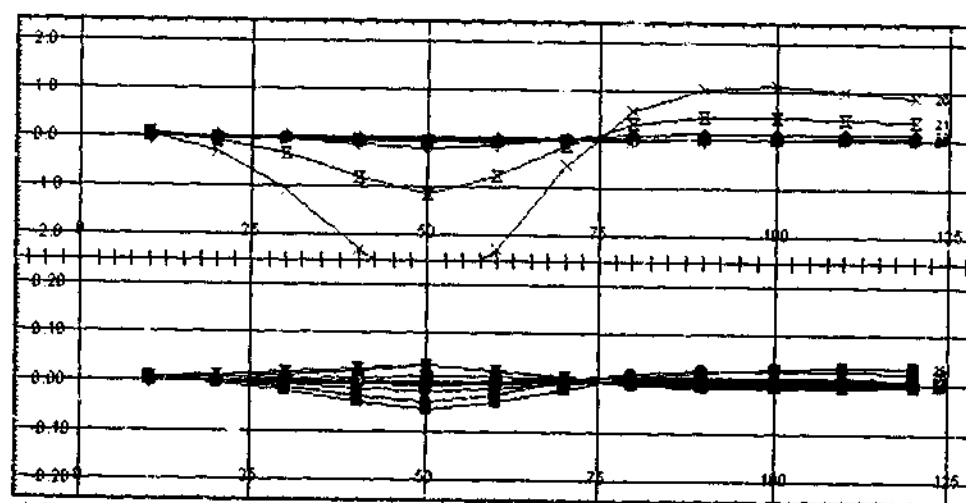
APPENDIX D.2: DOWNHOLE TEM MODEL DATA - PLATE 1.
 (See Table 6.2 for specifications of the dual-plate model)



a) Time windows 1 to 5.

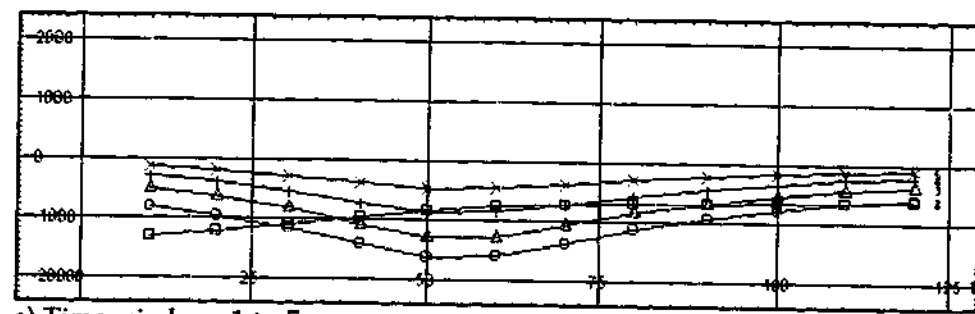


b) Time windows 5 to 10, 10 to 15 and 15 to 20.

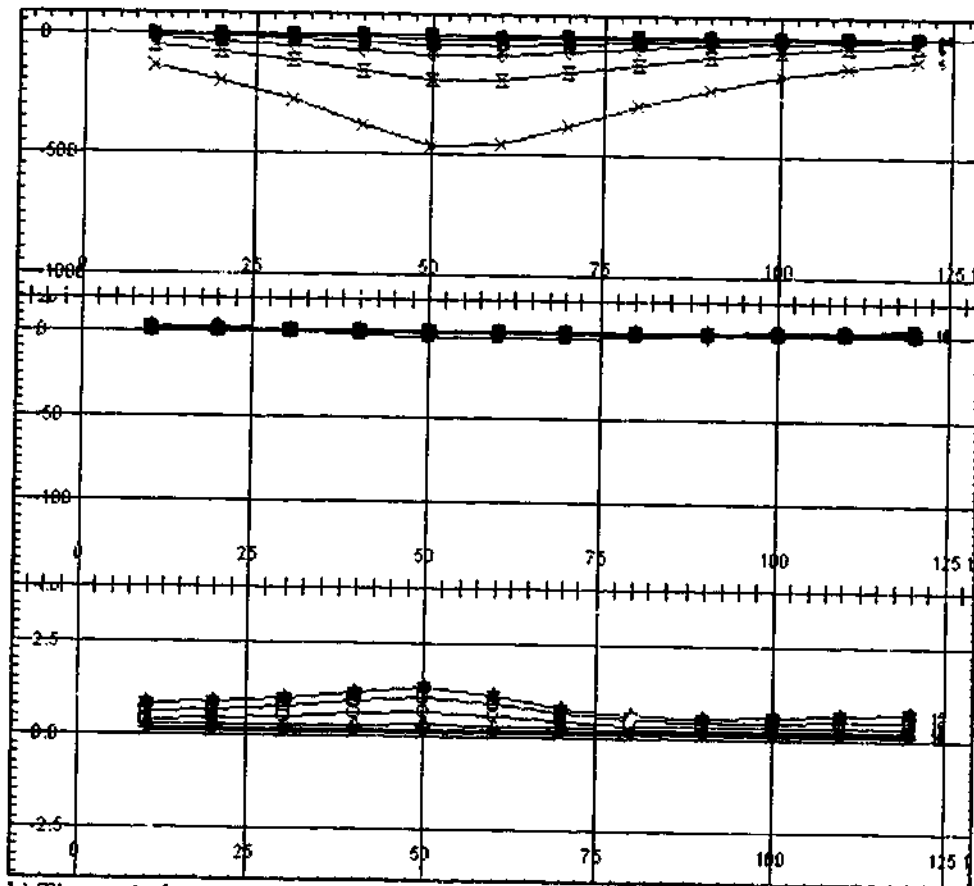


c) Time windows 20 to 25 and 25 to 32.

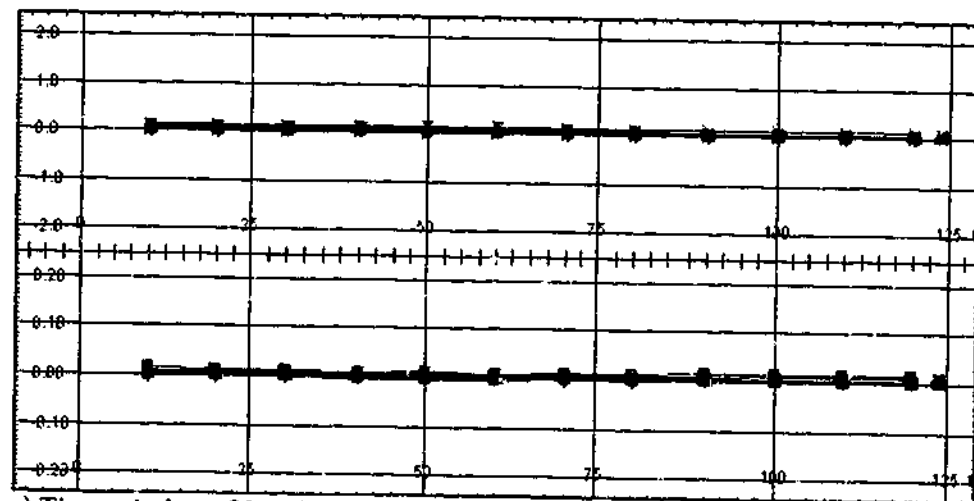
Figure D.2.1: Linear profiles of the axial component DHTEM Plate 1 model data, computed with program LEROI, for Borehole ID3039 with Loop 1.



a) Time windows 1 to 5.

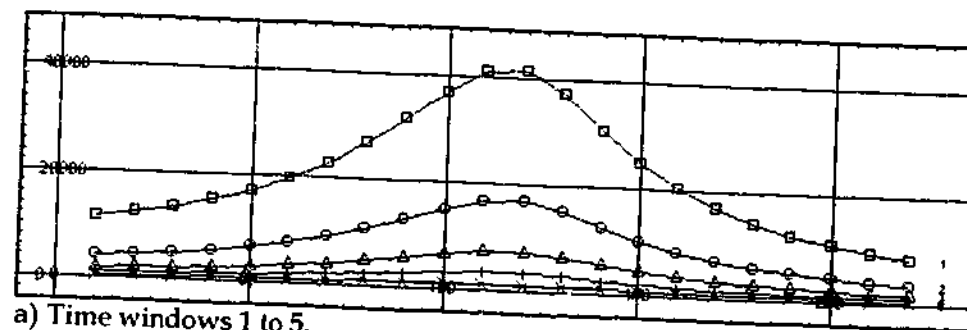


b) Time windows 5 to 10, 10 to 15 and 15 to 20.

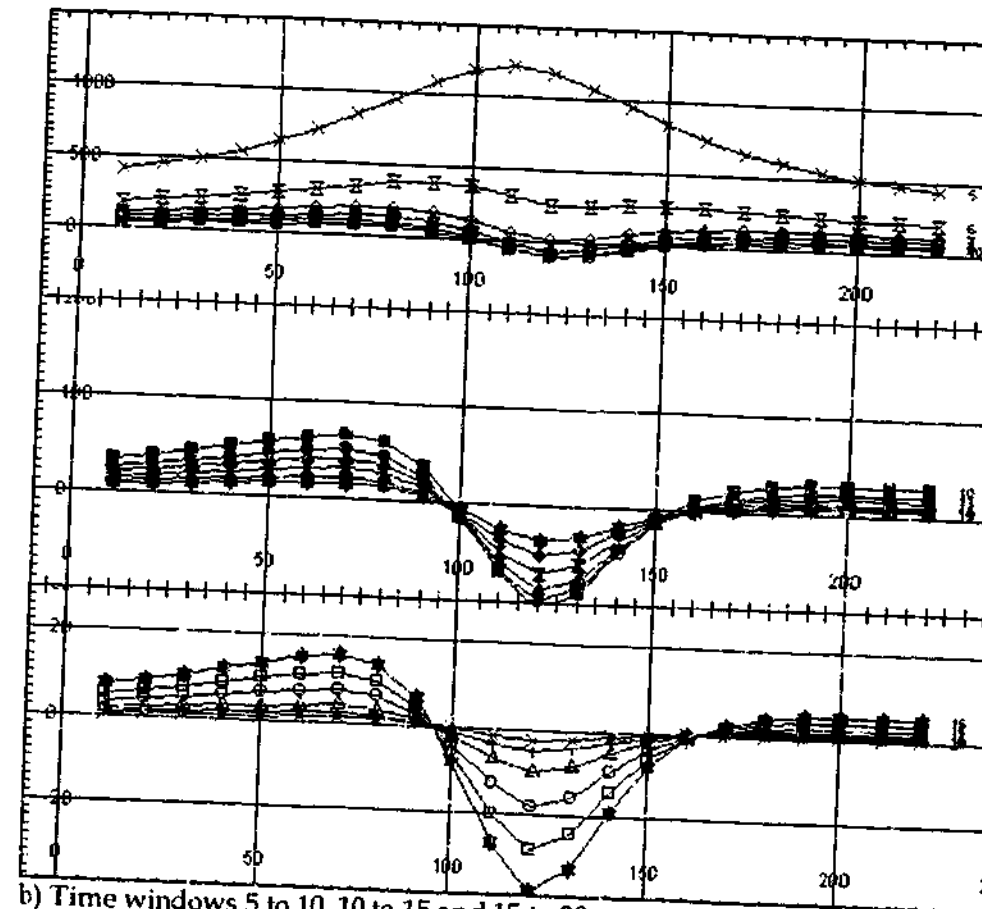


c) Time windows 20 to 25 and 25 to 32.

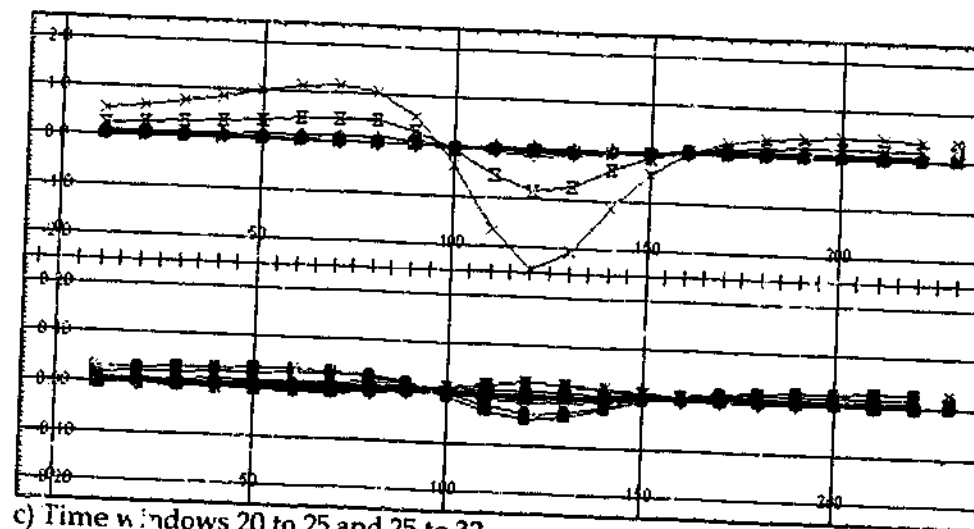
Figure D.2.2: Linear profiles of the axial component DHTM Plate 1 model data, computed with program LEROI, for Borehole ID3039 with Loop 3.



a) Time windows 1 to 5.



b) Time windows 5 to 10, 10 to 15 and 15 to 20.

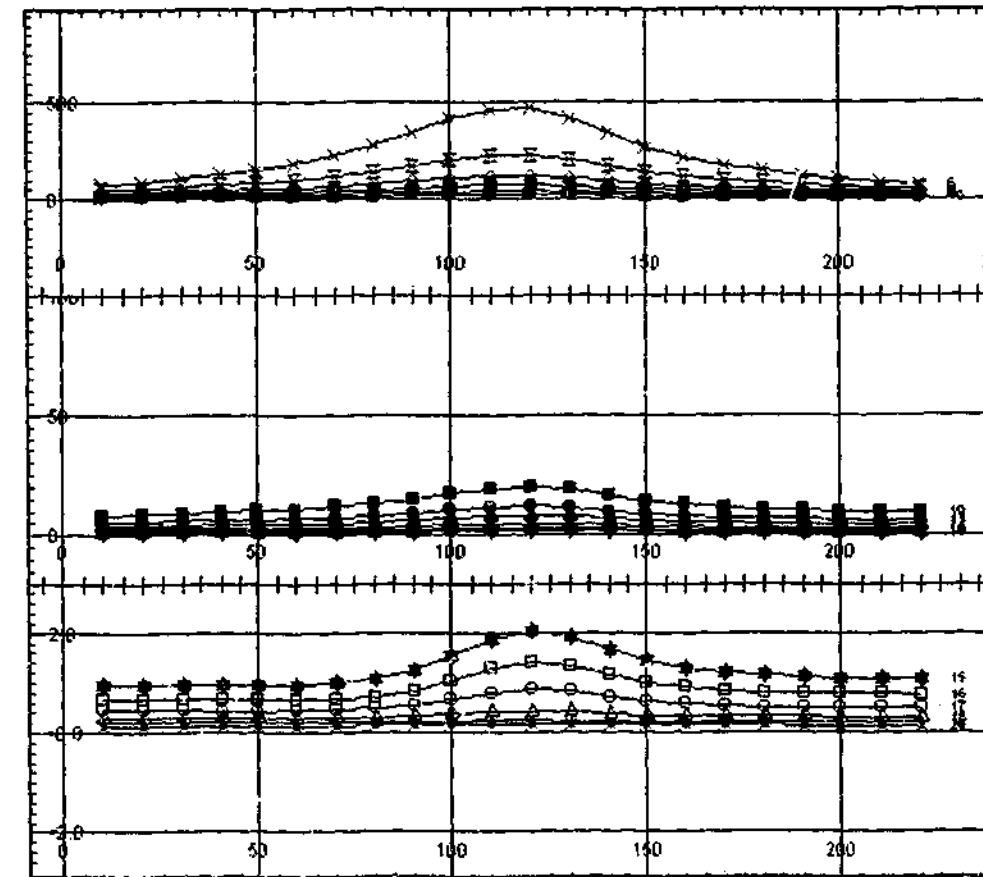


c) Time windows 20 to 25 and 25 to 32.

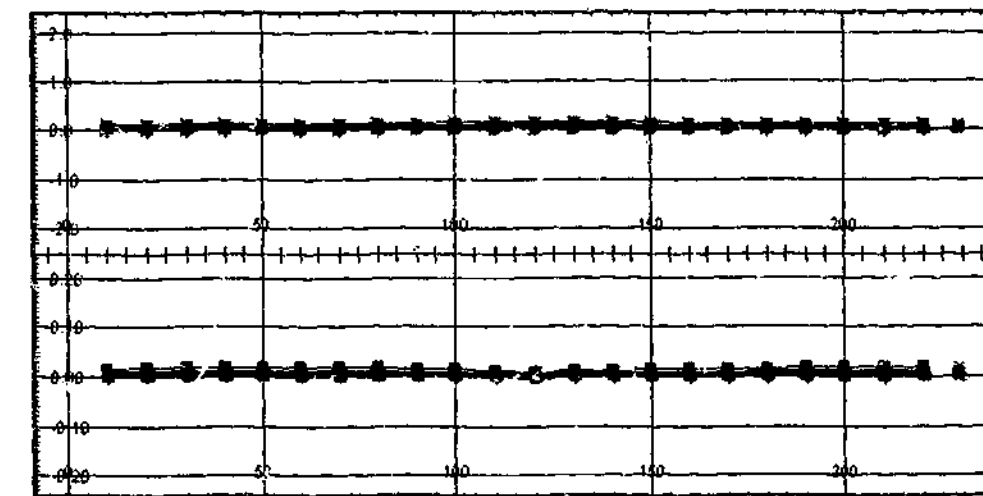
Figure D.2.3: Linear profiles of the axial component DHTM Plate 1 model data, computed with program LEROI, for Borehole ID3071 with Loop 1.



a) Time windows 1 to 5.



b) Time windows 5 to 10, 10 to 15 and 15 to 20.



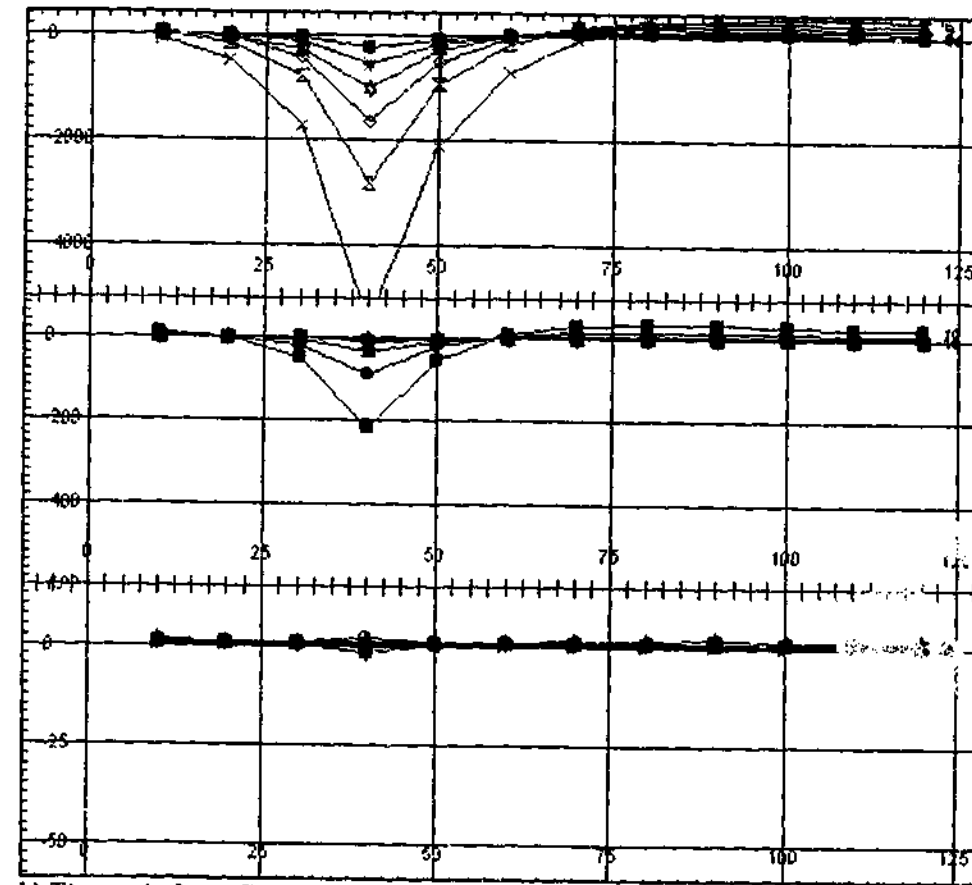
c) Time windows 20 to 25 and 25 to 32.

Figure D.2.4: Linear profiles of the axial component DHTM Plate 1 model data, computed with program LEROI, for Borehole ID3071 with Loop 3.

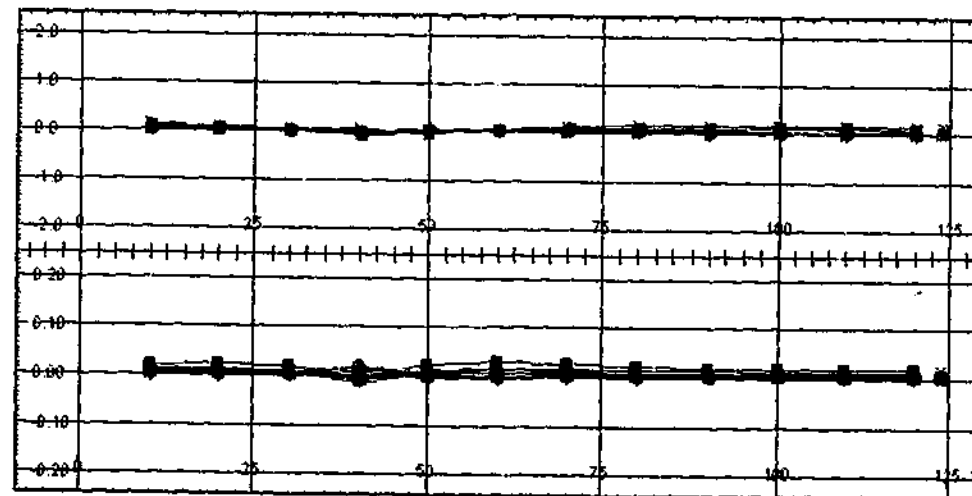
APPENDIX D.3: DOWNHOLE TEM MODEL DATA - PLATE 2.
(See Table 6.2 for specifications of the dual-plate model)



a) Time windows 1 to 5.

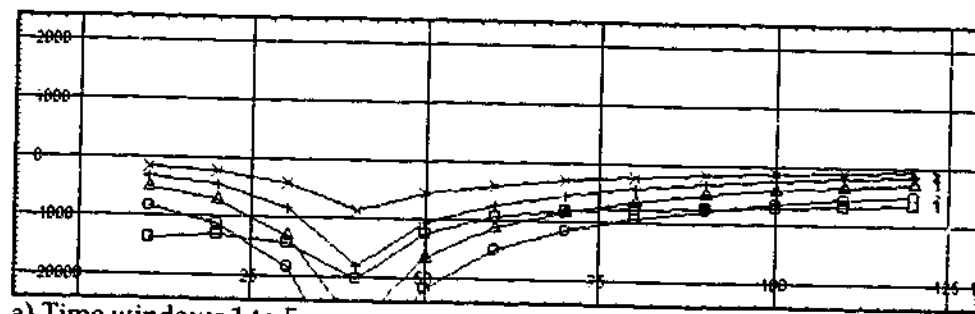


b) Time windows 5 to 10, 10 to 15 and 15 to 20.

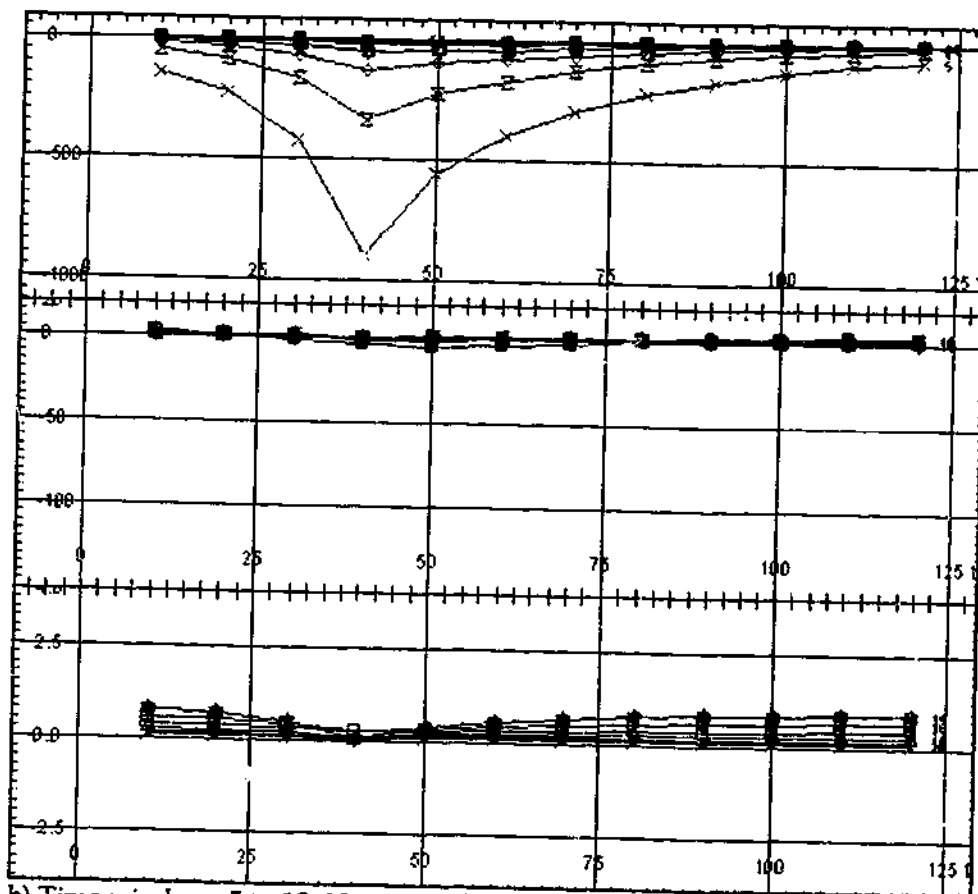


c) Time windows 20 to 25 and 25 to 32.

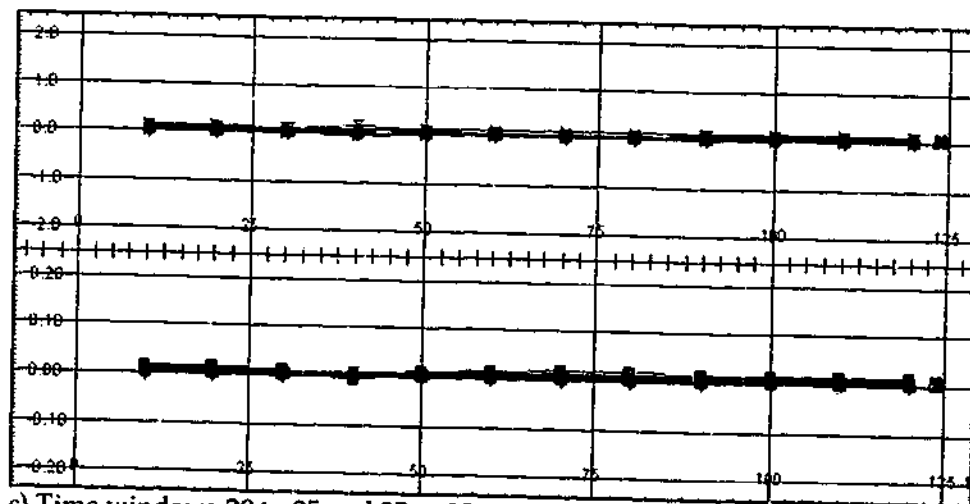
Figure D.3.1: Linear profiles of the axial component DHTM Plate 2 model data, computed with program LEROI, for Borehole ID3039 with Loop 1.



a) Time windows 1 to 5.

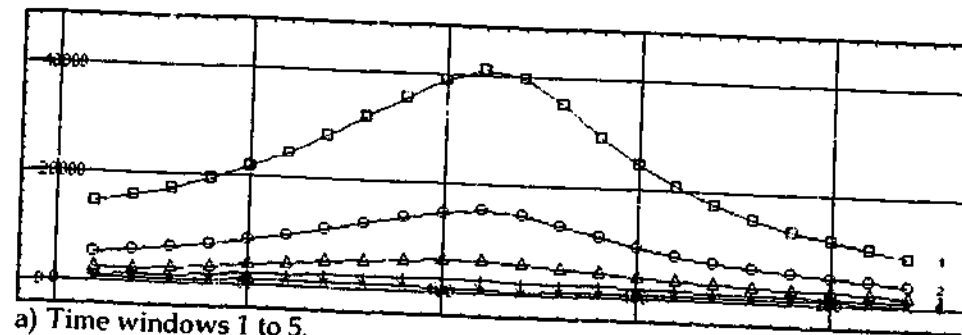


b) Time windows 5 to 10, 10 to 15 and 15 to 20.

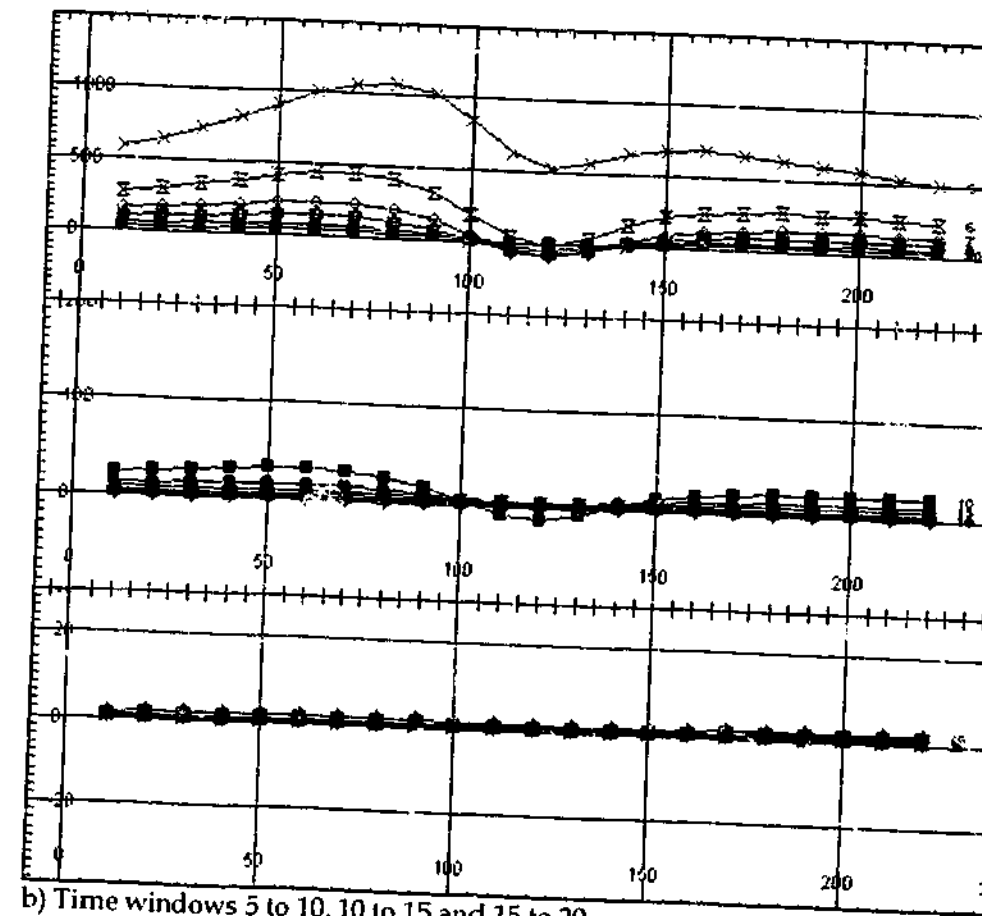


c) Time windows 20 to 25 and 25 to 32.

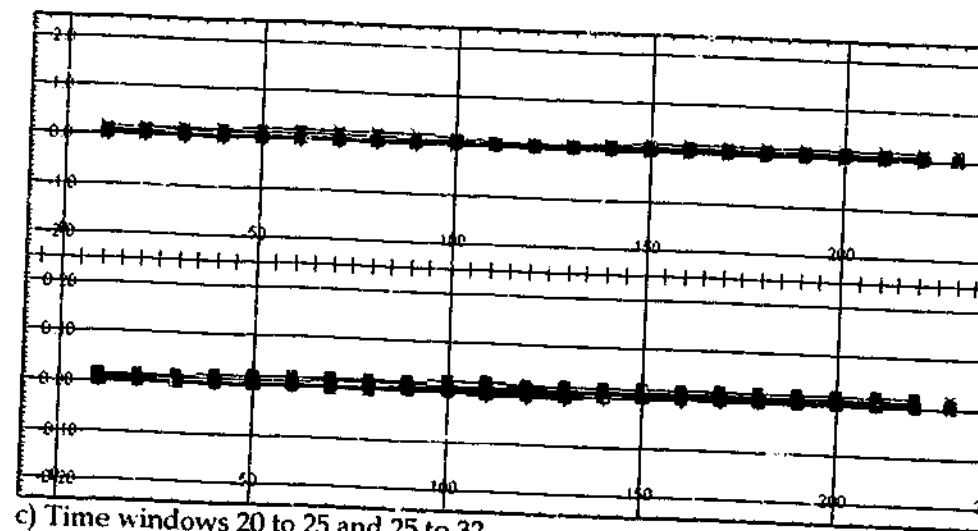
Figure D.3.2: Linear profiles of the axial component DHTeM Plate 2 model data, computed with program LEROI, for Borehole ID3039 with Loop 3.



a) Time windows 1 to 5.

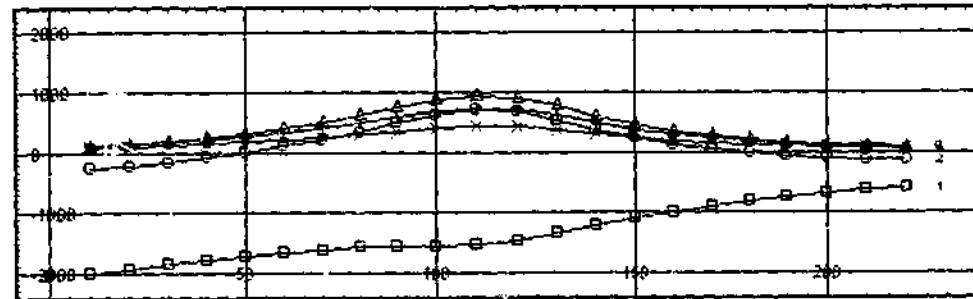


b) Time windows 5 to 10, 10 to 15 and 15 to 20.

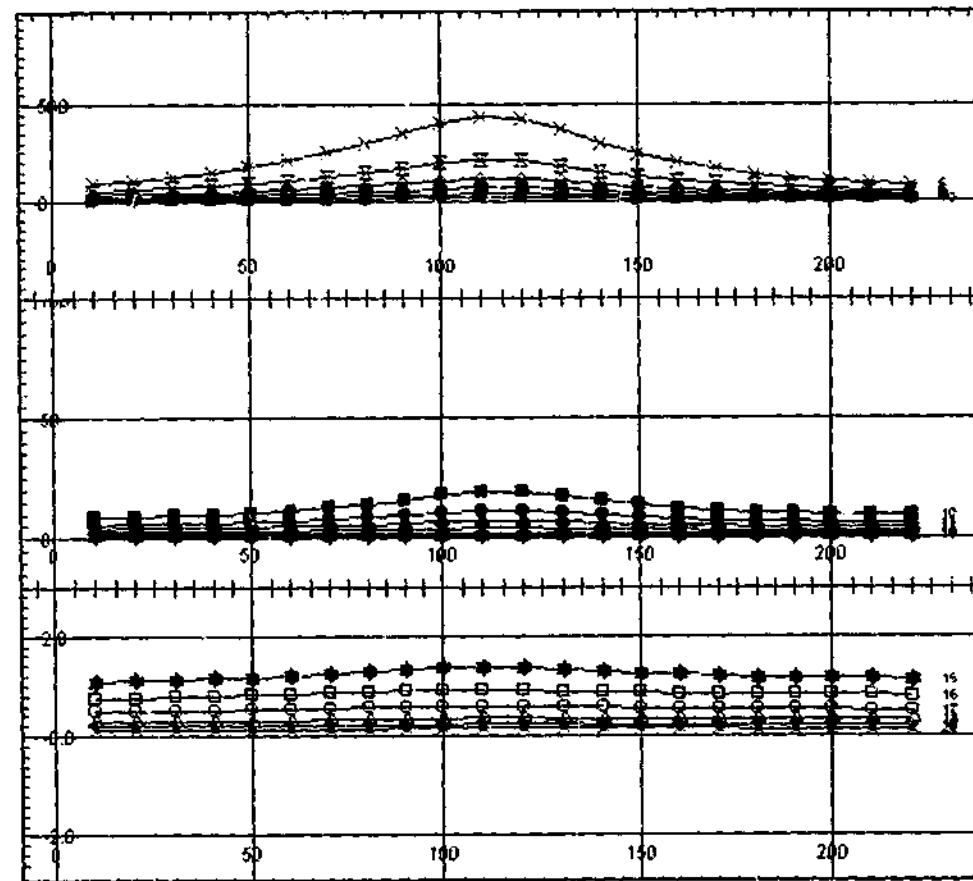


c) Time windows 20 to 25 and 25 to 32.

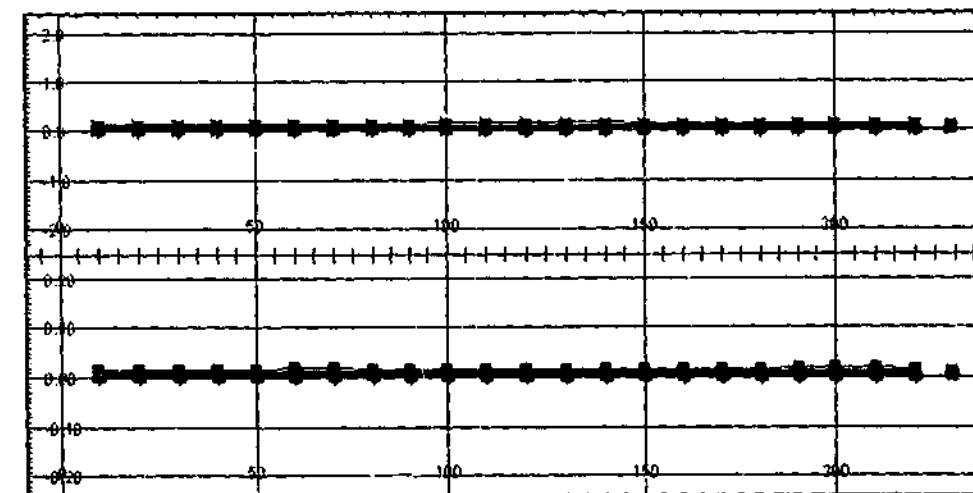
Figure D.3.3: Linear profiles of the axial component DHTeM Plate 2 model data, computed with program LEROI, for Borehole ID3071 with Loop 1.



a) Time windows 1 to 5.



b) Time windows 5 to 10, 10 to 15 and 15 to 20.



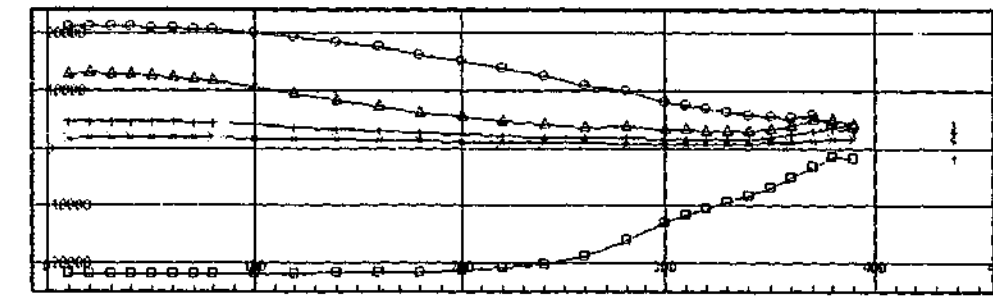
c) Time windows 20 to 25 and 25 to 32.

Figure D.3.4: Linear profiles of the axial component DHTM Plate 2 model data, computed with program LEROI, for Borehole ID3071 with Loop 3.

APPENDIX E

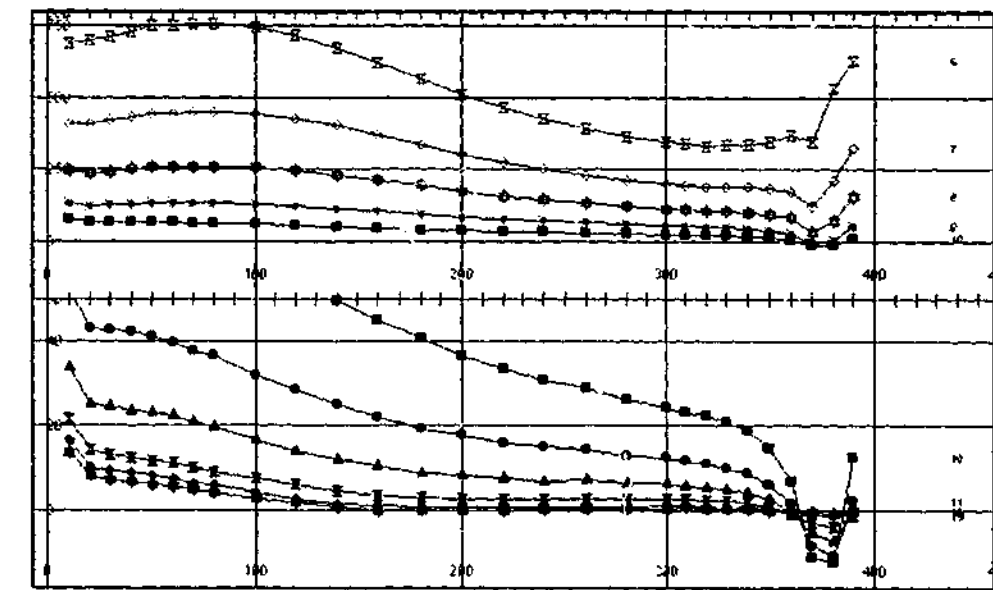
[DATA FOR FLYING DOCTOR DEPOSIT - LOWER LENS.]

APPENDIX E.1: DOWNHOLE TEM FIELD DATA.



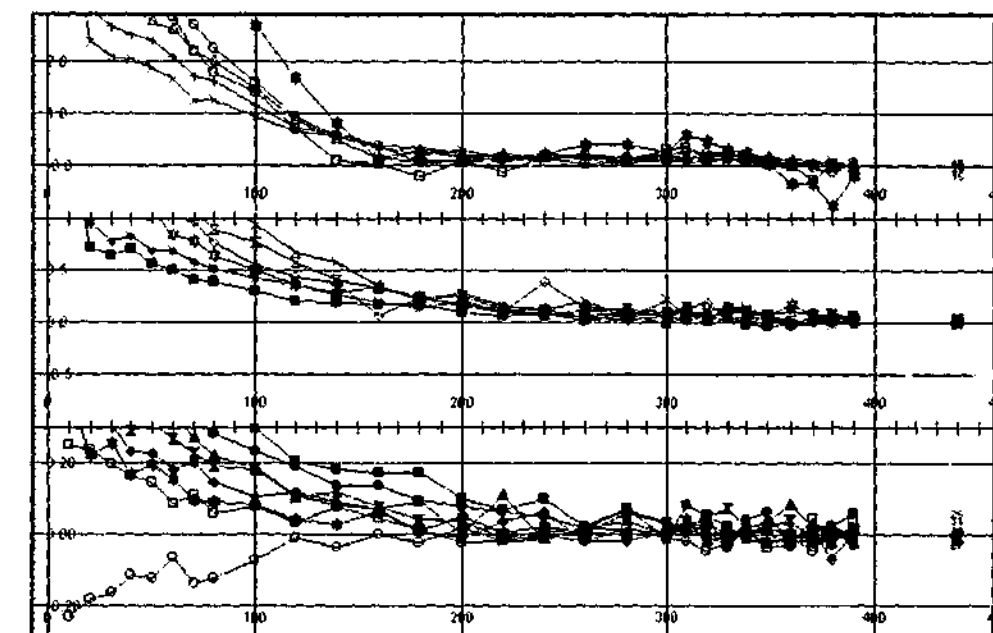
a) Time windows 1 to 5.

- 1 (0.120 ms)
- 2 (0.170 ms)
- △ 3 (0.220 ms)
- + 4 (0.270 ms)
- × 5 (0.345 ms)



b) Time windows 6 to 10 and 10 to 15.

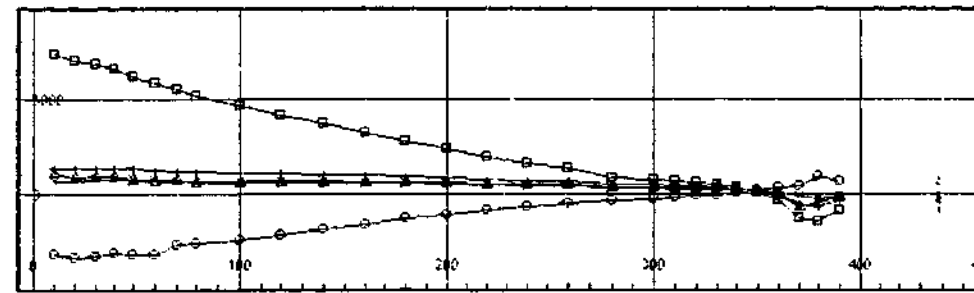
- ⊗ 6 (0.445 ms)
- ◇ 7 (0.545 ms)
- ☆ 8 (0.645 ms)
- * 9 (0.795 ms)
- 10 (0.995 ms)
- 11 (1.195 ms)
- ▲ 12 (1.395 ms)
- ⊗ 13 (1.695 ms)
- ◆ 14 (2.095 ms)
- ★ 15 (2.495 ms)



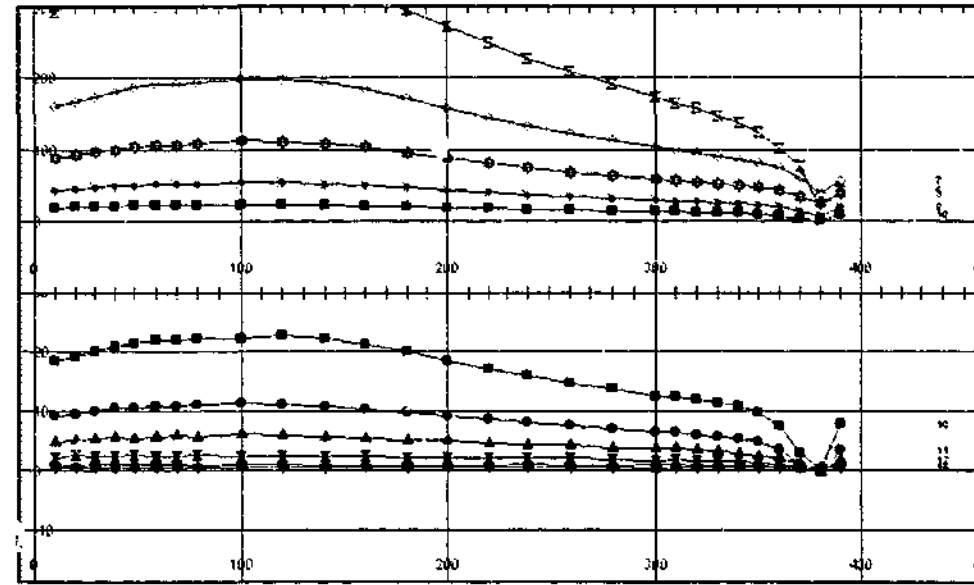
c) Time windows 15 to 20, 20 to 25 and 25 to 32.

- ★ 15 (2.495 ms)
- 16 (2.895 ms)
- 17 (3.495 ms)
- △ 18 (4.295 ms)
- + 19 (5.095 ms)
- × 20 (5.895 ms)
- ⊗ 21 (7.095 ms)
- ◇ 22 (8.695 ms)
- ☆ 23 (10.295 ms)
- * 24 (11.895 ms)
- 25 (14.295 ms)
- 26 (17.495 ms)
- ▲ 27 (20.695 ms)
- ⊗ 28 (24.695 ms)
- ◆ 29 (29.495 ms)
- ★ 30 (35.095 ms)
- 31 (41.495 ms)
- 32 (47.895 ms)

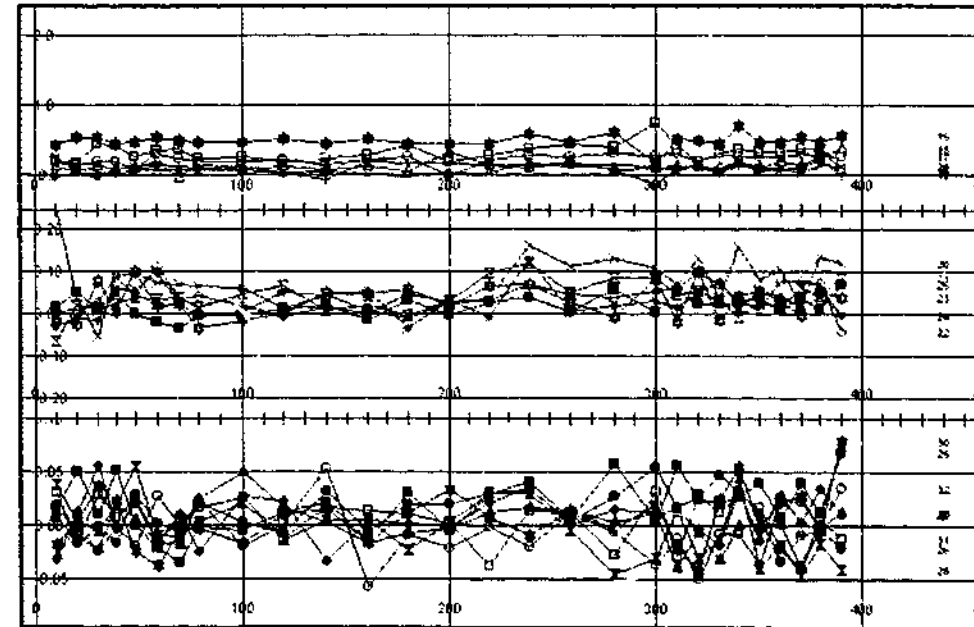
Figure E.1.1: Linear profiles of the axial component DHTM field data for Borehole ID3418 with Loop 1.



a) Time windows 1 to 5.

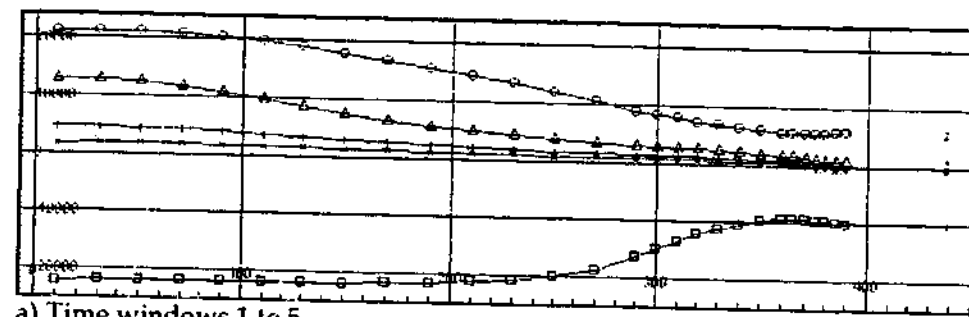


b) Time windows 6 to 10 and 10 to 15.

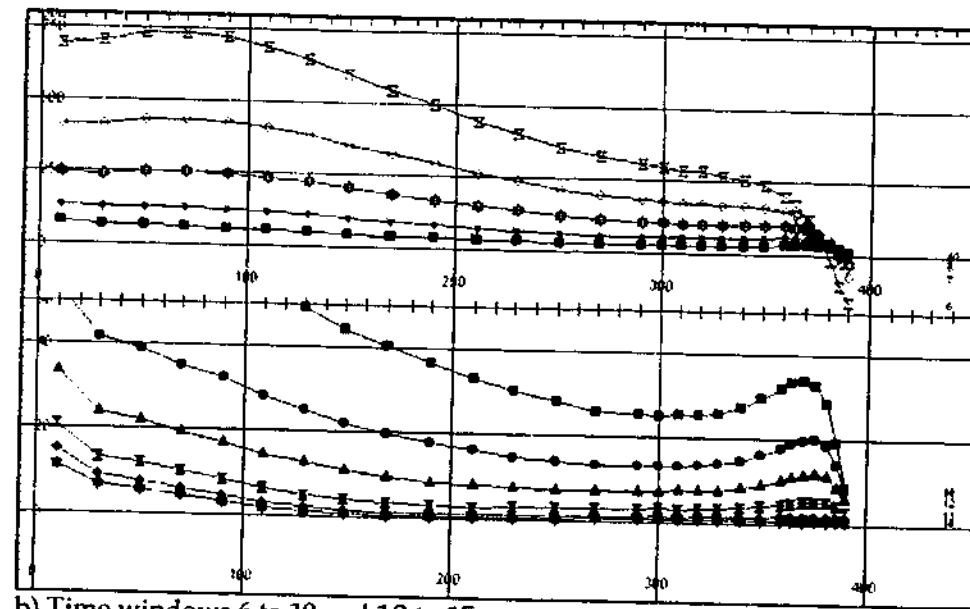


c) Time windows 15 to 20, 20 to 25 and 25 to 32.

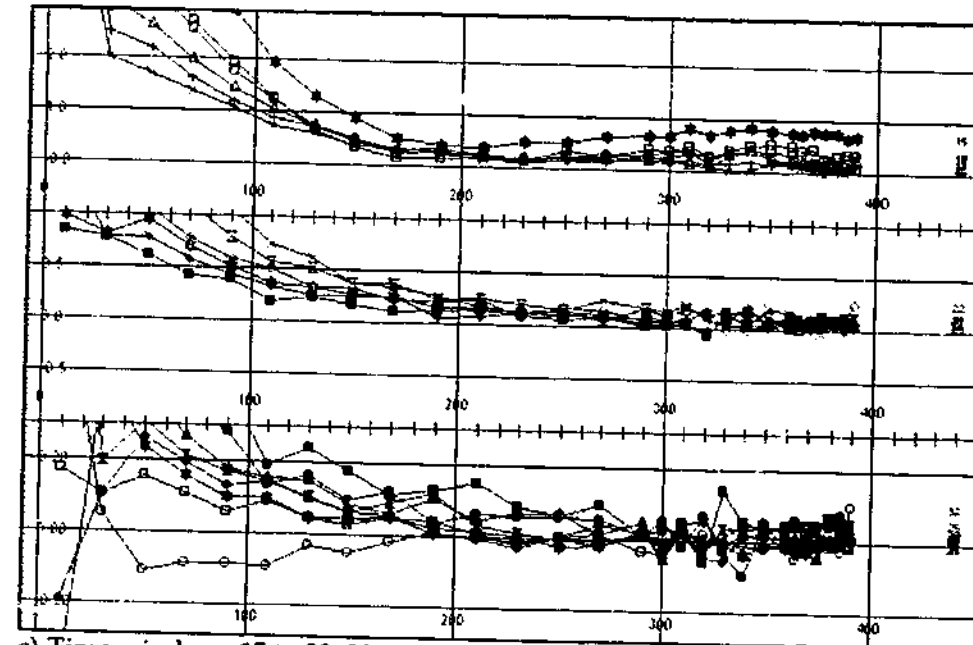
Figure E.1.2: Linear profiles of the axial component DHTEM field data for Borehole ID3418 with Loop 3.



a) Time windows 1 to 5.

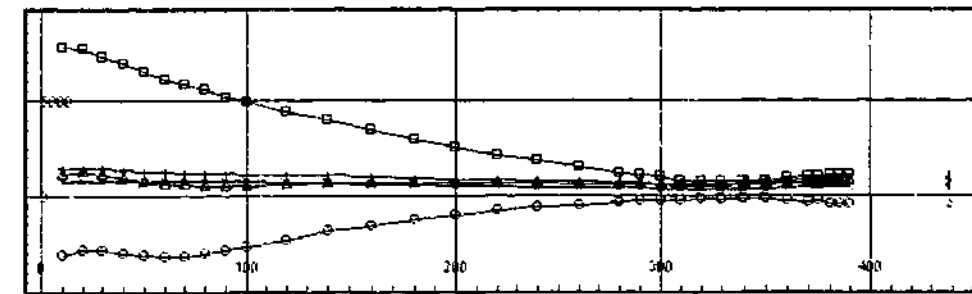


b) Time windows 6 to 10 and 10 to 15.

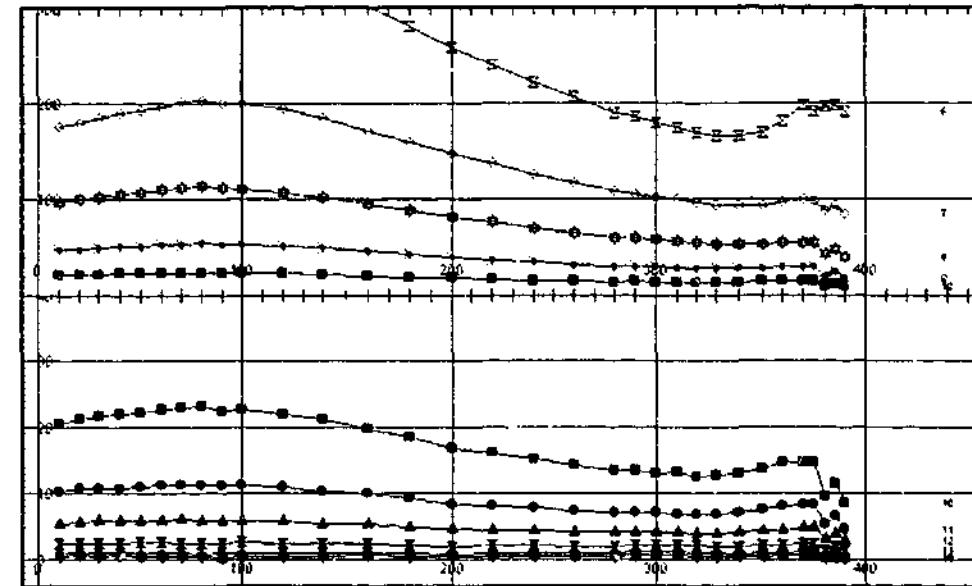


c) Time windows 15 to 20, 20 to 25 and 25 to 32.

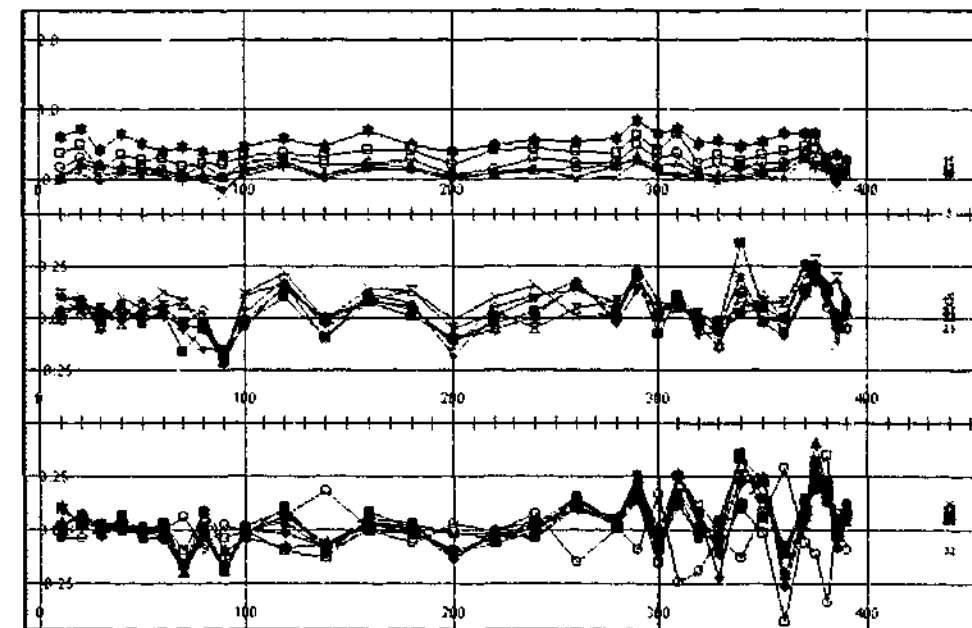
Figure E.1.3: Linear profiles of the axial component DHTEM field data for Borehole ID3419 with Loop 1.



a) Time windows set 1 to 5.



b) Time windows 6 to 10 and 10 to 15.

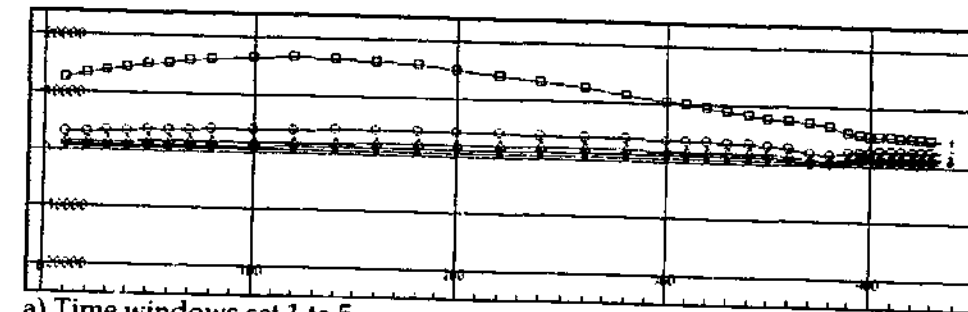


c) Time windows 15 to 20, 20 to 25 and 25 to 32.

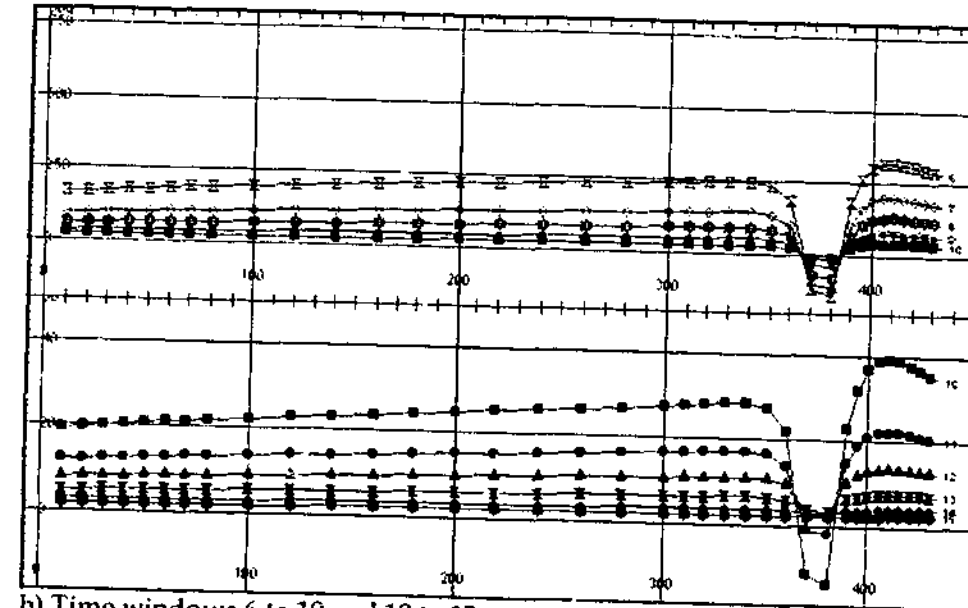
Figure E.1.4: Linear profiles of the axial component DHTEM field data for Borehole ID3419 with Loop 3.

APPENDIX E.2: DOWNHOLE TEM MODEL DATA.

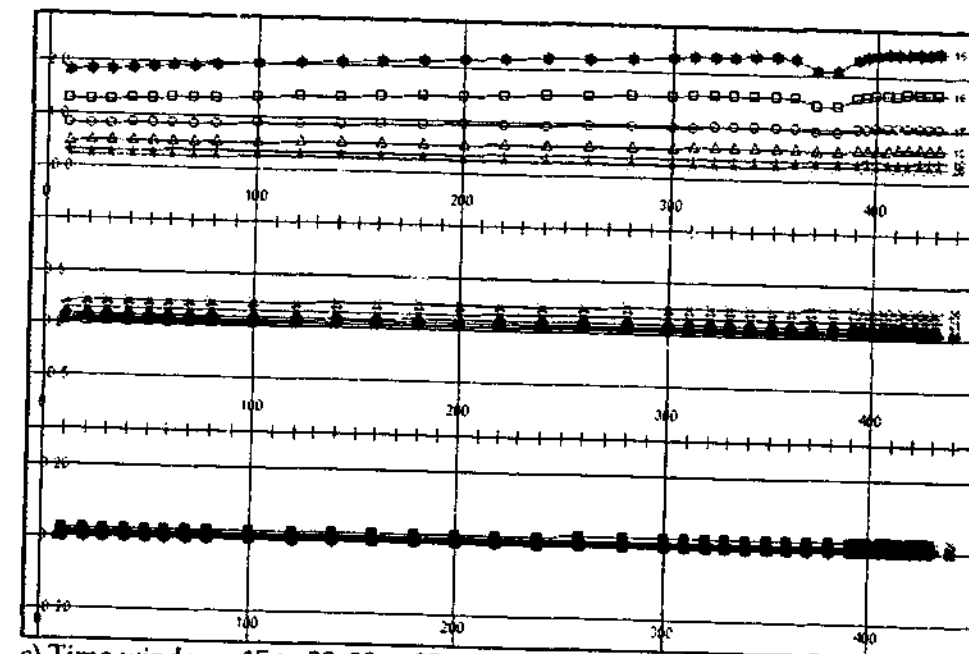
(See Table 8.1 for specifications of the single-plate model)



a) Time windows set 1 to 5.

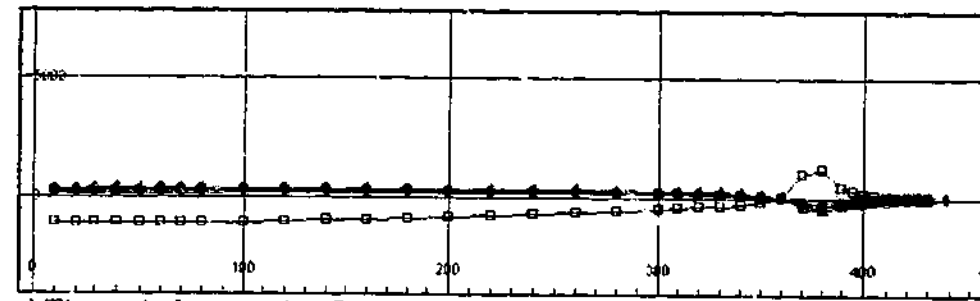


b) Time windows 6 to 10 and 10 to 15.

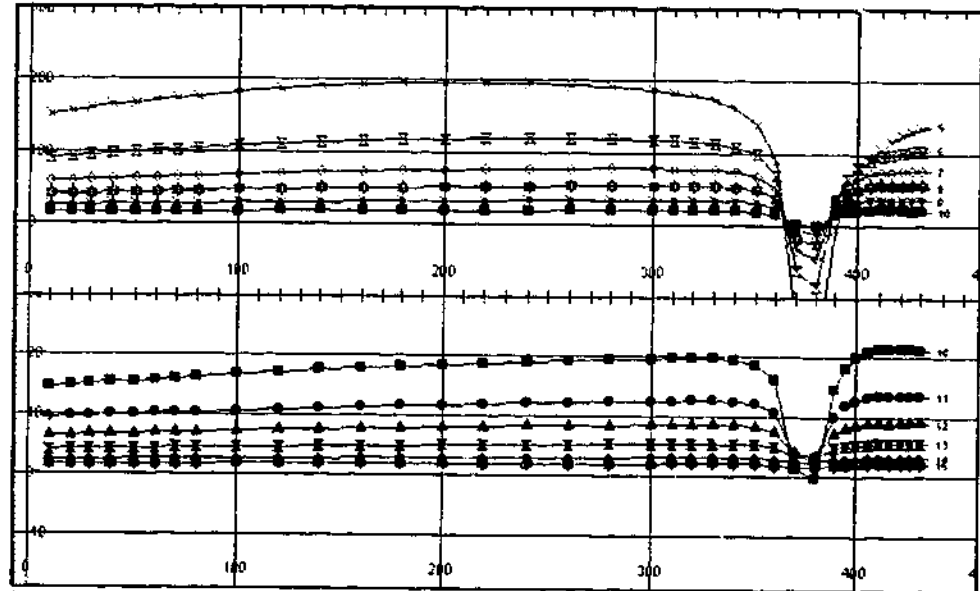


c) Time windows 15 to 20, 20 to 25 and 25 to 32.

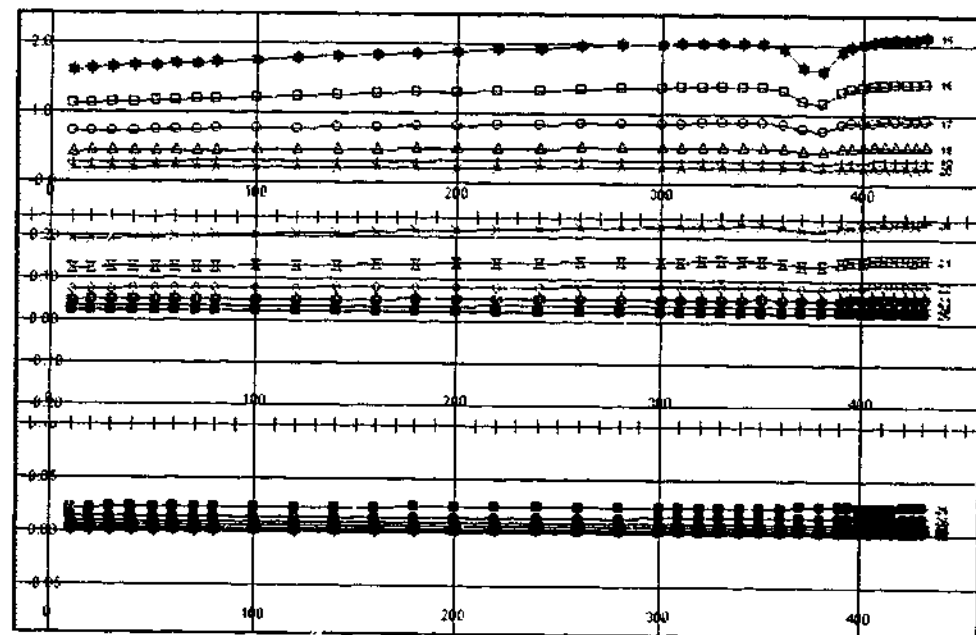
Figure E.2.1: Linear profiles of the axial component DHTEM model data, computed with program LEROI, for Borehole ID3418 with Loop 1.



a) Time windows set 1 to 5.

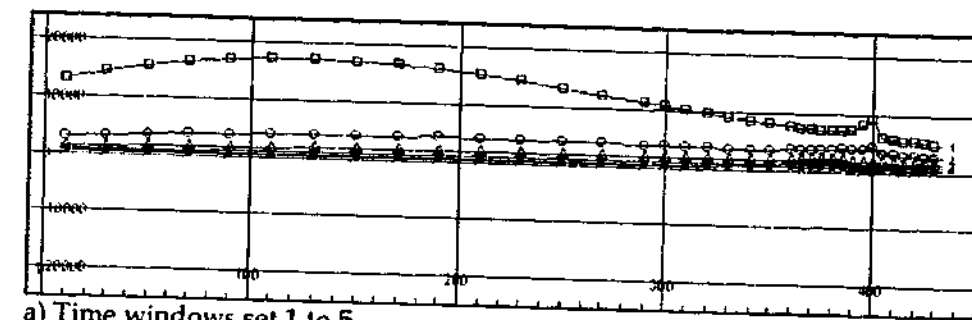


b) Time windows 6 to 10 and 10 to 15.

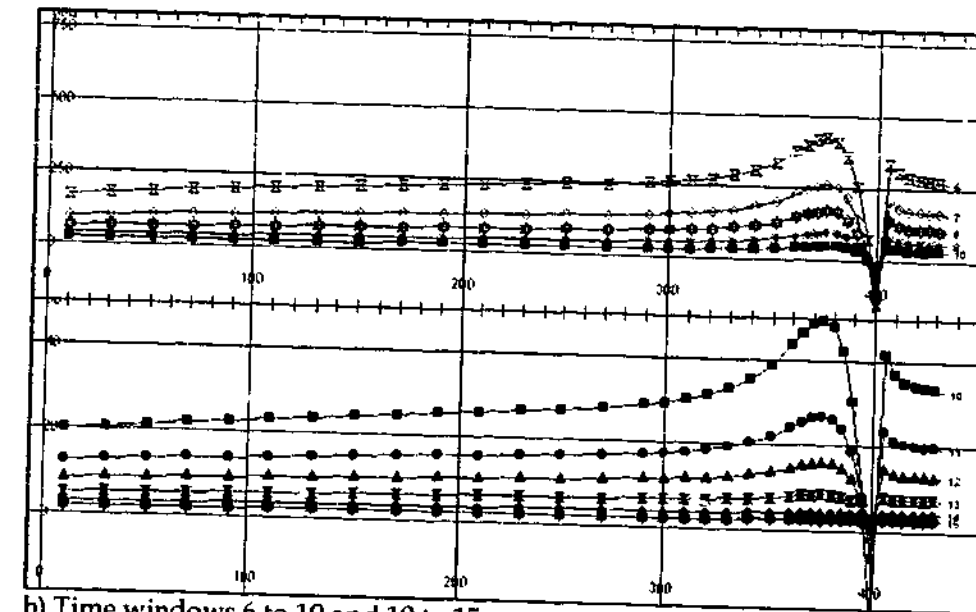


c) Time windows 15 to 20, 20 to 25 and 25 to 32.

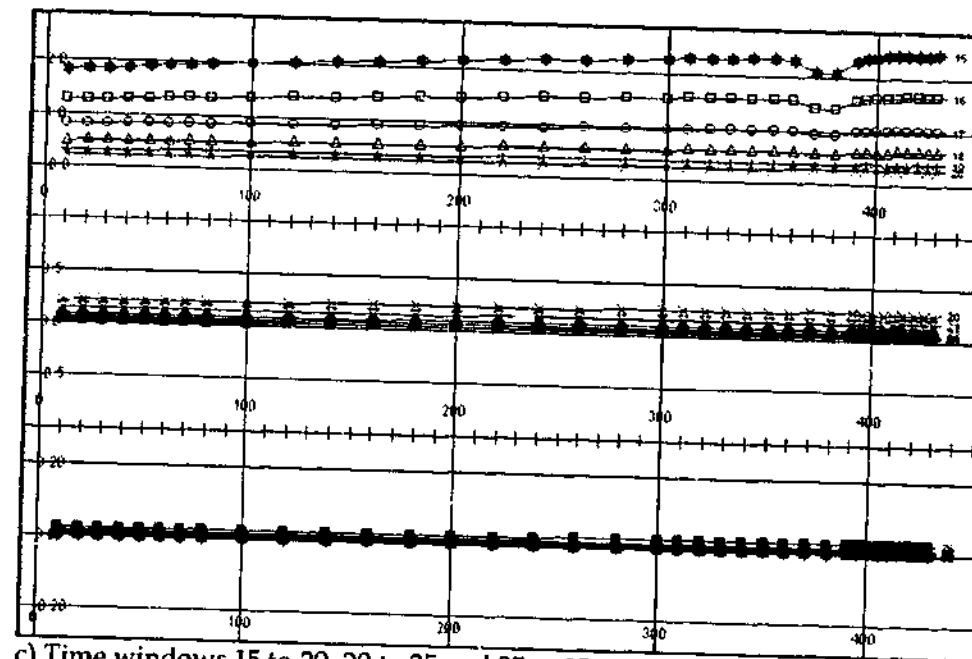
Figure E.2.2: Linear profiles of the axial component DHTM model data, computed with program LEROI, for Borehole ID3418 with Loop 3.



a) Time windows set 1 to 5.

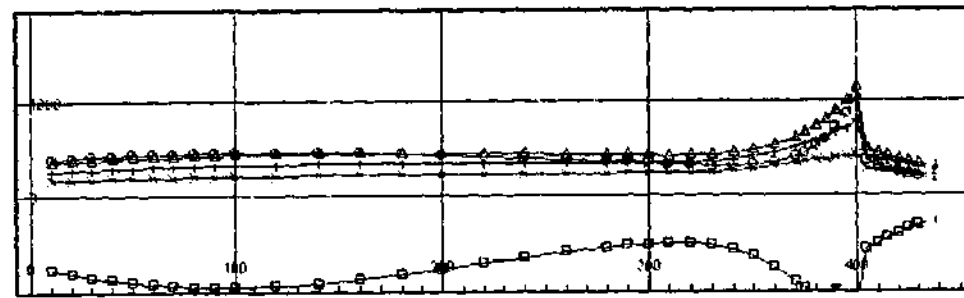


b) Time windows 6 to 10 and 10 to 15.

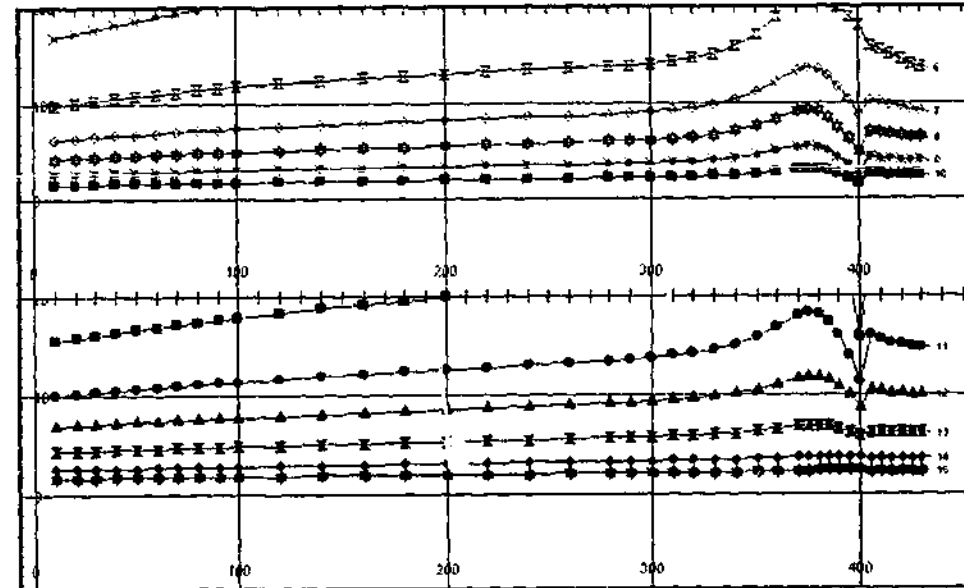


c) Time windows 15 to 20, 20 to 25 and 25 to 32.

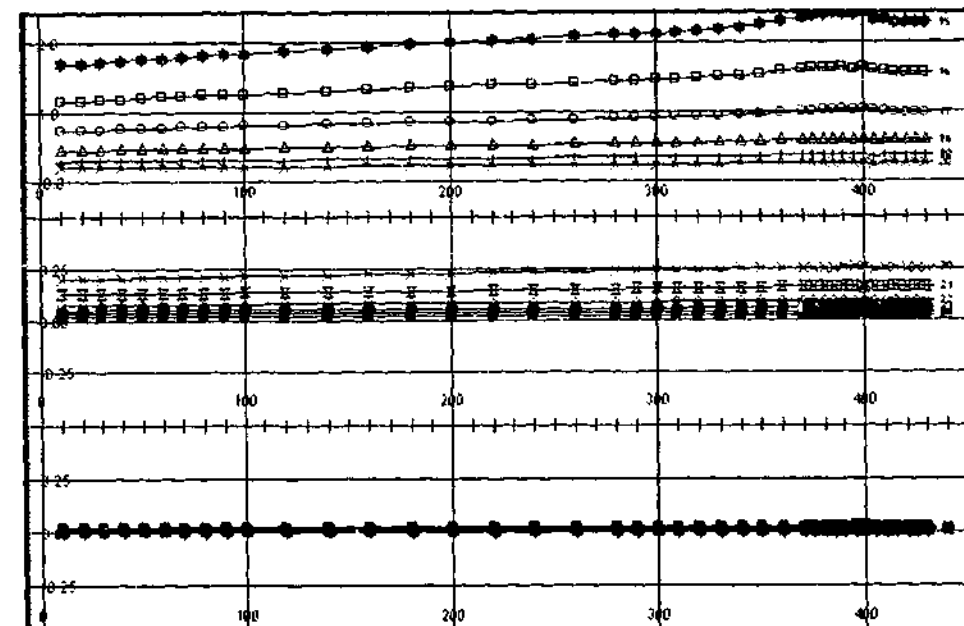
Figure E.2.3: Linear profiles of the axial component DHTM model data, computed with program LEROI, for Borehole ID3419 with Loop 1.



a) Time windows set 1 to 5.



b) Time windows 6 to 10 and 10 to 15.



c) Time windows 15 to 20, 20 to 25 and 25 to 32.

Figure E.2.4: Linear profiles of the axial component DHTM model data, computed with program LEROI, for Borehole ID3419 with Loop 3.

APPENDIX E.3: BOREHOLE STATION COORDINATES.

Table E.3.1: Receiver station coordinates for Borehole ID3039.

STATION.	EASTING. (m)	NORTHING. (m)	DEPTH. (m)
COLLAR	4775.6	20401.3	0.0
10	4782.1	20401.3	7.6
20	4788.5	20401.3	15.3
30	4795.0	20401.2	22.9
40	4801.5	20401.1	30.4
50	4808.1	20400.9	38.0
60	4814.6	20400.7	45.0
70	4821.3	20400.5	53.0
80	4828.0	20400.4	60.4
90	4834.9	20400.2	67.7
100	4841.8	20400.0	74.9
110	4848.8	20399.8	82.1
120	4855.8	20399.6	89.1

Table E.3.2: Receiver station coordinates for Borehole ID3071.

STATION.	EASTING. (m)	NORTHING. (m)	DEPTH. (m)
COLLAR	4695.7	20400.9	0.0
10	4700.7	20401.0	8.6
20	4705.8	20401.0	17.3
30	4710.9	20401.1	25.9
40	4716.0	20401.2	34.5
50	4721.1	20401.3	43.1
60	4726.2	20401.4	51.6
70	4731.6	20401.5	60.1
80	4737.2	20401.6	68.4
90	4742.9	20401.7	76.6
100	4748.9	20401.8	84.6
110	4755.0	20401.8	92.5
120	4761.3	20401.9	100.3
130	4767.9	20402.0	107.8
140	4774.6	20402.2	115.2
150	4781.7	20402.5	122.3
160	4788.9	20402.9	129.2
170	4796.3	20403.4	135.9
180	4803.9	20404.0	142.3
190	4811.8	20404.7	148.5
200	4819.7	20405.5	154.4
210	4827.9	20406.4	160.1
220	4836.3	20407.4	165.5

Table E.3.3: Receiver station coordinates for Borehole ID3418.

STATION.	EASTING. (m)	NORTHING. (m)	DEPTH. (m)
COLLAR	4618.0	20402.6	0.0
10	4620.6	20402.5	9.6
20	4623.3	20402.3	19.3
30	4625.9	20402.3	28.9
40	4628.5	20402.2	38.6
50	4631.1	20402.1	48.2
60	4633.8	20402.0	57.9
70	4636.4	20401.8	67.5
80	4639.0	20401.7	77.2
100	4644.2	20401.3	96.5
120	4649.4	20401.0	115.8
140	4654.8	20400.6	135.0
160	4660.2	20400.2	154.3
180	4665.6	20399.9	173.6
200	4671.0	20399.6	192.8
220	4676.6	20399.3	212.0
240	4682.2	20399.1	231.2
260	4687.9	20399.0	250.4
280	4693.8	20398.9	269.5
300	4699.8	20398.8	288.6
310	4702.8	20398.8	298.1
320	4705.8	20398.8	307.7
330	4708.8	20398.8	317.2
340	4711.9	20398.7	326.7
350	4715.0	20398.6	336.2
360	4718.0	20398.5	345.7
370	4721.1	20398.4	355.2
380	4724.2	20398.3	364.8
390	4727.3	20398.2	374.3

Extension†			
395	4728.9	20398.1	379.1
400	4730.4	20398.1	383.8
405	4732.0	20398.0	388.6
410	4733.5	20398.0	393.3
415	4735.1	20397.9	398.1
420	4736.6	20397.9	402.8
425	4738.2	20397.8	407.6
430	4739.7	20397.8	412.3
435	4741.3	20397.7	417.1
440	4742.8	20397.7	421.8
445	4744.4	20397.6	426.6
450	4745.9	20397.6	431.3

† Linear extension by use of Stations 380 and 390.

Table E.3.4: Receiver station coordinates for Borehole ID3419.

STATION.	EASTING. (m)	NORTHING. (m)	DEPTH. (m)
COLLAR	4618.4	20401.6	0.0
10	4620.0	20401.5	9.9
20	4621.6	20401.5	19.7
30	4623.4	20401.5	29.6
40	4625.1	20401.5	39.4
50	4626.9	20401.5	49.3
60	4628.6	20401.4	59.1
70	4630.3	20401.4	59.0
80	4632.0	20401.4	78.8
90	4633.8	20401.3	88.7
100	4635.5	20401.3	98.5
120	4639.0	20401.2	118.2
140	4642.4	20401.0	137.9
160	4645.8	20401.8	157.6
180	4649.3	20401.5	177.3
200	4652.8	20401.3	197.0
240	4659.9	20400.1	236.4
260	4663.5	20400.2	256.1
280	4667.1	20400.3	275.7
290	4669.2	20400.3	285.5
300	4671.5	20400.2	295.2
310	4673.8	20400.0	304.9
320	4676.2	20399.8	314.7
330	4678.7	20399.6	324.4
340	4681.1	20399.5	334.1
350	4683.5	20399.4	343.7
360	4686.0	20399.3	353.4
370	4688.4	20399.1	363.1
375	4689.7	20399.0	368.0
380	4690.9	20399.0	372.8
385	4692.1	20398.9	377.7
390	4693.4	20398.8	382.5

Extension†			
395	4694.7	20398.7	387.3
400	4696.0	20398.6	392.2
405	4697.3	20398.5	397.0
410	4698.6	20398.4	401.8
415	4699.9	20398.3	406.6
420	4701.2	20398.2	411.5
425	4702.5	20398.1	416.3
430	4703.9	20398.0	421.1
435	4705.2	20397.9	425.9
440	4706.5	20397.8	430.8
445	4707.8	20397.7	435.6
450	4709.1	20397.6	440.4

† Linear extension by use of Stations 380 and 390.

APPENDIX E.4: SIROTEM COMPOSITE TIMES.

Table E.4.1: SMARTEM times with 60 ms OFFTIME.†

WINDOW.	DELAY. (ms)	WIDTH. (ms)
1	0.05	0.05
2	0.10	0.05
3	0.15	0.05
4	0.20	0.05
5	0.275	0.10
6	0.375	0.10
7	0.475	0.10
8	0.575	0.10
9	0.725	0.20
10	0.925	0.20
11	1.125	0.20
12	1.325	0.20
13	1.625	0.40
14	2.025	0.40
15	2.425	0.40
16	2.825	0.40
17	3.425	0.80
18	4.225	0.80
19	5.025	0.80
20	5.825	0.80
21	7.025	1.60
22	8.625	1.60
23	10.225	1.60
24	11.825	1.60
25	14.225	3.20
26	17.425	3.20
27	20.625	3.20
28	24.625	4.80
29	29.425	4.80
30	35.025	6.40
31	41.425	6.40
32	47.825	0.40

†To obtain the required window times add an initial-delay of 0.07 ms.

REFERENCES

- Annan, A. P., 1974, The equivalent source method for electromagnetic scattering analysis and its geophysical application: *Ph.D. thesis, Memorial University of Newfoundland.*
- Asten, M. W., King, A., and Peacock, J., 1987, Sign changes in DHEM surveys for cindered coal in the Sydney basin: Downhole exploration methods, *Australian Society of Exploration Geophysicists*, v. 18, p. 319-323.
- Asten, M.W., 1991a, A study of galvanic response in the TEM response of conductive ore-bodies: *Abstracts of the Australian Society of Exploration Geophysicists 8th Conference, Sydney*, p. 124.
- Asten, M. W., 1991b, Field examples of the downhole MMR method and comparison with the TEM method: Appendix to 'The magnetometric resistivity method', by R. N. Edwards and M. N. Nabighian, in Nabighian, M. N., Ed., *Electromagnetic methods in applied geophysics, 02: Society of Exploration Geophysicists*, p. 99-104.
- Asten, M. W., 1998, Lecture notes: EM methods for geologists and geophysicists, Flagstaff Geo-consultants and Monash University, presented at December Review Meeting of Monash University - SPIRT project with industry sponsors.
- Asten, M. W., 2001, Borehole TEM and MMR Methods for Weak Conductors - A Project Review, *Extended Abstracts, ASEG 15th Geophysical Conference and Exhibition, August 2001, Brisbane.*
- Barnett, C. T., 1984, Simple inversion of time-domain electromagnetic data: *Geophysics*, v. 49, p. 925-933.

Bishop, J., Carroll, N., Asten, M., Hatch, M., and MacInnes, S., 1997, Finding sphalerite at Broken Hill with drillhole magnetometric resistivity: 12th Geophysical Conference, Australian Society of Exploration Geophysicists, v. 28, p. 6-10.

Duncan, A., Amann, B., O'Keeffe, K., Williams, P., Tully, T., Wellington, A., and Turner, G., 1998, Examples from a new EM and electrical methods receiver system: *Exploration Geophysics*, Australian Society of Exploration Geophysicists, v. 29, p. 347-354.

Dyck, A. V., and West, G. F., 1984, The role of simple computer models in interpretations of wide-band drill-hole electromagnetic surveys in mineral exploration: *Geophysics*, Society of Exploration Geophysicists, v. 49, p. 957-980.

Eadie, T., 1987, The Downhole EM Response of the Hellyer Ore Deposit: *Exploration Geophysics*, v. 18, p. 255-264.

Eadie, E. T., Silic, J., and Jack, D. J., 1985, The application of geophysics to the discovery of the Hellyer Ore Deposit, *Exploration Geophysics*, v. 16, 207-209

Edwards, R. N., and Nabighian, M. N., 1981, Extensions of the magnetometric resistivity (MMR) method: *Geophysics*, v. 46, p. 459.

Elders, J., and Asten, M., 2000, Minimization of receiver noise in downhole MMR surveys, 70th Ann. Internat. Mtg: Society of Exploration Geophysicists, p. 336-339.

Elders, J.E., and Asten, M.W., 2001, A comparison of receiver technologies in downhole MMR surveys: Submitted to Geophysical Prospecting.

EM Vision, 1996, EM Vision Reference manual - EM Vision: Modelling programs. LEROI program description. Australia: Encom Technology.

REFERENCES.

Flis, M., 1987, IP effects in 3-D TEM data - Theory and case histories: 5th Geophysical Conference, Australian Society of Exploration Geophysicists, v. 18, p. 55-58.

Gallagher, P. R., Ward, S. H., and Hohmann, G. W., 1985, A model study of a thin plate in free space for the EM37 transient electromagnetic system: *Geophysics*, v. 50, p. 1002-1019.

Halliday, D., and Resnick, R., 1988, Fundamentals of Physics, ext.d 3rd edn, Wiley and Sons.

Hanneson, J. E., 1992, The transient EM step response of a dipping plate in a conductive half-space: *Geophysics*, Society of Exploration Geophysicists, v. 57, p. 1116-1126.

Hayt, W. H., 1981, Engineering electromagnetics, McGraw-Hill.

Hecht, E., 1987, Optics, 2nd edn., Addison-Wesley.

Hohmann, G. W., 1988, Numerical modeling for electromagnetic methods of geophysics, in Nabighian, M. N., Ed., Electromagnetic methods in applied geophysics, 01: Society of Exploration Geophysicists, p. 313-364.

Hopgood, J. D., and N. Hungerford, 1994, Geophysical Case History of the Discovery of the Aguas Tenidas East Massive Sulphide Deposit, SW Spain: *Exploration Geophysics*, v. 25, p. 1-17

Irvine, R. J., 1987, Drillhole TEM Surveys at Thalanga, Queensland: *Exploration Geophysics*, v. 18, p. 285-293.

Johansen, H. K., and Sorensen, K., 1979, Fast Hankel transforms: *Geophysical Prospecting*, v. 27, p. 876-901.

Keller, G. V., 1988, Rock and mineral properties. In *electromagnetic Methods in Applied Geophysics*, vol. 1, chap. 2, M. N. Nabighian, ed. Tulsa: *Society of Exploration Geophysicists*.

Kreyszig, E., 1988, *Advanced engineering mathematics*, 6th edn.: John Wiley & Sons, NY.

Lajoie, J. J., and West, G. F., 1976, The electromagnetic response of a conductive inhomogeneity in a layered earth: *Geophysics*, v. 41, p. 1133-1156.

Lamontagne, Y. L., 1975, Application of wideband, time-domain EM measurements in mineral exploration: *Ph.D. thesis, Univ. of Toronto*.

Lebel, A., 1987, Geophysical tests at Cadjebut 1987 (surface and downhole SIROTEM and IP): BHP Minerals International Exploration Dept..

Lorrain, P., and Corson, D. R., 1990, *Electromagnetism: Principles and applications*, 2nd edn, Freeman.

Macnae, J. C., Lamontagne, Y., and McGowan, P. D., 1991, UTEM case histories: Appendix E of 'Time domain electromagnetic prospecting methods', by M. N. Nabighian and J. C. Macnae, in Nabighian, M. N., Ed., *Electromagnetic methods in applied geophysics, 02: Society of Exploration Geophysicists*, p. 497-506.

McNeill, J. D., Edwards, R. N., and Levy, G. M., 1984, Approximate calculations of the transient electromagnetic response from buried conductors in a conductivity half-space: *Geophysics*, v. 49, p. 918-924.

Nabighian, M. N., 1979, Quasi - static transient response of a conducting half-space - An approximate representation: *Geophysics*, v. 44, p. 1700 - 1705.

REFERENCES.

Nabighian, M. N., and Macnae, J. C., 1991, Time domain electromagnetic prospecting methods, in Nabighian, M. N., Ed., *Electromagnetic methods in applied geophysics, 02: Society of Exploration Geophysicists*, p. 427-520

Nabighian, M. N., Oppliger, G. L., Edwards, R. N., Lo, B. B. H., and Chessman, S. J., 1984, Cross-hole magnetometric resistivity: *Geophysics, Society of Exploration Geophysicists*, v. 49, p. 1313-1326.

Newman, G. A., Anderson, W. L., and Hohmann, G. W., 1989, Effect of conductive host rock on borehole transient electromagnetic responses: *Geophysics, Society of Exploration Geophysicists*, v. 54, p. 598-608.

Newman, G. A., and Hohmann, G. W., 1988, Transient electromagnetic modelling of high-contrast prisms in a layered earth: *Geophysics*, v. 53, p. 29-42.

Oristaglio, M. L., 1982, Diffusion of electromagnetic fields into the earth from a line source of current: *Geophysics*, v. 47, p. 1585-1592.

Oristaglio, M. L., and Hohmann, G. W., 1984, Diffusion of electromagnetic fields in a two-dimensional earth: A finite-difference approach: *Geophysics*, v. 49, p. 870-894.

Palacky, G. J. 1988. Resistivity characteristics of geologic targets. In *electromagnetic Methods in Applied Geophysics*, vol. 1, chap. 3, M. N. Nabighian, ed. Tulsa: *Society of Exploration Geophysicists*.

Raiche, A. P., Sugeng, F., and Xiong, Z., 1997, Documentation for Program LEROI [computer software], ver. 5.0. Australia: Mathematical Geophysics Group, CRC AMET, Macquarie University. Released for sponsors of AMIRA project P223C.

Raiche, A. P., Sugeng, F., and Xiong, Z., 1998a, Documentation for Program MARCO [computer software], ver. 2.3P. Australia: Mathematical Geophysics Group, CRC AMET, Macquarie University. Released for sponsors of AMIRA project P223C

Raiche, A., Sugeng F., and Xiong, Z., 1998b, P223 software manual: Description and Use of P223C Software with P223D Updates - prepared for AMIRA project P223D & part 2 of P223C final report.

Reid, J. E., and Macnae, J. C., 1998, Comments on the electromagnetic "smoke ring" concept: *Geophysics*, v. 63, p. 1908-1913.

San Filippo, W. A., Eaton, P. A., and Hohmann, G. W., 1985, The effect of a conductive half-space on the transient electromagnetic response of a three-dimensional body: *Geophysics, Society of Exploration Geophysicists*, v. 50, p. 1144-1162.

Scott R. L., Whiting T. H., and Turner, R., 1994. Role of Geophysics in exploration for MVT lead-zinc deposits on the Leonard Shelf, Western Australia. In Dentith M.C., Frankcombe K.F., Ho S.E., Shepard J.M., Groves D.I., & Trench A. (eds), Geophysical signatures of Western Australian Minerals Deposits. Geology and Geophysics Department (Key Centre) & UWA Extension, *The University of Western Australia, Publication 26, and Australian Society of Exploration Geophysicists, Special Publication 7*, p. 3-27.

Seely, S., and Poularikas, A. D., 1979, Electromagnetics: classical and modern theory and applications: M. Dekker, New York.

Silic, J., 1989, Interpretation of TDEM data using first and second spatial derivatives and time decay analysis: *Exploration Geophysics*, v. 20, p. 57-64.

Silic, J. Y., Eadie, E. T., and Jack, D. J., 1985, Application of time-domain

REFERENCES

electromagnetic methods in the discovery of the Hellyer ore deposit, Tasmania, Australia, *55th Ann. Internat. Mtg: Society of Exploration Geophysicists, Session:MIN2.1*.

Silic, J., and Eadie, E. T., 1989, Downhole EM: The Que-Hellyer Volcanics Experience: *7th Geophysical Conference, Australian Society of Exploration Geophysicists*, v. 20, p. 65-69.

Staltari, G., 1986, The Que River TEM case-study: *Exploration Geophysics*, v. 17, p. 125-128.

Stratton, J. A., 1941, *Electromagnetic Theory*: McGraw-Hill Book Co.

Strauss, W. A., 1992, *Partial Differential Equations - An Introduction*: Wiley, New York.

Swift, C. M. 1988. Fundamentals of electromagnetic theory. In *Electromagnetic Methods in Applied Geophysics*, vol. 1, chap. 1, M. N. Nabighian, ed. Tulsa: Society of Exploration Geophysicists.

Telford, W. M., Geldart, L. P., Sheriff, R. E., and Key, D. A., 1990, *Applied Geophysics*, 2nd edn.: Cambridge Univ. Press.

Theodoridis, J.A., and Asten, M.W., 2001. Galvanic excitation of the Cadjebut Pb-Zn ore body: *Extended Abstracts of the ASEG 15th Geophysical Conference and Exhibition, 5-8 Aug. 2001, Exploration Geophysics*, v. 32, p. 176-180.

Walker, P. W., and G. F. West, 1992, Parametric estimators for current excitation on a thin plate: *Geophysics*, v. 57, p. 766-773.

Ward, S. H., and Hohmann, G. W., 1988, Electromagnetic theory for geophysical applications. In *Electromagnetic Methods in Applied Geophysics*, vol. 1, chap. 4,

M. N. Nabighian, ed. Tulsa: *Society of Exploration Geophysicists*.

Weeks, W. L., 1964, *Electromagnetic Theory for Engineering Applications*: John Wiley.

West, G. F., and Edwards, R. N., 1985, A simple parametric model for the electromagnetic response of an anomalous body in a host medium: *Geophysics*, v. 50, p. 2542-2557.

West, G. F., and Macnae, J. C., 1991, Physics of the electromagnetic induction exploration method, in Nabighian, M. N., Ed., *Electromagnetic methods in applied geophysics, 02: Society of Exploration Geophysicists*, p. 5-45.

West, G. F., Macnae, J. C., and Lamontagne, Y., 1984, A time-domain electromagnetic system measuring the step response of the ground: *Geophysics*, v. 49, p. 1010.

Xiong, Z., 1992, Electromagnetic modeling of 3-D structures by the method of system iteration using integral equations: *Geophysics, Society of Exploration Geophysicists*, v. 57, p. 1556-1561.

Xiong, Z., and Tripp, A. C., 1995, A block iterative algorithm for 3-D electromagnetic modeling using integral equations with symmetrized substructures (short note): *Geophysics, Society of Exploration Geophysicists*, v. 60, p. 291-295.

Xu, S., 2001, *The boundary Element Method*, n. 9, geophysical monograph series. USA: *Society of Exploration Geophysicists*.

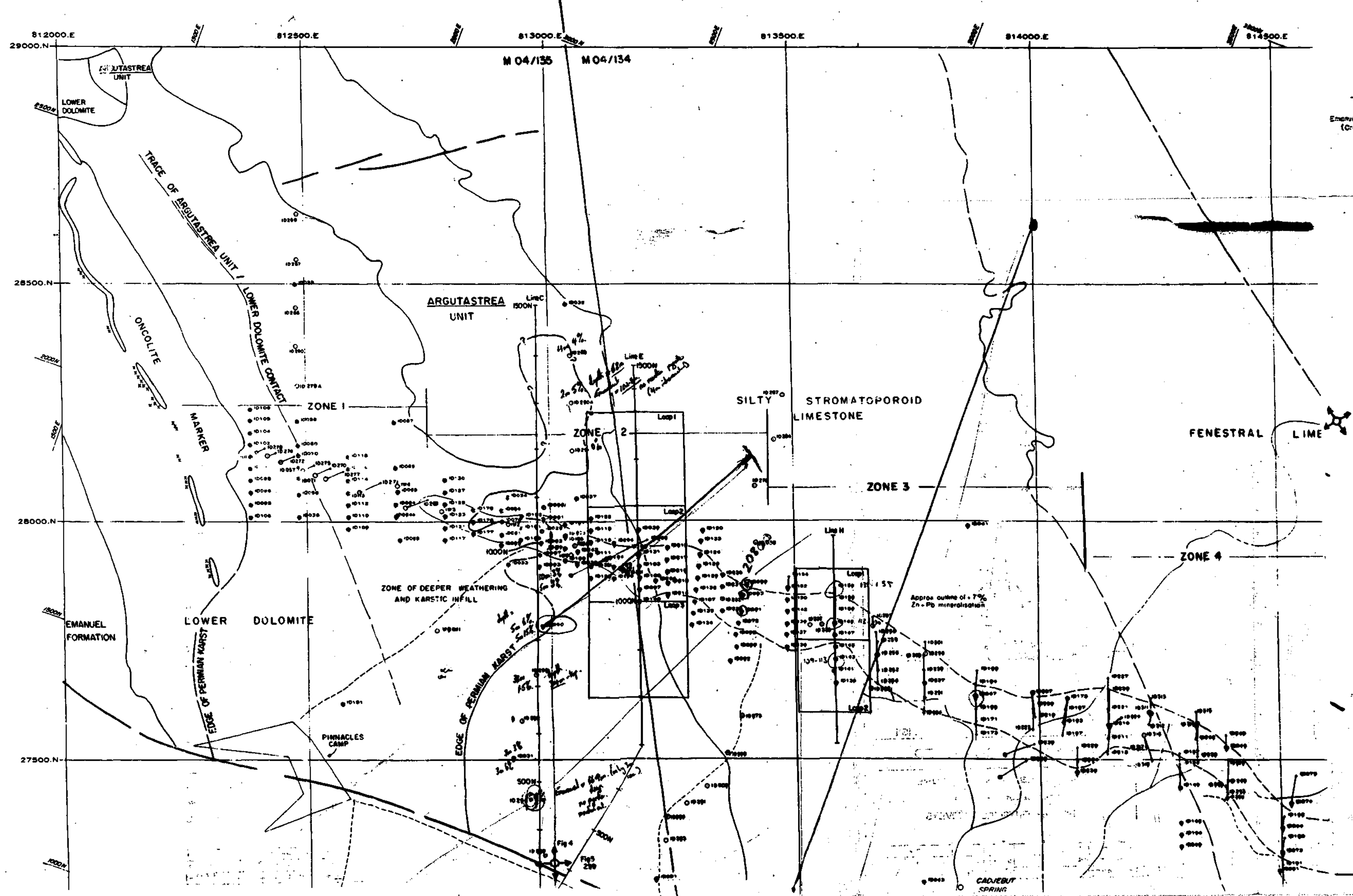
Zaky, A. A., and Hawley, R., 1974, *Fundamentals of Electromagnetic Field Theory*: Harrap.



PLATE I: CADJEBUT MINERALISATION (PLAN-VIEW).

- DOWNHOLE TEM SURVEY ELEMENTS:
 • BOREHOLE ID159;
 • LOOPS 1 & 2.
 COINCIDENT-LOOP SURVEY ELEMENTS:
 • LINE E (STN 300 TO STN 1450).

(AFTER LEVEL, 1987)



	cr	Vuggy Dolomite (0 metres thick)
Lower Dolomite	oo	
Dolomites and siltstones (DS)	oo	20 - 35 m thick
	oo	Dolomite Marker
	oo	mineralised zone - lens No. 1
	oo	Moat Spur Marker
	oo	mineralised zone - lens No. 2
Basal (arkasic) Siltstone	ud/ck	
Arkasic Siltstone (SL)	ud/ck	1-9 m thick
Emanuel Formation	ud	
Medular shale (NS)	ud	> 100 m thick

- LEGEND AND WORK DONE
- Hole collar
 - Trace
 - Hole number
 - Vertical hole and number
 - Water bore hole
 - Fault
 - Geological boundary
 - Geological boundary interpreted
 - Gossan
 - Joint Venture Boundary
 - + Hydrogeological waterbars
 - 27000, 440000 AMG coord
 - 30000, 45000 Mine Grid coord

Location of electrical soundings and TEM soundings. (Crossed directional pairs for VES: as described in separate memorandum.)
 Lines E and C: IP and TEM profiles
 Loops 1,2,3 (Line E): Large loop RVR profiles
 Loops 1,2 (Line H): Downhole logging of #143, #148, #159
 ID148 (Line H): Resistivity and IP log
 ID145, ID148 and ID159 (Line H): MMR logging

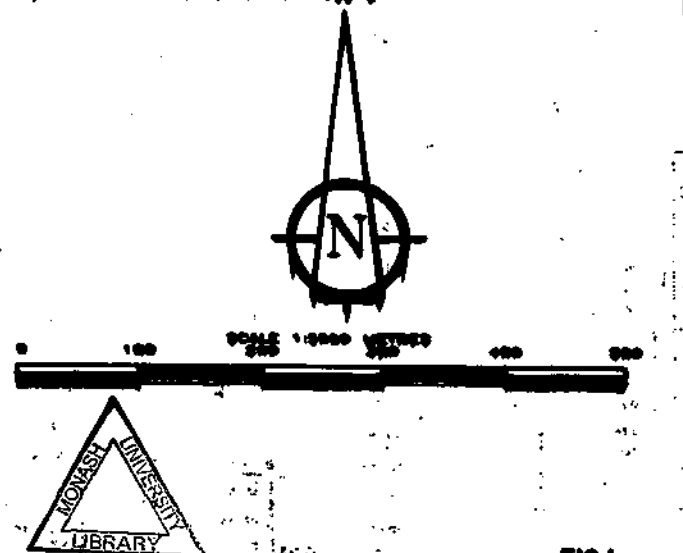


FIG.1

BHP MINERALS LTD.

PINNACLES JOINT VENTURE

CADJEBUT PROSPECT

1987 GEOPHYSICAL SURVEYS

DATE OF THIS 2	NOV 20-1987	BY: [signature]
DATE OF PREPARE	NOV 10	BY: [signature]
DATE OF PRINT	NOV 1987	BY: [signature]

John Theodoridis
Berehok Electromagnetic prospecting
for weak conductors. PhD 2000

PLATE II

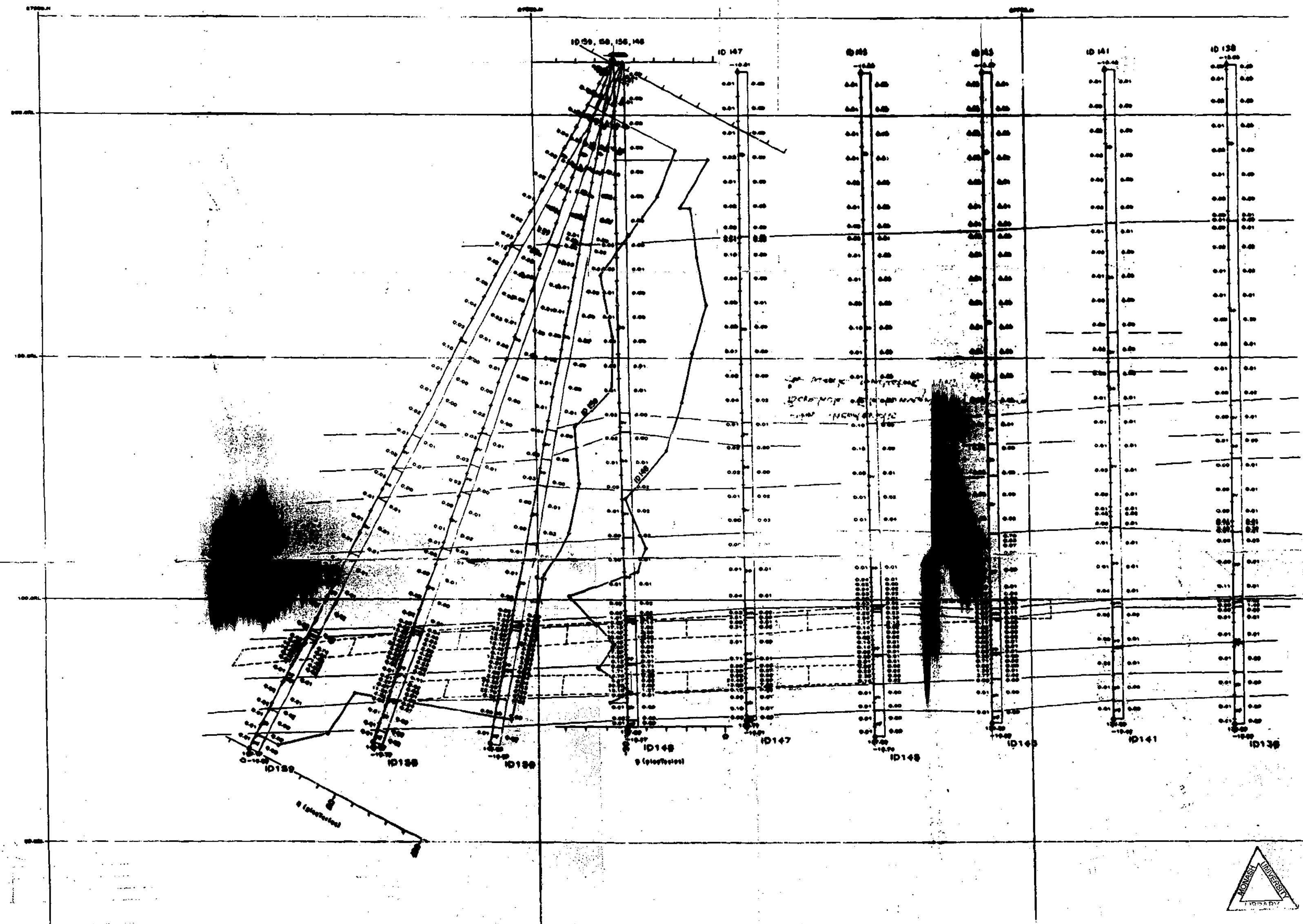


- BOREHOLE ID159;
- DELINEATED UPPER AND LOWER SLABS.

(AFTER LEBEL, 1987)

NORTH

LOOKING EAST



Stratigraphic Unit	Symbol	Notes
Permian till	ud	
Cyclic Limestone	cy	
Fenestral Limestone	fl	
Silty Stromatopora Limestone	sl	
Arctostichus Unit	cc	
Lower Dolomite	oo	
Goset (arctic) siltstone	us	
Emanuel Formation	ud	

Marker	Symbol	Notes
Vughy Dolomite	oo	
Dolomite Marker	oo	
mineralised zone - No. 1 Lens	oo	
Hard Soap Marker	oo	
mineralised zone - No. 2 Lens	oo	

Parameter	Symbol	Notes
Well Number	ID 145	
Distance east of section	2-00	
Well collar	ud	
Total depth	70-00	
Distance west of section	-0-15	

Picture Legend

Borehole collar marked by "o"

Borehole collar marked with HOLE NAME

Borehole collar marked with HOLE LENGTH

Borehole trace marked by "o"

Borehole trace marked with HOLE LENGTH

Borehole trace marked with DISTANCE TO SECTION

Borehole depth marked with HOLE LENGTH

Borehole depth marked with DISTANCE TO SECTION

Borehole depth marked with HOLE NAME

Borehole depth marked with HOLE LENGTH

Borehole depth marked with DISTANCE TO SECTION

Scale: 1:1000 METERS

PLATE 3

BHP MINERALS LTD

CADJEBUT, W.A.

LEG 5000 2

BORHOLES ID 148 AND 149

DOWNHOLE NMR PROFILES

(downhole transmitter)

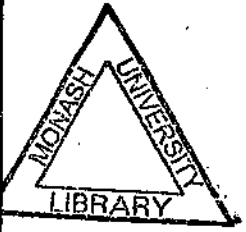
DATE OF SURV	NO. OF SURV	COMP
1987	48	AI-SSOR



John Theodoridis

PLATE III

Borehole electromagnetic prospecting
for weak conductors PhD 2004



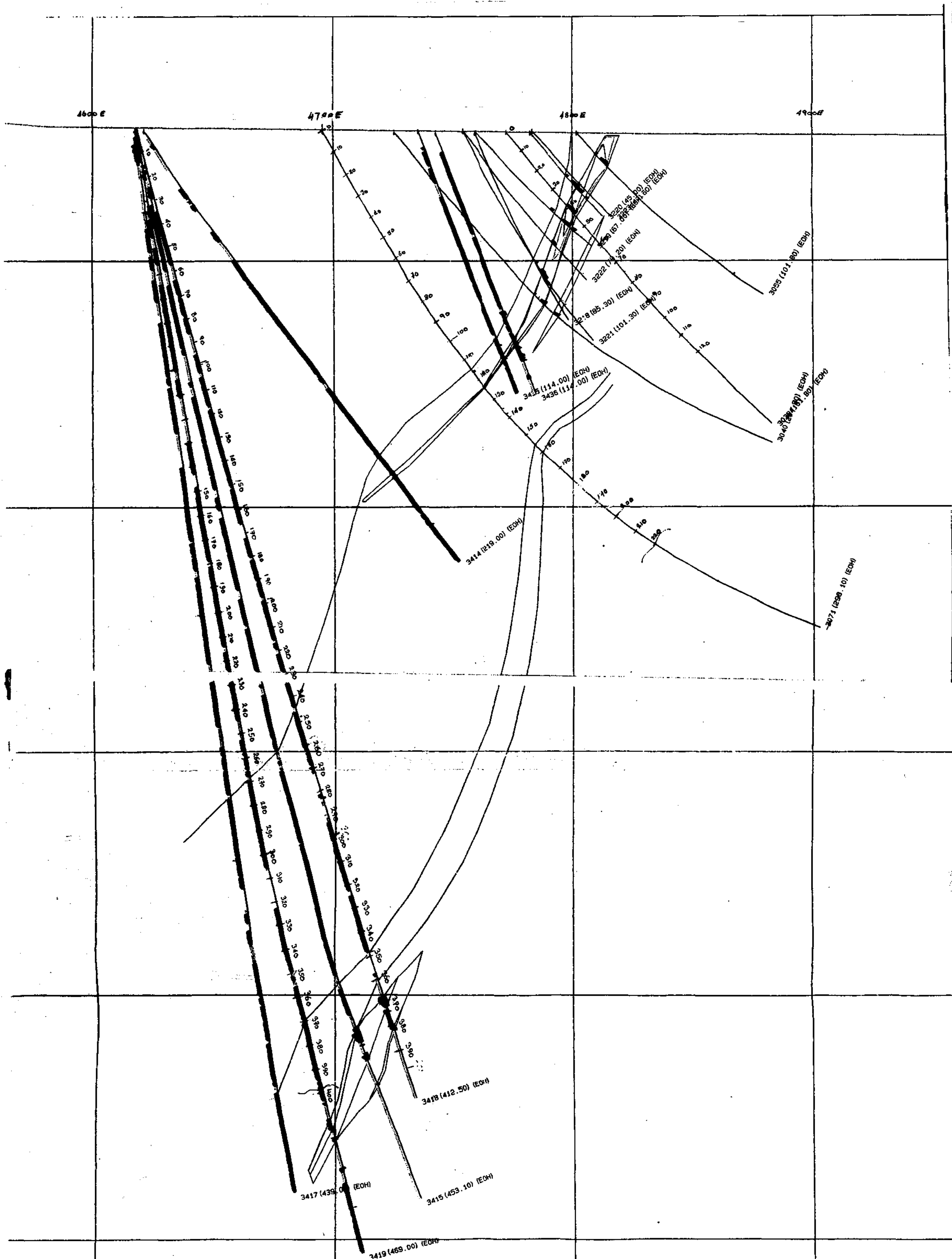


PLATE III: FLYING DOCTOR DEPOSIT (CROSS-SECTION).
 DOWNHOLE TEM SURVEY ELEMENTS:
 • BOREHOLES ID3039 & ID3071 - UPPER LENS;
 • BOREHOLES ID3418 & ID3419 - LOWER LENS.



(NOEL CARROLL - PASMINGO: PERSONAL COMMUNICATION, 2000)